Designing periodic and aperiodic structures for nanophotonic devices

Imanol Andonegui Artegui

Supervisors:
Prof. Angel J. Garcia-Adeva
Prof. Estibaliz Apiñaniz

Department of Applied Physics I

University of the Basque Country

This dissertation is submitted for the degree of

Doctor of Philosophy

April 2019

I would like to dedicate this thesis to my loving parents and to Itzi.

Declaration

I hereby declare that except where specific reference is made to the work of others, the contents of this dissertation are original and have not been submitted in whole or in part for consideration for any other degree or qualification in this, or any other University. This dissertation is the result of my own work and includes nothing which is the outcome of work done in collaboration, except where specifically indicated in the text.

Imanol Andonegui Artegui
April 2019

Acknowledgements

This thesis would have been impossible without the contribution of many colleagues and friends. First of all, I would like to acknowledge my advisors, Prof. Angel J. Garcia-Adeva and Prof. Estibaliz Apiñaniz Fernandez de Larrinoa. When I decided to start my PhD at the department of applied physics I met Angel for the first time. In our first meeting, his great energy and enthusiasm to do exciting research impacted me. I feel fortunate to be his first student and going working with him has been the most valuable experience that I gained in my PhD. I had access to Angel and Esti whenever I needed to discuss my problems, and their insights led to the success of my PhD work. I also want to thank all of my friends in the physics group: Adrian (" a PhD candidate never gets out of the lab until dusk" :)), Naiara, Sara, Raquel, Macarena and Itziar for their help, company and the entertaining discussions that we had about everything in general.

Probably the most significant part of my thesis has taken place in CUDOS laboratories at the University of Sydney. When I look back and recall memories of that time I promise myself that someday I will go back to this place where I had so many good times. That is why I would like to acknowledge Prof. Benjamin Eggleton, director of CUDOS who gave me the opportunity to form part of this excellent research group. Besides, I would like to express my sincere gratitude to my tutor in CUDOS, Prof. Andrea Blanco, for the continuous support of my Ph.D study and research, for her patience, motivation, enthusiasm, for the many good times we had. Very special thanks to my friends Alberto, Darren, Birgit, Alessio and Neetesh among many others. They made me feel at home from the very first day. Sincerely, thanks for all those times full of laughs and good times, not to forget that we established the climbing and running days. I had the privilege to learn a lot of things from Alberto, from his scientific knowledge up to climbling! we had really good times and I hope we can meet again soon.

I must express my very profound gratitude to my parents and my family for providing me with unfailing support and continuous encouragement throughout my years of study and through the process of researching and writing this thesis. This accomplishment would not have been possible without them. Thank you.

Last but not least, I would like to thank my Itzi for her support, she has been always proud of my every little success. Finally, I am deeply grateful to her for the love, care and

all the sacrifice she made during the time it took to me to finish this thesis. Her thrust on my decisions and her belief that I will be successful whatever I do was the most powerful force that has pushed me forward in any difficulty that I faced in my research and to reach my goals.

Thanks to all of you who have made me the person I am today, there is a piece of you in this thesis.

Contents

List of Figures

List of Tables

Introduction

The unstoppable miniaturization of electronic components over the last decades brought us the idea of micro-electronics, where transistors feature just a few microns, but the size shrinking trend of those transistors together with the advent of transistor grid lengths of just a few nanometers rapidly unveiled the so called nano-electronic technology. Furthermore, according to the prediction of Moore's law, the length of these transistor grids should be reduced by a factor of two every 18 months. Noticeably there does not exist a Moore's law for nanophotonic or optoelectronic components, which limit is usually naively imagined as featuring the size of wavelength. All in all, the incoming all optical networks and nanotechnology demand for a new scale of integration capable of dealing with light in a natural way. Current fiber networks require an electronic switching in order to commute the information that travels along optical links. In the absence of these components, the optical speed shrinks to electronic speeds of a few gigabytes per second. Therefore, in order to keep optical speeds and bandwidths in future telecommunication networks, it is mandatory to avoid electronic conversion of signals throughout the transmission path. Besides, all–optical networks will require to substitute the present electronic integrated circuitry by optical analogous devices that satisfy the compactness, throughput, latency and high transmission efficiency requirements in nanometer scale dimensions, outperforming the functionality of current networks. Moreover, future optical devices must be fabricated in a material system that is compatible with the existing integrated electronic manufacturing infrastructure. On the one hand, dielectric materials have resulted in successful architectures where a high bandwidth requirements can be satisfied even for long haul optical interconnections. However, far beyond the macroscopic optical device engineering, chip-level optical systems magnitude shrinks rapidly with every new integration of chip-manufacturing technology. Thereby, existing dielectric materials do not confine light in a sufficiently small scale and so the physical size of these links and devices becomes unacceptable. In fact, if the optical chip does not exist in the liking of the electronic chip, photonic crystals have recently led to great hopes for a large-scale integration of optoelectronic components. Accordingly, the first chapter of this thesis is devoted to introduce the reader into the exciting research

field of photonic crystals. To start with, we present these materials by considering the analogies between the study of electrons and photons in periodic media, followed by a short summary comprising some of the most meaningful milestones regarding to this research field. Subsequently, we detail the essential geometrical considerations corresponding to the two-dimensional lattices. Indeed, two-dimensional photonic crystals, and in particular two-dimensional photonic crystal slabs obtained through periodic structuring of a planar optical waveguide, feature many characteristics which bring them closer to electronic micro- and nanostructures. Moreover, when the overall periodicity of the lattice is suitably broken a new world of physical properties ranges for further controlling the flow of light within these complex materials. Though, exploring the light matter interaction within this complex inhomogeneous media requires to address a numerical method capable of successfully simulating the electromagnetic wave propagation subject to these boundary conditions of these materials. Chapter 2 is dedicated to grasp the theoretical background regarding to the set of computational methods that are used throughout this thesis to obtain novel photonic crystal structures. Calculating the unique physical properties resulting from the interaction between light and a complex media is often a tedious task unless one resorts to a rigorous analitical simulation tool to carry out numerical simulations. Among the vast set of tools that have been developed so far to deal with these complex media, we found that there are at least three computational tools that yield to excellent and reliable predictions of the propagation of light in PCs, namely the finite element method (FEM), the plane wave expansion method (PWEM) and the finite difference time domain (FDTD) method.

Subsequently, Chapter 3, is devoted to make a critical assessment of the finite element (FE) method for studying two-dimensional dielectric photonic crystals. Photonic band structures, transmission coefficients, and quality factors of various two-dimensional, periodic and aperiodic, dielectric photonic crystals are calculated by using the FE (real-space) method and the plane wave expansion or the finite difference time domain (FDTD) methods and a comparison is established between those results. It is found that, contrarily to popular belief, the FE method (FEM) not only reproduces extremely well the results obtained with the standard plane wave method with regards to the eigenvalue analysis (photonic band structure and density of states calculations) but it also allows to study very easily the time-harmonic propagation of electromagnetic fields in finite clusters of arbitrary complexity and, thus, to calculate their transmission coefficients in a simple way. Moreover, the advantages of using this real space method in the context of point defect cluster quality factor calculations are also stressed by comparing the results obtained with this method with those obtained with the FDTD one. As a result of this study, FEM comes out as an stable, robust, rigorous,

and reliable tool to study light propagation and confinement in both periodic and aperiodic dielectric photonic crystals and clusters.

Introducing defects into otherwise perfectly arranged dielectric patterns has proven to be a very handy way to create desired optical components, such as waveguides, light bends or micro-resonators, just to cite some. Admittedly, reality is more difficult than it appears, and designing efficient optical components requires to go one step beyond intuitive approaches, and thus, through this thesis we pose the photonic crystal design process as a NP-complete problem. Therein, the inherent complexity requires to address to non-convex combinatory optimization techniques. The subject of combinatorial optimization, which is i.e. the basis of any heuristic algorithm, is a long term discipline that has been extensively applied in computer science and engineering, specially during the las 10 years. Research in this area aims at developing efficient techniques for finding minimum or maximum values of a function of many independent variables comprising a NP or NP-complete problem. In Chapter 4 we openly approach the field of heuristic algorithms and to do so, we addressed to three different heuristic methods, namely the Fast Simulated Annealing (FSA), the Improved Harmoy Search method (IHS) and the Non Sorting Genetic Algorithm II (NSGA-II).

The algorithms introduced in Chapter 4 will serve to steam the inverse design strategy used through this thesis, and to unveil new nanophotonic structures that are listed in Chapter 5. More specifically, in Chapter 5 we report on the inverse design (ID) of ultra-wide bandwidth novel passive devices based on photonic crystal (PC) technology for efficiently performing the essential functionalities required by any future photonic integrated circuit (PIC). We utilize the heuristic and genetic optimization methods described in the previous chapter as a inverse design engine for achieving promising PC systems that outperform previous topologies devised on intuitive grounds. Ee combine the effectiveness of two alternative and well-proven optimization methods that will guide the inverse design process according to a certain pre-established criteria, with the flexibility and robustness of the FEM. With this proceeding we demonstrate that both algorithms suit perfectly to PC devising. PC topologies proposed throughout this chapter are constrained in order to fulfil the limitations imposed by lithographic manufacturing techniques. Therefore, these designs are not only interesting from a theoretical point of view but also of great practical importance, since they can be readily manufactured.

Having explored the capabilities of disrupting photonic crystal structures, we focused on one of the most critical bottlenecks of integrated nanophotonic and electrooptic devices, i.e. the inherent low efficiency of light coupling-decoupling systems. Nowadays, light conduits made of SOI waveguides are extensively used to guide light at micrometer scale in planar silicon integrated circuits and are also the last frontier between the PIC and an optical fibre.

Chapter 6 deals with the prospect of obtaining high integration photonic circuits provided with more effcient light coupling grating structures on these waveguides. This chapter starts with a brief introduction to SOI waveguides. Two typical optical waveguides are presented-strip and rib waveguides. Then, this unit describes the challenge of coupling light in and out of silicon photonic slab waveguides hereof, we review different coupling approaches and explore the physics behind the grating couplers. After, we use an FDTD method steamed by the ID methodology to design non-trivial coupling devices optimized to minimize insertion losses between optical fibres and integrated waveguides.

The final chapter of this thesis, Chapter 7, explores periodic arrangements from a new perspective and reports on the first experimental evidence of topologically protected waveguiding in silicon. Furthermore, we propose and demonstrate that, in a system where topological and trivial defect modes coexist, we can probe them independently. Tuning the configuration of the interface, we observe the transition between a single topological defect and a compound trivial defect state. These results provide a new paradigm for topologically protected waveguiding in a complementary metal-oxide-semiconductor compatible platform and highlight the novel concept of isolating topological and trivial defect modes in the same system that can have important implications in topological physics.

Hitzaurrea

Azken hamarkadetan osagarri elektronikoak jasandako miniaturizazio-joerak gaur egungo mikro-elektronikaren teknologia eraldatu du. Honela, mikra gutxitako transistoreen tamainak are gehiago txikitu dira eta transistore sareak nanometro gutxiko neurrira murriztean, nano-elektronikaren teknologiaren iraultza sustatu dute. Horrez gain, Moore-n legearen arabera, transistore sare hauen tamaina-murrizpenaren joera honek jarraitu egingo luke 18 hilabetero. Hala era, Moore-n legea elektronikaren arloan formulatu zen eta oraindik ez dago honelako aurresanik nanofotonikan edo osagarri optoelektronikoetan aplikatu daitekeena. Hala era, ingurune hauetan, osagarrien tamainaren muga fisikoa, erabilitako uhin luzeraren neurrikoa dela esaten da. Beste alde batetik, etorkizuneko sare guztiz-optikoak eta nanoteknologian oinarritutako gailuek integrazioko atalase-maila berri bat behar dute, argiaren bitartez igorritako informazioa ohiko era batean maneiatzea posible izan dadin. Gaur egungo zuntz optikoko sareek oraindik kommutazio elektronikoa erabiltzen dute informazioa garraiatzeko bide optikoen artean.

Osagarri optiko hauek garatzen diren bitartean, zuntz-optikoen bitartez transmititutako informazioaren abiadura optikoa, elektroien abiadurara mugatuta dago, eta komunikazioaren banda-zabalera gigabyte-segundu gutxitara mugatzen da. Zentzu berean, beraz, etorkizuneko telekomunikazio-sareen abiadura eta banda-zabalera optikoak areagotzeko, seinaleen transmisioa eremu elektronikotik izaera optikora aldatzeak eragiten duen abiadura eta banda-zabalera murrizketa ahal den heinean ekidin behar da. Gainera, sare guztiz optikoak gaur egun erabiltzen dituzten zirkuitu elektroniko trinkoak nanometroen eskalan gailu optikoz ordezkatu beharko dituzte, trinkotasun, eraginkortasun, latentzia eta transmisio tasa eskakizunak betetzeko. Horrez gain, etorkizuneko gailu optikoak osagarri elektronikoak fabrikatzeko erabiltzen diren teknikekin sortu beharko dira. Alde batetik, material dielektrikoak arkitektura arrakastatsuak eskaini ditu; banda-zabalera handiko interkonexio-optikoak eskuragarri jarri ditu. Hala ere, gailu optiko makroskopiko hauetatik kanpo, txip-optikoen eskalak nabarmenki behera egiten du osagarri trinkoen fabrikazio-teknologiek ematen dituzten aurrerapauso bakoitzarekin. Integrazio-muga batetik aurrera, ordea, ohiko material dielektrikoak ez dute argia behar bezala konfinatzen hain eskala txikietan eta beraz, muga fisiko bat zeharkatu

beharko da nolabait. Izan ere, zirkuitu elektronikoen pareko txip-fotoniko hori bermatzen ez den artean, kristal fotonikoa integrazio opto-elektroniko bat ahalbidetu dezakeen teknologia izan daitekeela dirudi.

Horrenbestez, tesi honen lehen kapituluan zehar irakurleak kristal fotonikoen ikerketa-eremuko lehen urratsak aurkituko ditu. Material hauen berezitasunak aurkezteko, ingurune periodikoetan elektroien eta fotoien azterketaren antzekotasunak bereizten dira eta jarraian, ikerketa-eremu honetan jaso diren mugarri aipagarrienak deskribatzen dira. Geroago, bi-dimentsioko sareetan kontuan hartu beharreko hausnarketa geometrikoen xehetasunak eskaintzen dira. Izan ere, bi-dimentsioko kristal fotonikoak, eta, batez ere, bi-dimentsiotako kristal fotonikozko xaflak (2D PC *slab*), uhin-gida lau baten sare periodiko bat antolatuz sortutakoak, mikro eta nano uhin-gida bereziak sortzeko ezaugarri asko biltzen dituzte. Gainera, sarearen maiztasuna era egokian apurtzen denean, propietate berri ugari agertarazten dira. Maiztasun hori gordetzen ez dituzten material konplexu horiek, argiaren hedapena are gehiago kontrolatzeko ahalmena eskaintzen dute. Material inhomogeneo konplexu horietan argi-materiaren interakzioa aztertzeko, muga-baldintza berezien barruan hedatzen diren uhin elektromagnetikoak simulatzeko gai diren metodo numerikoak behar dira. Horregatik, 2. kapituluan, kristal fotonikozko egitura berriak lortzeko erabiliko diren metodo konputazionalen oinarri teorikoak biltzen dira. Ingurune konplexu baten eta argiaren arteko interakzioan ematen diren propietate fisiko bereziak kalkulatzeko eta simulazio numerikoak lortzeko metodo numeriko zehatzak erabiltzea beharrezkoa bait da. Material horien propietateen inguruko hausnarketa bat egiteko, gaur egun eskuragarri dauden metodo numerikoen artean, hiru tresna konputazional aukeratu ditugu, kristal fotonikoetan zehar argiak deskribatzen duen hedapena era zorrotz eta zehatz batean deskribatzeko gai direnak: elementu finituen metodoa (FEM), *plane wave expansion* metodoa (PWEM) eta denbora-domeinuko diferentzia finitoen metodoa (FDTD) erabili ditugu, hurrenez hurren. 3. kapituluan, bi-dimentsioko kristal fotonikoen ezaugarriak antzemateko, elementu finituen (FE) metodoak dituen gaitasunen azterketa kritiko bat egiten da. FE (espazio-errealean), *plane wave expansion* nahiz denbora-domeinuko diferentzia finitoen metodoak erabilita, banda fotonikoen egiturak, transmisio-koefizienteak eta kalitate-faktoreak kalkulatzen dira bi-dimentsioko hainbat egitura periodiko eta aperiodikoentzako. Horrez gain, metodo horiek eskaintzen dituzten emaitzen konparaketa bat egiten da.

Orain arte uste zenaren aurka, FE metodoak, horrelako egiturek dituzten ezaugarri bereziak era bizkorrean eta fidagarrian kalkulatu ditzake. Horretaz gain, FE metodoaren bitartez, konplexutasun arbitrarioa duten kluster finituetan eremu elektromagnetikoen denbora-harmonikoen hedapena aztertzea posiblea da eta beraz, transmisio koefizienteak eskuratu daitezke era erraz eta bizkor batean. Beste alde batetik, akats-puntu bat duten klusterren

kalitate-faktoreen kalkulua burutzeko espazio errealeko metodo bat erabiltzearen abantailak ere aipatzen dira. Horretarako FDTD teknikarekin lortutako emaitzekin konparaketa bat egin dugu. Ikerketa-emaitza horietatik, FE kristal fotoniko dielektrikoko kluster periodiko nahiz aperiodikoen argiaren lokalizazioa aztertzeko metodo egonkorra, sendoa, zorrotza eta fidagarria dela ondorioztatu dugu.

Sare periodikoetan akatsak sortuz, osagarri optiko berriak sortu daitezke, esaterako uhin-gidak, mikro-erresonadoreak eta kurbadura handiak dituzten uhin-gidak. Errealitatean ordea, era horretan osagarri optiko eraginkorrak sortzea eginkizun zaila da eta horrelako diseinuak sortzeko, intuizio soilaren bidez lortzen diren diseinuak baino askoz diseinu hobeagoak ahalbidetzen dituen metodo bat proposatzen da tesi honetan. Horretarako, kristal fotonikoen diseinu prozesua problema ez-polinomiko oso (NP-complete) bat bezala planteatzen da. Horrelako problemei dagokien konplexutasun mailak beharrezkoa egiten du optimizazio teknika ez-konbexu konbinatorioak erabiltzea. Optimizazio konbinatorioa, berez, edozein algoritmo heuristikoen oinarria, asko erabili da zientzia eta ingeniaritzako hainbat esparrutan, bereziki, azken hamarkada honetan. Esparru horretako ikerketak aldagai ugari dituzten NP edo NP-problemetan funtzio baten minimo nahiz maximo globalak era bizkor baten aurkitzean oinarritzen dira.

4. kapituluan mota horretako algoritmoetan murgiltzen gara eta bereziki hiru algoritmo aztertzen dira: *Fast Simulated Annealing* (FSA), *Improved Harmoy Search* metodoa (IHS) eta *Non Sorting Genetic Algorithm II* (NSGA-II) helburu-anitzetako algoritmo genetikoa. 4. kapituluan deskribatutako algoritmoak alderantzizko diseinua (ID) deritzogun metodologiaren bitartez nano-egitura fotoniko berriak aurkitzeko erabiliko dira. Bereziki, 5. kapituluan, ID metodologia erabiliz banda-zabalera handia duten kristal fotonikozko dispositibo pasibo berriak aurkezten dira. Hain zuzen ere, kapitulu horretan, zirkuitu integratu fotonikoetan behar-beharrezkoak diren funtzioak betetzeko gai diren egitura ugari diseinatu dira. Horretarako, ID metodoa aldez aurretik definitutako irizpide baten eta FE metodoaren fidagarritasunean eta malgutasunean oinarrituz eta bi optimizazio metodo alternatiboz baliatu gara. Gainera, bertan proposatutako topologiak litografia prozesu baten bidez fabrikatzea posible izan dadin, egituretan muga bereziak ezarri dira. Horren arabera, egitura horiek ez dira soilik esparru teorikoan aztertu daitezkeen ereduak, baizik eta izaera guztiz praktikoa izan dezaketenak, fabrikazio-prozesu batean gauzatu daitezkeelako. Kristal fotonikoen abantailak aztertu ostean, gailu opto-elektronikoak duten eragozpen handiena aztertu dugu: bi ingurune horien arteko argi-akoplamendu sistemen eraginkortasun eza.

Gaur egun, *silicon-on-insulator* (SOI) teknologian egindako uhin-gida optikoak erabiltzen dira, mikrometroko eskalan, siliziozko zirkuitu integratuetan zehar argia garraiatzeko, eta PIC eta zuntz-optiko baten arteko azken muga dira. 6. kapitulua zirkuitu fotonikoetan

argi-akoplamendu eraginkor bat lor dezaketen *grating* egitura berrietan ardazten da. Kapitulu honetan, hasteko, SOI uhin-gidak deskribatzen dira, *strip* eta *rib* uhin-gida motak bereiztuz. Geroago, SOI uhin-giden eta zuntz optikoen bitarteko akoplamendua lortzeko ezagutzen diren metodoak zehazten dira eta grating akopladoreak erabiltzen duten printzipio fisikoa azaltzen da. Azkenik, FDTD metodo ID metodologiarekin batera erabiltzen da akoplamendu eraginkorra sortu dezaketen grating sistema ez-tribialak diseinatzeko.

Tesi honen azkenengo kapituluak, 7. kapituluak, egitura periodikoak beste ikuspegi batetik aztertzen ditu eta bertan silizioan egindako topologikoki babestuta dagoen lehenengo gidapenaren frogapen esperimentala aurkezten da. Gainera, kapitulu honetan akats topologikoa eta akats tribiala aurkitzen diren sistema batean, bi akatsak bereiztu daitezkeela frogatu dugu. Horretaz gain, sistema horren konfigurazioa aldatuz gero, modu topologikoaren eta modu topologiko eta tribialaren arteko nahasketa lortzeko trantsizioa aurkitu dugu. Emaitza hauek gidaketa topologikoaren paradigma berria zabaltzen dute, alde batetik, *complementary metal-oxide-semiconductor* (CMOS) plataformarekin guztiz bateragarria bait da eta bestetik, modu topologikoak eta tribialak sistema berean isolatzea posiblea izateak fisika topologikoan inplikazio berriak izan ditzakelako.

Kapitulua 1

Band Gap Fotonikoa duten materialak eta Kristal Fotonikoak

Lehenengo kapitulu honetan, irakurleak kristal fotonikoaren ikerketa arloari buruzko oinarriak aurkituko ditu. Egitura periodikoen materialen ikerketak interes haundia sustatzen dutenez, gai honen inguruko argitalpen kopurua oso ugaria da eta beraz, kapitulu honetan soilik kristal fotonikoen ezaugarri nagusiak aztertuko ditugu. Kapitulu honetan, lehenengo eta behin, izaera periodikoa duten materialak zeharkatzen dituzten elektroien eta fotoien arteko analogiak deskribatzen dira. Gero, ikerketa hildo honen inguruan, horain arte emon diren aurrepauso garrantzitsuen kronologia aurkitzen da, eta azkenik, bi-dimentsioko sare periodikoen oinarrizko kontsiderazio geometrikoak azaltzen dira.

1.1 Band gap fotonikoa duten materialak eta kristal fotonikoak: Elektroien eta fotoien arteko analogia egitura periodikoetan

Solido kristalinoen barneko elektroien dinamika hausnartzeko, egoera solidoaren fisikaren edota fisika kuantikoaren oinarri teorikoetara jo beharra dago. Bereziki, material horietan zehar elektroien higidura deskribatzeko, eredu sinplifikatuak erabiltzen dira. Orokorrean, elektroien dinamika aztertzeko, periodikoki tartekatutako atomo-kate infinituetan murgilduta-ko elektroiak erabiltzen direnean, material horien modelo teoriko bat moldatzen da. Ohikoa den sinplifikazio hau onetziz, kate egituraren egoera-elektronikoaren konputazioa errez burutu daiteke, alegia, atomo-kate infinituen eredua potentzial periodikoak erabiliz adierazten bada. Sistema horren maiztasuna eta traslazio simetria, a sare-parametroaren bidez deskribatzen da.

Traslazio-simetria, Schrödingerren formularekin konbinatuz gero, solidoen ezaugarri fisiko bereizgarriak aztertu daitezke. Honelako simetria duten egituretan, egoera aproposak ematen badira, energia-tarte debekatuak zabaltzen dira, horietan, elektroien agerpena inhibituta edo debekatuta dago. Ezaugarri hau erakusten duten materialei *Electronic Band-Gap* (EBG) materialak deritzegu. Hain zuzen ere, hauxe da aleazio semi-eroaleen propietaterik bereizgarriena: energi-tarte debekatua edukitzea. Honen bitartez, ezinbestekoa den elektroien hedapenaren kontrola izan dezakegu GaAlAs, InGaAs ed InAlAs bezalako sintesietan. Berezitasun hau ez da soilik elektroien inguruan jasotzen, periodikoki antolatutako material dielektrikoek antzeko propietatea adierazten dute, baina kasu honetan fotoien energia-tarteetan agertzen dira *gap* hauek. Material hauetan, uhin ekuazioak aztertuz gero, elektroiek eta fotoiek osatzen duten sistemen arteko analogia ugari aurkitu daitezke. Hartu dezagun hasteko Schrödingerren ekuazioa. Schrödingerren ekuazioa, $V(\vec{r})$ potentzial putzu-kate periodiko baten barne dagoen elektroiarentzat honela adierazi daiteteke

$$\left[-\frac{h^2}{8\pi^2 m}\nabla^2 + V(\vec{r})\right]\Psi(\vec{r}) = E\Psi(\vec{r}). \tag{1.1}$$

Bertan, ∇^2, h, Ψ, m eta E, Laplace-ren operadorea, Planck-en konstantea, uhin funtzioa, partikularen masa efektiboa eta energia totala dira, hurrenez hurren [1, 2]. Irispide teoriko bera erabili daiteke, elektroien ordez fotoiak ordezkatuz, dielektriko ezberdinez tartekatutako sistema periodiko baten uhin harmonikoaren ekuazioa ebazteko. Izan ere, Schrödingerren ekuazioaren berformulazio honek EBG materialen guztiz parekoa den sistema optikoa agertarazten du. Horretarako, egitura hauek ez magnetikoak direla kontuan hartuz, eta Maxwell-en ekuazioetan aldaketa gutxi batzuk eginez, hurrengo autobalio-kuazioa lortzen da

$$\left[\nabla \times \frac{1}{\varepsilon(\vec{r})}\nabla \times\right]\vec{H}(\vec{r}) = \left(\frac{\omega}{c}\right)^2 \vec{H}(\vec{r}), \tag{1.2}$$

$\vec{H}(\vec{r})$ eremu magnetikoarentzat $\varepsilon(\vec{r})$ permitibitatea duen profil dielektriko periodikoa zeharkatzen duenean. Bereziki azpimarragarriak dira (1.1) ekuazioaren eta (1.2) ekuazioaren arteko berdintasunak. Bi ekuazio hauek egitura periodiko baten antolatutako material bat zeharkatzen duen uhin funtzio bat adierazten dute eta beraz, edozein kasuan ebazpenean Bloch uhinak agertuko dira. (1.1) ekuazioak, Ψ probabilitate-funtzioa kalkulatzen du $V(\vec{r}) = V(\vec{r}+\vec{a})$ formako potentzial periodikoetan, non a lehen aipatutako sare-parametroa da. (1.2) ekuazioa ordea, $\varepsilon(\vec{r}) = \varepsilon(\vec{r}+\vec{a})$ permitibitatea duen egitura dielektriko periodikoa aztertzeko erabili daiteke.

Funtzio periodiko hauek bigarren ordeneko espazio-diferentzial operadore bat dute barnean, Hamiltonianoa eta Maxwellen operadorea, hurrenez hurren. Gainera, bi operadore hauek azpiespazio Hermitikoak osatzen dituzte [3].

Ekuazio honen ebazpenetik kalkulatu daitezkeen autobalio errealak elektroiaren energia, E, eta uhin elektromagnetikoaren frekuentziaren karratua, ω^2, dira, hurrenez hurren. Bi kasuetan, hedatutako uhinen superposizio koherenteak, elektroi eta fotoien deuseztapena deskribatzen dituzten autobalioak jaso daitezke. Egitura periodiko bat zeharkatuko duen fotoiaren kasu partikularrean (demagun orduan egituraren sare-parametroa fotoiaren uhin-luzeeraren parekoa dela) material honen errefrakzio-indizea periodikoki antolatuta egon ezkero eta errefrakzio indize honen aldakuntza nabaria bada, orduan, Bragg baldintzaren inguruan hedapen ezaugarri bitxiak aurkeztuko ditu fotoi honek. Konkretuki, aurreko kasuan, elektroiarentzat potentzial putzu periodikoen ondorioz sortutako energia debekatuen tarteen pareko tarteak sortuaraziko ditu honek, baina, kasu honetan debekaturiko fotoien energia buruz hitz egingo genuke.

Badira ere bi diferentzia nagusi mekanika kuantikoaren eta elektromagnetismo klasikoaren formulazio hauen artean. Alde batetik, (1.2) ekuazioko eremu elektrikoaren ekuazioa ebazteko guztiz bektorialak diren ebazpenak lortu behar dira, aldiz, Schrödingerren ekuazioaren soluzioak eskalarrak dira [1]. Beste alde batetik, Maxwell-en ekuazioetan ez dago neurri-eskala karakteristikorik, aldagai guztiak modu berean eskalatzen bait dira ekuazio horretan, baina, Schrödingerren ekuazioan konstante-fisikoek, Planck-en konstanteak edota elektroiaren masak esaterako, ekuazioaren aldagaien eskala finkatzen dute [3].

1.2 Kristal Fotonikoak

Kristal fotonikoek interes handia sustatu dute azken hamarkadan, fotoien garraioa kontrolatzeko aukera eskeintzen duten materialak bait dira [4–7]. Definizioz, kristal fotonikoak bi material edo gehiagoz osaturiko egitura inhomogeneo periodikoak dira eta osagai hauen konstante dielektrikoen artean diferentzia nabaria izaten da. Bereziki, konstante dielektriko (ε) periodikoaren aldakuntza dimentsio bakar batean gertatzen bada, honelako egiturei 1D PC deritzogu. Era berean, 2D eta 3D kristal fotoniak definitu daitezke, ε-en adakuntza bi eta hiru dimentsioetan gertatzen den kasuetarako, hurrenez hurren. 1.1 irudian aurkezten dira bat, bi eta hiru dimentsioetan agertzen diren egitura dielektriko inhomogeneoen eredu batzuk. Egitura horietan, sare-parametroaren pareko uhin-luzeera duen uhin elektromagnetiko bat hedatzen denean, ezuzteko jokaerak agertzen dira. Hauetatik interesgarrienak band-gap fotoniko oso (CPBG) bat sortzeko aukera, sare periodikoan defektuen bidez argia lokalizatzea

[1] Azalpen honetan spin-a alde batera utzi dogu.

[8, 9], edota talde-abiadura baxuak sorturiko argi materia interakzioak sustatutako fenomeno ez-linealak gertatzea [10, 11] aipagarriak dira, beste askoren artean.

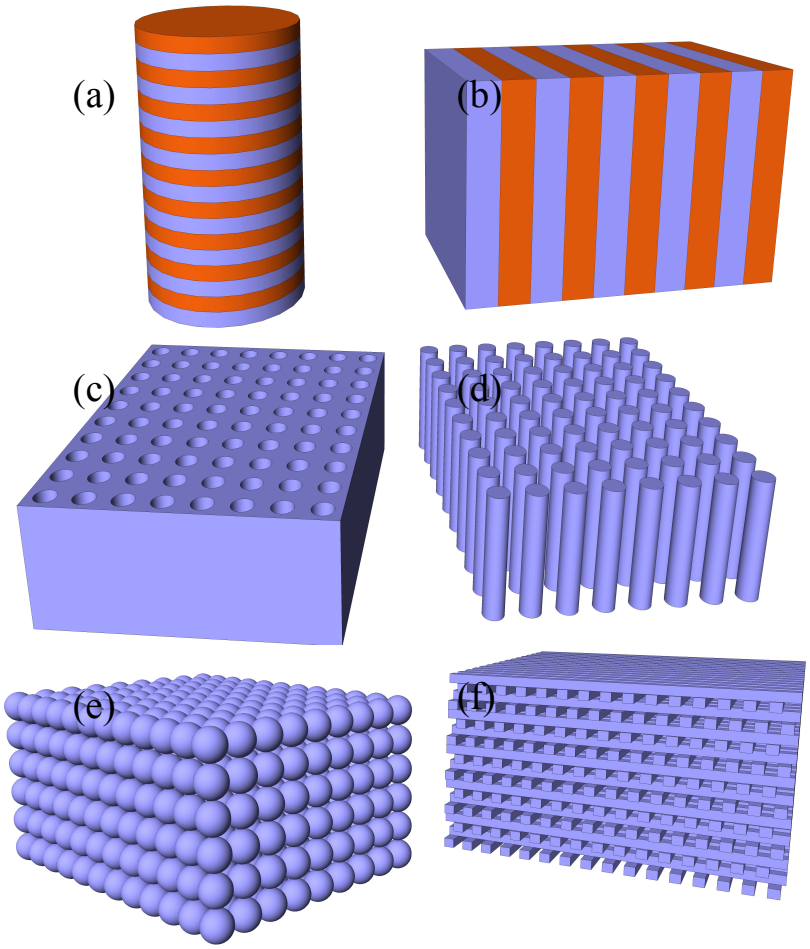

1.1. Irudia (a)1D, (b) 2D eta (c) 3D kristal fotoniko ezberdinen ereduak.

Fenomeno hauek potentzial teknologiko ugari izan ditzakete, esaterako, kristal fotonikoak ispilu hobeezinak garatzeko [12, 13], nahiz ioi aktiboen emisio espontaneoa kontrolatzeko [14–16] edota solitoiak garraiatzeko [11, 17].

Beste alde batetik, material hauek sustatzen duten argi materia interakzio gogorraz baliatuz kristal fotonikoetan ematen diren fenomeno ez-linealak aztertu daitezke, eta horiek aplikazio berrien hildoak zabaltzeko erabili daitezke. Esaterako, trinkoagoak diren kontsumo baxuko birsorgailuak sor daitezke [18, 19], sentsore eta biosentsore aurreratuak [20–22], eta zelula fotoboltaiko efizienteagoak garatu daitezke [23–25].

Zoritxarrez, gauza guzti hauek kontrapuntu bat dute: aipatutako aplikazio gehienetan, eta, batez ere, telekomunikazio maiztasunetan operatzen duten aplikazioetan, behar genukeen

kristal fotonikoen eskala-neurriak mikra baten azpikoak lirateke eta tamaina hain txikiko egiturak eraikitzeko prozesu konplexuak erabili behar dira. Are gehiago, ikuspuntu teknologiko batetik, honelako egitura periodikoak fabrikatzea askoz zailagoa bilakatzen da hiru dimentsioetako kristal fotonikoak planteatzen direnean. Ondorioz, kristal fotonikoen ikerketak bi dimentsioetako heteroegituetan jarri dira ikerketa ahalegin gehienak, batez ere, bi sustratoen artean inguratutako 2D kristal fotonikoez egindako hiru dimentsioetako egituretan, PC slab bezala ezagutzen direnak [26, 27]. Orain arte esandakoaren arabera, argudiatu daiteke beraz, kristal fotonikoen ikerketa ez dela soilik mundu akademikoaren inguruko ariketa batera mugatzen, baizik eta oinarrizko fisikan eta fisika aplikatuaneta teknologia berrien garapenean hildo garrantzitsu bat osatzen duen urratsa dela esan genezake.

1.2.1 Kristal Fotonikoen ikerketaren urratsak

Kristal fotonikoak ez dira hain material bitxiak. Guk egitura sintetikoen bidez argiaren hedapena manipulatzen hasi baino milloika urte lehenago, sistema biologikoek nanometroko eskalako egiturak erabiltzen zituzten efektu optiko liluragarriak sortzeko [28]. Zomorro espezie batzuen azalak sortutako iridiszentzia, pinpilinpauxen hegoen koloreak, nahiz opalo harribitxi erakargarriak daude periodikoki ordenatutako egiturez osatuak. Egitura konplexu hauek guztiak orden finko bat jarraitzen dute eta, orden horren barruan, batzuetan, defektu edo nolabaiteko kontrolpeko desordena ager daiteke, argiaren barreiadura sortzeko eta maiztasun zehatz batzuk deuseztekp.

Bereziki, animalia espezie batzuk sortutako urdin koloreak, 1.2 irudian agertzen diren modukoak, haien azaletan, periodikoki ordenatutako partikulen multzoak sortutako islapen elastikoan du jatorria, eta Tyndall islapenez ezagutzen da, edo Mie islapena, objektu horiek itxura esferikoa dutenean. Naturan sorturiko urdin kolorearen jatorriaren inguruan gehiago jakiteko irakurleak Simonis et al. -en idazkietan [29] aurkitu dezake deskribapen zehatza eta interesgarria. Oro har, naturak erakusten dituen egitura fotonikoen aniztasuna harrigarria da eta sarritan aplikazio berriak sortzeko erabiliak izan dira. Hortaz, kristal fotonikoak beti egon dira gure inguruan, era batean edo bestean, baina nahiz eta kristal fotonikoen ikerketa aspaldi hasi zen, gero eta ikerketa teoriko eta aplikatu gehiago egiten ari dira esparru honetan.

Gaur egun, kristal fotoniko terminoa argiaren hedapena kontrolatzeko eta argiaren eta materiaren interakzioa sustatzeko gai den edozein material periodiko inhomogeneo izendatzeko erabiltzen da. Gainera, aurreko definizioak ez ditu baztertzen periodizitatea nolabait etena dituzten materialak.

Beste alde batetik, kristal fotonikoen ikerketak, egoera solidoaren fisikatik oinordetzen ditu oinarri teoriko gehienak. Egoera solidoaren fisikan, dimentsio bakarreko potentzial hesi periodikoen katean higitzen den elektroiaren eredua, hots, Kronig-Penney eredua [31, 32],

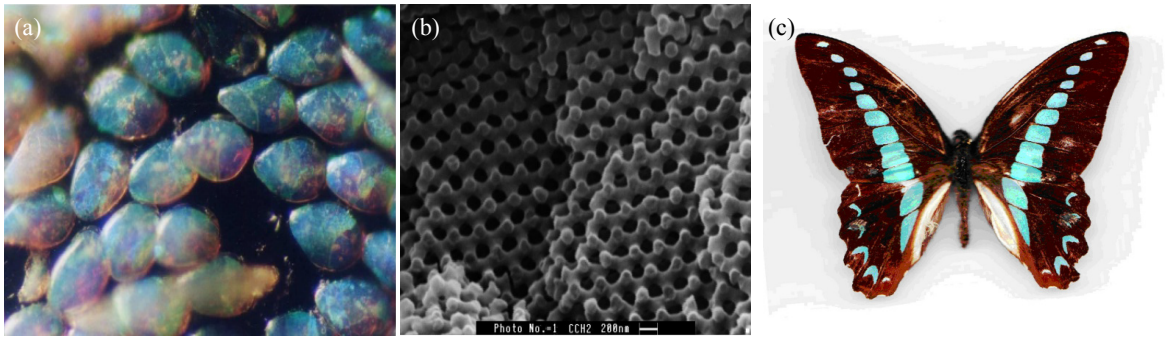

1.2. Irudia (a) Mikroskopioz hartutako eta (b) mikroskopio elektronikoz lortutako *Cyphus Handoki* gurgurioaren azal urdinaren irudiak. Bertan, sare kristalinoak isladapen fenomeno berezia sortzen du [30]. (c) *Graphium sarpedon* -en pigmentazio karakteristikoa hegoetan dituen eskaten ordenamenduak sortzen du [29].

energia-gakoen agerpena azaltzeko erabiltzen da. Optika mailan analogoa den eredua, hau da, material dielektriko ezberdinen pilaketaz sortutako ispiluak, Bragg erreflektore, *multilayer* pila, nahiz 1D PC izenez ezagutzen dira (Fig.1.1.a-b).

Argiak Bragg erreflektorea jotzen duenean, partzialki islatzen da, konstante dielektrikoaren aldakuntza bat ematen den puntu bakoitzean eta material dielektriko ezberdinen arteko kokapena periodikoa bada, orduan, islatutako konponenteak era suntsikorrean interferitzen dute, aurreruntz propagatzen den argi-uhina deuseztatuz. Fenomeno hau Lord Rayleigh-ek aztertu zuen lehenengoz 1887an [33] eta gaur egungo ispilu dielektrikoen [34, 35], Frabry-Perot filtroen [36, 37], erreflekzioak ekiditzeko geruzen [38], *distributed feedback laser*-en [39] nahiz kabitate optikoen [40] oinarria da.

Bi eta hiru dimentsioko kristal fotonikoen bidez, bi-hiru dimentsioko band-gap fotonikoak sortzea, Lord Rayleigh-en ikerketa eta ehun urte geroago proposatu zuten S. John and E. Yablonovich-ek ia aldi berean argitaratutako ikerketetan [41, 42]. Bi dimentsioko kristal fotonikoak material dielektrikoz edo metal-dielektrikoz osaturiko *array* erregularrak dituzte egituraren bi norabideetan; aldiz, homogeneoak eta infinituak dira beste norabidean. Azkenik, hiru dimentsioko kristal fotonikoak, hiru dimentsiotan zabaltzen diren material dielektrikoz edo metal-dielektrikoz osaturiko tartekatze erregularrez sortzen dira. Azken egitura hau da band-gap osoa sortzeko aukera duen bakarra, hau da, uhin elektromagnetikoen hedapena hiru dimentsioetan eta noranahi inhibitzeko ahalmena duen egitura da.

Geroago, 90.hamarkadaren hasieran, ikerketa ahalmen gehienak band-gap osoak (CPB) lortzearen saiaketan ardaztu ziren [47, 48]. Horretarako kristal sare ezberdinen banda-egiturak aztertu ziran [49, 50] eta fotoien lokalizazioa eta gidaketa sortzeko gai diran egitura berriak identifikatu ziren. Kristal fotonikoen aurkikuntza teorikoekin batera, fabrikazio-prozesu berriak garatu ziren, nanometroko eskalako kristalak sortzeko. Honen inguruan,

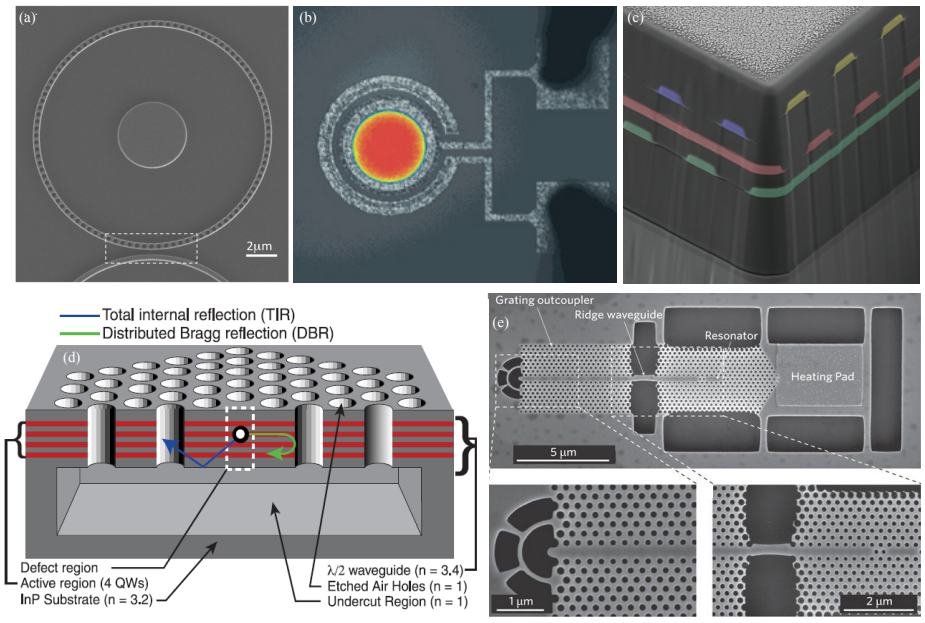

1.3. Irudia (a) Materia eta argiaren arteko interakzioa sustatzen duen 1D kristal fotonikoko erresonadore eraztun batez osatutako biosensore optiko baten SEM (Scanning electron microscopy) irudia [20]. (b) p-motatako Si nano uhin-gidaz eginiko elektoluminiszentzia sortzeko gailua, n-motatako ZnO erabiliz dopatutako aluminiozko elektrodoz osaturikoa. Material hauen artean Si-ko zutabez osaturiko kristal fotoniko bat kokatu da [43]. (c) SEM bidez lortutako 3D-ko *woodpile* egituran antolatutako kristal fotonikoaren irudia, SU-8 polimeroan egindakoa [45]. (d) Bi dimentsioko kristal fotoniko baten sortuarazitako akats puntual baten bitartez egindako laserra. Egitura honetan putzu energetiko bat agertzen da fotoientzat, hari kuantiko baten egituran elektroientzat sortzen den parekoa dena [44]. (e) Kristal fotoniko hutsune bat kristal fotoniko uhin-gida batekin akoplatuta eta honen muturrean uhinak kanporantza gidatzen dituen egitura bat du 1D kristal fotoniko batez osaturikoa [46]

self-assembly metodoa[51] eta erresinen bi fotoien xurgapenaren bidezko laser-idazketa zuzenaren teknikak [52] garatu ziren kalitate haundiko kristal fotonikoak fabrikatzeko. Bi metodo horiek, etorkizun handiko metodoak dira 3D PC egiturak sortzeko eta beraz, CPB baten beharra duten aplikazioetarako dispositiboak sortzeko.

Beste alde batetik, kuasi-2D kristal fotonikoak edo slab kristal fotonikoak, harreta handia jaso dute ikerketa mailan, zirkuito fotonikoak eraikitzeko plataforma bikainak izateko potentziala bait dute. Egitura horietan, nahita sortutako *akatsak* erabiliz, zirkuito fotoniko integratuetarako dispositibo pasiboak (filtroak [53–55] esaterako) eta aktiboak (laserrak [39, 56, 57] esaterako), inplementatu daitezke egitura konplexuak sortzeko [58]. Ondorioz, kristal fotonikoen ikerketa-arloa oso dinamikoa dela esan genezake, bertan aurkikuntza eta aplikazio berriak asmatzen bait dira erregularki.

Gainera, material hauek beste hildo batzuetara jauzia eman dute, hauen artean biologian PC biosensoreen [21] erabileran dute aplikazio nabaria, horien sensitibitate karakteristikoagatik; edota, ingenieritza zibilaren arloko aplikazioetan [59, 60], beste hainbat arloetako aplikazio ereduen artean. Hala eta guztiz ere, orain arte aipatutako aplikazio teknologikoen artean, arrakastatsuena kristal fotonikoen zuntz optikoetan aukitzen da. Mota honetako zuntz optikoak *core* hutsa (airea) erabiliz argia gidatzeko gai dira, propagazio galerak bortizki murriztuz [61, 62]

1.2.2 Bi dimentsioko sare periodikoak

Orain arte ikusi dugun moduan, kristal fotonikoak espazioko norabideetan periodikoki errepikatzen diren patroiez osaturiko materialak baino ez dira. Kristal arruntetan errepikatzen den patroia atomo edo molekulaz osatzen da, kristal fotonikoetan ordea, errepikatzen den elementua konstante dielelektriko ezberdina duten bi material edo gehiagok osatzen dute. Band-gap-en sormena eta horien zabalera faktore batzuen menpe dago: sarearen barne simetria, kristal fotonikoaren simetriarekiko topologia partikularra eta material dielektrikoen arteko indizearen kontrastea, batik bat. Hortaz, oso garrantzitsua da sare periodikoaren berezitasun geometrikoak ulertzea kristal fotoniko bakoitzaren ezaugarri fotonikoak ulertzeko. Bestalde, ikuspegi praktiko batetik, sarearen ezaugarri geometrikoen ulermenak, simulazioen domeinua murriztea ahalbidetzen du, gelaxka-unitate bakarra erabiliz eta bigarren pauso baten, sare osoa berregin ahal izateko, sareko simetriaz baliatuz.

Hiru dimentsioko sareetako ezaugarri geometrikoak idazki ugarietan lantzen dira [1]. Baina bi dimentsioko sareen kontsiderazio geometrikoak lantzen dituzten testu liburuak aurkitzea ez da hain erreza izaten. Hau dela eta, atal honetan, bi dimentsioko kristalen propietate geometrikoak laburbilduko ditugu. Sare karratua, gelaxka-unitatea definitzen duten sare-bektoreak erabiliz deskribatzen da (begiratu 1.4.a irudia)

$$\vec{a}_1 = a\,\hat{i}, \tag{1.3}$$

$$\vec{a}_2 = a\,\hat{j}. \tag{1.4}$$

Sarritan, beste gelaxka-unitate bat erabiltzen da ere, Wigner-Seitz gelaxka-unitatea, hain zuzen ere. Gelaxka-unitate honek, sare beraren simetria partekatzen dute. Beste ere batera definituta, gelaxka hau sare-puntuetatik hurbilen dauden puntuek osatutako gelaxka da. Tesi honetan zehar gelaxka hau erabiliko dogu gelaxka-unitate bat izendatzen dogun bakoitzean. Sare karratuan, gelaxka-unitate hau, sarearen puntu arbitrario baten zentratutako karratu batez osatzen da eta karratuaren aldeak a (sare parametroa) luzeera izango du. gelaxka-unitate

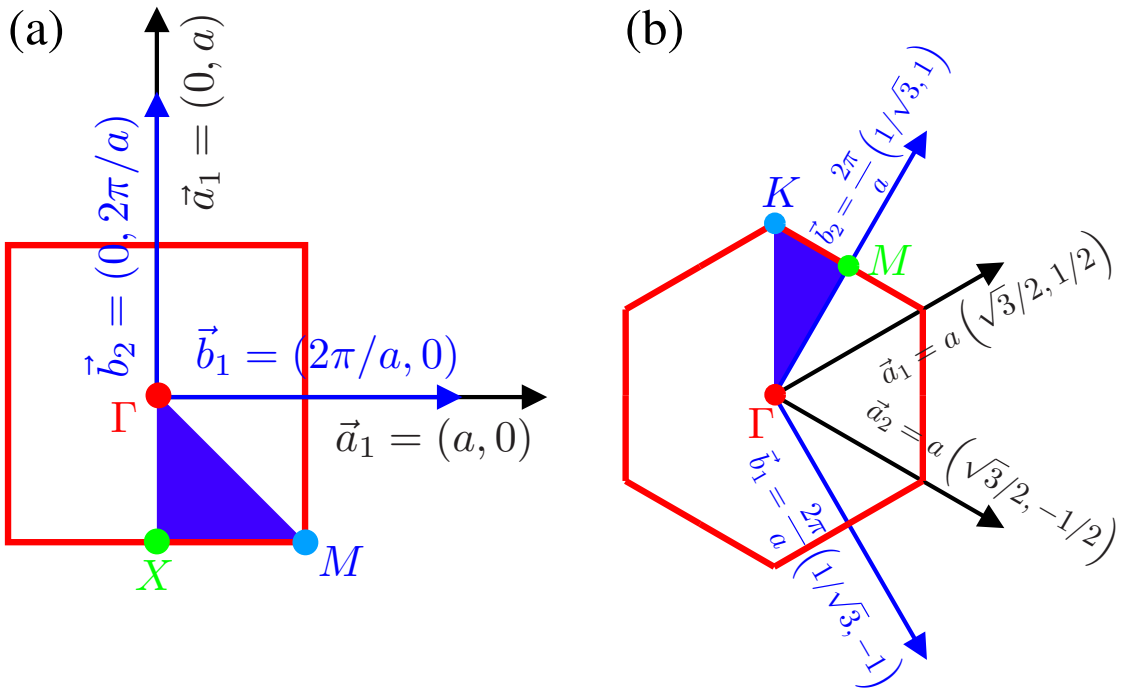

1.4. Irudia (a) Sare-bektoreak (beltzez), sare-erreziprokoaren bektoreak (urdinez), lehenengo Brillouin gunea (karratu gorria), zatiezina den 1BZ (triangelu urdina), eta sare karratuaren simetriaren puntu bereziak (Γ, X, eta M). (b) Sare-bektoreak (beltzez), sare erreziprokoaren bektoreak (urdinez), lehenengo Brillouin gunea (karratu gorria), zatiezina den 1BZ (triangelu urdina), eta sare triangeluarraren simetriaren puntu bereziak (Γ, M, eta K).

honi lotutako sare erreziprokoa (uhin-bektore espazioan) honako bektoreak osatuta dago:

$$\vec{b}_1 = \frac{2\pi}{a}\hat{\imath}, \tag{1.5}$$

$$\vec{b}_2 = \frac{2\pi}{a}\hat{\jmath} \tag{1.6}$$

eta hauek ortogonalitate baldintzak betetzen dituzte:

$$\vec{a}_i \cdot \vec{b}_i = 2\pi, \qquad \vec{a}_i \cdot \vec{b}_j = 0. \tag{1.7}$$

Espazio erreziprokoaren gelaxka-unitatearentzat bestelako geometria aukeratu genezake, lehenengo Brillouin gunea hautatuz (1BZ). Azken hau, espazio erreziprokoan proiektatutako Wigner-Seitz gelaxka-unitatea da. Gelaxka-unitate hau 1.4.a irudian ikusi daiteke, $\frac{\pi}{a}$ alboko karratu gorriz mugatutako gunean. Banda-egituretako kalkuluetan erabiltzen diren simetria-puntu bereziak, simetria-operaketetan erabiltzen direnak, 1.4.a irudian azaltzen dira ere bai.

Simetria puntu hauek honela adierazi daitezke:

$$\Gamma \equiv \vec{0}, \tag{1.8}$$

$$X \equiv \frac{\vec{b}_1}{2}, \tag{1.9}$$

$$M \equiv \frac{\vec{b}_1}{2} + \frac{\vec{b}_2}{2}. \tag{1.10}$$

Hiru puntu hauekin mugatutako espazio erreziprokoaren zatiari 1BZ-ren espazio zatiezina deritzogu. Uhin-bektorearen menpe dagoen edozein aldagai edo kopuru, zatiezin guneko uhin-bektoreen arabera kalkulatu daiteke eta, geroago, espazio erreziproko guztian errepikatu daiteke, simetria-operaketen bidez. Izan ere, banda-egitura operaketetan, hau da, uhin-energian uhin-momentuarekiko kalkuluetan, orokorrean energia dispertzioa 1BZ-ren zatiezin gunearen parametroarekiko kalkulatzen da.

Sare triangularrari dagokionez, horrela adierazi daiteke (begiratu 1.4.b irudia)

$$\vec{a}_1 = \frac{\sqrt{3}}{2} a\hat{i} - \frac{a}{2}\hat{j}, \tag{1.11}$$

$$\vec{a}_2 = \frac{\sqrt{3}}{2} a\hat{i} + \frac{a}{2}\hat{j}. \tag{1.12}$$

Sare ereziprokoari dagozkion bektoreak honela osatu daitezke

$$\vec{b}_1 = \frac{2\pi}{a}\left(\frac{1}{\sqrt{3}}\hat{i} - \hat{j}\right), \tag{1.13}$$

$$\vec{b}_2 = \frac{2\pi}{a}\left(\frac{1}{\sqrt{3}}\hat{i} + \hat{j}\right). \tag{1.14}$$

berriro ere, bektore hauek ortogonalizazio baldintzak betetzen dituzte. Sare honen 1BZ, $\frac{\pi}{a}$-ko apotema duen hexagono bat da 1.4.b irudian, simetria puntu bereziekin batera, irudikatzen den modukoa. Simetria puntu hauen izenak eta posizioak hauek lirateke

$$\Gamma \equiv \vec{0}, \tag{1.15}$$

$$M \equiv \frac{\vec{b}_2}{2}, \tag{1.16}$$

$$K \equiv -\frac{\vec{b}_1}{3} + \frac{\vec{b}_2}{3}. \tag{1.17}$$

Egitura-bandetako kalkuluetan sarearen periodizitatea ziurtatzeko eta era berean simulazio esparrua gelaxka-unitate batera mugatzeko, Bloch-en teorema aplikatu behar da simulazioaren

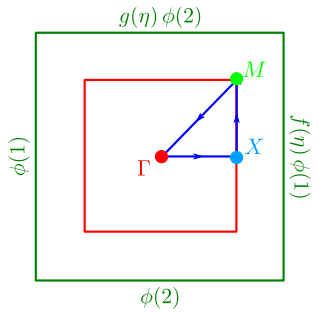

$\vec{k}$	$f(\eta)$	$g(\eta)$
$\overline{\Gamma X}$	$e^{i\pi\eta}$	1
$\overline{XM}$	-1	$e^{i\pi\eta}$
$\overline{M\Gamma}$	$e^{i\pi(1-\eta)}$	$e^{i\pi(1-\eta)}$

1.5. Irudia Bloch-en teorema sare karratu baten Wigner-Seitz gelaxka-unitatean aplikatuta. Berdez: Wigner-Seitz gelaxka-unitatea. Gorriz: Lehenengo Brillouin gunea (espazio erreziprokoaren Wigner-Seitzgelaxka-unitatea). Urdinez: zatiezina den 1BZ-ren partearen mugak. $\phi(i)$ balioak $\phi(\vec{r})$ (E_z edo H_z) kopurua hartzen du gelaxka-unitatearen i. mugan.

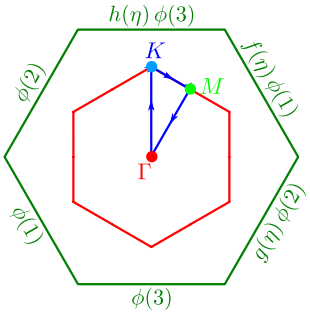

$\vec{k}$	$f(\eta)$	$g(\eta)$	$h(\eta)$
$\overline{\Gamma M}$	$e^{i\pi\eta}$	1	$e^{i\pi\eta}$
$\overline{MK}$	$-e^{-i\frac{\pi}{3}\eta}$	$e^{-i\frac{2\pi}{3}\eta}$	$-e^{i\frac{\pi}{3}\eta}$
$\overline{K\Gamma}$	$e^{i\frac{2\pi}{3}(1-\eta)}$	$e^{-i\frac{2\pi}{3}(1-\eta)}$	$e^{i\frac{4\pi}{3}(1-\eta)}$

1.6. Irudia Bloch-en teorema sare triangeluar baten Wigner-Seitz gelaxka-unitatean aplikatuta. Berdez: Wigner-Seitz gelaxka-unitatea. Gorriz: Lehenengo Brillouin gunea (espazio erreziprokoaren Wigner-Seitz gelaxka-unitatea). Urdinez: zatiezina den 1BZ-ren partearen mugak. $\phi(i)$ balioak $\phi(\vec{r})$ (E_z edo H_z) kopurua hartzen du ugelaxka-unitatearen i garren mugan.

mugetan. Uhin-luzeera konkretu batentzat, muga-baldintza hauek uhin elektromagnetikoaren hedapen norabidearen araberakoak dira, hau da, espazio erreziprokoaren uhin-bektorearen norabidearen menpekoak dira. Muga badintza hauek, sare karratu eta triangularrarentzat, 1BZ-ren gune zatigaitzan 1.5 eta 1.6 irudietan azaltzen dira, hurrenez hurren.

Kapitulua 2

Metodo numerikoak nanofotonikan

Atal honek tesiak jorratzen dituen kristal fotonikoko egitura berriak sortzeko erabiliko ditugun metodo konputazionalen oinarriak ezartzen ditu. Argiaren eta materialen egitura konplexuen arteko interakzioan gauzatzen diren fenomeno fisiko bereziak kalkulatzeko, eta propiete hauen simulazioak era zorrotz batean egiteko, simulazio tresna analitikoen erabileraren beharra dago. Dagoeneko hainbat simulazio-teknika ezberdin garatu izan dira material konplexu hauetan egin beharreko simulazioak aurrera eramateko. Hauen artean hiru simulazio teknika ezberdin erabili izan ditugu, teknika hauek, kristal fotonikoetan zehar hedatzen diren argi uhinen ezaugarriak era fidagarrian aurreikusteko orduan emaitz apartak eskaintzeko gai dira. Hiru metodo numeriko hauek elementu finitoen metodoa (FEM), uhin planoen espantsio metodoa (PWEM) eta denboraren araberako diferentzia finituen metodoa (FDTD) dira, hurrenez hurren.

2.1 Egitura nanofotonikoen azterketa teorikoa

Ikuspuntu teoriko batetik silizioan oinarritutako fotonikaren ikerketaren inguruko ekarpen garrantzitsuenetako bat, material heterogeneoen barruan, Maxwellen ekuazioak formulatzen dituzten uhin elektromagnetikoen hedapena deskribatzeko metodo numerikoen garapena da. Metodo numeriko horiek, prozesu experimentaletan lortutako emaitzak eta bertako sistemen fenomenologia modu bizkor eta era fidagarrian erreplikatzeko, ezinbesteko tresnak bilakatu dira.

Zoritxarrez, sistema hauetan hedatzen diren uhin elektromagnetikoak deskribatutako uhin ekuazioak, sistema homogeneoetan erabiltzen direnak baino konplexuagoak dira, hauetan ematen den konstante dielektrikoaren eta espazioarekiko menpekotasuna dela eta. Ondorioz, uhin-ekuazio hauek, modu analitiko batean ebaztea prozesu zaila da eta soilik kasu sinpleenetan, 1D PC-an esaterako, ebatzi daitezke konputagailu bidezko metodo numerikoak

erabili barik. Beraz, metodo numeriko hauek ezinbestekoak dira, alde batetik, orokorrean emaitz kuantitatiboak lortzeko bide bakarra direlako, eta beste alde batetik, PC konkretu baten predikzio numerikoa lortzea, neurketa esperimentalak egitea baino azkarragoa eta merkeagoa delako.

Kristal fotonikoen arloko metodo numerikoen garapenak, semi-eroaleen banda-egitura elektronikoa kalkulatzeko metodoek izandako bidearen parekoa izan da. Hasieran, ikerketa ahalegin gehienak kristal fotoniko ideal eta infinituek erakarri zituzten. Sistema hauetan, maiztasun espazialeko teknikak oso ondo moldatzen dira, adibidez uhin lauen metodoa (PWE) [4, 63, 85], edota *tight binding* metodoan oinarritutakoak. Laster, ordea, kristal fotonikoetako egituretan nolabaiteko desordena sartzeak ezaugarri fisiko bereziak sortarazten zituztela ikusiz, maiztasun eremuko metodoak erabili ziren, akatsak dituzten kristal fotonikoen banda egiturak nahiz egoera fotonikoen dentsitatea kalkulatzeko, gehien bat puntu edo lerro akatsez osaturiko supergelaxka egituretan oinarrituz [65]. Argiaren lokalizazioa sortzen duten akats hauetan ez ezik, kristal fotonikoen fabrikazio prozesuetan gertatzen den antzerako osagaien zorizko desplazamenduak sortutako desordena aztertzeko, aurreko metodo hauek ez dira aproposak. Gainera, sistema errealak beti luzera finitua dute eta beraz, metodo hauen sistema infinituen suposaketak beti errealitatearekin bat ez datozen kontsiderazioak dakartza.

Aurrekoak direla eta, ikertzaileak azken urte hauetan espazio errealean operatzen duten metodoak gero eta gehiago erabiltzen hasi dira. Metodo horiek beste metodoak ez bezala, periodikoak ez diren kluster finitoak erabiltzen dituzte. Azken horien artean, Maxwell ekuazioen hedapen multipolarrean oinarritutako zenbait algoritmo aipa ditzakegu, simetriaren arabera ardaztuta daudenak [66, 67] (harmoniko zilindriko edo esferikoak esaterako) edo denboraren eremuko diferentzia finituen metodoa [68]. Hedapen multipolarrean oinarritutako metodoak, oinarri simetrikoaren aukeraketaz mugatuta daude, simetria bera duten osagai dielektrikoak dituzten sistemei aurre egiteko. FDTD metodoa ordea, gero eta itxaropentsuagoa dirudi, metodo honen eragozpen garrantzitsuena denboraren araberako ekuazio-sistemetan hedatutako eremuek egoera egonkorrera iristeko beharrezko denbora, hau da, konputazio-denbora, luzea izaten ohi dela da. Nolanahi ere, metodo hauen erabilera askotan baztertu egin da, batez ere konputazionalki oso garestiak direlako, batez ere memoria erabilerari dagokionez. Hala ere, konputagailuen baliabide informatikoak gora egin ahala eta RAM memorien prezioen murrizketa ikusgarriak, FDTD metodoaren konputazio-kostuak areagotu ditu eta ondorioz, espazio errealeko metodoak aplikazio praktikoetan erabilpenean oso interesgarri egiten ditu.

Beste alde batetik, elementu finitoen (FE) metodoak [69–72, 74] arreta gutxi jaso du orain arte fisikaren arlo honetan, nahiz eta fisika eta ingenieritzako beste hainbat sailetan arrunki aplikatzen den. Izan ere, azken metodo honek baditu ingurune heterogeneo baten hedatzen

diren uhin elektromagnetikoen analisia egiteko onuragarriak diren alderdi ugari. Konkretuki, FE metodoak, modu natural batean, geometria arbitrarioen azterketa eta maiztasunaren araberako funtzio dielektrikoekin (adibidez, egitura inhomogeneo metalikoen kasuan) uhinen ebazpena ahalbidetzen du. Gainera, funtzio dielektrikoaren jarraitasun ezak ez dira FE metodoarentzat bereziki kaltegarriak eta kalkulatu beharreko kantitateak egoera egonkorrean aurkezten ditu uneoro. Metodoaren gabezi bakarra konputagailuaren memoriaren behar intentsiboa da. Hala eta guztiz ere, baliabide honen eskakizunak ez dira asko aldatzen egitura hauetan akatsak aztertzen direnean. Beraz, metodo honen erabilpena oso abantailagarria izan liteke sare desordenatuen azterketan [72]. Ondorioz, gaur egun, band gap fotonikoen arloan, FE metodoaren erabilgarritasuna aztertzea garrantzitsua da, honen bidez kristal fotonikoen propietate fisikoak ikertzeko, ikuspegi fundamental eta aplikatutik aurkezten dituen xehetasunak jakinarazteko.

2.2 Ingurune inhomogeneoetan uhin elektromagnetikoen hedapenari buruzko oinarri matematikoak

Ingurune heterogeneo baten hedatzen den uhin elektromagnetikoaren ezaugarriak deskribatzeko Maxwellen ekuazioak erabiltzen dira. Karga libreen eta kanpo korronte elektrikoen gabezian, Maxwellen ekuazioak, ingurune ez-magnetiko eta isotropikoan, hurrengo eran idatzi daitezke:

$$\nabla \cdot \vec{B} = 0 \tag{2.1}$$

$$\nabla \times \vec{E} = -\frac{d\vec{B}}{dt} \tag{2.2}$$

$$\nabla \cdot \vec{D} = \rho \tag{2.3}$$

$$\nabla \times \vec{D} = \vec{J} + \frac{d\vec{D}}{dt}, \tag{2.4}$$

non $\vec{E}$ eremu elektrikoa da eta $\vec{B}$ dentsitate magnetikoaren fluxua da. μ hutsaren permitibitatea da, $\varepsilon_0/\mu_0 = 1/c^2$ non, ε_0 hutsaren konstante dielektrikoa da. $\vec{D}$ desplazamendu eremua da, azken hau $\vec{E}$ eremu elektrikoarekin lotzen da ε konstante dielektrikoaren bitartez. Bereziki, bi-dimentsioko sistemetan, edozein eremu elektriko edo magnetiko bat, zeharkako eremu elektriko (TE) bat eta zeharkako eremu magnetiko (TM) baten konbinaketa linela erabiliz adierazi daiteke. Zeharkako eremu elektrikoa, kristal fotonikoaren plano perpendikularraren norabidea hartzen du – era berean, zeharkako eremu magnetikoa kristal fotonikoaren plano berean kokatzen da– eta kanpo iturrien ezean, Maxwell-en ekuazioak eremu elektrikoarentzat

Helmhotz-en ekuaziora murriztu daitezke hurrengo eran

$$\nabla^2 E_z(\vec{r}) + k_0^2 \epsilon_r(\vec{r}) E_z(\vec{r}) = 0, \tag{2.5}$$

non $E_z(\vec{r})$, z-norabidean hedatzen den eremu elektrikoa da $\vec{r}$ posizioan, $\epsilon_r(\vec{r})$ kristal fotonikoaren konstante dielektriko inhomogeneoa da, eta $k_0 = \omega/c$-n, ω eremu elektriko eraginkorraren maiztasun angularra da, c espazio hutseko argi abiadura izanik. (2.5) ekuazioa idazterakoan kristal fotonikoa ez magnetikoa ($\mu_r = 1$) eta ez-eroalea ($\sigma = 0$) dela onartu da. (2.5) ekuazioa ebatzi eta gero, denbora-harmonikoko eremu elektriko eta magnetikoak errez kalkulatu daitezke

$$\vec{E}(\vec{r}, t) = E_z(\vec{r})\, e^{-i\omega t}\, \hat{z} \tag{2.6}$$

$$\vec{H}(\vec{r}, t) = \frac{i}{k_0} \nabla \times \epsilon_r(\vec{r}) \vec{E}(\vec{r}, t). \tag{2.7}$$

Beste alde batetik, TM polarizazioaren kasuan, eremu magnetikoa kristal fotonikoaren planoarekiko perpendikularra da–eremu elektrikoa plano horretara mugatzen den neurrian –eta Maxwellen ekuazioak, kanpo iturrien ezean, eremu magnetikoarentzako Hemholz-en ekuaziora murriztu daiteke

$$\nabla \left(\frac{\nabla H_z(\vec{r})}{\epsilon_r(\vec{r})} \right) - k_0^2 H_z(\vec{r}) = 0, \tag{2.8}$$

non $H_z(\vec{r})$, z norabidean hedatzen den eremu magnetikoaren osagaia da, $\vec{r}$ posizioan. Eremu elektriko eta magnetikoen denbora-harmonikoak erraz kalkulatu daitezke (2.8) ekuazioa ebatzi eta gero

$$\vec{H}(\vec{r}, t) = H_z(\vec{r})\, e^{-i\omega t}\, \hat{z} \tag{2.9}$$

$$\vec{E}(\vec{r}, t) = -\frac{i}{k_0 \epsilon(\vec{r})} \nabla \times \vec{H}(\vec{r}, t). \tag{2.10}$$

Simulazio elektromagnetiko baten, simulazio domeinuaren muga-baldintza egokiak erabiltzea, alderdi garrantzitsu bat da. Muga-baldintza hauek, simulatutako eremu elektromagnetikoen izaera, problema fisiko bakoitzaren ezaugarri espezifikoetara egokitzen dituzte. Adibidez, banda-fotonikoen egiturak kalkulatzeko, muga-baldintza hauek, egitura infinitu baten propietateak sortzeko gai izan behar dira eta aldi berean, kristal fotonikoaren periodizitatea errepikatu behar dute. Aldiz, mota honetako muga- baldintzak ezin dira berrerabili izaera finitua duten egituretan. Egitura infinitu bat simulatzeko, muga-baldintza magnetiko perfektuak (PMC) edo elektriko perfektuak (PEC) erabiltzen dira, simulazio-eskualdea islatzeko. PMC baldintzak, eremu elektromagnetikoaren TE polarizazioarentzat erabiltzean, simulazio-

eskualdearen mugan tangentea den eremu magnetikoa deuseztatu beharko litzateke, hau da

$$\hat{n} \times \vec{H} = \vec{0}, \tag{2.11}$$

non $\hat{n}$ simulazio domeinuaren kanpoaldeko puntu bakoitzarekiko perpendikularra den unitate-bektorea da. Beste alde batetik, PMC baldintzak eremu elektromagnetikoaren TE polarizazioarentzat erabiltzen dira, simulazio-eskualdearen mugan tangentea den eremu elektrikoa deuseztatuko litzateke, hau da

$$\hat{n} \times \vec{E} = \vec{0}. \tag{2.12}$$

Kristal fotonikoaren sarearen periodizitatea, Bloch-en teorema erabiliz kristal fotonikoaren gelaxka unitatearen mugetan eragin daiteke. Teorema honek adierazten duenez, eremu elektrikoa (magnetikoa), PC-ren puntu batetik gelaxka unitatearen beste aldera hedatzen denean, $\vec{R}$ espazioa zeharkatuz, eremu elektromagnetikoak jasatzen duen aldaketa bakarra bere fasean aurkitzen da

$$E_z(\vec{r}+\vec{R}) = e^{i\vec{k}\cdot\vec{R}} E_z(\vec{r}) \tag{2.13}$$

eta

$$H_z(\vec{r}+\vec{R}) = e^{i\vec{k}\cdot\vec{R}} H_z(\vec{r}). \tag{2.14}$$

TE eta TM polarizazioetarako, hurrenez hurren. Ekuazio hauetan, $\vec{R}$ kristal fotoniko sarearen bektorea da, eta $\vec{k}$ eremu elektromagnetikoaren uhi- bektorea da (3). Beste alde batetik, hurrengo kapituluetan aurkezten diren transmitantziaren kalkuluak egiteko, uhin bektorearekiko paraleloak diren kluster finitoak erabiltzen dira. Aldi berean, kluster hauek infinituak dira norabide perpendikularrean. Material hauen ezaugarriak erreplikatzeko, PMC eta PEC muga-baldintzak erabili dira simulazio eskualdearen kanpo ertzetan, uhin bektore eraginkorrarekiko perpendikularra den norabidean TE eta TM polarizazioarentzat, hurrenez hurren. Uhin elektromagnetikoak, muga hauek zeharkatzen dituzten kasuetan, kanpo muga-baldintzetan arreta handia jarri behar da, egituren izaera finituak sortutako eremuen islapen artifizialak ekiditzeko. Horretarako *perfectly matched layer* (PML) muga-baldintzak erabiltzen dira. Muga-baldintza horiek definitzen dituzten ekuazioak hauexek dira

$$\hat{z} \cdot \hat{n} \times (\nabla \times E_z \hat{z}) - i\beta E_z = -2i\beta E_{0z} \tag{2.15}$$

$$\hat{z} \cdot \hat{n} \times (\nabla \times H_z \hat{z}) - i\beta H_z = -2i\beta H_{0z}, \tag{2.16}$$

non E_{0z} eta H_{0z} eremu elektriko eta magnetikoen eremuko hasierako balioak dira, hurrenez hurren, eta $\beta = k_0$ propagazio konstantea da. Goiko ekuazioa TE polarizazioari aplikatzen zaio, behekoa TM polarizazioari dagokio. Eremu elektrikoa mugaren modu propioa bada, mugan ez da isladapenik emango.

2.3 Elementu finitoen metodoa

Aurkezpenean adierazi den bezala, elementu finituen metodoa (FEM) ekuazio partzial diferentzialak ebazteko metodo numeriko orokorra da. Metodo hau bereziki egokia da zorizko konplexutasuna duten geometrien problema elektromagnetikoei aurre egiteko. Edozein FE simulazioen muinean sare bat sortzeko algoritmoa dago, hau da, simulatu beharreko geometria-eskualdea forma konkretu batez osatutako *sare elementu*-etan zatitzen duen algoritmoa.

Dimentsio bakarrean, hau da 1D-an, sare hau simulazio-domeinua zati txikietan banatzearen emaitza da. Sare honen muturreko puntuei *sarearen erpinak* edo *sarearen nodoak* deitzen zaie. Bi dimentsioetan, simulazio domeinua sare elementu triangular edo laukizuzenekin osatzen da, adibidez. Triangeluen bidez osatutako sareari, *egituragabea* deritzogu eta laukizuzenez osatutakoari ordea *egituratuta* dagoen sarea dela esaten diogu, sarea honek patroi itxura zehatz bat osatzen bait du. Triangeluen edota laukizuzenen albo eta ertzei, *sarearen ertz* eta *sarearen erpin*, deitzen zaie, hurrenez hurren. Simulazio-domeinuaren mugak partzialki (gutxi gorabehera) sarea ertzetan partekatzen dira, *muga elementuak* deritzogunetan, eta hauek sarearen triangeluekin bat etorri behar dira ondoan azpi-domeinu bat badago. Era berean, 3D-an, simulazio-eremua tetraedro, hexaedro edo prisma-sarea elementuetan banatu daiteke, zeinen aurpegiak, ertzak eta erpinak *sare aurpegi*, *sarearen ertz* eta *sarearen erpin* terminoekin izendatzen dira, hurrenez hurren. 2.1 irudian bi dimentsioetarako osatutako sare ezberdinen adibideak erakusten dira.

Hautatutako geometriarentzat sare bat definitu eta gero, problemaren menpeko aldagaien hurbilpen bat egiten da. Pauso honen helburua, parametro kopuru batzuen bitartez interpolazio-funtzio bat osatzea da, honela menpeko aldagaien hurbilketa bat egiteko. Interpolazio-funtzioa osatzen duten parametro hauei *askatasun-gradua* deitzen zaie. Ekuazio partzial diferentzialean (PDE) hurbilketa hau erabiltzean, askatasun-gradu hauentzat, ekuazio algebraiko sorta bat sortzen du. Gero, ekuazio algebraiko hauek, *solver* egokia erabiliz ebatzi daitezke. Prozesu hau hobeto deskribatzeko, ondoren FEM erabiliz dimentsio bakarreko ekuazio diferentzialaren ebazpena aztertuko dugu

$$-\frac{d}{dx}\left(\alpha(x)\frac{d\phi}{dx}\right)+\beta(x)\phi(x)=0, \tag{2.17}$$

$\phi(x)$ ebatzi nahi dugun funtzioa da eta $\alpha(x)$ eta $\beta(x)$ soluzio-domeinuaren ezaugarri fisikoak deskribatzen dituzten eta ezagunak diren funtzioak dira. Egin dezagun beste suposaketa bat, $\phi(x)$ funtzioa, simulazio-eskualdearen mugetan hirugarren motatako muga-baldintza

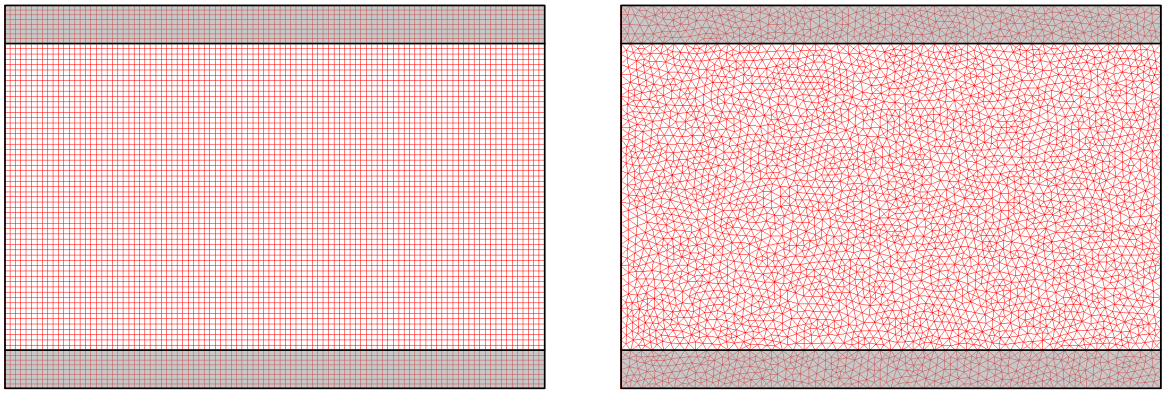

2.1. Irudia Ezkerrean: 2D sare-egitura baten eredua, 7400 sare elementu laukizuzenez osatutakoa. Eskuman: simulazio-eskualde bera 7722 sare-elementu triangeluarrez osatutako sare ez-egituratu batean zatituta dagoena. Geometria honen bidez uhin-gida plano axisimetriko baten uhin elektromagnetikoen hedapena simulatzeko erabili daiteke, adibidez. Simulazio eskualdearen gune ilunak, materialaren errefrakzio-indizeak balio altuak hartzen dituen tarteak irudikatzen ditu ($n = 3$), aldiz, kolore argiak dituzten guneak, aireak betetzen dituen tarteak adierazten ditu.

inhomogenoak emandako balioak hartzen dituela esanez

$$\alpha(0)\left.\frac{d\phi}{dx}\right|_{x=0} + \gamma(0)\phi(0) = q(0) \tag{2.18}$$

$$\alpha(L)\left.\frac{d\phi}{dx}\right|_{x=L} + \gamma(L)\phi(L) = q(L), \tag{2.19}$$

bertan $q(0)$ eta $q(L)$ parametroak ezagunak dira. Dimentsio bakarrean definitutako Helmholtz-en ekuazioa hurrengo eran idatzi daiteke

$$\frac{d^2\phi}{dx^2} + k_0^2\epsilon_r(x)\phi(x) = 0 \tag{2.20}$$

transparent influx motatako muga-baldintzak erabiliz (aurreko atalean deskribatutako PML baldintzen kasu berezia da hau, simulazio gunera igorritako eta simulazio gunetik irtetzen diren uhinen islapena ekiditzea ziurtatzen duten muga-baldintzak dira hain zuzen ere, $x = 0$ eta $x = L$-en, hurrenez hurren)

$$-\left.\frac{d\phi}{dx}\right|_{x=0} + ik_0\phi(0) = 2ik_0 \tag{2.21}$$

$$\left.\frac{d\phi}{dx}\right|_{x=L} + ik_0\phi(L) = 0 \tag{2.22}$$

(2.17)-ren kasu berezia da $\alpha(x) = -1$, $\beta(x) = k_0^2 \epsilon_r(x)$, $\gamma(0) = -\gamma(L) = ik_0$, $q(0) = 2ik_0$, eta $q(L) = 0$ direnean.

(2.17) ekuazioa (2.18) eta (2.19) muga-baldintzekin batera adierazteak, [69] aldakuntza-problema ebaztearen baliokidea da

$$\delta F(\phi) = 0, \tag{2.23}$$

eta bertan

$$F(\phi) = \frac{1}{2} \int_0^L \left[\alpha(x) \frac{d^2\phi}{dx^2} + \beta(x)\phi(x)^2 \right] dx + \Gamma(L) - \Gamma(0) \tag{2.24}$$

eta bereziki

$$\Gamma(x) = \frac{\gamma(x)}{2} \phi(x)^2 - q(x)\phi(x). \tag{2.25}$$

Horretarako, $F(\ phi)$-ren lehen aldakuntza sortuko dugu $\phi(x)$ funtzio fisikoaren arabera

$$\begin{aligned} \delta F(\phi) &= F(\phi(x) + \delta\phi(x)) - F(\phi) = \\ &= \int_0^L \left[\alpha(x) \frac{d\phi}{dx} \frac{d\delta\phi}{dx} + \beta(x)\phi(x)\delta\phi(x) \right] dx + \left[(\gamma(x)\phi(x) - q(x))\, \delta\phi(x) \right]_{x=0}^{x=L}. \end{aligned} \tag{2.26}$$

$\alpha(x)$ domeinu osoan jarraia dela suposatuz eta eskuinaldeko lehenengo terminoa zatietan integratuz, (2.26) hurrengo eran idatzi daiteke

$$\begin{aligned} \delta F(\phi) = -\int_0^L \left[\frac{d}{dx} \left(\alpha(x) \frac{d\phi}{dx} \right) + \beta(x)\phi(x) \right] \delta\phi(x) dx \\ + \left[\left(\alpha(x) \frac{d\phi}{dx} + \gamma(x)\phi(x) - q(x) \right) \delta\phi(x) \right]_{x=0}^{x=L} = 0. \end{aligned} \tag{2.27}$$

$\Delta\phi(x)$ aldakuntza arbitrarioa denez, integrazioa eta muga-terminoak desagertu egin behar dira eta jarraian (2.17) eta muga-baldintza homogeneoak, (2.18) eta (2.19) berreskuratzen dira. Elementu finituen metodoan, (2.23) ekuazioa ebazteko, soluzio-domeinua M luzeera berdineko sare-elementuetan zatitzen da [1], alegia, Δx elementuetan. Elementu bakoitzak n sare-nodoak edukiko ditu, x_i^l-ean kokatuta (ikusi 2.2 irudia). Elementu bakoitzean, interpolazio-funtzioa erabiliz $\phi(x)$-en hurbilketa kalkulatzen da

$$\tilde{\phi}^l(x) = \sum_{i=1}^{n} e_i^l \varphi_i^l(x), \tag{2.28}$$

[1] baldintza hau erraz erlaxatu daiteke baina honela eginez metodoaren formulazioa asko errazten da, beraz, tesi honetan zehar jokabide honekin jarraituko dugu.

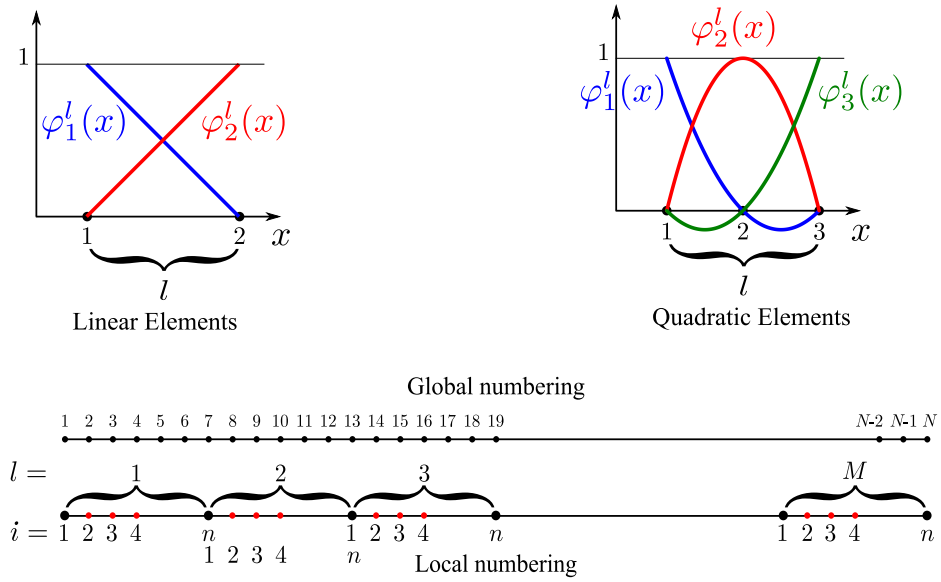

2.2. Irudia Azpikaldean: Simulazio eskualdea M sare-elementuetan zatituta, elementu hauek n nodo dituzte, zenbaketa eskema lokal eta globalean. Goikoan ezkerrean: Elementu linealen oinarrizko funtzioak l. sare-elementuarentzat. Goian eskuman: Elementu laukizuzenen oinarrizko funtzioak l. sare-elementuarentzat.

non e_i^l lehen definitutako askatasun graduak eta $\varphi_i^l(x)$ oinarrizko funtzioak hurrengo baldintzei lotuta daude

$$\varphi_i^l(x_j^l) = \delta_{ij} \qquad (i,j = 1,2,\ldots,N) \tag{2.29}$$

δ_{ij} Kronecker-en delta da. Oinarrizko funtzioak sortutako $\Phi(x)$ funtzio-sorta, funtzio linealen espazio bat da, *elementu finituen espazioa* izenekoa. Adierazpen hauetan, $l = 1,2\ldots,M$ sare-elementuen zenbakia da eta $i = 1,2,\ldots,n$ elementu konkretu baten barruko sareko nodoen zenbakia. Ordenamendu honi, zenbaketa lokalaren eskema deritzogu. Dimentsio bakarreko problemetan, zenbaketa lokalaren eskema hau erabiltzeak ez du abantaila haundirik ekartzen eta nahikoa izaten da soilik indize bakar bat erabiltzea elementuak eta nodoak bereizteko. Prozedura hau zenbaketa globalaren eskemaz ezagutzen da. Bertan, nodoak globalki ordenatzen dira 1-etik N-ra, N sortutako nodoen kopuru totala izanik. Zenbaketa lokalaren eskema erabiliz ordea, metodoa 2 eta 3 dimentsioetan formulatzerakoan, asko errazten du nodoen eta elementuen jarraipena egitea, eta beraz, aurrerantzean eskema hau jarraituko dugu tesi honetan zehar. (2.28) ekuazioa $F(\phi)$ funtzionalean ordezkatuz, hurbilketa funtzionala lortzen da

$$\tilde{F}(\tilde{\phi}) = \frac{1}{2}\sum_{l=1}^{M}\sum_{i,j=1}^{n} e_i^l K_{ij}^l e_j^l + \tilde{\Gamma}(L) - \tilde{\Gamma}(0), \tag{2.30}$$

bertan

$$K_{ij}^{(l)} = \int_{x_1^l}^{x_n^l} \left[\alpha(x) \frac{d\varphi_i^l}{dx} \frac{d\varphi_j^l}{dx} + \beta(x) \varphi_i^l(x) \varphi_j^l(x) \right] dx \tag{2.31}$$

eta

$$\tilde{\Gamma}(L) = \frac{\gamma(L)}{2} (e_n^M)^2 - q(L)\, e_n^M \tag{2.32}$$

$$\tilde{\Gamma}(0) = \frac{\gamma(0)}{2} (e_1^1)^2 - q(0)\, e_1^1. \tag{2.33}$$

Problemaren askatasun graduak kalkulatzeko beharrezkoak diren ekuazioak, egoera egonkorra edo estazionarioa inposatuz lortzen dira

$$\frac{\partial F}{\partial e_i^l}(e_1^1, \ldots, e_i^l, \ldots, e_n^M) = 0 \qquad (l = 1, 2, \ldots, M; i = 1, 2, \ldots, n). \tag{2.34}$$

Ekuazio aproposak lortzeko, hurrengo loturak kontuan izan behar ditugu

$$e_n^{l-1} \equiv e_1^l \qquad (l = 2, 3, \ldots, M), \tag{2.35}$$

eta beraz, askatasun gradu guztiak bikoiztuta egongo dira, lenehengoa eta azkena izan ezik, (2.34) ekuazioan. Honen bidez ondoko ekuazio linealak lortuko dira

$$\sum_{j=1}^{N} \left(K_{ij} + \gamma_{ij} \right) e_j = q_i \qquad (i = 1, 2, \ldots, N), \tag{2.36}$$

edo, era matrizialean

$$[\mathbb{K} + \mathbb{G}]\, \vec{e} = \vec{q}, \tag{2.37}$$

bertan

$$\mathbb{K} = \begin{bmatrix}
K_{11}^{(1)} & \dots & K_{1n}^{(1)} & \dots & 0 & \dots & 0 & \dots & 0 & \dots & 0 \\
\vdots & \ddots & \vdots & \ddots & \vdots & & \vdots & & \vdots & & \vdots \\
K_{n1}^{(1)} & \dots & K_{nn}^{(1)} + K_{11}^{(2)} & \dots & K_{1n}^{(2)} & \dots & 0 & \dots & 0 & \dots & 0 \\
\vdots & \ddots & \vdots & \ddots & \vdots & \ddots & \vdots & & \vdots & & \vdots \\
0 & \dots & K_{n1}^{(2)} & \dots & K_{nn}^{(2)} + K_{11}^{(3)} & \dots & K_{1n}^{(3)} & \dots & 0 & \dots & 0 \\
\vdots & & \vdots & \ddots & & \ddots & & \ddots & & & \vdots \\
\vdots & & \vdots & & \ddots & & \ddots & & \ddots & & \vdots \\
\vdots & & \vdots & & & \ddots & & \ddots & & \ddots & \vdots \\
0 & \dots & 0 & \dots & 0 & \dots & K_{11}^{(M-1)} & \dots & K_{1n}^{(M-1)} + K_{11}^{(M)} & \dots & K_{1n}^{(M)} \\
\vdots & & \vdots & & \vdots & & \vdots & \ddots & \vdots & \ddots & \vdots \\
0 & \dots & 0 & \dots & 0 & \dots & 0 & \dots & K_{n1}^{(M)} & \dots & K_{nn}^{(M)}
\end{bmatrix}, \tag{2.38}$$

$$\mathbb{G} = \begin{bmatrix}
-\gamma(0) & 0 & \dots & 0 & 0 \\
0 & 0 & \dots & 0 & 0 \\
\vdots & \vdots & \ddots & \vdots & \vdots \\
0 & 0 & \dots & 0 & 0 \\
0 & 0 & \dots & 0 & \gamma(L)
\end{bmatrix}, \tag{2.39}$$

$\vec{q} = \left(-q(0), 0, \dots, 0, q(L)\right)^T$, eta $\vec{e} = \left(e_1^{(1)}, \dots, e_{n-1}^{(1)}, e_1^{(2)}, \dots, e_{n-1}^{(2)}, e_1^{(3)}, \dots, e_n^{(M)}\right)^T$, azkenik *solver* egokia erabiliz ebatzi daitekeena. $\mathbb{K}$ matrizearen elementu ugarik zero balioa dute. Matrize honen tamaina mallaren elementu kopuruak zehazten du. FEM ekuazioak formulatzeko erabili dogun metodoari askotan Ritz FEM esaten zaio. FEM formulatzeko beste metodo batzuk ere badaude, adibidez, oso ezaguna den Galerkin metodoa. FEM metodo ezberdinak, antzeko ekuazio sistemetara hailegatzen dira. Metodo hauetan hausnartzean interesatuta dagoen irakurleak xehetasun gehiago aurkituko ditu ref. [69] erreferentzian.

Elementu finituen metodoaren alderdi garrantzitsuenetako bat (2.28) funtzio oinarrien aukeraketa da. Hautatutako oinarrizko funtzioen formulaketan, ohikoa da konpromezu bat bilatzea, funtzioaren ebazpenerako esleitzen duten hurbilketa ona izatea bilatzen da, baina baita oinarrizko funtzio hauek ahal den moduan funtzio sinpleak izatea ere espero da, beraz, bi helburu hauen arteko konpromezua da orokorrean hautagairik onena. Orokorrean, oinarrizko funtzioetarako (p) gradu jakin bateko polinomioak erabiltzen dira, hauek konputazio-metodo eraginkorra ahalbidetzen dutelako. Gradu jakin bateko polinomio baterako, sarean behar diran nodo kopurua $p+1$ da. Azter dezagun xehetasunez polinomio hauen bi aukera tipikoak: jarraian elementu linealak eta laukizuzenen erabilera aztertuko da, (2.17) adibidea erabiliz.

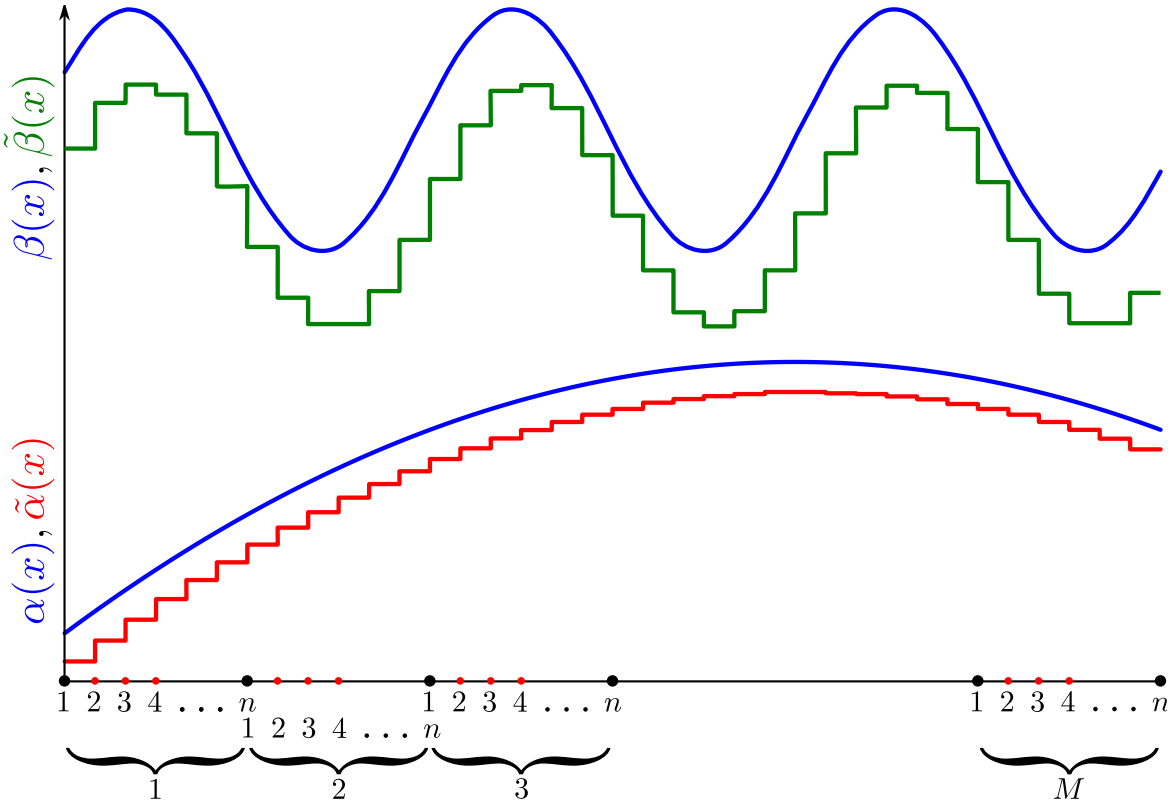

2.3. Irudia $\alpha(x)$ eta $\beta(x)$ funtzioen zatikako hurbilpenak. Hurbildutako funtzioak norabide bertikalean irudikatu dira, irudia ulerkorragoa izan dadin.

2.3.1 Elementu linealak ($p = 1$)

Teoria elektromagnetikoan erabiltzen diren ohiko oinarrizko funtzioak, batez ere hiru dimentsioetan erabiltzen direnak, elementu linealak dira, hauek elementu finitoen metodoaren efizientzia sustatzen bait dute. Elementu linealak erabiltzean, elementu bakoitzeko 2 nodo egongo lirateke eta oinarri funtzioak hauek izango lirateke (ikus 2.2) irudia).

$$\varphi_1^l(x) = \frac{x_2^l - x}{\Delta x}, \tag{2.40}$$

$$\varphi_2^l(x) = \frac{x - x_1^l}{\Delta x} \tag{2.41}$$

eta proba funtzioa honela idatzi daiteke

$$\tilde{\phi}^l(x) = e_1^l \varphi_1^l(x) + e_2^l \varphi_2^l(x). \tag{2.42}$$

$K_{ij}^{(l)}$ integrala ebaluatzeko, $\alpha(x)$ eta $\beta(x)$ funtzioen emaitz zehatza jakitea beharrezkoa da. Hala eta guztiz ere, kasu batzuetan ez da beharrezkoa datu hau jakitea, horretarako funtzio hauen zatikako hurbilketa egiten bada– 2.3 irudian argitzen den bezala–hau egiteko funtzio hauen balioa $[x_1^l, x_n^l]$ bitartean hurbiltzen da $\tilde{\alpha}_l = \alpha(x_1^l)$, $\tilde{\beta}_l = \beta(x_1^l)$ konstanteen bitartez, hurrenez hurren. Gainera, hurbilketa mota hau guztiz aproposa da hurrengo kapituluan proposatutako problemetarako, alegia kristal fotonikoen eremu elektromagnetikoen ebazpenerako. Problema hauetan, $\beta(x)$ kristal fotonikoaren errefrakzio-indizearekiko proportzinala da (dagoeneko definizioz zatietan definitutako funtzio bat dena) domeinuko sarea osatzean sarearen elementuen nodoak errefrakzio-indizearen aldaketa puntuekin bat badatoz. Baldintza honen arabera, $K_{ij}^{(l)}$ integralak analitikoki ebaluatu daitezke. Elementu linealak erabiliz, hurrengo emaitzara ailegatuko gara

$$K_{11}^{(l)} = K_{22}^{(l)} = \frac{\tilde{\alpha}_l}{\Delta x} + \tilde{\beta}_l \frac{\Delta x}{3}, \tag{2.43}$$

$$K_{12}^{(l)} = K_{21}^{(l)} = -\frac{\tilde{\alpha}_l}{\Delta x} + \tilde{\beta}_l \frac{\Delta x}{6}. \tag{2.44}$$

Adibide praktiko bat aipatzeko, elementu linealen bidez ebatzitako 1D Helmholtz ekuazioa, (2.37) ekuazio linealentzako FEM soluzioak ematen du, hurrengoarekin batera

$$\mathbb{K} = \frac{-1}{\Delta x}\begin{bmatrix} 1 & -1 & 0 & 0 & \dots\dots & 0 \\ -1 & 2 & -1 & 0 & \dots\dots & 0 \\ 0 & -1 & 2 & -1 & \dots\dots & 0 \\ \vdots & & \ddots & \ddots & \ddots & \vdots \\ 0 & \dots\dots & -1 & 2 & -1 & 0 \\ 0 & \dots\dots & 0 & -1 & 2 & -1 \\ 0 & \dots\dots & 0 & 0 & -1 & 1 \end{bmatrix}$$

$$+ \frac{k_0^2 \Delta x}{6}\begin{bmatrix} 2c_1 & c_1 & 0 & 0 & \dots\dots & 0 \\ c_1 & 2(c_1+c_2) & c_2 & 0 & \dots\dots & 0 \\ 0 & c_2 & 2(c_2+c_3) & c_3 & \dots\dots & 0 \\ \vdots & & \ddots & \ddots & \ddots & \vdots \\ 0 & \dots\dots & c_{M-2} & 2(c_{M-2}+c_{M-1}) & c_{M-1} & 0 \\ 0 & \dots\dots & 0 & c_{M-1} & 2(c_{M-1}+c_M) & c_M \\ 0 & \dots\dots & 0 & 0 & c_M & 2c_M \end{bmatrix}, \tag{2.45}$$

$$\mathbb{G} = \begin{bmatrix} -ik_0 & 0 & \dots & 0 & 0 \\ 0 & 0 & \dots & 0 & 0 \\ \vdots & \vdots & \ddots & \vdots & \vdots \\ 0 & 0 & \dots & 0 & 0 \\ 0 & 0 & \dots & 0 & -ik_0 \end{bmatrix}, \tag{2.46}$$

(2.47)

eta $\vec{q} = (-2ik_0, 0, \dots, 0)^T$ honekin batera $c_l = \tilde{n}_l^2 = n^2(x_1^l)$.

2.3.2 Elementu kuadratikoak ($p = 2$)

Soluzioaren zehaztasuna hobetzeko, maila handiagoko oinarrizko funtzioak erabili daitezke. Bereziki, elementu kuadratikoak problema fisiko ugarietan erabiltzen dira. Kasu honetan, sareko bitarte bakoitzean $p+1 = 3$ nodo aurkituko dira. Oinarrizko funtzioak (2.29) baldintzaz

mugatuta daude, hurrengoko ekuazioetara helduz (ikusi fig. 2.2 irudia)

$$\varphi_1^l = \frac{(x-x_2^l)(x-x_3^l)}{(x_1^l-x_2^l)(x_1^l-x_3^l)} = \frac{2(x-x_2^l)(x-x_3^l)}{\Delta x^2}, \tag{2.48}$$

$$\varphi_2^l = \frac{(x-x_1^l)(x-x_3^l)}{(x_2^l-x_1^l)(x_2^l-x_3^l)} = -\frac{4(x-x_1^l)(x-x_3^l)}{\Delta x^2}, \tag{2.49}$$

$$\varphi_3^l = \frac{(x-x_1^l)(x-x_2^l)}{(x_3^l-x_1^l)(x_3^l-x_2^l)} = \frac{2(x-x_1^l)(x-x_2^l)}{\Delta x^2} \tag{2.50}$$

$$\tag{2.51}$$

eta hurbilketa funtzioak honela idatzi daitezke

$$\tilde{\phi}^l(x) = e_1^l\,\varphi_1^l(x) + e_2^l\,\varphi_2^l(x) + e_3^l\,\varphi_3^l(x). \tag{2.52}$$

Suposatuz, berriro ere $\alpha(x)$ eta $\beta(x)$ zatikako funtzio baten bidez hurbildu daitezkela, $\mathbb{K}$ matrizeko elementuak erraz kalkulatu daitezke

$$K_{11}^{(l)} = \frac{7\tilde{\alpha}_l}{3\Delta x} + \frac{2}{15}\tilde{\beta}_l\Delta x, \qquad K_{12}^{(l)} = -\frac{8\tilde{\alpha}_l}{3\Delta x} + \frac{1}{15}\tilde{\beta}_l\Delta x, \qquad K_{13}^{(l)} = -\frac{\tilde{\alpha}_l}{3\Delta x} + \frac{1}{30}\tilde{\beta}_l\Delta x, \tag{2.53}$$

$$K_{21}^{(l)} = K_{12}^{(l)}, \qquad K_{22}^{(l)} = \frac{16\tilde{\alpha}_l}{3\Delta x} + \frac{8}{15}\tilde{\beta}_l\Delta x, \qquad K_{23}^{(l)} = -\frac{8\tilde{\alpha}_l}{3\Delta x} + \frac{1}{15}\tilde{\beta}_l\Delta x, \tag{2.54}$$

$$K_{31}^{(l)} = K_{13}^{(l)}, \qquad K_{32}^{(l)} = K_{23}^{(l)}, \qquad K_{33}^{(l)} = \frac{7\tilde{\alpha}_l}{3\Delta x} + \frac{2}{15}\tilde{\beta}_l\Delta x. \tag{2.55}$$

$\alpha(x)$ eta $\beta(x)$-en hurbilketa egokia kalkulatu ez den sare-elementuetan, ezinbestekoa da zuzenean integralak numerikoki kalkulatzea. Kasu hauetan, ohikoa da Gaus–Legendre-ren kuadraturaren metodoa erabiltzea integral hauek ebaluatzeko, metodo hau zehatza bait da polinomioen integralen kasuetarako [69].

2.3.3 Koordenatu lokalak eta Lagrange-ren elementuak

Oinarrizko funtzioak normalean *koordenatu lokalak* erabiliz deskribatzen dira. Koordenatu hauek ohiko d-dimensioko simplex-en bitartez definitzen dira

$$\xi_1 \geq 0, \xi_2 \geq 0, \ldots, \xi_d \geq 0, \xi_1 + \xi_2 + \ldots + \xi_d \leq 1, \tag{2.56}$$

koordenatu lokalaren espazioan aurkitzen dira. Espazio hau $\xi_1, \ldots, \xi_d$ koordenatu lokalez parametrizatuta dago. Bitarte unitarioa $d = 1$ simplex-a da. $d = 2$ simplex-a 45°-ko bi angelu osatzen dituen triangelua da, eta $d = 3$ simplex-a tetraedro bat da. Sare-elementuak simplex estandar hauen transformaketa linealak direla esan genezake. Honela, espazio globalaren koordenatuak x_i koordenatu lokalen funtzio linealak izatera moldatuz, sarearen-elementuak sinplex estandarren irudietatik lortu daitezke. Oinarri funtzioak, koordenatu lokalen arabera deskribatzen direnean forma basikoetatik geometria bat hartzen dute. Forma hauek *forma-funtzioak* dira. Funtzio hauek erraz lortu daitezke 1D-an. Kasu honetan, koordenatu lokalak transformazio linealen bitartez definitzen dira

$$\xi = \frac{x - x_1^l}{\Delta x}, \tag{2.57}$$

sare-elementu bakoitzean. Koordenatu lokalen arabera, $K_{ij}^{(l)}$ elementuen integralaren tartea $[0, 1]$ da. (2.57) ordezkatuz (2.40)-ean, elementu linealentzat forma-funtzioak lor daitezke

$$\varphi_1^l(\xi) = 1 - \xi, \tag{2.58}$$

$$\varphi_2^l(\xi) = \xi. \tag{2.59}$$

Bigarren ordeneko elementuentzat, (2.57) ordezkatuz (2.48)-ean, lor daitezke forma-funtzioak

$$\varphi_1^l(\xi) = (2\xi - 1)(\xi - 1), \tag{2.60}$$

$$\varphi_2^l(\xi) = 4\xi(1 - \xi), \tag{2.61}$$

$$\varphi_3^l(\xi) = \xi(2\xi - 1). \tag{2.62}$$

Orain arte erabilitako onarri funtzio lineal edo kuadratikoak *Lagrange-ren interpolazio-polinomioen* kasu bereziak izan dira edo, elementu finitoen terminologian, *Lagrange elementuak*. Lagrange elementu bat bere ordena edo gradua kontuan izanik bereizten da, p zenbaki positiboaren bidez adierazten dena. Φ funtzioa, elementu finitoen espazioan zatietan definitutako p graduko polinomioak dira. Funtzio hau deskribatzeko bere baloreak p graduko *Lagrange puntuetan* definitu behar dira. Puntu hauen koordenatu lokalak $1/p$-ren multiplo

osoak dira. Adibidez, 2D-ko sare triangeluar batean, $p = 2$ izanik, nodoen puntuak sarearen triangelu bakoitzaren ertzetan eta triangeluaren albo bakoitzaren erdian kokatuta daute. P_i^l nodo-puntu bakoitzarentzat, DOF $e_i^l = \Phi(P_i^l)$ bat eta oinarrizko funtzio bat $\varphi_i^l(x)$ definitzen da. Sareko elementu batentzat, ϕ_i^l oinarrizko funtzioa polinomio bat da, eta bere gradua (gehienez) k da koordenatu lokaletan, horrela i nodoan, $\phi_i^l = 1$ bete daiten, eta aldi berean, beste nodo guztietan $\phi_i^l = 0$ beteko da. Beraz, oinarri funtzioak jarraiak dira eta hauetako bat da

$$\Phi(x) = \sum_l \sum_i e_i^l \varphi_i^l(x). \tag{2.63}$$

Lehenengo graduko Lagrange elementuak elementu linealak deitzen dira. Bigarren gradukoak ordea, Lagrange elementu laukizuzenak deitzen dira. Azken hauek dira bi dimentsioetan problema elektromagnetikoak ebazteko erabiltzen direnak, aitzitik, elementu linealak hiru dimentsioetako problemetan erabiltzen dira sarritan, metodoa efizienteago egiteko. Lagrange elementuak zorizko graduetaraino definitu daitezke baina ohiko integrazio formulazioan $k \leq 5$ gradurainoko elementuak erabiltzen ditu normalean.

2.4 Plane Wave Expansion (PWE) metodoa

Plane Wave Expansion metodoa, kristal fotonikoen ikerketan gehien erabiltzen diren metodo numerikoen artean dago (baliteke ere arlo honetan erabilera handiena duen metodoa izatea). Teknika honek geometria periodiko inhomogeneoetan formulatutako Maxwellen ekuazioetatik dispertsio-diagrama eta modu optikoen soluzioak kalkulatzea ahalbidetzen du. Horretarako, materialean hedatzen diren uhin elektromagnetikoen autobalioen dekonposaketa egiten du maiztasun finitu moduak erabiliz[85]. Izan ere, PWE metodoaren bidez eremu baten eta automaiztasunen distribuzioa kalkulatzeko, funtsean, funtzio dielektrikoa eta eremu bektorearen hiru konponenteak Fourier serietan berridazten dira.

Prosezu hau azaltzeko 1D kristal fotonikoaren eredua erabili dezakegu eta puntu horretatik abiatuz, teknika bera bi eta hiru dimetsioko kasu periodikoetarako garatu daiteke modu erraz batean. Har dezagun beraz 1D kristal fotoniko bat, 2.4 irudian erakusten den modukoa.

Egitura sinple hau dielektriko ezberdinez eta era periodikoan antolatutako material dielektrikoz osatuta dago. Kristal hau ez-magnetikoa dela suposatuko dugu, PWE metodoaren planteamendua errazagoa izan dadin. 2.1 ekuazioa beste lau ekuazioetan banatu daiteke, honela, ekuazio bakoitzak eremu bakar bat soilik izango du kontuan. Horretarako eremu elektriko eta magnetikoen dibergentzia kalkulatu eta ordezkapenak eginez, hurrengo ekuazio-

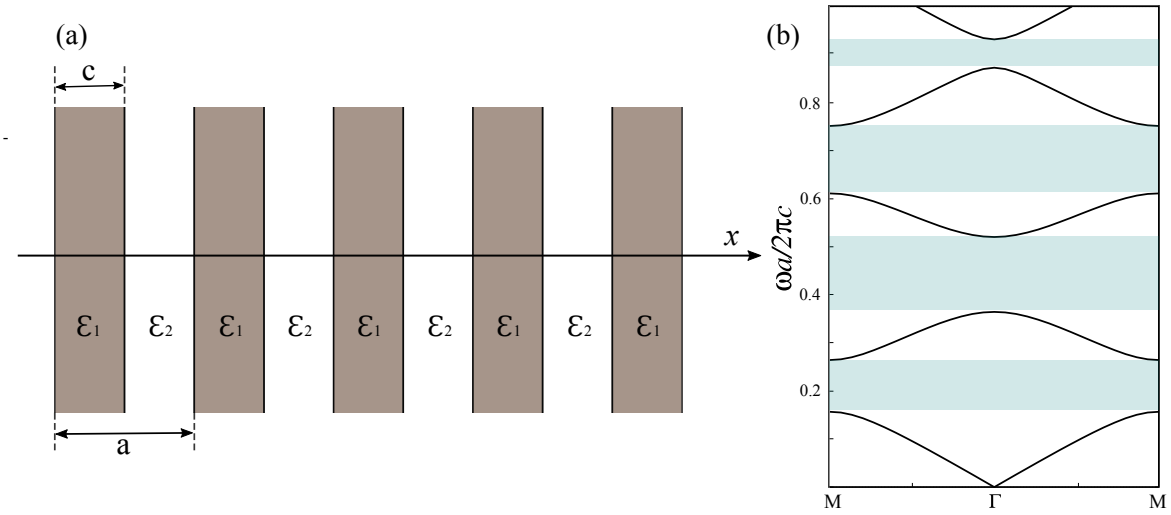

2.4. Irudia (a) Si materiala ($\varepsilon = 11.56$) eta airez ($\varepsilon = 1$) osaturiko guneak tartekatuz sortutako kristal fotonikoa. Eredu honetako egituraren gelaxka-unitatea bi material hauen artean berdin banatuta dago, hau da, $a = 2c$. (b) PWE metodoa erabiliz lortutako dispertsio diagrama. Diagrama honetan maiztasun ω eta uhin-luzeera k dimentsio gabeko unitateetan azaltzen dira. Diagrama honek 4 band gap erakusten ditu, kolore urdinez irudikatu direnak.

etara ailegatzen da:

$$\frac{1}{\varepsilon_r}\nabla\times\nabla\times\vec{E} = \frac{\omega^2}{c^2}\vec{E} \tag{2.64}$$

$$\nabla\times\nabla\times\frac{1}{\varepsilon_r}\vec{D} = \frac{\omega^2}{c^2}\vec{D} \tag{2.65}$$

$$\nabla\times\frac{1}{\varepsilon_r}\nabla\times\vec{H} = \frac{\omega^2}{c^2}\vec{H} \tag{2.66}$$

$$\nabla\times\frac{1}{\varepsilon_r}\nabla\times\vec{B} = \frac{\omega^2}{c^2}\vec{B}, \tag{2.67}$$

eremuak denborarekiko harmonikoak direla suposatuz. Gero, katearen erregela aplikatuz hiru dimentsioetako Maxwell-en ekuazioak ondorengo eran adierazi daitezke:

$$\frac{1}{\varepsilon_r}\left(-\frac{\partial^2 E_x}{\partial y^2} - \frac{\partial^2 E_x}{\partial z^2} + \frac{\partial^2 E_y}{\partial x\partial y} + \frac{\partial^2 E_z}{\partial x\partial z}\right) = \frac{\omega^2}{c^2}E_x \tag{2.68}$$

$$\frac{1}{\varepsilon_r}\left(-\frac{\partial^2 E_x}{\partial y^2} - \frac{\partial^2 E_x}{\partial z^2} + \frac{\partial^2 E_y}{\partial x\partial y} + \frac{\partial^2 E_z}{\partial x\partial z}\right) = \frac{\omega^2}{c^2}E_x \tag{2.69}$$

$$\frac{1}{\varepsilon_r}\left(-\frac{\partial^2 E_x}{\partial y^2} - \frac{\partial^2 E_x}{\partial z^2} + \frac{\partial^2 E_y}{\partial x\partial y} + \frac{\partial^2 E_z}{\partial x\partial z}\right) = \frac{\omega^2}{c^2}E_x, \tag{2.70}$$

$$\left(\frac{\partial}{\partial y}\frac{1}{\varepsilon_r}\right)\left(\frac{\partial H_y}{\partial x}-\frac{\partial H_x}{\partial y}\right)+\left(\frac{\partial}{\partial z}\frac{1}{\varepsilon_r}\right)\left(\frac{\partial H_z}{\partial x}-\frac{\partial H_x}{\partial z}\right)+\frac{1}{\varepsilon_r}\left(-\frac{\partial^2 H_x}{\partial y^2}-\frac{\partial^2 H_x}{\partial z^2}+\frac{\partial^2 H_y}{\partial x\partial y}+\frac{\partial^2 H_z}{\partial x\partial z}\right)=\frac{\omega^2}{c^2}H_x \tag{2.71}$$

$$\left(\frac{\partial}{\partial x}\frac{1}{\varepsilon_r}\right)\left(\frac{\partial H_x}{\partial y}-\frac{\partial H_y}{\partial x}\right)+\left(\frac{\partial}{\partial z}\frac{1}{\varepsilon_r}\right)\left(\frac{\partial H_z}{\partial y}-\frac{\partial H_y}{\partial z}\right)+\frac{1}{\varepsilon_r}\left(-\frac{\partial^2 H_y}{\partial x^2}-\frac{\partial^2 H_y}{\partial z^2}+\frac{\partial^2 H_z}{\partial y\partial z}+\frac{\partial^2 H_x}{\partial x\partial y}\right)=\frac{\omega^2}{c^2}H_y \tag{2.72}$$

$$\left(\frac{\partial}{\partial x}\frac{1}{\varepsilon_r}\right)\left(\frac{\partial H_x}{\partial z}-\frac{\partial H_z}{\partial x}\right)+\left(\frac{\partial}{\partial y}\frac{1}{\varepsilon_r}\right)\left(\frac{\partial H_y}{\partial z}-\frac{\partial H_z}{\partial y}\right)+\frac{1}{\varepsilon_r}\left(-\frac{\partial^2 H_z}{\partial x^2}-\frac{\partial^2 H_z}{\partial y^2}+\frac{\partial^2 H_x}{\partial x\partial z}+\frac{\partial^2 H_y}{\partial y\partial z}\right)=\frac{\omega^2}{c^2}H_z \tag{2.73}$$

$$-\frac{\partial^2}{\partial y^2}\frac{D_x}{\varepsilon_r}-\frac{\partial^2}{\partial z^2}\frac{D_x}{\varepsilon_r}+\frac{\partial^2}{\partial x\partial y}\frac{D_y}{\varepsilon_r}+\frac{\partial^2}{\partial x\partial z}\frac{D_z}{\varepsilon_r}=\frac{\omega^2}{c^2}D_x \tag{2.74}$$

$$-\frac{\partial^2}{\partial y^2}\frac{D_x}{\varepsilon_r}-\frac{\partial^2}{\partial z^2}\frac{D_y}{\varepsilon_r}+\frac{\partial^2}{\partial y\partial z}\frac{D_z}{\varepsilon_r}+\frac{\partial^2}{\partial x\partial y}\frac{D_x}{\varepsilon_r}=\frac{\omega^2}{c^2}D_y \tag{2.75}$$

$$-\frac{\partial^2}{\partial x^2}\frac{D_z}{\varepsilon_r}-\frac{\partial^2}{\partial y^2}\frac{D_z}{\varepsilon_r}+\frac{\partial^2}{\partial x\partial z}\frac{D_x}{\varepsilon_r}+\frac{\partial^2}{\partial y\partial z}\frac{D_y}{\varepsilon_r}=\frac{\omega^2}{c^2}D_z. \tag{2.76}$$

Ondoren, aurreko ekuazio hauetan deskribatzen diren eremuak Fourier serietan zabaldu ditzakegu sare periodikoen mugetan Bloch baldintzak ezarriz. 2.4 irudian aurkezten den 1D kristal fotonikoaren kasuan, materialaren konstante dielektrikoa, ε_r, x norabidean baino ez du aldakuntzarik jasotzen, eta beste norabideetan beraz, konstante izaten jarraitzen du. Arrrazoi hau dela eta, eremu elektriko eta magnetikoak ere konstante izango dira xy planoan zehar. Oro har, bi eremu hauen espazioarekiko deribatuak ezabatu egingo lirateke aurreko ekuazioetatik eta Maxwell-en ekuazioak ondorengo era sinplifikatuan adierazi ditzakegu:

$$\begin{gathered}
\frac{1}{\varepsilon_r}\frac{\partial^2 E_y}{\partial x^2}+\frac{\omega^2}{c^2}E_y=0\\
\frac{1}{\varepsilon_r}\frac{\partial^2 E_z}{\partial x^2}+\frac{\omega^2}{c^2}E_z=0\\
\frac{\partial}{\partial x}\left[\frac{1}{\varepsilon_r}\frac{\partial H_y}{\partial x}\right]+\frac{\omega^2}{c^2}H_y=0\\
\frac{1}{\varepsilon_r}\frac{\partial^2 H_z}{\partial x^2}+\frac{\omega^2}{c^2}H_z=0\\
\frac{\partial^2}{\partial x^2}\frac{D_y}{\varepsilon_r}+\frac{\omega^2}{c^2}D_y=0\\
\frac{\partial^2}{\partial x^2}\frac{D_z}{\varepsilon_r}+\frac{\omega^2}{c^2}D_z=0.
\end{gathered}$$

Bi ekuazio-sorta hauen simetria kontuan hartuz, eremuen ekuazioak lortzeko nahikoa da ekuazio hauetatik bakar bat ebaztea. Ekuazioen simetria, norabide normalean igortutako uhin bateko bi polarizazioen degenerazioak sortzen du, hori dela eta zoriz hautatutako E_z eta H_y osagaiak erabiliz jarraituko dugu azalpen hau.

$$\begin{aligned} \frac{1}{\varepsilon_r}\frac{\partial^2 E_z}{\partial x^2} + \frac{\omega^2}{c^2}E_z = 0, \\ \frac{\partial}{\partial x}\left[\frac{1}{\varepsilon_r}\frac{\partial H_y}{\partial x}\right] + \frac{\omega^2}{c^2}H_y = 0, \end{aligned} \tag{2.77}$$

Gainera, eremu magnetikoaren operadore diferentziala Hermitikoa da. Hau dela eta, ω^2/c^2 autobalioak errealak izango dira eta beraz, automaiztasuna bera duten eremuak ortogonalak izan beharko dira, operadore Hermitikoa erabiliz. Honela, kalkuloak are gehiago sinplifikatuko ditugu. H_y eremu hermitikoa duen ekuazioa erabiliz,

$$\frac{\partial}{\partial x}\left[\frac{1}{\varepsilon_r}\frac{\partial H_y}{\partial x}\right] + \frac{\omega^2}{c^2}H_y = 0, \tag{2.78}$$

Egitura periodikoaren dispertsio-erlazioa kalkulatzeko, 1D kristalaren plano periodikoa, hots x planoa, zeharkatuko duten uhin-zapal sorta bat kontsideratuko dugu. Kasu partikular honetan, ertzetako uhin-bektoreen osagaiak ezabatu daitezke, hau da $k_y = k_z = 0$, egitura honen periodizitatea dimentsio bakar batean soilik gertatzen bait da, eta beraz, k_x izango da ezabatzen ez den uhin-bektore bakarra. 1.2.2 atalean azaldu zan bezala, sarearen jatorrizko bektorea eta sare erreziprokoaren bektorea, a eta b, hurrengo eran adierazi daitezke, hurrenez hurren

$$\mathbf{a} = a\hat{i} \tag{2.79}$$

$$\mathbf{b} = b\hat{i} = \frac{2\pi}{a}\hat{i}. \tag{2.80}$$

Beste alde batetik, bektore erreziprokoaren lehenengo Brillouin gunea $[\frac{-\pi}{a}, \frac{\pi}{a}]$ tartera mugatuta dago eta 1BZ-ren zatiezina den gunea $[0, \frac{\pi}{a}]$ tartean definituta dago. 1D kristalaren simetria eta periodizitatea kontuan hartuz, x norabideko uhin-bektorearen konponentea Brillouin guneko gune zatiezinean definitu daiteke eta gero, ondorengo kalkuluak egindakoan, traslazio, rotazio eta islapen simetria operaketak aplikatuz, bektore reziprokoaren espazio osoan definituko ditugu ebaztutako eremuak [4, 85]. Banda diagramaren kalkuluekin jarraitzeko, espazio erreziprokoan definitutako konstate dielektrikoa, $1/\varepsilon_r$, zabalduko dugu, horretarako uhin plano sorta bat hedatuko dugu gelaxka-unitatean zehar [75]. Egituraren baldintza periodikoak adierazteko espazio osoan zehar, berriro ere Bloch baldintzak erabiliko ditugu. Horrela,

konstante dielektrikoa $\varepsilon_r = \varepsilon_r(x+a)$ moduan formulatuko dugu, eta beraz, eremuen ekuazioak ere funtzio dielektriko periodikoaren eta uhin-zapalen arabera formulatuko ditugu

$$\frac{1}{\varepsilon_r} = \sum_{n=-\infty}^{+\infty} \kappa(n) e^{jnbx} \tag{2.81}$$

$$H_y(k_x, x) = \sum_{m=-\infty}^{+\infty} h(k_x, m) e^{j(k_x+mb)x}, \tag{2.82}$$

non $h(k_x, m)$ uhin-zapal sortaren anplitudeak dira $e^{j(k_x+mb)x}$ adierazpenean. Hauek, m eta n zenbakiekin indizatuta daude, hurrenez hurren, eta b sare erreziprokoaren bektorearen modulua da, 2.79 ekuazioan definitutakoaren arabera. Funtzio dielektriko erreziprokoan zabaldutako Fourier koefizienteak $\kappa(n)$-ren bidez adierazten dira, eta hauek kalkulatzeko Fourier-ren alderantzizko transformatuen bidez kalkulatu daitezke

$$\kappa(n) = \frac{1}{a} \int_0^a \frac{1}{\varepsilon_r(x)} e^{-jnbx} dx \tag{2.83}$$

2.4 irudian erakusten den 1D kristal fotonikoaren kasu partikularrarekin jarraituz, konstate dielektriko periodikoa gelaxka-unitate sistema honen bidez berridatzi daiteke

$$\varepsilon(x) = \begin{cases} \varepsilon_1, & \text{for } 0 < x < c \\ \varepsilon_2, & \text{for } c < x < a \end{cases}$$

funtzio dielektriko hau erabiliz koefizienteak ondorengo moduan berridatziko ditugu

$$\kappa(n) = \frac{1}{a}\left(\int_0^c \frac{1}{\varepsilon_1} e^{jnbx} dx + \int_c^a \frac{1}{\varepsilon_2} e^{jnbx} dx \right) \tag{2.84}$$

(2.81) eta (2.82) ekuazioak (2.78) ekuazioan ordezkatuz eta uhin planoaren $e^{j(k_x+mb)x}$ faktoreari zero balioa aplikatuz $\ldots h_{-1}, h_0, h_1, h_2$ koefizienteen ekuazio linealak sortzen dira [76].

$$(k_x + bn)^2 h(k_x, m) - \sum_{m=-\infty}^{\infty} \left(\frac{\omega}{c}\right)^2 \kappa(n-m) h(k_x, m) = 0 \tag{2.85}$$

Hauen soluzioak aurkitzeko ω-k hurrengo baldintzak bete behar ditu

$$det\begin{bmatrix} \dots & \dots & \dots & \dots & \dots \\ \dots & (k-b)^2-\left(\frac{\omega}{c}\right)^2\kappa_0 & -\left(\frac{\omega}{c}\right)^2\kappa_{-1} & -\left(\frac{\omega}{c}\right)^2\kappa_{-2} & \dots \\ \dots & -\left(\frac{\omega}{c}\right)^2\kappa_1 & k^2-\left(\frac{\omega}{c}\right)^2\kappa_0 & -\left(\frac{\omega}{c}\right)^2\kappa_{-1} & \dots \\ \dots & -\left(\frac{\omega}{c}\right)^2\kappa_2 & -\left(\frac{\omega}{c}\right)^2\kappa_1 & (k-b)^2-\left(\frac{\omega}{c}\right)^2\kappa_0 & \dots \\ \dots & \dots & \dots & \dots & \dots \end{bmatrix} = 0. \tag{2.86}$$

Matrize honen tamainak k puntu bakoitzean lortuko diren autobalio kopurua finkatzen du. k aldatzen denean, autobalio bakoitza gradualki aldatzen da ere, $\omega_1(k)$, $\omega_2(k)$, $\omega_3(k)$, … funtzio jarraien arabera, 1D kristalaren sistemako banda-fotonikoen dispertsio-banden diagrama osatzeko. Horregaitik, $\omega_n(k)$ adierazpenean agertzen den n indizeari, banda-indizea ere esaten zaio [76].

2.4 irudiak Si materialez ($\varepsilon_1 = 11.56$) eta airez osaturiko hutsunez ($\varepsilon_2 = 1$) eta zabalera berdineko gerusez ($a = 2$) egindako *multilayer* baten banda diagrama aurkezten du. Dispertsio diagrama hau kalkulatzeko, 15 uhin lauak erabili izan dira, eta beraz, (2.86) ekuazioko matrizea n indizeko terminoak -12-tik 12-rako balioak ditu. Matrize sekularrean uhin lau gehiago erabiltzen direnean, maiztasun osagai gehiago kontuan hartuko dira eta dispertsio-diagraman uhin-luzeera laburragoeak ere adieraziko dira. Hortaz, dispertsio-diagraman maiztasun tarte handiagoa kalkulatu behar denean, matrize sekularraren tamaina handiagotu beharko da.

2.5 Denbora-domeinuko diferentzia finituen metodoa

Dembora-domeinuko diferentzia finituen metodoa (FDTD) uhin elektromagnetikoen inguruko problemak ebazteko erabiltzen diren metodoen artean gehien erabiltzen den metodo numerikoa da. FDTD metodoa Yee-k proposatu zuen 1996an [79] eta azken hamarkadan teknika honen ospeak gora egin du, gaur egungo ordenagailuetako baliabide konputazionalak handitu egin bait dira. FDTD metodoak nabarmenki frogatu du metodo boteretsu eta gaitasun anitzeko tresna dela, nahiz eta problema konkretu baten memoria baliabideen eskaera, simulatutako egituren bolumenarekin proportzionala den. FDTD metodoak handiak eta irregularrak diren egiturak, nahiz kristal fotonikoen kasuetan aurkitzen diren sistema periodikoen analisiak egitea ahalbidetzen du. Metodo hau Maxwell-en errotazionalen ekuazioetan oinarritzen da eta bereziki, ekuazio espazial eta denbora-ekuazioak bigarren ordeneko diferentzia finitoen bidez hurbiltzean datza. Abiapuntu hau jarraituz, domeinu konputazionala diskretizatu egiten da, problemak aztertzen dituen uhin-luzeerak baino txikiagoak diren tarteak osatzen dituen

sare bat erabiliz, eta bertako puntu guztietan materialaren propietateak zehazten dira. Jarraian, eremu elektrikoa, denboran eta espazioan desplazatutako eremu magnetikoarekin kalkulatzen da simulazio eskualdearen puntu guztietan [78].

FDTD metodoan eremuen iturriak zehaztu behar dira, gero eremu hauek eskualde konputazional osoa betetzen duen sare konputazionalaren denbora-espazio puntu guztietara hedatzeko. Horretarako, FDTD metodoan, denbora domeinuko iturri jarraiak, sinusoidalak eta monokromatikoak erabiltzen dira, gehien bat dispertsio-diagramak kalkulatzeko, nahiz iragankorrak diren iturriak, izpi gaussianoak edota dipolo itxurako iturriak erabiltzeko aukera dago, azken hauek sistemaren aspektu fisikoak aztertzeko erabilzen dira, esaterako, kristal fotoniko baten konfinatutako energia kalkulatzeko.

Metodoaren oinarri matematikoak aurkezteko, lehenbizi Maxwell-en ekuazioen diferentzia zentralaren adierazpenak deskribatuko ditugu, hauek bait dira FDTD formulazioaren ardatzak. Oinarri hauetatik abiatuz, PWE metodoan bezala, 1D kristal fotoniko baten Maxwell-en ekuazio diferentzialen kasua aztertuko dugu. Azkenik, atal honen bukaeran, 2D kristal fotoniko periodiko baten ekuazioetara helduko gara.

2.5.1 Maxwellen ekuazioen diferentzia zentralen adierazpenak

Lineala, isotropikoa eta kanpo iturririk ez duen sistema batean, Maxwell-en denboraren menpeko ekuazioak honela idatzi daitezke

$$\mu \frac{\partial \vec{H}}{\partial t} = -\nabla \times \vec{E}, \tag{2.87}$$

$$\varepsilon \frac{\partial \vec{E}}{\partial t} = \nabla \times \vec{H} - \sigma \vec{E}, \tag{2.88}$$

non μ, ε, σ, $\vec{E}$ eta $\vec{H}$ permeabilitatea, konduktibitatea, permitibitatea eta denboraren menpeko eremu elektriko eta magnetikoak diren, hurrenez hurren. Erabili dezagun horain f funtzio bat denbora eta espazioaren araberako eremu-osagaiak izendatzeko, hau da $f = f(u, v, w, t)$. Espazioaren araberako diferentzia koordinatu sistema honetan Δu, Δv, eta Δw diferentziak erabiliz adierazi daitezke, eta bitartean, denboraren araberako diferentziak Δt aldakuntzarekin izendatuko dira. Beraz, espazioaren eta denboraren araberako deribatuen hurbilketa puntu diskretuetan, bi puntu tarteen arteko diferentzia finituen bidez egin daiteke, bigarren ordeneko zehaztasunarekin

$$f(u, v, w, t) = f(i\Delta u, j\Delta v, k\Delta w, n\Delta t) = f^n_{i,j,k}. \tag{2.89}$$

Hemen, diferentzia zentralaren adierazpenean n azpi-indizearen notazioa erabili da denboraren indizea zehazteko eta i, j, k azpi-indizeak erabili ditugu espazioaren indizeak adierazteko.

Soilik f-ren lehenengo deribatuak kontsideratu ezkero, u espazioko indize eta $n\Delta t$ denbora tarte zehatzan aztertu ezkero [75, 79],

$$\frac{\partial f(i\Delta u, j\Delta v, k\Delta w, n\Delta t)}{\partial u} = \frac{f^n_{i+1/2,j,k} - f^n_{i-1/2,j,k}}{\Delta u} + O[(\Delta u)^2], \tag{2.90}$$

non $\pm(1/2)$ gehikuntzak f funtzioaren diferentzia finitua adierazten du $\pm(1/2)\Delta u$ tartean, u koordinatuaren i indizean, eta bitartean, azken terminoa, bigarren ordeneko eta orden handiagoko terminoak batzeko erabiltzen da Δu-n. Notazio honek, eremu elektriko eta magnetikoak espazioan banatzen ahalbidetzen du, eremu hauek tartekatuz espazioaren sarean, $\Delta u/2$-ko tarteetan. Ondorioz, E eremu elektrikoa ondoz ondoko H eremu puntuen tarteen arteko diferentizaren bidez kalkulatu daiteke eta banatze distantzia hau Δu izango da beti ere. Beste alde batetik, f-ren denboraren araberako lehenengo deribatu partziala, sarearen (i, j, k) puntuan

$$\frac{\partial f(i\Delta u, j\Delta v, k\Delta w, n\Delta t)}{\partial t} = \frac{f^{n+1/2}_{i,j,k} - f^{n-1/2}_{i,j,k}}{\Delta t} + O[(\Delta t)^2], \tag{2.91}$$

izango da. Kasu honetan, aldakuntzaren erdiak n denbora-indizeetan ematen dira. Algoritmoak beraz, eremu elektrikoak eta magnetikoak kalkulatzen ditu, denbora-pausuak txandakatuz, denbora tarteak $\Delta t/2$ izanik.

2.5.2 Dimentsio bakarreko kasua: TEM modua

Algoritmoaren formulaketa hau eredu sinple batez azaltzeko, espazioaren indize kopurua bakar batera mugatuko dugu eta arbitrarioki eremuen hedakuntzan galerarik ez dagoela suposatuko dugu ($\sigma = 0$), eta demagun iturri hau z norabidean hedatzen dela x ardatzeko polarizazioarekin. Beraz, berezitasun hauen arabera, Maxwell-en ekuazioak eremu elektriko eta magnetikoentzat ondokoak lirateke

$$\frac{\partial E_x}{\partial t} = \frac{-1}{\varepsilon}\frac{\partial H_y}{\partial z} \tag{2.92}$$

$$\frac{\partial H_y}{\partial t} = \frac{-1}{\mu}\frac{\partial E_z}{\partial z}. \tag{2.93}$$

Jarraian, diferentzia finitoen hurbilketa zentrala aplikatuz ekuazio hauetan, eta Δx eta Δt espazio eta denbora diskretuen tarteetan:

$$\frac{E_x^{n+1/2}(k) - E_x^{n-1/2}(k)}{\Delta t} = \frac{-1}{\varepsilon}\frac{H_y^n(k+1/2) - H_y^n(k-1/2)}{\Delta z}, \tag{2.94}$$

$$\frac{H_y^{n+1/2}(k) - H_y^n(k+1/2)}{\Delta t} = \frac{-1}{\mu}\frac{E_x^{n+1/2}(k+1) - E_x^{n+1/2}(k)}{\Delta z} \tag{2.95}$$

(2.94) eta (2.95) ekuazioetatik eta 1D kasuaren 2.5 irudian erakusten den Yee-ren eskemaren arabera, E eremuaren deribatuak $n\Delta t$ denboran, diferentzia zentralaren bidez adierazi daitezke E eremuaren balioak $\left(n+\frac{1}{2}\right)\Delta t$ denboretan erabiliz. Bereziki, (2.94) ekuazioaren ezkerreko

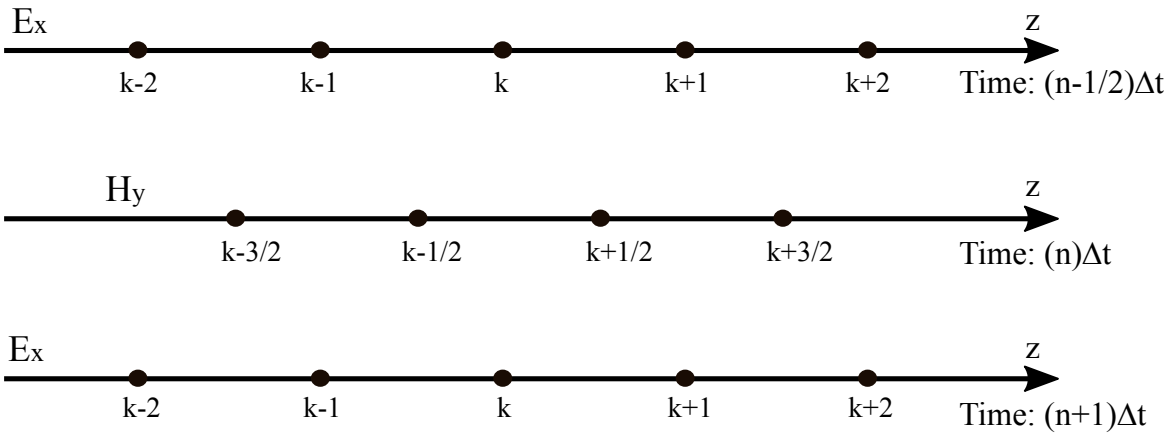

2.5. Irudia Dimentsio bakar bat aztertzerako orduan, Yee-ren eskemak hemen adierazi den eskema sinplearen itxura hartzen du. E eta H eremuak espazioan eta denboran konfigurazio hau jarraituz kalkulatuko dira.

terminoak, $\frac{\partial E_x}{\partial t}$ ekuazio zatiak E eremuaren diferentzia zentralaren hurbilketaren bidez ordezkatu daitekeela adierazten du, $\frac{\left(n+\frac{1}{2}\right)}{\Delta t}$ eta $\frac{\left(n-\frac{1}{2}\right)}{\Delta t}$ denbora tarteetan, hurrenez hurren. Ekuazioaren eskumako terminoak, H eremuari aplikatzen dio diferentzia zentralaren hurbilketa espazioko $\frac{\left(k+\frac{1}{2}\right)}{\Delta x}$ eta $\frac{\left(k-\frac{1}{2}\right)}{\Delta x}$ puntuetan, hurrenez hurren. Prozesu hau salto edo *leap frog* algoritmo izenez ere ezagutzen da, Maxwell-en ekuazioen espazio eta denborako hurbilketak egiteko lehenbizi H eremu magnetikoaren ekuazioak ebatzi behar diralako, jarraian E eremuko balio guztiak kalkulatzeko, E eta H eremuak espazioan $\frac{\Delta x}{2}$ tartez banatuta daudela jakinda. 2.5 irudiak *leap frog* algoritmoaren eskema aurkezten du. Hemendik abiatuz, (2.94) eta (2.95) FDTD ekuazio esplizituak erabiliz lortu daitezke

$$E_x^{n+1/2}(k) = E_x^{n-1/2}(k) + \frac{\Delta t}{\varepsilon \Delta z}(H_y^n(k-1/2) - H_y^n(k+1/2)) \tag{2.96}$$

$$H_y^{n+1}(k) = H_y^n(k+1/2) + \frac{\Delta t}{\mu \Delta z}(E_x^{n+1/2}(k) - E_n^{n+1/2}(k+1)). \tag{2.97}$$

E eta H eremuen anplitude ezberdinak sortzen dituzten errore numerikoak murrizteko, A.-Taflove-k normalizazio faktore bat proposatu zuen, E eremuak maila berdineko magnitudea

izan dezan [86]:

$$\tilde{E} = \sqrt{\frac{\varepsilon_0}{\mu_0}} E, \tag{2.98}$$

Beraz, normalizazio faktore hau erabiliz (2.94) eta (2.95) ekuazioetan, eta $\sim E$ baztertuz

$$E_x^{n+1/2}(k) = E_x^{n-1/2}(k) + \frac{1}{\sqrt{\varepsilon\mu}} \frac{\Delta t}{\Delta z} (H_y^n(k-1/2) - H_y^n(k+1/2)) \tag{2.99}$$

$$H_y^{n+1}(k) = H_y^n(k+1/2) + \frac{1}{\sqrt{\varepsilon\mu}} \frac{\Delta t}{\Delta z} (E_x^{n+1/2}(k) - E_n^{n+1/2}(k+1)) \tag{2.100}$$

2.5.3 Bi dimentsioko FDTD metodoa

Bi dimensioko FDTD metodoaren oinarriak erakusteko, atal honetan, z norabidean aldaezina den koordenatu sistema baten kasu partikularra aurkezten da. Beraz, z norabideko deribatu partzialak ezabatu daitezke Maxwell-en ekuazioetatik

$$-\frac{\partial E_z}{\partial y} = \mu_0 \frac{\partial H_x}{\partial t} \tag{2.101}$$

$$\frac{\partial E_z}{\partial x} = \mu_0 \frac{\partial H_y}{\partial t} \tag{2.102}$$

$$\frac{\partial H_y}{\partial x} - \frac{\partial H_x}{\partial y} = \varepsilon \frac{\partial E_z}{\partial t} + \sigma E_z \tag{2.103}$$

$$\frac{\partial H_z}{\partial y} = \varepsilon \frac{\partial E_x}{\partial t} + \sigma E_x \tag{2.104}$$

$$-\frac{\partial H_z}{\partial x} = \varepsilon \frac{\partial E_y}{\partial t} + \sigma E_y \tag{2.105}$$

$$\frac{\partial E_x}{\partial y} - \frac{\partial E_y}{\partial x} = \mu_0 \frac{\partial H_z}{\partial t}. \tag{2.106}$$

Berriro ere material ez magnetikoak, hau da $\mu = \mu_0$, hausnartzen ditugu, kristal fotoniko gehienetan ontzat hartu dezakegun sinplifikazio bat bait da, hain zuzen ere, uhin-luzeera optikoak aztertzen ditugunean. Aurreko bi ekuazio multzoetan, (2.101) eta (2.104) ekuazioak, eremu elektriko eta magnetikoen osagai bertikalak eta planoan hedatzen diren osagaiarekin erlazionatzen dituzte. (2.101) ekuazioetako kasu partikularrerako, E_z eremua da z norabideko osagai bakarra. Eremu magnetikoen kasurako, H_x eta H_y, xy planuko osagaiak dira. Beraz, osagai hauek TM polarizazioko moduak direla esango dugu. Beste alde batetik, (2.104) ekuazioetan TE polarizazioko osagaiak aurkituko ditugu. TM moduaren ekuazio diferentzialak

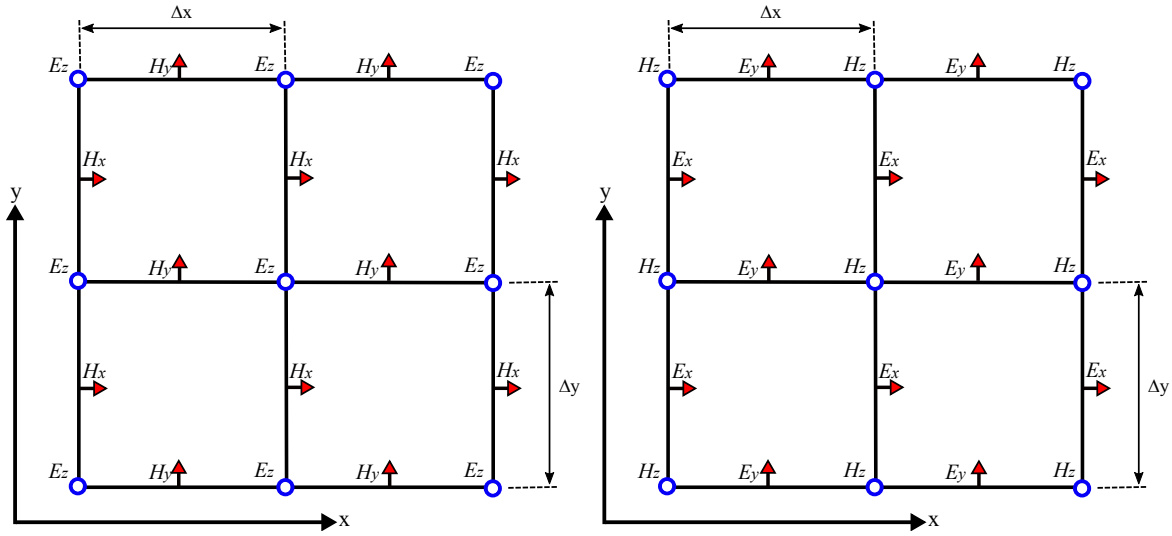

2.6. Irudia Yee-ren sarea bi dimentsioko (a) TM eta (b) TE moduen kasuetarako, hurrenez hurren. Geziek planoan hedatzen diren eremuen osagaiak adierazten dituzte, aldiz, zirkuluek planotik kanpoko norantzako konponenteak bereizten dituzte. Eremuen puntuak tartekatuta daude, $\frac{\Delta_x}{2}$ eta $\frac{\Delta_y}{2}$ banaketa erabiliz, TM eta TE sareetarako, hurrenez hurren.

diferentzia zentralaren adierazpenak erabiliz lortu daitezke

$$H_x|_{i,j}^{n+1/2} = H_x|_{i,j}^{n-1/2} - \frac{1}{\mu_0}\frac{\Delta t}{\Delta y}(E_z|_{i,j+1/2}^{n} - E_z|_{i,j-1/2}^{n}) \tag{2.107}$$

$$H_y|_{i,j}^{n+1/2} = H_y|_{i,j}^{n-1/2} - \frac{1}{\mu_0}\frac{\Delta t}{\Delta x}(E_z|_{i,j+1/2}^{n} - E_z|_{i,j-1/2}^{n}) \tag{2.108}$$

$$E_z|_{i,j}^{n+1} = \frac{\varepsilon_{i,j} - \sigma_{i,j}\Delta t/2}{\varepsilon_{i,j} + \sigma_{i,j}\Delta t/2} E_z|_{i,j}^{n} + \frac{\Delta t}{\varepsilon_{i,j} + \sigma_{i,j}\Delta t/2}\left(\frac{H_y|_{i+1/2,j}^{n+1/2} - H_y|_{i-1/2,j}^{n+1/2}}{\Delta x} - \frac{H_x|_{i,j+1/2}^{n+1/2} - H_x|_{i,j-1/2}^{n+1/2}}{\Delta y}\right) \tag{2.109}$$

non eremu elektrikoaren osagaiak $t = \frac{n}{\Delta t}$ denbora-tarteetan eta eremu magnetikoaren konponenteak $t = \frac{n+\left(\frac{1}{2}\right)}{\Delta t}$ tarteetan ebaluatzen bait dira. Jarraian, TE modurako, diferentzia

zentralaren formulazioa aplikatuz, ondorengo adierazpen diferentzialak lortuko dira

$$E_x|_{i,j}^{n+1} = \frac{\varepsilon_{i,j} - \sigma_{i,j}\Delta t/2}{\varepsilon_{i,j} + \sigma_{i,j}\Delta t/2} E_x|_{i,j}^{n} + \frac{\Delta t}{\varepsilon_{i,j} + \sigma_{i,j}\Delta t/2} \left(\frac{H_z|_{i,j+1/2}^{n+1/2} - H_z|_{i,j-1/2}^{n+1/2}}{\Delta y} \right) \tag{2.110}$$

$$E_y|_{i,j}^{n+1} = \frac{\varepsilon_{i,j} - \sigma_{i,j}\Delta t/2}{\varepsilon_{i,j} + \sigma_{i,j}\Delta t/2} E_y|_{i,j}^{n} + \frac{\Delta t}{\varepsilon_{i,j} + \sigma_{i,j}\Delta t/2} \left(\frac{H_z|_{i+1/2,j}^{n+1/2} - H_z|_{i-1/2,j}^{n+1/2}}{\Delta y} \right) \tag{2.111}$$

$$H_z|_{i,j}^{n+1/2} = H_z|_{i,j}^{n-1/2} + \frac{\Delta t}{\mu_0} \left(\frac{E_x|_{i,j+1/2}^{n} - E_x|_{i,j-1/2}^{n}}{\Delta y} - \frac{E_y|_{i+1/2,j}^{n} - E_y|_{i-1/2,j}^{n}}{\Delta x} \right) \tag{2.112}$$

Kapitulua 3

Sare infinitu eta finituen simulazio numerikoa

Orain arte, aurreko kapituluaetan kristal fotonikoen fisikan murgildu gara eta material bitxi hauen ezaugarriak simulatzeko metodo numerikoak deskribatu ditugu. Atal honek ordea, bi dimentsioko kristal fotonikoen azterketarako elementu finituen metodoaren azterketa kritiko bat jorratzen du. FE, PWE eta FDTD metodoen bitartez, banda-egitura fotonikoak, transmisio koefizienteak eta kalitate faktoreak kalkulatzen dira bi dimentsioko egitura periodiko eta aperiodikoentzat. Atal honetan aurkezten denez, FE metodoa, orain arte pentsatu denaren kontra, *Plane Wave* metodoaren autobalioen bitartez lortu daitezkeen emaitzen heineko emaitzak erreproduzitzeko gai den teknika da; izan ere, hemen aurkezten diren emaitzei begiratuz, banda-egiturak edota estatu fotonikoen dentsitateak kalkulatzeko tresna egokia dela ondorioztatu daiteke. Gainera konplexutasun arbitrarioko kluster finitoetan, eremu elektromagnetikoen denbora-harmonikoen hedapena ikertzeko baliabide erosoa da eta transmisio koefizienteak era erraz batean kalkulatzea ahalbidetzen du.

Gainera, espazio errealeko metodo hau, puntu-akatsen kalitate faktorearen kalkulurako ere erabil genezake. Azken hauek FDTD metodoarekin lortutako emaitzekin konparatzen dira. Ondorioz, FE metodo numerikoa, material konplexuetan hedatzen den argiaren azterketarako metodo numeriko fidagarria, sendoa eta zorrotza dela aurkitu dugu, egitura periodiko eta aperiodikoetan aplikatzen denean.

3.0.1 Lan honetan erabilitako FE metodoaren inplementazioa

Elementu finitoen metodoaren inplementazio libre ugari daude gaur egun [80–82], hala eta guztiz ere, gehienak elektromagnetismora, magnetoestatikara, antenen diseinura eta elektroestatikara bideratuak. Hau dela eta, kapitu honetan deskribatzen diren kalkuluak aurrera

erameteko, FE metodoaren inplementazio komertzial bat erabiltzea erabaki dugu, bereziki COMSOL multiphysics paketea [83] erabili dugu. Software hau erabiltzaearen arrazoien artean, bere CAD inguruneak egitura konplexuak sortzeko bide ezin hobea ematen duelako da. Bertan, simulatuko den egitura sortzeko tresnak ematen dira, uhin elektromagnetikoen hedapena kalkulatzeko ebazpen moduloa gehitzen du (2D eta baita 3D sistemetarako), post-prosezaketa eta eratze moduluak ditu eta MATLAB softwarrarekin lotu daiteke modu erraz batean.

Bi dimentsioetan, COMSOL-ek sare ez-egituratuak (sareko elementu triangeluarrak erabiliz) sortzeko sare eragile bat erabiltzen du Delaunnay algoritmoetan oinarritzen dena. Sarea sortu eta gero, aldagai dependienteak funtzio baten bidez (forma funtzioak) hurbiltzen dira. Hauek parametro kopuru finitu batzuen bidez deskribatu daitezke, *degrees of freedom/ askatasun graduak* deitutakoak. Hurbilketa hauek ekuazio originaletan sartuz, askatasun gradu hauentzat ekuazio sistema bat sortzen du eta ekuazio hauek *solver* edo ebazle egokiarekin ebatzi daitezke. Bereziki, hemen aurkeztuko den lehenengo problemarako, forma-funtzioak bigarren graduko Lagrange elementuak dira eta problema linealaren ebazketarako UMFPACK [84] ebazlea erabiltzen da, sistema ez simetrikoetan etekin haundiko ebazlea bait da.

Aldi berean, *Plane Wave* metodoarekin konparatzeko, MIT Photonic-Bands (MPB) softwarra erabili da, kristal fotonikoen ikerketan ohikoa [85]. Software hau guztiz bektoriala da, egitura dielektriko anisotropikoekin lan egin dezake eta gelaxka-unitate ez-ortogonalak erabiltzeko aukera aurkezten du. Gainera, konputazio paraleloa erabili daiteke, MPI-ren bitartez eta erabiltzaileak egitura dielektrikoaren ezaugarriak deskriba ditzake *script* lengoai baten bidez idatzitako kodeak sortuz. Azkenik, FE metodoaren bitartez egitura finito eta aperiodikoetan lorturiko kalitate faktoreak baieztatzeko, *harmonic inversion* metodoarekin eta FDTD [68] metodoarekin konparatu dira, azken software hauek ere MIT-en garatutakoak.

3.1 Sare karratuan oinarrituriko kristal fotonikoen simulazioen emaitzak

Lan honetan aztertutako lehenengo egitura sare karratu baten kokatutako elementu dielektriko zirkularrez osatuta dago, 3.1 irudian erakusten den modukoa. Material dielektrikoa lineala, isotropikoa eta ez-magnetikoa dela suposatzen da[1]. Zutabe zirkular hauen konstante dielektrikoaren balioa 9 da. $\frac{r}{a}$ erlazioa 0.38-koa da, non r zilindroaren erradioa bait da eta a sare parametroa. Guztiz ezaguna den egitura hau McCall-ek [94] aztertu zuen lehenengoz. Bertan,

[1] Hemendik aurrera erakusten diren materialetan ere kontsiderazio hauek inposatu dira

argiaren lokalizazioaren predikzio teorikoen eta emaitz esperimentalen arteko konparaketa zorrotza aurkeztu zuen.

Gure kasuan, topologia hau FE metodoaren eraginkortasuna frogatzeko hautatu dugu eta horretarako PWE metodoarekin konparatuko dugu, azken hau banda fotonikoen egitura kalkulatzeko metodoa bait da. Lehenengo bederatzi banda fotonikoak polarizazio transbertzal elektrikoarentzat (TE) kalkulatu ditugu, lehenengo Brillouin guneko (1BZ) ertzak delimitatzen dituzten mugetan zehar. FE kalkuluetarako, gelaxka-unitate karratua 3720 sare-elementuetan zatitu da eta Bloch-en teoremaren araberako muga-baldintza periodikoak inposatu dira gelaxka-unitatearen mugetan. MPB bidezko kalkuluetarako, 64×64 (= 4096) zatietan banatutako erresoluzioa duen sare bat osatu dugu, eta konstate dielektrikoa 9 sare-elementuetan zatitu da. Kalkulatutako banda fotonikoen egitura 3.1. irudian erakusten da. Ohikoa denez, $\omega a/2\pi c = a/\lambda$ dimentsiorik gabeko kantitatea erabili da igortutako uhin eleketromagnetikoaren maiztasuna karakterizatzeko; ω igorritako uhin elektromagnetikoaren maiztasuna eta λ uhin-luzeera direlarik.

Eremu elektrikoaren z norabidean, E_z, autobalioak kalkulatu dira 1BZ-ko simetria puntuetan, batik bat, Γ, M, eta K puntuetan eta 3.1 irudian adierazten dira. Irudi hau aztertuz, FE metodoaren bidez kalkulatutako banda fotonikoen egitura modu zehatz baten MPB-ren bidez lortutako diagrama bera aurkezten duela ondorioztatzen da. Hiru gap fotoniko zabaltzen dira egitura honetan eta hauen zabaleraren definizioan ere bi metodo numerikoak bat datoz. Gainera, FE metodoa erabiliz lortutako moduak eta MPB-ren bidez lortutakoak guztiz pareko eremuak aurkezten dituzte, soilik simetria operaketa tribial batez edota modu degeneratuen konbinaketa linealez ezberdintzen direnak.

Nahiz eta bi metodo hauen zehaztasuna eta arintasuna konparatzea ez den lan honen helburu nagusia, ezinbestekoa da honelako konparaketa bat burutzea FE metodoaren etekinaren erreferentzia bat edukiteko. MPB metodoarekiko zehaztasun erlatiboa kalkulatzeko, X simetria puntuaren bederatzigarren bandako autobalorearen errorea kalkulatu dugu, sare karratuko gelaxka-unitatearen diskretizazioaren elementu kopurua handitzen genuen bitartean. FE metodoaren kasuan, 254, 414, 928, eta 1502 elementu dituzten sare ezberdinak erabili dira eta MPB kalkuluetarako, 16×16 (= 256), 32×32 (= 1024), 48×48 (= 2304), eta 64×64 (= 4096) elementuetako sareak erabili dira. MPB-ren bidez 256×256-eko erresoluzioaz eta 25-eko sarearekin kalkulatutako autobalioak hartu ditugu erreferentzia zehatz moduan.

Konparaketaren emaitzak 3.2.a irudian erakusten dira. Azpimarragarria da FE metodoaren bidez lortutako emaitzak zehaztasun handiagoa eskuratzen duela konputazio MPB-ko metodoan erabilitako sare trinkoagoa aplikatzen denean. Emaitz hau bigarren ordeneko Lagrange elementuak erabiltzean lortzen da. Hala eta guztiz ere, bi metodoen arteko diferentziak arbuiagarriak dira aplikazio gehienetarako. Noski, FE metodoak lortutako zehaztasun honek

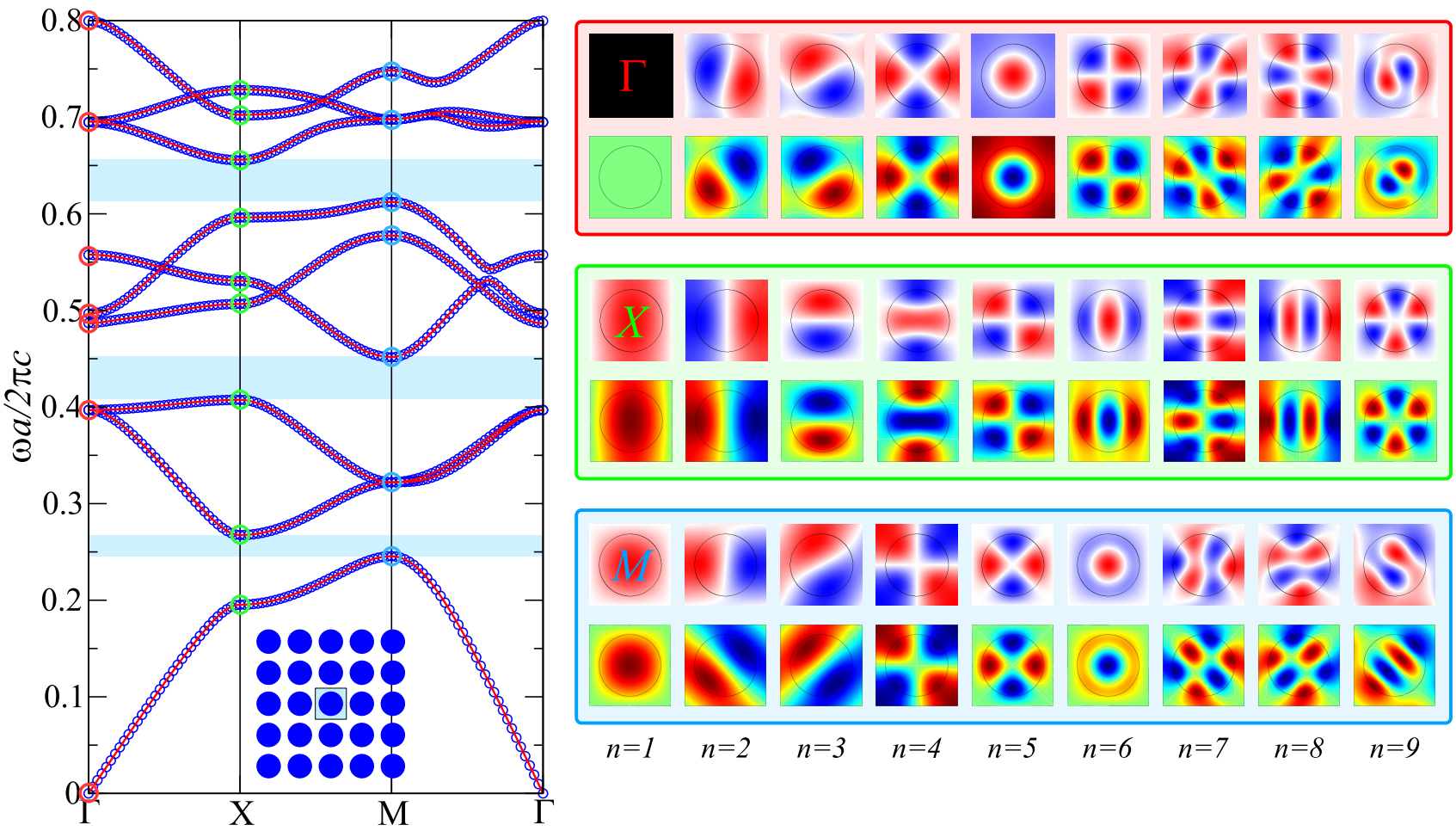

3.1. Irudia Ezkerrean: MPB (zirkulu urdinak) erabiliz eta COMSOL (zuzen gorriak) erabiliz kalkulatutako banda-egitura TE polarizatutako uhin elektromagnetikoentzat. Eskuman: MPB-ren bidez kalkulatutako E_z moduen patroiak gelaxka-unitatean (laukizuzen bakoitzeko goiko errenkadan) eta COMSOL-en bidez lortutakoak, simetria puntu berezietarako, hau da, Γ, *X*, eta *M* puntuetarako.

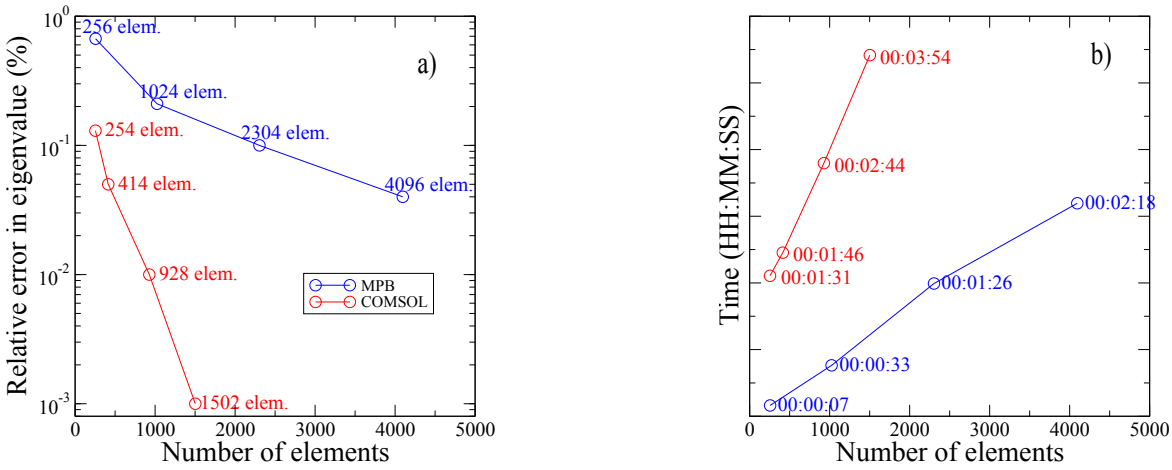

3.2. Irudia (a) Sarearen diskretizazioa egiteko erbilitako sare-elementu kopuruen araberako errore erlatiboaren eboluzioa. (b) Sarearen diskretizazioa egiteko erebilitako sare-elementu kopuruen araberako beharrezkoa izan den simulazio denboraren eboluzioa.

konputazio denbora gehiago eskatzen du, MPB metodoarekin konparatuz, 3.2.b irudian ikusi daitekeen bezala. Bertan, sarearen elementu kopuruaren araberako simulazio-denboraren garapena aurkezten da FE eta MPB metodoentzat, hurrenez hurren.

FE metodoaren bidez kristal fotoniko finituaren transmitantzia kalkulatu daiteke baita ere. Horretarako 9×9 tamainako airez inguratutako material dielektrikoko zilindroz osatutako kluster bat eraiki da. Bertan, TE polarizatutako argia hedatzen da ΓX norabidean. Kalkulu hau egiteko, 9×9-ko material dielektrikoen zilindroak 19140 sare-elementuetan diskretizatu dira[2]. Honek esan gura du konputazio honen eremu elektromagnetikoaren uhin-luzeera txikienarentzat ere ($\lambda_{\min} \approx a$) 15 sare-elementu inguru ($\omega a/2\pi c = a/\lambda = 0.25$-rentzat ≈ 35 elementu) egongo dira.

Kluster honen transmitantzia kalkulatzeko adierazpena

$$T = \frac{1}{L_y}\int_0^{L_y} E_z(L_x,y)\times E_z^*(L_x,y)\,dy, \tag{3.1}$$

eta L_α, norabidearen luzeera da α. kanpo mugan($\alpha = x,y$) norabidean. Simulazio-domeinu honen muga baldintzak honela ezarri dira: sarrera eta irteerako mugetan (ezkerreko eta eskumako mugetan, hurrenez hurren) *perfectly matched layers* baldintzak ezarri dira fisikoak ez diren erreflekzio espurioak ekiditzeko. Eremu elektrikoaren z konponenteak 1 eta 0 balioa hartzen du, simulazioaren hasierako baldintzetan, sarrera-mugan eta irteera-mugetan, hurrenez hurren.

[2]Izan ere 27644, 30392, eta 44876 sare-elementuz osatutako simulazio domeinuak ere erabili dira baina transmitatziaren ebazpenean ez da aldakuntza nabaririk aurkitu

Beste alde batetik, eroankortasun magnetiko perfektuko muga-baldintzak ezarri dira goiko eta beheko simulazio-mugetan, eremu magnetikoaren osagai tangentziala deusezteko [3], honela norabide hauetan klusterra infinituraino luzatzen dela egokitzeko.

3.3 irudiak transmitantziaren kalkulua erakusten du, kluster honetan 3.1 ekuazioa aplikatuz lortutako $[0,0.8]$ maiztasunen tartean. ΓX norabidean kalkulatutako banda-egitura ere erakusten da bertan, transmitantziak iruditutako espektroaren konparaketa egiteko. Modu honetan, transmitantziaren espektroak gap fotonikoak argi errepikatzen dituela nabaritzen da. Beste alde batetik, $\frac{\omega a}{2\pi c} = 0.4$ eta 0.7 maiztasun-tarteen inguruan soilik modu antisimetrikoak existitzen dira eta beraz, ezin dira igorritako uhin elektromagnetikoen bitartez sustatu eta beraz, banda-diagramako maiztasun tarte opakoetan aurkitzen dira. Gertaera hau sakonki aztertzen du Sakodak [5]. Zoritxarrez, MPB-ren bidez ezin daiteke transmitantzia-kalkulurik egin eta hortaz, ezinizezkoa da bi metodoen konparaketa zehatzago bat egitea aspektu honetan. 3.3 irudiko eskumaldean E_z moduaren hiru patroi aurkezten dira, a/λ maiztasun ezberdinetarako. Behekaldean irudikatutako modua $a/\lambda = 0.1$ maiztasunaren patroia aurkezten du. λ honetan, dispertsio linealaren inguruan aurkitzen denez, eremuaren patroiak ingurune homogeneo baten zehar hedatzen den uhin lau baten itxura bera du. Erdiko aldean dagoen eremuaren patroiak ordea, $a/\lambda = 0.45$ maiztasunerako kalkulatu da eta gap fotonikoan murgildutako eremuaren itxura karakteristikoa aurkezten du: eremua esponentzialki murrizten da argia kristalan zehar hedatzen den heinean, eta beraz, transmitantziaren balioa bertan zero da. Azkenik, $a/\lambda = 0.75$-eko patroi konplexuak egituraren izaera inhomogeneoaren irudi karakteristikoa aurkezten du.

3.2 Sare triangeluarran oinarritutako kristal fotonikoen simulazioen emaitzak

Kristal fotonikoen egituretan, ohikoa den beste egitura bat sare triangeluarraz osaturikoa da, sare hau aplikazio praktiko gehienetan erabiltzen bait da [4]. Arrazoi hau dela eta, garrantzitsua da FE metodoak emaitz zehatzak lortzen dituen jakitea ez-ortogonala den sare honetan. Horretarako, banda fotonikoen egitura eta transmizio-koefizienteak kalkulatu ditugu sare triangeluarran oinarritutako kristal fotoniko sorta batentzat. Kalkulu hauek ere MPB-ren bidez lortutako emaitzekin konparatu dira, metodoaren zehaztasuna frogatzeko. Konparaketa hori ez denez posiblea egitea transmitantzia emaitzetarako, lehenengo atalean deskribatutako pauso berdinak jarraitu ditugu, gap fotonikoen eta transmitantziaren espektroaren arteko zuzenezko erlazioak bilatuz. Ondorengo simulazio guztietan 12 balioa duen konstante

[3] Beste muga baldintza batzuk ere frogatu izan dira goiko eta beheko mugetan eta transmisio espektroan ez da aldaketa nabaririk sumatu

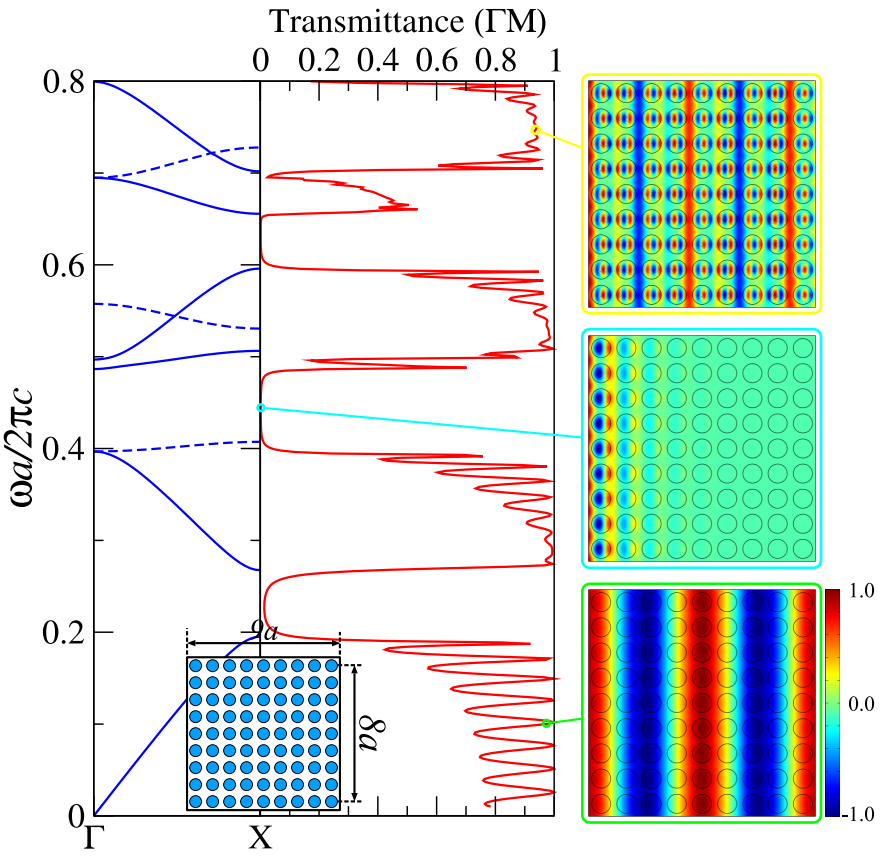

3.3. Irudia Sare karratuan antolatutako eta airez inguratutako zutabez osatutako kristal fotonikoaren dispertsio-diagramaren (ezkerraldean) eta transmitantzia-diagramaren (erdikaldean) arteko konparaketa. Diagrama hauetan TE-polarizatutako uhin elektromagnetikoak ΓX norabidean kontsideratu dira. Banda-egituran agertzen diren zuzen etenak akoplatu ezin diren moduak adierazten dituzte. Irudiaren xehetasunean transmitantzia kalkulatzeko erabili den kristal fotonikoaren klusterra erakusten da. Zirkulu urdinak material dielektrikoa adierazten dute eta karratuak simulazio-eskualdearen mugak erakusten ditu. Eskumaldean E_z eremuaren hiru patroi erakusten dira, $\omega a/2\pi$-ren hiru baliorentzat, 0.1, 0.45, eta 0.75, azpitik gora, hurrenez hurren.

dielektrikoko materiala erabili da. Atal honetan aztertu den lehenengo egitura fotonikoa, sare hexagonal baten antolatutako eta airez inguratutako zilindro dielektrikoz osatutako sistema da (ikusi 3.4 irudiko xehetasuna). Zilindro hauen erradioa $0.12a$ da. Simulazioaren konfigurazioa sare karratuan erabilitakoaren oso antzekoa da: FE banda fotonikoen kalkulurako, gelaxka-unitate 1086 elementuetan zatitu da eta muga-baldintza periodikoak ezarri dira simulazioaren ertzetan. ΓM norabidean kalkulatutako transmitantziaren emaitzak lortzeko, 12×8-ko gelaxka-unitate dituen kluster bat sortu da eta hau 60748 sare-elementuetan zatitu da. ΓK norabidean kalkulatutako transmitantzia lortzeko, 11×10-ko gelaxka-unitate dituen klusterra erabili da 67282 sare-elementuetan banandua izan dena. Sare karratuan erabilitako muga-baldintza berak erabili ditugu kasu honetan ere. 3.4 irudian banda fotonikoen egitura, ΓM eta ΓK norabideetan transmitantzia espektroa eta baita TE polarizatutako uhin elektromagnetikoen eremu patroiak erakusten dira. FE metodoaren bidez kalkulatutako banda-egiturak era oso fidagarri baten erreproduzitzen ditu MPB-ren bidez lortutako emaitzak. Egitura honek, TE polarizazioarentzat, lehenengo eta bigarren banden artean gap bat aurkezten du eta gap hau argi ikus daiteke ere transmizio espektroa aztertuz gero, bai ΓM, eta baita ere ΓK norabideetan marrazten bait ditu opakoak diren maiztasun tarte hauek.

Gainera, badaude beste gap partzial batzuk ere, bigarren eta hirugarren banden artean, nahiz laugarren eta bostgarren banden artean agertzen diren modukoak. Hauek ΓM norabidean ikus daitezke, baina ΓK norabidean aldiz, desagertzen dira. Beste alde batetik, gap hauekin erlaziorik ez duten gune opakoak ere badaude. Banda-egituran agertzen diren gune opako hauek akoplatu ezin diren moduekin erlazionatzen dira, bostgarren bandan agertzen denaren modukoa, ΓK norabidean desakoplatuta dagoena.

Sare hexagonalean aztertutako bigarren egitura $r = 0.25a$ erradioko zilindro dielektrikoz osaturiko sistema da (ikusi 3.5-an adierazten den egituraren xehetasunak) eta kasu honetan TM polarizatutako uhin elektromagnetikoaz irradiatutako fenomenoak aztertu ditugu. Banda fotonikoen egitura kalkulatzeko, 942 sare-elementu erabili dira. Nahiz eta sare-elementu kopuru hau baxua den, konputazioaren zehaztasun-maila harrigarria da, MPB-rekin konparatu ezkero, 3.5 irudian ikus daitekeen moduan. Gainera, FEM-en bidez kalkulatutako H_z modu-patroiak eta MPB-ren bidez kalkulatutakoak guztiz bat datoz.

Transmitantziaren kalkuluetarako orain arte jarraitutako pausu berdinak errepikatu ditugu, baina kasu honetan PEC muga baldintzak erabili dira goiko eta beheko mugetan, kristalaren muga fisikoak infinituraino luzatzearen efektu bera sortzeko. Horretaz aparte, transmitantzia kasu honetan honela definitu dugu

$$T = \frac{1}{L_y} \int_0^{L_y} H_z(L_x, y) \times H_z^*(L_x, y)\, dy. \tag{3.2}$$

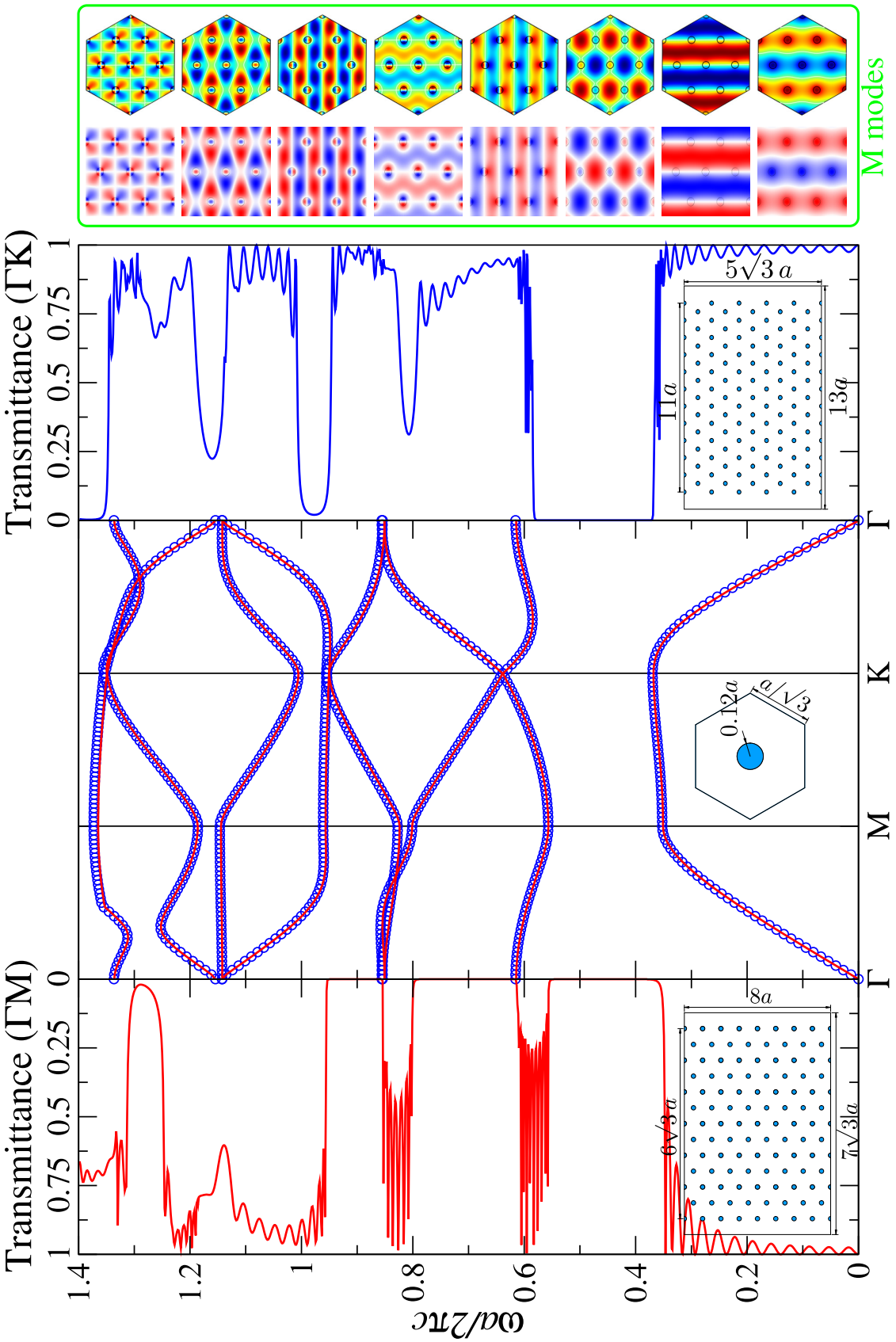

3.4. Irudia Ezkerrean: Xehetasunean agertzen den kristal fotonikoaren klusterrean burututako TE-polarizazio duten uhinen transmitantzia diagrama Γ*M* norabidean. Erdiko partean: COMSOL (zuzen gorriak) eta MPB (zirkulu urdinak) erabiliz lortutako banda-egituraren arteko konparaketa TE polarizatutako uhin elektromagnetikoentzat 1BZren mugettan zehar. Irudiaren barneko xehetasunean kalkulu hauek burutzeko erabili dan gelaxka-unitatea aurkesten du. Eskuman: Γ*K* norabidean kalkulatutako transmitantzia TE polarizazio duten uhin elektromanetikoentzat, xehetasunean agertzen den kluster hexagonalean kalkulatu da. Rektangulo berdearen barruan: MPB (ezkerrean) eta FE (eskuman) metodoak erabiliz, *M* puntuan kalkulatutako E_z eremu patroien arteko konparaketa, lehenengo zortzi bandetarako (banda indizeak azpitik gora ordenatuta daude).

ΓM eta ΓK norabideetan erabilitako sare-elementu kopuruak, 37760 eta 42270 izan dira, hurrenez hurren. Aztertutako egitura honek ez du gap osorik aurkezten maiztasun tarte honetarako behintzat. Aitzitik, gap partzial batzuk aurkezten ditu, 3.5 irudiko transmisio espektroak adierazten duen bezala.

Sare hexagonalean oinarritutako hirugarren egiturak, dielektriko xafla baten zulotutako eta airez betetako zilindroz osatzen da. Zulo zilindriko hauen erradioa $r = 0.34a$ da. Sistema honen diagrama 3.6 irudian ikusi daiteke. Kasu honetan TE polarizatutako uhinak kontsideratu ditugu. FE metodoaren bidez banda fotonikoen egitura lortzeko, gelaxka-unitatea 896 sare-elementuetan zatitu da eta muga baldintza periodikoak ezarri dira hexagonoaren simulazioaren mugetan. Aurreko kasuetan bezala, FE metodoa erabiliz lortutako emaitzak eta MPB-ren bidez lortutakoak konparatuz ez da kontraesanik aurkitzen. Transmitantzia kalkulatzeko ere ohiko konfigurazioa erabili dugu simulazioa egiteko. Kasu honetan, 26528 eta 29984 sare-elementu erabili dira ΓM eta ΓK norabideetan transmisio koefizienteak kalkulatzeko, hurrenez hurren.

Aurreko kasuetan bezala, bi norabide hauetan zehar transmitantziaren kalkuluak dispertsio-diagraman lortutako gap-ekin erlazionatzen dira, modu ezinobean. Nolanahi ere, maiztasun tarte batzuetarako modu batzuk ezin dira akoplatu, bostgarren eta zazpigarren bandetan gertatzen den moduan, ΓM eta ΓK norabideetarako).

Bukatzeko, laugarren egitura bat ere aztertu da. Sare hexagonala jarraitzen duen sistema hau, $r = 0.23a$ erradioko airezko zulo zilindrikoz osatzen da eta 3.7 irudian bereizten da egitura hau. Kasu honetan TM polarizatutako uhin elektromagnetikoak erabili dira. FE metodoa erabiliz banda fotonikoen egitura kalkulatzeko, gelaxka-unitatea 620 sare-elementuetan zatitu da eta muga baldintza periodikoak erabili dira hexagonoaren mugetan. Transmitantziaren espektroa kalkulatzeko, aurreko konfigurazio bera erabili izan dugu, bereziki, TM argiaz irradiatutako dielektriko zilindroz osaturiko sisteman erabilitakoa. Transmitantian erabilitako sare-elementu kopurua, kasu honetan, 40690 eta 45488 da, ΓM eta ΓK norabideetan, hurrenez hurren. Aurreko kasuetan bezala, FE metodoa erabiliz lortutako banda fotonikoen egitura eta MPB bidez lortutakoa bat datoz. Gainera, transmitantziak bi norabide hauetan argi adierazten ditu banda-egituraren xehetasunak.

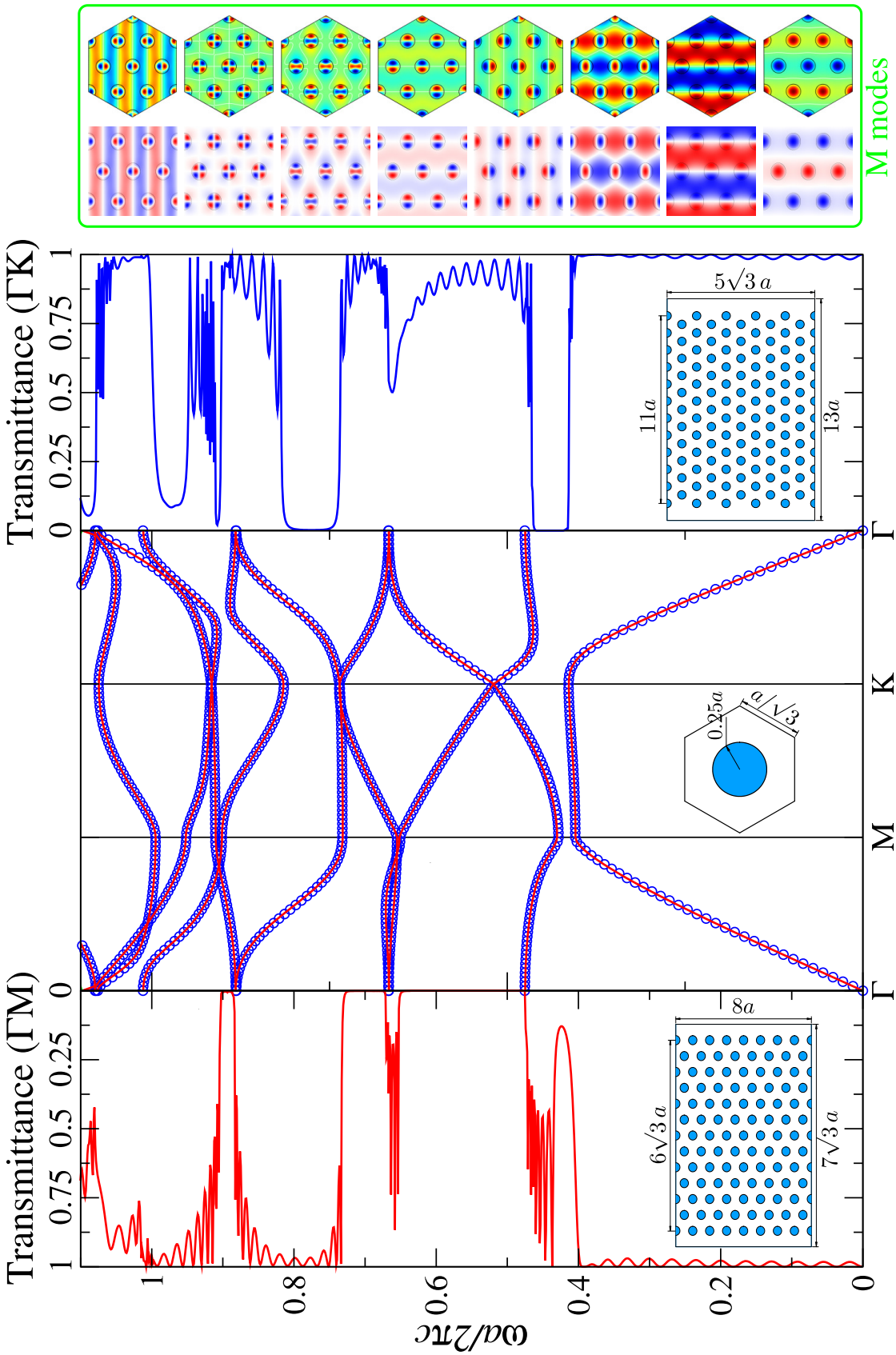

3.5. Irudia 3.4 irudiaren antzeko simulazioa, baina kasu honetan TM-polarizatutako uhin elektromagnetikoak erabili dira. Gainera, zilindroen erradioak $0.25a$-ko neurria du horain eta H_z eremuaren patroiak M puntuan kalkulatu dira.

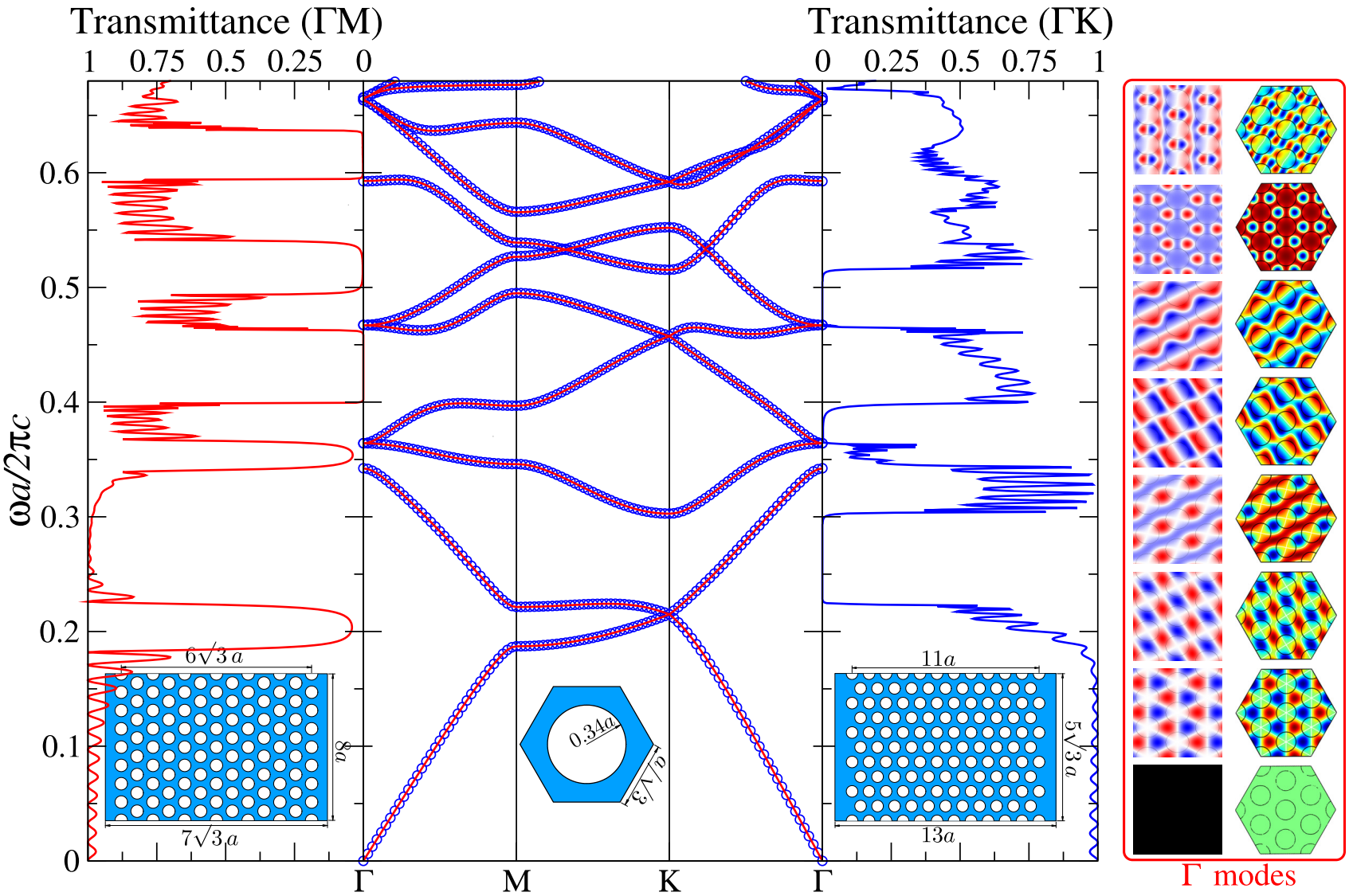

3.6. Irudia 3.4 irudiaren antzeko simulazioa, baina kasu honetan airez betetako zuloz osatu da kristal fotonikoa, material dielektriko baten xafla baten gainean (beraz, alderantzizko egitura da hau). Gainera, airea duten zuloen erradioa $0.34a$-ko neurria du horain eta E_z eremuaren patroiak Γ puntuan kalkulatu dira.

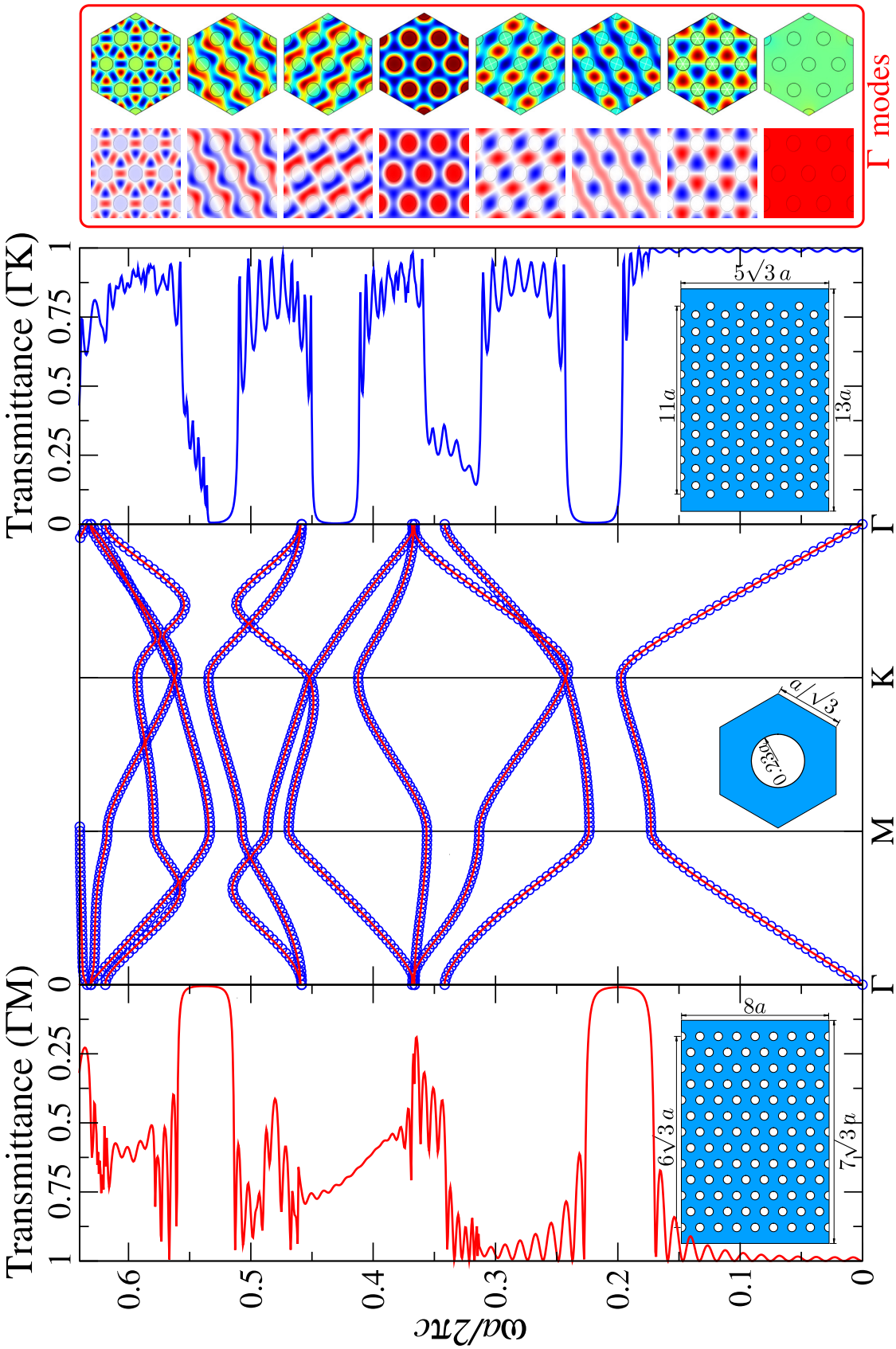

3.7. Irudia 3.6 irudiaren antzeko diagrama, baina kasu honetan TM-polarizatutako uhin elektromagnetikoak erabili dira. Zilindroen erradioa horain $0.23a$-koa da eta eremuaren patroiak H_z konponentearenak dira Γ puntuan.

3.3 2D kristal fotonikoen supersareetan egindako akatsak

Orain arte ikusi dugunez, kristal fotonikoen propietate fisikoak oso interesgarriak dira eta aplikazio berrien iturri izateko potentzial haundia dute. Hala eta guztiz ere, semieroaleetan gertatzen den bezala, desordenatutako kristal fotonikoen fisikak aplikazio berrien eta interesgarriagoen oinarria da. Kristal fotoniko hauen artean, akats puntualen bitartez argiaren lokalizazioa sustatzen duten egiturak bereziki interesgarriak dira telekomunikazio arloko aplikazioetan. Akats hauen egitura garrantzitsuak eraikikiteko sistema bikainak dira, argia akatsan lokalizatzeko egitura aproposak bait dira. Hauen bitartez faktore kalitate haundiko mikro–kabitate optikoak egin daitezke, gaur egundo beste kabitateak baino askoz ere dimentsio txikiagotan eta intentsitate handiagotan lokalizatzen bait dute argia. Gainera, akats hauek lerro batean irudikatuz gero, uhin elektromagnetikoen gidaketa bikaina lortzeko egiturak era erraz batean lortzeko aukera ematen dute, zuntz optikoen bidez lortzen den gidaketan baino galera baxuagoak eragiten dituztenak. Egitura hauek sortzen dituzten argiaren lokalizazioaren propietate fisikoak oso ulergarriak dira.

Prozesua errazteko, sortu dezagun lehenengo puntu akats bat egitura guztiz periodiko baten oinarrituz. Akats gabeko egitura periodiko baten, aurreko kasuetan ikusi dugun bezala, gap fotonikoak agertzen dira hau da modu optikoak desagertzen diren maiztasun tarte bat zabaltzen da. Bertan, agertaratzen diren modu optikoak uhin bektore konplexuak dituzte, eta beraz esponentzialki murrizten da haien anplitudea gune hauetan. Horrelako egituretan akats puntual bat sortzerakoan, modu zehatz baten agerpena baimentzen da gap honen barruan. Akats honetatik kanpo berriro ere moduaren anplitudea esponentsialki galtzen da. Sistema erreal batean ordea, modu hauen galera esponentsialak kristalaren mugetara helduko dira eta denborarekin, Akatsean lokalizatuta dagoen argiak ihes egingo du. Arrazoi hau dela eta, ohikoa denez, puntu akatsetanf kokatutako modu optikoak modu erresonante deitzen dira, denboran mugatutako existentzia bait dute modu hauek. Puntu akatsak sortzeko, normalean, kristal fotonikoaren elementuetan aldaketa batzuk sortarazten dira, esaterako, elementu baten edo batzuren konstante dielektrikoa nahiz hauen tamaina aldatzen da, edota bi aukera hauek konbinatuz egiten da.

Lerro akats bat sortzeko prozesu berdina aplikatu daiteke, jarraian dauden elementu sorta batzuk hautatuz. Gap honen barruko argia lerro akatseko norabidean hedatu daiteke soilik eta lerro honen albo mugetan argia konfinatuta egongo da. Ondorioz, argiaren gidaketa bikaina sortzen da, eta indizearen gidaketa-mekanismoaren limitazioz kanpo dagoen argiaren kontrol osoa eskuratu daiteke. Guzti hau dela eta ulergarria da egitura hauen eaugarri fisikoak antzemateko tresna numerikoen garapenak duen garrantzia azpimarratzea. Orain arte, akatsak dituzten kristal fotonikoen azterketa egiteko gehien erabilitako teknika numerikoen artean

supergelaxka baten aplikatutako maiztasun metodoak izan dira, aurreko kapituluan azaldu diren modukoak. Jokaera hau oso ezaguna da akatsak dituzten beste material batzuetan tradizionalki aplikatzen bait da, esaterako semieroaleen elektronikan edo ez-purutasun ez-magnetikoen azterketarako magnetismoko esparruan.

Puntu akats bat duten kristal fotonikoen azterketaren hildoa asko eta luze landu da dagoeneko, beste aplikazioen artean, puntu kuantikoen eta erresonantzia kabitateen arteko bateratzea sustatzeko modu aproposa bait da, eta sistema honen bitartez puntu kuantikoen argi igorleak sortu daitezkelako [87]. Gainera, laser igorleen atalasea murrizteko ere proposatu dira egitura hauek [88]. Beste alde batetik, fisikaren beste atal eta aplikazioetarako ere proposatu dira puntu defektodun kristal fotonikoak. Beste akoren artean, antenen direkzionalitatea sustatzeko [89], memoria optikoak sortzeko [90, 91], PC-VCSEL laser berriak sortzeko [92] eta bio-sentsore [93] gailuak sortzeko erabili daitezke.

Atal honetan erabili izan diran simulazioetan, egituraren periodizitate ohia apurtu egin dugu, akats puntual bat sortzeko eta band gap gunearen bitartean estatu lokalizatu bat sortzeko asmoarekin. Argi hau kaiolatuta geratuko da band gap efektuaren eraginez, behintzat, galera dakarren beste mekanismorik egongo ez balitz. Kristal fotoniko hau oraindik gelaxka-unitatearen metodologia erabiliz aztertu genezake, baina horretarako, gure gelaxka-unitatean kokatzen diren dielektriko zutabe kopuruaren hautaketa egokia egin behar da. Kopuru hau nahikoa denean, ggelaxka-unitatearen errrepikamen prozesuan, ondoko akatsen eragina arbuiagarria izan behar da, hau da muga baldintza periodikoek sorturiko defektruen gainazarmena ekiditzeko gai izan behar da. Beste alde batetik, zutabe bakarra aldatuarazi den kristal hauetan, simetria rotazionala mantendu egiten da. Hortaz, nahiz eta ondorengo kristal fotonikoetan sarearen periodizitatea hautsi dugun, oraindik, posiblea da hauen banda fotonikoen egiturak kalkulatzea eta hauek aurreko kristal fotonikoekin konparatzea, 1BZ-ren ertzeko estatuak ahusnartuz.

3.3.1 Sare karratuan antolatutako zutabeetan egindako akatsa-puntua: McCall-en esperimentua

Zutabe dielektrikoz osaturiko sare periodiko baten barruan lortutako argiaren lokalizazioa McCall-ek [94] aurkeztu zuen, bertan saiakera esperimentalen bidez emaitzak jakinaraziz. Gure lan honetan, McCallek aztertutako kasutik abiatu gara. Egitura horren ezaugarriak FE eta PWE [85] metodoen ikuspegitik aztertu ditugu eta emaitzen konparaketa aurkezten dugu. 3.8 irudian McCallen esperimentuan erabilitako konfigurazioari dagokion dispertsio-diagrama erakusten da. Bertan, sare karratua duen kristalaren erdian kokatutako dielektriko zutabe zilindriko bakar bat kendu da. Sare horretako zilindroen erradioa $0.38a$-koa da

eta konstante dielektrikoak 9 balioa hartzen du, McCallen konfigurazioan adierazten dan bezala. FE metodoaren bidezko kalkuluetarako 5×5 tamainako super-gelaxka bat osatu da. Simulazio-eskualde hori 95903 sare-elementuetan zatitu da. MPB-ri dagokion super-gelaxkarako 3096 sare-elementu dituen sare bat sortu da. Eremu elektrikoaren z-osagarriaren zati erreala kalkulatu da, $a/\lambda = 0.4686$ maiztasunean 1BZ-ko Γ simetria puntuan.

Super-gelaxka bat erabiltzearen eragozpen nagusia *band-folding* efektuaren agerpena da. Efektu horren eraginez gelaxka-unitatearen banda-fotonikoak N biderrez dolezten dira dispertsio-diagraman (N super-gelaxkaren dimentsio lineala delarik). Efektu hau dela eta, beharrezko konputazio-denborak gora egiten du, kalkulatutako autobalioen kopurua $\sim N$ biderrez handitzen bait da. Hortaz, K-espazioan 211 puntuetarako 100 banda kalkulatu ditugu, bi metodoen bitartez.

3.8 eta 3.9 irudietan aurkezten den moduan, McCall-en emaitzatarako MPB-ren bidez lortutakoak eta FE metodoa erabiliz jasotako emaitzak guztiz bat datoz.

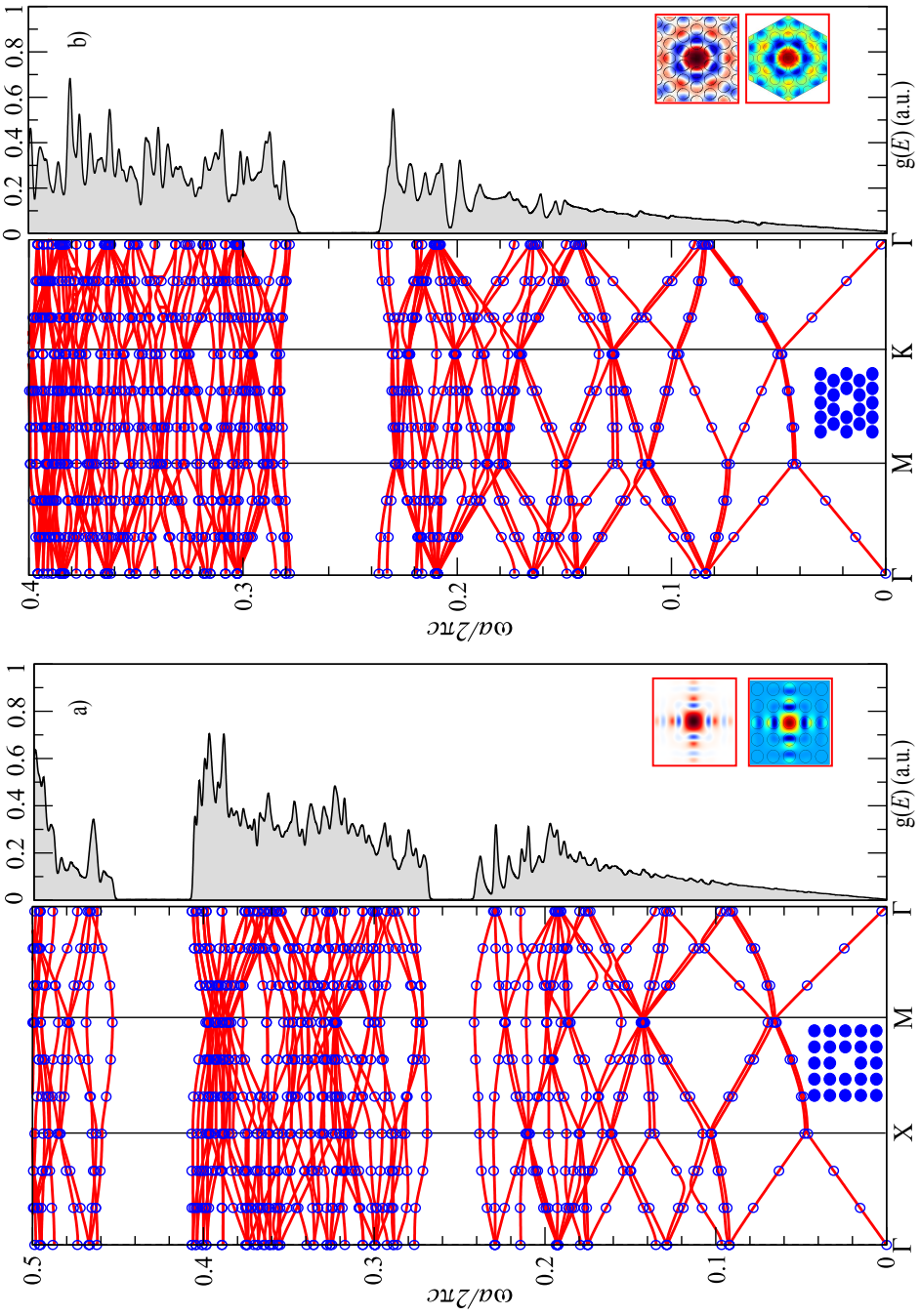

3.8. Irudia (a) Ezkerrean: 5×5 sare karratuan antolatutako super-gelaxkaren banda-diagrama, MPB-ren bidez kalkulatu izan dana (zirkulu urdinak) eta baita FE metodoa erabiliz (zuzen gorriak) simulatutakoa. Egitura honek modu defektu bat dauka $\frac{\omega a}{2\pi c} = 0.466 \pm 0.002$ inguruan. Eskuman: FE metodoa erabiliz lortutako estatu fotonikoen dentsitatea (DOS). Grafiko honetan erraz antzeman daiteke kristalak sortutako gap tartea, baita akats-modua ere. Irudi honen barruko xehetasunak 5×5-eko super-gelaxkan FE eta MPB erabilita lortutako E_z eremuen patroiak, M simetria puntuarentzat, erakusten dira. (b) Ezkerrean: 5×5-eko sare triangeluarran antolatutako super-gelaxkaren banda-diagrama, MPB-ren bidez kalkulatuta (zirkulu urdinak) eta baita FE metodoaren bidez (zuzen gorriak) lortutakoa. Berriro ere defektu bakar bat agertzen da, kasu honetan $\frac{\omega a}{2\pi c} = 0.285 \pm 0.003$ inguruan. Eskuman: FE metodoa erabiliz lortutako estatu fotonikoen dentsitate diagrama. Irudi honen barruko xehetasunak 5×5-eko super-gelaxkan FE eta MPB erabilita lortutako E_z eremuen patroiak, Γ simetria puntuarentzat, erakusten dira. FE metodoaren kalkulu hauek egiteko super-gelaxka hexagonal bat erabili da.

Egitura honek bi band-gap ingurune azaltzen ditu, $\frac{a}{\lambda} = 0$ eta $\frac{a}{\lambda} = 0.5$, dimentsio gabeko maiztasunetan, ($\tilde{\omega} = \frac{a}{\lambda}$), hurrenez hurren. Band gap tartea zeharkatzen duten bi modu ikusi daitezke 3.8.a irudian, baina soilik akats-moduak kontzentratzen du energia geometriaren hutsunearen inguruan. Estatuen dentsitate diagramak (DOS) zutabe bakar baten aldaketaren eragina aurkezten du ere. Hain zuzen ere, estatu defektuaren maiztasunean kokatutako Dirac motatako perturbazioak sortzen direla erakusten du. DOS kalkulu horiek ere FE metodoa erabiliz lortu izan dira, 1IBZ gunean k-puntu aleatorioen energiak erabiliz, sare bakoitzean. Uhin-luzera altuen limitean, kantitate honek bi dimentsioko material dielektriko homogeneoetan ohikoa den hedapen egoera aurkezten du.

3.3.2 Zutabez osatutako sare triangeluar baten sorturiko akats puntuala

Antzeko egoera sortu daiteke sare triangeluar baten zutabe bat ezabatzen denean. 3.8.b irudiak Smith et al.-ek [95] sare karratuetan eta triangeluarretan sortutako akatsen propietateak ikertzeko erabilitako parametroen araberako kristal fotonikoen simulazioen emaitzak adierazten dira. Super-gelaxka triangeluar horretako kristal fotonikoaren konstante dielektrikoen parametroak eta zutabeen erradioak, lehen, 3.8a irudiko sare ortogonalean erabilitakoen berdinak dira, eta berriro ere FEM kalkuluak eta PWE metodoaren bidez lortutako emaitzak guztiz bat datoz.

Simulazio-eskualdearen ezaugarriak, lehen sare karratuan erabilitakoaren berdinak dira, salbuespen batekin, orain super-gelaxkaren diskretizazioan 71376 sare-elementu erabili dira. Gainera, super-gelaxka hexagonal bat erabili da FEM kalkuluetarako, geometria horrek sare triangeluarraren sare erreziprokoarekin bat datorrelako. Bi kasuetan, sare karratu eta triangeluarrean egindako akats puntuala duten super-gelaxketan, eremu elektrikoaren z–osagarria akatsaren inguruan lokalizatuta dago, eta hortik kanpo, hutsunetik kanpo, bildutako energia esponentzialki galtzen da.

Gainera, sarearen ingurunetik kanpo, auto-funtzioak berezko simetria bat aurkezten du, konkretuki, bi sare hauetan modu defektuak monopolo patroi baten itxura du, zutabe dielektrikoaren erdian plano nodal bat bait du [4]. Akats-puntu horren simetriaren ezaugarrietaz xehetasun gehiago irakurteko irakurleak [96]-n aurkituko du informazio gehiago.

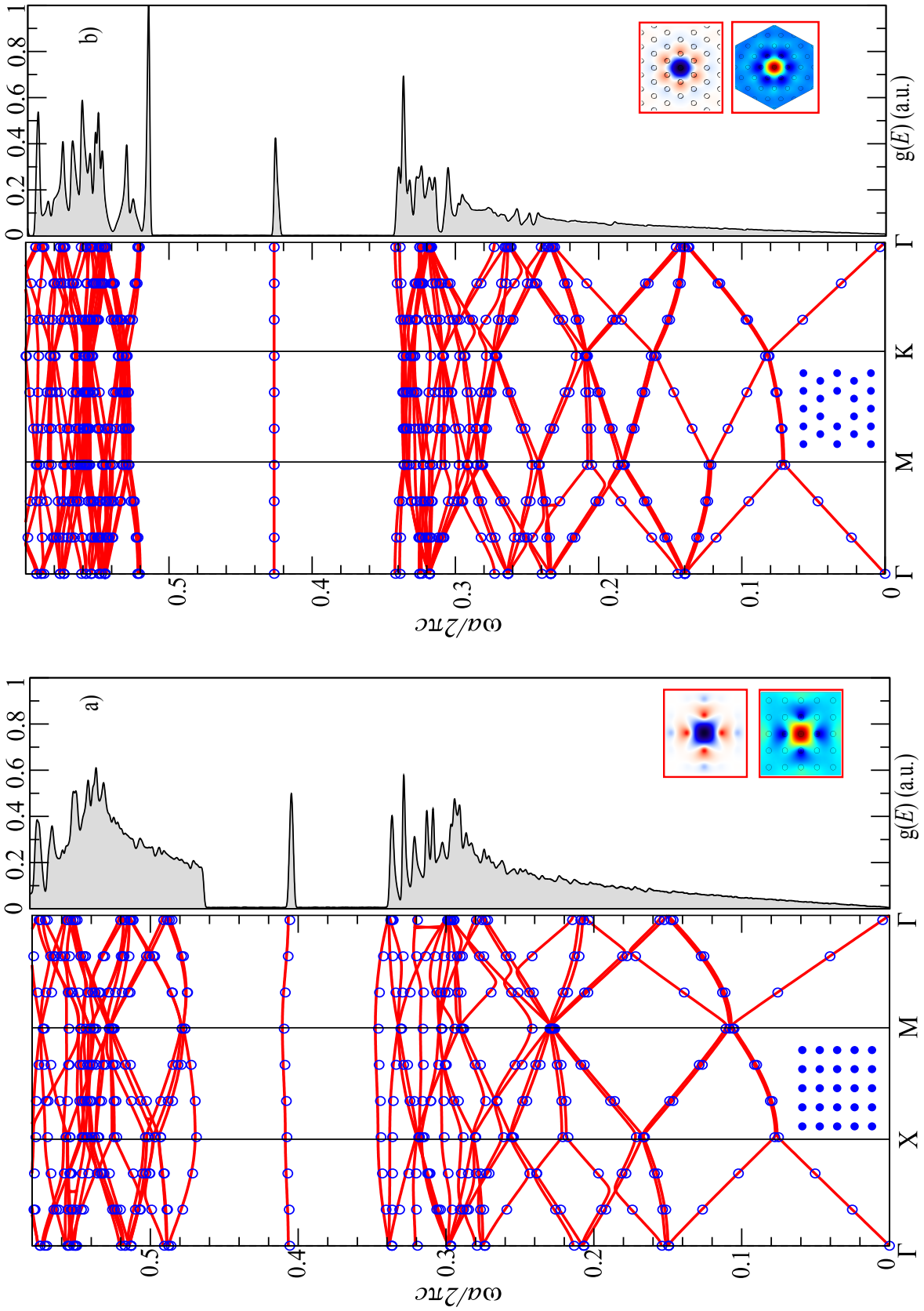

3.9. Irudia (a) Ezkerrean: 5×5 sare karratuan antolatutako super-gelaxkaren banda-diagrama, MPB-ren bidez kalkulatu izan dana (zirkulu urdinak) eta baita FE metodoa erabiliz (zuzen gorriak) simulatutakoa. Kasu horretan, zutabeen erradioa $0.17a$-ra aldatu da, honela lokalizazio hobeagoa lortzen bait da. Eskuman: FE metodoa erabiliz lortutako estatu fotonikoen dentsitatea (DOS). Grafiko horretan erraz antzeman daiteke kristalak sortutako gap tartea, baita modu defektua ere. Irudi honen barruko xehetasunak 5×5-eko super-gelaxkan FE eta MPB erabilita lortutako E_z eremuen patroiak, M simetria puntuarentzat, erakusten dira. Eremu patroi horiek bat datoz 3.8.a irudian aurkeztutakoekin, baina $0.17a$ erradioko zutabez osatutako egitura honetan, bolumen modala nabarmenki murrizten da. (b) $0.17a$ erradiodun zutabez osaturiko sare triangeluarreko kristala. Kristal horren erdian hutsune bat sortu da. Egitura horren band-gap-aren zabalera handiagoa da, eta hortaz, akatsaren argi lokalizazioak ere gora egiten du.

Egituraren hutsuneak eragiten duen eremu elektrikoaren konfinamendua sarearen band-gap indarrarekin erlazionatuta dago. Hau da, band-gap zabalagoa duten egiturak moduaren lokalizazioa sustatzen dute. Efektu hau oso aproposa da aplikazio praktikoen jardueretarako, *gap-mid-gap* erlazioa modu erraz baten aldatu daitekeelako, alegia zutabeen erradioa edota konstante dielektrikoa aldatuz. Aurreko kasuan bezalako materiala erabiliz, hau da 9-ko konstante dielektrikoa duten zilindroz osaturiko kristaletan, hauen erradioa $0.17a$-ra aldatu ezkero, TE polarizazioan gap-mid-gap erlazioa areagotzen da. 3.9a eta 3.9b. irudietan sare karratuan eta sare triangeluarrean ordenatutako $0.17a$-ko erradiodun zilindroz osaturiko kristalen banda eta DOS diagramak aurkezten dira, hurrenez hurren. Irudi horietan ikusi daitekeenez, band-gap handiagoa duten egitura horietan, banda-akatsen lokalizazioa maximizatzen da. Gainera, akats-modu horiek maiztasunean mugituarazi daitezke, sarearen eta defektuaren arteko konstante dielektrikoaren erlazioa egokitu ezkero [4].

Modu horren egokitzapen gaitasunaz baliatuz, kristal fotonikoen propietate batzuk sustatu daitezke. Hain zuzen ere, algoritmoen bitartez gidatutako diseinu prozedura inkrementalak sarritan erabili izan dira defektuen funtzio dielektrikoak egokitzeko, diseinuaren beharren arabera [97–99].

3.4 2D kristal fotonikoen klusterretan sortutako akats-moduak

Orain arte aztertutako akatsak dituzten egitura guztiak, infinitura luzatzen dira, espazioko norabide guztietan. Aitzitik, errealitate fisikoan, kristal fotonikoak luzera jakin bat dute eta beraz, defektuan kokatutako moduaren lokalizazioa ere mugatuta egongo da. Defektu horietan barreiatutako energia hutsunetik kanpo irradiatuko da. Egoera hori kuantifikatzeko kristal fotonikoaren erresonadorearen kalitate faktoreaz, Q, hitz egin beharra dago. Kalitate faktoreak denbora ziklo bakoitzeko, kristal fotonikoan gordetako energiaren eta irradiaturik galdutako energiaren arteko erlazioa kuantifikatzen du. Aztertzen ari garen egitura horietan, ez dugu zertan norabide transbertsalean irradiatzen den eremua kontuan hartu behar, kristala norabide horretan infinituraino luzatzen bait da. Dena den, planoaren norabide tangentzialean egitura N periodoetako luzera du, eta beraz eremu elektromagnetikoak kristalaren kanpo mugetaraino irradiatuko dira denbora zikloak aurrera egin ahala. Ikuspegi kuantitatibo batetik, bi galera mekanismo horiek ez dute inolako korrelaziorik eta hortaz, bereziki aztertu daitezke.

Beste alde batetik, gure kontestu honetan, absortzioak sortutako galerak arbuiatu dira eta baita sare kristalinoak eduki ditzakeen inperfekzioak sortutakoak. Beraz, kalitate faktorearen muga bakarra hutsuneak jasandako modu erradiatiboak eragindakoan datza. Transmitantzia diagramak FE metodoa erabiliz lortu dira. 3.8 eta 3.9 irudietan sare karratuan eta

triangeluarran sortutako kristalen transmitantzia erakusten dira, hurrenez hurren. Aurreko kasuetan ez bezala, atal honetan aztertutako transmitantzien kalkuluetarako luzera finitudun sare kristalinoak erabili dira. Hau dela eta, PMC eta PEC muga baldintzen ordez, PML muga baldintzak erabili dira, uhin igorlearekiko perpendikularrak diren mugetan eta uhin elektromagnetikoa sartu eta irteten den ertzetan *Transparent influx conditions* baldintzak inposatu dira, eta TE polarizatutako uhina hedatu da $\Gamma - X$ norabidean.

Muga baldintza horiekin islapen espurioak ekidin dira. Muga baldintza horiek ondorengo ekuazioz deskribatzen dira

$$\vec{z}\cdot\hat{n}\times(\nabla\times E_z\hat{z}) - ik_0E_z = -ik_0(1-\vec{k}_0\cdot\hat{n})E_{0z}e^{-i\vec{k}_0\cdot\vec{r}} \tag{3.3}$$

$$\vec{z}\cdot\hat{n}\times(\nabla\times H_z\hat{z}) - ik_0H_z = -ik_0(1-\vec{k}_0\cdot\hat{n})H_{0z}e^{-i\vec{k}_0\cdot\vec{r}}, \tag{3.4}$$

E_{0z} eta H_{0z} eremu eletriko eta magnetikoaren hasierako anplitudeak dira, sarrerako mugetan, hurrenez hurren eta $\vec{k}_0$ hedapen konstantea da.

Kristal fotonikoaren egitura luzatu egiten bada, alegia periodo gehiago jarriz, transmitantziaren espektroak argi azaltzen du modu defektuaren maiztasunean kokatutako erpin zorrotz bat. Simulazioan erabilitako klusterra handitzen denean, modu defektua estutzen da eta limitean Dirac delta baten itxura hartuko du. Aldi berean, akats-moduaren maiztasunean aldakuntza bat emoten da, egituraren batazbesteko konstante dielektrikoa aldatu egiten bat da. Gainera, aldaketa honek modu lokalizatu berriak agertarazi ditzake, goiko nahiz beheko banda fotonikoetatik.

$0.38a$-ko erradioa eta 9-ko konstante dielektrikoa duen sare karratuko kristal batean, kristala luzatzen den heinean, $\frac{a}{\lambda} = 0.4686$ maitasunean aurkitzen den hutsunean bildutako energia $\frac{a}{\lambda} = 0.49$ bandaren energiarekin parteiatzen da. Kalitate faktorea kristalaren transmitantzia espektroari begira kalkulatu da, definizioz

$$Q = \frac{f_c}{FWHM}, \tag{3.5}$$

f_c akats-moduaren maiztasun zentrala da eta FWHM akatsaren anplitudearen maximoaren erdiko balioa duten anplitudeen distantzia da. Kalitate faktorearen kalkulo bakoitzarentzat, FWHM balioa zehaztasunez lortu da Brent-en metodoa erabiliz [100]. Metodo honek erdibideketa, regula–falsi eta interpolazio kuadratikoa erabiltzen ditu FWHM-ko bi puntuen balioa zehazteko. Q faktorea transmitantzia espektrotik zuzenki kalkulatzeko metodoa sarritan eztabaidan jarri da [106, 107], denboraren domeinuko tekniketan metodo honek dituen efizientzia eta zehaztasun gabetasunak direla eta. Aldiz, FE metodoa transmitantziaren kalkulua lortzeko teknika bizkorra da eta beraz, Q-ren balioak zuzenean lortu daitezke

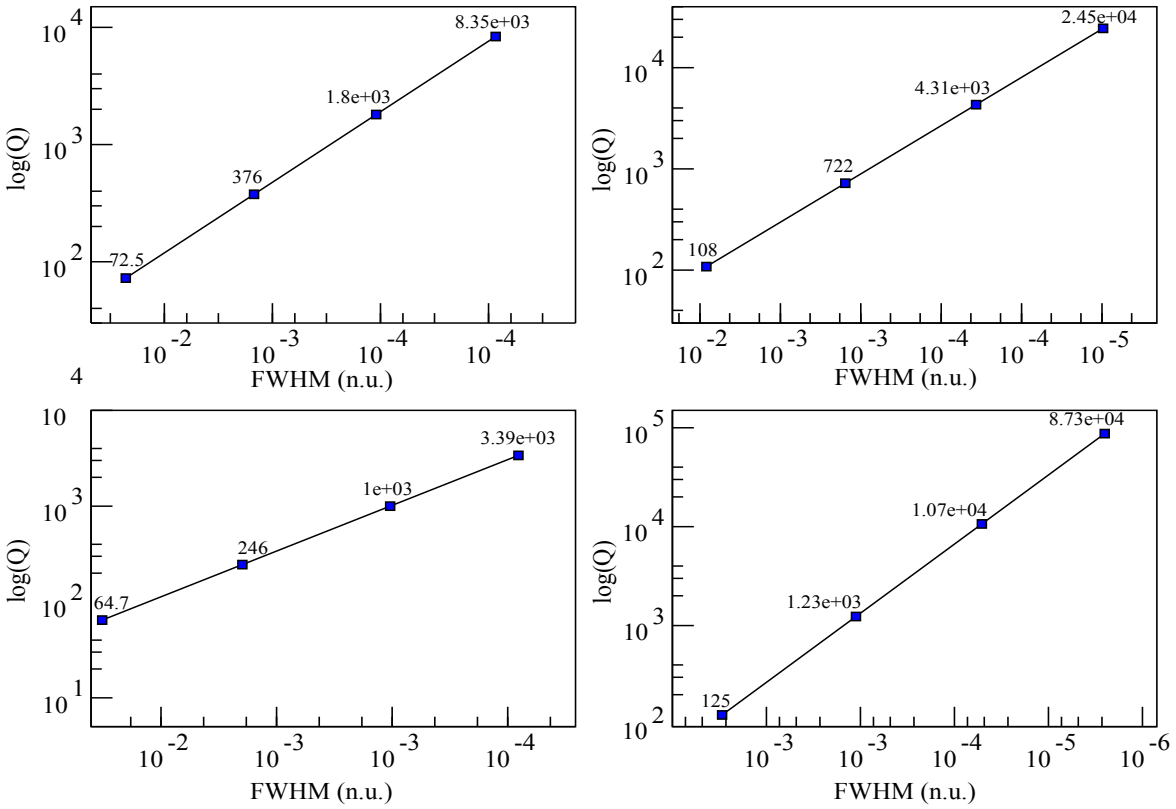

3.10. Irudia Goian: itxura Lorentzianoa duten erresonantzien FWHM kopurua erabiliz lortutako kalitate faktoreen estimazioa tamaina ezberdineko (a) 0.38a eta (b) 0.17a erradioko zutabeetako kluster karratueetarako. FWHM kopurua a/λ dimentsio gabeko unitateetan emoten da. Eskala logaritmitkoa erabili da bi ardatzetan. Behean: sare triangeluarretan egindako kalkulu analogoak (c) 0.38a eta (d) 0.17a erradioetarako.

3.5 ekuazioa aplikatuz. Hurrengo atalean, FEM, FDTD eta denbora eremuko seinaleen inbertsio harmonikoaren tekniken bitartez lorturiko Q balioak eztabaidatzen dira, eta hauen arteko konparaketa bat egiten da. Akatsa inguratzen duten periodo kopurua handitzean, akatsean bildutako energia galerak esponentzialki murrizten dira. 3.10 irudian, sare karratu eta triangeluarran, sarearen periodoak handitu ahala, sortutako akatsen kalitate faktoreen garapena adierazten da. Irudi honen arabera, akats-moduaren banda zabalera esponentzialki murrizten da, band gapa zabaltzen den heinean, eta beraz hau litzateke kalitate faktorearen sustatzaile fisiko nagusia. Beste talde batetik, akats-nodutik kanpo emoten den energiaren irradiazaioak transmitantzi espektroan forma Lorentzianoa duen erpin bat irudikatzen du beti. Efektu hau argiago ikusten da akatsa mid-gap maiztasunera mugituarazten denean eta FWHM estutzen denean N handitzean.

3.5 Denboraren domeinuko metodoa: FDTD

FDTD metodoa argiaren hedapena irudikatzeko metodorik ezagunena denez, FE metodoaren bidez kalkulatutako Q-ko faktoreak baieztatzeko erabili dugu. Atal honetan egindako FDTD simulazioak MEEP [107], softwarraren bitartez egin dira. FDTD metodoaren ospea eta baliagarritasuna, bere malgutasunari eta geometria aperiodiko eta irregularretara moldatzeko trabetasunari atxikitu daiteke. Orokorrean, FDTD metodoa maiztasun multzo bat konputazio beran ebazteko gai da eta espektro honetatik moduak lortu ditzake. Horrexegaitik metodo hau kristal fotonikoen egituretan Q faktore handiak kalkulatzeko metodorik erabiliena da. Hala eta guztiz ere, 3.5 ekuazioa aplikatuz Q faktoreak kalkulatzea zaila izan daiteke. FDTD metodoan transmitantzia, simulazio-eskualdearen amaieran kalkulatzen da, PML muga baldintzak baino nonbait lehenago. Gainera, transmitantzia hau kalkulatzeko eremuak denboran eboluzionatu eta gero, era nabariki galtzen hasten direnerarte martxan jarraitu behar du simulazioak, ($|E_z|^2$ edo $|H_z|^2$ eremuak gutxienez $\frac{1}{1000}$ faktoreko murrizketara ahilegatu arte, egoera estazionarioa dela suposatzeko). Gero, lortutako fluxua normalizatu beharra dago eta horretarako simulazioa berriz egin behar da, baina kasu honetan hutsune gabeko egitura bat simulatuz.

Beste alde batetik, transmizioaren simulazio zuzena kalkulatzeko beharrezkoa den denborak gora egiten du erresonantzia kabitateko kalitate faktoreak balio altuak hartzen dituenean, Fourier-en teoremaren arabera, simulazioan definitzen diren denbora tarteak maiztasunaren erresoluzioaren alderantzizkoarekin eskalatzen bait du [107]. Hortaz, transmitantziaren espektroa erabiliz, FDTD metodoarekin Q faktoreak kalkulatzea ez da aukera azkarra, ezta fidagarria ere ez. Bestela ere, Q faktoreak kalkulatzeko, denboraren domeinuan hedapen transitoriaren analisi zuzenaren bidez lortu daiteke. Hala ere, FDTD-ren bidezko

beste prozedimentu honek baditu nahiko eragozpen ere. Izan ere, FDTD metodoan espazioa eta denbora sare erregular baten zatitzen dira, aurreko kapituluan azaltzen den moduan. Gero, eremuak garatzen dira aurrerapauso diskretuak erabiliz.

FDTD metodoaren simulazio domeinuaren ertzak muga baldintza aproposak behar ditu, mugetako islapen efektu ez-fisikoak ekiditzeko, FE metodoak beharrezko dituen baldintzen antzera. Gainera, FDTD metodoan *split-field* PML baldintzak ezartzen dira simulazioaren kanpo azalera baten, mugetara heltzen diren huinak zurgatzeko, Berengerrek proposatutakoak esaterako [104]. Zoritxarrez, kalitate faktoreari dagozkion konputazioak simulazio-eskualdearen diskretizazio mailarekiko oso aldakorrak dira, eta beraz, igortutako uhin elektromagnetikok islapen espurioak sortuarazten baditu simulazio mugetan, norabide normalean irradiatutako uhinak islatutako uhinekin nahastuko lirateke eta simulazioaren konbergentzia ezegonkorra izango litzateke. FDTD metodoan banda zabaleko uhin iturria edo izaera monokromatikodun uhinak erabili daitezke, banda zabaleko iturria delarik erresonantzia bat sustatzeko gehien erabiltzen den iturria. Lan honetan erabilitako FE metodoak ordea, soilik uhin monokromatikoak erabili ditzake, erregimen harmoniko estazionarioan. Hortaz, aurreko atalean azaldutako FE metodoko emaitzak eta FDTD-ren bidez kalkulatutakoak konparatzeko, aurretik FDTD kalkuluetan zer nolako uhin iturri erabili behar den zehaztu behar dugu. Puntu hau aztertzerakoan, kontuan izan behar da denboraren domeinuan transmitantzia era iteratibo baten kalkulatzea (hau da, maiztasun bakoitzari dagokion uhin plano bat hedatzea, simulazio bakoitzean) etekin oso baxua duela eta konputazio arazoak sor ditzakela. Hau dela eta, honelako uhin iturri bat aukeratu ezkero, FDTD eta FEM arteko konparaketa ez litzateke pareko baldintzetan ezarriko; FDTD metodoa desabantaila nabarian egongo litzateke. Horregaitik, bidezko konparaketa bat egiteko, Q faktoreak kalkulatzetko, FDTD-ren kasuan banda zabaleko uhin iturri bat erabili da eta FE metodoaren kasuan uhin monokromatiko sorta bat erabilida, aurreko ataletan erabilitakoen modukoa.

Bereziki, FDTD konputazioak egiteko puntu formako iturri Gaussiano bat erabili da, akats hutsunean kokatuta dagoena. Pultso hau denboran laburra izan behar du (beraz maiztasunean zabala izateko) akats modua sustattu dezan kuster bakoitzean. Iturri Gaussiano hau pizterakoan, eremua hasi egiten da eta denbora tarte txiki bat igaro eta gero, uhin iturria amatatu egiten da.

Uhin iturriaren eraginez, erresonantzia efektua emoten da kristalaren akatsean, hau da, argia akatsean konfinatuta egongo da ziklo optiko kopuru zehatz batzuetan zehar. Bitartean, harrapatuta dagoen energia hori denboran esponentzialki murrizten da (begiratu 3.11 irudia). FDTD-ren prozesuan puntu honetaraino heldutakoan, kalkulatutako eremuaren aldakuntza txikia aurkezten duen konponentea, hau da eremu elektrikoaren portadoraren norma erabiliz,

kalitate faktorea kalkulatu daiteke, t denbora zehatz baten bildutako energia eta T periodo baten ostean galdutako energiaren arteko erlazioa erabiliz.

$$Q = 2\pi \frac{|E(t)|^2}{|E(t)|^2 - |E(t+T)|^2}. \tag{3.6}$$

Lan honetan, FDTD kalkuluak burutzeko *Uniaxial Perfectly Matched Layers* (UPML) [105, 106] motatako PML baldintzak erabili dira, hain zuzen ere MEEP jatorriz, islatutako uhinak desagertarazteko erabiltzen dituen kanpo muga baldintzak direnak. Ingurune artifizial honetan zehar, PML-a ε eta ν efektibo anisotropikoen arabera adierazten da [107]. Puntu honetan, garrantzitsua da azpimarratzea UPML eta kristal fotonikoaren klusterra banatzen duen distantzia guztiz kritikoa dela kalitate faktorearen kalkuluan. Hau da, UPML-a oso gertu kokatzen bada, baliteke hedatzen den eremuaren konponente ugari ezeztatzea edo, UPML-ren zabalera txikiegia bada, agian UPML-ak ez ditu behar beste konponente deusezten. Gustira, UPML-aren konfigurazioak erresonantziaren galera faktorean efektu zuzena dauka. 3.1-ko taulan jasotzen diran FDTD kalkuluen bitartez lorturiko emaitzetan, $2a$ lodierako UPML-a erabili da egitura inguratzeko. Gainera, UPML eta kristal fotonikoaren arteko distantzia, kasu hauetan $0.8 \leq d \leq 1.1$ izan da. Kalkulatutako eremu elektrikoa muestreatzen bada, erresonantziaren periodoaren arabera, funtzio kuasi-periodiko bat lortzen da eta bertatik Q faktorea kalkulatu daiteke 3.6 ekuazioa aplikatuz, baina prozedura hau oso aldakorra da. Baliteke, ezegonkortasun hauek klusterraren translazio simetriaren apurketan izatea jatorria. Dena dela, ziklo optikoak aurrera egin ahala, eremu elektrikoaren murrizketa esponentzialaren joera filtratu eta interpolatu egin dugu. Beraz, lortutako eremu diskretuaren interpolazioan, 3.6 ekuazioa modu iteratiboan aplikatu ezkero, bataz besteko Q faktorea eta honi lotutako errore teorikoa kalkulatu daitezke, hurrenez hurren.

Gainera, FE eta FDTD metodoen bitartez lortutako Q faktoreen kalkuluen konparaketaz gain, eremu seinaleen inbertsio harmonikoen bidez (`Harminv`) [108] lortu daiteke Q-ren estimazio bat. Software honek diagonalizazio filtraketa metodoa (FDM) erabiltzen du maiztasun tarte bateko sinusoide funtzioaren dekonboluzioa aurkitzeko. Simulazio ingurunea FDTD kalkuluetarako erabili dan berdina da: akatsean kokatutako pultsu Gaussiano zabal bat hedatuz kabitatearen TE moduak sustatzen dira eta PML muga baldintzak simulazio-eskualde osoa inguratzen dute. Bereziki, $\frac{a}{\lambda} = 0.02$ zabalera duen pultsu Gaussianoko argi iturri bat erabili da, egitura guztietan, eta pultsu hauen maiztasun zentrala kabitatearen erresonantzia maiztasunera ajustatu da. Argi iturria amatatu eta gero, PML-en eraginez eremua ezabatzen denean, `Harminv`-ek kabitatean geratzen diren eremuen seinale prozesamendua egiten du. Modu honetan, ezabatzear dauden modu erresonanteen maiztasuna eta gainbehera ratioa kalkulatuko ditu. Egoera hau emoten denean, metodo honek Q faktoreak era bizkor eta fidagarrian kalkulatu ditzake, baina oraindik eremuen hedapen osoa eta hauen ahulketa

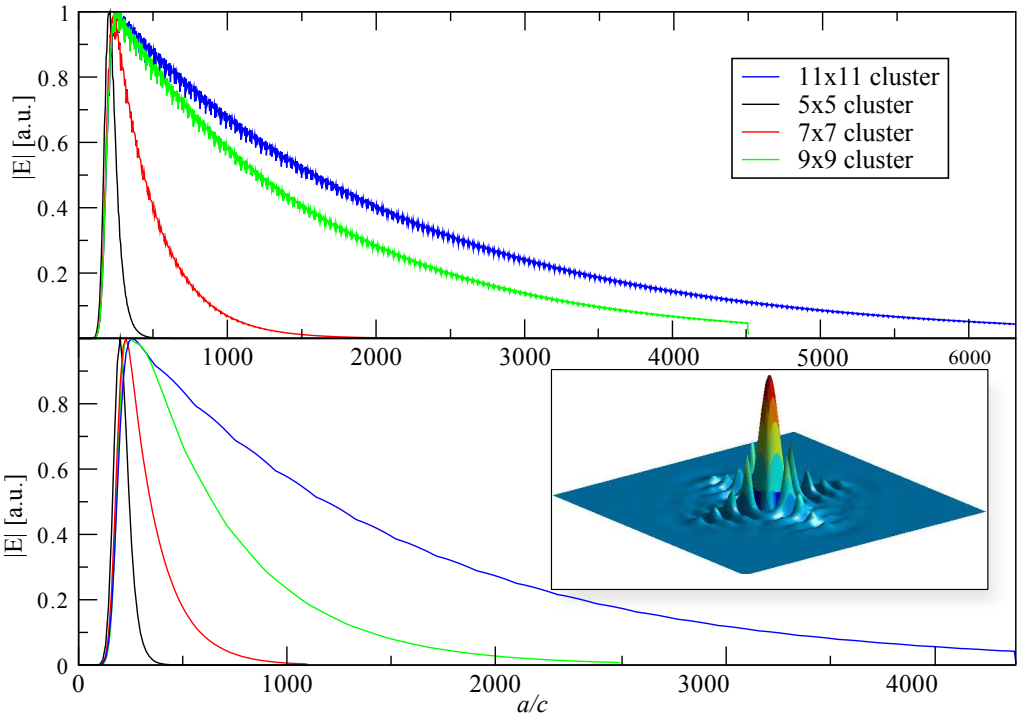

3.11. Irudia (a) 0.38a erradioko zutabeen egituran sortutako akatsaren barneko eremu elektromagnetikoaren eboluzioa eta honen aldakuntza klusterraren tamainaren arabera. Argi iturri puntual bat kokatu da kluster hauen erdian eta periodo gutxi batzuk pasatu eta gero, argi iturria itzali egiten da. Hutsuneak sorturiko erresonantziak argi iturriaren galera esponentziala sortzen du. (b) Antzeko simulazioak kluster triangeluar baten simulatuta.

gertatzen den unerarte itxarotea eskatzen du. Konputazio denbora gainera, asko luzatzen da simulazio-eskualde handiago bat erabiltzerakoan. Hau paliatzeko ordea, egituraren simetria ardatzak erabili ditzakegu, konputazio eskualdea murrizteko.

Beste alde batetik, pultsu Gaussiano zabal bat erabiltzeak ebazpen espurioen agerpena bultzatzen du, baina, aldi berean, pultsuak zabalera nahikoa izan behar du nolabait ezezaguna den maiztasun erresonanteak sustatzeko. Dena den, azpimarragarria da FE, FDTD eta Harminv metodoen bidez lortutako Q faktoreen balioen adospena. 3.1 Taulan kapitulu honetan erabilitako egituretan, hiru metodoen bidez lortutako emaitzak biltzen dira. Bi dimentsioetan kalkulatutako FE metodoaz lortutako Q faktoreak FDTD eta Hamrminv bidez lortutako emaitzekin bat datoz, baina FEM-ek modu azkar eta efizientean lor ditzake balio hauek. FDTD metodoak ordea, Q faktorean kalkulatzeko, bitarteko simulazio ziklo ugari egin behar ditu egoera estazionariora heldu baino lehen eta bitarteko simulazio ziklo hauek deuseztu egiten dira, ez bait dute interesik Q kopuruaren kalkuluan. Beste alde batetik, FDTD metodoaren, eta beraz Harminv metodoaren kalkuluan, hainbat faktore heurisitikok hartzen dute parte, alegia UPML-en zabalerak, iturriaren kokapenak, maiztasun zentralak eta zabalerak, dira Q balioaren emaitzan aldakortasuna ezartzen duten faktore batzuk, beste askoren artean. Faktore hauetaz gain, kabitatearen modu erresonanteak kalkulatzerako orduan, FDTD metodoa erabili ezkero, argi iturriaren karakteristikak hautatzean kontuz ibili behar da. Argi iturri hau modu erresonantearekiko ortogonalitasunik aurkezten badu, metodoak ez bait du modu erresonantea aurkituko. Honen inguruan, FE metodoak abantail ugari aurkezten ditu, ez bait du aurreko berezitasunen zehazpenik egin behar. Beraz, abantail haeui dagokionez, FE metodoa kalitate faktoreen kalkuluak egiteko modu fidagarria, sendoa eta efiziente dela argudiatzen dugu, material dielektriko konplexuen kasurako.

3.6 Kristal fotonikoen bidez egindako argi-uhinen gida

Puntu defektodun sareetan sortutako perturbazioean antzera, sare kristalinoetan perturbazioak lerro oso baten zehar sortu daitezke. Honelako egituretan, geldikorrak, desagerkorrak edo hedagarriak diren uhin monomodoak edo multimodoak agertu daitezke band gap fotonikoaren bitartean. Egoera honetan, argia uhin luzeera baino txikiagoko eskaladun espazioan hedatzzen da hedapen galera oso baxuekin. Uhin-gida hauek sortzeko ohiko bidea kristal fotoniko periodiko baten zulo edo dielektriko zutabe bakar bat kentzean datza. Orain arteko ikerketa teoriko gehienak kristal fotonikoen klusterretan honelako uhin-gidak hartu dituzte abiapuntutzat, eta orokorrean, airez inguratutako dielektrikoko zutabez osaturiko kristal fotonikoak erabili izan dituzte. Egitura hauetan sorturiko uhin-gida mekanismoak modu bakar bat gidatzeko duintasuna dute, kasu gehienetan. Kasu hauetan, bide zuzena deskribatzen

Taula 3.1 Sare karratu eta triangeluar ezberdinetako zutabe-motatako kristal fotonikoetan egindako puntu-akatsen kalitate faktorearen kalkulua, kluster tamainaren arabera, FEM, FDTD eta inbertsio harmonikoaren metodoak erabiliz.

	Sare karratua r=0.38a			Sare karratua r=0.17a		
Kluster tamaina	FEM	FDTD	Harminv	FEM	FDTD	Harminv
5	73	80±1	88	108	113±13	107
7	376	350±3	347	722	727±6	723
9	1800	1773±24	1765	4310	4312±31	4308
11	8350	7677±83	7674	24500	24561±74	24559
	Sare triangeluarra r=0.38a			Sare triangeluarra r=0.17a		
5	97	107±2	103	134	130±1	126
7	358	320±1	316	1280	1171±8	1166
9	1240	1211±5	1209	11100	11241±42	11238
11	5270	5656±74	5650	90200	83903±84	83892

duen uhin-gidaz beste, edozein norabide hartzen duen uhin-gida bat sortzea tribiala da. Beste alde batetik, dielektrikoz osaturiko zilindro zutabedun sare periodikoan egindako uhin-gidapenak galera erradiatibo ugari aurkezten ditu 3D-xafla bat erabiltzen denean. Aldiz, dielektriko material baten egindako zuloz osaturiko kristal fotonikoetan, uhin-gidak guztiz kontrako jokaera aurkezten du: 3D-xafla batean argiaren konfinamenduak ez du hainbesteko galera erradiatiborik sortzen, baina bertan sorturiko uhin-gidetan kurbaturaren bat sortzean, ezberdintasun geometrikoak direla eta, hedapen galera garrantzitsuak sortuarazten ditu. Beraz, honelako egituretan kurbaturak edota argiaren banaketa bat egiterako orduan, konfigurazio konplexuak diseinatzea beharrezkoa da.

3.12 irudian silizio materialean 0.35a erradioko aire zuloz osaturiko sare triangeluarra jarraitzen duen kristal fotonikoaren dispertsio-diagrama aurkezten da; a sarearen periodoa da eta Si materialaren errefrakzio-indize lineala, isotropikoa eta ez-magnetikoa 3.46 da. Kasu honetarako, bi dimentsioko sistema bat osatu dugu. Bertan, Bloch muga baldintzak ezarri dira, planoko periodizitatea formultzeko, eta bitartean, egitura hau z norabidean infinitu luzatzen dela suposatu dugu. Si materialaren eta zuloetako airearen arteko indizeen kontrasteak band gap fotoniko baten agerpena ziurtatzen du, [0.22 – 0.31] maiztasun tartean zabaltzen dena. Kristal honetan uhin-gida bat sortzerakoan, akats-moduak agertarazten dira band gap honen barruan. Berriro ere PWE metodoa erabili dugu dispertsio-diagrama hau lortzeko 1BZ-ko $\Gamma - K$ proiekzioan zehar, bertan traslazio simetria mantendu egten bait da. 3.12 irudiaren xehetasunean, lerro akatsaren eskema kontzeptual bat adierazten da, kristal fotonikoaren $\Gamma - M$ norabide kristalinoan ezabatutako aire zuloak adierazten dituena. W sinboloak uhin-gidaren zabalera zehazten du. Zabalera hau, lerro bakar bat ezabatutako uhin-gidaren

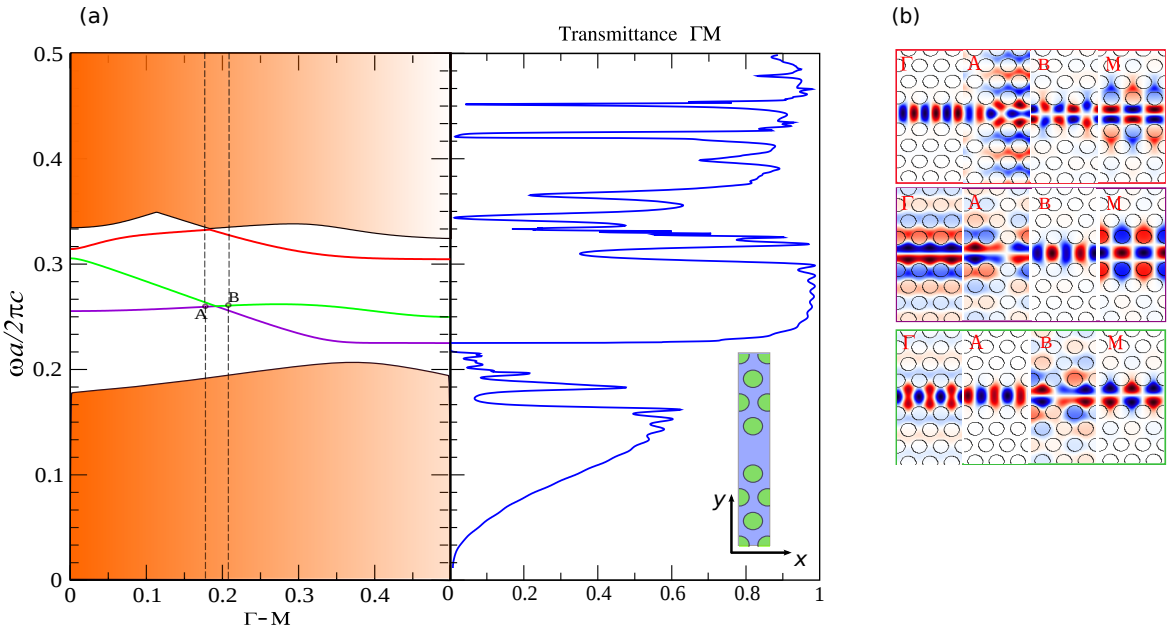

3.12. Irudia (a) Ezkerrean: Si materialan (n=3.46) egindako (0.35a erradioko zuloz osatutako 2D kristal fotonikoan zulo lerro bakar bat ezabatuz sortutako uhin-gidaren dispertsio-diagrama. Irudiaren barneko xehetasunak dispertsio-diagrama hau sortzeko erabili den gelaxka-unitatea erakusten du. (b) H_z eremuaren modua Γ, M eta anti-crossing puntuetarako. Azken hauek moduaren profilaren aldaketa nabarmena antzematen dute.

arabera neurtzen da, alegia, sare triangeluarran, $W = a\sqrt{3}$ zabalera duen uhin-gidaren arabera. Simulazio honetarako, zortzi zulo dituen kluster bat erabili da, baina konputazio baliabideetan eskaera murrizteko, kristal fotoniko uhin-gida (PCWG) hau simetria-planoarekiko banatu da. Beraz, simetria hau kontuan izanda, bakarrik simulazio domeinuaren erdia kontsideratu da. Egituraren ispilu simetria erabiltzeko, PEC muga baldintzak erabili dira simetria-planoan zehar. Modu honetan, mugarekiko tangenteak diren eremu elektrikoaren konponenteak eta mugaz kanpo dauden eremu elektrikoaren konponenteak ezabatzen dira. Gainera, PML muga baldintzak erabili dira simulazioa inguratzen gainerako mugetan, krusterraren luzeera finitoak sortutako islapen ez-fisikoak ekiditzeko.

Banda-diagrama hau kalkulatzeko 32×32 (=1304) sare-elementuko erresoluziodun diskretizazioa erabilida eta konstante dielektrikoa 9 sare puntuen bitarteko bataz bestekoa eginez osatzen da. Eremu magnetikoaren, z–konponentearen, H_z, automoduak ere kalkulatu ditugu $k = 0$, $k = 0.5$ eta *anti-crossing* puntutik hurbil dagoen posizioetarako. Beste alde batetik, 3.12.a irudian W1 PCWG klusterrari dagokion transmitantzi espektroa ere erakusten da, $[0, 0.5]$ maiztasun tartean. Hemen ere transmitantzia grafikoak argi adierazten ditu egituraren propietate optikoak, esaterako $[0.216, 0.224]$ maiztasun bitartean dagoen gap partziala argi ikus daiteke bai banda-diagraman, bai transmitantzia espektroan ere. Beste alde

batetik, espero genuen moduan, akats lineala sortzean, gap fotonikoaren barruan hiru modu gidatu sustatzen ditu. Modu hauek kolorez adierazi dira, gainerako bandetatik bereizteko. Hiru modu gidatu hauek simetria patroi ezberdinak dituzte. Automodu hauen simetria, eremu magnetikoaren z–konponenteak definitzen du, uhin-gidaren ispilu simetriaren planoaren arabera. Kolore gorridun moduak, aire banda eta gidatutako banda lotzen ditu. Ondorioz, bien arteko energia transferentzia sortzen du. Banda gap bitartean dagoenean, simetria bikoitia aurkezten du. Beste bi moduak interesgarriak dira ere, $\Gamma - M$ norabidean guztiz gidatuta bait daude. Gainera, bi moduen arteko interakzioa emoten da *anti-crossing* puntuan. *Anti-crossing* puntura heldu baino lehen, bi modu hauek modu fundamentalaren patroia aurkezten dute. *Anti-crossing* puntua eta gero ordea, haien arteko simetria eraldatu egiten da eta hauen arteko patroiak trukatu egiten dituzte eta bigarren ordeneko moduen patroia jasotzen dute. Fenomeno hau argi ikus daiteke 3.12 irudian. 3.12 irudian aurkezten dan W1 uhin-gidan, *anti-crossing* puntua 0.188-tik gertu aurkitzen da. Bertan, simetria bikoitia eta bakoitia duten modu gidatuen arteko interakzioa emoten da. Interakzio honek bi supermodu sortzen ditu, gap bidez sorturiko eta indizearen bitartez gidatutako moduen arteko nahasketa, fasean eta anti-fasean sortzen dituena.

Hemen aurkeztutakoak bezalako uhin-gida periodikoak oso interesgarriak dira beste hainbat aspektu direla eta. Bereziki adierazgarria denez, modu honetan sorturiko uhin-gidatuak *slow-light* erregimenaren barruko moduak sortuarazten ditu, banden ertzetan gehienbat. Modu hauek talde abiadura oso baxua dute eta aldi berean argi-materiaren interakzioa sustatzen duen erregimenan kokatzen dira eta honek efektu ez-linealak sustatzeko tresna ezinobea bihurtzen ditu.

3.6.1 Kristal fotoniko xafla baten egindako argi-uhin gida

Orain arte planteatutako 2D kristal fotonikoak z–norabidean infinitura luzatzen dira eta beraz, egitura irreal hauetan kristalen propietate teorikoak baino ez ditugu aurreikusten. Bitartean, aplikazio praktikoetan aurkitu daitezkeen egiturak 3 dimentsioetan mugatuta daude. 3D kristal fotoniko ugari aztertu dira jadanik, esaterako [110, 111], baina orain arte behintzat 3D PC praktikoak eraikitzeak fabrikazio prozesua asko konplikatzen du [112]. Askoz ere praktikoak diren PC xafla egiturak sarritan erabiltzen dira 3D kristal fotonikoen ordez, hauek litografia metodo arrunten bitartez sortzeko aukera ematen bait dute.

PC xafla egiturak bi dimentsioetan izaera periodikoa mantentzen dute eta, planoz kanpoko norabidean, indizearen bidezko gidaketa-mekanismoa erabiltzen dute argia materialan zehar konfinatzeko. Horrela, 2D-PC-ren propietate asko aurkizen dira 2D PC xafla egituretan. 3.12 irudian ikus daitekeen moduan, 2D eta 2D xafla egituretako propietateak erlazio zuzena

aurkezten dute. Noski, z–planoan xafla egiturak mugatuta daudenez, planoaz kanpo hedatzen diren moduetarako ez dago band-gap bat sortzerik [26].

PC xafla egituretan modu guztietako akatsak sortu daitezke ere, orain arte azaldutakoen modukoak. Egitura hauek gainera, erraz fabrikatu daitezke, eta horren froga, orain arte litografia metodoaren bitartez sortutako PC xafla experimental sorta haundiak osatzen du. Planoz kanpoko norabideko luzeera mugatua denez argi-kono bat definitzen da banda-diagraman. Argi-konora lotutako modu gidatuen energia airera erradiatuko da, eta beraz, uhin-gidaren diseinu egokitzen ez bada, uhin-gidako argi guztia mekanismo honen eraginez galdu egin daiteke. Atal honetan, Si materialan osatutako eta airez inguratutako PC xafla bat konsideratu dugu. Sistema hau $z = 0$ planoarekiko islapenei dagokionez aldagaitza da. Simetria honek modu optikoak *TE-like* (bikoitiak) eta *TM-like* (bakoitiak) bezala bereizteko aukera ematen digu. Era honetan osaturiko kristal fotonikoak *air bridge* izenez esagutzen dira. Air bridge PC xafla egiturak modu bertikalen argi konfinaketa oso ona lortzeko aukera ematen dabe eta gidatutako uhinen galera erradiatiboak murrizteko eta zuloen difrakzioari lotutako galerak ekiditzeko egitura apartak dira. 3.13 irudian W1 PCWG xafla baten 1BZ-ko Γ-M proiekzioan kalkulatutako banda-egitura aurkezten da. Ikus daitekenez, 3.12 irudian kalkulatutako 2D kristal fotonikoaren antzeko banda fotonikoak lortzen dira hemen. Kasu honetan, banda-diagramaren $\omega \geq c|k|$ argi-konoaren kurbak, gainetik limitatzen du dispertsio-diagrama. Kono honen gaineko moduak airean hedatzen bait dira. Gainera, z norabidean egiturak zabalera finitoa duenez, indize dielektriko efektiboa 2D kasuan baino txikiagoa da eta honen eraginez bandak maiztasun ardatzan desplazatuta aukitzen dira. Egituraren periodizitatea planoan baino agertzen ez denez, band-gap fenomenoa ere bertan bakarrik aurkituko da. Hau dela eta, gidatutako moduak beheko eta goiko mugetatik argia irradiatuko dute.

W1 PCWG xafla honen dispertsio-diagramak hiru modu gidatu aurkezten ditu. Hauek ere 3D FE metodoarekin lortutako transmitantzia kalkuluen bitartez antzeman daitezke, 3.13 irudian erakusten den bezala. Simulazio hauek egiteko $2a$ zabalera duen aire guneak definitu dira W1 xaflaren goikaldean eta azpikaldean. Egituraren simetria kontutan hartuz, simulazio-eskualdea 3.13 irudian xehetzen dan egiturara murriztu da. PMC muga baldintzak erabili ditugu z= 0 ebakuntza planoan. Simulazio-eskualdea 236.399 sare-elementuetan zatitu dugu eta *Generalized Minimal Residual method* (GMRES) solver bat erabiliz ebatzi dugu problema.

Xafla baten lodieraren hautapena ez da tribiala. Xafla honen dielektrikoaren lodiera finegia bada, orduan uhinen gidapena lerro akatsean zehar oso ahula izango da, hots, argi-konotik kanpo irradiatuko dira eta baliteke, inolako gidapenerik ez lortzea ere. Beste alde batetik, xafla honen lodiera zabalegia bada, orduan aireko moduak band-gap-aren barruan

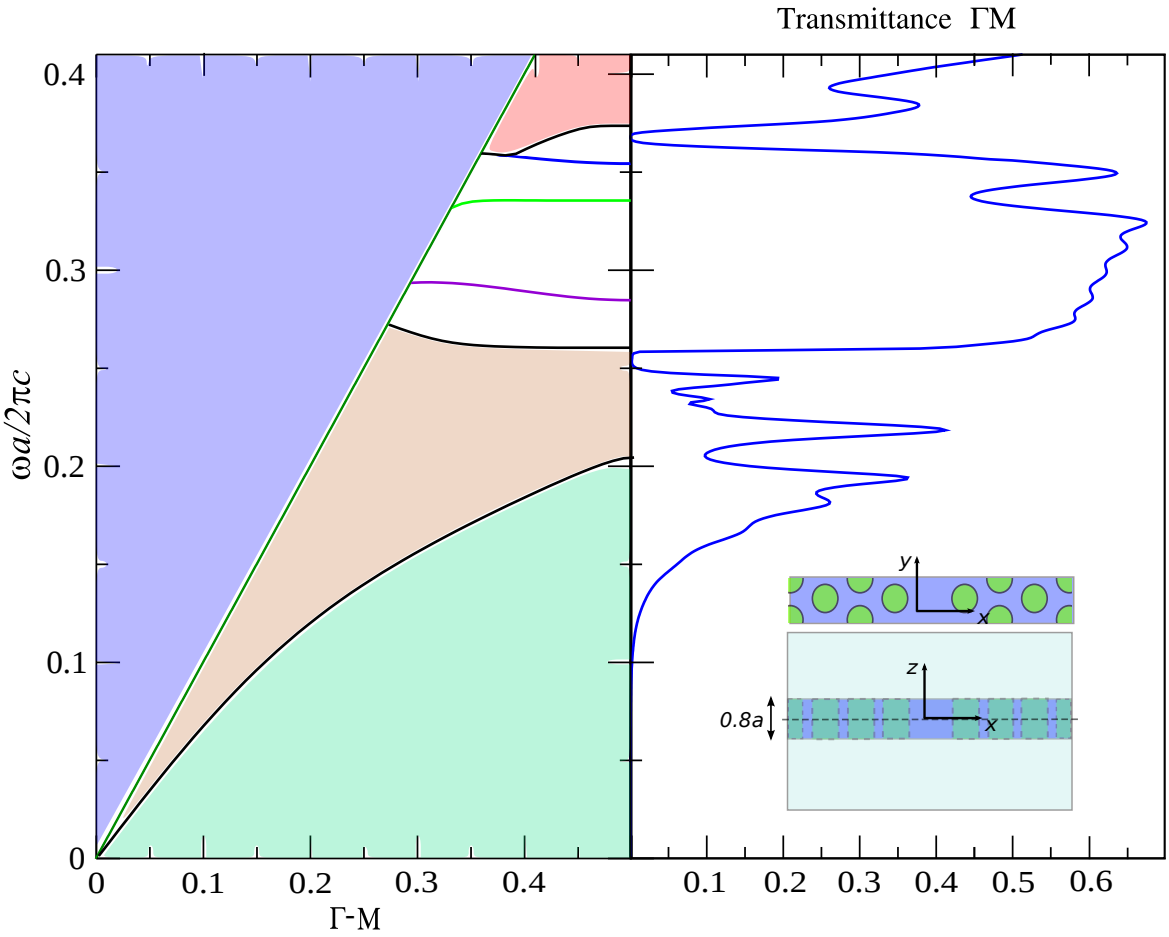

3.13. Irudia Ezkerrean: TM-like (z-odd) estatuen banda-diagramaren proiekzioa W1 akatsa duen eta zuloz osatutako xafla kristal fotonikoarentzat. Kristal honetan zulo lerro bat ezabatu da y–norabidean. Kristalaren altuera d=0.8a-koa da eta airez inguratuta dago. Eskualde urdinak argi-konotik kanpo dauden moduak estaltzen ditu, $\omega \geq c|k|$. Kolore gorri argiak *bulk* moduen gunea adierazten du. Gidatutako moduak gap tartearen barruan eta kristalaren *extended* moduen azpikaldean daude (eskualde berdean). Gune berdearen barruko modu gehieneak indizearen mekanismoaren bitartez gidatutako moduak dira eta z–bikoiti edo z–bakoiti moduan sailkatzen dira $z = 0$ simetria-planoaren eta uhin-gidaren ebakuntza planoaren arabera. Eskuman: W1 PCWG honen transmitantzia diagrama.

jausiko lirateke. Orokorrean, 0.6a lodiera hautatzen da [4] PC xafla egituretan, edo beste askotan, fabrikazio-metodoak berak ezartzen du xafla hauen lodieraren limitazioa. Kasu honetan, eta aurrerantzean aurkeztuko diren 3D PC xafla egituretan 0.8a lodiera duten egiturak proposatu dira.

Kapitulua 4

Baldintzatutako metodo heuristiko eta genetikoak egitura nanofotonikoen diseinuan

Algoritmo heuristikoak eta genetikoak ohiko optimizazio-teknikak erabiltzen dituzten metodo zuzenez kanpoko hautabideek eskaintzen dituzte problema konplexuetan ebazpen optimoak bilatzeko. Partzialki desordenatuta dauden osagarrien bidez egindako gailu nanofotonikoetan, kristal fotonikoetan esaterako, sare periodikoaren maiztasunaren apurketak onura garrantzitsuak sortarazi ditzake, esaterako, argiaren lokalizazioa sustatuz eta argia ez-ohizko era batean gidatuz. Desorden honek aldiz, honelako egituren diseinua bortizki konplikatzen du. Hau dela eta, kapitulu honetan, egitura fotonikoen alderantzizko diseinua garatzeko erabilitako algoritmo heuristiko eta genetikoak deskribatzen ditugu.

4.1 Konplexutasun konputazionala

Konplexutasun konputazionalaren teoriaren esparruan, NP (non-deterministic polynomial-time) moduan sailkatutako problemak [114], soilik ez-determinitistikoa den Turing-en makina baten bitartez ebatzi daitezke denbora-tarte polinomiko batean. Horrelako makinak aldiz, gailu kontzeptual bat baino ez dira eta funtsean, horrelako problema baten ebazpena lortzeko, problemaren egoera bakoitzarentzat, aukera anitzen artetik jarraitu behar diren erregelak definitzen dituzte. Beraz, aurreko definizioaren arabera, NP motatako problema bat ebazteko ez dago gaur egun ezagutzen diren metodo deterministikoak erabiliz ebazterik, horretarako beharrezkoa litzatekeen konputazio-denbora probleman planteatutako ezezagun kopuruekin esponentzialki handitzen bait da. Hala ere, Turing-en makinaren pareko funtzionalitateak

eskaintzen dituen algoritmo batek ebazpen *egokia* lortzeko aukera eskaini dezake, denbora-tarte onargarri batean. Beste alde batetik, NP problemen artean, NP-osoak deritzogun problemak ere aurkitzen dira eta hauek NP problemak baino konplexutasun maila handiagoan sailkatzen dira. Izan ere, orain arte inork ez du NP-osoak diren problemak denbora-tarte polinomikoan ebatzi daitezkeenik frogatu, eta berez, matematika arloan ebaztear dauden problemarik garrantzitsuenen artean dagoen erronka bat da.

Dena dela, problemaren ebazpen espazioaren hausnarketa zorrotz bat egiteko konputazio-denbora oso luzeak beharko lirateke eta are gehiago, kasu batzuetan, konputazio-denbora horiek esponentzialki luzatzen dira N aldagaien arabera, eta beste hainbat kasuetan egoera hau are larriagoa bihurtu daiteke [115]. Problema mota hauek sarritan aurkitu daitezke aplikazio esparru ugarietan, errepideen trafikoaren kudeaketan [116–118], edota bestelako produktu salmenta eta garraioen plangintzan [119, 120], nahiz multi-prozesadoreen eginkizunen bideraketan [121, 122] eta programazioan [123, 124], beste arlo askoren artean. NP motatako problemetan bi ezaugarri hartu behar dira kontuan: ebazpen optimoa lortzeko helburua era adierabakarrean zehaztea eta helburu horretara ailegatzeko beharrezkoa den konputazio-denboraren mugaketa, hurrenez hurren. Honen ildoan, orain arte, hurbilketa-metodo asko proposatu izan dira, problema hauetan egokiak diren ebazpenak ahalik eta modu bizkorrenean (beti ere denbora super-polinomialean) aurkitzeko gai diren algoritmoak garatzeko. Ikuspuntu praktiko batetik, baliabide konputazionalak ebazpen optimo baten bilaketan erabiltzean baino, ebazpen egoki (baina potentzialki optimoaren azpitik dagoena) bilatzea posiblea da, ondorengo hurbilketa-metodoak erabiliz:

- Zorizkotasuna: aldagaien balio optimoen bilaketa egiteko, behin eta berriro aldagaiei zorizko balioak ezarriz ebazpen numeriko hobeagoak aurkitzean datza. Zorizkotasun irizpide honen bidez, Monte Carlo [125–127] metodoak, nahiz Markov katean oinarritutako Monte Carlo metodoak ebazpen optimoaren hurbilpen bat eskaintzen dute. Metodo hau sarritan erabiltzen da, gehien bat zerrenda honetan aipatzen diren beste metodoekin konbinatuta, askatasun-gradu ugari maneiatu behar direnen kasuetan.

- Hurbilketa-metodoak: algoritmo hauek problemaren aurre ezagutza batetik abiatzen dira, aldagai batzuen balioa xehetuz problemaren askatasun-graduak murrizten du era bizkorrago batean ebazpen egoki bat aurkitzeko. Aitzitik, bilaketa-espazioaren mugaketa hori, intuizioan oinarritzen bada soilik (ohikoa denez) baliteke ebazpen optimoak bilaketa-esparru horretatik kanpo geratzea.

- Metodo Heuristikoak: mota honetako metodoak ebazpen optimoa aurkitzeko beste biderik ezagutzen ez denean, edota soluzio optimoaren bilaketan beharrezkoa den konputazio-denbora tartearen mugaketak garrantzia handia duenean erabiltzen dira

normalean. Nahiz eta algoritmo hauek problemaren soluzio optimoa bilatzeko helburua duten, ez dago ebazpen optimo hori lortuko dutenen ziurtasunik eta horren ordez, egokitzat hartzen den ebazpena aurkitzeko baliabideak inplementatzen dituzte. Orokorrean, metodo hauek NP-osoak diren problemetan aplikatzean, emaitza egokiak edo behar adina egokiak diren emaitzak ahalbidetzen dituzte. Bilaketa-prozesu iteratiboa kontrolatzeko operadore probabilistiko batzuk erabiltzen dituzte. Metodo hauen erabilera asko zabaldu da, gehien bat bi arrazoi direla eta. Alde batetik, algoritmo heuristikoak era errazean aldatu eta moldatu daitezke problema berrietara eta beste alde batetik, konputazio-denboraren eta lortutako ebazpenaren kalitatearen arteko oreka egoki bat eskaintzen dute.

4.2 Metodo Heuristikoak

Algoritmo heuristikoak, funtsean, optimizazio-konbinatorioan oinarritzen dira eta berez, optimizazio-konbinatorioaren esparruko problemak dagoeneko konputazio zientziaren ildoan nabarmenki landu dira, batez ere azken hamarkada honetan. Gai honetan egindako ikerketak NP nahiz NP-osoko problemetako aldagaiek osatzen duten formulatutako funtzioen minimo edo maximoak aurkitzeko teknika efizienteak aurkitzean ardaztu dira batez ere. Orohar, tesi honetan zehar, horrelako funtzioa sarritan kostu-funtzioa edota helburu-funtzio bezala izendatuko dugu eta optimizazio-prozesuaren iterazioetan, kostu-funtzioan aldagai zehatz batzuk erabiltzean lortzen den neurketa kuantitatiboa, *fitness* terminoa erabiliz izendatuko dugu, orain arteko literaturaren terminologia erabiliz [128]. Optimizazio-konbinatorioaren eredu sinple eta klasiko bat saltzaile bidaiariaren problema da. Demagun saltzaile honek N hiri guztietatik behin bakarrik igaro behar dela, hasierako hirira itzuli baino lehen, bere salmentak egiteko. Hiri guzti hauen artean guztira egin behar duen ibilbidea saltzailearen bidaiaren kostu-funtzioa definitzen du eta beraz, saltzailearen ibilbide optimoa planteatzean datza problema hau, edo beste era batean esanda, kostu-funtzioaren minimo globala edota fitness balio onena lortzeko ibilbidea definitzen duten aldagaiak asmatu beharra dago. Saltzaile bidaiariaren probleman eta berez NP-osoak diren azpimultzo guztietako problemetan, hurbilpen deterministiko bat erabiltzen denean, ebazpena aurkitzeko beharrezkoa den kostu-konputazionala probleman kontuan izandako aldagai kopuruaren arabera era esponentzialean handitzen da (N hiriak kasu honetan). Beraz, ebazpen determinista eta zehatza aurkitzeko, probleman planteatutako aldagai kopurua oso mugatuta egon behar da. Are gehiago, NP-osoak diren problemak ebazteko, N potentziara mugatutako konputazio baliabideak erabili ezkero ez dago ebazpen zehatzik lortzeko biderik, hala ere, noizbait honelako problema bat ebazteko bide bat lortuko balitz, orduan baliteke mota honetako problema guztiak

ebazteko prozedura bat izatea. Hala eta guztiz ere, oraingoz ez dago honelako ebazpenak egiterik eta gainera ez dago ezta argi NP-ososko problema baten zailtasuna definitzen dituzten ezaugarriak ezberdintzerik. Gainera, NP-osoak diren problemak ezaugarri praktiko garrantzitsuak dituzten problematika anitzetan aurkitu daitezke. Horregatik, metodo heuristikoak garatu dira, hain zuzen ere, horrelako problemen aurrean N ordenaren adinako baliabide konputazionalen bidez problemaren ebazpen *egokiak* aurkitzeko asmoz [128].

Algoritmo heuristikoak normalean bi estrategia ezberdin erabiltzen dituzte optimo globala aurkitzeko: *divide and conquer* deritzoguna, hau da, problemaren bilaketa-espazioa azpi-problema mugatuagoetan zatitzea, eta gero, bigarren pauso baten hobekuntza iteratiboak egiten dira. Jatorrizko problema, azpi-problema txikiago eta sinpleagoetan zatitu daiteke, baldin eta azpi-problemak ez-korrelatuak badira, bestela, azpi problemen ebazketa egindakoan, berriro ere azpi-multzo hauek batzen direnean, ez genuke inolako abantailarik lortuko honelako irizpide bat erabilita. Bestalde, hobekuntza iteratiboak egiteko, algoritmoak hasierako konfigurazioaren kostu-funtzioa ebaluatzen du. Gero, prozesu iteratiboan, algoritmoak aldagaiak aldaraziko ditu, kostu-funtzioan hobekuntza bat lortzen duen konfigurazio bat lortzen duen arte. Jarraian, algoritmoak *downhill/uphill* mugimenduak sortuko ditu eta prozesua errepikatzen da inolako hobekuntzarik aurkitzen ez den arte, edota aldez aurretik ezarritako iterazio-kopuru batera heldu arte. Noski, ez dago inongo ziurtasunik algoritmoak bi mekanismo hauen bitartez optimo globala lortuko duela ziurtatzeko. Hain zuzen ere, bi mekanismo hauek ez dute optimo-lokaletatik ihes egiteko baliabide eraginkorrik hornitzen. Horretarako, optimizazio-prozesua behin baino gehiagotan burutu daiteke, hasiera puntu ezberdinak hautatuz, eta bertatik emaitza egokiena hautatu daiteke. Metodo heuristiko gehienak ez dute honen beharrik, dagoeneko optimo-lokaletatik ihes egiteko baliabideak inplementatzen dituztelako. Tresna hauek operadore probabilistikoak dira eta haietan kontrolpenean dagoen zorizkotasun maila batek eragiten du. Operadore probabilistiko hauek direla eta, algoritmo heuristiko baten saiakera bakoitzean lortutako emaitzak ez dute zertan bat etorri eta baliteke algoritmoak konbergentziarik ez lortzea ere, edota arinegi konbergentzia puntura iristea, bitartean optimo globala aurkitu gabe. Beraz, algoritmo heuristikoak erabiliz kristal fotonikoen esparruko problemak ebazteko orduan, ezin daitekeenez aldez aurretik jakin zein algoritmok jasoko dituen emaitzarik onenak, hiru algoritmo heuristiko erabili ditugu, Fast Simulated Annealing (FSA) [129], Improved Harmoy Search metodoa (IHS) [130] eta Non Sorting Genetic Algorithm II (NSGA-II)[132], azken hau helburu anitzetako problemak ebazteko.

FSA algoritmo heuristiko klasiko bat da, aspaldi garatu izan zena eta gaur egun bere erabilera nabarmenki murriztu da, algoritmo berriak agertu diren heinean. Hala ere metodo hau oso eraginkorra dela frogatu da, aplikazio ezberdin ugarietan [133–139] , baina kristal

fotonikoen kasuan ez dagoenez aldez aurretik egindako frogaketarik, algoritmo honek eskainitako emaitzen etekina aztertuko dugu tesi honetan eta horretarako, gaur egun ospe handia jaso duen IHS algoritmoaren emaitzekin konparatuko dugu. Beste alde batetik, NSGA-II metodoa algoritmo konplexuago bat da, aldi berean helburu bat baino gehiagoren gaineko optimizazioa egitea ahalbidetzen duena.

4.2.1 Fast Simulated Annealing metodoa

Simulated annealing (SA) optimizazio-teknika meta-heuristikoen artean oso ezaguna den teknika bat da eta dagoeneko optimizazio-konbinatorio motatako problema anitzetan frogatu da [140–145]. Simulated annealing terminoak metalurgian erabiltzen den *annealing* prozesutik dator. Prozesu honetan, materialak tenperatura altuetaraino berotzen dira eta gero era kontrolatu batez astiro hozten dira, materialen egitura kristalinoaren akatsak minimizatzeko. Beroak, atomoak hasierako posizioetatik (barne-energiaren minimo lokala) mugituarazten ditu, eta zorizko ibilbideak jarraituz energia altuagoko estatuetara ailegatzeko aukera dute. Jarraian, hozketa prozesu leun baten bidez, hasierako konfigurazioak baino barne energia baxuagoa duten konfigurazio berriak aurkitzeko aukerak handitzen ditu edo beste era batera esanda, minimo global bat aurkitzeko aukerak sustatzen ditu prozesu honek. Bilaketak espazioko optimo-lokalak ekiditeko aukera eskaintzen du, *Hill Climbing* (HC) bezalako beste hainbat optimizazio-teknika sinpleagoak aurkezten duten ahultasunak gainditzeko. Horretarako, energia altuagoetara salto egiteko probabilitate ez-nuluko mekanismoa erabiltzen du, hau da, sistemaren energia minimizatzeko joera hausten duten soluzioak esleitzen ditu operadore probabilistiko batzuen arabera. SA-ren oinarri teorikoak Kirkpatrick et al.-ek ezarri zituzten 1983an [128]. Lehenbiziko SA-ren inplementazio horretan, Metropolis Monte Carlo algoritmoa [146] erabiltzea proposatu zuten tenperaturaren parametro artifiziala kudeatzeko, eta horren bidez energia altuagoetara mugiarazteko onarpen-probabilitatea kontrolatzeko[1]. Simulated annealing metodoa erlazionatutako hiru baliagarri erabiltzen ditu, batik bat [149]:

1. $g_T(x)$: D parametroen energia estatu-espazioko probabilitate dentsitatea $x = x^i; i = 1, \ldots, D$, non T azpi-indizeak tenperatura parametroa adierazten du.

2. $h(\Delta E)$: Kostu-funtzio berria onartzeko probabilitatea, soilik aurreko kasuaren balioa kontuan hartuz.

3. $T(k)$: T tenperatura parametroaren annealing prozesuaren planifikazioa, k annealing denbora-tarteen araberakoa dena.

[1] Hala eta guztiz ere, metodo honen oinarrien lehenbiziko proposamenak ere beste hainbat egileei esleitzen zaizkie, era independientean eta aldi berean antzeko lanak aurkeztu bait zituzten, [147, 148] esaterako.

Konfigurazio berri bat onartzeko probabilitatea, aurreko E_k energia estatutik, E_{k+1} energia duen estatu berri bat lortzeko aukeren araberakoa da. Kostu-funtzio berri bat onartzeko probabilitateak Boltzman-en distribuzioa jarraitzen du eta ondorengo eran idatzi daiteke [150]:

$$h(\Delta E) = \frac{e^{\frac{-E_{k+1}}{T}}}{e^{\frac{-E_{k+1}}{T}} + e^{\frac{-E_k}{T}}} = \frac{1}{1 + e^{\frac{-\Delta E}{T}}} = e^{\frac{-\Delta E}{T}}, \tag{4.1}$$

non ΔE kostu-funtzioaren gaitasun maila edo fitness-aren eta aurreko kostu-funtzioaren fitness-aren arteko energia diferentzia da, funtsean, ΔE = fitness$_{k+1}$ - fitness$_k$. Hasieran, T tenperatura parametroari balio altu bat ezartzen zaio. Tenperatura altu honek, optimizazio-prozesuaren hasierako pausoetan fitness balio txarrago bat ematen duten parametroak onartzeko probabilitate handia eskaintzen du. Prozesuaren fase honi dibertsifikazio fasea deitzen zaio. Bertan algoritmoak bilaketa-espazioan zehar araketa zabal bat egiten saiatzen da, optimo-lokal batzuk alde batera ustearen truke. Gero, hozketa prozesuan, energia altuagoetarantz egindako mugimenduak gero eta gutxiago izango dira, eta beraz, algoritmoak kostu-funtzioaren fitness-a hobetzen saiatuko da batez ere, minimo lokalen inguruan bideratuz bilaketa. Dagoeneko SA algoritmoarentzat hainbat metodo alternatibo proposatu izan dira [151, 152], baina honelako algoritmo gehienak SA inplementazioan aldaketa garrantzitsuak inposatzen dituzte. Aldiz, Fast Simulated Annealing (FSA) algoritmoak [129], SA algoritmo originalak normalean behar duen konputazio-denbora murriztea lortzen du, bilaketa semi-lokal bat erabiliz eta optimizazio-prozesuaren eraginkortasuna sustatzen du, energia altuagoetarantz egindako saltoen kontrola hobetuz, beraz minimo lokalen inguruko bilaketa sakonduz. Hau guztia, jatorrizko SA algoritmoaren oinarriak mantenduz egitea lortzen du. Izan ere, kostu-funtzioak minimo bakar bat duenean, jatorrizko SA algoritmoak modu bizkor batean aurkitu dezake oinarrizko estatu hori, gradienteaz baliatutako minimizazio metodoak egiten duten bezala jokatuz. Baina, kostu-funtzioak minimo ugari dituen kasuetan, ez-konbexua den optimizazio-teknika bat behar da, metodoak minimo lokaletatik ihes egiteko tresnak izan behar dituelako. Szu et al.–ek SA metodoa birformulatu zuten, FSA metodoan [129] D-dimentsioetako espazioko kostu-funtzio berrien onarpen-probabilitatea, $g(\Delta x)$, Cauchy-Lorentz probabilitate distribuzio bat jarraituz antolatzea proposatu zuten:

$$g(\Delta x) = \frac{T}{((\Delta x)^2 + T^2)^{\frac{D+1}{2}}}. \tag{4.2}$$

Cauchy distribuzioak distribuzio normalak edo Gaussianoak (Boltzman) baino emaitza hobeagoak lortzen ditu, izan ere, funtzioaren muturrak zapalagoak direnez minimo lokalak era intentsiboago baten hausnartzeko aukera ematen bait du [129]. Ondorioz, FSA metodoak duen annealing prozesua jatorrizko SA algoritmoarena baino esponentzialki bizkorragoa

da. Optimo-lokal bat aurkitu orduko, FSA algoritmoak SA algoritmoaren ohiko prozesua jarraitzen du, funtsean, tenperatura parametroaren araberako energia altuagoko konfigurazioak onartzeko aukeraz gidatutako optimizazio zikloa jarraituko du. Gero, tenperatura parametro hau txikiagotzen da, hozketa prozesu leun bat jarraitzeko. Bereziki, algoritmoak tenperatura parametro hau sistematikoki txikiagotuko du, k annealing parametroaren balio bakoitzerako. k parametroa algoritmoaren ziklo kopuruaren bestelakoa izango da, re-annealing prozesu bat inplementatzen ez bada behintzat. Tenperatura parametroa orduan, honela berridazten da:

$$T = \frac{T_0}{k}, \tag{4.3}$$

non T_0, i—aldagaiaren hasierako tenperatura balio da, eta k, i—aldagaiaren annealing parametroa da. Tenperatura baxuagoak onarpen-probabilitate baxuagoak suertatzen dituzte. Era berean, Δ handiago batek ere onarpen-probabilitate baxuak suertatzen ditu. Pauso ez-intuitibo honek, batzuetan bilaketa eremu berri bat aurkitzeko gaitasuna ematen du, funtsean, kostu-funtzioaren balioa txikiagotzen ez duten konfigurazioak ere noizbehinka onartuz, hasierako iterazioetan aurkitutako minimo lokal batetik ihes egiteko aukera dago, minimo global baten bila jarraitzeko.

Gainera, gure FSA algoritmoaren inplementazioan re-annealing eskema bat ere erabili da. Re-annealing-ak bilaketa-espazioaren inguruko parametroen artean, emandako aldaketen sumagaitz diren efektuak aurkitzeko erabiltzen da, eta bestetik, kostu-funtzioan efektu gehien duten parametroetan ardazteko gaitasuna eskaintzen du. Re-annealing-ak annealing parametroak iterazio zenbakia baino balio txikiagora ezartzen ditu eta tenperatura parametroa handitu egiten du dimentsio bakoitzean, funtzio objetiboaren gradientearen arabera, dimentsio bakoitzean. i, k_i osagarriaren annealing parametroa hurrengo formularekin kalkulatzen da:

$$k_i = \log\left(\frac{T_0}{T_i}\frac{max(s_j)}{s_i}\right), \tag{4.4}$$

non T_i, i aldagaiaren tenperatura parametroa da, eta s_i helburu-funtzioaren gradientea da i norabidean, i norabideko tarteen arteko diferentziaz biderkatuta dagoena. Azkenik, aldez aurretik zehaztutako iterazio-kopurua betetzean edota fitness helburutik gertu dagoen balioa, Δx, lortu denean algoritmoa gelditukoa da. 4.1 irudian lan honetan erabilitako FSA algoritmoaren pseudo-kodigoa eta diagrama erakusten dira.

4.2.2 Improved Harmony Search (IHS) algoritmoa

Harmony Search (HS) algoritmoa, musikaren inprobisazio prosezuan inspiratutako optimizazio-algoritmo meta-heuristiko bat da. HS algoritmoa Geem et al.-ek proposatu zuten 2001. urtean

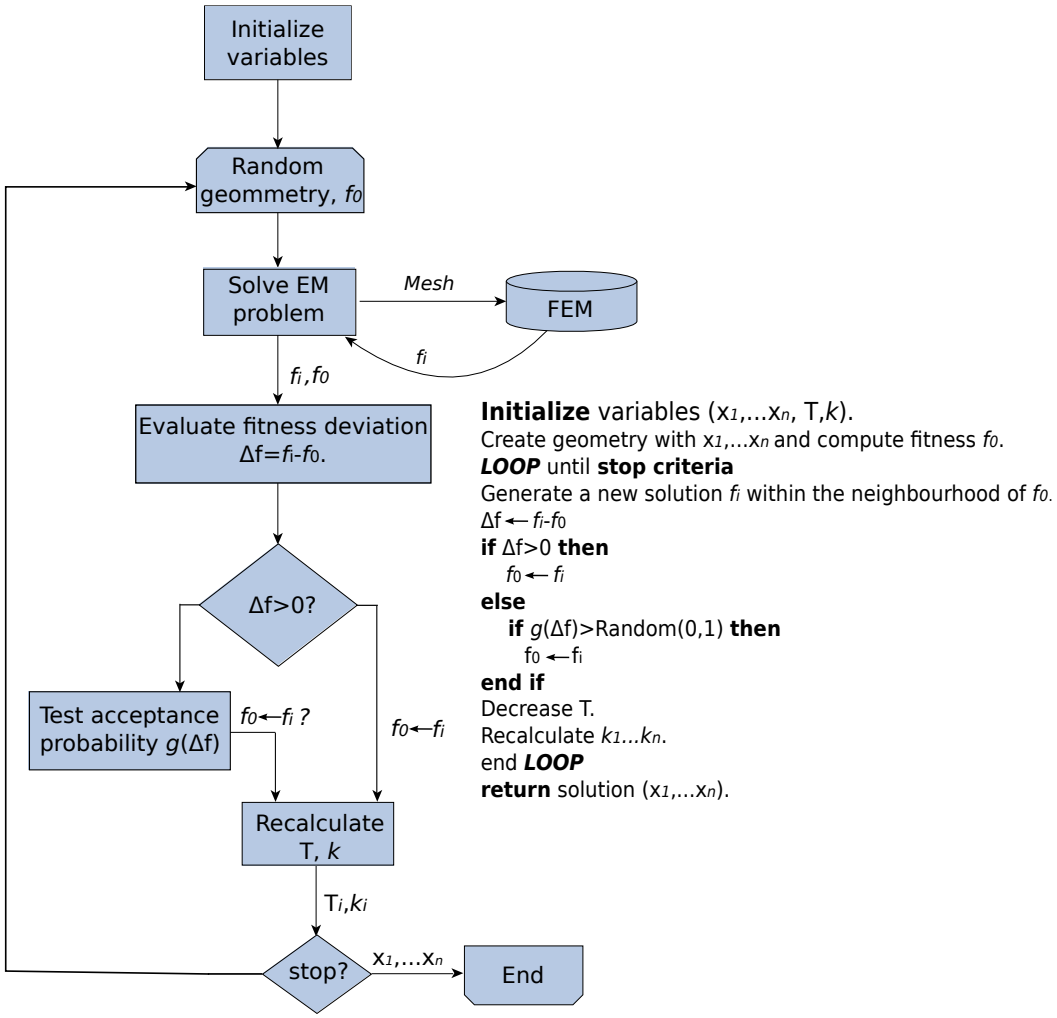

4.1. Irudia Testu honetan erabilitako FSA algoritmoaren fluxu-diagrama.

[153]. Ordutik hona algoritmo hori optimizazio-konbinatoriozko problema ugarietan aplikatu da [154–156]. HS algoritmoa, izaera jarraiko aldagaiak maneiatzeko asmoz proposatu zen eta funtzio objetiboaren deribatuak erabili beharrean, bilaketa-prozesu estokastiko aleatorioan oinarritzen da. Kontzeptualki, HS algoritmoak jazz musika talde batek melodia baten harmonia hobetzearren egiten duen ekintzak imitatzen ditu, melodien parekoak diren funtzio berriak sortzeko prozesuan, optimizazio helbururantz hurreratuz. Hau egiteko, musikariak egiten dituen ekintzak hautaketa aldagai multzo batez adierazten dira, une baten inprobisatutako harmonia iterazio konkretu baten sortutako soluzio-bektoreaz osatzen da eta harmoniaren musikalitatea kostu-funtzioaren fitness-aren balioarekin parekatzen da analogia horretan. Beraz, musika taldeak batera jotzean melodia bat hobetzeko jarraitzen dituzten ekintzak imitatuz, batik bat, nota edo akorde berriak sortuz, edota nota hauek aldatuz, Harmony Search algoritmoak ere antzerako eredua jarraituko du fitness balioak problemaren

optimo globalarekin bat egiteko [157]. Gainera, musika berri baten inprobisazio prozesuan hiru egoera ematen dira: musikari batek doinu bat aurrez aurretik ikasi duen modu berean jo dezake, edo antzerako doinu bat jo dezake, bertako nota edo horien tonuren bat aldatuz; bestela ere, nota aleatorio berriak sartu ditzake doinuan, betiere, melodiaren musikalitatea hobetzearren. Hiru egoera horiek kontuan hartuz Geem et al.-ek optimizazio-prozesu berri bat proposatu zuten. Optimizazio-algoritmo honek hiru tresna erabiltzen ditu: harmonia ezberdinen memoria bat, tonuaren aldaketa eta zorizkotasuna. Bapatean sortutako musikaren analogiarekin jarraituz, HS algoritmoak musikak erabiltzen duen terminologia bera erabiltzen du, esaterako, hautagai den soluzio-bektore bakoitza harmonia bat da eta harmonia bakoitza notaz osatuta dago, algoritmoan berez aldagaien balio multzoz osatuta daudenak. Beste alde batetik, Improved Harmony Search (IHS) algoritmoa [130] jatorrizko HS algoritmotik sortutako beste bertsio bat da.

IHS algoritmoak, jatorrizko HS algoritmoaren soluzio-bektoreak sortutako zehaztasuna eta konbergentzia-denborak hobetzeko helburua duen metodoa da. IHS algoritmoaren prozedura hurrengo puntuetan laburbiltzen da:

- Hasi optimizazio-problema eta algoritmoaren parametroak- Optimizazio-problema orokorrean minimisazio funtzio eran formulatzen da

$$\text{Minimize}, f(x): \quad \text{s.t.}: x_i \in X_i, \quad i = 1, 2, ..., N, \tag{4.5}$$

  non $f(x)$ helburu-funtzioa bait da; x aldagai multzoa x_i optimizazio-problemaren aldagai bakoitzarentzat, non ${}_L x_i \leq X_i \leq_U x_i$ (domeinu jarrai baten formulatutako problemarentzat), eta ${}_L x_i$ eta ${}_U x_i$, i aldagaiaren azpi eta goiko mugak bait dira, hurrenez hurren. Pauso honetan ere HS algoritmoak erabiltzen dituen parametroak ere zehazten dira:

  - Harmonien memoria (HM): hautagai diren soluzio-bektore guztiak biltzen dituen matrize bat da. Hasierako pauso honetan matrizeko aldagai guztiak balio aleatorioak hartuko dituzte, betiere ${}_L x_i$ eta ${}_U x_i$, baldintzen artekoak izango direnak.
  - Harmonien memoriaren tamaina (HMS): harmonien memoriaren barnean egokituko diren soluzio-bektore kopurua definitzen du.
  - Harmonien memoriaren kontsiderazio-indizea (HMCR): HM-tik nota bat aukeratu eta harmonia berri bat sortzeko probabilitatea definitzen duen operadore estokastikoa da.
  - Tonua ajustatzeko indizea (PAR): HM-n gordetako harmoniatik hautatutako nota baten tonua aldatzeko probabilitatea definitzen duen operadorea da.

– Hautaketa aleatorioaren indizea (RSR)[131]: HM-ko nota baterako balio aleatorio berri bat ezartzeko probabilitatea definitzen du. Operadore hau ez da HS algoritmo originalean, ezta IHS algoritmoan proposatzen. Hala eta guztiz ere, operadore berri hau gure inplementazioan sartzea erabaki genuen, zorizkotasun iturri osagarri bat izan dadin.

– Algoritmoa gelditzeko irizpidea: normalean iterazio-kopuru (NI) bat betetzean prozesua gelditzeko irizpidea hartzen da.

HMCR, PAR, RSR operadore estokastikoak xehetasun gehiagoz deskribatzen dira ondorengo 4.2.3 atalean:

- Sortu balio aleatorioak HM harmonia matrizean goiko eta beheko limiteen barneko balioekin. Gero, aldagai bektore bakoitza ebaluatu egiten da eta matrizeko bektoreak fitness balioaren arabera sailkatzen dira,

$$HM = \begin{bmatrix} x_1^1 & \cdots & x_n^1 & | & f(\mathbf{x}^1) \\ \vdots & \ddots & \vdots & | & \vdots \\ x_1^{HMS} & \cdots & x_n^{HMS} & | & f(\mathbf{x}^{HMS}) \end{bmatrix}. \tag{4.6}$$

- Harmonia berri bat inprobisatu. Harmonia berria HM-ko harmoniak erabiliz sortzen da, $x' = (x'_1, x'_1, \ldots, x'_N)$. Diseinuaren aldagai baten, x'_i, balioa, harmonia berria sortzeko erabili dadin, modu arbitrarioan. Nota berriak sortzeko, HMCR parametroa erabili daiteke. HMCR-k 0 eta 1 bitarteko balioa hartu dezake:

$$x' = \begin{cases} x'_i \in x_i^1, x_i^1, \cdots, x_i^{HMS} \\ x'_i \in X_i \quad \text{with probability} \quad (1 - HMCR) \end{cases} \tag{4.7}$$

Oro har, x'_1 nota berri bat sortzeko, HM-tik balio zehatz bat aukeratzeko probabilitatea HMCR probabilitate operadoreak zehazten du; bestela $(1 - HMCR)$ probabilitateaz, nota berri horrek balio aleatorio bat hartuko luke, HM memoriako notaz beste dagoena. Hurrengo pausoan, harmonia berriaren nota bakoitza aztertzen da, nota hauen tonua aldatu behar den erabakitzeko. Prozesu honek PAR parametroa erabiltzen du, HM-ko noten tonua aldatuko du PAR probabilitateaz, edo bestela ez du aldaketarik egingo $(1 - PAR)$ probabilitatearekin. Oro har, nota baten tonua aldaketa egitea esleitzen bada, x'_1 nota horrek aldameneko tonu balioa hartuko du, tonuaren aldakuntza banda-zabaleraren tarte arbitrario bat (bw) erabiliz. Gure IHS algoritmoaren inplementazio partikularrean, zorizkotasun tresna gehigarri bat erabili izan dugu, Hautaketa Aleatorioaren indizea (RSR), [158]-ean proposatu zena. Operadore probabilistiko honek SA algoritmoan

annealing-a edota algoritmo genetikoen (GA) mutazio operadoreak [159] (ikusi geroago azaltzen den algoritmo genetikoaren azalpena, 4.2.4-ean) bezalako funtzioak egiten ditu; funtsean, nota aleatorioak sor ditzake harmonia berrian RSR probabilitatearekin.

- HM eguneratu. Harmonia bektore berria, HM-n gordetako harmonien kostu-funtzio baliorik txarrena duen harmonia baino hobeagoa bada, orduan, harmonia berriak HM memorian gordetako harmonia ordezkatzen du. Jarraian, HM matrizea berriz sailkatzen da helburu-funtzioaren fitness balioaren arabera.

- Aurreko pausoak ziklikoki errepikatzen dira, algoritmoa gelditzeko irizpidea betetzen den unea ailegatzen den arte.

IHS algoritmoak ohiko algoritmo heuristikoen osagaiak biltzen ditu. Izan ere, Tabu-search metodoarekin [160] parekotasun ugari ditu, adibidez, aurreko soluzio-bektoreak gorde egiten ditu harmonia-memorian. Gainera, HMCR parametroaren erabilerak, SA algoritmoaren moldagarritasuna ekartzen du IHS algoritmora. Beste alde batetik, IHS algoritmoak, algoritmo genetikoek egiten duten moduan, aldi berean soluzio ugari kudeatzeko gai da. Gaitasun hau oso komenigarria da, arkitektura paraleloko konputazioa erabiliz iterazio bakoitzean kalkulatzen diren soluzio-bektoreak aldi berean ebazteko aukera ematen bait du. Aldiz, IHS algoritmoaren inprobisazio operadoreak beste algoritmoetatik bereizten du eta azken finean, hauek dira metodoaren optimo globalaren bilaketa gidatzen duten tresnak. Ondorengo atalean, operadore hauek sakonki aztertuko ditugu.

4.2.3 IHS: inprobisazio-operadoreak

- **Harmonien-memoriaren kontsiderazio-indizea, (HMCR)**: HM-n dauden noten arteko nahasketa indizea definitzen du. Parametro honek, bapatekotasun prozesuan, nota zehatz batek HM memorian geratzen diren beste nota baten balioa hartzeko probabilitatea ezartzen du.

  Harmonia-memoriaren erabilerak garrantzia handia du, algoritmo genetikoetan ere (ikusi 4.2.4 atala) hoberen moldatzen diren banakoen jarraipena ziurtatzen du. HMCR parametroak balio baxua hartzen duenean, problemaren aldagaietan bilaketa zabal bat egingo da, eta aurreko soluzioen erabilera urria egingo da. Aldiz, HMCR operadoreak balio altua hartzen badu, soluzioen sakabanaketa galdu egiten da eta algoritmoa era azkarregi batean konbergentziara heldu daiteke. Beraz, HMCR operadorea problema bakoitzaren menpeko balioa hartu behar du, gure kasu partikularrean, 0.9-ko balioa izango du.

- **Tonua ajustatzeko indizea, (PAR)**: tonuaren banda-zabalera, bw_{range}, parametroaren bidez tonu-aldaketa kontrolatzen duen operadorea da. Musikan, nota baten tonua ajustatzean, bere soinuaren maiztasuna apur bat aldatzen ariko ginateke. IHS algoritmoan, tonua aldatzeak HM-n gordetako aldagai baten balioan, notaren alfabetoko aldameneko balio berri bat egokitzen zaio nota horri.[2]. Notaren tonuaren aldaketa hau gauzatu dadin, PAR operadoreak honako aldakuntza zehazten du

$$x_i' = x_i + bw \times \epsilon, \tag{4.8}$$

non x_i HM memorian gordetako nota bait da, bw banda–zabalera da, ε distribuzio uniforme batetik aleatorioki sortutako balio bat da, $[-1, 1]$ bitartean dagoena, eta x_i'-k tonu berria duen nota izendatzen du. Egile askoren iritziz parametro honen erabilerak dibertsifikazioa eta intentsifikazioa orekatuz egindako bilaketa lokal bat egitearekin parekatu daiteke [130]. PAR balio baxu batek IHS algoritmoaren konbergentzia-tartea luzatu dezake, bilaketa-espazioa azpiespazio estu batera mugatuko litzatekeelako. Beraz, PAR operadorearentzat, ohiko balioak $0.1 \leq 0.5$ ingurukoak dira, aplikazio gehienetan. Tonuaren ajusteak algoritmo genetikoetan ematen den mutazio-operadorearen pareko rola betetzen du.

Geem-ek [153] proposatutako jatorrizko HS algoritmoan, PAR eta banda-zabaleraren balioak finko mantentzen dira eta ez dute aldaketarik sufritzen optimizazio-prozesuan zehar. Beraz, operadore hauen hautaketa kritikoa izaten da, emaitzaren konbergentzia eta kalitatearen ikuspuntutik. Hau dela eta, jatorrizko HS algoritmoak iterazio asko behar izaten ditu optimo globala aurkitzeko. Aldiz, IHS algoritmoak [130], *PAR* eta *bw* parametroen balioak ziklikoki aldatzen ditu, bilaketa-prozesuaren konbergentzia leuna izan dadin. FSA algoritmoarekin analogia eginez gero, operadore hauen moldaketak, FSA-an erabiltzen den Cauchy-Lorentz probabilitate distribuzioaren pareko eragina sortzen du. Beraz, IHS algoritmoan *bw* parametroak balio altu bat hartzen du algoritmoaren hasierako zikloetan, honela soluzioen dibertsifikazio lortzen bait du. Gero, zikloak aurrera egin ahala, *bw*-ari balio baxuak ezartzen zaizkio, dibertsifikazioaren ordez, bilaketa lokalak burutu ditzan. Hau dela eta, IHS algoritmoan, PAR operadorea n zikloan honela kalkulatzen da:

$$PAR(n) = PAR_{min} + \frac{PAR_{max} - PAR_{min}}{N} \times n, \tag{4.9}$$

[2]Kasu honetan, *alfabeto* terminoak, nota batek izan dezakeen eta muga balio konkretu batzuen bitartean dauden balio diskretu edo jarraiei deritzogu.

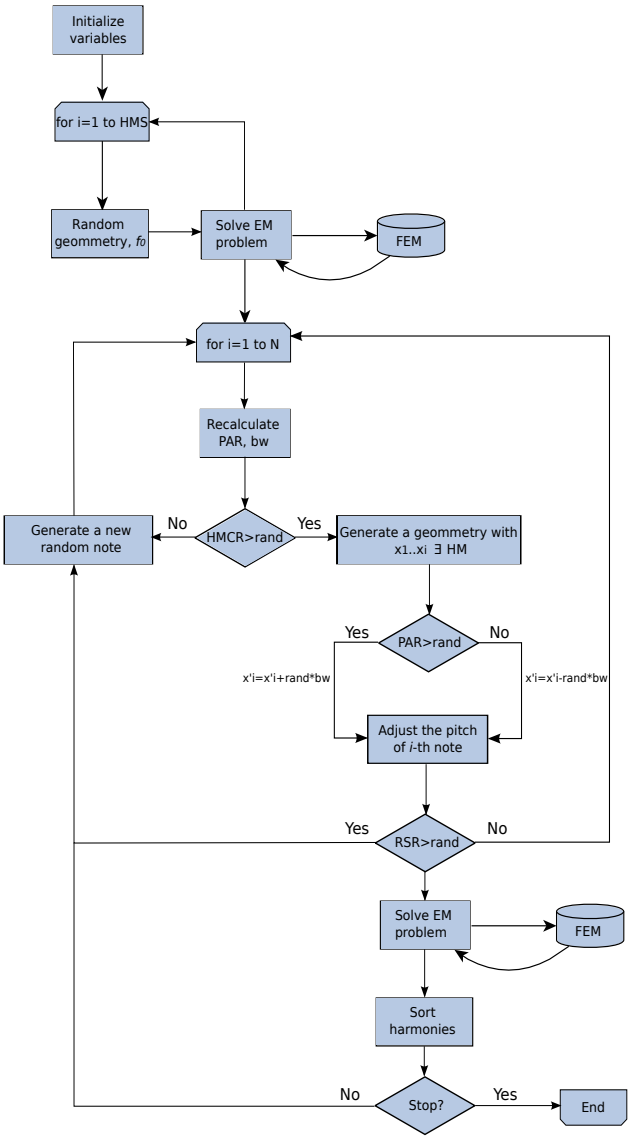

Initialize variables (x*1*,...x*n*, HM, HMCR, PAR, bw, RSR).
Fill HM with random harmonies and resolve cost functions.
LOOP until **stop criteria**
Readjust PAR and bw parameters
if HMCR>rand **then**
  x'$_i$=HM(rand(1...HM), rand(1...n))
  if PAR>rand **then**
    if 0.5>rand **then**
      x'$_i$=x'$_i$+rand*bw
    else
      x'$_i$=x'$_i$+rand*bw
    end if
  if RSR>rand **then**
    x'$_i$=random value within variable bounds
    return x'$_i$
  else
    return x'$_i$
  end if
else
  x'$_i$=random value within variable bounds.
end if

Solve harmony.
sort HM according to f_1...f_{HM}
end **LOOP**

4.2. Irudia Tesi honetan inplementatutako IHS algoritmoaren fluxu-diagrama eta pseudo-kodea

non N guztira egingo diren iterazio edo ziklo kopurua bait da (algoritmoa gelditzeko irizpidea). Beste alde batetik, banda-zabalera n iterazioan ondoko era ez-linealan kalkulatzen da:

$$bw(n) = bw_{max} \times e^{c \times n}, \tag{4.10}$$

eta c koefizientea iterazio bakoitzean berriro kalkulatzen da,

$$c(n) = \frac{\ln \frac{bw_{min}}{bw_{max}}}{N}. \tag{4.11}$$

Soluzioen aniztasuna mantentzeko eta bilaketa-espazioa larregi mugatu ez dadin, PAR_{min} parametroari 0.4 balioa ezarri diogu lan honetan, eta $(PAR)_{max}$-ari 0.9 balioa eman zaio. Banda-zabalera minimoa eta maximoari, BW_{min} eta BW_{max}, 0.0001 eta 1 balioak ezarri dizkiegu, hurrenez hurren.

- **Hautaketa aleatorioaren indizea, (RSR):** zorizkotasunak algoritmoak proposatutako soluzioen aniztasuna sustatzen du eta beraz, optimo globala lortzeko soluzio ezberdinak hausnartzea bideratzen du. Nahiz eta PAR operadoreak antzeko eginkizuna duen, PAR-a alfabeto batez mugatutako eremu batera mugatuta dago eta beraz, bilaketa-prozesu lokal batean aritzen da. RSR $\in [0, 1]$ erlazioak, aldagaien domeinutik nota berri bat aleatorioki hautatzeko probabilitatea zehazten du. Operadore honek, SA algoritmoan energia altuagoetara salto egiteko probabilitatearen pareko eginkizuna betezen du, baina, kasu honetan, HM harmonien memorian sortutako perturbazioa, harmoniaren fitness baliorekiko modu independientean egiten da, RSR probabilitatea jarraituz soilik. Lan honetan RSR parametroari balio baxu bat, 0.1 ezarri diogu, algoritmoaren konbergentzia ziurtatzeko.

HS algoritmoak baldintza matematiko gutxi eskatzen ditu eta ez du hasierako baldintzen balio konkretuen ezarpenik behar. HS algoritmoak bilaketa-prozesu aleatorio estokastikoa erabiltzen duenez, deribatuen bidezko informaziorik ere ez du behar.

4.2.4 Helburu ugarien optimizazioa

Helburu-anitzetako optimizazioak kontraposizioan egon litezkeen helburuak, aldi berean optimizatzea ahalbidetzen duten algoritmoak dira. Orokorrean, helburu-anitzetako optimizazio-algoritmoak helburu bakarreko algoritmoak baino askoz ere konplexuagoak izaten dira. Soluzio optimo bakarraren ordez n helburu dituen optimizazio-problema baten ekuazioa honela adierazi daiteke:

$$c(n) = \frac{\ln \frac{bw_{min}}{bw_{max}}}{N}. \tag{4.12}$$

Izan ere, helburu-anitzen optimizazio-problema batean, helburu ezberdinentzat egoera optimo baten orekara daraman ebazpena aurkitzeko, helburu ezberdinen kostu-funtzioan era onenean egokitu daitezkeen aldagai ezberdinen balioak aurkitzean datza. Honelako problemak ebazteko, hasierako hurbilpen bat eginez, helburu-ugariren optimizazio-problemaren ekuazioa,

(4.12), helburu ezberdinen kostu-funtzioen haztatutako batuketa formara pasatzen da:

$$\min_{\mathbf{X}\in\mathcal{X}} f(\mathbf{X} = \sum_{i=1}^{n} \omega_i f_i(x)) \tag{4.13}$$
$$\text{subject to } g_i(\mathbf{X}) \leq c_i, \quad i = 0, \ldots, m.$$

eta beraz, (4.13)-ko helburu-anitzen problemaren ekuazioa, helburu bakarreko optimizazio-problema erara bihurtu da. Haztatutako batuketaren metodoak ω_i pisuak ezartzen dizkio helburu bakoitzaren kostu-funtzioari $f_i(x)$. Horretarako, $f_i(x)$ kostu-funtzioaren garrantzia estimatzen da, probleman kontsideratutako beste kostu-funtzioen eragin orokorrarekin konparatuz. Hala eta guztiz ere, pisu horientzat balio aproposenak bilatzea, orokorrean, zeregin ez-tribial bat da, eta optimizazio-problemaren naturaren ezagutza sakonean oinarritzen da. Beraz, helburu-anitzen optimizazio-problema bat modu honetan formulatzea sinplea dirudien arren, ebazpen-prozesua asko konplikatu dezake, $f_i(x)$ kostu-funtzioen ω_i pisuen ezarpenaren arbitrarietatea ez bait da batere argia. Beste alde batetik, Pareto-optimoen fronteak erabiltzea askoz ere hurbilpen xeheagoa da. Metodo honek, helburu-anitzen problemaren hautagaiak diren soluzio-bektoreen ($X = \{X_1, X_1, \ldots, X_N\}$), bilaketa, $X_n \in \mathcal{X} \forall n \in \{1, \ldots, N\}$ moduan adierazten du, $f(X) = \{f_1(X), f_2(X), \ldots, f_L(X)\}$ ebazpenak optimizatzeko [157]. Beste modu batean esanda, ebazpen bat Pareto-optimoa, edo ez-gainditutako Pareto-optimoa dela esaten da, baldin eta helburu batekiko hobekuntza batek beste edozein helburu batekiko degradapen bat sortzen ez duen beste inongo ebazpenik ez badago. 4.3 irudian Pareto-optimo fronte baten eredua aurkezten da. Bertan, agertzen den karratuaren barruko puntuak, helburu-anitzen optimizazio-problema bateko minimizazio prozesu baten aurkitutako hautagai ebazpenak lirateke. Problema honek bi helburu kontuan hartzen ditu aldi berean, f_1 and f_2 kostu-funtzioak kuantifikatzen dituzten helburuak, hurrenez hurren. Kasu honetan, C puntua ez lirateke Pareto-frontearen barruan egongo, A eta B puntuez gaindituta dagoen puntua bait da. Aldiz, A eta B puntuak ez daude domeinatuta beste edozein puntuz, eta beraz Pareto frontean kokatutako puntuak dira. Kasu idealean, Pareto-puntuak modu uniformean sakabanatuko lirateke frontean zehar, baina praktikan, hau ez da beti betetzen optimizazio-problema guztietarako.

Pareto-fronte zehatz baten baliagarritasuna estimatzeko modu konkreturik ez dago. Horretarako, ziklikoki Pareto-fronte ezberdinak lortuz, Pareto-fronteen arteko konparaketa egin daiteke. Beste alde batetik, optimizazio metodo klasikoak (*multicriterion decision-making methods* barne) helburu-anitzen optimizazio-problemak, helburu bakarreko optimizazio-problema eran formulatzea proposatzen dute, horretarako, soilik Pareto-optimoko frontearen ebazpen bakar bat kontuan hartuz. Ebazpen multzo bat hausnartzeko, horrelako metodo bat

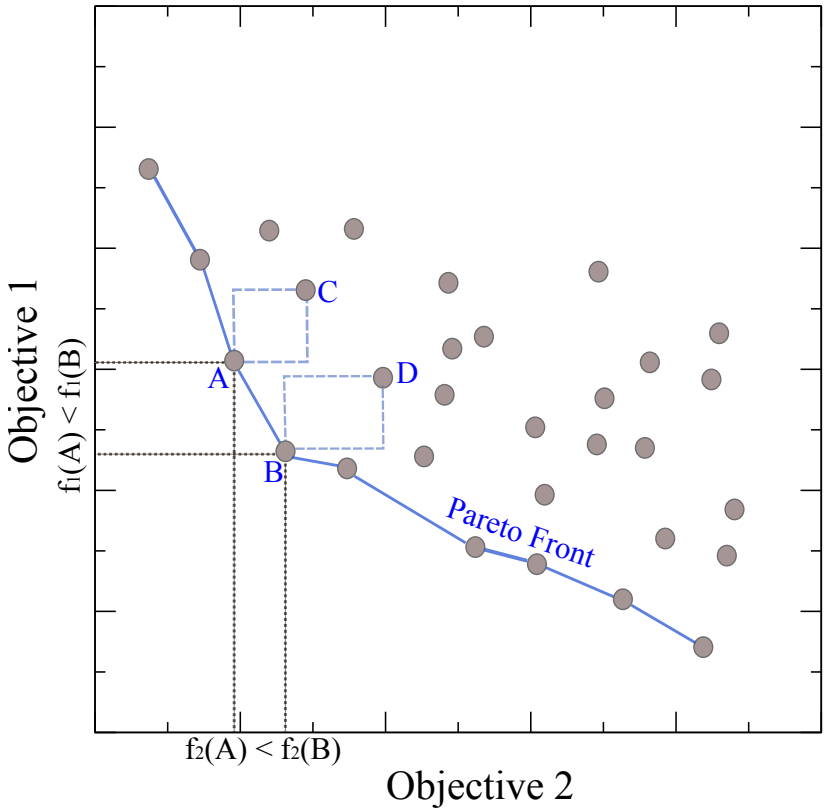

4.3. Irudia Pareto-fronte baten eredua, hau da, bestelako soluzioz menperaturik ez dauden soluzio-puntuen multzoa.

erabiltzean, prozesua behin eta berriro errepikatzea beharrezkoa da, ebazpen ezberdin bat lortzeko asmoarekin simulazio aldi bakoitzean [161].

4.2.5 Algoritmo Genetikoak (GA)

Algoritmo ebolutiboak natura eta genetikan inspiratutako algoritmo heuristiko moldakorrak dira, mutazio eta hautaketa bezalako, bio-inspiratutako operadoreak erabiltzen dituztenak optimizazio-prozesuan. Bereziki, algoritmo genetikoak, algoritmo ebolutiboen azpimultzo bat dira, eta hauen jatorria John Henry Holland-ek 70.hamarkadan aurkeztutako lana da [162]. Algoritmo hauek *machine learning* eta adimen artifizialean gehien erabiltzen diren algoritmo motak dira [163–167]. Normalean, algoritmo genetiko baten hasierako biztanleriaren (soluzio-bektoreen multzoa, algoritmo genetikoen terminologian) aleatorioki sortutako aldagaiez betetzen dira [3]. Soluzio-bektore hauek, gizabanakoak edo fenotipoak deitzen dira, GA-en terminologian. Fenotipo bakoitzak parametro sorta bat biltzen du, parametro

[3]Bilaketa-espazioaren inguruko informazioren bat izan ezkero ere erabili daitezke hasiera pauso horretan.

hauek kromosoma izena hartzen dute eta optimizazio-problemaren baldintzez mugatuta daude. Belaunaldi (iterazio) bakoitzean, algoritmoak fenotipoen fitness balioa ebaluatzen du, helburu-funtzioen arabera. Gero, algoritmoak hurrengo belaunaldian iraungo duten fenotipoak hautatzen ditu, hau da, bizirik iraungo duen biztanleria zein den erabakiko du. Hurrengo pausoan, algoritmoak belaunaldi horren fenotipoen genomak (optimizazio-problemaren aldagai bakoitzari deritzo) aldatuko ditu konbinaketa eta mutazio aleatorioak erabiliz, ondorengo belaunaldiko gizabanakoak sortzeko. Belaunaldi-kopuru maximo bat sortutakoan, biztanleriak konbergentzia lortzen duenean edota onargarria den fitness balio bat lortutakoan, algoritmoak bilaketa-prozesua amaitzen du. Algoritmo genetikoak hiru operadore estokastiko erabiltzen dituzte orokorrean optimo globalaren bilaketako bidean.

Operadore hauetatik bik hautagai soluzioetan aldakuntzak eginez soluzio berriak sortzen dituzte eta hirugarren operadoreak aldiz sortutako soluzioen artetik zeintzuk izango diren hurrengo belaunaldiak sortzeko erabiliko diren arbasoak hautatzen ditu. Algoritmo ebolutibo (EA) estandarren eta GA kanonikoen arteko desberdintasun garrantzitsuenetako bat, algoritmo ebolutiboetako biztanleria ordezkatzeko estrategiaren gabezia da. Genetikoetan ordean, biztanleria hutsik hasten bada ere, betez joaten da gurasoetan *crossover* eta mutazioa aplikatuz. Hain zuzen ere, guraso-bikote bakoitzeko bi haur berri sortzen dira, eta hauek biztanleriaren memorian sartuko dira [157]. Operadore hauek era sekuentzialean aplikatzen dira biztanleriaren fenotipoetan iterazio bakoitzean ondoren azaltzen den eran:

- **Hautaketa-estrategia**. Hurrengo belaunaldian bizirik jarraituko duen fenotipoak hautatzeko prozedura zehazten du. Nahiz eta hautaketa hau egiteko estrategia ugari dauden, ondokoak dira sarritan erabiltzen diren estrategiak algoritmo genetikoetan:

  a) Fitness balioaren araberako hautaketa (FPS), erruletaren hautaketa metodoa ere deitutakoa. Hautaketa-estrategia hau Holand-ek proposatu zuen [162] eta proposatutako fenotipoen artean soluzio bat hautatzeko probabilitatea ezartzen du, gizabanako bakoitzaren fitness balioarekiko proportzionaltasuna ezarriz egiten du. Kromosoma biztanleriaren barruan dagoen i kromosoma baten f_i fitness balioarentzat, metodo honek p_i hautaketa-probabilitate bat esleitzen dio i kromosomari, horretarako p_i kalkulatuz $p_i = \frac{f_i}{\sum_{j=1}^{N} f_j}$, non N biztanleriaren gizabanako kopurua da. Prozesu hau, kontzeptualki kasino baten erruleta batekin parekatzen da. Erruleta hori biztanlerian dauden gizabanako kopuruaren adineko zatietan banatzen da eta zati bakoitzaren zabalera gizabanako bakoitzaren fitness balioarekiko proportzionala da. Beraz, hurrengo belaunaldian bizirik iraungo duten gizabanakoak hautatzeko, erruleta biratu egiten da eta saritutako gizabanakoa hautatutzat hartuko da. Prozesu hau N aldiz errepikatzen da N gizabanako

hautatzeko, bide batez biztanlerian zeuden gizabanako kopurua mantentzeko optimizazio-prozesuan zehar. Metodo honetan, fitness balio onena duten hautagai soluzioak baztertuta izateko probabilitate gutxi badute ere, badago hauek hurrengo belaunaldiko haurrak sortzeko hautatuta ez izateko probabilitatea. Beste alde batetik, estrategia honek soluzio ahulei ere hurrengo hautaketa-prozesura pasatzeko probabilitateak eskaintzen die. Hau, berez, abantaila bat izan daiteke, soluzio ahulen osagarri (gen) batzuk ere interesgarriak izan daitezkeelako hurrengo birkonbinaketa prozesuetan. Beste hautaketa teknika batzuk erruleta metodoaren teknika garatzen dute, James Baker-ek [168]-en proposatutako *stochastic universal sampling* metodoa esaterako.

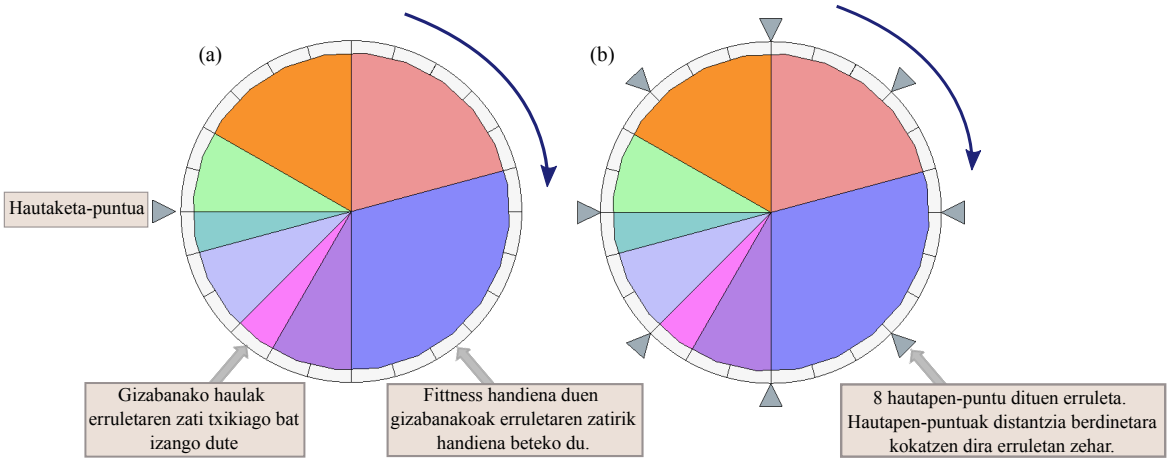

4.4. Irudia (a) Fitness-aren araberako hautaketa metodoaren ilustrazioa. Hautagaiak diren soluzioak erruletan kokatzen dira, bakoitzaren fitness balioaren araberako zabalera duen lekua hartuz. Gero, erruleta biratu egiten da eta hautatuta izango den kromosoma suertatzen da. (b) *Stochastic universal sampling* teknika. Metodo honek modu berdinean sakabanatutako N selektore erabiltzen ditu (kasu honetan N=8) eta hortaz, erruletaren bira bakar batean hautatuak izango diren guraso guztiak aurkitzen dira. Metodo honetan fitness balio onena duten soluzioak hautagai espazioa asetzea ekiditzen du. Irudi hau [169]-tik moldatu da.

b)*Stochastic universal sampling* (SUS): Erruletaren metodoaren hobekuntza bat da. Soluzio onenen hautaketa egiten du metodo honek, baina aldi berean, soluzio onak hautatutako soluzioen multzoa betetzea ekiditzen du. FPS metodoak errendimendu eskasa aurkeztu dezake biztanleriaren memorian gordetako gizabanakoen artean zenbait kromosomek fitness balio oso handia dutenean, gizabanako ahulei hautagai izateko aukera gutxi uzten dizkio, alegia azken horiei hautaketa-probabilitate oso baxuak esleitzen bait dizkio. Stochastic universal sampling metodoan, hautatutako gizabanakoa adierazten duen identifikadore

bakar bat erabili beharrean, berdin tartekatutako N identifikadore erabiltzen dira, eta beraz, erruletaren bira bakar batean hurrengo belaunaldia sortzeko erabiliko diren guraso guztiak hautatzen ditu. Horrela, hautaketa-prozesua eraginkorragoa eta doia egiteko aukera eskaintzen du.

c)Torneoa: *torneo* hautaketa-prozesuak behin eta berriro aleatorioki hautatutako biztanleriaren azpimultzo batetik fitness onena duten gizabanakoak hautatzean datza. Jarduera hau gizabanako hauen arteko torneo lehiaketa bat egitearekin irudikatzen da. Lehenengo, k gizabanakoak hautatzen dira biztanleriaren multzo artetik aleatorioki, non $k \leq N$ aldez haurretik ezarritako balio osoa da. Gero, p probabilitatearekin torneoaren multzoko gizabanakorik onena hautatzen da. Hurrengo pausoan, torneoaren multzo horretatik bigarren gizabanakorik onena hautatzen da $p \times (1-p)$ probabilitatearekin, eta hirugarren hautagai bat balego torneo multzo horretan, $p * (1-p)^2$ probabilitatearekin hautatuko da. Hautaketa-prozesuak beraz, irizpidea hori jarraituko du hurrengoko hautagaientzat. Hautaketa hori modu errez batean moldatu daiteke torneo hautaketa metodoan. Horretarako k torneoaren multzoko hautagai kopurua xehetu daiteke, p hautaketa-probabilitatearekin batera. k kopuruak balio baxua hartzen badu, bakarrik fitness balio altua duten gizabanakoak hautatuko dira; balio altua hartzen badu ordea, beste hainbat gizabanako kontuan hartuko ditu, beti ere hauentzat hautaketa-probabilitatea baxuago bat erabiliz. GA algoritmoan, torneoaren tamainak 2 balioa hartzen du. [157].

- **Gurutzaketa**. Gurutzaketa kromosomen birkonbinaketa prozesua kontrolatzen duen operadore genetikoa da algoritmo genetikoetan. Operadore honek kromosoma berriak sortzen ditu (umeak), gurasoen kromosomen genak nahastuz fitness balio hobeagoa duten soluzioak sortuz, hain zuzen ere. Gurutzaketa hau egiteko teknika ugari daude, bakoitzak birkonbinaketa modu ezberdinetan egiten dutenak:

  b) Puntu-bakarreko gurutzaketa: metodo honek gurutzaketa egiteko erreferentzia-puntu bakar bat hartzen du aintzakotzat. Puntu hori aleatorioki hautatzen da, kromosoma baten gen kopuru totalaren artean. Gero, puntu horretatik aurrera dauden kromosoma zatiak bi kromosomen artean trukatzen dira, bi soluzio berri sortuz.

  c) Bi-puntuen bidezko gurutzaketa: Kasu honetan bi puntu erabiltzen dira, aleatorioki hautatutakoak, trukaketa egiteko. Beraz, bi puntuen artean dauden gen guztiak gurasoen artean trukatzen dira, hurrengo belaunaldirako bi soluzio berri sortuz.

d) Gurutzaketa uniformea: Puntu bakarreko eta bi puntuen arteko gurutzaketako tekniketan ez bezala, gurutzaketa uniformean ez da inongo punturik hautatu behar genen trukaketa aurrera eramateko. Horren ordez, teknika honek gen bakoitza ebaluatu egiten du eta trukatu egiten ditu p probabilitatearekin.

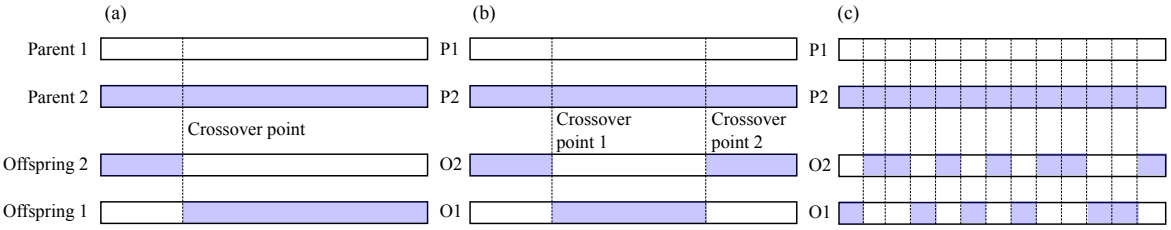

4.5. Irudia (a) Puntu bakarreko gurutzaketaren metodoa. Marra etenak aleatorioki hautatutako gurutzapen puntua adierazten du. Bertatik osatuko dira soluzio berriak.(b) Bi-puntuen bidezko gurutzaketaren metodoaren eskema. (c) Gurutzaketa uniformeak ez du ebasketa punturen beharrik, horren ordez, genak trukatuko ditu p_c probabilitate baten arabera. Irudi hau [170]-tik moldatuta dago.

- **Mutazioa**. Operadore genetiko hau aniztasun genetikoa sustatzeko erabiltzen da. 4.2.2 atalean azaldutako RSR operadorearen eta 4.2.1 atalean azaldutako energia altuenganantz ematen diren jausien pareko eginkizuna du operadore honek algoritmo genetikoen kasuan. Mutazio operadorearen eredu klasikoan mutazioak bit batek kontrako egoera bitarraren balioa hartzeko probabilitatea zehazten du. Mutazioaren bitartez, algoritmo genetikoak minimo lokaletatik ihes egiteko eta aukera berriak hausnartzeko ahalmena jasotzen du eta aldi berean, algoritmoak konbergentziara iristeko behar duen denbora murrizten du. Beste era batean esanda, operadore honek genen arteko permutazioa sustatzen du, gurasoengandik guztiz ezberdinak izan daitezkeen semeak sortzeko. Kodifikazio bitarraren ordez kodifikazio uniformea erabiltzen denean, mutazio operadore estandarrak distribuzio normala erabiltzen du, genaren balioari zarata ahul bat batuz edo kenduz p_M probabilitatearekin.

Algoritmo genetiko ohiaren erronka jarraituz, gaur egunerarte helburu-anitzen algoritmo ebolutibo (MOEA) asko proposatu dira [171–174]. Algoritmo hauek arrakasta itzela izan dute, hautagai soluzioen dibertsitatea mantentzeko potentzial handia bait dute, Pareto-optimo eskualderantz abiatzen diren heinean. *Non-dominated sorting genetic* algoritmoa (NSGA) [132]-en proposatu izan zena, algoritmo ebolutiboetatik arrakasta handia lortu zuen aurreneko algoritmoetako bat da. Hala eta guztiz ere, hurrengo hiru arrazoiengatik kritikak jaso ditu algoritmo honek:

I Algoritmo honen konplexutasunak $O(MN^3)$ erregela jarraitzen du, non M eta N, helburu kopurua eta biztanleria kopurua diren, hurrenez hurren. Arrazoi hau medio, algoritmo hau konputazio ikuspegitik garestia da biztanleria handietarako. Konplexutasunari dagokionez, *non-dominated sorting* irizpidea ezartzen du belaunaldi bakoitzean.

II NSGA algoritmo originalak ez-elitista den hurbilketa bat erabiltzen du. Elitismoa, belaunaldien artean, genotipo onenen iraupena ziurtatzen duen prozedura da, hain zuzen ere.

III Elkarbanaketa parametro bat, σ_{share}, zehaztea eskatzen du NSGA-k, biztanleriaren dibertsitatea ziurtatzeko eta soluzio baliokideen kopurua murriztua izateko.

NSGA-II algoritmoak, zailtasun guzti hauek ekiditzen ditu, ahal den neurrian. HSGA originalaren konplexutasunean, N tamainako biztanleria kontuan hartuz, ez-dominatutako lehenengo frontean egon behar diren soluzioak identifikatzeko, soluzio bakoitza beste soluzio guztiekin konparatu behar da, honela jakin bait daiteke soluzio hau dominatua dagoen ala ez. Beraz prozesu honek, soluzio bakoitzeko $O(MN)$ konparaketa egitea suposatzen du. Gainera, prosezu hau ez-dominatua den lehenengo mailako soluzio guztientzat errepikatu behar da, problemaren konplexutasuna igoz $O(MN^2)$-ra. Hau guztia amaitzean, lehenengo fronteko ez-dominatuak diren soluzio guztiak identifikatuta egongo lirateke. Hurrengo frontean dauden ez-dominatutako soluzioak aurkitzeko, berriro ere prozedura errepikatzen da. Kasu txarrenean, aurrerantzeko fronteen bilaketak $O(MN^2)$ konputazio [132] beharko lituzke. Azkenik, eta beti ere kasu txarrenean, N fronteko problema baten konplexutasun konputazionala $O(MN^3)$-koa litzateke. Guzti hau kontutan izanda, NSGA-II metodoak ez-dominatutako ordenaketa bat egiteko era bat eskaintzen du, eta aldi berean, problema ebazteko beharrezko konplexutasun konputazionala mugatu egiten du $O(MN^2)$-ra. Hau egiteko, NSGA-II algoritmoak bi entitate erabiltzen ditu, dominatuen zenbaketa egiten duten n_p eta S_p, alegia p soluzioak dominatzen dituen soluzio sorta, hurrenez hurren. Geroago, hurrengo atalean, ordenaketa metodo honi buruz xehetasun gehiago aurkitu daitezke. NSGA algoritmo originalaren bigarren ahultasuna, algoritmoaren elitismo eza da. Aldiz, NSGA-II algoritmoak elitismoan oinarritutako hautaketa bat egiten du, belaunaldien arteko biztanleriaren konbergentzia errazteko.

Azkenik, NSGA-II algoritmoak dibertsifikazio ezaren problemari aurre egiten dio, eta horretarako inolako parametro finkorik erabili barik egiten du. Jatorrizko NSGA metodoan, dibertsitatea σ_{share} banaketa parametroaren bitartez lortzen zan. Parametro honen balioak pareko fitnes balioa izango duten bi soluzioen arteko distantzia geometriko maximoa adierazten du. Bertan, erabiltzaileak berak ezartzen du parametro honen balioa, nahiz eta balio hau aldez aurretik ezartzeko inongo erreferentziarik ez dagoen. NSGA-II-n ordea,

parametro honen ordez, *crowed-comparison* deitutako hurbilketa erabiltzen da. Honek, biztanleriaren soluzio konkretu bakoitzaren inguruneko soluzioen dentsitatearen estimazioa egiten du. Beraz, metodo honek ez du erabiltzailearen partaidetzaren beharrik, belaunaldi bakoitzean berriz kalkulatzen den parametro bat erabiltzearekin parametroaren finkotasun eta ziurgabetasunak ekiditzen ditu.

4.2.6 NSGA-II algoritmoaren prozesua

Lehenbizi algoritmoak biztanleria sortu egiten du, gizabanako bakoitza mugatutako espazioaren barruko balio aleatorioekin betez. Gero, gizabanako bakoitza ebaluatu egiten da, M helburuen funtzio objektiboen arabera. Jarraian, biztanleria Pareto-fronte ezberdinetan ordenatu egiten da, horretarako ez-domeinatuen ordenaketa irizpidea jarraitzen da. Konkretuki, soluzio bakoitzari fitness balio bat ezartzen zaio, soluzio horiek fronteetan duten kokapenaren araberakoak izango dira. Fitness balioaz aparte, parametro berri bat kalkulatzen da, *crowding* distantzia, eta hau ere gizabanako bakoitzarentzat independienteki kalkulatzen da. Lehenengo belaunaldian, gurasoak torneo bitarraren teknika erabiliz hautatzen dira (beraz $k = 2$), horrela hurrengo belaunaldiko umeak sortu daitezen, gurasoen arteko gurutzaketa eta mutazio operadoreak aplikatu eta gero. Hurrengo pausoan, biztanleria eta sortu berriak diren umeen bitarteko biztanleriak ordenatu egiten dira berriro ere, ez-dominatuaren metodoa jarraituz. Horrela biztanlerian dauden gizabanako guztietatik bakarrik N gizabanakok jarraituko dute bizirik hurrengo belaunaldian, eta beste guztiak baztertuko dira. Bigarren iterazioan aldiz, prozesua ez da guztiz berdin egiten. Bigarren belaunalditik aurrera elitismoa erabiliko da, beraz, crowding distantzia eta fitness onena duten gizabanakoak zuzenean hurrengo belaunaldiko biztanlerian agertuko dira, inongo hautaketa-prozesutik pasatu gabe.

Azpiatal honetan algoritmoaren iterazio prozesuan potentzialki hautagai diren soluzioen ordenaketa metodoaren xehetasunak deskribatzen dira. Ondoren deskribatutako prozedura, [132, 175] lanetan proposatutako urratsak jarraitzen ditu hain zuzen ere. Lehenengo, P biztanleriako p gizabanako bakoitzarentzat hurrengoa egiten da:

- S_p zenbagailua, p soluzioak domeinatzen dituen soluzio sorta, eta n_p, hau da, p soluzio domeinatzen duten soluzio sorta hasieratzen dira, $S_p = 0$ and $n_p = 0$, hurrenez hurren. Gero, gizabanako bakoitzarentzat $q \neq p$ non $q \in P$ eta P biztanleriako gizabanako totalaren kopurua izanik:
  - p gizabanakoak q domeinatzen badu, orduan gehitu q domeinatuen S_p sortaren kontagailuan, hau da. $S_p = S_p \cup \{q\}$.
  - Aldiz q gizabanakoak p domeinatzen badu, orduan gehitu n_p kontagailuan unitate bat, i.e. $np = np + 1$.

Konparaketa konbinaketa guztiak egin eta gero, agian ez dago p domeinatzen duen beste gizabanakorik, hau da $n_p = 0$. Kasu horretan, p lehenengo frontean kokatuta egongo litzateke eta beraz, p gizabanakoaren rangoak 1 balioa izango luke ($p_{rank} = 1$). Gainera, lehenengo fronteari p gizabanakoa ere gehitzen zaio $F_1 = F_1 \cup \{p\}$. Ondoren, algoritmoak hurrengo Pareto-frontearen bilari ekingo dio.

- Fronteen kontagailuak, i, 1 balioa hartuko du hasiera batean, $i = 1$, eta i frontea hutsik ez dagoen bitartean, hau da, $F_i \neq 0$, hurrengoa egingo da:

  - Q aldagaia hasierazten da. $(i+1)^{th}$ fronteko gizabanakoak gordetzeko erabiltzen den aldagaia da hau eta hasieran zero balioa izango du, $Q = 0$.
  - Gero, F_i fronteko p gizabanako bakoitzarentzat eta q gizabanako bakoitzarentzat, non $q \in S_p$:
    - q gizabanakoaren menpekotasun-kontagailua gutxitu unitate batean, $n_q = n_q - 1$.
    - $n_q = 0$ bada, orduan hurrengo fronteetan kokatutako gizabanakoak ez dute q domeinatuko. Beraz, q-ri hurrengo rango balioa ematen zaio, $q_{rank} = i + 1$ eta Q sorta eguneratzen da, hau da $Q = Q \cup q$.
  - Iterazio bat bukatzen den bakoitzean, fronteen kontagailuari unitate bat gehitzen zaio, $i = i + 1$, eta Q multzoa i_{th} fronteari esleitzen zaio, hau da. $F_i = Q$.

4.2.7 *Crowding* distantziaren kalkulua

Menpekotasunik gabeko ordenaketak, gizabanakoak fronte ezberdinetan sailkatzen ditu, hauen egokitasun (fitness balioa) balioaren arabera. Baina, parametro baten xehetasunik gabe biztanleriaren dibertsitate-egonkortasun baldintzak betetzeko, NSGA-II metodoak *crowding* distantzia deitatutako trena erabiltzen du. *Crowding* distantzia hau, M helburuen arabera fronte ezberdinetan sailkatutako gizabanakoen arteko M dimentsioetako hiper-espazioko distantzia euklidearra kalkulatzean datza [175, 176]. F_i fronteko N gizabanako ezberdinen arteko crowding distantzia kalkulatzeko prozedura hurrengo pausoetan deskribatzen da:

- Distantzia euklidearrak zero balioa hartzen du hasiera batean, F_i fronteko gizabanakoentzat, $F_i(d_j) = 0$, non j gizabanako zehatz bat litzateke F_i frontean.
- m funtzio objektibo bakoitzarentzat:
  - F_i-ko gizabanakoak ordenatu m helburuaren fitnessaren arabera, $I = sort(F_i, m)$.

- Frontearen mugetan kokatutako balioei distantzia infinitu bat esleitzen zaio, horrela mugetako balioak beti hautatuak izango bait dira, $I(d_1) = I(d_n) = \inf$, eta beste gizabanakoentzat distantzia ondorengo moduan kalkulatuko da:

$$I(d_k) = I(d_k) + \frac{I(k+1) \times m - I(k-1) \times m}{f_m^{max} - f_m^{min}} \tag{4.14}$$

non $I(k) \times m$ balioa k^{th} gizabanakoaren m^{th} funtzio objektiboa da I-n [175].

4.2.8 NSGA-II algoritmoaren operadore genetikoak

NSGA-II-k *Simulated Binary Crossover* (SBX) [177, 178] eta mutazio polinomikoa [179], erabiltzen ditu gurutzaketa eta mutazio operadore giza, hurrenez hurren. SBX gurutzaketa metodoa bereziki egokia da optimo ugari dituzten problemetan eta baita aldez aurretik minimoen eta maximoen kokapenaren ezagutza eskaxa dagoen problemetan. Metodo honek bi seme osatzen ditu aldez aurretik hautatutako bi gurasoengandik, ondorengo transformazioak erabiliz [175]:

$$c_{1,k} = \frac{1}{2}\left[(1-\beta_k)p_{1,k} + (1+\beta_k)p_{2,k}\right] \tag{4.15}$$

$$c_{2,k} = \frac{1}{2}\left[(1+\beta_k)p_{1,k} + (1-\beta_k)p_{2,k}\right], \tag{4.16}$$

non $c_{i,k}$, i. umearen k aldagaia da, $p_{i,k}$ hautatutako gurasoa da, eta β_k aleatorioki egokitutako zenbaki aleatorioa da, ondorengo dentsitatea duena

$$p(\beta) = \frac{1}{2}(\eta_c + 1)\beta^{\eta_c}, \quad \text{if} \quad \leq \beta \leq 1 \tag{4.17}$$

$$p(\beta) = \frac{1}{2}(\eta_c + 1)\frac{1}{\beta^{\eta_c+2}}, \quad if \quad \beta > 1 \tag{4.18}$$

Distribuzio hau (0, 1) bitartean uniformeki muestreatutako u zenbaki aleatoriotik lortu daiteke. η_c gurutzaketa operadorearen distribuzioaren indizea da eta umeen eta gurasoen aldagaien arteko sakabanaketa neurria kontrolatzen du. Ondorengo eran formulatu daiteke:

$$\beta(u) = (2u)^{\frac{1}{\eta+1}} \tag{4.19}$$

Mutazio polinomikoak c_k ume berri bat sortzen du p_k gurasotik ondorengoa jarraituz

$$c_k = p_k + (p_k^u - p_k^l)\delta_k \tag{4.20}$$

non p_k^u gurasoaren aldagai baten goiko muga-baldintza eta p_k^l azpiko muga-baldintza dira eta δ_k distribuzio polinomikotik jasotako aldakuntza txiki bat da [175]

$$\delta_k = (2r_k)^{\frac{1}{\eta_m+1}} - 1, \quad \text{if} \quad r_k < 0.5 \tag{4.21}$$

$$\delta_k = 1 - [2(1-r_k)]^{\frac{1}{\eta_m+1}}, \quad \text{if} \quad r_k \geq 0.5, \tag{4.22}$$

non r_k uniformeki muestreatutako zenbaki aleatorioa da $(0,1)$ bitartean eta η_m mutazio distribuzioaren indizea da.

Ondoren, algoritmoak, sortu berri den biztanleria aurrekoarekin batzen du. Hau eginez, aurreko biztanleriako gizabanako onenak eta baita belaunaldi berriko gizabanako onenak hautatu ditugunez, elitismoa bermatuta dago. Belaunaldi berria sekuentzialki fronte bakoitzarekin osatzen da, biztanleriaren tamaina gainditzen den arte. F_j fronteko gizabanako guztiak biztanleriara gehitzean biztanleriaren tamaina maximoa, N, gainditzen bada, orduan, F_j fronteko gizabanakoak *crowding* distantziaren arabera hautatzen dira, biztanlerian N gizabanako hautatzen diren arte. Prozedura hau belaunaldiz-belaunaldi errepikatzen da, biztanleriaren konbergentzia lortzen den arte edota aldez aurretik ezarritako iterazioak betetzen diren arte.

Kapitulua 5

Kristal fotoniko zirkuituen alderantzizko diseinuaren bidezko optimizazioa

Kapitulu honetan kristal fotonikoetan egindako eta alderantzizko diseinuan (ID) oinarritutako banda-zabalera handiko dispositibo pasiboen diseinatutako egiturak aurkezten dira. Egitura horiek, bereziki zirkuitu trinko fotonikoetan (PIC) ezinbestekoak diren funtzioak era eraginkor baten betetzeko burutu dira. Egitura hauetan, aurreko kapituluetan deskribatutako optimizazio metodo heuristiko eta genetikoak erabili dira ID prozesuaren araketa gidatzeko. Lortutako egiturak, intuizioan oinarritutako egiturak baino eraginkortasun eta funtzionalitate hobeagoak aurkezten dituzte. Metodoak, dagoeneko luzaro frogatu izan diren bi optimizazio metodo alternatiboen baliabideak erabiltzen ditu, aldez aurretik ezarritako irizpide baten araberako bilaketa bat gauzatzeko, beti ere FE metodoaren fidagarritasunaz eta bizkortasunaz baliatuz. Lortutako emaitzak aztertuz, PC egituren diseinurako, bi metodo hauen fidagarritasuna eta eraginkortasuna baieztatzen da. Gainera, kapitulu honetan proposatutako egiturak litografia prozesuak dituen mugak optimizazio-prozesuan kontuan hartu dira. Beraz, diseinu hauek ez dira bakarrik esparru teorikoan aztertu daitezkeen emaitzak, baizik eta fabrikatu daitezkeen egitura praktikoak ere badira.

5.1 Alderantzizko diseinuaren metodoa (ID)

Zientzia esperimentalak jarraitzen duen ohiko prozesuan, antzemandako fenomeno fisiko batek hipotesiak formulatzera eramaten gaitu eta hipotesi hauen baieztapenetik, aldagai batzuen menpe dagoen sistemaren eredu bat lotzen duen teoria berri bat garatzen da. Eredu teoriko hori problema era zuzenean ebazteko erabiltzen da, modeloaren aldagaien balioak ezartzen dira eta datu esperimentalak kalkulu teorikoekin konparatzen dira. Beraz, eredu teorikoa era zuzenean planteatutako problemaren formulazioa da. Aldiz, neurtutako datuen

bitartez aztertu beharreko sistemaren propietateak antzematea, hau da, alderantzizko problema ebaztea, askoz ere sailagoa izaten da, zientzia esperimentalaren ohiko prozesuaren urratsak alderantzizko eran jarraitzen bait ditu. Material baten propietateak, material honen egitura sortzeko parte hartzen duten aldagaien menpe daude. Bereziki, kristal fotoniko batean, sarearen maiztasunak edota materialaren indize dielektrikoak, egituraren propietateak baldintzatzen ditu. Beraz, material berezi bat diseinatze-prozedura zuzena jarraitu ezkero, aldagaien pisuak iteratiboki doitzen dira, behar den konfigurazio horretara ahal den gehien hurbiltzeko. Bide hau problema linealetan aplikatu daiteke soilik, hurbilketa ugari aztertzea suposatzen bait du.

Problema linealetatik kanpo, planteatutako problemak ebazpen bat izan dezake edo ez, ebazpen hori bakarra izan daiteke edo ez eta ebazpen hori egonkorra izan daiteke edo aldakortasun nabarmena aurkeztu dezake aldagaietan aldaketa txikiak jasan ezkero. Alderantzizko diseinuan aitzitik, aurreneko ebazpen batetik abiatuz, eskuratu gura ditugun propietate fisikoak definitzen dituzten aldagaien balioak ondorioztatzen dira. Beste alde batetik, problema zuzenean ebazpen bakar bat duen problemak, alderantzizko diseinuan ebazpen ugari izan ditzake [180]. Gaur egun, helburu zehatz batzuk betetzen dituen PC egitura bat lortzeko, batez ere intuizioan oinarritutako erabakiak jarraitzen dira, teknika matematiko zorrotzetan oinarritutako argibideak erabili barik. Funtsean, ekintza hori diseinu zuzenean kokatu daitekeen jokabidea da. Horrela, aurreneko ikerketa ugarik kristal fotonikoen aldagaietan eragindako aldaketa batzuen bitartez lorturiko abantaila optikoak aurkezten dituzte. Hala ere, egoera batzuetan, frogaketa-hutsegite eran oinarritutako bilaketa bat eginez ezaugarri zehatz baten hobekuntza adierazgarri bat lortzea, eragiketa saila eta neketsua bilakatzen da. Gainera, ez-korrelatuta dauden helburu bat baino gehiago betetzen dituzten egitura fotonikoak diseinatzea ez da eskuragarria horrelako metodoak erabiliz gero . Beste alde batetik, maiztasun zehatz bat jarraitzen ez duten kristal fotonikoen egiturak diseinatzeko orduan, konfigurazio posibleen kopurua asko handitzen da eta beraz, parametro gutxi batzuekin bakarrik jolasteak zentzua galtzen du. Ikus dezagun adibidez ez-periodikoa den PC baten eredua. Hartu dezagun oinarriz material dielektrikoan zulatutako hutsunez osatuta dagoen PC bat. Bertan, argiak ibilbide zehatz bat jarraitu dezan zulo batzuk material dielektrikoz estali egin beharko dira. Kasu horretan, posibleak diren konfigurazioen kopuruak gora egiten du kluster hori osatzen duten zuloen kopuruak (N) gora egin ahala. Zehazki, kasu horretani, konfigurazio kopuruak 2^N araua jarraitzen du. Nahiz eta aurreko adibidea hasiera batean ariketa sinple bat baino ez zirudien, argi ikus daiteke problemaren konfigurazio kopuru hori aztertzea ez dela bideragarria N zulo kopurua maiztasun tarte gutxi batzuetan aurkitu daitezkeen zuloak kontuan hartzen dituenean. Zailtasun honen aurrean, ohikoa izaten da problema askatasun gradu gutxi batzuetara mugatzea, eta parametro gutxi

horien bilaketa-ingurune osoa banan-banan arakatzea. Azkenik, aldagai horien araberako egituretatik, emaitzik interesgarriena eskaintzen duen egitura aukeratzen da. Metodo hori beraz, konputazionalki oso garestia da, eta kasu gehienetan ezin da era zuhur batean aplikatu. Bestalde, alderantzizko diseinuaren teknika erabilita eta bilatzen ari garen materialaren helburuak ezarriz, helburu hauek betetzen dituzten egiturak aurkitu daitezke, askatasun gradu kopuru arbitrarioak izanik ere [181–183]. Metodo hau da, hain zuzen ere, lan honetan jorratu dugun teknika kristal fotoniko egitura konplexuak diseinatzeko. Horretarako, metodo heuristikoen eta ebolutiboen konbinaketak erabili ditugu, elementu finituen metodoarekin batera [184], helburu zehatz batzuekin bat datozen egitura fotonikoak aurkitzeko. Teknika honen bitartez eraginkortasun handiko zirkuitu integratu fotonikoak diseinatu ditugu. Hauek, integrazio dentsitatearen aldetik eta baita kostu aldetik hobekuntza nabariak aurkezten dituzte. Algoritmo heuristikoak oinarrizko bi baliabide erabiltzen dituzte: zatitu-eta-menderaketa prozesua, hau da, problema azpiproblema sinpleagoetan zatitzea, eta optimizazio-prozesu sekuentziala. Algoritmo horiek, optimizazio globalaren ildoan eta baita ingeniaritzako beste esparru askotan, ibilbide luzea izan dute. Hala eta guztiz ere, optimizazio heuristikoan oinarritutako teknikak aplikatzeak oraindik konputazio baliabide handiak eskatzen ditu. Orokorrean, algoritmo heuristikoak, ebazpen hautagai bat kalkulatzeko makinaren prozesaketa-denbora bitarte tribiala behar denean soilik aplikatzen dira. Material heterogeneo konplexu baten denboraren domeinuko metodoak erabiliz Maxwell-en ekuazioak ebazteak ordea ez du horrelako azkartasunik onartzen.

Eremu elektromagnetikoen hedakuntzaren kalkuluan, konputazio denborak luzeak izaten dira eta eremu horiek kalkulatzeko konputazio baliabideak era intentsiboan erabiltzen dira. Bi arrazoi horiengaitik, metodo heuristikoak ez dute hasiera batean eraginkortasun handirik lortuko mota horretako problemak ebazteko orduan. Elementu finituen bitartez ordea, sistema luze eta konplexuetan hedatzen diren eremu elektromagnetikoak egoera egonkorrean aztertu daitezke, eta beraz, uhin EM-en ebazpenak era azkarrean aurkitu daitezke [184] optimizazio iteratibo bat burutuz. Bestalde, ondoren deskribatzen diren PC egiturak diseinatzeko erabili izan den ID teknikaren bidez, egituraren aldagaietan, CMOS fabrikazio teknologiarekin bat datozen muga fisikoak ezarri daitezke. Horretaz aparte, metodo honek, PC diseinuen problema anitzetan aplikatu daiteke, metodoak ez bait du problemaren natura ezagutu beharrik ezarritako helburura iristeko. Beraz, prozesu estokastiko baten bidez gidatutako optimizazioaren abantailak, elementu finituaren metodoaren (FEM) zehaztasun eta bizkortasunarekin batera erabiliko ditugu osagarri optiko pasibo funtzionalak diseinatzeko [184]; 3.46 errefrakzio indizea duen material baten $0.35a$ erradioko zuloz egindako sare triangeluar baten antolatutako 2D kristal fotoniko baten oinarrituz. Ondorengo

topologiak, ezinbesteko funtzionalitateak hobetzen dituzte eta ibilbide konplexuetan zehar argia garraiatzeko gai dira.

5.2 Argi-potentzia banatzaileak

Sistema elektronikoetan, oinarrizko funtzioak egiteko ezinbestekoak diren gailu optikoen artean, argi-potentziaren banaketa ahalbidetzen duten osagarri optikoak funtsezko eginkizunak betetzen dituzte. Alde batetik, uhin-gida batetik garraiatzen den argia zatitzen dute eta beste alde batetik, Match-Zhender interferometroak (MZI), edota interkonektore optiko integratuak bezalako gailu konplexuagoak sortzeko ezin besteko elementuak dira. Funtsean, potentzia-banatzaile baten eginkizun nagusia jasotako argia neurri berean irteeratako uhin-gidetan banatzea da. Aurreneko ikerketa lanen arabera, PC teknologia erabiliz, elektro-optikoki kontrolatu daitezkeen banatzaile/ akopladoreak nahiz *switch*-ak nano-eskalan eskuratzeko aparteko materialak izan daitezke [185–188]. Uhin-gida zuzenak eta kurbadurak dituzten uhin-giden ezaugarriak jadanik sakonki aztertuak izan diren esparruan diren bitartean, banatzaile eta akopladore optikoen ikerketak ez dute hainbesteko arretarik jaso orain arte. Bereziki, orain arte proposatu izan diren konfigurazioak batez ere mikro-uhinen esparruan kokatzen dira [185, 186], eta egitura hauek sistema fotonikoetara moldatzeak zailtasun handiko lana lirateke. Gainera, dielektrikozko zutabez osatutako kristal fotonikoetan, T eta Y motatako akopladoreak emaitza bikainak aurkezten dituzten egiturak dira, zoritxarrez PC-slab egituretan, banatzaile horien eraginkortasunak bortizki behera egiten du. Beste alde batetik, zuloz osatutako dielektrikoetan, modu ugari sustatu daitezke uhin-gidetan eta beraz, modu multzo horiek era optimoan banatzeko oinarrizko egitura hauek ez dute behar bezalako eraginkortasunik lortzen [186]. Argia jatorrizko uhin-gidak zehazten duen ibilbidetik desbideratzen denean norabide kristalino ezberdin baterantz, modu berriak gidatzen dira, edota jatorrizko moduen konbinaketak sortzen dira. Modu berri horien eta jatorrizko uhin-gidak gidatzen dituen moduen arteko eremuen ezberdintasunak transmititutako argi-kopurua bortizki murrizten du. Are gehiago, oinarrizko T eta Y akopladoreak erabiltzen direnean. Y akopladore estandarrean akats bakarreko kristal fotonikoz osatutako hiru uhin-gida elkartzen dira, 120°-ko egitura osatuz. Geometria honek islapen handiak sortzen ditu eta bere erabilpena banda-zabalera estuetara mugatzen da soilik. Antzeko eraginak izaten dituzte *multi-mode interference* motatako potentzia-banatzaileen konfigurazioak.

MMI banatzaileak argiaren barreiatze naturak duen izaera periodikoaz baliatzen dira argiaren banaketa gauzatzeko. Horretarako modu bikoiti baten irudi bikoitza irteeran kokatutako uhin-gida pare batera fokalizaten dute. Zoritxarrez, argi-irudi hauen simetrikoak posizio ezberdinetan aurkitzen dira maiztasun ezberdineko argi izpientzako, eta beraz, banda-

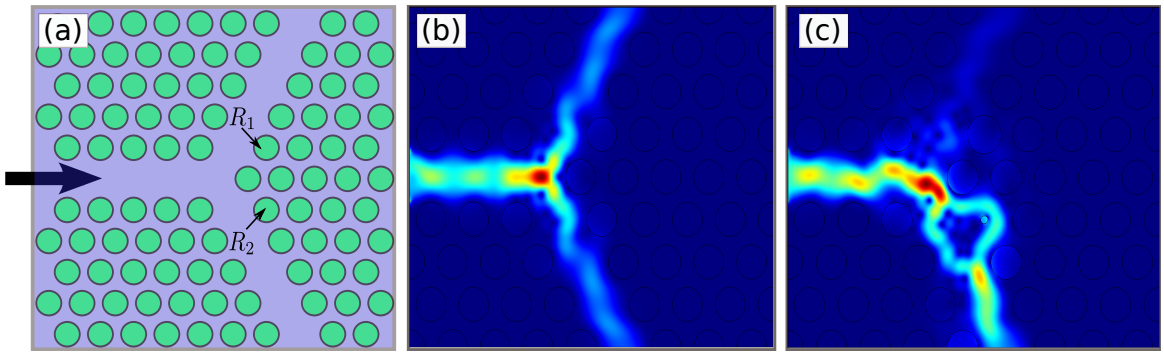

5.1. Irudia (a) *Toy-model* banatzailearen irudi eskematikoa. Bertan, R_1 eta R_2 bezala izendatutako zuloen erradioa aldatu da atzera-isladatzen den argi portzentaia murrizteko. Gezi beltzak argiaren jatorria adierazten du W1 uhin-gidan. (b) Hasierako Y–banatzailearen konfigurazioan simulatutako denboran bataz-besteko potentzia-fluxua. (c) ID metodoaren bidez lortutako emaitza baten denboran bataz-besteko potentzia-fluxua. Bertan, argi gehiena Y–banatzailearen irteerako portu batera bideratzen da.

zabalera handia lortzea ez da posiblea honelako dispositiboak erabilita. Ondoren, aurreko kapituluan azaldutako metodo heuristikoak erabiltzen dituen ID metodologia erabiliz, *Y*–eran eta MMI sistemetan oinarritutako egitura berriak aurkezten dira. Hala ere, diseinu praktikoetara jo baino lehen, oraindik konputazionalki konplexuak diren egitura tribial batzuk aztertu ditugu, ID metodoaren eraginkortasuna aztertzeko.

5.2.1 Y-banatzaile baten eredu sinplifikatua

Askatasun gradu ugari dituzten problemak ebazteko, alderantzizko diseinuko (ID) teknika erabiltzeak alagai guztien domeinuko araketa sakon bat egitea ekiditzen du eta bitartean, optimo globala aurkitzeko bide bakarra izaten da, kasu gehienetan. Horrelako kasuetan ere, zaila edota konputazionalki ezinezkoa izaten da lortutako ebazpena optimo lokal edo global baten kokatuta dagoen jakitea. ID metodoaren bidez jaso daitezkeen emaitzak frogatzeko, *brute-force* bilaketa zorrotz bat aplikatzea posiblea den eredu sinple batetik abiatu gara, bertan lortutako emaitzak optimo globalera ailegatzen diren edo ez frogatzeko, egitura konplexuagoetan ID metodoa aplikatu baino lehen. Abiapuntutzat hartutako *toy–model* egitura sinple hauen artean, aldez aurretik metodo semi-analitikoak erabiliz proposatu diren PC konfigurazioak hautatu dira.

Jarraian, ID metodoa erabiliz *Y* motatako akopladoreen diseinua aurkezten da. Gainera, era honetan eraldatutako egiturak, kasu batzuetan, orain arte jasotako ebazpenak baino emaitza hobeagoak eskaintzen dituela ikusiko da.

Nahiz eta ondorengo *toy–model* egiturak sinpletasun nabaria duten, oraindik, honelako ereduetan bilaketa sakon bat egitea konputazionalki ariketa luze eta astuna da, behintzat klusterizatu gabeko baliabideak erabiltzen badira.

5.1.a irudian lehenengo egitura sinplea aurkezten da. Egitura hau uhin-gida batez eta Y motatako akopladore bat irudikaten du, jatorrizko uhin-gidarekin $60\,^{\circ}$-ko angelua osatzen duten bi W1 uhin-gida elkartuz. Egitura horretatik abiatuz, irteeretako portuetarantz argi potentzia gehiena zuzendu dadin, eta beraz, sarrerako uhin-gidarantz barreiatzen den argi potentzia minimizatzea posiblea egiten duen konfigurazioa aurkitzean datza gure helburua. Berez, egitura hau ezin da Y akopladore moduan sailkatu, ez bait du potentziaren banaketa eragiketarik egiten. Halere, egitura teoriko honek ID metodoaren prozesua antzemateko baliogarria da.

5.1.a irudian, argia W1 uhin-gidako portu bateteik igortzen da eta irteerako portu baten transmitantzia kalkulatzen da 3.1 ekuazioa erabiliz. Eremu elektro-magnetikoen hedakuntzaren kalkuluan FE metodoa erabililtzen da, erregimen egonkorrean.

Emaitza hau hautagaitzat hartutako geometria bakoitzaren egokitasuna ebaluatzeko erabiltzen da, *fitness* balioa deritzogunean. Bereziki, *fitness* balioa kalkulatzeko*root-mean-square desviation* (RMSD) erabiliko dugu.

$$\mathrm{RMSD}(\theta_1,\theta_2) = \sqrt{\mathrm{MSE}(\theta_1,\theta_2)} = \sqrt{T((\theta_1-\theta_2)^2)} = \sqrt{\frac{\sum_{i=1}^{n}(x_{1,i}-x_{2,i})^2}{n}}. \qquad (5.1)$$

Kasu honetan, bi algoritmoen bidez lortutako emaitzen egokitasuna kalkulatzeko, Si materialean egindako $0.35a$ erradioko zuloz W1 uhin-gida zuzenaren transmitantzia hartu dugu oinarritzat.

Hiru askatasun gradu baino gehiago dituzten azpiespazioak irudikatu ezin direnez, gure lehenengo saiakera honetan, sistema hau zeharkatuz argiaren garraioa hobetzen duten R_1 eta R_2 elementuen erradioa aurkitzera mugatuko dugu problema (ikusi 5.1 irudia). Horrela, 4.2.2 eta 4.2.1 ataletan azaldutako IHS eta FSA algoritmoetan 60 Monte Carlo saiakera eginez alderantzizko diseinuaren metodoa frogatu da. Bi algoritmo hauen bitartez optimo globala aurkitu da ia kasu guztietan, 5.2 irudian ikusi daitekeen moduan. Ebazpen-espazioaren araketa sakona egiteak 24 ordu baino gehiago behar izan ditu. Aldiz, ID metodoaren bitartez egindako saiaketa bakoitza minutu gutxi batzuetan egin daiteke, *i*3 ordenagailu estandar bat erabiliz. 5.1.b irudian abiapuntutzat hartu dugun egitura ez-optimizatutan simulatutako argi potentziaren denboraren batezbesteko diagrama aurkezten da, eta 5.1.c irudian magnitude bera optimo globalarekin bat datorren egiturarentzat adierazten da. Optimizatutako egituran, igorritako argia irteerako uhin-gidarantz hedatzea lortzen da eta atzera isladatzen den eremua arbuiagarria da. Egitura horren simetria bikoitia denez, optimo globalaren grafikoak ere

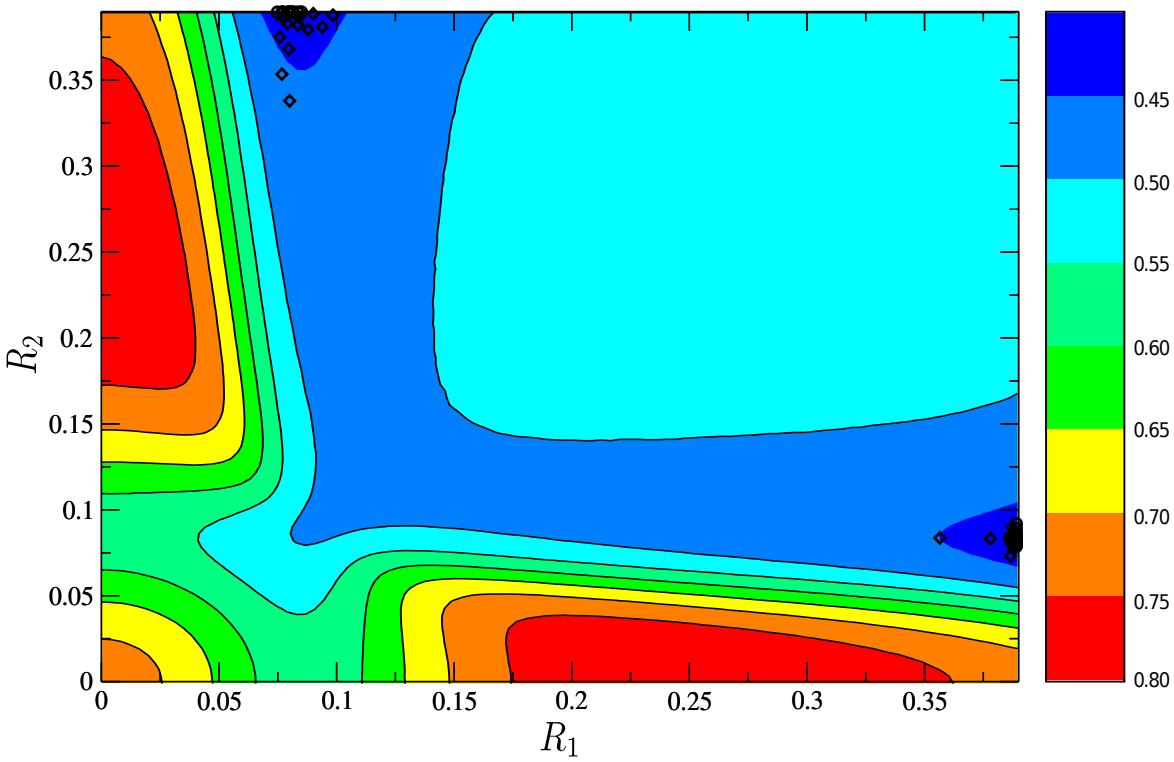

5.2. Irudia Dentsitate mapak optimizazio funtzioaren kostu funtzioaren balioa adierazten du kalkulatutako ebazpen-espazio osoan. Horretarako, bilaketa-espazioa 10.000 puntuetan zatitu da. Zirkulu batez inguratutako puntuak eta diamante forma duten puntuak IHS metodoaren bidez eta FSA metodoaren bidez lortutako ebazpenak dira, hurrenez hurren.

simetria bikoitza izango du. Horrelako egoeretan, gradienteetan oinarritutako teknikak hasierako puntuaren hautaketaren menpekotasun larria izaten dute. Aldiz, erabili ditugun optimizazio algoritmo heuristikoak inplementatzen dituzten operadore estokastikoen bitartez, bilaketa-espazioan zehar ingurune zabalago bat arakatu daiteke, eta hasierako baldintzak ez dute eragin zuzenik lortutako emaitzetan. Orokorrean, bi algoritmo hauek erabiliz, optimo globalak aurkitzen dira, optimo global bakoitza %50-eko probabilitatearekin. Bereziki, IHS algoritmoak konbergentzia puntua lortutakoan, HM harmonia-memorian bi optimo globalak zehazten dituzten aldagai balio osagarriekin betetzen da, %50-eko probabilitatearekin.

5.3.c irudiak, optimizazioaren bilakaera adierazten du, 5, 10, 20 eta 30 iterazio burutakoan. Saiakera bakoitzaren egokitasuna edo *fitness* balioa aldagai sorta bakoitzarentzat kalkulatzen da, elementu finituen metodoaren bitartez eremu EM-ak ebatziz.

5.3 irudian, bi metodo hauen batezbesteko eraginkortasuna, iterazio bakoitzean eta horien maximo eta minimoak adierazten dira. Bi metodoen konbergentzia bizkorrak *toy-model* problemaren konplexutasuna iterazio gutxi batzuetan era errezean ebazten duela adierazten du. *Fitness* funtzioak ere ez du ezegonkortasun handirik aurkezten saiaketa bakoitzean, nahiz

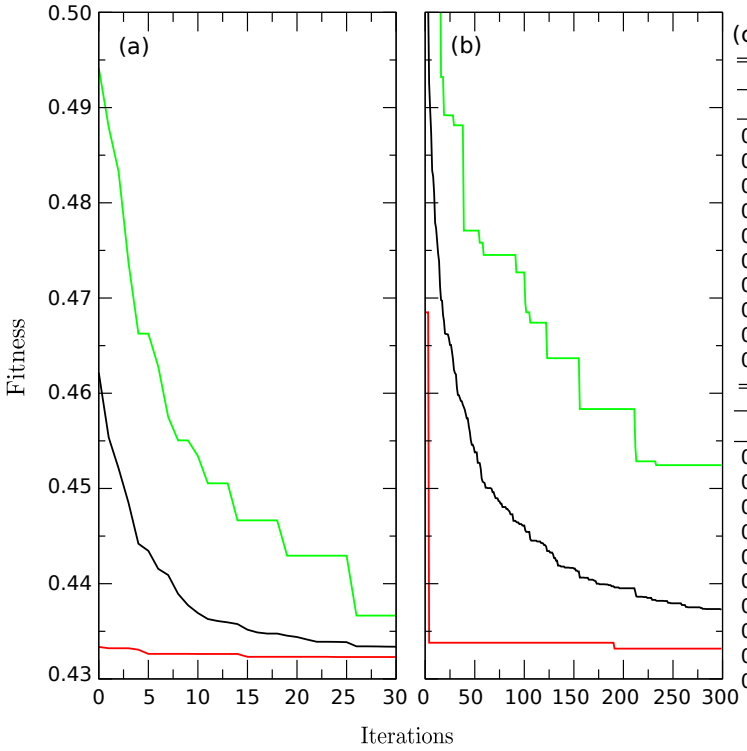

(c)

Iteration1			Iteration10		
R_1	R_2	fitness	R_1	R_2	fitness
0.083	0.334	0.457	0.39	0.088	0.434
0.315	0.084	0.463	0.07	0.387	0.441
0.078	0.305	0.472	0.072	0.387	0.441
0.101	0.268	0.473	0.101	0.384	0.448
0.154	0.108	0.488	0.101	0.384	0.448
0.154	0.134	0.495	0.364	0.079	0.448
0.065	0.334	0.498	0.364	0.076	0.451
0.197	0.356	0.516	0.072	0.373	0.451
0.203	0.226	0.517	0.101	0.373	0.453
0.197	0.305	0.518	0.101	0.370	0.454

Iteration20			Iteration30		
R_1	R_2	fitness	R_1	R_2	fitness
0.39	0.088	0.434	0.39	0.079	0.433
0.072	0.387	0.445	0.39	0.079	0.433
0.072	0.387	0.441	0.39	0.088	0.434
0.101	0.384	0.448	0.072	0.387	0.441
0.101	0.384	0.448	0.072	0.387	0.441
0.364	0.079	0.448	0.072	0.387	0.441
0.364	0.076	0.451	0.072	0.387	0.441
0.072	0.373	0.451	0.39	0.071	0.442
0.101	0.373	0.453	0.101	0.387	0.447
0.101	0.370	0.454	0.101	0.387	0.447

5.3. Irudia (a) 60 Monte Carlo-ren bidez lortutako balioen bataz-besteko konbergentzia IHS algoritmoa erabilita (zuzen beltza), ebazpenik txarrena (zuzen berdea) eta ebazpenik onena (zuzen gorria). (b) FSA algoritmoa 300 Monte Carlo erabiliz lortutako emaitzak. (c) IHS memorian gordetako ebazpenak 1, 10, 20 eta 30 iterazio egindakoan. Urdinez azpimarratutako emaitzak maximo global batean kokatzen diren ebazpenak dira eta gorriz azpimarratutakoak problemaren simetriak sortzen dituen maximo global osagarriak dira, hurrenez hurren.

eta algoritmo hauek prozesu estokastiko baten oinarritzen diren. Eredu jakin honetan, IHS algoritmoa fitness balio baxuago batera iritzi da baina kapitulu honetan aurkezten diren egituretan jasotako beste emaitzen arabera, (IHS) eta (FSA) metodoen eraginkortasunaren bidezko konparaketa bat egitea zaila da, eta problema konkretuaren arabera bata edo bestea hobeto moldatu daitezke; tamalez aldez aurretik zein moldatuko den hobeto jakiterik ez dugu. Beste alde batetik, (IHS) eta (FSA) metodoentzat iterazio-kopuru ezberdina erabili da, IHS algoritmoak ebazpen gehiago hartzen bait ditu kontuan iterazio bakoitzean eta FSA metodoak ordea ebazpen bakar bat onartzen du.

Ondorengo ataletan, potentzia-banatzaile eskema berriak proposatzen dira. Horrelako topologietan simetria ezaugarriak mantentzen dira eta, gainera, (PIC) baten bete beharreko integrazio-tamainaren eskakizunak ere kontuan hartuko dira.

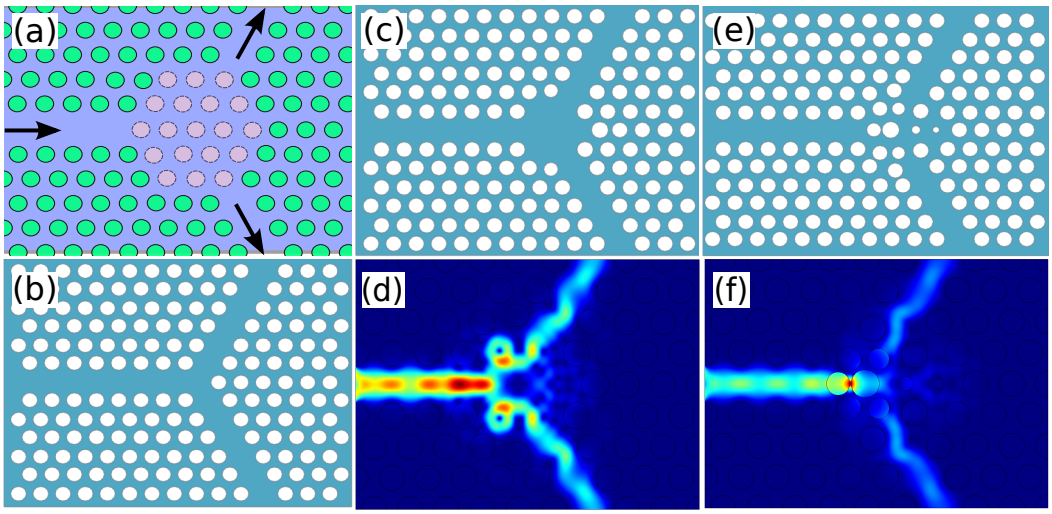

5.4. Irudia (a) Banatzaile eraginkorrago bat sortzeko ID metodoan erabili den PC klusterraren irudi eskematikoa. (b) Optimizatu gabeko Y–banatzailea. (c) IHS algoritmoa erabiliz optimizatutako Y–banatzailea. (d) Simulatutako potentzia-fluxua (c) erabiliz. (e) FSA algoritmoa erabiliz optimizatutako Y–banatzailea. (f) Simulatutako potentzia-fluxua (e) erabiliz.

5.2.2 Kristal fotonikozko Y-banatzaileak/zatitzaileak

Atal honetan, *Y* akopladore moduan antolatutako egiturak berregin dira ID metodoa erabiliz. Jatorrizko banatzaile egitura baten diagrama 5.4.a irudian ikusi daiteke eta hiru W1 uhin-gidaz osatuta dago. Horrelako banatzaileek kritika ugari jaso dituzte, haien transmitantzia-eraginkortasuna oso baxua izaten dalako [188]. Transmisioaren kalitatea uhin-giden eta bateratzaile sekzioaren akoplazio-mailaren araberakoa da. Kristal fotonikoetan sortutako uhin-gidak, band-gap fenomenoa erabiltzen dute argiaren hedakuntza kontrolatzeko eta egitura horien konfigurazioa eraldatu ezkero, argia kurbatura handiko ibilbideetan zehar garraiatu daiteke (ikusi 5.3 atala gai honen inguruko xehetasun gehiago irakurtzeko). Hala ere, 5.4-ko egituretan igorritako argia irteerako uhin-gidetara moldatzeko, 120°-ko kurbadura batzuk zeharkatu behar ditu. 120°-ko kurbadura duten uhin-gidetan zehar argi moduak akoplatzerakoan atzera-isladapen larriak sortzen dira.

Topologia horiek planteatzen dituzten erronkak gainditzeko, egitura horietan ID metodologia aplikatu dugu. ID metodoak geomertriak sortu, ebaluatu eta *fittness* balioen arabera sailkatu eta hautatzen ditu egoera bakoitzean. Horrez gain, ID metodologiak ID parametroaren bilaketa mugatua onartzen du eta, ondorioz, CMOS fabrikazioaren teknologiarekin guztiz bateragarriak diren PC topologiak proposatzeko ahalmena du. Orokorrean, ondorengo baldintzak inposatu dira:

- Zuloen erradioak. Ohiko fabrikazio tekniken bidez sortu daitezkeen egiturak proposatzeko eta beraz fabrikatu ezin diren soluzio arbitrarioak saihesteko, aldagaien bilaketa-eremua mugatu egin da,

$$0.1 < r_{ij} \geq 0.39. \tag{5.2}$$

  5.2-ko azpiko mugak, fabrikazio metodoaren atalasea gainditzen duten eta arbuiagarriak diren zuloak ekiditzeko ere, ondorengo baldintza ezarri da

$$\epsilon_{ij}\{n_{air} if r_{ij} \geq 0.1 n_{Si} otherwise. \tag{5.3}$$

  Hori dela eta, 0.1 erradioa baino txikiagoko zuloaak, material dielektrikoaz betetzen dira. Zulo hauek ezabatuz, arguiagarriak liratekeen islapenak ekiditzen dira, eta oso aldakorrak diren interferentzia patroiak erabiltzea saihesten da.

- Zulo bakoitzaren desplazamendu erlatiboa, sare triangeluarraren kokapenareko. Desplazamendu hori modu independientean eragiten da eta ndorengo mugimenduetara mugatuta dago

$$-0.2 < x_{ij} \geq 0.2. \tag{5.4}$$

  Desplazamendu negatiboak elementua ezkerrerantz mugituko du, eta positiboa eskuin aldera mugitzen du.

- Ordenatu-ardatzean eragindako desplazamenduko mugekin batera abzisa-ardatzean ere horrelako mogimenduak baldintzatzen dira.

$$-0.2 < y_{ij} \geq 0.2. \tag{5.5}$$

Horrela planteatutako egiturak, batzutan zuloen arteko gainezartzea sortu dezake geometrietan, hau da, behar bada eraginkorrak izan daitezkeen egiturak sortu ditzake baina, aldi berean, fabrikatzeko ezinezkoak izan daitezke edota zuloen arteko tarte txikiak hauskorrak diren topologiak proposatu ditzake. Hala eta guztiz ere, ebazpen horiek baztertu beharrean, ebazpen horiei fitness balio handiago bat ezartzen zaie. Egitura horiek, hurrengo iterazioetan sortutako aldaketen bitartez, topologia askoz ere hobeagoak eta sendoagoak lortzeko aukera eskaintzen dute. Bestela ere, elementu bakoitzaren erradioa eta inguruko elementuen erradioak eta kokapen erlatiboa kontuan hartu daitezke, gainezarpenik ez duten zuloen bidez sortutako geometriak bakarrik onartzeko. Hala ere, beste aldagai askoren arabera baldintzatutako aldagai baten bilaketa-espazioa mugatuz, optimizazio metodoaren aniztasuna

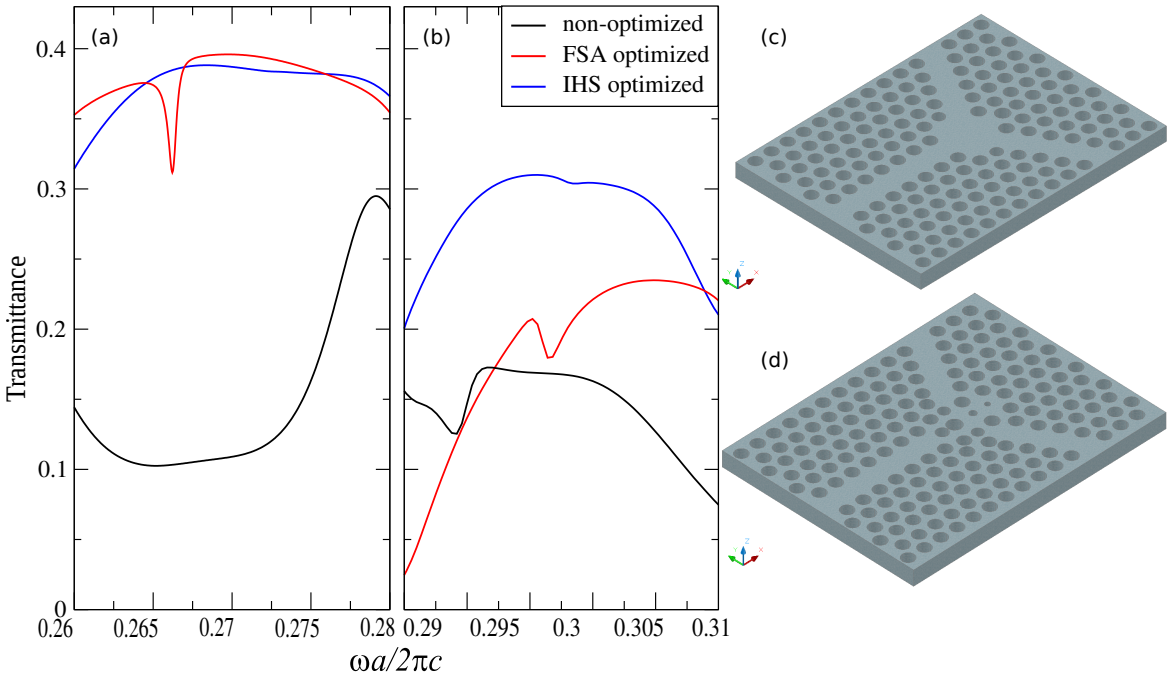

5.5. Irudia Optimizatu gabeko eta IHS eta FSA metodoak erabiliz optimizatutako egituren transmitantzia espektroaren konparaketa, (a) 2D PC egituretan eta (b) 3d PC egituretan, hurrenez hurren. 3D-ko egiturak (c) IHS eta (d) FSA topologientzat, hurrenez hurren.

gehiegi murrizten da. Gainera, problema planteatzeko modu horrek, intuizioan oinarritutako hierarkia bat sortzea suposatzen du, optimizazio heuristikoen prozeduren kontraesanean.

5.5 irudian, IHS eta FSA algoritmoen bidez optimizatutako eta baita optimizatu gabeko konfigurazioen transmitantzien emaitzak aurkezten dira. Optimizatu gabeko egituraren kasuan, argi ikusi daiteke bihurgune zorrotzak argiaren hedakuntza oztopatu egiten du. Bereziki, geometria horrek gehienez %30-eko transmitantzia eskaintzen du 0.278-ko maiztasun normalizatuaren inguruan eta gidatutako beste uhin-luzeretan berriz, %10-eko transmitantzia minimoa aurkezten du; ez da beraz konfiguraziorik aproposena dispositibo trinkoetan erabiltzeko. Aitzitik, FSA eta IHS algoritmoen bidez sortutako egiturak etekin askoz hobea lortzen dute. Egitura horien transmitantziak izaera laua aurkezten dute gidatutako moduaren banda-zabalera osoan zehar eta irteerako portu bakoitzean sarreratik txertatutako argiaren %45-a jasotzen da. FSA algoritmoa erabiliz lortutako egituraren transmitantzia grafikoa aztertuz, 0.267 maiztasun normalizatuan minimo adierazgarri bat dagoelaa antzeman daiteke. Minimo hori, sortutako uhin-gidan argiaren hedakuntza oztopatzen duen zuloak sortzen duen erresonantziak eragiten du, 5.4.e irudian ikusi daitekeen moduan. Dena dela, erresonantzia horren eragina arbuiagarria da, optimizatu gabeko sistemarekin konparatu ezkero.

Aurretik aipatu den bezala, zuloz osaturiko sareetan oinarritutako egiturak erabiltzeak abantaila garrantzitsu bat du zutabez osaturikoekin konparatu ezkero: 2D PC-etan kalkulatuta-

ko gida egituren gaitasunak mantendu egiten dira aplikazio optikoetan erabiltzen diren 3D-ko egituretara moldatu ezkero. Ohikoa denez, PC xafla egiturak erabili ditugu optimizatu gabeko eta IHS eta FSA metodoen bidez optimizatutako konfigurazioen ezaugarriak aztertzeko. 3D FEM erabiliz burututako simulazioak 5.5 irudian aurkezten dira. 3D-ko kasuan, aipagarria da optimizatu gabeko egiturak eraginkortasun baxua izaten jarraitzen duen bitartean, IHS-ren bidez optimizatutako egiturak, berriz ere, 2D-ko simulazioetan aurkezten zuen argi-banaketa bikaina eskaintzen du. Aitzitik, FSA-ren geometriak eragozpen larriak ditu maiztasun baxuagoetan, alegia, gidatutako moduen simetriaren aldaketa dela eta. Izan ere, moduak bere simetria bikoitza galtzen duenean, argiaren fluxua zatitzea oso zaila bihurtzen da. Egoera hori 2D ingurune batean aurreikustea ere zaila izaten da eta beraz, banatzaile batek izan behar dituen trinkotasun eskakizunak betearazten dituen hasierako konfigurazio batek ID algoritmoarentzat abiapuntu hobeagoa izan daitekeela uste dugu. Irizpide hau jarraituz, hurrengo atalean, galera oso baxuak dituen 3 dB-ko zatitzaile baten eredua azaltzen da.

5.2.3 Uhin-luzeran hautakortasunak diren eta banda zabalera altuak dituzten akopladore/zatitzaileen eta baita akats linealen bidez garatutako potentzia-zatitzaileen optimizazioa

Azpiatal honetan, 120° graduko uhin-giden konfigurazioan oinarrituta ez dauden banatzaile/akopladore batzuk azaltzen dira. Ondorengo egiturak sortzeko, [186]-en azaltzen den *multimode interference* (MMI) banatzailea erabili da, hasierako egituraren banda-zabalera handitzeko asmoarekin. MMI motatako banatzaileak dielektriko baten zuloz osatutako multi-modu diren PCWG-etan egitura optimizatuak diseinatzeko abiapuntu bikaina dirudi, *self-imaging* printzipioarekin bat datozen ebazpenak lortu daitezkeelako. *Self-imaging* fenomenoaren bidez, argi izpi bat erregularki tartekatutako izpi-kopietan banatzen da. Kopia hauek era erraz batean zuzendu daitezke sistemaren irteeran paraleloki kokatutako bi uhin-gidetarantz. Irteeran kokatzen diren uhin-giden eta sarrerako uhin-gidaren arteko hurbiltasunak super-modo berriak sustatzen ditu eta beraz, giden arteko ingurunea aldatuz gero, eremu elektriko/ magnetikoaren patroia irteerako uhin-gidek onartzen dituzten moduetara moldatu daiteke. MMI eredurik sinpleena hiru PCWG paraleloekin osatzen da: jatorritik argia garraiatzen duen uhin-gida bat eta irteera ezberdinetara eramaten dituzten bi uhin-gida paralelo izango ditu, argi moduak egokitzeko bereziki diseinatu behar den ingurune batez bananduta daudenak. Ingurune horrek, kasu honetan W5 uhin-gida baten zabalera izan dezan egokitu da. Era horretan, dispositiboak bere trinkotasunaren eta uhin-giden arteko isolaketa (*cross-talk* galeren) konpromisoak ziurtatuko ditu. 5.6 irudian, W5 uhin-gida baten dispertsio-diagrama ikusi daiteke, orain arte erabilitako parametro berdina erabiiz osatutako

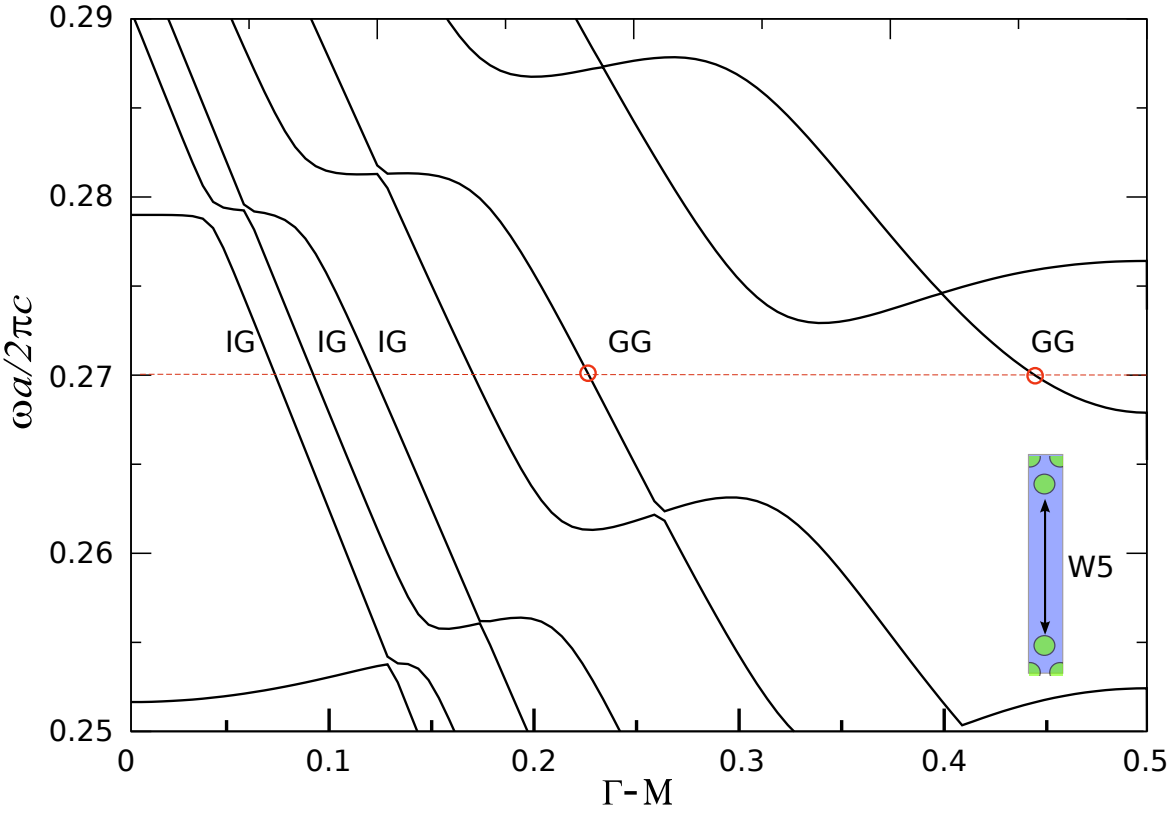

5.6. Irudia W5 PCWG-aren dispertsio diagrama. Gida honek modu ugari onartzen ditu bere banda gidatuetan. Modu batzuk gap bitartez gidatzen dira (GG) eta beste batzuk errefrakzio indizearen kontrastearen mekanismoa erabiliz gidatzen dira (IG). a/λ=0.27 maiztasun arbitrarioan, modu fundamentala eta lehenengo irudiko moduak zirkulu gorriekin adierazi dira.

PC egitura baten kalkulatu izan dana. Uhin-gidaren zabalera handitzerakoan, egiturak oinarrizko moduetatik sortzen diren modu gehiago onartzen ditu. Modu berri horiek simetria bikoitia edo bakoitia izan ditzakete. Gure kasu jakin honetan, argi potentziaren banaketa bi uhin-gidetara zuzendu gura denez, bikoitiak diren moduak bilatuko ditugu. W5 PCWG-an, a/λ_0=0.27-ko maiztasuneko bandan modu bikoitiak nahiz bakoitiak aurkitu daitezke. Bi uhin-gidez osatutako banatzaile bat sortzeko, nahikoa litzateke maiztasun horretan aurkitu daitezkeen lehenengo modu pare simetrikoak bilatzea, hau da, modu fundamentala eta bigarren ordeneko modua, hurrenez hurren. Ondoren, modu horren lehenengo kopia sortzeko behar den distantzia kalkulatzeko, hurrengo formula aplikatu daiteke:

$$MMI_{spacing} = \frac{1}{(k_0 - k_2)}, \tag{5.6}$$

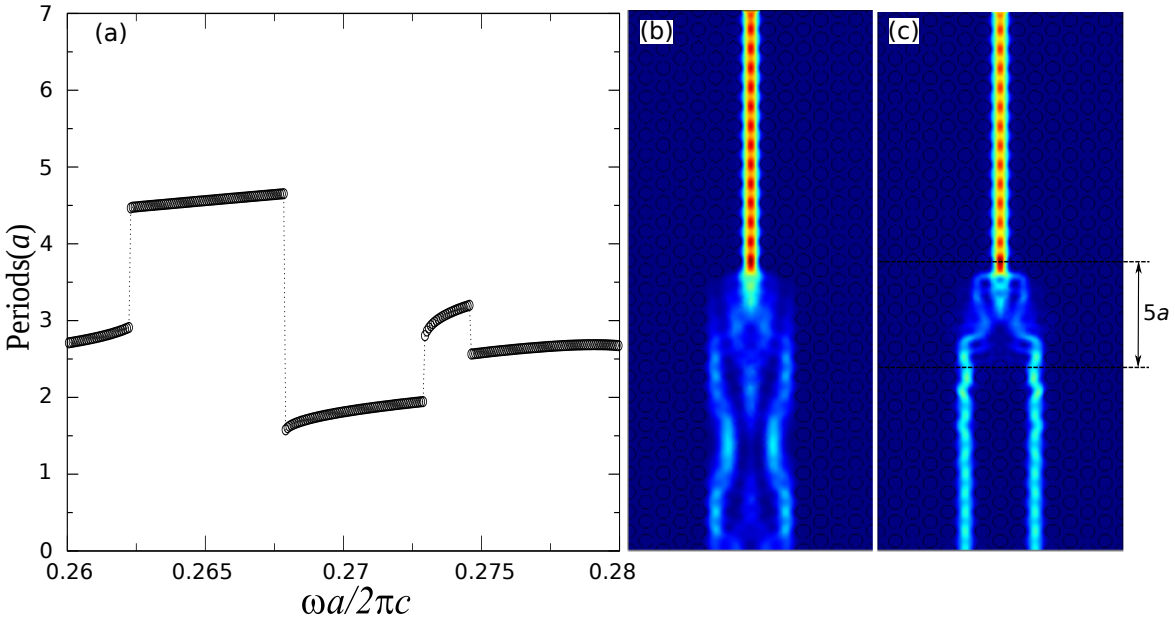

5.7. Irudia (a) W1 PC uhin-gida W5 uhin-gida zabalago batekin elkartzen denean modu sorta berri bat agertzen da. Bi uhin-gida hauen bitarteko akoplazio guneak, modu fundamentalaren irudi berriak sortzen ditu eta simetria bikoitza duen lehenengo irudia berehala kalkulatu daiteke 5.6 ekuazio erabiliz. Grafiko honek $[0.26 - 0.28]$ maiztasun tartean dauden maiztasunetarako argi banaketa egokia lortzeko beharrezkoak diren periodoak aurkezten ditu. (b) a/λ=0.27 maiztasunan simulatutako potentzia-fluxua eta (c) PC egitura bat erabiliz lortutako potentzia banaketa.

non k_0 eta k_2 modu fundamentalaren eta bigarren ordeneko moduaren uhin bektorean dira, hurrenez hurren. 5.6 ekuazioa aplikatu ezkero, simetria bikoitia duten irudien maiztasun tarteak (a) aurkitu daitezke eta, horrela, W1 uhin-gida pareetara gidatzeko egitura osatu daiteke. Kalkulu hauek aplikatuz lortu daitekeen emaitza 5.7 irudian ikusi daiteke.

Jarraian, material dielektrikoan zulo sare batez osatutako akopladore soil bat osatu da, 5.7.c irudian aurkezten den bezalakoa, potentziaren zatiketa eraginkor bat lortzeko. Hala ere, 5.7 irudian ikusi daitekeenez, simetria bikoitiko moduaren tartea, maiztasunaern menpekotasun handia aurkezten du eta beraz, banda zabalera estuetara mugatuta dago, behintzat, PC klusterraren konfigurazioa egonkorra eta mugiezina bada eta erregimen linealean lan egin ezkero. Modu bikoitien tartekotasunarekin bat datozen MMI konfigurazio ezberdinak frogatu izan dira $[0.26 - 0.28]$ maiztasunen bitartean. Egitura horien emaitzen kalkuluak 5.9 irudian aztertzen dira.

$[0.262 - 0.267]$ maiztasun normalizatuen bitartean, MMI banatzailearen irudi bikoitia 5 periodoen inguruan aurkezten du, baina $[0.268 - 0.273]$ maiztasunetarako bi periodoen distantzian aurkitu daiteke irudi simetriko hori. Hortaz, maiztasun tarte horretarako, ez dirudi MMI zatitzaile estandar batek horrelako simetria baldintzarik ziurtatu dezakeenik. Gainera,

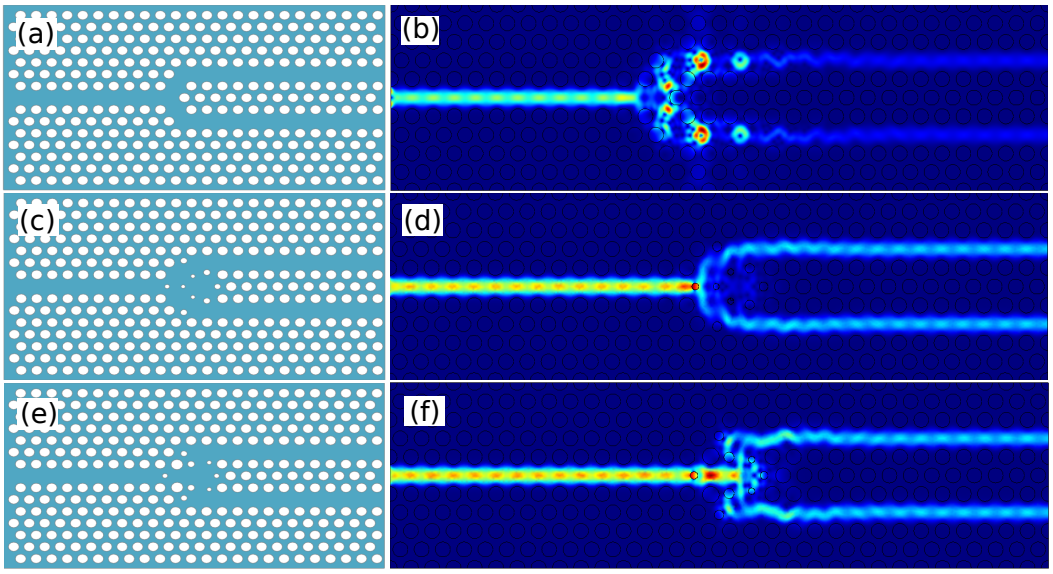

5.8. Irudia (a) Optimizatu gabeko MMI motatako banatzaileak galera nabargarriak sortzen ditu. (b) a/λ=0.27 maiztasun normalizatuan optimizatu gabeko banatzaile egiturak prestazio baxuak eskaintzen ditu. (c) IHS erabiliz, optimizatutako egiturak argi potentziaren banaketa era egokian egitea ahalbidetzen du (d)-n ikusi daitekeen moduan. (e) FSA algoritmoaren bidez lortutako banatzailea. (f) Potentzia-fluxuaren simulazioa (e) erabiliz.

operaketa maiztasun *anticrosing* puntu batetik gertu balego, (5.6) ekuazioko hurbilketak ezusteko emaitzak lortuko lituzke. Bereziki, *anti-crossing* puntuetan, moduen simetriak trukatzen dira, modu bikoitiak izatetik bakoitiak izatera igarotzen dira.

Sistema hauen etekina hobetzearren, alderantzizko diseinuaren metodoa aplikatu dugu. ID prozesuak 5.8 irudian ikusi daitezkeen egiturak hornitu ditu. Bereziki, IHS metodoak emandako egiturak, [187] lanean aurkezten den egituraren antza handia dauka. Bertan,Y-motatako bateratzailea antzeman daiteke, hiru zuloz osatutako akopladerez osaturikoa. Horretaz aparte, IHS ereduak irteerako uhin-giden arteko akats bat ere gehitzen du, 60◦ graduko dolezdura duen uhin-gida elkarketak sortutako galerak saihesteko. Beste alde batetik, FSA algoritmoak diseinu guztiz ezberdin bat proposatzen du. Azken egitura horrek *Multiple Line Defect Waveguide* (LDW) uhin-gidak dituzten antzeko topologia bat proposatzen du, hain zuzen ere [188]-en lanean proposatzen direnen modukoak. Konfigurazio hori oso komenigarria da, konplikatuegia izan litezkeen edo galera garrantzitsuak sor ditzaketen dolezdurak erabiltzea ekiditzen duelako eta sare triangeluarraren $\Gamma - K$ norabidean egindako W1 uhin-gidetan oinarrituz, parametro gutxi batzuk aldatuz lortu da. Egitura hori, eta baita IHS algoritmoak eskainitako konfigurazioak, ustekabeko emaitzak izan dira, hau da, ID metodoak 5.8 irudian ikusi daitezkeen egituraren topologiak hautatu ditu, soilik 5.8.a irudiko hasierako egitura abiapuntutzat hartuz.

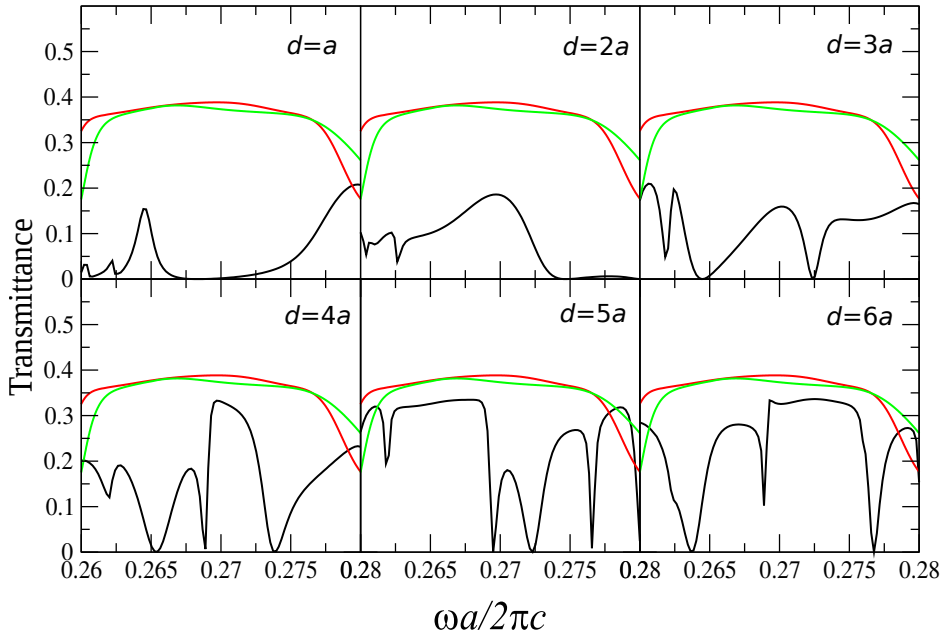

5.9. Irudia 5.8.c irudiko (gorriz) IHS banatzailearen, 5.8.e irudiko (berdez) FSA banatzailearen eta ohiko MMI banatzaile (beltzez) egituren transmitantzia espektroen konparaketa. Ohiko MMI-aren kasuan, banaketa distantzia d ezberdinak erabili dira 1-etik a distantzietarako tartean, non a sarearen maiztasuna da.

5.10 irudian, egitura hauen bidez kalkulatutako transmitantzia espektroak aurkezten dira. Nabargarria denez, ID metodoaren bitartez lortutako egituretan, sarrerako uhin-gidatik jasotako argi gehienak irteerako uhin-giden artean banatzen dira eta atzera-isladatutako argi-kopurua arbuiagarria da. Gainera, funtzionalitate hau uhin-giden banda-zabalera guztian zehar, $[0.26-0.28]$ bitartean, gertatzen da eta ondorioz, transmitantzia espektroak izaera ia laua aurkezten du. Ezaugarri horietaz gain, sistema hauek integrazio maila oso altua eskaintzen dute. Izan ere, biek akoplamendu akoplamendu eskualdea periodo gutxi batzuetara mugatzen dute eta aurreko ikerketa lanetan aurkeztutako konfigurazioek akoplamendu espazio handiagoak erabiltzen dituzte. Izaera hau 3D-PC xafla plataforman ere errepikatzen da, 5.10.b irudian ikusi daitekeen bezala. Y-banatzailearen kasuan ez bezala, kasu honetan, bai IHS eta bai FSA metodoaren bidez lortutako egiturak menbrana motatako ingurune hauetan eraginkortasun handia eskaintzen dute.

5.3 Kurbadura zorrotzetako PCWG osagarriak

Orain arte, 3.6 atalean, kristal fotoniko baten egindako lerro akatsen bidez sortutako uhin-giden ezaugarriak deskribatu dira. Horrelako uhin-gidak, kristal fotoniko baten, era zuzen

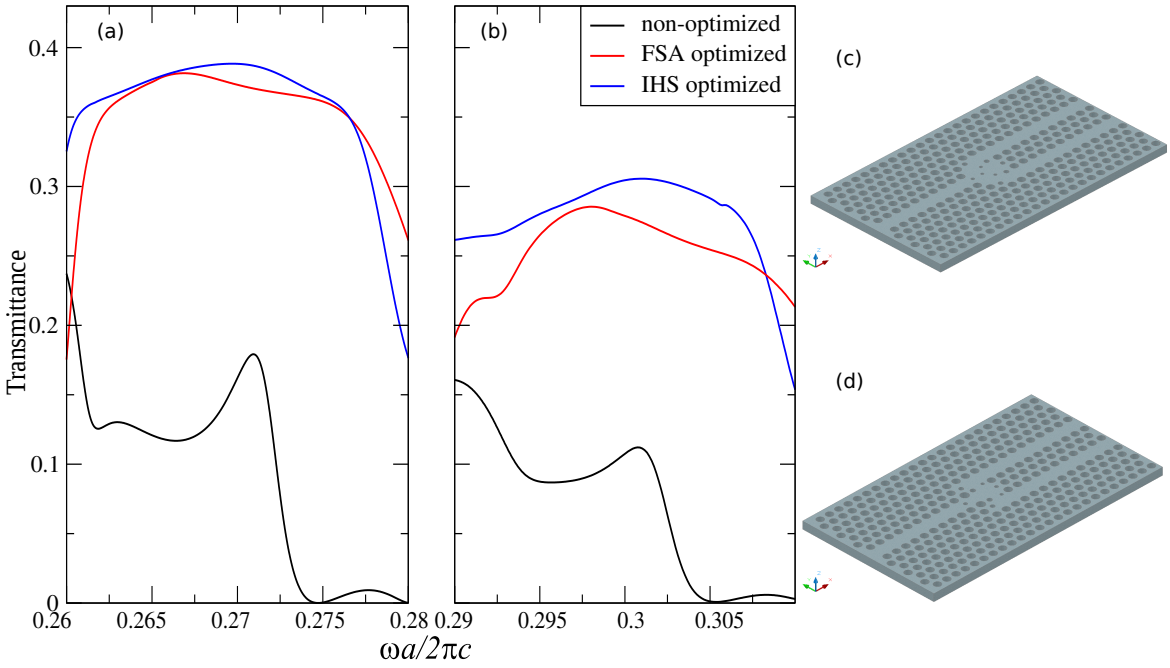

5.10. Irudia (a) Optimizatu gabeko egituraren eta IHS eta FSA metodoak erabiliz optimizatutako 2D-PC banatzaile egituren transmitantzia espektroen konparaketa. (b) PC xafla banatzaileen transmitantzia kalkuluak, (c) eta (d) egiturentzat, hurrenez hurren. (c) IHS eta (d) FSA topologiak PC xafla konfigurazioan.

batean argia gidatzeko elementu apartak dira. Aldiz, ikuspuntu praktikoago batetik, uhin-gida batek seinale optikoa norabide arbitrarioetarantz gidatzeko ahalmena izan behar du, dispositibo fotoniko fisiko guztietan kurbatura ugari dituzten uhin-gidez osatuta bait daude. Ohiko uhin-gidak, hurrengo kapituluan azaltzen diren hari fotonikoak esaterako, errefrakzio indizearen gidaketan oinarritzen dira argia ibilbide okertuetan zehar garraiatzeko. Gidaketa-mekanismo horretan ordea, dolezdura angelu kritiko baten limite fisikoa agertzen da. Angelu horretatik haurrera, guztizko barne isladapen mekanismoren baldintzak ezeztatzen dira eta, hortaz, dolezdura zorrotz horietan argiaren gidapena deuseztatzen da.

PCWG dolezduretan, uhin-gida dielektriko konbentzionaletan ez bezala, milimetroen mailako dolezdura angelu kritikoen mugak saihestu daitezke. Horren ordez, PCWG egiturak, dolezdura zorrotzetan zehar argia garraiatzeko sistema trinkoagoak eskaintzen dituzte [189], eta beraz, gailu opto-elektronikoen integrazio dentsitatea hobetzeko aukera zabaltzen dute. Uhin-gidetako dolezdurak sortutako atzera-isladapena murrizteko era ugari aztertu dira gaur egun arte [110, 111, 190–193]. PC uhin-gidetako dolezduretan garatutako lehenbiziko ikerketa lana Mekis et al.-ek aurkeztu zuen 1996an [190]. Bertan, sare karratu baten antolatutako 2D-ko kristal fotonikoan egindako 90° -ko dolezduren transmisioa ikertu zan. Lan horretatik gaur egunerarte, kurbatura hauen transmisio etekina hobetzeko hainbat

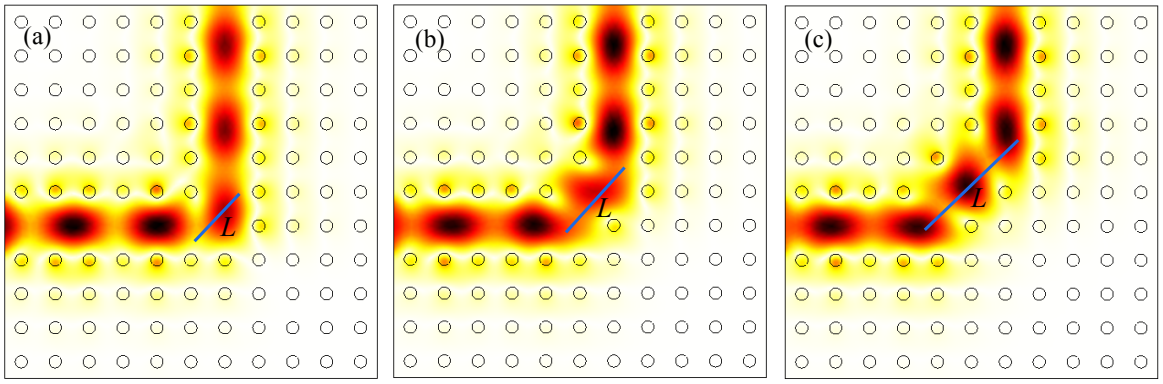

5.11. Irudia (a) 90°ko dolezdura duen kristal fotoniko uhin-gida. Egitura honetan GaAs zutabez (n=3.4) osatutako sare karratu baten bi uhin-gida zuzen elkartu dira, Mekis et al.-ek proposatu zuten modukoa [190]. Argia uhin-gida horizontaletik sustatzen da ([10 norabidean]). uhin-gida horren tarte diagonala, L luzeraz adierazi da. Eremu elektrikoa uhin-gida bertikalerantz ([01] norabiderantz) zuzendu dadin konfiguratu da (b) eta (c) grafikoetan.

teknika proposatu dira [110, 194, 195]. Gehienak, airez inguraturiko dielektriko zutabez osatutako egituretan oinarritu dira. Horrelako konfigurazioetan oinarritutako uhin-gidak, normalean, mono-modu izaera izaten dute. Horrelako kasuetan, transmisioa areagotzeak ez du hainbesteko konplexutasunik. Mekis et al.-ek, [190]-en, 5.11 irudian ikusi daitekeen egituran, 90° kurbaturaren transmisio propietateak deskribatzeko, dimentsio bakarreko isladapen teoriaren eredu sinplifikatu bat proposatu zuten. Horrelako uhin-gidetan, band-gap fotonikoaren eraginez, jasotako argi-izpiak ez dute uhin-gidatik kanpora argirik erradiatzeko biderik, barreiatutako moduak ezin baitira hedatzen diren moduetara akoplatu. Beraz, uhin-gidan igorritako argia transmititu edo isladatu daiteke soilik. Faktore hauek kontuan hartuz, Mekis-ek problema hau isladapen problema baten eran planteatu zuen eta isladapen koefizientea honela estimatu zuen

$$R(\omega) = \left[1 + \left(\frac{2k_1(\omega)k_2(\omega)}{[k_1^2(\omega) - k_2^2(\omega)]\sin k_2(\omega L)}\right)^2\right]^{-1}, \tag{5.7}$$

non $k_1(\omega)$ bi uhin-gidetan hedatu daitekeen moduaren uhin bektorea da, [10] eta [01] norabideetan heda daitekeena, hain zuzen ere. $k_2(\omega)$ [11] norabidean, hau da kurbatura norabidean, hedatu daitekeen moduaren uhin bektorea da eta, L parametroak bi uhin-giden arteko kurbaduraren luzera efektiboa adierazten du. Beraz, egitura honetan, kurbadurak sortutako isladapena minimizatzeko, 5.7 ekuazioan, hautatutako maiztasunerako, 5.7 ekuazioaren zeroak aurkitzera mugatzen da problemaren ebazpena.

Berriro ere, teknika hau erabilita, dielektrikoan buruturiko zuloz osatutako PC-etan, banda-estuko ebazpenak areagotzea baino ez da posiblea eta banda z-zabaleko ebazpenak

aurkitzeko beste era batera jo beharko litzateke. Hau egiteko bide bat, uhin-gida mono-modu izatera bultzatzea litzateke. Horretarako, uhin-gidaren zabalera murriztu daiteke. Hala eta guztiz ere, uhin-gida estuak hedapen-galera handiagoak aurkezten dituzte [192] eta beraz, dolezdura zorrotzen egituren analisia dagoeneko galera nabariak dituzten uhin-gidetara mugatzea ez dirudi jokabiderik praktikoena. Problematika honen inguruan, atal honetan, kurbadura zorrotza duten W1 uhin-gidetan eta banda-zabalera handian zehar, transmisio etekin optimizatuak aurkitu daitezkeela azalduko dugu. Aurretik, beste egile batzuk argitaratu dituzten lanen artean teknika ezberdinak proposatu dira. Ezagunen artean, kurbadura gunetik gertu puntu akatsak erabiltzea proposatzen dituztenak aurkitu daitezke [194, 196, 197], zulo batzuen erradioa aldatuz transmisio etekina hobetzea lortzen dituzten aurrekariak [198], akatsen inguruko akopladore adiabatikoak sortzen dituztenak [192] edota kurbaduraren ondoko zuloak topologia exotikoekin ordezkatzen dituztenak [195, 199] azpimarratu daitezke. Aurrekari hauen estrategiak jarraitu ezean, atal honetan, ID prozesua jarraituko dugu maiztasun optikoen transmisioa hobetzeko, 60° eta 120°-ko kurbadurak dituzten egituretan.

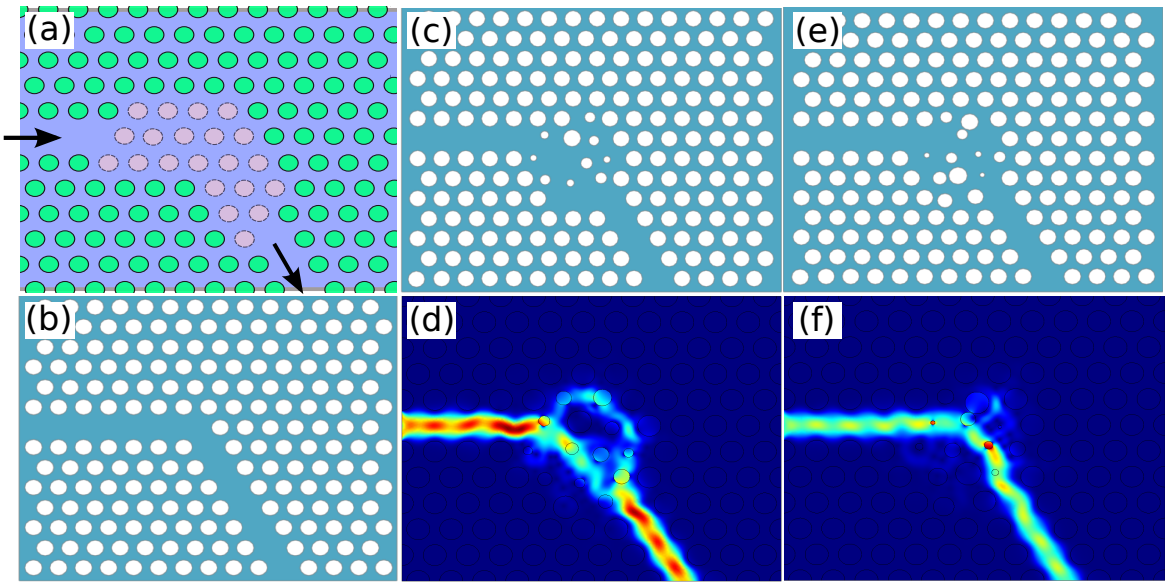

5.12. Irudia (a) 60°-ko dolezdura duen kristal fotonikozko uhin-gida diseinatzeko erabili den PC klusterraren eskema. Optimizazioan erabili diren airezko zuloak kolorez adierazi dira. (b) Optimizatu gabeko PCWG dolezdura. (c) IHS algoritmoa erabiliz optimizatu den egitura eta (d) horren bitartez simulatutako potentzia-fluxua. (f) FSA algoritmoa erabiliz optimizatu den egitura eta (g) horren bitartez simulatutako potentzia-fluxua.

Hasteko, **??** atalean deskribatzen den 2D kristal fotonikoaren sareaz abiatuz, zulo sorta bat ezabatu da 60° kurbaduraz lotzen diren bi uhin-gida elkartzeko, 5.12 irudian azaltzen den moduko egituran. Kristalaren sarearen apurketa bortitza sortzen duen dolezdurak ispilu ia ezin hobe baten moduko efektua sortzen du, sarrerako uhin-gidako potentzia optiko

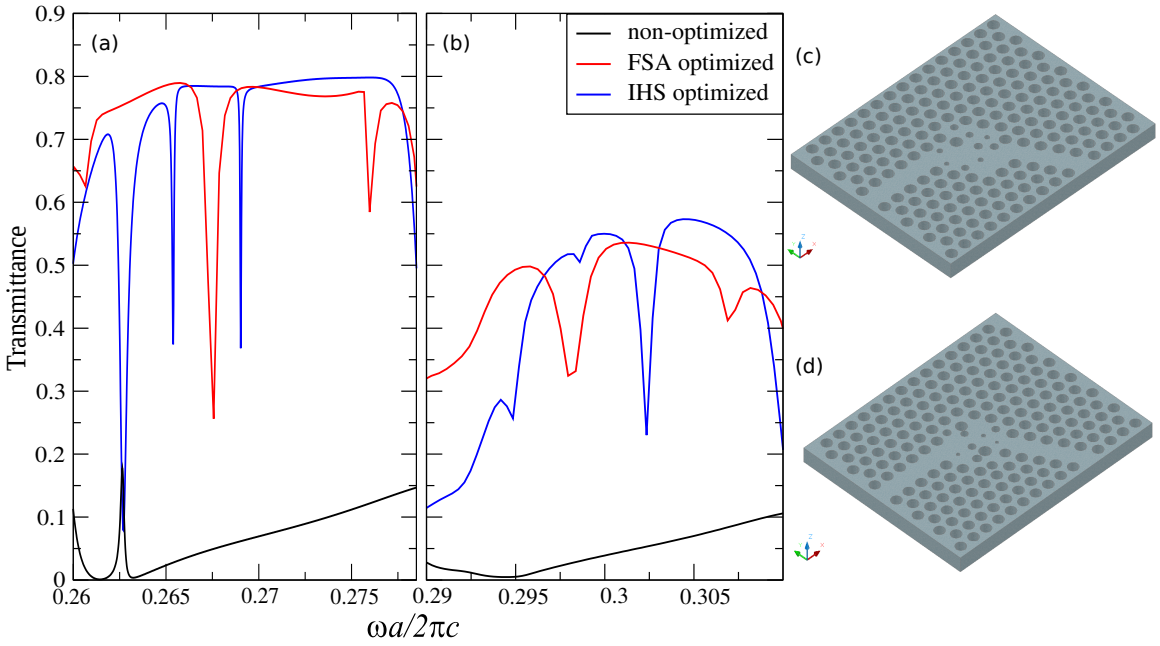

5.13. Irudia 60°-ko kurbadura duten egituren transmitantzia, IHS FSA eta optimizatu gabeko egiturentzat, hurrenez hurren. (b) Aurreko kalkuluak PC xafla plataforman kalkulatutakoak. (c) IHS eta (d) FSA algoritmoak proposatutako egiturak.

gehiena isladatu egiten da. Transmisio baxu hori ere 3.12 irudian azaltzen den 2D W1 uhin-gidaren dispertsio diagrama hausnartuz arrazoitu daiteke. Dispertsio diagraman ikusi daitekeen moduan, Γ–K norabideko, band-gap barneko moduak Γ–M norabidean ezin dira gidatu, edota zuzenean modu desagerkorrak izatera bilakatzen dira eta material dielektrikoan esponentzialki gainbeheratzen dira. Honek denak transmisio espektroan galera adierazgarriak sortzen ditu, 5.13 irudian ikusi daitekeen moduan.

Egoera hau aldiz erabat aldatzen da optimizazio algoritmoak erabiltzen direnean. IHS eta FSA algoritmoak erabilita sortutako egiturak 5.13 adierazten dira, hurrenez hurren. 5.13 irudiak egitura hauek eskaintzen duten transmitantzia espektroaren areagotzea erakusten du, uhin-gidak onartzen duen maiztasun zabalean, hau da 0.26-tik 0.28-ra. Funtsean, 5.12 irudian adierazten den dolezdura ingurunea, partzialki desordenatutako zuloz osatuta dagoena, Γ–M eta Γ–K norabideetan hedatu daitezkeen moduen arteko akoplamendu eraginkorra eskaintzen du. Printzipioz, izaera multi-modoa duen W1 uhin-gida bat erabiltzean, gutxienez modu bat akoplatzea lortu dezakeen egitura bat aurkitzea errazten du. Hala ere, 5.13 irudian aurkezten diren kongigurazioak eskaintzen duten transmitantzia diagramak forma laua dute eta hortaz, akoplazioa gidatuak diren modu guztietarako gertatzen dela baieztatu daiteke. Hau dena kontuan hartuta, 5.13 irudian agertzen diren transmisio koefizienteak W1 PCWG zuzenean kalkulatutako erreferentziazko balioetatik oso gertu daude, optimizatutako banda-zabalera

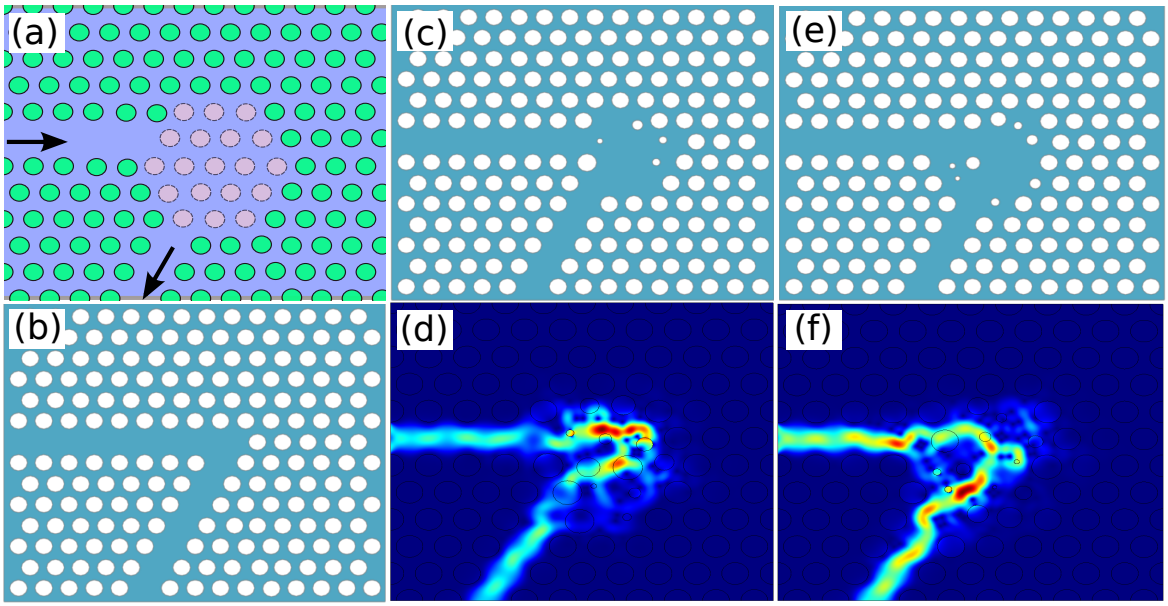

5.14. Irudia (a) 120°-ko kurbadura duen PCWG diseinatzeko erabili den klusterraren eskema. Optimizazio-prozesuan erabili diren elementuak kolorez adierazi dira. (b) Optimizatu gabeko egitura. (c) IHS algoritmoaren bidez optimizatutako egitura eta (d) egitura horretan simulatutako bataz-besteko potentzia fluxua. (e) IHS algoritmoaren bidez optimizatutako egitura eta (f) egitura horretan simulatutako bataz-besteko potentzia fluxua.

ingurune osorako. Emaitza honek, teknika heuristikoak PC topologien optimizazioan aplikatu daitekeen metodo oso moldakorra dela baieztatzen du.

Dolezduraren kurbatura handitzean, gidatutako moduen akoplamenduaren gabeziak are kritikoagoak bihurtzen dira. Hain zuzen ere, 120°-ko dolezdura zorrotzen bidez argia zuzentzea eginkizun zaila bihurtzen da eta bi uhin-giden arteko lotura bortizki eraldatzea suposatzen du. Bestalde, problematik hau garatzen duten ikerketa lan gutxi aurkitu daitezke, [200] eta [201] bezalakoak. Izan ere, lan hauetan egituretan aldaketa garrantzitsuak ezartzen dira banda-zabaleko transmisio gaitasunak hobetzeko. Horregatik, espazio-simetria osoa hautsi beharrik gabe, banda-zabalera osoan argia transmititzea ahalbidetzen duten konfigurazio berriak aurkitzea funtsezkoa da. Berriki, horrelako kurbadura duen uhin-gida bat aurkeztu zan, fotonika topologikoa erabiliz diseinatu izan dana [202]. Tesi honen azken kapituluan ere babes-topologikoa aztertzen da.

Dolezdura zorrotz hauetan argia gidatzeko, alderantzizko diseinuaren prozedura erabili dugu berriro ere, oraingo honetan 5.14.a irudian agertzen den 2D 120°-ko egituratik abiatuz. 5.14.c eta 5.14.e irudian IHS eta FSA algoritmoen bidez jasotako 2D topologia optimizatuak errepresentatzen dira, hurrenez hurren. Bihurgunerik gabeko W1 uhin-gidaren eta 120°-ko dolezdura duten egituretan kalkulatutako transmisioak antzekotasun handia aurkezten

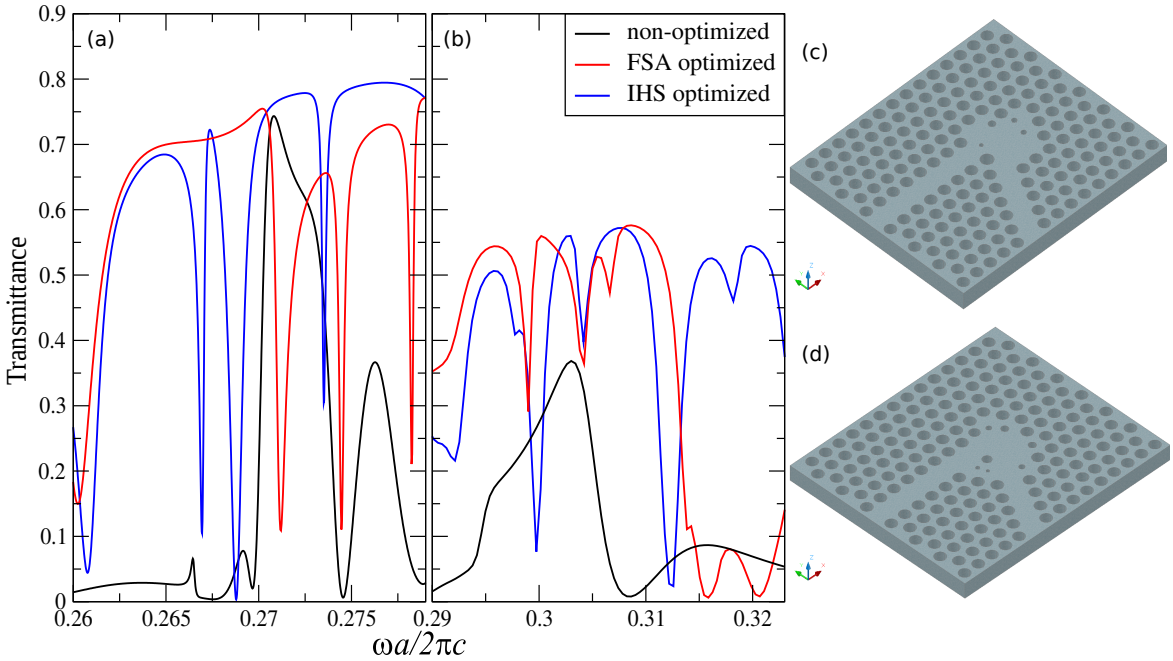

5.15. Irudia (a) 120° -ko kurbatura osatzen duen uhin-gida baten transmitantzia espektroaren konparaketa IHS, FSA eta optimizatu gabeko PCWG egituretan. (b) PC xafla plataforman egitura hauek eskaintzen duten transmitantzia espektroa. (c) IHS eta (d) FSA algoritmoak proposatutako egituraren eskema.

dute berriro ere. Gainera, 5.15 irudian adierazitako transmisioen konparaketak, egitura optimizatuak, dolezdura zorrotzak izanik, aurkezten dituzten galerak minimoak direla baieztatzen du. $\omega = 0.273$ inguruan modu erresonante bat dagoela antzeman daiteke. Bertan, egitura ez-optimizatuak ere transmisioan maximo bat azaltzen du. Lortutako emaitzak, xafla kristal fotoniko baten ere kalkulatu dira eta transmitantziaren espektroaren hobekuntza esanguratsuak sortzen dituztela frogatu da. 5.13 eta 5.15 irudietan lortutako espektroak hiru dimentsioko FE metodoaren bidez egiaztatu dira.

Azkenik, 5.13.b eta 5.15.b irudietan, 2D eta 3D-n kalkulatutako simulazioen arteko lotura bikaina adierazten du. Hala eta guztiz ere, xafla egituraren indize efektiboa eta 2D egiturarenak bat ez datozenez, egiturek aurkezten duten band-gap tartea eta horren barruan dauden modu gidatuak maiztasun ezberdinetan aurkitzen direla arrazoitu daiteke.

5.4 *Channel-drop* motatako iragazkiak

Banda-zabalera handiko argi-komunikazioak ahalbidetzea ezinbesteko faktorea da komunikazio aplikazio berrietan. Modu berean, selektibitate hobeagoa duten iragazkiak sortzea bereziki garrantzitsua da banda-zabalera zabala duten uhin-gidetan modu aberasgarri modulazio

teknika berriak eskaintzen dituzten onuren abantailak erabiltzeko. Beste alde batetik, *channel-drop* motatako iragazkiak behar-beharrezko elementuak dira uhin-luzerako demultiplexazio-sistemetako (DWDM) demultiplexazio trinkoen gaitasunak ustiatzeko [203, 204]. Kristal fotonikoak, horrelako egiturak sortzeko material hobezinak dira, alde batetik, PBG fenomenoak uhin luzera sorta asko bereizteko erabili daitezke eta beste alde batetik, sare periodikoaren eraldaketa minimoak Q-faktore altuko modu lokalizatuak sortzeko gaitasuna azaltzen dute. Modu lokalizatu horiek, uhin-gida batetik jasotako eremuak beste uhin-gida baten alokatzeko erabili daitezke. Horretarako, uhin-luzeraren arabera argiaren ibilbidea kontrolatu ditzaketen PC egiturak egin ditugu, hau da, elektronikan interkonexio elektronikoek egiten duten eginkizunaren analogia optikoa lortzen duten egiturak direnak. Orain arte, superprisma efektua erabiliz horrelako dispositiboak egitea posiblea dela frogatu duten ikerketa lanak argitaratu dira [205, 206], eta baita erresonantziak erabiliz antzeko emaitzak sortu dituztenak aurkitu daitezke, [207, 208] esaterako. Superprisma efektua erabiltzen dituztenak sare zabalak behar izaten dituzte eta beraz, (PIC) baten trinkotasun baldintzaren aurkako joera azaltzen dute. Erresonantziak erabiliz ordea, integrazio trinkotasun handia sortzen da, baina banda-estuko erabilpenetara mugatuta daude.

5.4.1 Oinarrizko *Channel-drop* iragazki baten diseinua

[203]-en, Ren-ek eta bere lankideek hiru portuz osatutako *add-drop* bat proposatu zuten, kristal fotoniko baten parametro gutxi batzuk aldatuz lortutakoa. 5.16.a irudian, Ren et al.-ek proposatutako jatorrizko geometria irudikatzen da. Egitura hori, 3.4 errefrakzio indizeko, eta $0.2a$ erradioa duten zutabe errenkada bat ezabatuta duen W1 PCWG batez eta perpendikularki kokatutako beste uhin-gida batez osatzen da. Honen bidez, uhin-gida horizontaletik igorritako uhin EM-ak modu ezabakorren bidez akoplatzen dira irteerako uhin-gidarantz. Modu ezabakor horiek, egituraren barrunbearen maiztasun erresonantearen bidez akoplatzen dira. Egitura horretan, *time coupled mode theory* metodoa aplikatu zuten, kristal fotonikoaren barrunbea osatzen duen zutabearen eta uhin-gida bakoitzetik gertu dauden zutabeen erradioa kalkulatzeko.

5.16.b irudian Ren et al.-ek proposatutako geometrian, maiztasun erresonantean kalkulatutako denboraren batez-besteko potentzia fluxua aurkezten da. Bertan $R_1 = 0.042a$ eta $R_2 = 0.211a$ parametroak erabili dira. Ren-ek egindako analisi teorikoa, 5.18.a irudian erakusten dan uhin-gida transbertsalaren transmitantzia espektroarekin baieztatu daiteke. Espektro horretan, transmitantziaren jausi bortitza modu erresonantearen akoplazioaren eraginari dagokio. Ren-ek iradoki zuenaren arabera, aire akatsaren eta bi uhin-giden ingurunean sortzen diren barrunbeen kalitate faktoreak orekatuz, uhin-giden moduen akoplazioa optimizatu daiteke. Konfigurazio sinple horretan bi parametro baino ez dira kontuan hartzen. Hau

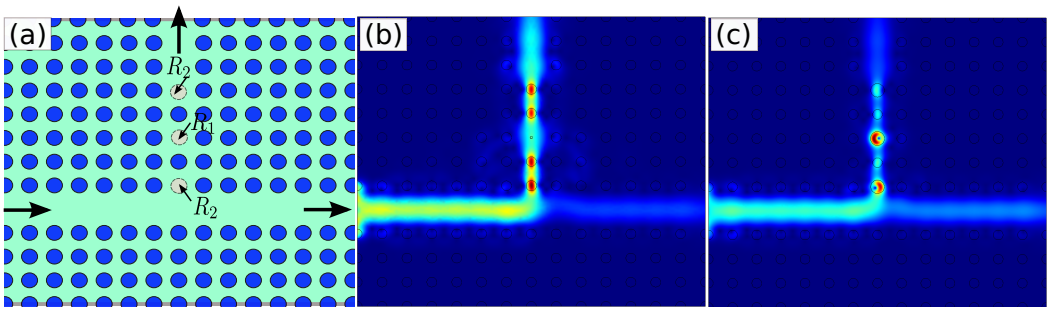

5.16. Irudia (a) Bi huin-gida transbertsalez eta R_1 eta R_2 erradioen aldaketaz sortutako *add-drop* filtroaren irudi eskematikoa. Denboran bataz-besteko potentzia fluxua, $a/\lambda = 0.37$ erresonantzia maiztasunean (b) Ren et al.-ek proposatutako konfigurazioan, non $R_1 = 0.042a$ eta $R_2 = 0.211a$ eta (c) IHS algoritmoak sortutako konfigurazio batentzat, non $R_1 = 0.388a$ eta $R_2 = 0.276a$.

horrela izanik, ebazpen-espazio osoa arakatu daiteke. 5.17 irudian, 10.000 ebazpenen fitness balioen bidez osatutako mapa ikusi daiteke. Kalitate faktore altuak dituzten PC barrunbeen modu erresonanteak ebazteko, zehaztasun handia behar da eta beraz, simulazio denborak nabarmenki gora egiten du, nahiz eta horretarako metodo azkarrak erabili diren [184]. Ondorioz, 5.17 irudian jasotako informazioa eskuratzeko ia 250 ordu behar izan ziran. Hala ere, ID metodoa erabiltzean prozesua azkartu egiten da, hau da, IHS, nahiz FSA-z gidatutako ID prozesu bakar batek, 17 minutu baino gutxiagotan konbergitzen du ebazpen egokira.

5.18 irudiak ID metodoak proposatutako ebazpen batzuk aurkezten ditu. Emaitza hauek, Ren et al.-ek proposatutako ebazpenetik oso gertu daude eta batzuk Ren-en emaitzak baino akoplazio hobeagoa lortzera ailegatu dira.

Fan et al.-ek Wang-ek planteatutako prozesua jarraitu zuten eta hiru kanaletako filtro batetik lau kanaletako filtro simetriko batera zabaldu zuten haien aurrekarien lana[207]. Fan et al.-ek erabilitako akopladore sistemaren diagrama 5.19 irudian ikusi daiteke. Bertan, aluminiozko zutabez osatutako kristal fotoniko sare baten *A* uhin-gidatik hedatu daitekeen modu bat (ikusi Fig. 5.19.a diagrama), era konstruktibo batean eragin dezake *D* uhin-gidan, gainerako uhin-gidetan modu ezabakor batean eragiten duen bitartean. Nabarmenki, Fan et al.-ek proposatutako sistema Ren et al.-en erakutsitakoaren antza handia dauka, baina, kasu horretan, Fan-ek zutabeen erradioa ez ezik (R_1 elementuak 5.19.a irudian), 5.19.a irudian koloreztatutako elementuen errefrakzio indizea ere aldatzea proposatzen du.

Guztira, eredu horrek hiru askatasun gradu ditu, eta hortaz, sistema horren ebazpenak Ren-en egiturak baino konplexutasun handiagoa inplikatzen du. Hori dela eta, bilaketa-espazioen araketa sakona egiteak gehiegizko kalkulu kopurua egitea inplikatzen du. Hala ere, ID metodoaren eraginkortasuna frogatzeko esparru honek praktikotasun handia du. 5.20

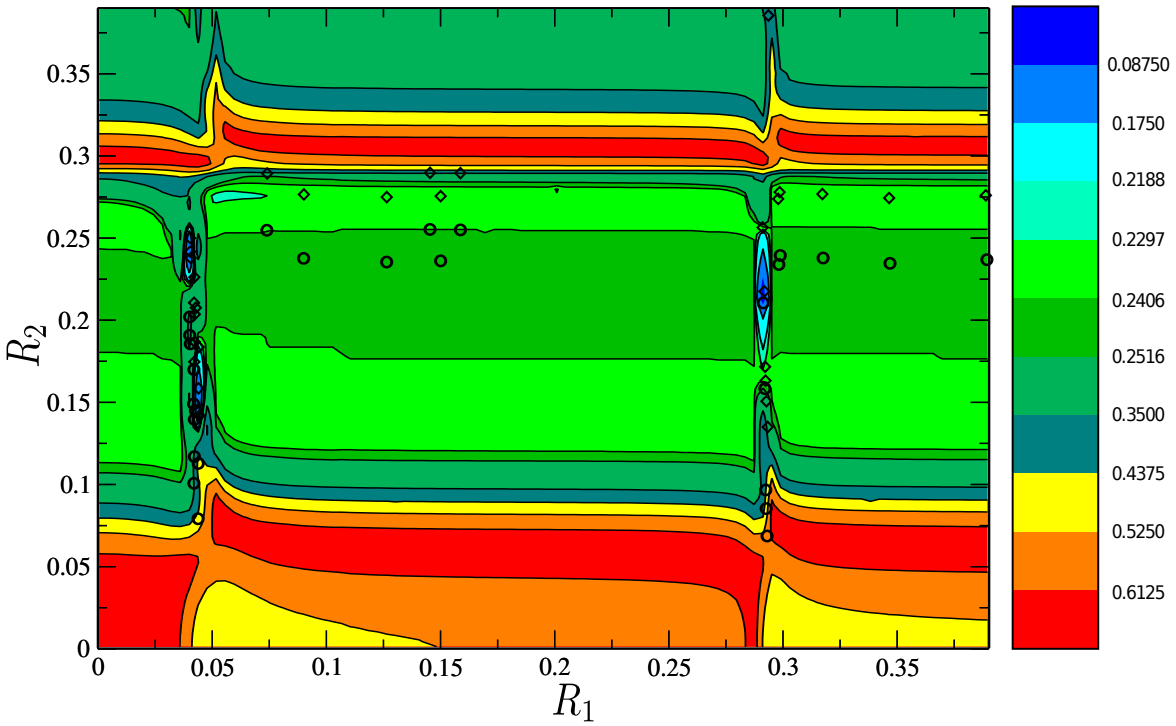

5.17. Irudia Kostu funtzioaren balioaren adierazpena kalkulatutako bilaketa-espazioko puntu bakoitzarekiko. Horretarako, bilaketa-espazioa 10.000 puntuetan diskretizatu da. Zirkulu batez eta diamante itxurako puntuekin adierazitako ebazpenak, ID metodoa IHS eta FSA algoritmoekin erabiliz lortutako ebazpenak adierazten dituzte, hurrenez hurren.

irudian Fan et al.-ek proposatutako topologiaren eta ID metodoaren bitartez lortutakoen transmitantzia kalkuluen emaitzak aurkezten dira. Oinarrizko topologian ID metodoak eskainitako parametroak ezartzen direnean, filtroaren operaketa maiztasunaren inguruan patroi interesgarri bat aurkezten du, hots, C eta B kanaletara zuzentzen den argia era ezabakorrean interferitzen du eta D kanalean berriz, era konstruktiboan jokatzen du, argi transferentzia osoa lortuz.

Bereziki, Fan et al.-ek proposatutako ebazpena sare karratu baten antolatutako 11.56-ko konstante dielektrikoko zutabetan garatzen da. Bertan, R_1=0.05a, n_1=6.6 and n_2=9.5 ebazpena proposatzen da. Bitartean, ID algoritmoak R_1=0.0727, n_1=2.32 and n_2=10.69 parametroak proposatzen ditu. Laburbilduz, Fan-ek proposatutako kabitate erresonantzia sistema erabilita, argi transferentzia eraginkorra lortzen duten egiturak lortu dira. Metodo analitikoen bidez ebatzi daitezkeen eredu hauek, ID metodoaren bitartez modu erraz eta bizkor baten ebatzi daitezke. Gainera, kasu honetan, gure ebazpenak Fan-ek [207]-en proposatutako emaitzak baino zertxobait hobeagoak dira. Emaitza hauen arabera, ID metodoak, IHS nahiz FSA metodoak erabiliz, PC klusterren diseinurako erabilgarria dela ondorioztatu daiteke.

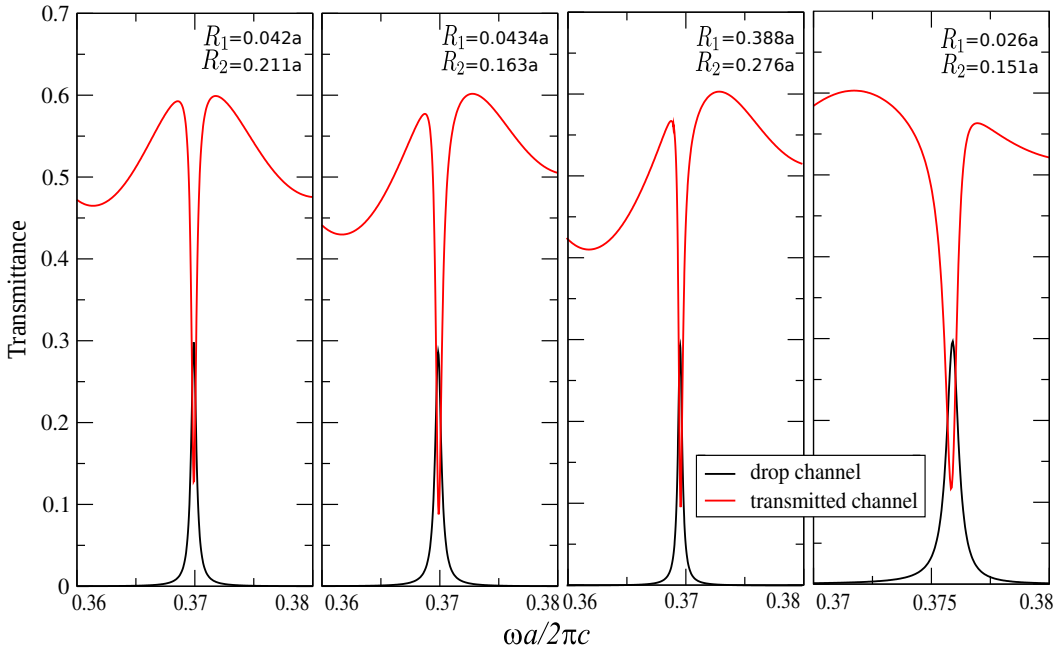

5.18. Irudia Ezkerretik eskumara: kanal bakoitzaren transmitantzia espektroa Ren et al.-ek proposatutako egiturarentzat, IHS metodoaren bidez lortutako egiturarentzat, FSA algoritmoaren bidez lortutako ebazpenarentzat eta IHS metodoak proposatutako beste egitura osagarri batentzat.

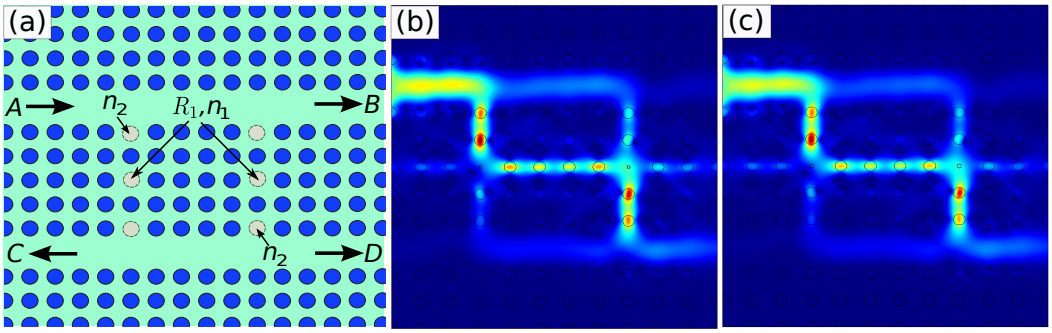

5.19. Irudia (a) Fan et al.-ek bi uhin-gida paralelo erabilita argia filtratzeko proposatu zuten egitura [207]. (b) Denboraren bataz-besteko potentzia-fluxua Fan et al.-ek proposatutako egiturarentzat eta (c) ID algoritmoak proposatutakoarentzat, a/λ=0.373 maiz-tasun normalizatuaren inguruan.

Gainera, hurrengo atalean, metodo hauen erabilgarritasuna askatasun gradu asko dituzten konfigurazio konplexuen kasuaetan areagotzen dela erakusten da.

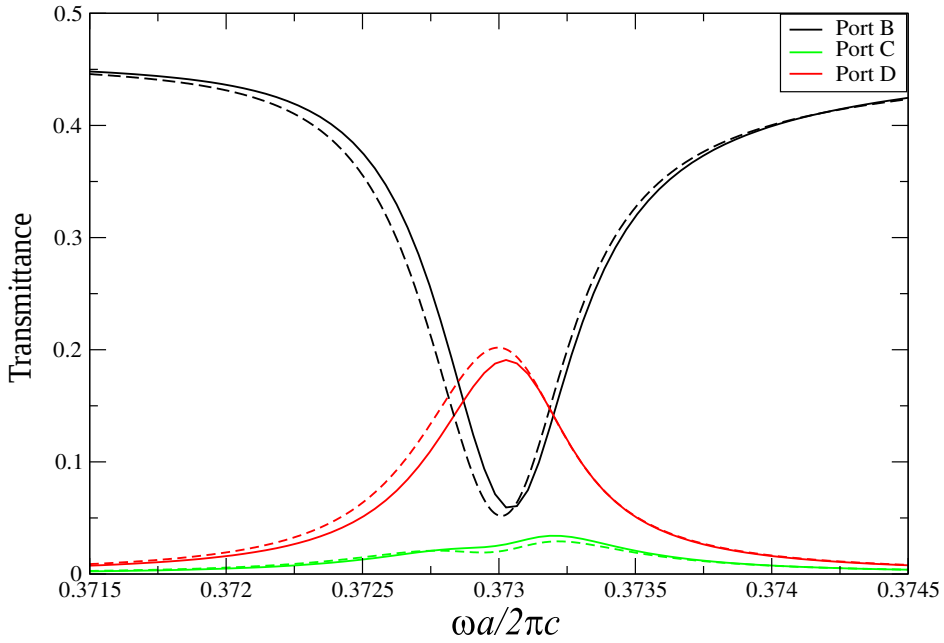

5.20. Irudia Fan et al.-ek proposatutako egituran kalkulatutako *B*,*C*, *D* portuen transmitantzia (zuzen jarraiak) eta IHS-ren bidez lortutako egituraren emaitzak (zuzen etenak).

5.5 PCWG taperren alderantzizko diseinua

Bi uhin-gida optikoen arteko akoplamendu eraginkorra eskuratzea funtsezko zeregin bat da zirkuitu optiko integratu konplexuen garapenerako. Horrez gain, PCWG-etan hedatzen diren emphslow-light moduen akoplaketa sustatzeak ere garrantzi handiko helburua da [209], argi-materiaren interakzioa *slow-light* erregimenean areagotzen bait da [210–212] eta, beraz, *optical delay lines* konpaktuagoak eta aldakorrak sortzeko erabili daitezke [192, 213]. Hala eta guztiz ere, *slow-light* erregimenean, PCGW-en arteko akoplazioak atzera-isladapen bortitza sortzen du [209, 214]. Hain zuzen ere, PCWG konfigurazio ezberdinetan egindako uhin-gidak aurkezten duten talde-indize diferentzia handiak sortzen du efektu hori eta, askoz nabariagoa da abiadura oso baxuko moduak hedatzen direnean [215].

Berriki, sekzio ezberdinak dituzten PC uhin-giden arteko akoplazio eragingarria lortzeko teknika eta egitura ugari proposatu dira. Zenbait kasutan, [216]-en bezala, ohiko siliziozko uhin-giden arteko akoplamendua obetzeko, uhin-giden moduen moldaketa bultzatzen da (hurrengo kapituluan siliziozko uhin-gida trinkoei buruzko informazio gehiago ematen da) PCWG-etan modu eraginkor batean argia txertatzea ere interes handiko gai bat da eta dagoeneko ikerketa lan batzuetan landu da, bai teorikoki [215], bai esperimentalki, [214]-ean esaterako. Bereziki, [214]-en, Vlasov et al.-ek *strip* motatako uhin-gida batetik PCWG batera argia akoplatzeko elementu batzuk moldatuz lortu daitekeela frogatzen dute. Gainera,

prozedura horrek abiadura oso baxuko argi moduen kasuan ere aplikatu daitezkeela frogatzen dute. Aldiz, bi uhin-giden arteko trantsizioa errazten duten egitura adiabatikoetan oinarritutako ebazpenak arreta gehiago jaso dute. Gailu horien funtzionamenduaren printzipioa zulo/zutabeen diametroa pixkanaka doitzean datza. Moldaketa horiek, indize-efektiboaren gradiente leuna simulatzen dute eta ondorioz, horrelako egiturak erabiliz, bi uhin-giden arteko indizeen ezberdintasunak sortutako islapenak minimizatu daitezke. Printzipioz, moduen moldaketa gradualak uhin-gida klasikoen eta PCWG-en arteko akoplazioa egitea bideratzen du [192, 217] eta baita zabalera ezberdina duten PCWG-ak bateratzea ahalbidetzen du, argi modua uhin-gida horietan ondo konfinatuta egon ezkero [218]. Gainera, metodo horrek emaitza ikusgarriak lortzen ditu abiadura ertaineko argiarekin, baina, abiadura-baxuko argia hedatzerakoan, uhin-gida ezberdinen inpedantzia diferentziak nabarmenagoak egiten dira eta sortu beharrezko taper-aren luzera handitu egin behar da akoplamenduko galerak murrizteko [219, 220]. Beste alde batetik, kristal fotonikoen egituretan diseinu adiabatikoak sortzea fabrikazio metodo oso zehatzak eskatzen ditu, egitura adiabatikoak akats estrukturalen aurrean erantzun guztiz ezberdin bat aurkezten bait dute. Beste motatako taper egiturak diseinatzeko, algoritmo genetikoak ere erabil izan dira, algoritmoaren bitartez egituraren zilindro batzuen kokapena aldatuz [221, 222]. Aurretik egindako ikerketek soluzio hurbilak aurkitzean ardazten dira (sarritan intuizioan oinarritutakoak izan direnak) edo, kasu askoz sinpleagoetarako, konponbide erdi-analitikoak aurkezten dituzte, baina azken horiek elementu ugariz osatutako kristal fotoniko xafla batean sortutako uhin-gidetan aplikatzea oso zaila izaten da. Hala ere, [209]-en, Oskooi et al.-ek adierazten dutenez, askatasun gradu asko dituzten kasuetan, horrela lortzen diren topologiak fabrikazio-akatsen menpekotasun handia dute. Hori dela eta, taper egiturak diseinatzeko orduan parametro gutxi batzuk baino ez dira kontuan hartzen. Baldintza eta limitazio horiek kontuan hartuz, [209]-en, kasu-txarrenaren optimizazio metodoa proposatzen da. Metodologia hori fidagarria eta egonkorra dela dirudien arren, kapitulu honetan azaltzen diren bezalako sistema konplexuagoetara estrapolatzea oso zaila izaten da.

5.5.1 Akopladore sinple baten eredua

Kasu horretan, 5.21 irudian aurkezten den *toy-model* problema planteatzen da. Bertan, zabalera apur bat ezberdinak dituzten bi uhin-giden arteko moduen akoplamendua aztertuko da. Kristal fotonikoko egitura horrek lerro akats bat du Γ - M norabidean. Horrela, $\sqrt{3}a$-ko zabalera duen uhin-gida bat sortzen da, normalean W1 izenez ezagutzen dena. Notazio horren arabera, hurrengo zulo errenkada ere ezabatzen denean, uhin-gida zabalagoa sortzen da, W3 bezala izendatzen dena. Bertan, modu gehiago hedatzeko aukera agertzen da, baina orokorrean, modu berri horiek ezin dira zuzenean W1 uhin-gidara akoplatu. Horrela, bi uhin-

giden arteko ezberdintasunak sortutako argi isladapena ekiditzeko eta transmisioa hobetzeko, ezaugarri horiek betearazten dituen egitura lotura batez hornitu behar da sistema.

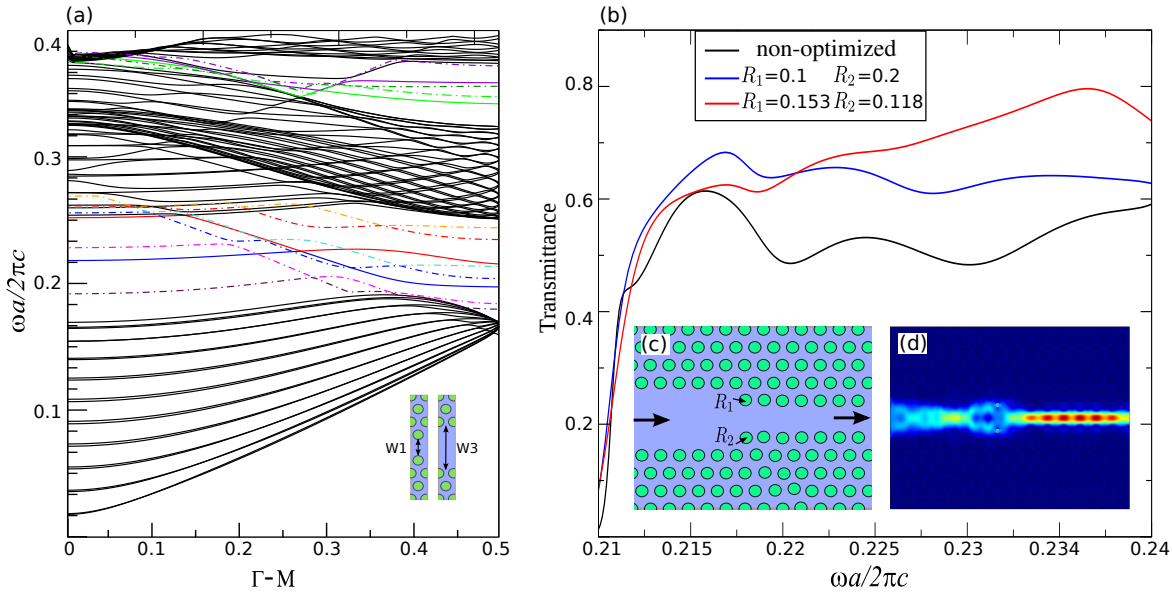

5.21. Irudia (a) 3.5-eko errefrakzio indizea duen material baten $0.295a$ erradioko zuloz egindako sare triangeluarrean zulo errenkada bat estali da, W1 uhin-gida bat sortzeko. Sare berean 3 errenkada estaliz W3 uhin-gida bat sortu da ere. Irudian, uhin-gida horien banda-diagrama erakusten da. W1 egituran, modu gidatu batzuk agertzen dira (koloreztatutako marra jarraiekin adierazita), baina W5 uhin-gidan modu-gidatu gehiago hedatzen dira gand-gap bitartean (koloreztatutako marra etenez adierazita). (b) Optimizatu gabeko W3-W1 egituraren, ID prozesuak proposatutako egituraren eta Talneau et al.-ek proposatutako egituren transmitantzia espektroa. (c) R_1 eta R_2 erradioen menpe dagoen oinarrizko taper egitura. (d) ID metodoak proposatutako konfigurazioaren potentzia fluxuaren simulazioa.

[223]-en Talneau et al.-ek izaera adiabatiko duten *taper* egiturafk proposatzen dira, W3-ko sekzioa duten uhin-gidetatik, estuagoak diren w1 uhin-gidetara argia akoplatzeko. Talneau et al.-ek proposatutako eredua, gero eta diametro txikiagoko zuloak dituen egitura batean oinarritzen da. Horren bidez, material artifizial baten mailakako indize efektibo baten efektua sortzen da. Talneau et al.-ek proposatutako egiturarik sinpleena 5.21.c irudian ikus daiteke. Egitura hori 3.5-eko errefrakzio indizea duen GaInAsP materialean egindako zulo sare baten sortutakoa. W1-eko gidatik W3-ko uhin-gidara dagoen trantsizioa diametro txikiagoa duten bi zuloen bidez lortu da, R_1 eta R_2 bezala izendatu direnak, hurrenez hurren. Talneau et al.-ek uhin-gidaren egitura optimizatu zuten, atzera-isladatzen diren argi eremuak ekiditzeko. Eredu hori *toy-model* eredu gisa aukeratu dugu, simetria bikoitza duen diseinu sinplea delako eta beraz, simetria horrek problema are gehiago sinplifikatzea ahalbidetzen duelako. ID metodoaren kalkuluak egin baino lehen, uhin-gida bakoitzan hedatu daitezkeen moduak

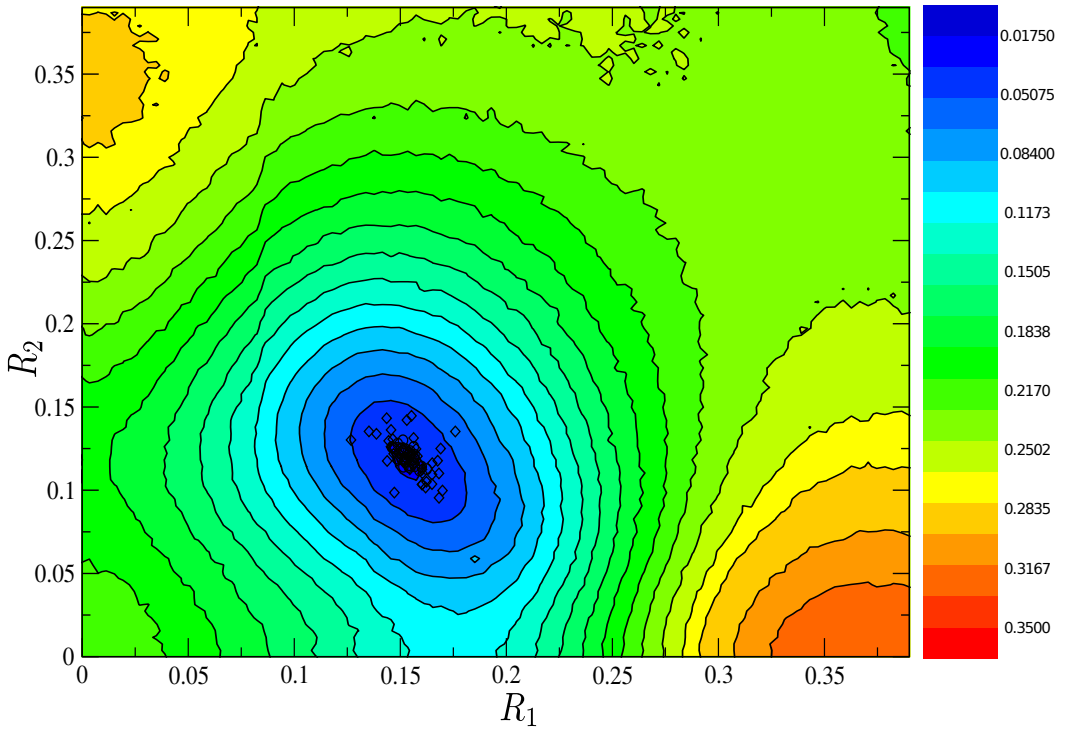

5.22. Irudia Kostu funtzioaren balioa kalkulatutako bilaketa-espazioko puntu bakoitzarekiko. Horretarako, bilaketa-espazioa 10.000 puntuetan diskretizatu da. Zirkulu batez eta diamante itxurako puntuekin adierazitako ebazpenak, ID metodoa IHS eta FSA algoritmoarekin erabiliz lortutako ebazpenak dira, hurrenez hurren.

aztertu dira. 5.21 irudian W1 eta W3 uhin-giden dispertsio diagramak aurkezten dira, lerro jarraiak eta etenak erabiliz, hurrenez hurren. PCWG bi horien akoplamendu eragingarria sortzeko, bi uhin-gida horietan hedatu daitezkeen moduak moldatu egin behar dira, lehenengo uhin-gidan aurkitu daitekeen moduaren forma, bigarren uhin-gidan aurkitzen denarekin bat egin dezan. Nabarmenki, a/λ =0.215 puntuaren inguruan W1 eta W3 gidetako moduak bat egiten dute, maiztasunean eta forman. Hala eta guztiz ere, egoera hori maiztasun gutxi batzuetarako baino ez da ematen eta beraz, 5.21.b irudiko diagraman ikusi daitekeenez, transmitantzia azkar galtzen da puntu horren inguruan.

Kasu horretan, R_1 eta R_2 aldagaien balio optimoa aurkitzeko, bilaketa-espazioaren arakaketa zorrotza egitea posiblea da, *brute-force* eran eta horretarako 10.000 ebazpen kalkulatu dira. Kalkulu horien bidez, optimo globala $R_1 = 0.1531$ eta $R_2 = 0.118$ balioak ezartzerakoan dagoela aurkitu da. Berriro ere, IHS eta FSA algoritmoak bilaketa-espazioaren optimoan kokatutako aldagaien balioak aurkitzen dituzte, baina, kasu honetan, ebazpen horiek ez datoz bat Talneau et al.-ek proposatutako ereduarekin. Hain zuzen ere, 5.21.b irudian ikusi daitekeenez, Talneau et al.-ek proposatutako konfigurazio adiabatikoa erabiliz, non $R_1 = 0.1$ eta $R_2 = 0.2$ diren, transmitantziaren eraginkortasunak ID metodoaren bidez

aurkitutako ebazpenak sortutako transmitantziaren adinako hobekuntza sortzen du. Hala ere, lan honetan erabilitako optimizazio metodoetarako, konponbide adiabatikoak dakarren ebazpena oraindik ere maximo lokal batean kokatzen da. Behar izanez gero, ID metodoaren optimizazioak puntu horretatik ihes egiten du eta optimizazio globala aurkitzen du iterazio gutxi batzuetan. 5.22 irudiak IHS metodoa erabiliz arakatutako 60 Monte Carlo fitness frogapen eta FSA metodoa erabiliz kalkulatutako beste 60 Monte Carlo erakusten du. Erabilitako bi metodoen bidez, w1 uhin-gidako akoplazioa maximizatzea lortzen duten optimo globalen egiturak aurkitzea lortu da.

5.5.2 W5 eta W1 kristal fotoniko uhin-giden arteko akopladore eraginkorra

Normalean, siliziozko fotonika arloan, ohikoa da SOI uhin-gidak erabiltzea osagarri trinkoen arteko argiaren gidaketa egiteko. Uhin-gida horien bideragarritasuna osagarri trinkoetan luzaro frogatu bait da. Beraz, kristal fotoniko baten sarean egindako uhin-gida bat (PIC) batean erabiltzean, SOI uhin-gida horietara konektatu behar izango da, baina SOI uhin-giden sekzioak W3 PCWG baino zabalera askoz handiagoa du. Bestela ere, SOI uhin-gidak W5-eko zabalera duten gidekin konektatu daitezke, kasu horretan, antzeko zabalera dutenez akoplazio kalterik larrienak ekidin daitezke. Geroago, W5-eko uhin-gidetatik W1 uhin-gidetara akoplatu daitezke taper gailu bat erabiliz. Halaber, zabalera hain desberdina duten uhin-giden arteko akoplazioa lortzea, aurreko *toy-model* ereduan egindako hausnarketa baino prozesu konplexuagoa da eta parametro gutxi batzuk aldatzeak ez du eraginik izango atzera-isladapenaren arazoan. 5.23.b. irudian akopladore berria garatzeko erabili den hasierako konfigurazioa aurkezten da. Berriro ere, ohiko kristal fotoniko sare triangeluar bat erabili da, $0.35a$ erradioko zuloz osaturikoa, non a sarearen maiztasuna da. Zulo horiek 3.46 indizea duen Si materialean antolatzen dira. Bertan, W5 uhin-gida bat W1 uhin-gidarekin elkartzen da. Ingurune bi horien arteko akoplazioa hobetzeko, ID algoritmoari 5.23.a irudian koloreztutako zuloen kokapena eta erradioa aldatzea utzi zaio. Bi uhin-gidak $[0.26-0.28]$ maiztasunen arteko moduak onartzen dituzte eta banda-zabalera horretan ID metodo aplikatzen dugu, maiztasun tarte horretan transmisio laua azaltzen dituzten egiturak aurkitzeko. Guk dakigula, hemen proposatu den egitura litzateke hainbesteko banda-zabala eskaintzen duen lehenengoa. 5.23.a irudian aurkezten den kluster-ak simetria-plano bat dauka eta beraz, geometria erdia simulatzea nahikoa da sistema hori ebazteko. Simetria hori simulatzeko, *perfect electric* muga baldintzak (PEC) ezarri dira plano simetrikoaren mugan eta *perfectly matched layers* baldintzak erabili dira beste muga guztietan, klusterraren izaera mugatuak sortutako islapen ez-fisikoak saihesteko. Simulatutako eredu hau ezkerreko

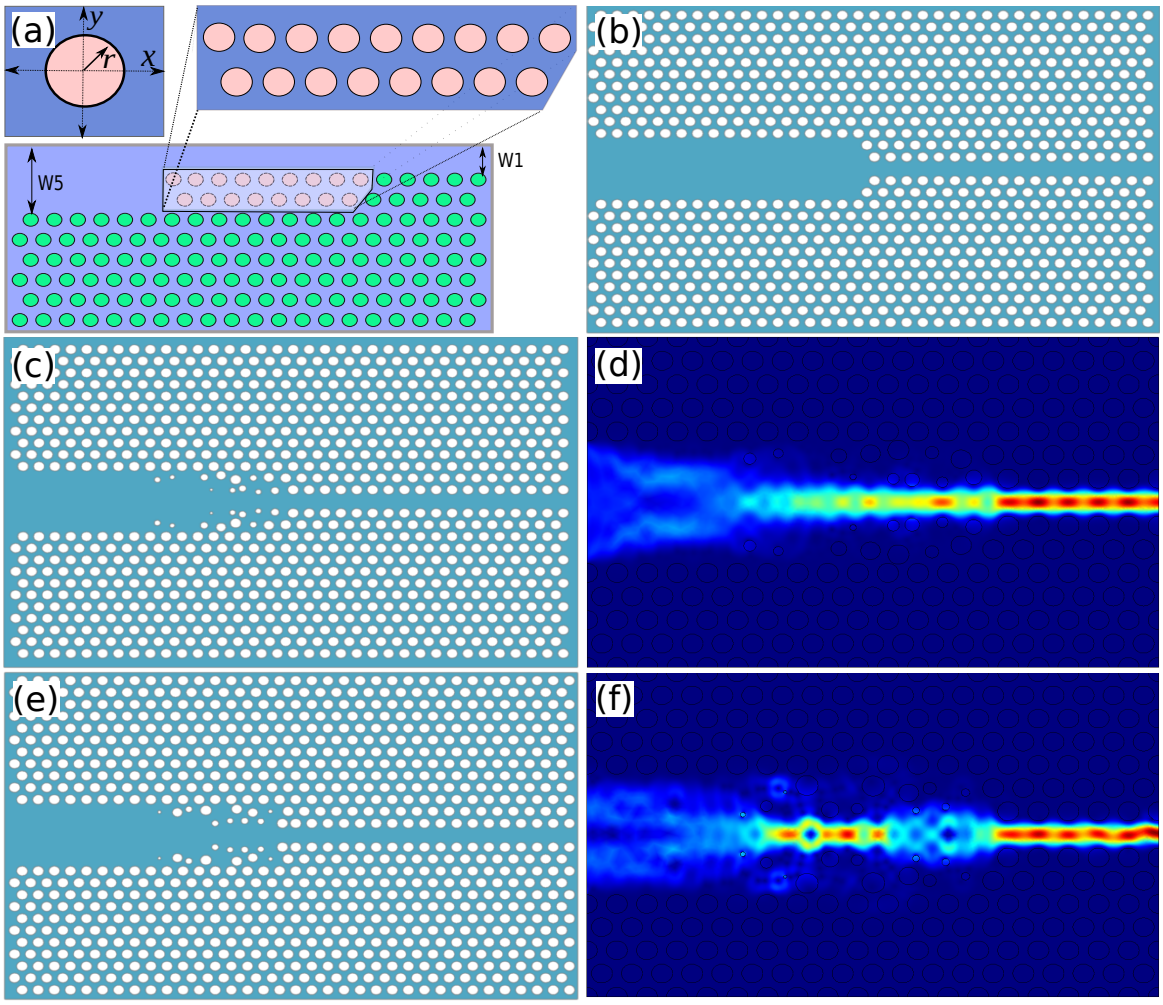

5.23. Irudia (a) Taper egituraren akoplazio eskualdearen irudi eskematikoa bere simetria ardatzetik zatituta. Optimizazioan erabilitako zuloak kolorez adierazi dira eta irudi honen xehetasunean sarearen unitate-zelda bat ikusi daiteke. (b) Optimizatu gabeko *horn* taper baten egitura. Taper honek argi gehiena atzera-isladatzen du W5 uhin-gidarantz. (c) IHS algoritmoaren bidez optimizatutako egiturak ia %100-eko akoplazio etekina lortzen du (d) a/λ =0.265 maiztasun normalizatuan. (e) FSA algoritmoaren bidez optimizatutako egitura. (f) Denboran bataz-besteko potentziaren fluxua (e) konfigurazioa erabiliz.

simulazio mugatik sustatutako uhin plano monokromatiko batekin argitu da. Gero, IHS eta FSA metodoak erabilita, alderantzizko diseinua erabili da. Optimizatutako diseuniak 5.23.c-. 5.23.e irudietan ikusi daitezke.

5.24.irudiak 5.23.c- 5.23.e-etako topologiak erabiliz lortutako transmitantzia espektroak aurkezten ditu, 5.23.b irudian ikusi daitekeen optimizatu gabeko W5-W1 taper egituraren taperraren espektroarekin batera. Alde batetik, akoplamendu etapa barik lotutako eta zabalera ezberdineko uhin-gidak erabiltzean, islapen bortitzak agertzen dira eta transmisioaren inten-

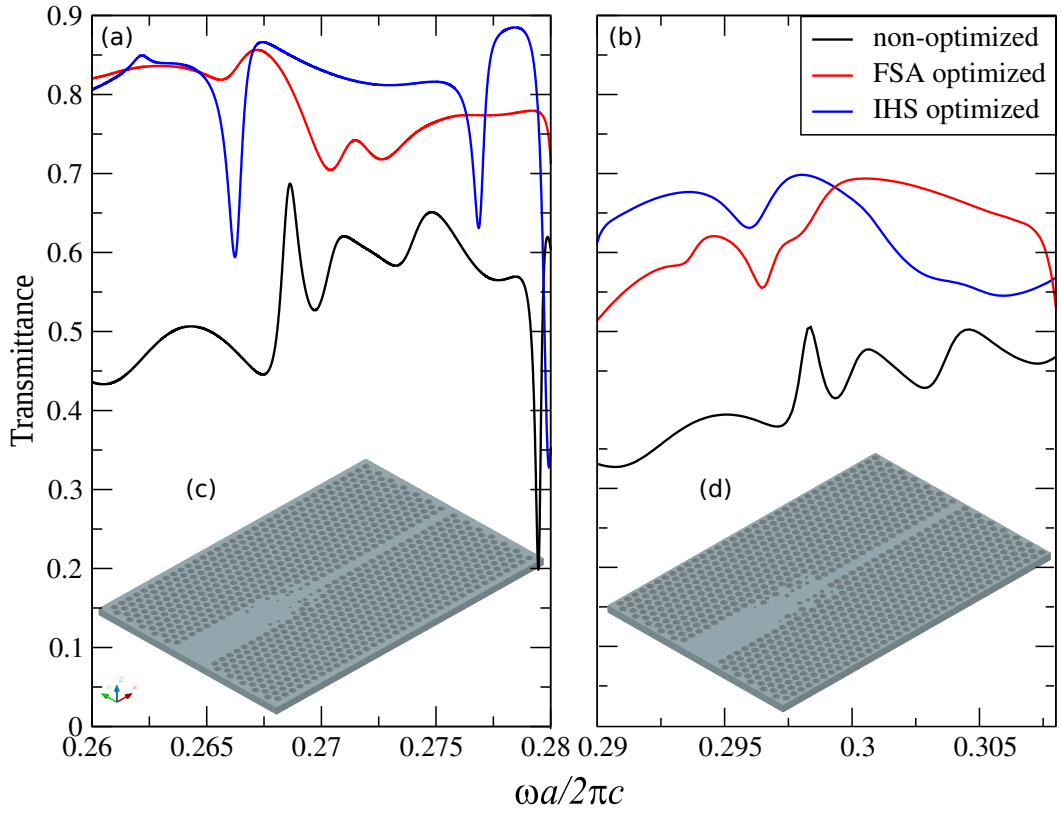

5.24. Irudia (a) Optimizatu gabeko (beltza), IHS (urdina) eta FSA (gorria) algoritmoen bidez optimizatutako akopladore egituren anplitude eta transmitantzia espektroen konparaketa, Si (n=3.46) materialean egindako $0.35a$ erradioko zuloz osatutako 2D kristal fotonikoan diseinatutakoak. Barneko irudiak IHS metodoak proposatutako 3D PC xafla egitura aurkezten du. (b) Xafla egituretan kalkulatutako transmitantzien konparaketa. Barneko irudiak, FSA metodoak proposatutako egitura 3D PC xafla konfigurazioan aurkezten du.

tsitatean galera handiak azaltzen dira. Beste alde batetik, argiaren akoplamendua nabarmenki hobetzen da taper egiturak erabiltzen direnean. Gainera, transmisio espektroak, gure erreferentzia dan W1 uhin-gidaren simulazioak eskaintzen duen transmisio emaitzetatik oso gertu dagoen emaitza aurkezten du. W1 PCWG-aren transmitantziari dagokionez, kalkulatutako transmitantziaren maximoak 0.9 balioaren azpitik daude. Izan ere, egoera hori absortzio mugak sortzen dute 2.kapituluan deskribatutako PML muga baldintzek.

Taper egiturrik gabeko sistemak, transmisioan konfiguratutako gailuetan erabiltzeko adinak izan daitezke. Aitzitik, islapenan operatzen duten gailuetan, islapen txikiek Gires-Tournois bezalako interferentziak sortu ditzake eta beraz, sistema eragileetan kalteak sortu ditzake. Kasu horietan, orain arte proposatutako taper egiturak arbuiagarria diren islapenak aurkezten dituzte. Horrez gain, bi kasuetan, taper egitura kristal fotonikoaren zirkuituan integratzen da eta, beraz, egitura osoaren fabrikazioak ez du beste teknika konplexurik behar

osagarri hori fabrikatzeko. Gainera, proposatutako diseinuak PCWG-etan erabilitako objektu geometrikoak erabiltzen ditu, hau da, ez du inolako geometria exotikorik erabiltzen. Azkenik, taper sekzioaren luzerak ez du osagarria gehiegi luzatzen, 8 periodoz ez besterik osatuta bait dago. Orain arte aurkeztu diren taperrak izaera adiabatikoa duten egitura luzez osatzen dira, zabalera tarte gutxiagoko bi uhin-gidak lotzeko (gehien bat W3-W1 bitarteko akoplazioa lortzeko taperretan oinarritutakoa), [192]-en bezala. Gainera, optimizatutako taper egituren 3D-ko simulazioak egin dira, $0.6a$-ko lodiera duen kristal fotoniko xafla bat erabiliz. Egitura hauek sortutako transmitantzia diagramak 5.24.b irudian ikusi daitezke. Emaitza horietatik, 2D PCWG-etan kalkulatutako egiturak 3D xafla plataforman ere ezaugarri berak mantentzen dituztela ondorioztatu daiteke. Gainera, xafla egituraren lodiera handitzen denean, gidatutako bandak maiztasun baxuagoetan aurkitzen dira eta taper-aren eraginkortasunak gora egiten du, 5.24.a irudian aurkezten den transmitantzia balioetara hurbilduz.

5.6 Ondorioak

Kapitulu honetan, alderantzizko diseinua erabiliz diseinatutako osagarri pasibo berriak aurkeztu dira. Gailu hauen eraginkortasuna eta banda-zabalera optimizatu egin da, etorkizuneko zirkuitu trinko fotonikoen funtsezko zereginak burutzeko aproposak izan daitezen. Aurreko diseinu gehienak intuizioan oinarrituta daude gehien bat. Hemen azaldutako diseinuak berriz metodo heuristikoak erabiltzen dituzte alderantzizko diseinuaren metodoa gidatzeko eta gailu horien aurrekariak baino emaitza hobeagoak lortzeko. Izan ere, horrelako teknikak, kasu bakoitzean planteatutako helburuaren optimo globala aurkitzeko erabilgarriak dira. Beste alde batetik, optimizazio teknika horiek kristal fotonikoen uhin-gidetara ere aplikatu ditugu. Esparru horretan, dielektriko baten zuloz osatutako kristal fotonikoen uhin-gidak bereziki garrantzitsuak dira. Kasu horretan, ohikoa da uhin-gida multi-modu izaera edukitzea eta beraz, norabide kristalino ezberdinen arteko nahiz neurri ezberdineko uhin-giden artean modu horiek akoplatzea ez da posiblea bitarteko gailu bat erabili barik. ID metodologia luzaro erabili izan da ingeniaritzako beste hainbat esparruetan, baina oso kasu gutxietan erabili da kristal fotonikoetan oinarritutako osagarri fotoniko konplexuak diseinatzeko. ID metodoarekin batera, FSA eta IHS algoritmoak optimizazio-problema horietan oso aproposak direla frogatu da. FSA eta IHS algoritmoen etekina aurkeztu den arren, kapitulu honetan ez da metodo horien arteko konparaketa zehatzik planteatzen, ebatzitako problemak ez baitira testuinguru estandar batean kokatzen eta horrelako konparaketa bat egitea lan honen ildotik kanpo dago. Hala ere, teknika horien baliagarritasuna frogatzeko, PC egitura sinple batzuk aurkeztu dira. Bertan, maneiatu beharreko askatasun graduak gutxi direnez, araketa metodo zehatzak erabili daitezke oraindik ID metodoaren emaitzekin

konparaketa bat egiteko. Eredu sinple horietan ere literaturan aurkitu daitezkeen kasu batzuetan oinarritu gara. Azpimarragarria denez, kasu batzuetan ID metodoak aurkitutako ebazpenak literaturako adibide hauetan jasotako kasuak baino emaitza hobeagoak lortzea bideratu du.

Eredu sinple horietaz gain, egitura askoz konplexuagoak aurkeztu dira. Egitura horiek irizpide teoriko batetik ikusita interesgarriak izan daitezke, baina gainera, ezinbesteko funtzio praktikoak betetzeko gailu interesgarriak izan daitezke, zirkuituetan oinarrizkoak diren eginkizunak betetzen bait dituzte. Kasu horien adibide garbia kapitulu honetan aurkeztutako akopladoreetan dago. Egitura horiek, gidatutako moduak jatorrizko gida batetik beste gida batera moldatzeko gai dira, gida horien loturak sortutako atzera-isladapena murriztuz. Izan ere, atzera-isladatzen den argia ekiditzea ezinbestekoa da *slow-light* erregimenean oinarritzen diren *delay-line* uhin-gidetan. ID metodoaren bitartez lortutako egituretan akoplazio etekina %100-etik hurbil dago, gidatutako moduen maiztasun guztietarako. Gainera, taper horiek guztiz trinkoak dira eta PC sarearen periodo gutxi batzuetan osatzen dira soilik, bitartean, horrelako taper adiabatikoak antzekotasun gehiago duten uhin-gidak bateratzeko, luzera handiagoak erabiltzen dituzte. 2D egituretan lortutako emaitza horiek, 3D-FEM erabilita ere xafla egituretan eraginkortasun handia izaten jarraitzen dutela frogatu da. Beste alde batetik, ID metodoa dolezdura zorrotzak dituzten uhin-gidak sortzeko ere erabili da. Bertan, maiztasun tarte zabal batean transmitantzia maximizatzea izan da helburua. Izan ere, dolezdura zorrotz horietan argia gidatzeko gaitasunak PCWG-en abantaila garrantzitsuenetarikoa da, baina gidatu daitekeen banda-zabalera osoan horrelako erantzuna lortzeko geometria bereziak erabili behar dira. Kapitulu honetan, sare exotikorik behar ez dituzten geometriak erabili dira eta beraz, ohiko metodo litografikoak erabiliz fabrikatu daitezke. Horretaz gain, guk dakigula, hemen aurkeztutako 120°-ko dolezdura duten PCWG-ek, banda-zabalera osoan efizientzia optimoa lortzen duten lehenengo egiturak dira. Horiek, gailu opto-elektroniko berrietan erabili daitezkeen eskala-txikiko zirkuitu optiko trinkoak sortzeko erabilgarriak izan daitezke. Eredu hauekin batera, banatzaile topologia berriak ere aurkeztu dira. Egitura hauek, irteerako uhin-gidetako moduen hedapena eta eszitazioa kontrolatzean ardazten dira. Egitura sinple hauek galera baxuak eskaintzen dituzte moduen banda-zabalera optikoan eta (PIC) baten argiaren banatzaile moduan nahiz interferometro baten edota *switch* optikoetan erabilgarriak izan daitezke. Emaitza hauek kontuan hartuz, era intuitibo baten horrelako emaitzak lortzea zaila izango litzatekeen bitartean, ID metodoak era bizkorrean aurkitzen dituela ondorioztatu daiteke eta beraz, ID metodoa osagarri optikoen diseinurako tresna oso egokia dela baieztatu daiteke.

Chapter 1

Photonic band gap materials and photonic crystals

This first chapter is devoted to introduce the reader into the research field of photonic crystals. To start with, we present these materials by considering the analogies between the propagation of electrons and photons in periodic one dimensional media. Inasmuch as the particular physical properties of periodic media have attracted substantial attention from the research community, there is already a vast body of work about them, and thus it is hard to compose a short review chapter. Therefore, we have summarized some of the most relevant milestones regarding to this research field.

1.1 Photonic band gap materials and photonic crystals: The analogy between electrons and photons in periodic media

Solid state physics and, in a more general sense, quantum mechanics, gave us the theoretical understanding of the dynamics of electrons in crystalline solids. Assuming a great simplification, the atomic structure of such materials can be described by a regular, periodic and infinite arrangement of atoms. The later permits to reduce the computation of electronic states to the much simpler and general case of an electron under a periodic potential. The periodicity of the system is commonly represented by a lattice parameter, a, which defines the discrete translational invariance of the so called *primitive cell*, i.e. the smallest segment of space of length a that is periodically repeated along the (assumed) infinite lattice. These symmetry considerations can be combined with Schrödinger's equation to get a qualitative idea of the physical features of electron dynamics in these solids. Under some circumstances, materials possesing these discrete periodic potentials can induce the appearance of intervals

of forbidden energy, i.e. energy ranges for which no electron states can exist, which are often referred to as electronic band gap materials (EBG). These band gaps constitute the property which distinguishes semiconductors alloys, such as GaAlAs, InGaAs or InAlAs just to cite some of them, from other materials, providing them with the mechanism that permits to control and restraint the flow of electrons .

It is rather straightforward to examine the direct analogy between electron and photon dynamics within periodic structures from the wave-equation point of view. The Schrödinger's equation for an electron in a periodic potential $V(\vec{r})$ reads

$$\left[-\frac{h^2}{8\pi^2 m}\nabla^2 + V(\vec{r})\right]\Psi(\vec{r}) = E\Psi(\vec{r}), \tag{1.1}$$

where ∇^2, h, Ψ, m and E, stand for the Laplace operator, the Planck constant, the wave function, particle's effective mass and the total energy, respectively [1, 2]. Further, the very same theoretical approach works when these electrons are replaced by an harmonic electromagnetic wave in a periodic dielectric medium. Indeed, it is rather straighforward to reformulate Schrödinger's equation for waves in inhomogeneous dielectric media as an optical analogue of the EBG materials. In the absence of magnetic media, some manipulations of Maxwell's equations yield to the following eigenvalue expression

$$\left[\nabla \times \frac{1}{\varepsilon(\vec{r})}\nabla \times\right]\vec{H}(\vec{r}) = \left(\frac{\omega}{c}\right)^2 \vec{H}(\vec{r}), \tag{1.2}$$

for the magnetic field $\vec{H}(\vec{r})$ in a periodic dielectric medium described by the periodic permittivity $\varepsilon(\vec{r})$. Noticeably equations eq. (1.1) and eq. (1.2) unveil numerous similarities. Both equations solve a wave function in a periodic space featuring solutions characterized by the inherent periodicity of the material, that is solutions of these equations are, in both cases, Bloch waves. Eq. (1.1) serves to calculate the probability density function Ψ in a periodic potential that is usually represented as $V(\vec{r}) = V(\vec{r}+\vec{a})$, being a the lattice parameter introduced before, whereas eq. (1.2) applies to a periodic dielectric medium with permittivity $\varepsilon(\vec{r}) = \varepsilon(\vec{r}+\vec{a})$. These periodic functions appear within second order space-differential operators, the Hamiltonian and Maxwell operators, respectively, which are both Hermitian[3]. The corresponding real eigenvalues are the electron energy E and the squared frequency of the electromagnetic wave ω^2, respectively. In both cases, the coherent superposition of propagating and scattered waves can lead to eigenvalues for which electrons are inhibited. In the particular case of a photon propagating in a periodic microstructure (lattice constant of the order the optical wavelength), whose distinguising feature is a very large modulation depth of the refractive index, it will exhibit anomalous propagation effects in the vicinity of its Bragg

condition, i.e. it exhibits ranges of wavevectors where propagation is forbidden, likewise electrons within potential barriers are for certain energies. However, there also two main differences between the quantum mechanic and classic electromagnetic field formulation. First, the electromagnetic field in eq.(1.2) requires full-vector wave solutions, whereas the wave function in Schrödinger equation is a scalar quantity[1]. Second, there is no characteristic length scale inherent to Maxwell's equations, while Schrödingers equation is subjecto to the fundamental physical constants, such as Planck's constant or the electron mass [3].

1.2 Photonic Crystals

Photonic crystals (PhC) have generated a surge of interest in the last decades because they offer the possibility to control the propagation of photons to an unprecedented level [4–7]. In its simplest form, a photonic crystal is an engineered inhomogeneous periodic structure made of two or more materials with very different dielectric constants. In the case where the periodical variation of the dielectric constant (ε) occurs along one direction, we call it a 1D PC. Similarly, we define 2D and 3D PCs, corresponding to the respective cases where ε varies along two and three directions. Several examples of how mixed dielectric media can be arranged periodically forming PhCs in one, two, and three dimensions are shown in Fig. 1.1. When an electromagnetic wave (EM) propagates in such a structure whose period is comparable to the wavelength of the wave, unexpected behaviors occur. Among the most interesting ones are the possibility of forming a complete photonic band gap (CPBG), to localize light by introducing several types of defects in the lattice [8, 9], or enhancing certain non-linear phenomena arising due to stronger light-matter interactions caused by small or anomalous group velocity effects[10, 11].

The potential technological applications of these phenomena seem to be limitless and they range from simply using photonic crystals as perfect mirrors [12, 13] to controlling the spontaneous emission of an optically active ion [14–16] or propagation of solitons [11, 17]. Exploiting the strong light-matter interaction in PhCs, opens the possibility to explore exciting non-linear effects which are steaming a huge range of fascinating applications, such as, more efficient, compact, and low-power consuming optical regenerators [18, 19], enhanced sensing and biosensing devices [20–22], and more efficient photovoltaic cells [23–25].

Unfortunately, all these nice features come at a price: the length scales required in order to fabricate a photonic crystal appropriate for most applications, such as the ones involving telecommunication frequencies, are below the micron, so that ingenious innovations were required in order to actually fabricate such structures. Furthermore, fabricating devices based

[1] if the spin degrees of freedom are neglected

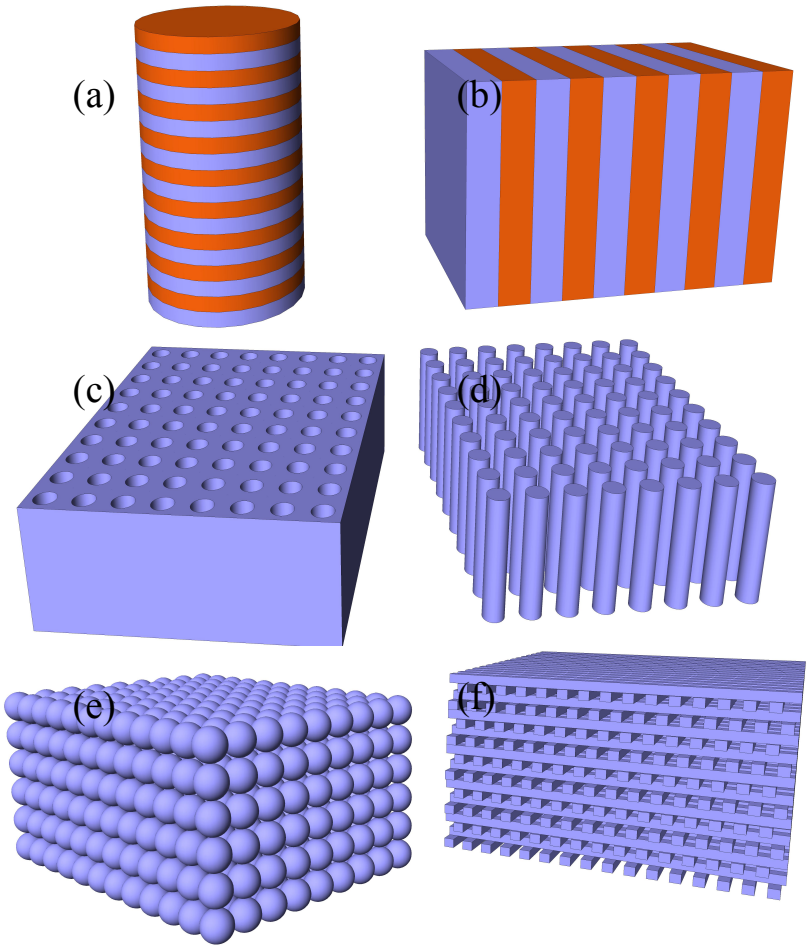

Figure 1.1 Schematics of representative a-b) 1D , c-d) 2D and e-f) 3D photonic crystals

on these lattices is even more challenging from a technological point of view, especially in three dimensions. This has resulted in a lot of effort being devoted to investigating 2D photonic crystal devices based on two-dimensional heterostructures, such us three-dimensional waveguides made of a two-dimensional photonic crystal core sandwiched between two layers of substrate that confines light by simple refraction index matching [26, 27]. Therefore, investigating photonic crystals is not a mere academic exercise but an important task, both at the fundamental and applied levels.

1.2.1 A short summary about the long road to Photonic Crystals

Photonic crystals are less exotic than they may appear to be. Millions of years before we began to manipulate the flow of light using synthetic structures, biological systems were using nanometre-scale architectures to produce striking optical effects [28]. From the marvelous

iridiscence produced by the shell scales of some species of beattles to the colorful wings of butterflies or the most eyecatching gem opals are indeed formed by ordered domains of stacked layers forming a precise lattice-like structure. These complex structures, provided with multiscale effects (and certain degree of disorder) produce light diffusion, forcing light waves to go through to inhibit the reflected light at certain frequency. In particular, the bluish decoloration shown in Fig.1.2 by some species of animals, is due to the elastic scattering at periodically ordered particles known as Tyndall scattering (or Mie scattering if this is produced by spherical objects). For a more detailed explanation of how nature produces the blue color, the reader is referred to [29]. Altogether, the variety of the natural photonic showcase is astonishing and it is a continuous inspiration for new technological applications. Therefore, photonic crystals have always been around us in one form or another and, thus, it has been an old research field that continues to attract researchers into the theoretical and practical possibilities enabled by these materials. It is not straightforward to determine an starting point, neither a date, in the timeline of photonic crystals research, from which this topic began to be the scope of many research efforts. Nowadays, the word photonic crystal stands for any ingenious photonic scheme that uses an engineered lattice aimed to customize the propagation of light and exploit the strong light matter interaction around periodic subwavelength scale scatterers. However, this definition does not discriminate any other material in which the inherent periodicity is broken up to some point.

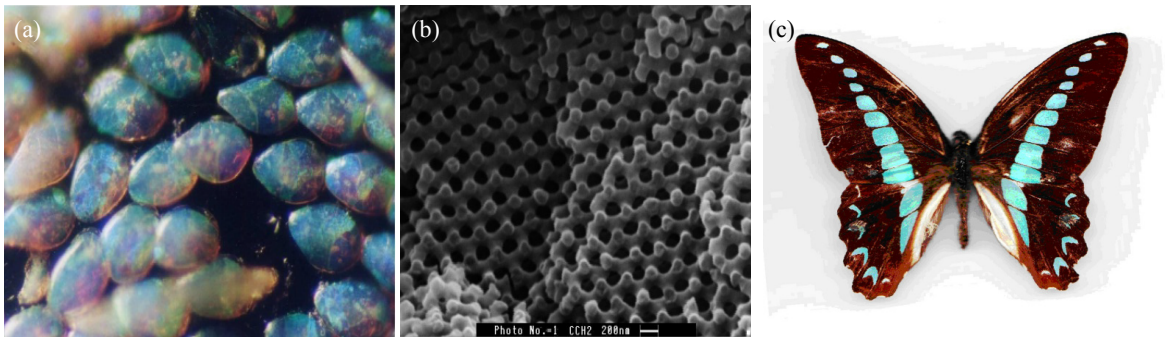

Figure 1.2 Microscope view (a) and electron microscope image (b) of the blue scales of the weevil *Cyphus handoki*, wherein the crystal lattice creates this particular scattering phenomena [30]. (c) The Swordtail *Graphium sarpedon* shows its characteristic pigmentation due to the tapestry of scales that covers the wings [29].

On the other hand, the foundations of PhC research inherits most of its theoretical background from solid state physics. In solid-state physics, the electron motion in a one-dimensional periodic array of potential barriers, i.e. the Kronig-Penney model [31, 32] is commonly used for understanding the formation of energy gaps. The optical analogous structure formed by a multilayer dielectric mirror, is commonly known as a Bragg reflector,

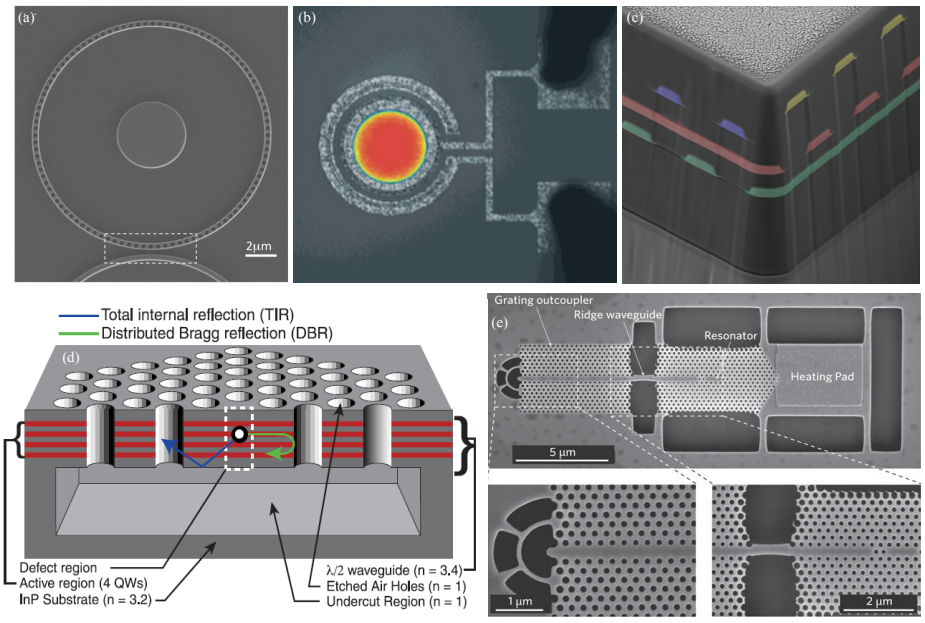

Figure 1.3 (a) A SEM image of a label free optical biosensor based on a one dimensional photonic crystal microring resonator with enhanced light-matter interation [20].(b) Electroluminisence device using p-type Si nanowires with a transparent n-type aluminium doped ZnO top electrode. Between these layers a photonic crystal comprised by Si pillars is sandwidched [43]. (c) Scanning electron microscopy view of a 3D woodpile photonic crystal made in a SU-8 polymer [45]. (d) This schematic shows a crosss section through the middle of a laser cavity formed from a single defect in a two dimensinoal photonic crystal.The structure forms an energy well for photons similar to that for electrons in a quantum wire structure [44]. (e) A device consisting of a photonic crystal cavity coupled to a photonic crystal waveguide terminated with a grating out-coupler [46]

multilayer stack or, according to the terminology used throughout this thesis hereafter, a 1D photonic crystal. Such structure is formed by alternating layers of material with different dielectic constants (see Fig.1.1.a-b).

When light impinges into the multilayer stack, it will be partially reflected at each dielectric discontinuity and, if the spacing is periodic, multiple reflections of the incident wave interfere destructively to inhibit the forward-propagating wave. This well-known phenomenon, first explained by Lord Rayleigh in 1887 [33], is the basis of many devices, ranging from dielectric mirrors [34, 35], dielectric Fabry–Perot filters [36, 37], antireflection coatings [38], distributed feedback lasers [39] to cavities [40]. The possibility to create two- and three-dimensional photonic crystals with two- and three-dimensional forbidden band gaps needed one hundred years since Lord Rayleigh's experiments to be proposed almost simultaneously by S. John and E. Yablonovich [41, 42]. Two-dimensional photonic crystals consist of a regular array of dielectric or metaldielectric materials in two directions while

the structure is homogeneous and infinite in the other direction. Finally, three-dimensional photonic crystals consist of a regular array of dielectric or metal-dielectric materials in the three directions. This structure is the only one that can exhibit a complete band gap, that is, a frequency range where the propagation of electromagnetic waves is forbidden, irrespective of the propagation direction [45].

Further, in the early 1990s, most of the research focused on the mechanism of creating a complete photonic bandgap(CPB) [47, 48], studying the band structure of different crystal lattices [49, 50] and enhancing the localization and guiding of photons within these structures. Together with the theoretical understanding of PCs, new fabrication processes were required to achieve nanometer length features. Regarding to this, the self-assembly method [51] and the laser direct writing techniques through the two-photon absorption of resin [52] were developed to fabricate high-quality photonic crystals. These two methods are some of the most promissing methods for obtaining high quality 3D PC structures and the realization of optical devices based on crystals possesing a complete band gap. On the other hand, quasi-2D photonic crystals, also known as photonic crystal slabs (PCS) have received a considerable attention as they have the potential to serve as an integration platform for densely packed photonic circuits. By introducing *defects* in a PC in a controlled manner, it is possible to implement passive, as well as active, building blocks (e.g. filters [53–55] or lasers [39, 56, 57]), just to cite some. These can then be combined to form large-scale complex structures [58]. Therefore, the study of photonic crystals is a very active research field in which new discoveries and applications are observed regularly. Besides, these materials have made the leap to some other fields, such as biology, mainly due to the high sensitivity of PhC biosensors [21], or to civil engineering [59, 60] among others. Yet, in spite of the numerous advances achieved regarding to the development of new devices based on photonic crystal technology, thus far, the most successful field of application is in photonic crystal fibers. These fibers allow light to be guided within a hollow core, minimizing the effect of losses, undesired nonlinearities, and many other unwanted properties of the bulk materials [61, 62].

1.2.2 The two-dimensional lattices

A photonic crystal receives its name from the fact that it is nothing but the periodic repetition of certain pattern along the space directions. The difference with standard crystals is that, in these, the repeated pattern is a set of atoms or molecules, whereas in a photonic crystal, the repeated pattern is a portion of, at least, two dielectric materials of different dielectric constants. The formation of a photonic band gap and its size depends on various factors: the symmetry of the underlying crystal lattice, the topology of the photonic crystal for a

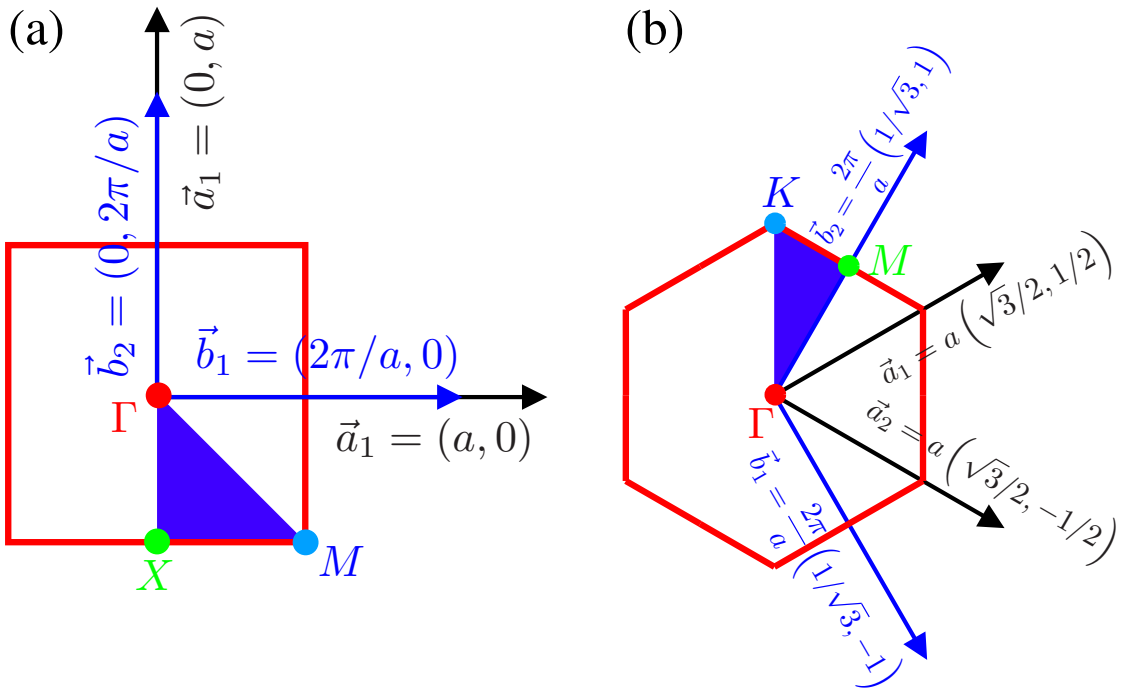

Figure 1.4 (a) Lattice vectors (black), reciprocal lattice vectors (blue), 1st Brillouin Zone (red square), irreducible part of the 1BZ (blue triangle), and special symmetry points (Γ, *X*, and *M*) of the square lattice. (b) Lattice vectors (black), reciprocal lattice vectors (blue), 1st Brillouin Zone (red square), irreducible part of the 1BZ (blue triangle), and special symmetry points (Γ, *M*, and *K*) of the triangular lattice.

particular lattice symmetry, and the dielectric constant contrast [2]. Therefore, it is important to understand the geometrical details of the lattice in order to fully grasp the photonic properties of a particular photonic crystal. Also, from a practical point of view, understanding the geometrical details of the lattice allows one in some cases to reduce the simulation domain to a single unit cell and, later, reconstruct the whole domain by applying symmetry operations.

It is relatively easy to find all the details about three dimensional lattices in well known textbooks [1]. Surprisingly, it is not so easy to do so for two-dimensional lattices. For this reason, we have decided to summarize in this section the main geometrical properties of the crystal lattices studied in this work.

The square lattice is defined by the lattice vectors that define the unit cell (see figure 1.4a)

$$\vec{a}_1 = a\,\hat{i}, \tag{1.3}$$

$$\vec{a}_2 = a\,\hat{j}. \tag{1.4}$$

[2] $\Delta\varepsilon = |\varepsilon_2 - \varepsilon 1|$

Another, often more useful, choice for the unit cell is the Wigner-Seitz unit cell, that is, the unit cell that possesses the symmetry of the underlying lattice. Alternatively, this cell can be defined as the set of points closer to a given lattice point than to any other point. This is actually the unit cell that is used in this work for the band structure calculations. For the square lattice, this unit cell is a square centered at an arbitrary lattice point and side a.

The corresponding reciprocal lattice (wave-vector space) is spanned by the basis vectors

$$\vec{b}_1 = \frac{2\pi}{a}\hat{i}, \tag{1.5}$$

$$\vec{b}_2 = \frac{2\pi}{a}\hat{j} \tag{1.6}$$

and they fullfill the orthogonality conditions

$$\vec{a}_i \cdot \vec{b}_i = 2\pi, \qquad \vec{a}_i \cdot \vec{b}_j = 0, \tag{1.7}$$

Another possible choice for the reciprocal space unit cell is the 1st Brillouin Zone (1BZ), which is the Wigner-Seitz unit cell in reciprocal space. This cell is illustrated in figure 1.4 as the region delimited by a red square of side $\frac{\pi}{a}$. There some especial symmetry points in the reciprocal lattice commonly used in band structure calculations whose positions –up to a symmetry operation– and names are given by

$$\Gamma \equiv \vec{0}, \tag{1.8}$$

$$X \equiv \frac{\vec{b}_1}{2}, \tag{1.9}$$

$$M \equiv \frac{\vec{b}_1}{2} + \frac{\vec{b}_2}{2}. \tag{1.10}$$

The portion of reciprocal space delimited by these three points is an instance of what is called the *irreducible part* of the 1BZ. Any quantity that depends on the wave vector can be calculated for wave vectors in the irreducible part of the 1BZ and later extended over the rest of the reciprocal space by using symmetry operations. In fact, for band structure calculations, that is, calculation of the wave energy as a function of the wave momentum, it is customary to calculate the energy dispersion relations along the perimeter of the irreducible part of the 1BZ.

The triangular lattice is defined by the lattice vectors (see figure 1.4)

$$\vec{a}_1 = \frac{\sqrt{3}}{2} a\hat{i} - \frac{a}{2}\hat{j}, \tag{1.11}$$

$$\vec{a}_2 = \frac{\sqrt{3}}{2} a\hat{i} + \frac{a}{2}\hat{j}. \tag{1.12}$$

The corresponding reciprocal lattice is spanned by the basis vectors

$$\vec{b}_1 = \frac{2\pi}{a}\left(\frac{1}{\sqrt{3}}\hat{i} - \hat{j}\right), \tag{1.13}$$

$$\vec{b}_2 = \frac{2\pi}{a}\left(\frac{1}{\sqrt{3}}\hat{i} + \hat{j}\right). \tag{1.14}$$

and, again, they fulfill the orthogonality conditions (1.7). The 1BZ for this lattice is an hexagon of apothem $\frac{\pi}{a}$, as can be seen in figure 1.4 together with its irreducible part and some special points that will be used for the photonic band calculations below. The names and positions of these points are

$$\Gamma \equiv \vec{0}, \tag{1.15}$$

$$M \equiv \frac{\vec{b}_2}{2}, \tag{1.16}$$

$$K \equiv -\frac{\vec{b}_1}{3} + \frac{\vec{b}_2}{3}. \tag{1.17}$$

In order to ensure the periodicity of the underlying lattice in the band structure calculations so that one can reduce the simulation domain to a single unit cell, it is necessary to enforce Bloch's theorem at the boundaries of the simulation domain. For a given wavelength, these boundary conditions depend on the propagation direction of the electromagnetic wave, that is, the direction of the wavevector in reciprocal space. A summary of these boundary conditions for the Wigner-Seitz unit cells of the square and triangular lattices along the boundary of the irreducible part of the 1BZ are depicted in figures 1.5 and 1.6, respectively.

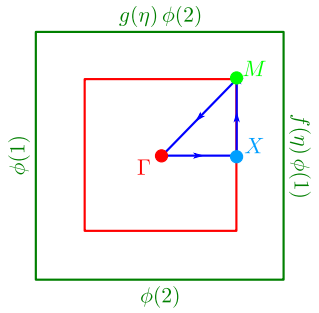

$\vec{k}$	$f(\eta)$	$g(\eta)$
$\overline{\Gamma X}$	$e^{i\pi\eta}$	1
$\overline{XM}$	-1	$e^{i\pi\eta}$
$\overline{M\Gamma}$	$e^{i\pi(1-\eta)}$	$e^{i\pi(1-\eta)}$

Figure 1.5 Bloch's theorem applied to the Wigner-Seitz unit cell of the square lattice. In green: the Wigner-Seitz unit cell. In red: the first Brillouin zone (Wigner-Seitz unit cell of the reciprocal space). In blue: boundary of the irreducible part of the 1BZ. $\phi(i)$ stands for the value that takes the quantity $\phi(\vec{r})$ (E_z or H_z) on the i-th boundary of the unit cell.

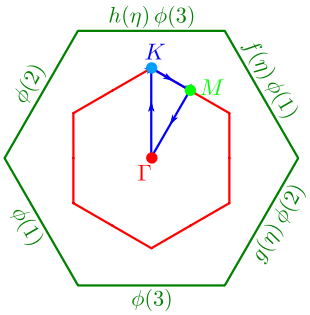

$\vec{k}$	$f(\eta)$	$g(\eta)$	$h(\eta)$
$\overline{\Gamma M}$	$e^{i\pi\eta}$	1	$e^{i\pi\eta}$
$\overline{MK}$	$-e^{-i\frac{\pi}{3}\eta}$	$e^{-i\frac{2\pi}{3}\eta}$	$-e^{i\frac{\pi}{3}\eta}$
$\overline{K\Gamma}$	$e^{i\frac{2\pi}{3}(1-\eta)}$	$e^{-i\frac{2\pi}{3}(1-\eta)}$	$e^{i\frac{4\pi}{3}(1-\eta)}$

Figure 1.6 Bloch's theorem applied to the Wigner-Seitz unit cell of the triangular lattice. In green: the Wigner-Seitz unit cell. In red: the first Brillouin zone (Wigner-Seitz unit cell of the reciprocal space). In blue: boundary of the irreducible part of the 1BZ. $\phi(i)$ stands for the value that takes the quantity $\phi(\vec{r})$ (E_z or H_z) on the i-th boundary of the unit cell.

Chapter 2

Numerical methods in nanophotonics

This chapter is intended to grasp the theoretical background regarding the set of computational methods that are used throughout this thesis to obtain novel photonic crystal structures. Calculating the unique physical properties resulting from the interaction between light and a complex media is often a tedious task unless one resorts to a rigorous analitical simulation tool to carry out numerical simulations. Among the vast set of tools that have been developed to deal with these complex media so far, we found that there are at least three computational tools that yield excellent and reliable predictions of the propagation of light in PCs, namely the finite element method (FEM), the plane wave expansion method (PWEM), and the finite difference time domain (FDTD) method.

2.1 Introduction

From a theoretical perspective, one of the most important venues of research in silicon photonics is to develop numerical methods to solve Maxwell's equations of an EM wave propagating in a heterogeneous media that are reliable, fast, and capable of dealing with large systems as close as possible to the real ones employed for experiments. The reason why numerical methods are so important in this field is rooted on the fact that the predictions of Maxwell's equations for these systems are in excellent qualitative and quantitative agreement with experiments and they are able to describe the ample phenomenology exhibited by these systems. Unfortunately, the wave equations that describes the propagation of the EM field in these structures is not as simple as for homogenenous media due to the spatial dependence of the dielectric constant, which renders these equations very difficult to solve analytically except in the simplest cases (such as one dimensional PCs) and makes it necessary to resort to numerical techniques in the general case. Therefore, developing such methods is important mainly for two reasons: firstly, because usually is the only way to obtain quantitative results

and, more importantly, because obtaining reliable numerical predictions for the properties of a given PC is cheaper and faster than performing the experiments to measure the corresponding quantities.

The development of numerical methods for photonic crystals has undergone an evolution that mimics to a certain extent the one underwent by the techniques used to calculate the electronic band structure of semiconductors: initially, the main interest were ideal infinite periodic photonic crystals, for which techniques on the frequency space are ideally suited (such as the plane wave method (PW) [4, 63, 85] or algorithms based on the tight binding method). Very soon, however, it was realized that the real interest of these systems is disordered photonic crystals. Frequency methods can be used to address the calculation of certain quantities (such as the photonic band structure or density of states) for some types of disorder, mainly point or line defects, by performing supercell calculations [65] but they are not very useful for studying disorder that is not localized (such as random displacements of the dielectric constituents of the photonic crystal or compositional disorder), which are of great practical interest, as these types of disorder are usually associated to the fabrication techniques themselves. Furthermore, frequency methods, in principle, are only applicable to infinite systems whereas real systems are always finite. For these reasons, people have started to pay attention during the last years to real space methods. These methods differ from the previous ones in that they work with a finite cluster which does not need to be periodic. Among them, they can be cited certain algorithms based on a multipolar expansion of Maxwell's equations in a basis with a particular symmetry [66, 67] (such as spherical or cylindrical harmonics) or the finite difference time domain method [68]. The former is limited by the choice of the symmetric basis to deal with systems that are made of dielectric constituents that possess that same symmetry. The later seems more and more promising, being its main inconvenient the fact that is rather time consuming, because it is necessary to let the system evolve for a long time before the stationary state is reached. In any case, the use of these methods has been traditionally precluded mainly because they are very demanding computationally, especially with regards to memory usage. However, with the advent of more and more powerful computers and the spectacular decrease in the price of RAM memory, this problem has been partially alleviated and, as a consequence, real space methods have started to look very promising for practical applications. Interestingly, a method that has received very little attention in this field even though is has been known and extensively used in other areas of Physics and Engineering is the finite element (FE) method [69–72, 74]. Indeed, there are a number of reasons that seem to suggest that it could be applied well to the study of the propagation of EM waves in inhomogeneous media. In particular, this method allows one to study geometries of arbitrary complexity, it can deal with

frequency dependent dielectric functions (metallic inhomogeneous structures) in a natural way, discontinuities in the dielectric function are not especially detrimental for convergence of the method, and the quantities are already calculated in the stationary regime. The only shortcoming of the method is its extensive computer memory usage. However, the demand of this resource is quite insensitive to the presence of defects, which could render this technique very advantageous for studying disordered lattices [72]. Therefore, at the present status of the photonic band gap materials field, it is important to assess whether this method could be useful to investigate the properties of photonic crystals from both the fundamental and applied points of view.

2.2 The mathematics behind the propagation of EM waves in inhomogeneous media

The propagation of an electromagnetic wave through an inhomogeneous medium is described by Maxwell's equations. In the absence of electric current and free charges, Maxwell's equations for nonmagnetic and isotropic media can be written as:

$$\nabla \cdot \vec{B} = 0 \tag{2.1}$$

$$\nabla \times \vec{E} = -\frac{d\vec{B}}{dt} \tag{2.2}$$

$$\nabla \cdot \vec{D} = \rho \tag{2.3}$$

$$\nabla \times \vec{D} = \vec{J} + \frac{d\vec{D}}{dt}, \tag{2.4}$$

where $\vec{E}$ is the electric field and $\vec{B}$ is the magnetic flux density. μ is the permeability of vacuum $\varepsilon_0/\mu_0 = 1/c^2$, with ε_0 the dielectric constant of vacuum. $\vec{D}$ is the displacement field, which is related to $\vec{E}$ throug ε. In particular, for two-dimensional media, any electric or magnetic field can always be expressed as a linear combination of a transversal electric (TE) and a transversal magnetic field (TM). In the first case, the electric field is perpendicular to the photonic crystal plane –whereas the magnetic field is constrained into this plane– and the sourceless Maxwell's equations are reduced to a Hemholtz equation for the electric field given by

$$\nabla^2 E_z(\vec{r}) + k_0^2 \epsilon_r(\vec{r}) E_z(\vec{r}) = 0, \tag{2.5}$$

where $E_z(\vec{r})$ is the z-th component of the electric field at position $\vec{r}$, $\epsilon_r(\vec{r})$ is the inhomogeneous relative dielectric constant of the photonic crystal, and $k_0 = \omega/c$ with ω the angular frequency of the incident electric field and c the speed of light in free space. In writing down equation (2.5), it has been assumed that the photonic crystal is non-magnetic ($\mu_r = 1$) and non-conducting ($\sigma = 0$). Once equation (2.5) is solved, the time-harmonic electric and magnetic fields are easily calculated as

$$\vec{E}(\vec{r},t) = E_z(\vec{r})\, e^{-i\omega t}\, \hat{z} \tag{2.6}$$

$$\vec{H}(\vec{r},t) = \frac{i}{k_0}\nabla \times \epsilon_r(\vec{r})\vec{E}(\vec{r},t). \tag{2.7}$$

On the other hand, in the case of TM polarization, the magnetic field is perpendicular to the photonic crystal plane –whereas the electric field is constrained into this plane– and the sourceless Maxwell's equations reduce to a Hemholz equation for the magnetic field given by

$$\nabla\left(\frac{\nabla H_z(\vec{r})}{\epsilon_r(\vec{r})}\right) - k_0^2 H_z(\vec{r}) = 0, \tag{2.8}$$

where $H_z(\vec{r})$ is the z-th component of the magnetic field at position $\vec{r}$. The time-harmonic electric and magnetic fields are easily calculated once equation (2.8) is solved and they are given by

$$\vec{H}(\vec{r},t) = H_z(\vec{r})\, e^{-i\omega t}\, \hat{z} \tag{2.9}$$

$$\vec{E}(\vec{r},t) = -\frac{i}{k_0\epsilon(\vec{r})}\nabla \times \vec{H}(\vec{r},t). \tag{2.10}$$

An important aspect of any electromagnetic simulation is the use of appropriate boundary conditions at the interfaces. These bondary conditions will adequate the simulation of EM fields according to the nature of each physical problem, e.g., in order to calculate photonic band structures, it is necessary to implement boundary conditions that mimic an infinite simulation domain together with the periodicity of the photonic crystal lattice, whereas these conditions are not valid for the simulation of finite size objects. An infinite medium is simulated by using perfect magnetic (PMC) or perfect electric conductor (PEC) boundary conditions that mirror the simulation domain. The former condition is used for TE polarization of the EM field and ensures that the component of the magnetic field tangent to the boundary is identically zero at the outer interface, that is,

$$\hat{n} \times \vec{H} = \vec{0}, \tag{2.11}$$

where $\hat{n}$ is a unit vector perpendicular to the outer simulation domain surface at each point. The later is used for TM polarization of the EM field and ensures that the component of the electric field tangent to the boundary is identically zero at the outer interface, that is,

$$\hat{n} \times \vec{E} = \vec{0}. \tag{2.12}$$

The periodicity of the photonic crystal lattice is ensured by an adequate use of Bloch's theorem at the boundaries of the photonic crystal unit cell. This theorem states that when the electric (magnetic) field propagates from one point in the PhC to another one separated from the previous one by a lattice vector, $\vec{R}$, the only effect on the EM field is a change of its phase,

$$E_z(\vec{r} + \vec{R}) = e^{i\vec{k}\cdot\vec{R}} E_z(\vec{r}) \tag{2.13}$$

and

$$H_z(\vec{r} + \vec{R}) = e^{i\vec{k}\cdot\vec{R}} H_z(\vec{r}) \tag{2.14}$$

for TE and TM polarization, respectively. In these expressions, $\vec{R}$ is a vector of the photonic crystal lattice and $\vec{k}$ is the wavevector of the electromagnetic wave (see section 3).

On the other hand, for the transmittance calculations reported in the following chapters, finite clusters in the direction parallel to the incident wave vector were used, whereas the clusters are of infinite extension in the perpendicular direction. In order to mimic such a material, PMC and PEC boundary conditions were used for the outer interfaces that limit the simulation domain in the direction perpendicular to the incident wave vector for TE and TM polarization, respectively. For the interfaces at which the EM wave enters and exits the cluster, the situation is a little more involved because it is necessary to avoid unphysical reflections due to the finite size of the cluster and, thus, perfectly matched layers were used at these interfaces. The equations that describe such boundaries are given by

$$\hat{z} \cdot \hat{n} \times (\nabla \times E_z \hat{z}) - i\beta E_z = -2i\beta E_{0z} \tag{2.15}$$

$$\hat{z} \cdot \hat{n} \times (\nabla \times H_z \hat{z}) - i\beta H_z = -2i\beta H_{0z}, \tag{2.16}$$

where E_{0z} and H_{0z} are the initial values of the electric and magnetic fields at the boundaries, respectively, and $\beta = k_0$ is the propagation constant. The upper condition applies to TE polarization, whereas the lower one corresponds to TM polarization. If the electric field is an eigenmode of the boundary, the boundary is exactly non-reflecting.

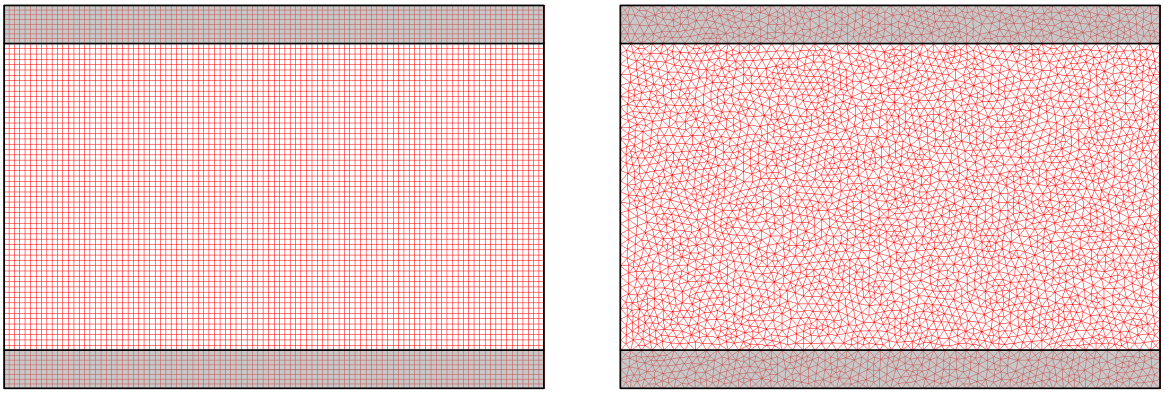

Figure 2.1 On the left: an example of a 2D structured mesh with 7400 quadrilateral mesh elements. On the right: the same simulation domain partitioned with an unstructured mesh consisting of 7722 triangular mesh elements. This geometry could be used, for example, to simulate propagation of an EM wave in a planar or axysimmetric waveguide. The dark regions represent high refraction index regions ($n = 3$), whereas the white region represents air.

2.3 The finite element method

As commented in the Introduction, the finite element method (FEM) is a general purpose numerical method for solving partial differential equations that it is especially well suited for dealing with electromagnetic problem in geometries of arbitrary complexity.

At the core of any FE simulation is the algorithm for generating a mesh, that is, a partition of the geometry into small units of known shape called *mesh elements*. In 1D, a mesh is a partition of the simulation domain into smaller intervals. The endpoint of the resulting mesh elements are called *mesh vertices* or *mesh nodes*. In 2D, the domain can be partitioned into triangular or quadrilateral mesh elements, to quote some examples. In the first case the mesh is referred to as *unstructured*, whereas in the second case the mesh is called *structured* because the resulting pattern possesses a structure. The sides of the triangles and quadrilaterals are called *mesh edges* and their corners are *mesh vertices*. The boundaries of the simulation domain are partitioned (approximately) into mesh edges, the so-called *boundary elements*, which must conform with the triangles if there is an adjacent subdomain. Similarly, in 3D, the simulation domain can be partitioned into tetrahedral, hexahedral, or prism mesh elements whose faces, edges, and corners are called *mesh faces*, *mesh edges*, and *mesh vertices*, respectively. Examples of two dimensional meshes can be seen in figure 2.1.

Once a mesh is defined, an approximation for the dependent variables of the problem is introduced. The central idea is to approximate the dependent variables with interpolation functions that can be described with a finite number of parameters, the so-called *degrees of*

freedom. Inserting this approximation into the governing partal differential equation (PDE), generates a set of algebraic equations for the degrees of freedom that is then solved with an appropriate *solver*.

To illustrate this, we will concentrate on the FEM solution of the one dimensional differential equation

$$-\frac{d}{dx}\left(\alpha(x)\frac{d\phi}{dx}\right)+\beta(x)\phi(x)=0, \tag{2.17}$$

where $\phi(x)$ is the function we want to determine and $\alpha(x)$ and $\beta(x)$ are known functions that describe the physical properties of the solution domain. Let us further assume that $\phi(x)$ at the boundaries is fixed by the inhomogenenous boundary conditions of the third kind [73]

$$\alpha(0)\left.\frac{d\phi}{dx}\right|_{x=0}+\gamma(0)\phi(0)=q(0) \tag{2.18}$$

$$\alpha(L)\left.\frac{d\phi}{dx}\right|_{x=L}+\gamma(L)\phi(L)=q(L), \tag{2.19}$$

where $q(0)$ and $q(L)$ are known parameters. The standard one-dimensional sourceless Hemholtz equation

$$\frac{d^2\phi}{dx^2}+k_0^2\epsilon_r(x)\phi(x)=0 \tag{2.20}$$

with transparent influx boundary conditions (a special case of the perfectly matched layers described in the previous section that ensures transparency for the incoming wave at $x=0$ and for the outgoing wave at $x=L$)

$$-\left.\frac{d\phi}{dx}\right|_{x=0}+ik_0\phi(0)=2ik_0 \tag{2.21}$$

$$\left.\frac{d\phi}{dx}\right|_{x=L}+ik_0\phi(L)=0 \tag{2.22}$$

is a special case of (2.17) when $\alpha(x)=-1$, $\beta(x)=k_0^2\epsilon_r(x)$, $\gamma(0)=-\gamma(L)=ik_0$, $q(0)=2ik_0$, and $q(L)=0$.

Equation (2.17) together with the boundary conditions (2.18) and (2.19) are equivalent to solving the variational problem [69]

$$\delta F(\phi)=0, \tag{2.23}$$

where

$$F(\phi)=\frac{1}{2}\int_0^L\left[\alpha(x)\frac{d^2\phi}{dx^2}+\beta(x)\phi(x)^2\right]dx+\Gamma(L)-\Gamma(0) \tag{2.24}$$

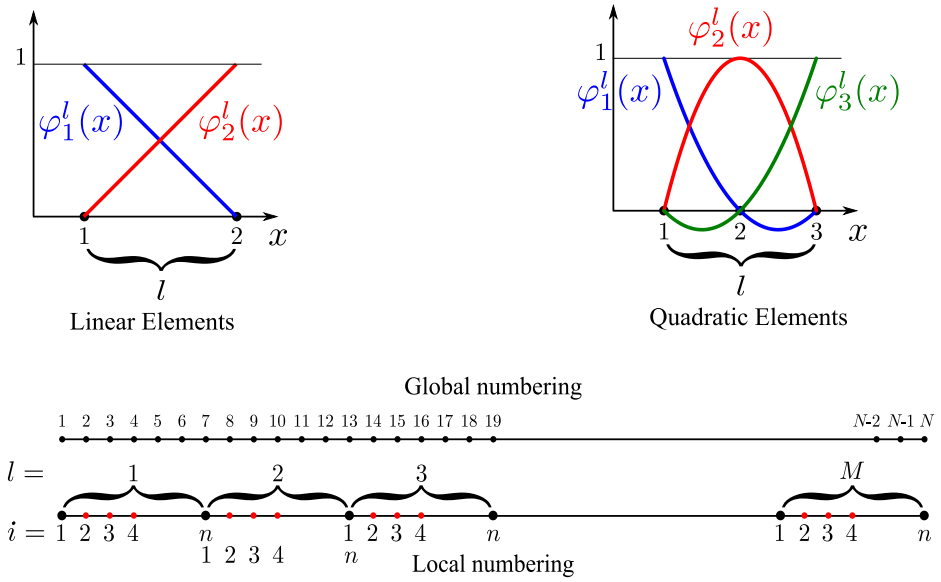

Figure 2.2 On the bottom: Simulation domain divided into M mesh elements with n nodes each in both the local and global numbering schemes. Upper left: Linear elements basis functions for the l-th mesh element. Upper right: Quadratic elements basis functions for the l-th mesh element.

with

$$\Gamma(x) = \frac{\gamma(x)}{2}\phi(x)^2 - q(x)\phi(x). \tag{2.25}$$

To see this, let us construct the first variation of $F(\phi)$ with respect to the physical $\phi(x)$

$$\begin{aligned}\delta F(\phi) &= F(\phi(x)+\delta\phi(x)) - F(\phi) = \\ &= \int_0^L \left[\alpha(x)\frac{d\phi}{dx}\frac{d\delta\phi}{dx} + \beta(x)\phi(x)\delta\phi(x)\right]dx + \left[(\gamma(x)\phi(x) - q(x))\,\delta\phi(x)\right]_{x=0}^{x=L}.\end{aligned} \tag{2.26}$$

Assuming that $\alpha(x)$ is continuous in the entire domain and integrating by parts the first term on the right hand side, (2.26) can be written as

$$\begin{aligned}\delta F(\phi) = -\int_0^L \left[\frac{d}{dx}\left(\alpha(x)\frac{d\phi}{dx}\right) + \beta(x)\phi(x)\right]\delta\phi(x)dx \\ + \left[\left(\alpha(x)\frac{d\phi}{dx} + \gamma(x)\phi(x) - q(x)\right)\delta\phi(x)\right]_{x=0}^{x=L} = 0.\end{aligned} \tag{2.27}$$

Because $\delta\phi(x)$ is an arbitrary variation, both the integrand and boundary terms must vanish and one immediately recovers equation (2.17) and the inhomogeneous boundary conditions (2.18) and (2.19).

In the spirit of the finite element method, in order to solve equation (2.23) the solution domain is divided into M mesh elements of equal length[1], Δx, each containing n mesh nodes located at x_i^l (see figure 2.2). On each element, $\phi(x)$ is approximated by the interpolation function

$$\tilde{\phi}^l(x) = \sum_{i=1}^{n} e_i^l \varphi_i^l(x), \tag{2.28}$$

where e_i^l are the degrees of freedom defined above and the basis functions $\varphi_i^l(x)$ are subject to the conditions

$$\varphi_i^l(x_j^l) = \delta_{ij} \qquad (i, j = 1, 2, \ldots, N) \tag{2.29}$$

with δ_{ij} the Kronecker delta. The set of functions $\phi(x)$ spanned by the basis functions is a linear function space called the *finite element space*. In these expressions, $l = 1, 2 \ldots, M$ stands for the mesh element number and $i = 1, 2, \ldots, n$ stands for the node number inside a given element. This is known as the local numbering scheme. In one-dimensional problems, using the local numbering scheme is not strictly necessary and one only needs one index to label both elements and nodes. This is known as the global numbering scheme, where the nodes are globally numbered from 1 to N, being N the total number of nodes. Using the local numbering scheme, however, makes it easier to formulate the extension of the method to 2 and 3 dimensions and we will stick to it in the following.

Substituting (2.28) into the functional $F(\phi)$ gives us the approximated functional

$$\tilde{F}(\tilde{\phi}) = \frac{1}{2} \sum_{l=1}^{M} \sum_{i,j=1}^{n} e_i^l K_{ij}^l e_j^l + \tilde{\Gamma}(L) - \tilde{\Gamma}(0), \tag{2.30}$$

where

$$K_{ij}^{(l)} = \int_{x_1^l}^{x_n^l} \left[\alpha(x) \frac{d\varphi_i^l}{dx} \frac{d\varphi_j^l}{dx} + \beta(x) \varphi_i^l(x) \varphi_j^l(x) \right] dx \tag{2.31}$$

and

$$\tilde{\Gamma}(L) = \frac{\gamma(L)}{2} (e_n^M)^2 - q(L)\, e_n^M \tag{2.32}$$

$$\tilde{\Gamma}(0) = \frac{\gamma(0)}{2} (e_1^1)^2 - q(0)\, e_1^1. \tag{2.33}$$

[1] This requirement can be easily relaxed but it keeps the formulation of the method very simple, so we will use it throughout this thesis.

The set of equations that allows one to calculate the physical degrees of freedom is obtained by imposing the stationarity conditions

$$\frac{\partial F}{\partial e_i^l}(e_1^1,\ldots,e_i^l,\ldots,e_n^M)=0 \qquad (l=1,2,\ldots,M; i=1,2,\ldots,n). \tag{2.34}$$

In order to obtain the correct set of equations, one needs to take into account the ligatures

$$e_n^{l-1} \equiv e_1^l \qquad (l=2,3,\ldots,M), \tag{2.35}$$

so that all but the first and last degrees of freedom are duplicated in (2.34). This results into the set of linear equations

$$\sum_{j=1}^{N}\left(K_{ij}+\gamma_{ij}\right)e_j = q_i \qquad (i=1,2,\ldots,N), \tag{2.36}$$

or, in matrix form

$$[\mathbb{K}+\mathbb{G}]\,\vec{e}=\vec{q}, \tag{2.37}$$

where

$$\mathbb{K}=\begin{bmatrix}
K_{11}^{(1)} & \ldots & K_{1n}^{(1)} & \ldots & 0 & \ldots & 0 & \ldots & 0 & \ldots & 0 \\
\vdots & \ddots & \vdots & \ddots & \vdots & & \vdots & & \vdots & & \vdots \\
K_{n1}^{(1)} & \ldots & K_{nn}^{(1)}+K_{11}^{(2)} & \ldots & K_{1n}^{(2)} & \ldots & 0 & \ldots & 0 & \ldots & 0 \\
\vdots & \ddots & \vdots & \ddots & \vdots & \ddots & \vdots & & \vdots & & \vdots \\
0 & \ldots & K_{n1}^{(2)} & \ldots & K_{nn}^{(2)}+K_{11}^{(3)} & \ldots & K_{1n}^{(3)} & \ldots & 0 & \ldots & 0 \\
\vdots & & \vdots & \ddots & & \ddots & & \ddots & & & \vdots \\
\vdots & & \vdots & & \ddots & & \ddots & & \ddots & & \vdots \\
\vdots & & \vdots & & & \ddots & & \ddots & & \ddots & \vdots \\
0 & \ldots & 0 & \ldots & 0 & \ldots & K_{11}^{(M-1)} & \ldots & K_{1n}^{(M-1)}+K_{11}^{(M)} & \ldots & K_{1n}^{(M)} \\
\vdots & & \vdots & & \vdots & & \vdots & \ddots & \vdots & \ddots & \vdots \\
0 & \ldots & 0 & \ldots & 0 & \ldots & 0 & \ldots & K_{n1}^{(M)} & \ldots & K_{nn}^{(M)}
\end{bmatrix}, \tag{2.38}$$

$$\mathbb{G}=\begin{bmatrix}
-\gamma(0) & 0 & \ldots & 0 & 0 \\
0 & 0 & \ldots & 0 & 0 \\
\vdots & \vdots & \ddots & \vdots & \vdots \\
0 & 0 & \ldots & 0 & 0 \\
0 & 0 & \ldots & 0 & \gamma(L)
\end{bmatrix}, \tag{2.39}$$

$\vec{q} = \left(-q(0), 0, \ldots, 0, q(L)\right)^T$, and $\vec{e} = \left(e_1^{(1)}, \ldots, e_{n-1}^{(1)}, e_1^{(2)}, \ldots, e_{n-1}^{(2)}, e_1^{(3)}, \ldots, e_n^{(M)}\right)^T$, that can be solved with an appropriate solver. It is important to notice that the $\mathbb{K}$ matrix is a sparse matrix. Its size is determined by the number of mesh elements, whereas its bandwidth is determined by the number of nodes inside a given mesh element.

The method presented here for formulating the FEM equations is usually known as the Ritz finite element methods. There are other methods that lead to slightly different FEM equations that will not be described here (notably the Galerkin method). We refer the interested reader to ref. [69] for more details.

One of the most important aspects of the finite element method is the choice of the basis functions in (2.28). These basis functions are often selected as a compromise between trying to keep them as simple as possible and obtaining a good approximation to the solution function. A standard choice is to use polynomials of a given degree (p) because they allow for an efficient computational implementation of the method. For a given polynomial degree, the number of nodes one needs on each mesh elements is $p+1$. Let us analyze in detail two typical choices of these polynomials: linear and quadratic elements, applied to our particular example (2.17).

2.3.1 Linear elements ($p = 1$)

A common choice of basis functions in electromagnetics, especially in three dimensions, is the use of linear elements because they allow for an extremely efficient implementation of the method. In this case, the number of nodes in each element is 2 and the basis functions are given by (see figure 2.2)

$$\varphi_1^l(x) = \frac{x_2^l - x}{\Delta x}, \tag{2.40}$$

$$\varphi_2^l(x) = \frac{x - x_1^l}{\Delta x} \tag{2.41}$$

and the trial function can be written as

$$\tilde{\phi}^l(x) = e_1^l \, \varphi_1^l(x) + e_2^l \, \varphi_2^l(x). \tag{2.42}$$

In order to evaluate the $K_{ij}^{(l)}$ integrals, one needs to know the exact value of the functions $\alpha(x)$ and $\beta(x)$. However, this can be avoided in some cases by using a piecewise approximation for these functions –as shown in figure 2.3– consisting of approximating the value of these functions in the interval $[x_1^l, x_n^l]$ by the constant values $\tilde{\alpha}_l = \alpha(x_1^l)$, $\tilde{\beta}_l = \beta(x_1^l)$, respectively. As an aside, it is important to notice that this approximation is an excellent one for the type

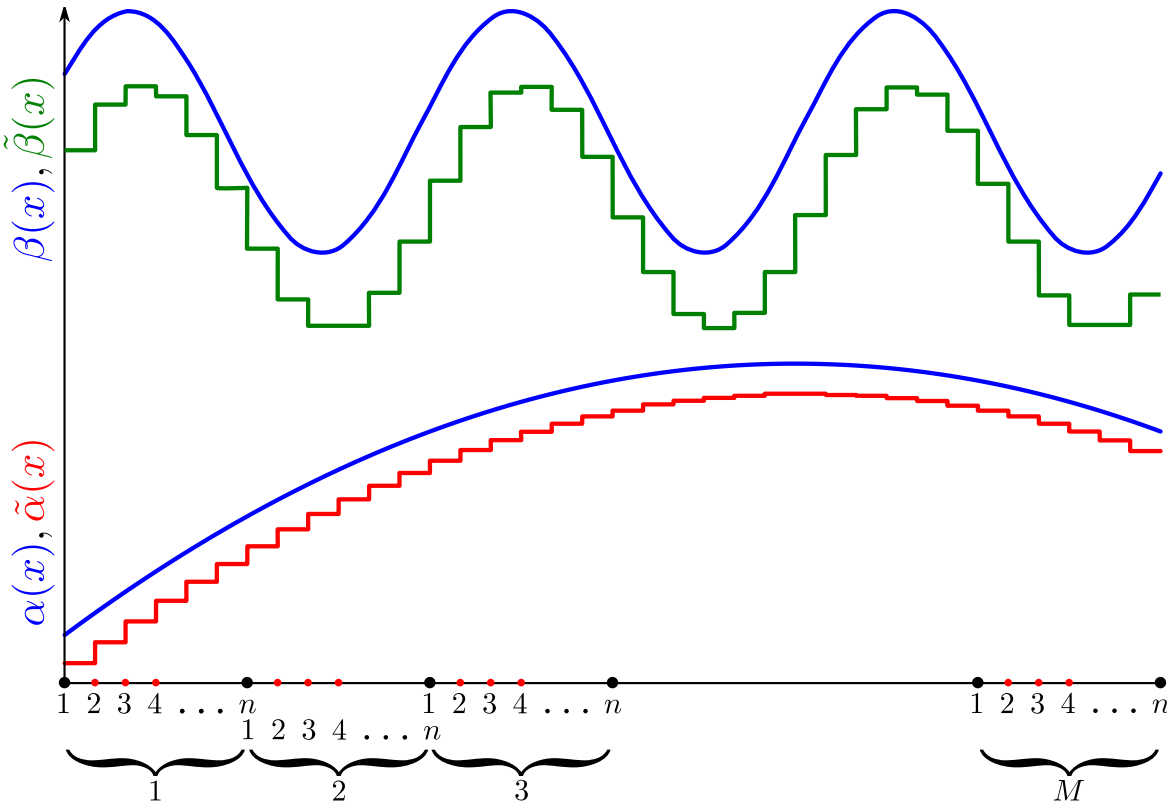

Figure 2.3 Piecewise approximation of the $\alpha(x)$ and $\beta(x)$ functions. The approximated functions have been shifted in the vertical direction for clarity.

of problem analyzed below where $\beta(x)$ is proportional to the index of refraction of a photonic crystal (a piecewise function by definition) if one chooses the mesh partition of the domain in such a way that the discontinuities of this quantity coincides with node points. Under this condition, the integrals $K_{ij}^{(l)}$ can be evaluated analytically. For linear elements, the result is

$$K_{11}^{(l)} = K_{22}^{(l)} = \frac{\tilde{\alpha}_l}{\Delta x} + \tilde{\beta}_l \frac{\Delta x}{3}, \tag{2.43}$$

$$K_{12}^{(l)} = K_{21}^{(l)} = -\frac{\tilde{\alpha}_l}{\Delta x} + \tilde{\beta}_l \frac{\Delta x}{6}. \tag{2.44}$$

To quote a practical example, the solution of the 1D sourceless Hemholtz equation employing linear elements is given by the FEM solution of the linear set of equations (2.37) with

$$\mathbb{K} = \frac{-1}{\Delta x}\begin{bmatrix} 1 & -1 & 0 & 0 & \ldots\ldots\ldots & 0 \\ -1 & 2 & -1 & 0 & \ldots\ldots\ldots & 0 \\ 0 & -1 & 2 & -1 & \ldots\ldots\ldots & 0 \\ \vdots & & \ddots & \ddots & \ddots & \vdots \\ 0 & \ldots\ldots\ldots & -1 & 2 & -1 & 0 \\ 0 & \ldots\ldots\ldots & 0 & -1 & 2 & -1 \\ 0 & \ldots\ldots\ldots & 0 & 0 & -1 & 1 \end{bmatrix}$$

$$+ \frac{k_0^2 \Delta x}{6}\begin{bmatrix} 2c_1 & c_1 & 0 & 0 & \ldots\ldots\ldots & 0 \\ c_1 & 2(c_1+c_2) & c_2 & 0 & \ldots\ldots\ldots & 0 \\ 0 & c_2 & 2(c_2+c_3) & c_3 & \ldots\ldots\ldots & 0 \\ \vdots & & \ddots & \ddots & \ddots & \vdots \\ 0 & \ldots\ldots\ldots & c_{M-2} & 2(c_{M-2}+c_{M-1}) & c_{M-1} & 0 \\ 0 & \ldots\ldots\ldots & 0 & c_{M-1} & 2(c_{M-1}+c_M) & c_M \\ 0 & \ldots\ldots\ldots & 0 & 0 & c_M & 2c_M \end{bmatrix}, \tag{2.45}$$

$$\mathbb{G} = \begin{bmatrix} -ik_0 & 0 & \ldots & 0 & 0 \\ 0 & 0 & \ldots & 0 & 0 \\ \vdots & \vdots & \ddots & \vdots & \vdots \\ 0 & 0 & \ldots & 0 & 0 \\ 0 & 0 & \ldots & 0 & -ik_0 \end{bmatrix}, \tag{2.46}$$

$$\tag{2.47}$$

and $\vec{q} = (-2ik_0, 0, \ldots, 0)^T$ with $c_l = \tilde{n}_l^2 = n^2(x_1^l)$.

2.3.2 Quadratic elements ($p = 2$)

In order to improve the accuracy of the solution, higher-order basis functions can be used. In particular, quadratic elements is a common choice for many physical problems. The number of nodes on each mesh interval in this case is $p + 1 = 3$. The basis functions are fixed by the conditions (2.29), which yield (see figure 2.2)

$$\varphi_1^l = \frac{(x - x_2^l)(x - x_3^l)}{(x_1^l - x_2^l)(x_1^l - x_3^l)} = \frac{2(x - x_2^l)(x - x_3^l)}{\Delta x^2}, \tag{2.48}$$

$$\varphi_2^l = \frac{(x - x_1^l)(x - x_3^l)}{(x_2^l - x_1^l)(x_2^l - x_3^l)} = -\frac{4(x - x_1^l)(x - x_3^l)}{\Delta x^2}, \tag{2.49}$$

$$\varphi_3^l = \frac{(x - x_1^l)(x - x_2^l)}{(x_3^l - x_1^l)(x_3^l - x_2^l)} = \frac{2(x - x_1^l)(x - x_2^l)}{\Delta x^2} \tag{2.50}$$

$$\tag{2.51}$$

and the trial functions can be written as

$$\tilde{\phi}^l(x) = e_1^l \varphi_1^l(x) + e_2^l \varphi_2^l(x) + e_3^l \varphi_3^l(x). \tag{2.52}$$

Assuming, again, that $\alpha(x)$ and $\beta(x)$ can be approximated by a piecewise function, the elements of the $\mathbb{K}$ matrix can be easily calculated to be

$$K_{11}^{(l)} = \frac{7\tilde{\alpha}_l}{3\Delta x} + \frac{2}{15}\tilde{\beta}_l \Delta x, \qquad K_{12}^{(l)} = -\frac{8\tilde{\alpha}_l}{3\Delta x} + \frac{1}{15}\tilde{\beta}_l \Delta x, \qquad K_{13}^{(l)} = -\frac{\tilde{\alpha}_l}{3\Delta x} + \frac{1}{30}\tilde{\beta}_l \Delta x, \tag{2.53}$$

$$K_{21}^{(l)} = K_{12}^{(l)}, \qquad K_{22}^{(l)} = \frac{16\tilde{\alpha}_l}{3\Delta x} + \frac{8}{15}\tilde{\beta}_l \Delta x, \qquad K_{23}^{(l)} = -\frac{8\tilde{\alpha}_l}{3\Delta x} + \frac{1}{15}\tilde{\beta}_l \Delta x, \tag{2.54}$$

$$K_{31}^{(l)} = K_{13}^{(l)}, \qquad K_{32}^{(l)} = K_{23}^{(l)}, \qquad K_{33}^{(l)} = \frac{7\tilde{\alpha}_l}{3\Delta x} + \frac{2}{15}\tilde{\beta}_l \Delta x. \tag{2.55}$$

In those cases where $\alpha(x)$ and $\beta(x)$ are not adequately approximated by constant values inside a mesh element, one has to resort to evaluate the integrals numerically. A commonly used method to perform these integrals is Gauss–Legendre quadrature because this method is exact for polynomial integrands [69].

2.3.3 Local coordinates and Lagrange elements

The description of the basis functions is usually simplified by using the *local coordinates*. These coordinates are defined in terms of the standard d-dimensional simplex

$$\xi_1 \geq 0, \xi_2 \geq 0, \ldots, \xi_d \geq 0, \xi_1 + \xi_2 + \ldots + \xi_d \leq 1, \tag{2.56}$$

that resides in the local coordinate space parametrized by the local coordinates $\xi_1, \ldots, \xi_d$. The $d = 1$ simplex is the unit interval. The $d = 2$ simplex is the triangle with two 45° angles, and the $d = 3$ simplex is a tetrahedron. The mesh elements can be considered as linear transformations of the standard simplexes. Namely, by letting the global space coordinates x_i be suitable linear functions of the local coordinates, one gets the mesh elements as the image of the standard simplexes.

When described in terms of the local coordinates, the basis functions assume one of a few basic shapes. These are the *shape functions*. These are especially simple to obtain in one dimension. The local coordinates in this case are defined by the linear transformation

$$\xi = \frac{x - x_1^l}{\Delta x}, \tag{2.57}$$

on each mesh element. In terms of the local coordinates, the integration interval in the definition of the $K_{ij}^{(l)}$ elements is $[0, 1]$. Substituting (2.57) into (2.40) one gets the shape functions for the linear elements

$$\varphi_1^l(\xi) = 1 - \xi, \tag{2.58}$$

$$\varphi_2^l(\xi) = \xi. \tag{2.59}$$

For second order elements, substituting (2.57) into (2.48) one gets the corresponding shape functions

$$\varphi_1^l(\xi) = (2\xi - 1)(\xi - 1), \tag{2.60}$$

$$\varphi_2^l(\xi) = 4\xi(1 - \xi), \tag{2.61}$$

$$\varphi_3^l(\xi) = \xi(2\xi - 1). \tag{2.62}$$

The linear and quadratic basis functions used so far are special cases of *Lagrange interpolation polynomials* or, in the terminology of the finite element method, *Lagrange elements*. The Lagrange element is characterized by its *order*, a positive number p. The functions Φ in this finite element space are piecewise polynomials of degree p. To describe

such a function it is necessary to give its values at the *Lagrange points* of order p. These are the points whose local coordinates are integer multiples of $1/p$. For example, for a triangular mesh in 2D with $p = 2$, the node points are located at the corners and side midpoints of each mesh triangle (labelled by l). For each of these node points P_i^l, there exists a DOF $e_i^l = \Phi(P_i^l)$ and a basis function $\varphi_i^l(x)$. The restriction of the basis function ϕ_i^l on a given mesh element is that it is a polynomial of degree (at most) k in the local coordinates such that $\phi_i^l = 1$ at node i and $\phi_i^l = 0$ at all other nodes. Therefore, the basis function are continuous and one has

$$\Phi(x) = \sum_l \sum_i e_i^l \varphi_i^l(x). \tag{2.63}$$

The Lagrange elements of order 1 are called linear elements. The Lagrange elements of order 2 are called the quadratic Lagrange elements. Indeed, the later are the ones commonly used in electromagnetic problems in two dimensions, whereas the former ones are commonly used in electromagnetic problems in three dimensions to make the method more efficient. The Lagrange elements are available to any arbitrary order but the commonly used integration formulae usually limit its usefulness to $k \leq 5$.

2.4 The Plane Wave Expansion method (PWE)

The Plane Wave Expansion method is one of the most (if not the most) commonly used computational tool among the photonic crystal research comunity. This technique permits to calculate the dispersion diagram as well as the modal solutions of Maxwell's equations over periodic inhomogenerous geometries by performing an eigenmode decomposition of the electromagnetic propagation as a set of definite-frequency modes [85]. The basic approach for calculating the field distribution and eigenfrequencies using the PWE technique relies on expanding the dielectric function and the three components of the field vectors into Fourier series. This process is best illustrated by taking the simple example of a 1D PC, then it can be easily generalyzed to two- and three-dimensional periodic systems. Let us consider the 1D photonic crystal shown in Fig. 2.4.

This simple structure is comprised by an alternating layers of different dielectric, which we assume non-magnetic, for simplicity reasons. Equations eq. 2.1–2.4 can be further decoupled into four equations each involving only one type of field, by taking the curl on the electric and magnetic field equations and then performing a few subsittutions, to get to the following expressions:

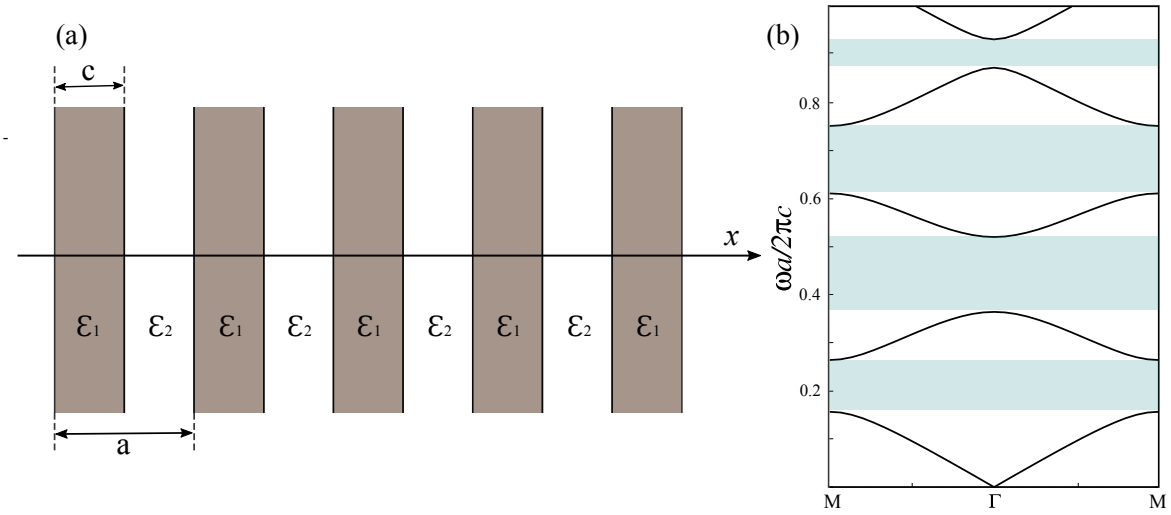

Figure 2.4 (a) One dimensional stack comprised of alternating layers of Si material ($\varepsilon = 11.56$) and air ($\varepsilon = 1$), whose unit cell is equally divided into these two materials, i.e $a = 2c$. (b) Dispersion diagram computed using the PWEM method. Both the frequency ω and the wavenumber k are shown in dimensionless units. The resulting dispersion diagram shows 4 band gaps, highlighted in blue.

$$\frac{1}{\varepsilon_r}\nabla\times\nabla\times\vec{E} = \frac{\omega^2}{c^2}\vec{E}$$
$$\nabla\times\nabla\times\frac{1}{\varepsilon_r}\vec{D} = \frac{\omega^2}{c^2}\vec{D}$$
$$\nabla\times\frac{1}{\varepsilon_r}\nabla\times\vec{H} = \frac{\omega^2}{c^2}\vec{H}$$
$$\nabla\times\frac{1}{\varepsilon_r}\nabla\times\vec{B} = \frac{\omega^2}{c^2}\vec{B},$$

in which we assumed that the fields are time harmonic. Now, if we iteratively apply the chain rule we get to the full set of three dimensional Maxwell's equations

$$\frac{1}{\varepsilon_r}\left(-\frac{\partial^2 E_x}{\partial y^2} - \frac{\partial^2 E_x}{\partial z^2} + \frac{\partial^2 E_y}{\partial x\partial y} + \frac{\partial^2 E_z}{\partial x\partial z}\right) = \frac{\omega^2}{c^2}E_x \tag{2.64}$$
$$\frac{1}{\varepsilon_r}\left(-\frac{\partial^2 E_x}{\partial y^2} - \frac{\partial^2 E_x}{\partial z^2} + \frac{\partial^2 E_y}{\partial x\partial y} + \frac{\partial^2 E_z}{\partial x\partial z}\right) = \frac{\omega^2}{c^2}E_x \tag{2.65}$$
$$\frac{1}{\varepsilon_r}\left(-\frac{\partial^2 E_x}{\partial y^2} - \frac{\partial^2 E_x}{\partial z^2} + \frac{\partial^2 E_y}{\partial x\partial y} + \frac{\partial^2 E_z}{\partial x\partial z}\right) = \frac{\omega^2}{c^2}E_x, \tag{2.66}$$

$$\left(\frac{\partial}{\partial y}\frac{1}{\varepsilon_r}\right)\left(\frac{\partial H_y}{\partial x}-\frac{\partial H_x}{\partial y}\right)+\left(\frac{\partial}{\partial z}\frac{1}{\varepsilon_r}\right)\left(\frac{\partial H_z}{\partial x}-\frac{\partial H_x}{\partial z}\right)+\frac{1}{\varepsilon_r}\left(-\frac{\partial^2 H_x}{\partial y^2}-\frac{\partial^2 H_x}{\partial z^2}+\frac{\partial^2 H_y}{\partial x\partial y}+\frac{\partial^2 H_z}{\partial x\partial z}\right)=\frac{\omega^2}{c^2}H_x \tag{2.67}$$

$$\left(\frac{\partial}{\partial x}\frac{1}{\varepsilon_r}\right)\left(\frac{\partial H_x}{\partial y}-\frac{\partial H_y}{\partial x}\right)+\left(\frac{\partial}{\partial z}\frac{1}{\varepsilon_r}\right)\left(\frac{\partial H_z}{\partial y}-\frac{\partial H_y}{\partial z}\right)+\frac{1}{\varepsilon_r}\left(-\frac{\partial^2 H_y}{\partial x^2}-\frac{\partial^2 H_y}{\partial z^2}+\frac{\partial^2 H_z}{\partial y\partial z}+\frac{\partial^2 H_x}{\partial x\partial y}\right)=\frac{\omega^2}{c^2}H_y \tag{2.68}$$

$$\left(\frac{\partial}{\partial x}\frac{1}{\varepsilon_r}\right)\left(\frac{\partial H_x}{\partial z}-\frac{\partial H_z}{\partial x}\right)+\left(\frac{\partial}{\partial y}\frac{1}{\varepsilon_r}\right)\left(\frac{\partial H_y}{\partial z}-\frac{\partial H_z}{\partial y}\right)+\frac{1}{\varepsilon_r}\left(-\frac{\partial^2 H_z}{\partial x^2}-\frac{\partial^2 H_z}{\partial y^2}+\frac{\partial^2 H_x}{\partial x\partial z}+\frac{\partial^2 H_y}{\partial y\partial z}\right)=\frac{\omega^2}{c^2}H_z \tag{2.69}$$

$$-\frac{\partial^2}{\partial y^2}\frac{D_x}{\varepsilon_r}-\frac{\partial^2}{\partial z^2}\frac{D_x}{\varepsilon_r}+\frac{\partial^2}{\partial x\partial y}\frac{D_y}{\varepsilon_r}+\frac{\partial^2}{\partial x\partial z}\frac{D_z}{\varepsilon_r}=\frac{\omega^2}{c^2}D_x \tag{2.70}$$

$$-\frac{\partial^2}{\partial y^2}\frac{D_x}{\varepsilon_r}-\frac{\partial^2}{\partial z^2}\frac{D_y}{\varepsilon_r}+\frac{\partial^2}{\partial y\partial z}\frac{D_z}{\varepsilon_r}+\frac{\partial^2}{\partial x\partial y}\frac{D_x}{\varepsilon_r}=\frac{\omega^2}{c^2}D_y \tag{2.71}$$

$$-\frac{\partial^2}{\partial x^2}\frac{D_z}{\varepsilon_r}-\frac{\partial^2}{\partial y^2}\frac{D_z}{\varepsilon_r}+\frac{\partial^2}{\partial x\partial z}\frac{D_x}{\varepsilon_r}+\frac{\partial^2}{\partial y\partial z}\frac{D_y}{\varepsilon_r}=\frac{\omega^2}{c^2}D_z. \tag{2.72}$$

These fields can now be expanded into Fourier series along periodic lattices using Bloch conditions. For the particular case of the 1D photonic crystal shown in Fig. 2.4, the material dielectric constant, ε_r, varies only along the x direction, while it remains constant within the yz plane. Accordingly, it can be assumed that the magnetic and electric fields will be constant within these directions as well. Therefore, the spatial derivatives of both fields vanish from the above equations and the Maxwell's equations can be further reduced to this set of equations:

$$
\begin{aligned}
\frac{1}{\varepsilon_r}\frac{\partial^2 E_y}{\partial x^2} + \frac{\omega^2}{c^2}E_y = 0 \\
\frac{1}{\varepsilon_r}\frac{\partial^2 E_z}{\partial x^2} + \frac{\omega^2}{c^2}E_z = 0 \\
\frac{\partial}{\partial x}\left[\frac{1}{\varepsilon_r}\frac{\partial H_y}{\partial x}\right] + \frac{\omega^2}{c^2}H_y = 0 \\
\frac{1}{\varepsilon_r}\frac{\partial^2 H_z}{\partial x^2} + \frac{\omega^2}{c^2}H_z = 0 \\
\frac{\partial^2}{\partial x^2}\frac{D_y}{\varepsilon_r} + \frac{\omega^2}{c^2}D_y = 0 \\
\frac{\partial^2}{\partial x^2}\frac{D_z}{\varepsilon_r} + \frac{\omega^2}{c^2}D_z = 0.
\end{aligned}
$$

Considering the symmetry of these two sets of equations, only one of them is sufficient to obtain the field equations. This effect occurs because the two polarization states of the wave are degenerate for normal incidence, and we arbitrarily choose the set of E_z and H_y.

$$
\begin{aligned}
\frac{1}{\varepsilon_r}\frac{\partial^2 E_z}{\partial x^2} + \frac{\omega^2}{c^2}E_z = 0, \\
\frac{\partial}{\partial x}\left[\frac{1}{\varepsilon_r}\frac{\partial H_y}{\partial x}\right] + \frac{\omega^2}{c^2}H_y = 0.
\end{aligned}
\tag{2.73}
$$

Besides, the differential operator for the magnetic field is Hermitian and that ensures that the eigenvalues ω^2/c^2 will be real, and thus, the field distributions with the same eigenfrequency must be ortogonal. Thus, to further simplify the calculations we will proceed by using the equation regarding to the Hermitian H_y field, that is

$$
\frac{\partial}{\partial x}\left[\frac{1}{\varepsilon_r}\frac{\partial H_y}{\partial x}\right] + \frac{\omega^2}{c^2}H_y = 0, \tag{2.74}
$$

To study the dispersion relation of the periodic structure, we consider that a set of plane waves will propagate through the 1D crystaline periodicity, namely in the x direction. With respect to this, the transversal wavevectors components can be disregarded, i.e. $k_y = k_z = 0$, hence in this situation, k_x is the only non vanishing wavevector. As it was pointed out in sec. 1.2.2, the primitive lattice vector a and the reciprocal lattice vector b can be expressed as

$$\mathbf{a} = a\hat{i} \tag{2.75}$$

$$\mathbf{b} = b\hat{i} = \frac{2\pi}{a}\hat{i}. \tag{2.76}$$

On the other hand, the 1st Brillouin Zone of the reciprocal vector space is reduced to the interval $[\frac{-\pi}{a}, \frac{\pi}{a}]$, whereas the irreducible part of the 1BZ is reduced to $[0, \frac{\pi}{a}]$. Considering the symmetry and periodicity of the given 1D crystal, the wavevector component on the x direction can be reduced to the irreducible Brillouin zone, then, after fulfilling the ongoing calculations we can easily extend those to the entire reciprocal vector space by using symmetry operations, such as translation, rotation or mirror reflections [4, 85]. To proceed with the calculations of the band diagram we choose a set of plane waves as a basis to expand the reciprocal of the dielectric constant, i.e. $1/\varepsilon_r$, within the entire unit cell [75]. To replicate the periodic conditions over the entire space we refer once more to the Bloch condition. This results in a reformulation of the dielectric constant as $\varepsilon_r = \varepsilon_r(x+a)$, and thus the field equation can now be rewritten in terms of the periodic dielectric function and the plane wave basis as

$$\frac{1}{\varepsilon_r} = \sum_{n=-\infty}^{+\infty} \kappa(n) e^{jnbx} \tag{2.77}$$

$$H_y(k_x, x) = \sum_{m=-\infty}^{+\infty} h(k_x, m) e^{j(k_x+mb)x}, \tag{2.78}$$

where $h(k_x, m)$ represent the amplitudes of the set of plane waves displayed by $e^{j(k_x+mb)x}$, which are indexed by the integer indices m and n, respectively, and b is the modulus of the reciprocal lattice vector defined in Eq.2.75. Note that $\kappa(n)$ symbolyze the Fourier coefficients in the expansion of the reciprocal dielectric function, which can be calculated using the inverse Fourier transform

$$\kappa(n) = \frac{1}{a}\int_0^a \frac{1}{\varepsilon_r(x)} e^{-jnbx} dx \tag{2.79}$$

Following with the multilayer case shown in Fig. 2.4, the step index dielectric constant for the two alternating materials can be expressed as a piecewise equation over the periodic unit cell as

$$\varepsilon(x) = \begin{cases} \varepsilon_1, & \text{for } 0 < x < c \\ \varepsilon_2, & \text{for } c < x < a \end{cases}$$

which yields to the following expansion coefficients

$$\kappa(n) = \frac{1}{a}\left(\int_0^c \frac{1}{\varepsilon_1} e^{jnbx} dx + \int_c^a \frac{1}{\varepsilon_2} e^{jnbx} dx\right) \tag{2.80}$$

Inserting eq. (2.77) and eq. (2.78) into the wave equation eq. (2.74) and putting the prefactor of the plane wave $e^{j(k_x+mb)x}$ to zero one can construct the linear coupled equations for the set of coefficients $\ldots h_{-1}, h_0, h_1, h_2 \ldots$ [76].

$$(k_x + bn)^2 h(k_x, m) - \sum_{m=-\infty}^{\infty} \left(\frac{\omega}{c}\right)^2 \kappa(n-m) h(k_x, m) = 0 \tag{2.81}$$

The solutions exists only when ω satisfies

$$\det \begin{bmatrix} \ldots & \ldots & \ldots & \ldots & \ldots \\ \ldots & (k-b)^2 - \left(\frac{\omega}{c}\right)^2 \kappa_0 & -\left(\frac{\omega}{c}\right)^2 \kappa_{-1} & -\left(\frac{\omega}{c}\right)^2 \kappa_{-2} & \ldots \\ \ldots & -\left(\frac{\omega}{c}\right)^2 \kappa_1 & k^2 - \left(\frac{\omega}{c}\right)^2 \kappa_0 & -\left(\frac{\omega}{c}\right)^2 \kappa_{-1} & \ldots \\ \ldots & -\left(\frac{\omega}{c}\right)^2 \kappa_2 & -\left(\frac{\omega}{c}\right)^2 \kappa_1 & (k-b)^2 - \left(\frac{\omega}{c}\right)^2 \kappa_0 & \ldots \\ \ldots & \ldots & \ldots & \ldots & \ldots \end{bmatrix} = 0, \tag{2.82}$$

The size of this matrix sets the number of eigenvalues that are solved for each k point. As k varies each of the eigenvalues changes gradually according to a set of continuous functions $\omega_1(k), \omega_2(k), \omega_3(k), \ldots$, to form the dispersion curves of the photonic bands of the multilayer system. The subscript n of $\omega_n(k)$ is usually called a band index [76]. Fig. 2.4 shows the computed band diagram for a multilayer stack formed using alternating layers of Si ($\varepsilon_1 = 11.56$) material and air gaps of ($\varepsilon_2 = 1$) of equal widths ($a = 2c$). To calculate this dispersion diagram we used 15 plane waves, thus, the matrix of eq. (2.82) was filled with terms comprising n index ranging from -12 to 12. Accordingly, as long as more plane waves are incorporated to the secular matrix, more frequency components are taken into account and the contributions of the shorter waves are incorporated to the dispersion diagram. Therefore, if we need to compute the dispersion diagram for a large frequency range, the secular matrix will neccessarily increase in size.

2.5 The finite difference time-domain method (FDTD)

The finite difference time-domain method is arguably one of the most popular numerical methods for solving electromagnetic boundary value problems. The FDTD method was first

proposed by Yee in 1966 [79] and during the las decade, the popularity of this computational method has grown hand-in-hand with the scale down of the computational requirements. FDTD has proven to be a truly powerful and versatile numerical tool, in which the memory requirement is linear with the volume of the simulated structure. Furthermore, the FDTD method permits the analysis of large, irregular structures in addition to perfectly periodic structures such as PhCs. The basis of the method relies on solving Maxwell's curl equation by approximating spatial and temporal derivatives as second order accurate finite differences. With this regards, the computational space is discretized using a grid that features narrow intervals below all wavelengths under consideration and in which the material properties are specified at each point. Then, the electric field grid, which has an offset both spatially and temporally from the magnetic field H grid, is used to successively update the fields for all space points forward in time thorughout the entire computational domain [78]. Unlike the PWEM the finite difference time domain method requires to specify a source to excite the fields solved in the series of discrete time-space points comprising the computational grid in which the simulation model is discretized. FDTD enables continuous (typically sinusoidal in time and monochomatic) sources, which are primarily used to compute the dispersion relations, as well as transient sources, such as gaussian beams or dipole-like excitations, needed to stimate many physical features, such as the energy confinement factor of photonic crystals.

To introduce the mathematical background of this method, we first describe the Central difference expressions of Maxwell's equations, which comprises the core of the FDTD formulae. With this foundations it is straightforward to tailor the Maxwell's differential equations for the naive case of a multilayer stack. In the reminder of this section we present the finite difference expressions for a two-dimensional periodic lattice.

2.5.1 Central difference expressions of Maxwell's Equations

In a linear, isotropic and source free region, Maxwell's time dependent curl equations can be written as

$$\mu \frac{\partial \vec{H}}{\partial t} = -\nabla \times \vec{E}, \tag{2.83}$$

$$\varepsilon \frac{\partial \vec{E}}{\partial t} = \nabla \times \vec{H} - \sigma \vec{E} \tag{2.84}$$

where μ, ε, σ, $\vec{E}$ and $\vec{H}$ are the permeability, the conductivity, the permittivity and the time dependent electric and magnetic fields, respectively. Let us assume now a generalized f

expression to designate any field component in terms of space and time, i.e. $f = f(u,v,w,t)$. The spatial differences n this cartesian coordinate system can be expressed unsing the intervals Δu, Δv, and Δw, whereas the time intervals can be designated by the time time increment Δt. Therefore, the space and time derivatives can be approximated at the discrete points, by means of centered two point finite differences, with second order accuracy

$$f(u,v,w,t) = f(i\Delta u, j\Delta v, k\Delta w, n\Delta t) = f^n_{i,j,k}. \tag{2.85}$$

Here, the central difference expression uses a subscript n notation to denote the time index and the subscripts *i, j, k* to indicate the spatial indices. Considering only the first partial derivative of f with respect to the spatial index u at a fixed time $n\Delta t$ [75, 79]

$$\frac{\partial f(i\Delta u, j\Delta v, k\Delta w, n\Delta t)}{\partial u} = \frac{f^n_{i+1/2,j,k} - f^n_{i-1/2,j,k}}{\Delta u} + O[(\Delta u)^2], \tag{2.86}$$

where the $\pm(1/2)$ increment in the index i of the u coordinate indicates a finite difference of f over interval $\pm(1/2)\Delta u$, while the last term is used to gather all second order and higher terms in Δu. This notation permits to spatially separate the electric and magnetic fields by interleaving them in space lattice at intervals $\Delta u/2$. Consequently, the electric field E can be calculated as the difference between two adjacent H field grid points, separated by a distance Δu. On the other hand, the first partial time derivative of f at the grid point (i,j,k) is

$$\frac{\partial f(i\Delta u, j\Delta v, k\Delta w, n\Delta t)}{\partial t} = \frac{f^{n+1/2}_{i,j,k} - f^{n-1/2}_{i,j,k}}{\Delta t} + O[(\Delta t)^2], \tag{2.87}$$

This time, the half increments occur in time index n. The algorithm thus, computes the electric and magnetic fields at alternating time steps, separated by a time lapse of $\Delta t/2$

2.5.2 The one dimensional case: TEM mode

To quote a very simplified model, we will limit the spatial indices to just one, arbitrarily assuming that the propagation is lossless ($\sigma = 0$), following the z direction and the field is x-polarized. Therefore, the non vanishing Maxwell's curl equations for the electric and magnetic fields are

$$\frac{\partial E_x}{\partial t} = \frac{-1}{\varepsilon}\frac{\partial H_y}{\partial z} \tag{2.88}$$

$$\frac{\partial H_y}{\partial t} = \frac{-1}{\mu}\frac{\partial E_z}{\partial z} \tag{2.89}$$

Then, applying the central finite difference approximation to these equations, discretized by the spatial and time intervals, Δx and Δt, respectively:

$$\frac{E_x^{n+1/2}(k) - E_x^{n-1/2}(k)}{\Delta t} = \frac{-1}{\varepsilon} \frac{H_y^n(k+1/2) - H_y^n(k-1/2)}{\Delta z}, \tag{2.90}$$

$$\frac{H_y^{n+1/2}(k) - H_y^n(k+1/2)}{\Delta t} = \frac{-1}{\mu} \frac{E_x^{n+1/2}(k+1) - E_x^{n+1/2}(k)}{\Delta z} \tag{2.91}$$

From eq. (2.90) and eq. (2.91), and according to Yee's scheme shown in Fig. 2.5 for the one dimensional case, the the derivative of the E field at time $n\Delta t$ can be expressed as a central difference using E field values at times $\left(n + \frac{1}{2}\right)\Delta t$.

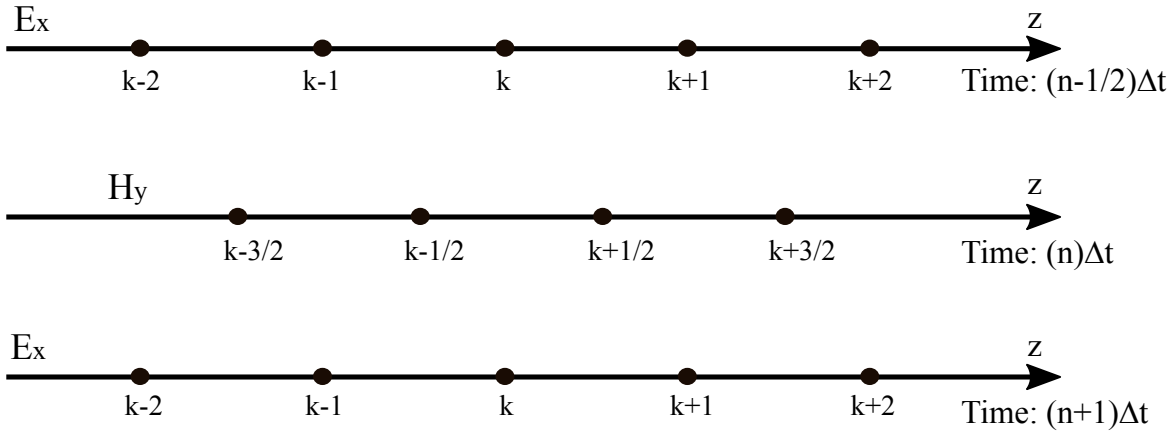

Figure 2.5 When considering only one dimension, Yee's scheme reduces to this scheme. E and H fields will be calculated in space and time according to this configuration.

In particular, the left term in equation eq. (2.90) states that $\frac{\partial E_x}{\partial t}$ can be substituted by a central differencee approximation of the E field values at times $\frac{\left(n+\frac{1}{2}\right)}{\Delta t}$ and $\frac{\left(n-\frac{1}{2}\right)}{\Delta t}$, whereas the right trem of the equation applies the central difference approximation to the H field in space, at points $\frac{\left(k+\frac{1}{2}\right)}{\Delta x}$ and $\frac{\left(k-\frac{1}{2}\right)}{\Delta x}$. This procedure is also known as leap from algorithm, meaning that to appproximate Maxwell's curl equations in space and time the algorithm must first solve the equation regarding to the magnetic field H, and then calculate all E field values, taking into account that fields E and H are shifted also in space by $\frac{\Delta x}{2}$. Fig. 2.5 shows schematically the scheme of the leap frog algorithm. Then, the explicit FDTD equations can be derived from eq. (2.90) and eq. (2.91), to obtain

$$E_x^{n+1/2}(k) = E_x^{n-1/2}(k) + \frac{\Delta t}{\varepsilon \Delta z}(H_y^n(k-1/2) - H_y^n(k+1/2)) \tag{2.92}$$

$$H_y^{n+1}(k) = H_y^n(k+1/2) + \frac{\Delta t}{\mu \Delta z}(E_x^{n+1/2}(k) - E_n^{n+1/2}(k+1)) \tag{2.93}$$

To reduce the numerical errors which arise from taking very different amplitudes of E and H, A. Taflove introduced a normalization factor to make E field of the same order of magnitude as [**?**]:

$$\tilde{E} = \sqrt{\frac{\varepsilon_0}{\mu_0}} E, \tag{2.94}$$

Thus, introducing the normalization factor into equations eq. (2.90) and eq. (2.91), and dropping the $\sim$ yields to

$$E_x^{n+1/2}(k) = E_x^{n-1/2}(k) + \frac{1}{\sqrt{\varepsilon\mu}} \frac{\Delta t}{\Delta z}(H_y^n(k-1/2) - H_y^n(k+1/2)) \tag{2.95}$$

$$H_y^{n+1}(k) = H_y^n(k+1/2) + \frac{1}{\sqrt{\varepsilon\mu}} \frac{\Delta t}{\Delta z}(E_x^{n+1/2}(k) - E_n^{n+1/2}(k+1)) \tag{2.96}$$

2.5.3 Two-dimensional FDTD method

To get insight of the two dimensional FDTD approach we will particularize it to a cartesian coordinate system in which the fields and geommetries will remain invariant within the z direction. Accordingly, those partial derivatives with respect to z will vanish from Maxwell's equations

$$-\frac{\partial E_z}{\partial y} = \mu_0 \frac{\partial H_x}{\partial t} \tag{2.97}$$

$$\frac{\partial E_z}{\partial x} = \mu_0 \frac{\partial H_y}{\partial t} \tag{2.98}$$

$$\frac{\partial H_y}{\partial x} - \frac{\partial H_x}{\partial y} = \varepsilon \frac{\partial E_z}{\partial t} + \sigma E_z \tag{2.99}$$

$$\frac{\partial H_z}{\partial y} = \varepsilon \frac{\partial E_x}{\partial t} + \sigma E_x \tag{2.100}$$

$$-\frac{\partial H_z}{\partial x} = \varepsilon \frac{\partial E_y}{\partial t} + \sigma E_y \tag{2.101}$$

$$\frac{\partial E_x}{\partial y} - \frac{\partial E_y}{\partial x} = \mu_0 \frac{\partial H_z}{\partial t} \tag{2.102}$$

$$\tag{2.103}$$

Once again we assumed non magnetic materials, i.e. $\mu = \mu_0$ everywhere, which is reasonable for most photonic crystal applications at optical wavelengths.

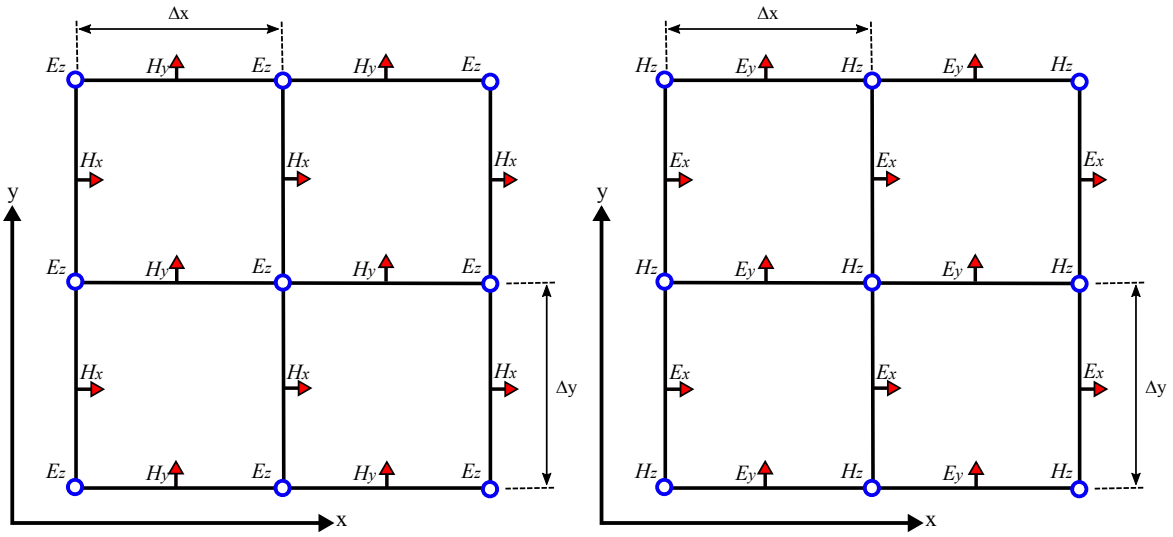

Figure 2.6 The Yee mesh for two-dimensional (a) TM and (b) TE modes, respectively. Arrows indicate the field components for the in-plane components, whereas circles do it for the out-of-plane components. The field points are interleaved with a spacing of $\frac{\Delta_x}{2}$ and $\frac{\Delta_y}{2}$, for the meshes of the TM and TE modes, respectively.

The former two sets of equations, i.e. eq. (2.97) and eq. (2.100) comprise electric and magnetic fields which relate the vertical field components with those corresponding to in-plane directions. In the particular case of the equations in eq. (2.97), the E_z field is the only field component designated to z direction, while the magnetic fields H_x and H_x remain within the xy plane. Therefore, canonically we will refer to them as the equations regarding to the TM polarized mode. On the other hand, the set of equations comprised in are designated for the TE polarization.

The difference equations corresponding to the TM mode are obtained by aplying the central difference expressions to the TM equations

$$H_x|_{i,j}^{n+1/2} = H_x|_{i,j}^{n-1/2} - \frac{1}{\mu_0}\frac{\Delta t}{\Delta y}(E_z|_{i,j+1/2}^{n} - E_z|_{i,j-1/2}^{n}), \tag{2.104}$$

$$H_y|_{i,j}^{n+1/2} = H_y|_{i,j}^{n-1/2} - \frac{1}{\mu_0}\frac{\Delta t}{\Delta x}(E_z|_{i,j+1/2}^{n} - E_z|_{i,j-1/2}^{n}), \tag{2.105}$$

$$E_z|_{i,j}^{n+1} = \frac{\varepsilon_{i,j} - \sigma_{i,j}\Delta t/2}{\varepsilon_{i,j} + \sigma_{i,j}\Delta t/2}E_z|_{i,j}^{n} + \frac{\Delta t}{\varepsilon_{i,j} + \sigma_{i,j}\Delta t/2}\left(\frac{H_y|_{i+1/2,j}^{n+1/2} - H_y|_{i-1/2,j}^{n+1/2}}{\Delta x} - \frac{H_x|_{i,j+1/2}^{n+1/2} - H_x|_{i,j-1/2}^{n+1/2}}{\Delta y}\right), \tag{2.106}$$

where the electric field components are evaluated at time steps $t = \frac{n}{\Delta t}$ while the magnetic fields are calculated at $t = \frac{n+\left(\frac{1}{2}\right)}{\Delta t}$. Then, applying the central-difference formulation to the TE mode yields the following difference expressions

$$E_x|_{i,j}^{n+1} = \frac{\varepsilon_{i,j} - \sigma_{i,j}\Delta t/2}{\varepsilon_{i,j} + \sigma_{i,j}\Delta t/2}E_x|_{i,j}^{n} + \frac{\Delta t}{\varepsilon_{i,j} + \sigma_{i,j}\Delta t/2}\left(\frac{H_z|_{i,j+1/2}^{n+1/2} - H_z|_{i,j-1/2}^{n+1/2}}{\Delta y}\right) \tag{2.107}$$

$$E_y|_{i,j}^{n+1} = \frac{\varepsilon_{i,j} - \sigma_{i,j}\Delta t/2}{\varepsilon_{i,j} + \sigma_{i,j}\Delta t/2}E_y|_{i,j}^{n} + \frac{\Delta t}{\varepsilon_{i,j} + \sigma_{i,j}\Delta t/2}\left(\frac{H_z|_{i+1/2,j}^{n+1/2} - H_z|_{i-1/2,j}^{n+1/2}}{\Delta y}\right) \tag{2.108}$$

$$H_z|_{i,j}^{n+1/2} = H_z|_{i,j}^{n-1/2} + \frac{\Delta t}{\mu_0}\left(\frac{E_x|_{i,j+1/2}^{n} - E_x|_{i,j-1/2}^{n}}{\Delta y} - \frac{E_y|_{i+1/2,j}^{n} - E_y|_{i-1/2,j}^{n}}{\Delta x}\right) \tag{2.109}$$

Chapter 3

Numerical simulation of infinite and finite 2D lattices

So far, we have devoted the previous chapters to introduce the reader into the physics of photonic crystals and to describe the numerical methods that permit to simulate these features. In the following, though, we make a critical assessment of the finite element (FE) method for studying two-dimensional dielectric photonic crystals. Photonic band structures, transmission coefficients, and quality factors of various two-dimensional, periodic and aperiodic, dielectric photonic crystals are calculated by using the FE (real-space) method and the plane wave expansion or the finite difference time domain (FDTD) methods and a comparison is established between those results. It is found that, contrarily to popular belief, the FE method (FEM) not only reproduces extremely well the results obtained with the standard plane wave method with regards to the eigenvalue analysis (photonic band structure and density of states calculations) but it also allows to study very easily the time-harmonic propagation of electromagnetic fields in finite clusters of arbitrary complexity and, thus, to calculate their transmission coefficients in a simple way. Moreover, the advantages of using this real space method in the context of point defect cluster quality factor calculations are also stressed by comparing the results obtained with this method with those obtained with the FDTD one. As a result of this study, FEM comes out as an stable, robust, rigorous, and reliable tool to study light propagation and confinement in both periodic and aperiodic dielectric photonic crystals and clusters.

3.0.1 Implementation of FEM used in this work

Even though there are freely available implementations of the finite element method for dealing with electromagnetic problems [80–82], they are more focused on other aspects of

electromagnetism, most noticeably magnetostatics, antennae design, electrostatics, and so on. For this reason, in order to perform the calculations described in this chapter, we decided to use a commercial implementation of the FE method, namely the COMSOL multiphysics package [83]. The main reasons to choose this software are the intuitive CAD environment it provides for designing the system to be simulated, there is an specific application mode for simulating propagation of EM waves in an arbitrary medium (including both 2D and 3D systems), its post-processing and visualization capabilities, and the fact that it can be easily interfaced with MATLAB. In two dimensions, COMSOL uses an unstructured mesh (triangular mesh elements) generator based on the Delaunay algorithm. Once a mesh is created, the dependent variables are approximated by a known function (shape functions) that can be described with a finite number of parameters called *degrees of freedom*. Inserting this approximation into the original equations generates a set of equations for the degrees of freedom that is then solved with an appropriate *solver*. In particular, for the present problem, the shape functions are second order Lagrange elements and the solver for the resulting linear problem is the so called UMFPACK solver, which is a very efficient direct solver for unsymmetric systems [84]. The MIT Photonic-Bands (MPB) implementation of the plane wave method has been also used as the standard to assess the accuracy of the finite element calculations [85]. Some of the nice features of this software package are that it is fully vectorial; it supports arbitrary, anisotropic dielectric structures and non-orthogonal unit cells; parallel computations are supported by using MPI, it provides a flexible user interface (extensible and scriptable), and it has been extensively tested by numerous researchers during the last 15 years. In order to compare the usefulness of the FEM method in the calculation of quality factor in these cavities, we have compared the results obtained via FEM with the results obtained by Time-Domain Finite Difference (FDTD) [68] method and the ones acquired using harmonic inversion method.

3.1 Simulation results for photonic crystals based on the square lattice

The first structure analyzed in this work is a 2D photonic crystal made of dielectric circles whose centers occupy the positions of a square lattice and is depicted in the inset of Fig. 3.1. The dielectric material was assumed to be linear, isotropic, and non-magnetic[1]. The dielectric constant of the rods has a value of 9. The ratio $\frac{r}{a}$, where r is the radius of the cylinders and a the lattice parameter, was taken as 0.38. This well known structure was first investigated

[1]This applies to the rest of photonic crystals considered in the present chapter

by McCall and coworkers in order to compare the predictions of theory with experimental results with regards to the localization of light in strongly scattering media. In the present context, we have studied this topology in order to check how well the FE method fares when compared with the plane wave method that, as stated before, is the one commonly used to calculate photonic band structures. The first nine photonic bands were calculated for transversal electric (TE) polarization along the path that delimits the irreducible part of the 1st Brillouin Zone (1BZ). For the FE calculation, the square unit cell was divided in 3720 mesh elements and periodic boundary conditions given by Bloch's theorem were implemented. For the MPB calculation, a resolution of 64×64 (= 4096) grid elements were used and the dielectric constant was average over 9 grid points. The resulting photonic band structure is depicted in Fig. 3.1. As it is customary, the dimensionless quantity $\omega a/2\pi c = a/\lambda$ has been used to characterize the frequency of the incident EM wave, where ω is the frequency of the incident EM wave and λ the associated wavelength. The corresponding eigenmodes of the z-component of the electric field, E_z, were also calculated at the Γ, M, and K points of the 1BZ and they are shown also in figure 3.1. It is clear from that figure that the band structure calculated with the FE method faithfully reproduces the one calculated with MPB to its minimum details. There are three photonic gaps in the band structure of this lattice whose sizes coincide with the calculated ones with MPB. Also, the modes calculated with the FE method closely resemble those calculated with MPB up to a trivial symmetry operation or linear combination of degenerate modes.

Even though that is not the main purpose of this paper, it is illustrative to compare to some extent the accuracy and speed of the FE calculations with the ones performed by using the PW method. To estimate the relative accuracy, we computed the percent error in the eigenvalue calculated at the X point for the ninth band for different discretizations of the square unit cell. In the FE case, meshes with 254, 414, 928, and 1502 elements were used, whereas for the calculations done with MPB, resolutions of 16×16 (= 256) grid elements, 32×32 (= 1024) grid elements, 48×48 (= 2304) grid elements, and 64×64 (= 4096) grid elements were used. We took the eigenvalue calculated with MPB by using a resolution of 256×256 and a mesh size of 25 as the exact one. The result of this comparison can be seen in Fig. 3.2a. It is noticeable that the FE method gets a better accuracy with coarser discretizations of the lattice than the PW does. This is due to the use of second order Lagrange elements. However, the differences between both methods should be negligible for most applications. Of course, this better accuracy comes at a price and the simulation times for the FE calculations are longer by a noticeable factor than those for the MPB ones, as can be seen in Fig. 3.2b, where we have depicted the evolution of the simulation runtime with the number of mesh elements and grid elements for the FE and MPB calculations, respectively.

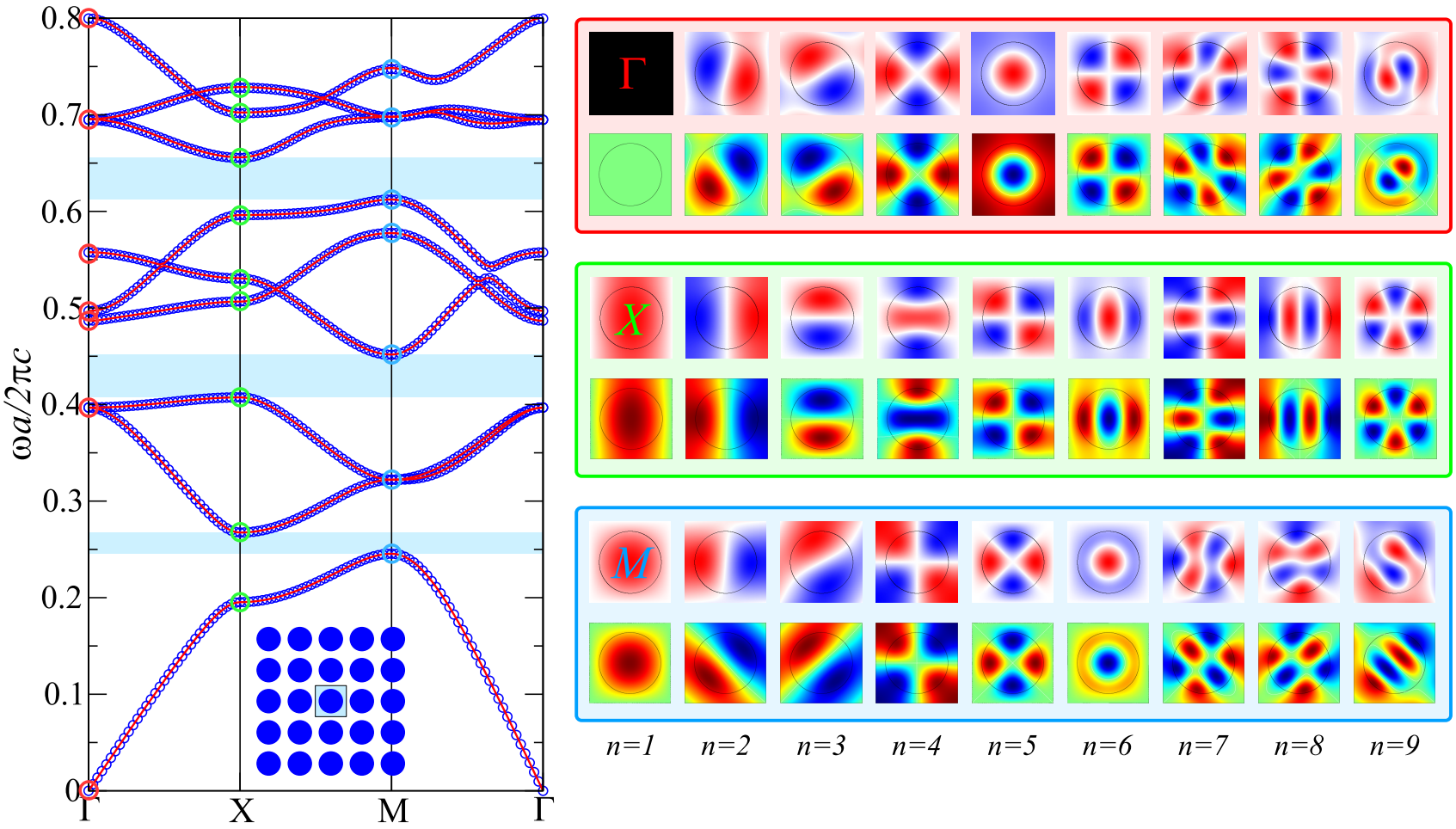

Figure 3.1 On the left: band structure calculated with the MPB (blue circles) and COMSOL (red line) software packages for TE-polarized EM waves. On the right: E_z patterns in the unit cell calculated with MPB (upper row in each rectangle) and COMSOL at the special symmetry points Γ, X, and M.

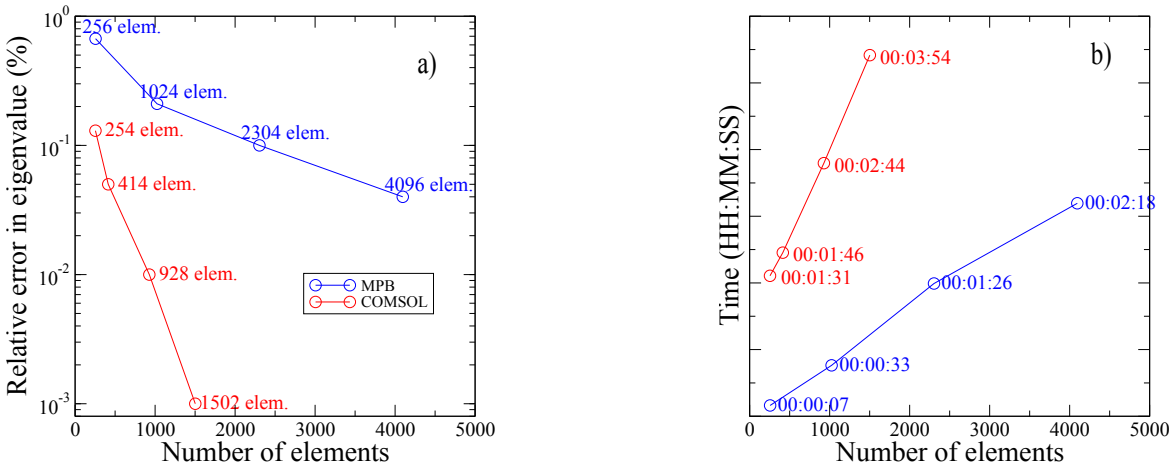

Figure 3.2 (a) Evolution of the relative error with the number of elements in which the lattice is discretized. (b) Evolution of the simulation run time with the number of elements in which the lattice is discretized.

Another quantity that can be readily calculated with the FEM method is the transmittance of a finite photonic crystal. A cluster comprised of 9×9 dielectric rods in air was studied. TE polarized light propagating in the ΓX direction was considered. In order to perform this calculation, a photonic crystal composed of 9×9 dielectric rods was discretized into a mesh containing 19140 elements[2]. This means that even for the shortest wavelength of the EM field considered in this calculation ($\lambda_{\min}\approx a$) there are roughly 15 mesh elements per wavelength (≈ 35 at $\omega a/2\pi c = a/\lambda = 0.25$), more than enough to simulate the inhomogeneous character of this system. The transmittance of the cluster was calculated with the expression

$$T = \frac{1}{L_y}\int_0^{L_y} E_z(L_x,y)\times E_z^*(L_x,y)\,dy, \tag{3.1}$$

where L_α is the length of the output boundary in the α-th direction ($\alpha = x,y$). The boundary conditions for the simulation domain were set as follows: on the input and output boundaries (left and right boundaries) a perfectly matched layer was used to avoid spurious reflections from non-physical boundaries. The z-component of the electric field was set to 1 and 0 at the initial time of the simulation on the input and output boundaries, respectively. On the other hand, perfectly magnetic conductor boundary conditions that set the tangential magnetic component of the magnetic field to zero were used for the upper and lower boundaries[3] in order to mimic an infinite stripe in that direction.

[2] In fact, meshes containing 27644, 30392, and 44876 mesh elements were also considered and no significant differences in the calculated transmittance were found

[3] Simulations using different boundary conditions for the upper and lower boundaries were performed and no significant differences in the calculated transmission spectra were found

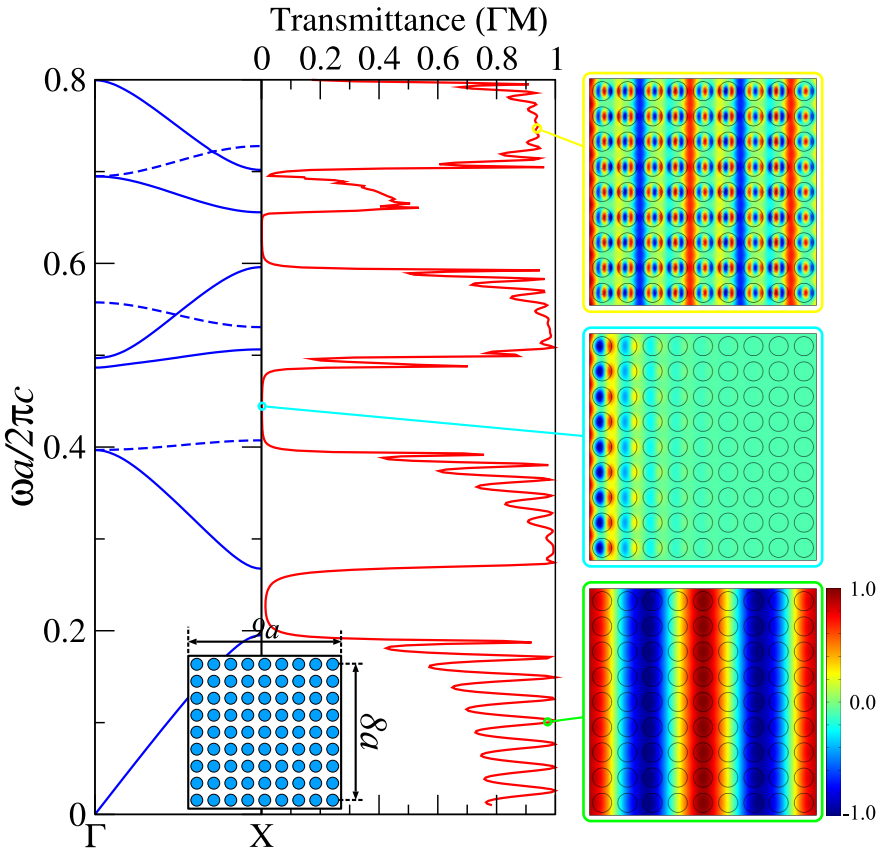

Figure 3.3 Comparison between the band structure (on the left panel) and transmittance (on the center panel) for TE-polarized EM waves propagating in the ΓX direction of a square lattice photonic crystal made of dielectric rods in air. Dashed lines in the band structure represent uncoupled modes (see text). The inset depicts the cluster used for computing the transmittance. Blue circles represent the dielectric material and the square is the boundary of the simulation space. Displayed on the right are three patterns of E_z that correspond to the values of $\omega a/2\pi c$ 0.1, 0.45, and 0.75 from bottom to top, respectively.

Fig. 3.3 shows the transmittance calculated by using equation 3.1 for this cluster in the frequency range $[0, 0.8]$. The band structure along the ΓX direction is also shown for comparison. It is easy to see that the transmittance clearly reproduces the partial gaps in the band structure as frequency regions where the transmitted intensity is very small. On the other hand, there are two narrow energy intervals (around $\frac{\omega a}{2\pi c} = 0.4$ and 0.7) in which only antisymmetric modes exist, so that these cannot be excited by the incident wave and, thus, they correspond to opaque frequency regions not found in the band diagram. This has been discussed in detail by Sakoda [5]. Unfortunately, MPB does not support transmittance calculations, so it is not possible to establish a comparison between both methods. Displayed on the right side of Fig. 3.3 there are three patterns of E_z in the stationary regime for different values of a/λ. The one at the bottom illustrates the field pattern for $a/\lambda = 0.1$. As expected, for this λ we are in the linear dispersion region and the field pattern is that of a plane wave propagating through a homogeneous medium. The one on the middle, on the other hand, was calculated at $a/\lambda = 0.45$ and it illustrates a typical pattern associated to a photonic gap: the field decays exponentially as it propagates across the crystal and, consequently, the transmittance is zero. Finally, the complex pattern at $a/\lambda = 0.75$ clearly reflects the inhomogeneous character of the underlying structure.

3.2 Simulation results for photonic crystals based on the triangular lattice

Another important class of two-dimensional photonic crystals is the one formed by those structures based on the triangular lattice because this is the symmetry most commonly used for practical applications [4]. For this reason it is important to test whether the FE method produces correct results for this non-orthogonal lattice. With this purpose, we have calculated the band structure and transmission coefficient of a number of photonic crystals based on the the triangular lattice. The former has been compared with the calculations performed with MPB to check the accuracy of the FE method. As such comparison is not possible for the transmittance, we have followed the same approach as in the previous section and compared the positions of the gaps predicted by this quantity with the ones obtained from the band structure. A value of 12 was used for the dielectric constant of the non-empty part of the photonic crystal in all subsequent calculations.

The first structure based on the hexagonal lattice that has been considered in the present work is a photonic crystal made of dielectric cylinders whose centers occupy the sites of an hexagonal lattice of lattice constant a (see the insets in Fig. 3.4). The radius of the cylinders is $0.12a$. The simulation setup was very similar to the one used for the square

lattice: For the FE band calculation, the unit cell was divided into 1086 mesh elements and periodic boundary conditions were implemented across the boundaries. For the transmittance calculation in the ΓM direction, a cluster comprising 12×8 unit cells (dielectric rods) was divided into 60748 mesh elements. For the transmittance calculation in the ΓK direction, a cluster comprising 11×10 unit cells was divided into 67282 mesh elements. The same boundary conditions as for the square lattice calculations described above were used. The photonic band structure, transmittances in the ΓM and ΓK directions, and E_z field patterns for TE-polarized EM waves are reported in Fig. 3.4. The band structure calculated with the FE method faithfully reproduces the one obtained with MPB. This structure possesses one gap between the first and second bands for TE-polarized EM waves that can be clearly seen in the transmission spectra for light propagating in both the ΓM and ΓK directions as wide opaque regions. There are also some partial gaps, as the ones occurring between the second and third bands and the fourth and fifth bands in the ΓM direction that, however, are not present in the ΓK direction. Also, there some opaque regions not related to gaps on the band structure but rather to the existence of uncoupled modes, such as the one associated to the 5th band, that is uncoupled in the ΓK direction.

The second hexagonal structure analyzed is a lattice made of dielectric cylinders of radius $r = 0.25a$ (see the insets in Fig. 3.5) and, in particular, its behavior under irradiation with TM-polarized EM waves. The number of mesh elements used in this case for the band calculations using the FEM was 942. In spite of this relatively small number of elements, the accuracy of the calculation is remarkable when compared with the bands calculated with MPB, as can be seen in the central panel of Fig. 3.5. Also, the H_z mode patterns calculated with FEM closely resemble those calculated with MPB. For the transmittance calculations, we followed the same approach as for the previous case. However, in this case, PEC boundary conditions were used in the upper and lower boundaries of the simulation cluster in order to mimic an infinite crystal in the vertical direction. Moreover, the transmittance is defined now as

$$T = \frac{1}{L_y} \int_0^{L_y} H_z(L_x, y) \times H_z^*(L_x, y)\, dy. \tag{3.2}$$

The number of mesh elements used in the transmittance calculations in the ΓM and ΓK directions were now 37760 and 42270, respectively. It is interesting to notice that this structure exhibit no complete gap in the analyzed frequency range. However, it exhibits some partial gaps that are correctly reproduced by the transmittance in the corresponding direction (left and right panels in Fig. 3.5), most noticeably, the wide partial gap occurring between the second and third bands in the ΓM direction.

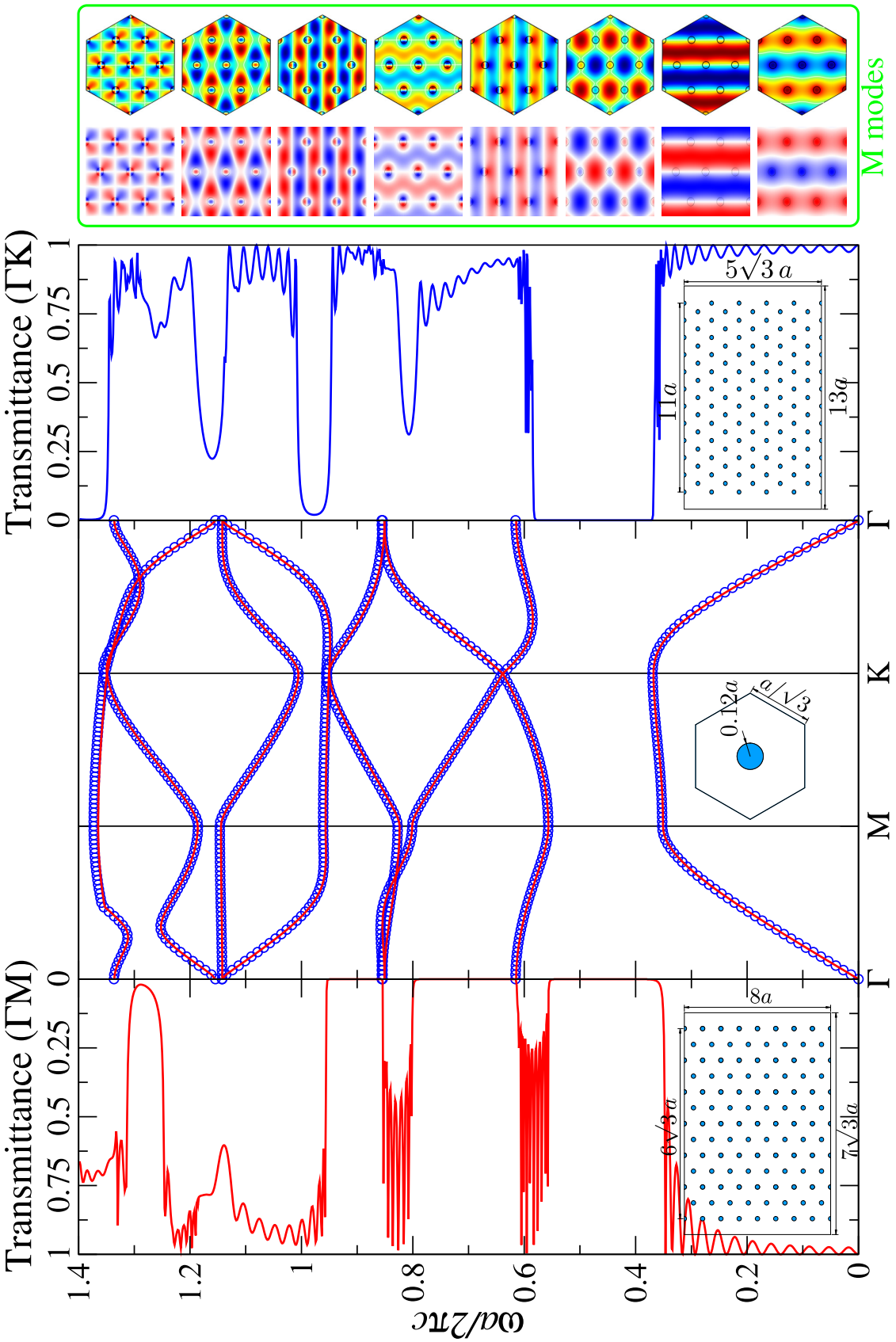

Figure 3.4 Left panel: Transmittance for TE-polarized waves propagating in the ΓM direction of the hexagonal photonic crystal cluster depicted in the inset. Central panel: Comparison between the band structure calculated with COMSOL (red line) and MPB (blue circles) for TE-polarized EM waves along the boundary of the irreducible part of the 1BZ. The inset shows the unit cell used for the calculations. Right panel: Transmittance for TE-polarized waves propagating in the ΓK direction of the hexagonal photonic crystal cluster depicted in the inset. Inside the green rectangle: Comparison between the E_z field patterns at the M point calculated with MPB (on the left) and FEM (on the right) for the first eight bands (the band index increases from bottom to top). A portion of the photonic crystal that contains 3×3 unit cells is displayed in order to show the hexagonal symmetry of the modes.

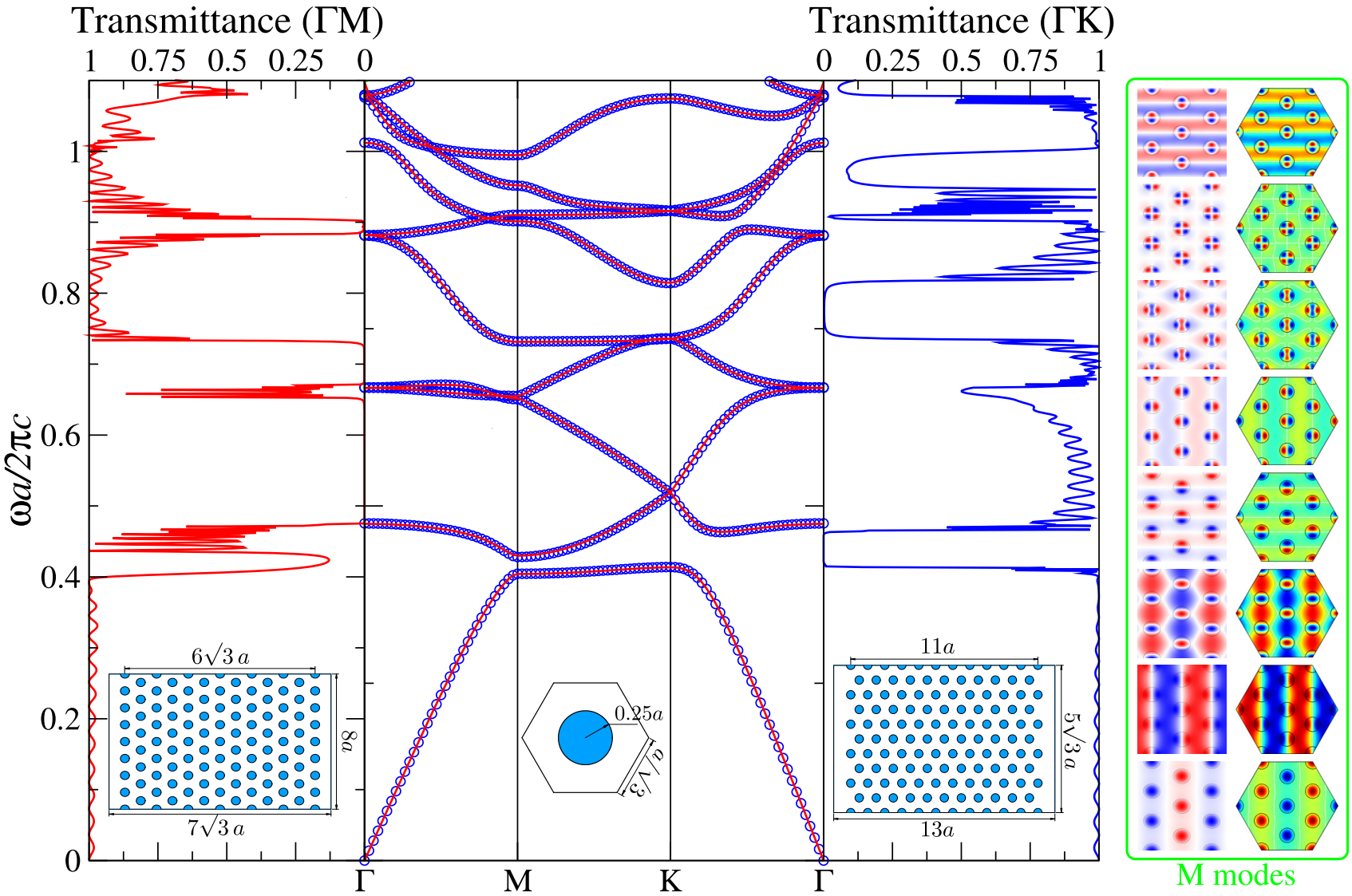

Figure 3.5 Similar to Fig. 3.4 but for TM-polarized EM waves. Also, the radius of the cylinders is now $0.25a$ and the displayed patterns are those for the H_z field at the M point.

The third structure studied in this work consists of an hexagonal lattice of air rods of radius $r = 0.34a$ that has been drilled into a sheet of dielectric material (see insets of Fig. 3.6). TE-polarized EM waves were considered in this case. For the band structure calculations using the FE method, the unit cell was divided into 896 mesh elements and periodic boundary conditions were implemented across the boundaries of the hexagon. As in the previous case, the accuracy of the band and mode calculations is very good when compared with the MPB ones. The simulation setup for the transmittance calculation was similar to the one used for the hexagonal lattice of dielectric rods under TE-polarized EM waves irradiation. The number of mesh elements employed in this case were 26528 and 29984 for the calculation in the ΓM and ΓK directions, respectively. As in the previous cases, the transmittances in both directions faithfully reproduce the features present in the band diagram, except for those frequency ranges in which uncoupled modes exists (such as the range between the 5th and 7th bands in both the ΓM and ΓK directions).

Finally, the fourth structure considered in this work is an hexagonal lattice of air rods of radius $r = 0.23a$ that has been drilled into a sheet of dielectric material (see Fig. 3.7). TM-polarized EM waves were considered in this case. For the band structure calculations using the FE method, the unit cell was divided into 620 mesh elements and periodic boundary conditions were implemented across the boundaries of the hexagon. The simulation setup for the transmittance calculation was similar to the one used for the hexagonal lattice of dielectric rods under TM-polarized EM waves irradiation. The number of mesh elements used in this case were 40690 and 45488 for the calculation in the ΓM and ΓK directions, respectively. As in the previous cases, the band structure calculated with the FE method faithfully reproduces the one calculated with MPB. Moreover, the transmittance in both considered directions clearly reproduce the details of the band structure and the existence of other opaque ranges due to the existence of uncoupled modes, just as in the previous cases.

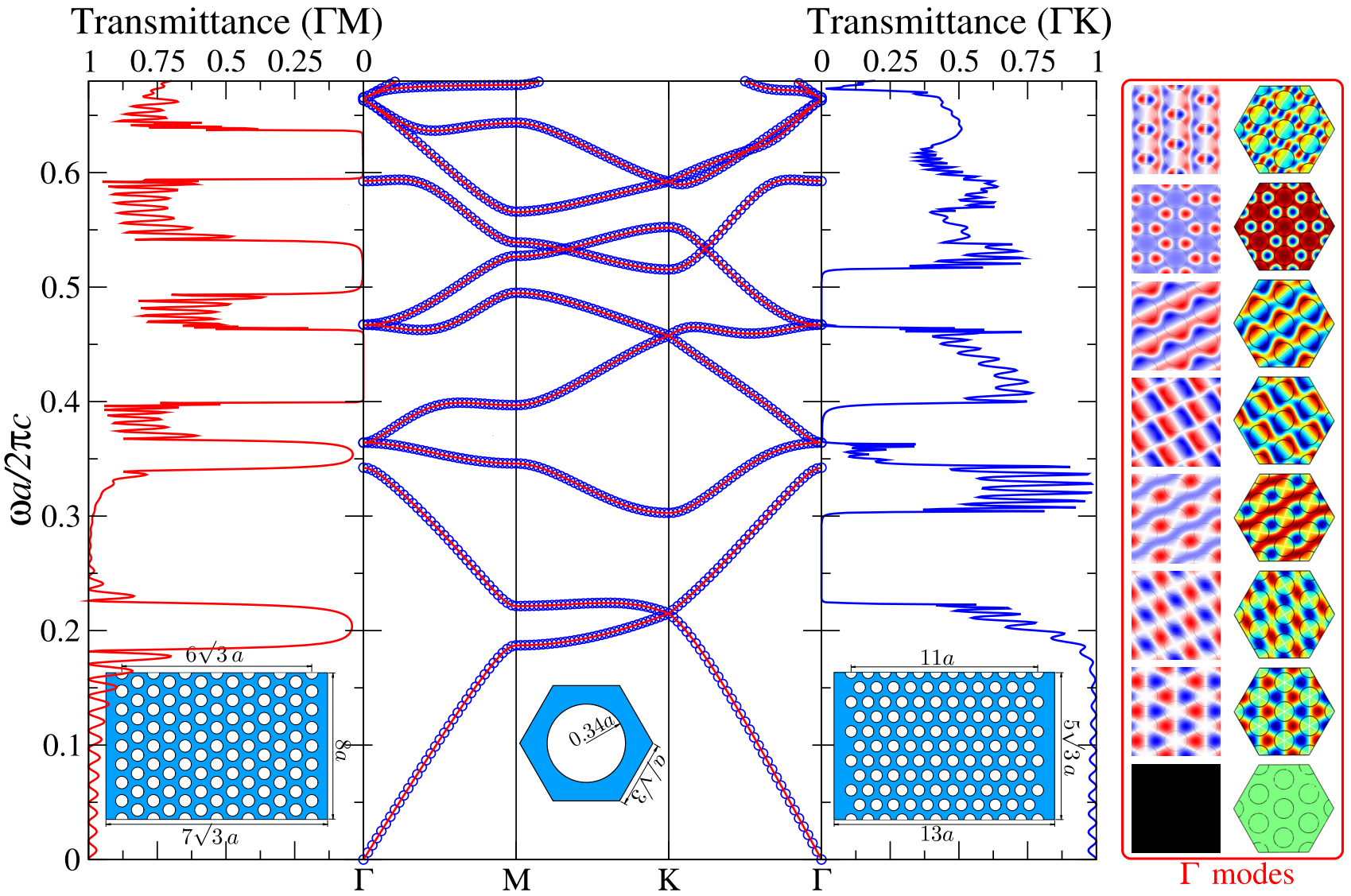

Figure 3.6 Similar to Fig. 3.4 but now air holes are drilled into a slab of dielectric material (so that an inverse structure is obtained). Also, the radius of the air cylinders is now $0.34a$ and the E_z field patterns are displayed at the Γ point.

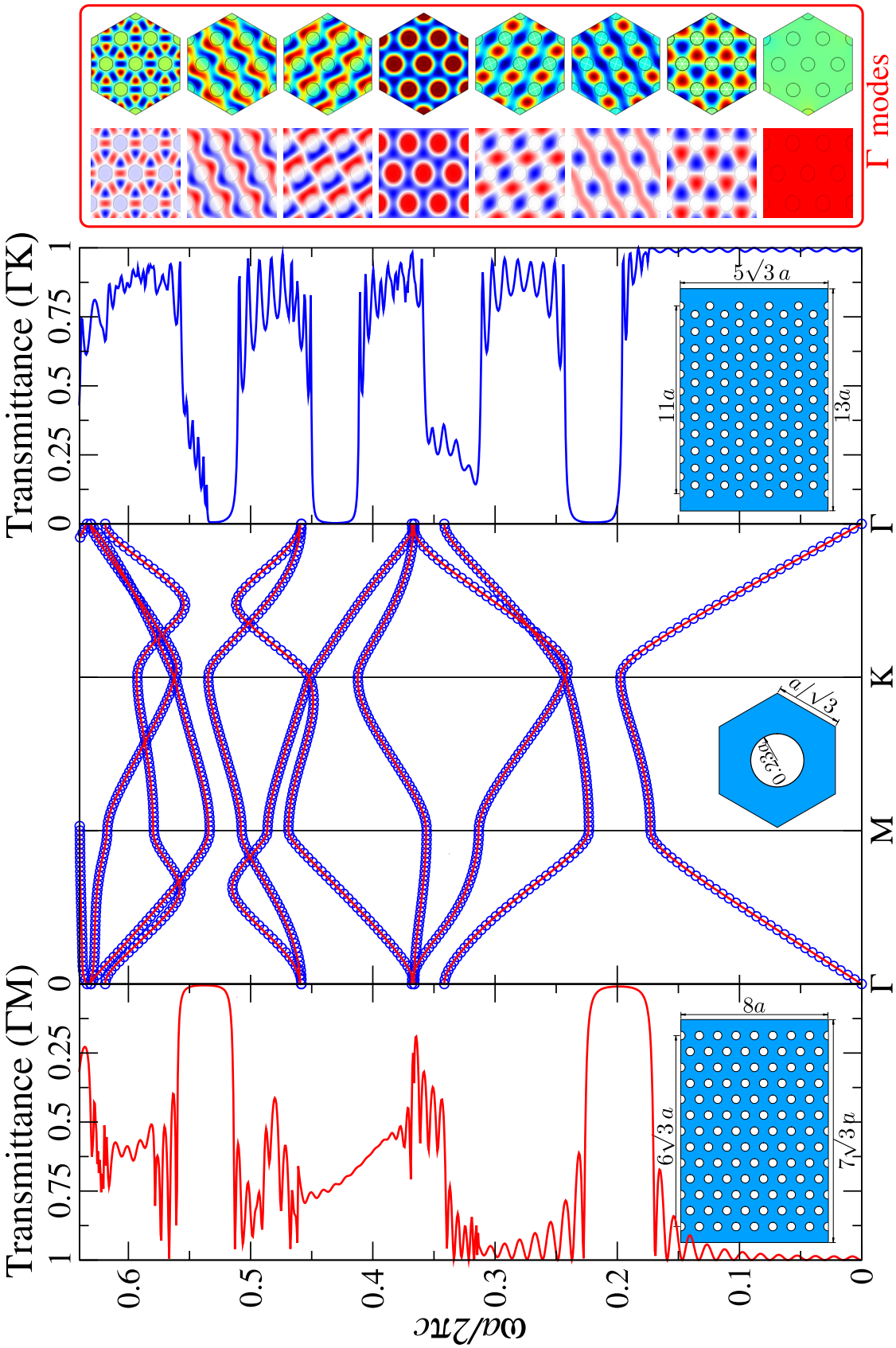

Figure 3.7 (color online) Similar to Fig. 3.6 but for TM-polarized EM waves. Also, the radius of the cylinders is now $0.23a$ and the displayed patterns are those for the H_z field at the Γ point.

3.3 Defect states in 2D photonic crystal superlattices

As seen so far, the physics of ideal periodic photonic crystals is very interesting and their potential applications very attractive. However, in complete analogy with semiconductors, the physics of disordered photonic crystals is even richer and their potential applications even more promising. Among these, photonic crystals in which defects are placed in a controlled way forming point or line defects are especially important for telecommunication applications. Their importance is rooted on the fact that these types of defects can lead to the formation of localized states inside the photonic gap that allows one to localize light around the defects. This can be used to fabricate optical microcavities with quality factors orders of magnitude larger than current generation ones and to guide light across the crystal along pathways that are impossible to attain using standard optical fibers.

The physics behind the localization of a state with frequency inside the gap is very easy to understand. For simplicity, let us first consider a single point defect in the otherwise perfect photonic crystal. Far away from this defect, the modes of the EM field are required to be eigenstates of the bulk crystal and, thus, modes with frequency inside the frequency range of the band gap cannot propagate in the crystal. Therefore, the only possibility is that any modes in that frequency range have complex wavevectors, so that they decay exponentially as one moves from the vicinity of the defect. In practice, any real photonic crystal has a finite size and a localized mode can escape from the defect region by its exponential tail. For this reason, these modes are usually called resonant modes, because they have a finite life-time. Typical ways of creating point defects include changing some of the constituents of the photonic crystal, such as the dielectric constant, their size, or both at the same time. On the other hand, a line defect can be built with a succession of point defects forming a path across the crystal. The light with frequency inside the gap can propagate along this path but is confined laterally and, thus, it acts as a perfect waveguide without the limitations imposed by the index-guiding mechanism used in conventional optical fibers.

It is easy to understand from these facts the importance of developing computational methods that allow one to understand the nature and features of such localized modes in an efficient and easy way. Traditionally, the methods most commonly used for calculating the photonic band structure and field modes for these photonic crystals with defects have been frequency methods such as the ones described above (based on an expansion in a certain complete basis) applied to a supercell that includes the defects. This is similar to what is done in other fields of physics to deal with defect states such as the ones resulting from defects in semiconductors for electrons or non-magnetic impurities in magnetism.

Point defect photonic crystal configurations have been widely studied as promising candidates for the enhancement of strong coupling between the resonance cavity and quantum dots light emitters [87] or to reduce the lasing threshold of a certain laser emitter [88]. Besides, they have been described as key elements for several applications in many areas of physics and engineering such as enhancing high directivity antennas [89], designing low power consumption and highly tunable optical buffering devices [90, 91], or constructing new PC-VCSEL lasers [92] as well as for biosensing applications [93], just to cite some examples.

In the simulations reported in this section, periodicity of the lattice has been intentionally broken and hence a defect is introduced into the otherwise perfectly ordered dielectric distribution, giving rise to localized states within the band gap region. When a single rod is removed from the dielectric lattice, light bounces back and forth in the disordered area, trapped by the surrounding band gap, whilst no other leakage mechanism is present. The resulting photonic crystal can still be classified on the basis of unit cell calculations, as long as the fundamental periodic cell hosts sufficient rods around the imperfection to make sure that the defect state does not overlap with neighboring replicas of itself. Furthermore, in these single rod perturbed cells, rotational symmetry remains invariant and thus comparative studies with previous perfect square and triangular lattice based calculations can still be performed at the edge of the 1BZ.

3.3.1 A square lattice of dielectric rods with a point defect: the McCall's experiment

The experimental evidence of spatial mode localization in an ordered dielectric lattice of rods in an air background was first given by McCall et al. [94]. In the present context, we have studied this topology by FE method and compared it to the predictions of the PWE method [85]. Figure 3.8 depicts the resulting dispersion diagram calculated for the experimental setup raised by McCall, where a single rod has been suppressed amidst the square lattice of dielectric rods, for which the normalized rod radius is $0.38a$. The rod dielectric constant has been set to 9, as in the original McCall's work.

A 5×5 supercell has been used for the FEM calculations reported in this section. It has been discretized into 95903 mesh elements. A 3096 element grid has been used for the corresponding MPB calculations. The real part of the z-component of the electric field for the defect mode located at $a/\lambda = 0.4686$ was calculated at the Γ point of the 1BZ. The main drawback of the supercell approach is the band-folding effect: redundant bands of the unit cell are folded back N times (N being the linear dimension of the supercell). This fact leads

to larger computational times since the amount of eigenvalues to be solved grows $\sim N$. We have therefore solved eigenvalues for 211 points in K-space for 100 bands by both methods. Experimental results obtained by McCall and coworkers, MPB calculations, and FEM results fully agree as it is shown in Figs. 3.8 and 3.9.

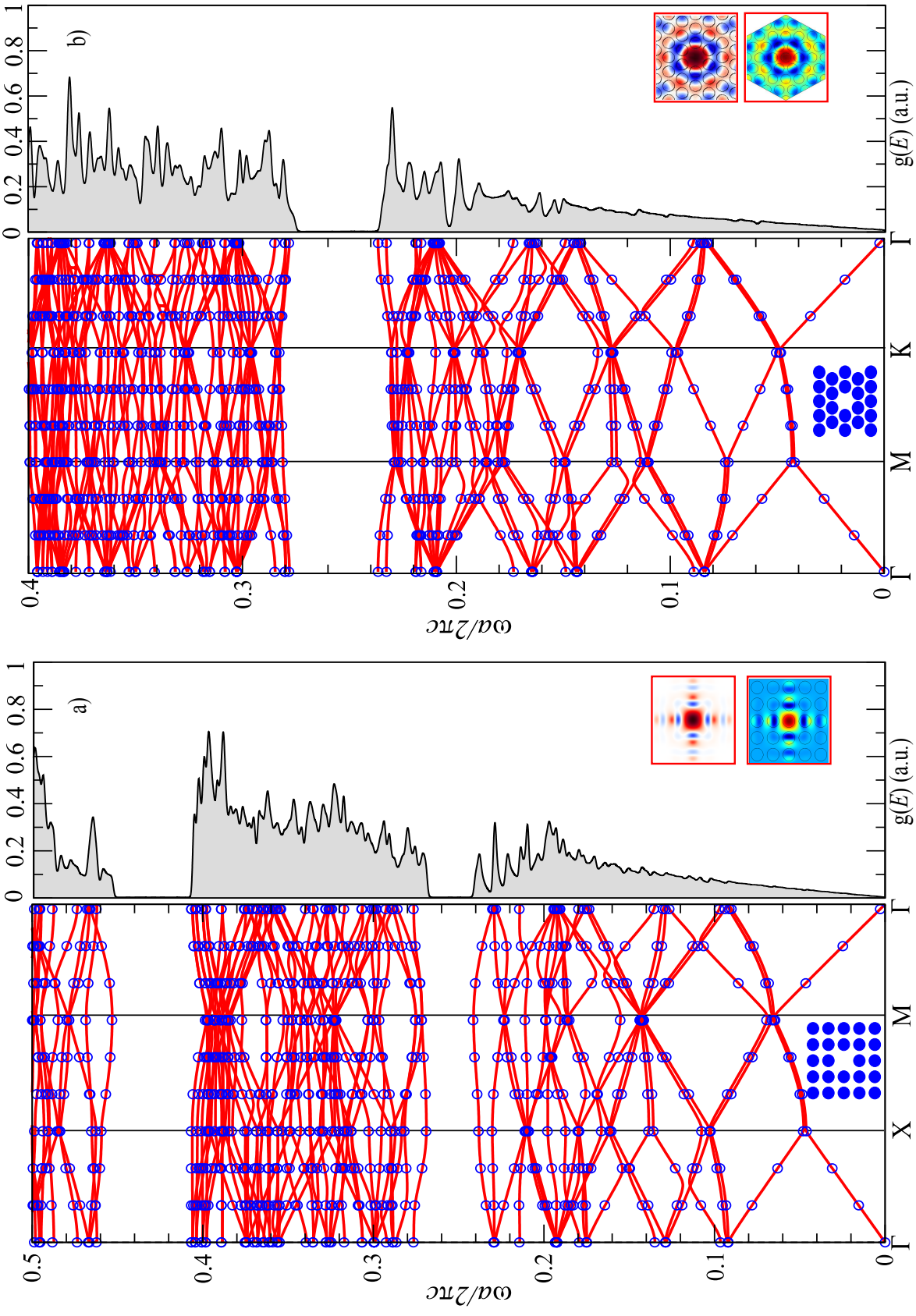

Figure 3.8 a) On the left: Band structure of a 5×5 square lattice periodic supercell calculated with MPB (blue circles) and FEM (red lines), wherein a defect state has been excited around $\frac{\omega a}{2\pi c} = 0.466 \pm 0.002$. On the right: density of photonic states (DOS), calculated by FEM. The band gap region is clearly distinguishable and a weakly localized defect mode merging from the upper band can be seen. In the inset, E_z patterns for a 5×5 supercell calculated by both methods are shown for the M symmetry point. b) On the left: band structure of a 5×5 triangular lattice calculated with MPB (blue circles) and FEM (red line). A single defect state merges at $\frac{\omega a}{2\pi c} = 0.285 \pm 0.003$. On the right: density of photonic states, calculated by FEM. In the inset, E_z patterns for the Γ symmetry point. An hexagonal supercell has been used for the FEM calculation .

Two modes make their way across the upper band gap region but only the defect mode depicted in Fig. 3.8a concentrates its energy around the missing rod.

The density of states (DOS) shows that perturbation of a single rod induces a series of sharp Dirac peaks centered at the frequencies where the defect state occurs. DOS calculations have been also computed via FEM by randomly sampling k-points constrained to the irreducible portion of the IBZ for each lattice. In the long wavelength limit, this quantity clearly exhibits the linear behavior expected for propagation in an homogeneous two-dimensional dielectric medium.

3.3.2 A triangular lattice of dielectric rods with a point defect

An analogous situation can be achieved by removing a single rod in a photonic crystal based on the triangular lattice. Fig. 3.8b shows the corresponding results for photonic crystal parameters adjusted just like Smith et al. [95] did in the investigation of defect mode structures in the square and triangular lattices. Rod radii and dielectric constant parameters of the triangular lattice supercell are the same as in the orthogonal case of Fig. 3.8a and, once again, FEM calculation and results obtained by means of PWE method coincide. The simulation setup was similar to the previously described one for the square lattice, but this time discretization of the supercell has been set to 71376 mesh elements. Furthermore an hexagonal supercell has been used for the FEM calculations, as its shape matches the reciprocal lattice of a periodical triangular arrangement. In both cases, square and triangular lattice point defect supercells, the electric field z-component is well localized around the defect neighborhood and rapidly decays to small amplitudes as one moves further from the defect. Also, the eigenfunction around the lattice irregularity clearly shows an inherent symmetry. Indeed, both lattices present a monopole pattern with a single nodal plane through each dielectric rod [4]. The symmetry of such point defect modes is analyzed in detail in [96].

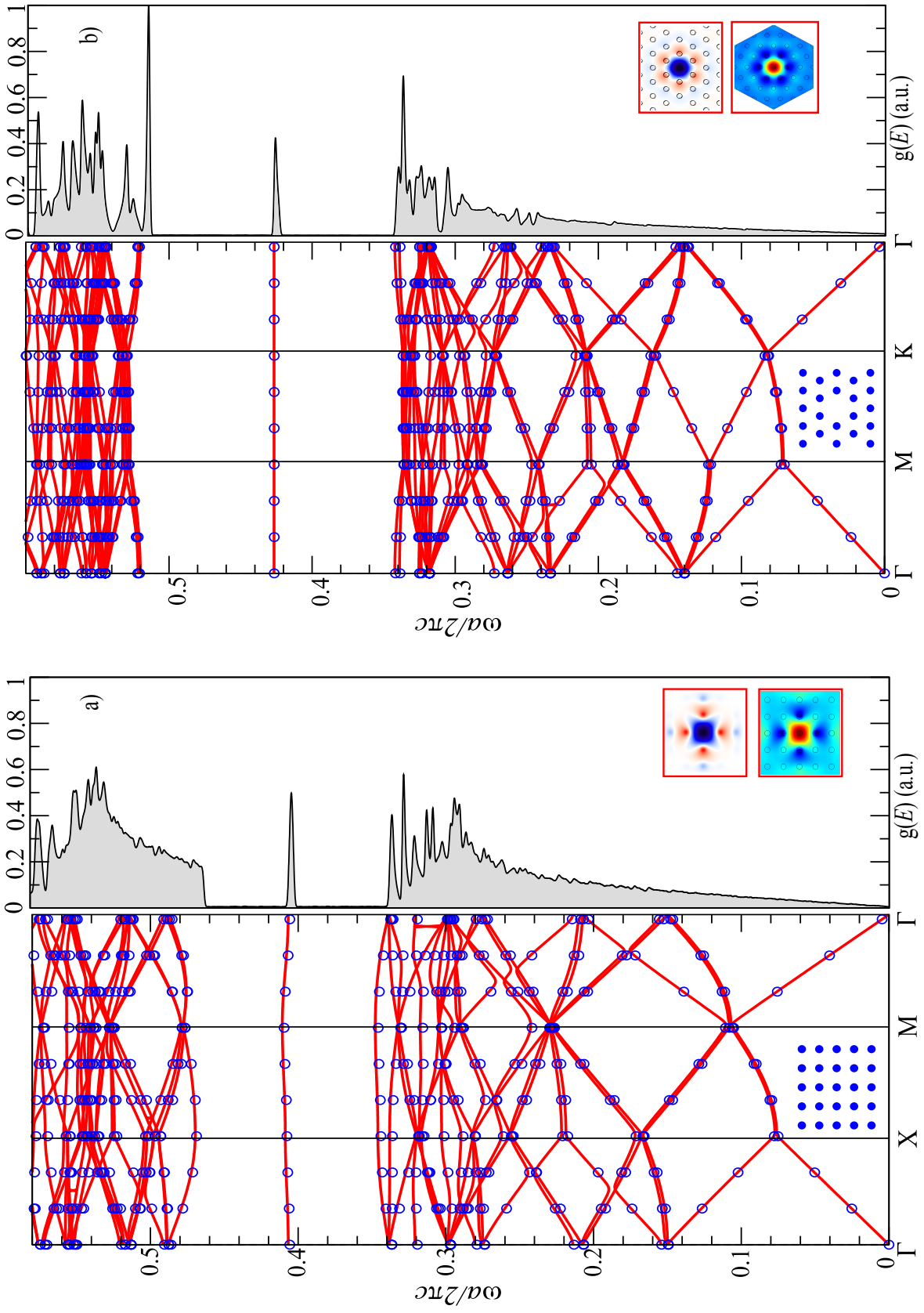

Figure 3.9 a) On the left: band structure of a 5×5 square lattice periodic supercell calculated with MPB (blue circles) and FEM (red lines). The rod radii has been set to $0.17a$, which ensures a better localization of the unique defect mode. On the right: density of photonic states, calculated by FEM. The defect mode clearly shows up in the gap region, since the defect state is strongly confined. In the inset, the E_z patterns for a 5×5 supercell calculated with both methods are shown for the M symmetry point. All these patterns match the ones presented in Fig. 3.8a but the modal volume decreases significantly for $0.17a$ rod lattices. b) Triangular lattice made of $0.17a$ rods where the central rod has been removed. The band gap increases and so it does the defect mode localization around the point defect.

The confinement of the electric field amplitude in the cavity is directly related to the band gap strength. Stronger mode localization has been observed for wider gap geometries. This is a highly desirable effect since the gap-mid-gap ratio can be easily tuned by adequately preselecting rod radii and dielectric contrast. For rods of dielectric contrast equal to 9 in square and triangular lattices, one can maximize the gap-mid-gap ratio for TE polarization by just adjusting the rod radii to $0.17a$. Band diagrams and DOS calculations for $0.17a$ radius rods for square and triangular lattice are reported in Fig. 3.9a and Fig. 3.9b. There, localized defect bands are strongly confined by a wider band gap. Moreover, these defect modes can be spatially translated into frequency by simply choosing the appropriate index contrast between lattice rods and point defect rod [4]. With regards to this mode tunability some important properties of photonic crystal cavities can be conveniently enhanced. Indeed, incremental design procedures have successfully been demonstrated by means of algorithmic techniques rather than using intuitive trial and error design methods, where the defect dielectric function is tuned according to design requirements [97–99].

3.4 Defect states in finite 2d photonic crystal clusters

All the structures studied so far had an infinite extension in all space directions. Nevertheless, an engineered photonic crystal must be finite sized. This fact limits defect mode confinement factor as stored energy will be finally radiated outside the cavity. This circumstance gives rise to a quantity of very much practical importance: the quality factor of a photonic crystal resonator, Q, which is just the ratio between the stored energy in the photonic crystal and the radiated energy per cycle. In the present context it is unnecessary to consider the radiated energy in the off-axis direction because the crystal has still infinite length in this direction, but inasmuch as the in-plane propagation will be limited to N periods of dielectric rods, electromagnetic fields will still be leaked outwards. Quantitatively, these energy decay mechanisms are uncorrelated to each other, and so they can be studied separately. On the other hand, in the present calculations no losses, absorptions, nor imperfections have been taken into account and, consequently, the quality factor is only limited by the inherent energy leakage from the cavity to the radiative modes.

When the photonic crystal sample is enlarged, by adding subsequent periods to the lattice, the transmittance spectra clearly reveals a sharp peak centered at the defect mode frequency. When one considers a larger cluster, the defect mode gets narrower, i.e. it converges to a Dirac delta. Simultaneously, there is a frequency shift due to the increment of the overall dielectric index percentage and new localized states may emerge from upper or lower transmission bands.

Transmittance diagrams have been obtained using the FEM but, in contrast with the transmittances reported above for ideal lattices, in this section a finite length design is regarded. Therefore, PMC and PEC boundary conditions were substituted by PML interfaces in the direction perpendicular to the incident wave vector as well as at the interfaces at which the EM wave enters and exits the structure. Accordingly, transparent influx conditions were imposed to the outer boundaries of the finite cluster and a TE polarized source propagating in the $\Gamma - X$ direction was considered. Spurious reflections are thus prevented from being injected back into the simulation domain by locating these artificial perfectly matched layers all around the simulation domain boundaries. The equations that describe such boundaries are given by

$$\vec{z}\cdot\hat{n}\times(\nabla\times E_z\hat{z}) - i\,k_0 E_z = -ik_0(1-\vec{k_0}\cdot\hat{n})E_{0z}e^{-i\vec{k_0}\cdot\vec{r}} \tag{3.3}$$

$$\vec{z}\cdot\hat{n}\times(\nabla\times H_z\hat{z}) - i\,k_0 H_z = -ik_0(1-\vec{k_0}\cdot\hat{n})H_{0z}e^{-i\vec{k_0}\cdot\vec{r}}, \tag{3.4}$$

where E_{0z} and H_{0z} are the initial values of the electric and magnetic fields at the boundaries, respectively, and $\vec{k_0}$ is the propagation constant. A set of monochromatic plane waves is excited for each frequency in the simulation domain. This way, a point defect is introduced in the topologies characterized in previous sections. The resulting transmittance results are depicted in Fig. 3.10.

When the size of the cluster is enlarged, the confinement of the defect mode increases and it converges to the previously discussed periodic case (Fig. 3.10). Additionally, the defect mode frequency is shifted due to the overall dielectric percentage change in the finite cluster which is indeed very convenient since it allows one to tune the resonance frequency according to dielectric index changes.

For the particular case of a square arrangement of dielectric rods with radius $0.38a$ and dielectric constant of 9, wherein its dimensions have been gradually modified, the energy stored in the defect mode centered around $\frac{a}{\lambda} = 0.4686$ is exchanged with the upper band energy situated around $\frac{a}{\lambda} = 0.49$. The sharpness of the defect mode transmittance in the case of a hexagonal structure yields a higher quality factor than the one exhibited by the rest of the clusters studied so far. This quality factor has been calculated by means of the transmittance response for each crystal, since by definition

$$Q = \frac{f_c}{FWHM}, \tag{3.5}$$

where f_c represents the central frequency of the defect mode and FWHM the difference between the two values in the transmittance function at which the transmittance is equal

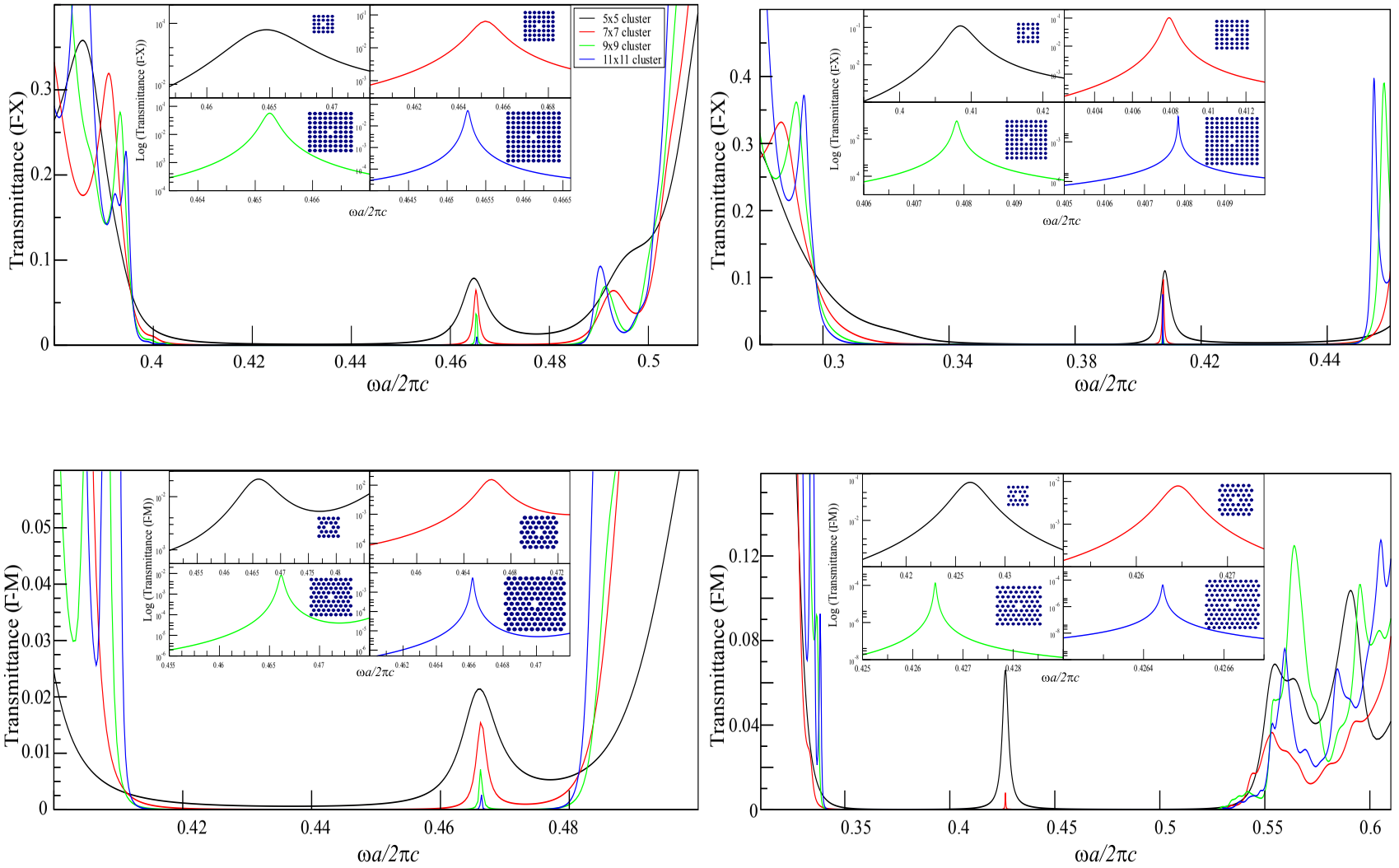

Figure 3.10 a) Top: transmittance diagrams for different cluster dimensions in a rectangular arrangement of dielectric rods with a central defect. On the left, rod radii is set to $0.38a$ while on the right $\frac{r}{a}$ is $0.17a$. In the inset, detailed defect mode curves are depicted.(b) Down: analogous transmittance diagrams in a triangular cluster.

to the half of defect mode maximum amplitude. For each quality factor calculation, the FWHM has been accurately determined by means of the Brent's algorithm [100], which combines bisection, regula falsi, and inverse quadratic interpolation methods for root finding. As the amount of dielectric rods surrounding the defect increases, the rate of the energy loss within the cavity relative to the energy confined in it decays exponentially. Figure 3.11 depicts the quality factor increment for these square and triangular clusters. According to that figure, the defect mode bandwidth decreases exponentially with the addition of new periods due to the strengthening of the band gap effect, which is the main contribution to the enhancement of the quality factor. The onset of the leakage mechanism transforms the localized modes transmittance spectra into distorted Lorentzian peaks. These peaks progressively tend to a Lorentzian curve when the defect mode gets closer to the mid-gap frequency and its FWHM gets narrower whenever N increases. Interestingly, a similarity can be established between a photonic crystal cavity, which is nothing but an air domain enclosed by rod-like mirrors, with a Fabry-Perot interferometer, where waves are refracted back and forth leading to a constructive interference pattern. In a Fabry-Perot etalon the radiation losses and hence the quality factor of the resonator is determined by the reflection coefficient of the surrounding mirrors when a phase matching condition is fulfilled. If the bouncing mode inside the etalon is assumed to be truly guided, i.e., losses from one mirror to another are disregarded, this reflection coefficient is limited by the mirrors reflectivity. Actually, it is very easy to demonstrate that a cavity formed within a 1D PC acts as the Fabry-Perot resonator. However it is not straightforward to establish such a connection in the case of a 2D PC. On the one hand, in Ref. [101] comparative results between Fabry-Perot model predictions, numerical data and experimental results suggest that a Fabry-Perot model is close enough to the light confinement in a PC microcavity. This fact could be truly advantageous for theoretical analysis, since the equations for a Fabry-Perot resonator are easier to solve than the EM field equations for a regular PC cavity. On the other hand, it could be a very useful mechanism to enhance certain aspects such as the reduction of radiative losses in the cavity or to decrease the group velocity of the localized mode. Finally, it is important to stress that this analogy should be exploited carefully, as certain cavities do not follow a Fabry-Perot model at all [101, 102].

3.5 Time domain approach: FDTD

As FDTD is the most popular method for the theoretical description of light propagation in these systems, we used FDTD in order to assess and compare the Q factor calculations attained so far using FEM. For the present manuscript, the FDTD simulations were performed

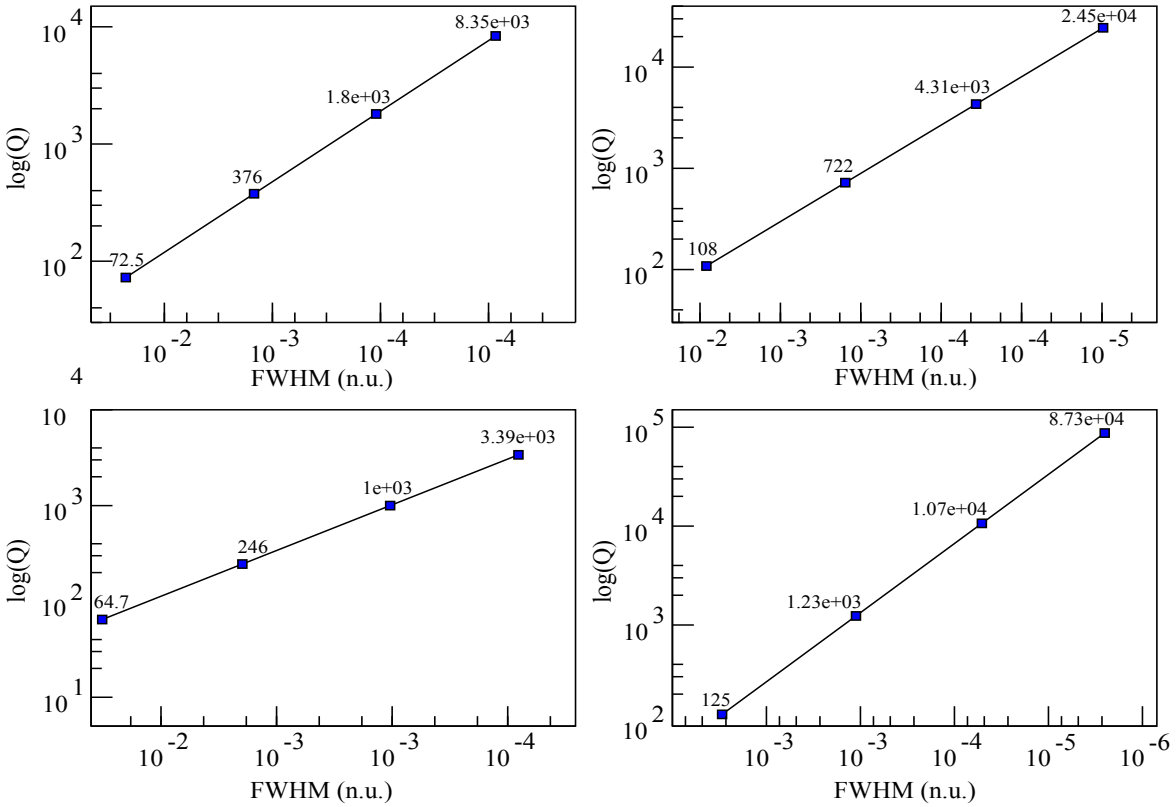

Figure 3.11 Top: quality factor estimation for a number of different sized square clusters of 0.38a radii dielectric rods (left) and 0.17a rods (right). Down: analogous computation results obtained for triangular arrangements.

using MEEP [107], a freely available implementation package of this method. The success of FDTD method is due to its flexibility and to its adaptability to irregular or aperiodic geometries. More generally, the FDTD method can compute a large number of frequencies at once and even extract modes of the spectrum. In FDTD space and time is divided into a finite rectangular grid and then fields are evolved in time using discrete steps. However, FDTD has serious limitations when the computational domain is finite whilst FEM convergence time is rather insensitive to this fact. In FDTD the computational domain must be terminated with some boundary conditions as it is the case in the FEM and, in order to simulate open boundaries in finite clusters, a wave absorbing mechanism, such as the split-field PML proposed by Berenger [104] has been used. Such an artificial region is needed so as to absorb outgoing spurious waves from the computational grid rather than reflecting them back into the photonic crystal. Moreover, quality factor calculations are very sensitive to the size of the computational grid and, thus, if the injected pulse experiences spurious reflections from the domain boundaries, radiated normal-incident waves will not be the dominant ones and they will be mixed with reflected waves. Using standard absorbing boundary conditions

(ABC), for which absorption is limited to waves radiated at some angles, a sizable part of the incoming flux is still reflected back, preventing the calculation of the quality factor of such a cavity. A later formulation of these absorbing layers, where artificial anisotropic absorbing materials are combined with ordinary PML layers known as Uniaxial Perfectly Matched Layers (UPML) [105, 106], partially overcome such problems. These UPML layers are in fact the ones implemented in MEEP. Along this artificial medium, the PML is expressed in terms of effective anisotropic ϵ and ν [107]. For the case of periodic media, not analyzed using MEEP in this report, the problem of reflective absorbing layers remains, but it can be mitigated by tuning the width of the so called *pseudo*-PML [107] and so attenuating the field during the reflection round-trip. For the present FDTD computation, a point Gaussian source has been placed inside the cavity. This excitation must be short enough (broad bandwidth) to excite the defect mode for each cluster. When this Gaussian source is switched on, the field grows and after some time this source is extinguished. Subsequently, a resonance effect occurs and the electromagnetic fields bounce back and forth for a limited amount of optical periods. Meanwhile, the energy trapped around the defect exhibits an exponential time decay (see Fig. 3.12). At this point, if one takes into account the slowly varying component only, i.e., the envelope of the electric field norm, the quality factor is determined by the ratio of the stored power divided by the loss power after one cycle:

$$Q = 2\pi \frac{|E_t|^2}{|E_t|^2 - |E_{t+T}|^2}. \tag{3.6}$$

In this type of calculations, the proximity of the UPML to the cluster significantly determines the decaying factor of the existing resonance. In the FDTD calculations reported in Table 3.1 an UPML of thickness $2a$ surrounds each structure. Besides, the distance between the UPML layer and the edge of the computational grid must be adequately tuned in order to avoid an unphysical field decay. According to this, a distance of $0.8 \leq d \leq 1.1$ has been used. Sampling the electric field response with a period relative to the resonance frequency, results in a quasi-periodic step function that induces some uncertainties in the Q factor determination if (3.6) is directly applied. These fluctuations could be due to the abruptly broken translational symmetry of the clusters. However, the marked decaying behavior of the electric field data can be easily filtered and interpolated. Therefore, by iteratively applying (3.6) to the interpolated sample field, an average Q factor and the corresponding theoretical error is obtained. Finally, in order to compare with previous Q factor calculations obtained via FEM transmittance results and FDTD decaying field value relations, an harmonic inversion of time signals (`Harminv`) [108] implementation has been used. This software package uses a filter diagonalization method (FDM) to find the deconvolution of sinusoidal functions near a given frequency interval. The simulation setup is the same as the one used in the

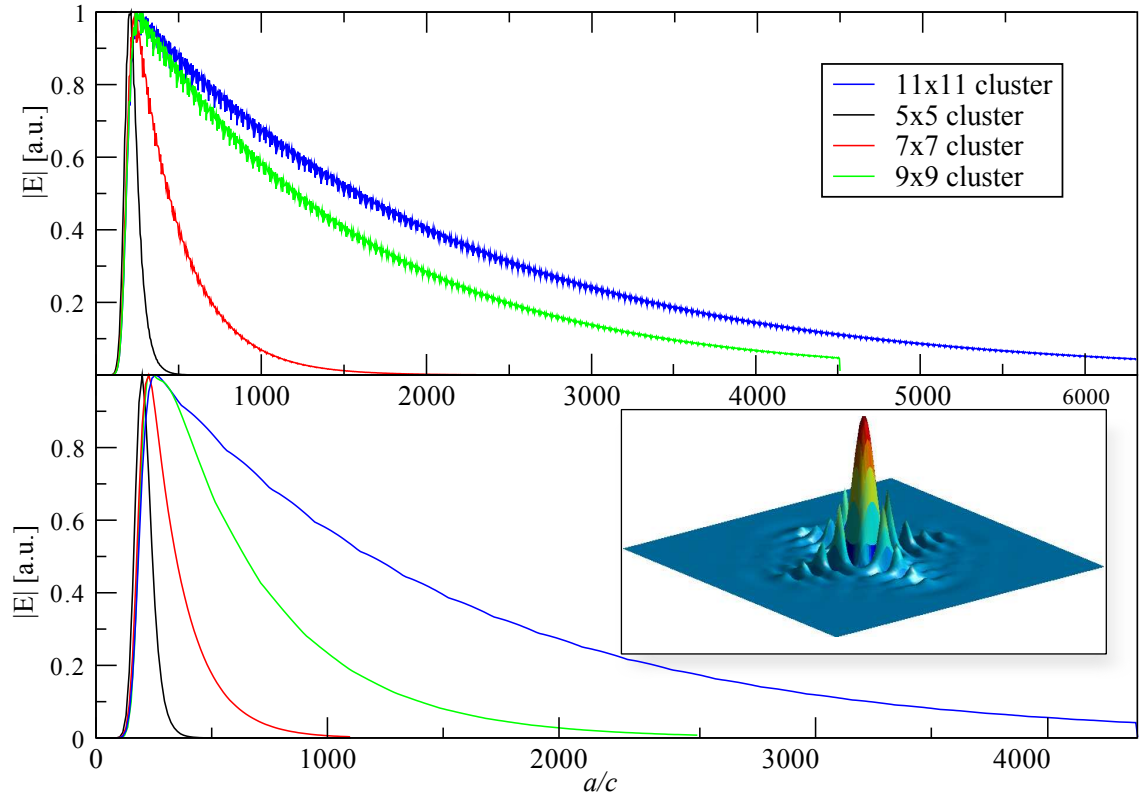

Figure 3.12 Top: evolution of the electromagnetic field inside the defect rod for a $0.38a$ arrangement and for different cluster dimensions. A point source is excited in the cavity but after some periods the source is extinguished and although the electromagnetic field still remains in the cavity it experiences an exponential decay. Down: analogous computation results obtained for triangular defect cluster.

standard FDTD calculations: a broad Gaussian point source located in the defect excites TE modes in the cavity and PML layers surrounding the cluster. In particular, a $\frac{a}{\lambda} = 0.02$ pulse width Gaussian source centered at the resonant frequency of each structure has been excited. When the source vanishes, `Harminv` performs the signal processing of the fields in the cavity. This way, it identifies the frequencies and decay rates of the excited resonant modes. This method is a fast and accurate way to determine the Q factors but still requires waiting until the fields have evolved and decayed to a certain small value. Computation time scales also with the cluster size, but this fact can often be overcome if symmetries are used to reduce the size of the computational cell. Besides, choosing a broad Gaussian source can yield to the appearance of spurious solutions but, at the same time, the source must be broad enough to excite the resonant frequency.

It is important to stress the remarkable agreement between FEM results, FDTD and Harminv calculations of the Q factor. Table 3.1 summarizes the results obtained using the

three methods described in this report. Two dimensional FEM calculation of Q factor offers satisfactory agreement with FDTD and `Harminv` results whilst providing substantial gain in solution robustness and efficiency. Indeed, FDTD is a powerful tool to calculate resonant frequencies and quality factors for complex cavity structures. However, it is very inefficient because one must discard many simulation cycles before reaching the stationary regime. Also, there are many heuristic factors that enter into the FDTD simulation process, such as the thickness of the UPML, the excitation source location and both its central frequency and width, that make the results from this method not as reliable as one would want. Moreover, when computing resonant modes in time domain special care must be taken to avoid choosing an excitation source nearly orthogonal to the resonant mode because FDTD is likely to miss it, otherwise. In this regard, FEM can be seen as an efficient, reliable and more rigorous alternative to FDTD for the analysis of quality factors and resonant modes in complex dielectric material.

	Square lattice r=0.38a			Square lattice r=0.17a		
Cluster size	FEM	FDTD	Harminv	FEM	FDTD	Harminv
5	72	80±1	88	108	113±13	107
7	376	350±3	347	722	727±6	723
9	1800	1773±24	1765	4310	4312±31	4308
11	8350	7677±83	7674	24500	24561±74	24559
	Triangular lattice r=0.38a			Triangular lattice r=0.17a		
5	97	107±2	103	134	130±1	126
7	358	320±1	316	1280	1171±8	1166
9	1240	1211±5	1209	11100	11241±42	11238
11	5270	5656±74	5650	90200	83903±84	83892

Table 3.1 Quality factor calculations for diferent cluster sizes in square and triangular lattice rod-type PC single-defect cavities using FEM, FDTD, and harmonic inversion methods.

3.6 Primitive PC light guiding structure

Likewise, in point defect lattices, the perturbations of the lattice can be created across one of the main crystalline directions of the photonic crystal. When this occurs, evanescent, standing waves or/and travelling single or multiple modes may break through the band gap. In this situation, the light is guided at subwalength scale with minimal propagation losses. A typical way to create such guiding devices consists in suppressing a single row of holes or rods in the periodic arrangement. Most theoretical studies performed so far have

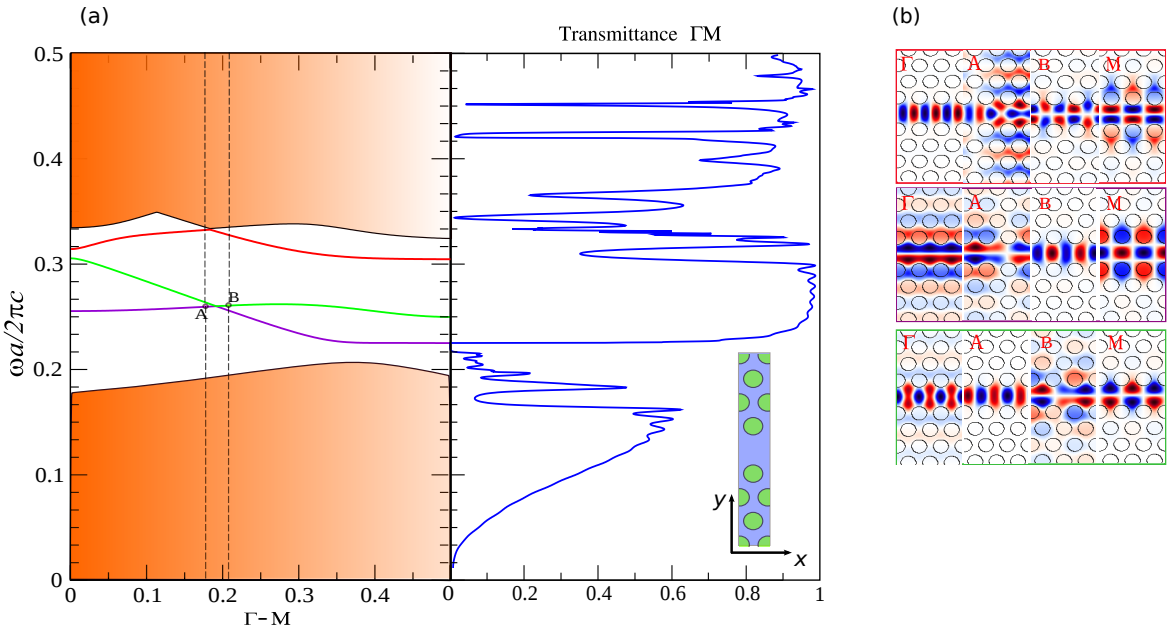

Figure 3.13 (a) Left: dispersion diagram for a one row missing infinite periodic 2D PCWG with 0.35a radius holes drilled in n=3.46 material. Right: Transmittance spectra. the insets shows the unit cell used for the calculation of the band diagram.(b) Hz field mode profile for the special directions Γ, M and near anti-crossing points that illustrated mode symmetry exchange.

investigated PC clusters comprised by dielectric rods-in-air geometries. Waveguides created from these topologies have the particularity of being single moded in the majority of cases. In these cases, guiding light through exotic paths is relatively straightforward. However, these configurations present serious radiative losses when a 3D-slab approach is used. In contrast, in holes-in-dielectric configurations the situation is reversed: the confinement of light in 3D-slab systems using these geometries is reasonably good while molding the flow of light in some bends, geometrical mismatches or splitting the light power requires using novel structures.

Fig. 3.13 depicts the dispersion diagram of a PC formed by a triangular lattice of 0.35a radius air holes drilled into Silica, being a the lattice period and 3.46 the refractive index of the Si material, which is assumed to be linear, isotropic and non-magnetic. We have considered a two-dimensional system where Bloch boundary conditions describe the in-plane periodicity and the z–direction extends infinitely. The index contrast between the Si and the air holes ensures the appearance of a photonic band gap for this PC in the frequency range $[0.22 - 0.31]$ whilst the line defect promotes some guided modes within the band gap. The PWEM was used once more to calculate this band diagram along the projected 1BZ, $\Gamma - K$, were the symmetry remains unbroken. In the inset of Fig. 3.13 a schematic

picture of a line defect is shown with one row of holes missing in the $\Gamma - M$ direction. W stands for the waveguide width, it is measured relative to a single row missing waveguide $W = a\sqrt{3}$. A cluster comprised of eight holes has been used. In order to save computational resources the PCWG cluster has been splitted by its symmetry plane and thus, only half of the cluster domain has been taken into account. So as to reproduce the mirror symmetry existing through the cut plane, perfect electric boundary condition has been set, which ensures that the component of the electric field tangent to the boundary is identically zero at the outer interface whereas perfectly matched layers are used for the outer interfaces in order to avoid unphysical reflection due to finite size of the cluster. For the band diagram calculation, a resolution of 32×32 (=1304) grid elements were used and the dielectric constant was average over 9 grid points. As it is customary, the dimensionless quantity $\omega a/2\pi c{=}a/\lambda$ has been used to characterize the frequency of the incident TM wave and λ the associated wavelength. The corresponding eigenmodes of the z–component of the magnetic field, H_z, were also calculated at $k = 0$, $k = 0.5$ and close to the anti-crossing point. On the other hand, Fig. 3.13.a shows also the transmittance spectra for a W1 PCWG cluster in the frequency range $[0, 0.5]$. It is easy to see that the transmittance clearly reproduces a partial gap in the band structure in the frequency region $[0.216, 0.224]$ where the transmitted intensity is very small. As expected, the introduction of the linear defect promotes three guided modes inside the band gap region. The guided modes of the present W1 PCWG are presented by thick coloured lines. The coloured area corresponds to the modes outside PBG region which in the air band are guided in the bulk PC and hence are not confined to the line defect and in the valence band are mainly index guided modes. There are three continuous dispersion curves in the PBG region with different symmetry profiles. The symmetry of the eigenmodes is defined by its magnetic field regards to the existing mirror plane in the waveguide center along the z–direction. The upper mode coloured in red leaks to the air band and them merges with even symmetry. The other modes are rather interesting because they are guided all along the $\Gamma - M$ direction and besides they interact with each other at an anticrossing point. Before the anticrossing occurs, both modes have a fundamental mode profile, then, after the anticrossing, the symmetry of both modes is exchanged and they acquire a shape of second order mode being. This phenomena is clearly appreciated in Fig. 3.13. In the W1 waveguide shwon in Fig. 3.13 the anticrossing occurs close to 0.188. There is an intrinsic interaction of even gap guided and index guided modes.This interaction forms two supermodes, which are represented by the sum of gap guided and index guided modes in phase and anti-phase.

Periodic waveguides like the one depicted here, are both useful and challenging for the same reason: a periodic waveguide has a slow-light band edge, for which the group velocity of light slows down as it approaches a certain frequency. Operating in this slow-light region

is useful because it increases the interaction of the light with the material, enhancing features like non-linearities gain and other effects. Due to the fast variation of the group velocity at the anticrossing point, the group velocity dispersion has a maximum near 0.1888. This effect is very similar to the coupling of two different waveguides except that here two modes from the same waveguide are coupled [109].

3.6.1 The photonic crystal slab waveguide

Two dimensional photonic crystals posses an infinite elevation in the z–direction and thus, they are theoretical structures that can hardly constitute practical materials for future real world applications. In regards to this fact, many 3D–PCs have been proposed so far [110, 111], however, complete 3D PCs are still very challenging due to their complex structure nature [112]. Alternatively, PC slabs are very handy as they can be fabricated using the standard lithography methods and they still offer satisfactory light guiding. PC slabs preserve the two-dimensional periodicity but rely on index guiding to further confine light in the out of plane direction. This results in a preservation of some desirable properties of the former 2D–PCs. It is still possible to relate the properties of PC–slabs with analogous 2D–PC structures as the one depicted in Fig. 3.13 [113], however, as the z–plane is no more infinitely extruded, and so, a continuum of states merge for every out-of-plane propagation [26]. Photonic crystal slabs can still allocate linear defects as the ones used hitherto to form PCWGs. Despite the resemblance to the former 2D-PCWGs, the later can lead to manufacturable PCWG devices. With such building blocks, many interesting devices have been experimentally realized using standard lithographic techniques based on two-dimensional patterns. This ease of fabrication comes at a a price, since the lack of periodicity in the z-direction raises new limiting factors. The primary difference between the case of a slab and the case of a truly two-dimensional photonic crystal is that the band diagram of the slab has a light cone. The light cone will force the leakage of guided modes into the air region and in some cases, if the PCWG is not rightly designed, can completely inhibit the localization of guided modes. Yet, the thickness of the slab assumes a prominent role in determining the properties of PC slabs. In this section a suspended membrane structure has been considered, i.e. a Si structure surrounded entirely by air. The system is invariant under reflections through the $z = 0$ plane. This symmetry permits to classify the modes as TE-like (even) and TM-like (odd). Air bridge PC slab waveguides provide very strong vertical mode confinement and can greatly reduce the losses associated with leaky waveguides and scattering from the bottom of the etches holes. Fig.3.14 plots the projected band structure along the Γ-M direction of the 1BZ of a W1 PCWG slab. Many features of this band diagram resemble to the one depicted in Fig.3.13. However, in this case, there is a light cone in $\omega \geq c|k|$ upper limits the diagram, covers extended modes that

propagate in air. Now, in a PC-slab, as the structure is no longer infinite in the z direction, the overall effective dielectric index is reduced and consequently the guided bands are pulled up. Moreover, due to the lack of periodicity in the elevation plane, the confinement of light in z-direction is only due to the index guiding phenomena. Inasmuch as the band gap operates only for in–plane confinement, leaky modes, namely, guided modes that suffer an exponential decay at the boundaries of the upper and lower surfaces of the PCWG arise. The reduction of the out-of-plane radiation losses is essential for applications. The dispersion diagram of

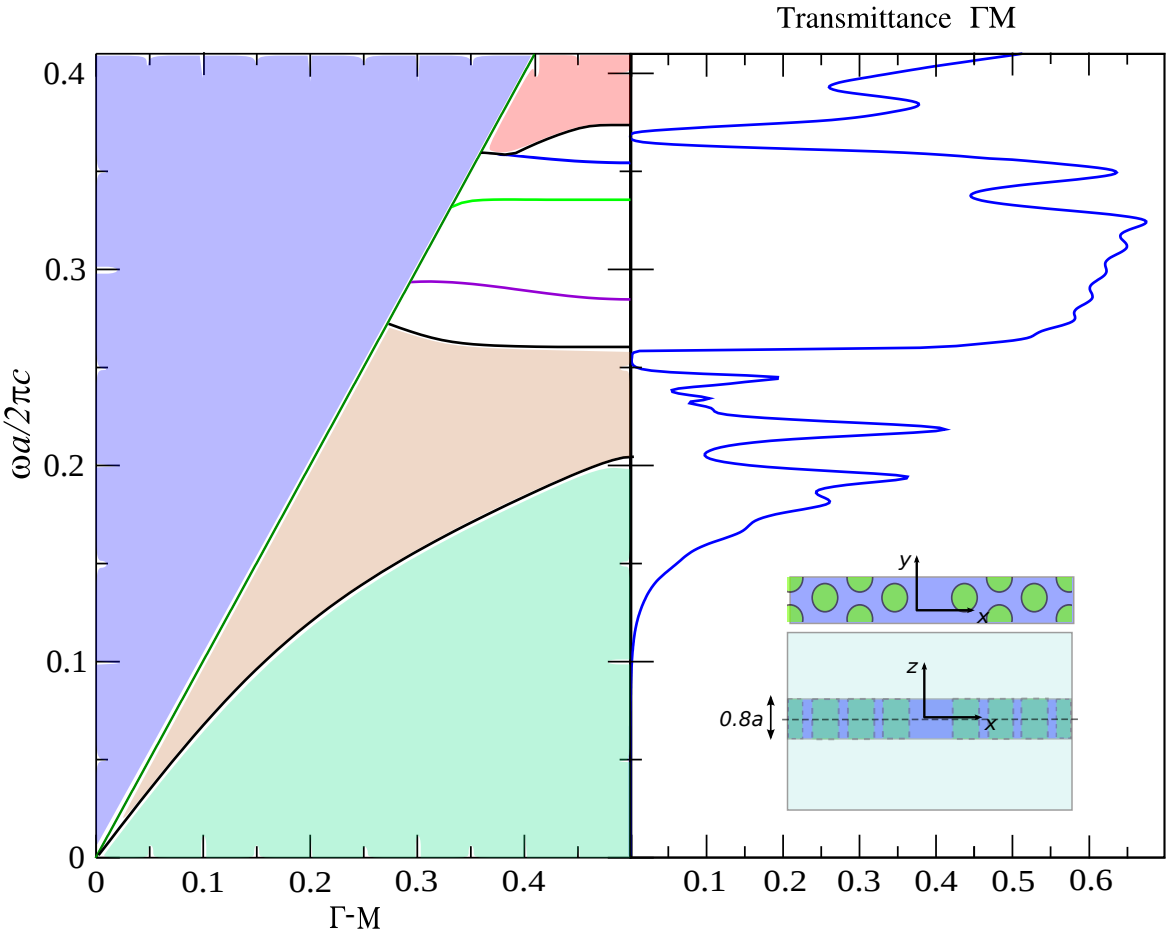

Figure 3.14 Left: Projected band diagram of TM-like (z-odd) states for a W1 defect in the hole slab, formed by a missing row of nearest-neighbour holes along the y–direction with a thickness of d=0.8a suspended in air. Blue region represents the modes above the light cone $\omega \geq c|k|$. Light-red shaded regions indicate bulk modes of the PC or extended TM-like modes of the crystal. Guided modes are introduced both in the gap and below all of the extended modes of the crystal (green region). Modes in the green region are mainly index guided modes. Guided modes are classified as z–even or z–odd according to the $z = 0$ mirror symmetry plane bisecting the waveguide. Right: transmittance diagram for a W1 PCWG.

the W1 PCWG slab clearly shows three guided modes. 3D-FEM transmittance calculations

also depicts these features (see Fig.3.14). In this model, a $2a$ thickness air region was placed covering the W1 slab. Owing to the symmetry of the structure, the simulation set up has been reduced to the one depicted in the inset of Fig.3.14. PMC boundary conditions were used in the z= 0 cut-plane. The remaining geometry was discretized in 236.399 elements and solved using a Generalized Minimal Residual method (GMRES) solver. The choice of the thickness of the slab should be considered carefully. If the slab is too thin, then bands are weakly guided and may not even be guided at all. States that lie just below the light line decay very slowly into the air regions. In some cases, the light line can even overlay the upper boundary of the band gap, and so the modes become completely delocalized regardless of the chosen in-plane geometry. On the other hand, the larger the thickness of the slab the more similar will be the band diagram to the case of a 2D-PCWG shown in Fig.3.13. However, for a thick slab, higher-order modes are pulled down and populate the gap. All the same, the bad gap size is not a critical limiting factor for PC slab structures and thus, it is not necessary to search for the strictly optimal thickness. Normally, a customary thickness is chosen for a PC slab as given in [26] it should be close to a value of $0.6a$ [4] or a thickness value constrained by the fabrication process. In this case and hereinafter, a value of $0.8a$ is used.

Chapter 4

Constrained heuristic and genetic techniques for Inverse Designing nanophotonic structures

Heuristic and genetic algorithms provide an alternative to custom optimization techniques using directed random searches to locate optimal solutions in complex landscapes. In complex photonic structures, such as photonic crystals, partial disorder plays a critical role in practical applications, specially in those where light is localized and guided in non trivial lattices. Whereas disorder discloses several advantages to control the flow of light and enchances non-linear features in these materials, breaking the peridicity makes the modelling process very hard. With this regards we devote this chapter to describe the heuristic and genetic algorithms used to generate optimized photonic structures shown in the next chapter.

4.1 Introduction to computational complexity

In computational complexity theory, a decision problem is classified as a NP (non-deterministic polynomial-time) decision problem [114], when it is only solvable in a polynomial amount of time using a non-deterministic Turing machine. Such machine though, is a mere abstract mathematical concept that determines the solution of a generic problem by following a set of rules that prescribes more than one action for a given situation. In esence, the former definition states that there is no known way to solve a NP-problem using a conventional deterministic approach, as the time required to solve the problem using any currently known method increases very quickly as soon as the size of the problem grows. Instead, an algorithm that displays the functionalities of a Turing machine, i.e., a transition function regarding a

number of predefined constraints, could lead to a *good enough* solution using a reasonable amount of time. Further, a subset of NP decision problems, known as NP-complete problems are one step beyond the complexity level of NP problems. In fact, nobody has yet been able to determine conclusively wether NP-complete problems are in fact solvable in polynomial time, making this one of the great unsolved problems of Mathematics. The thorough exploration of the solution in any of such problems involves an unaffordable amount of computational time that grows exponentially with the amount of N inputs (unknowns) considered by the problem (footnote: unless N=NP is proven)(and some problems may require even more time [115]). Unffortunately, this class of problems are rather common in real life applications such as vehicle routing [116–118], shop scheduling [119, 120], multiprocessor scheduling [121, 122], or integer programming [123, 124], just to cite some. Two subsidiary features are of general interest in NP-complete class problems: predicting the expected optimal solution and stimating or obtaining bounds for the computing effort necessary to determine that value. Nevertheless, there have been extensive effort to find substantially fast, though still superpolynomial time requiring algorithms to alleviate the search of good solutions to those problems. In practical uses, instead of spending computational resources looking for an optimal solution, a good enough (but potentially suboptimal) solution may often be found using some of the approaches assorted below:

- Randomization: this approach uses randomnes to get a faster average running time relying on repeated random sampling to obtain numerical results. From a sufficiently large number of samples, a Monte Carlo [125–127] based approach, or a more sophisticated encoding of a Markov chain Monte Carlo based predictions can be used to get to a stimated result. This approach in widely used, combined with other methods, in systems with many defrees of freedom such as in the disordered materials that are described in the next chapter.

- Approximated methods: these algorithms take advantage of some previous knowledge of the problem to do a restriction of the search space by fixing some of the parameters, and thus they lead to fast solutions. However, bounding the search, according to some degree of intuition, could also be misleading and there is no guarantee that no better solutions were disregarded in the optimization proccess due to the initial assumptions taken by the algorithm designer.

- Heuristic methods: these methods are typically used when there is no known way to find an optimal solution, or when it is acceptable to give up finding the optimal solution for an improvement in the run time. They do not attempt to find the best result to a certain problem, albeit they do their best in order to achieve a close to optimal solution, which is

normally more than enough in NP-Complete problems. These methods introduce some probabilistic operators to control the search process during an iterative optimization process. There are two fundamental reasons that promote the use of these methods. On the one hand, heuristic methods can be easily modified to be applied to a wide range of applications and problems. On the other hand they provide a good balance between the computational time required to converge to a solution and the quality of the obtained results. More insights about heuristic algorithms are given in the next section.

4.2 Heuristic methods

The subject of combinatorial optimization, which is the basis of any heuristic algorithm, is a long term discipline that has been extensively applied in computer science and engineering, specially during the last 10 years. Research in this area aims at developing efficient techniques for finding minimum or maximum values of a function of many independent variables comprising a NP or NP-complete problem. Throughout this thesis we will often refer to this function as the cost function or the objective function and to the fitness with regards to the quantitative measure of the *goodness* of the complex system under the optimization process [128].

The classic example, because it is so simply stated, of a combinatorial optimization problem is the traveling salesman problem. Given a list of N cities and a means of calculating the cost of traveling between two cities, one must plan the salesman's route, which will pass through each city once and return finally to the starting point, minimizing the total cost. When a deterministic approach is used to solve the traveling salesman problem (and indeed any problem belonging to the NP-complete subclass) the computation effort scales exponentially with the number of parameters (N cities in this case) considered in the route, so that in practice exact solutions can be attempted only on problems involving a few hundred cities or less.

No method for exact solution with a computing effort bounded by a power of N has been found for any of these problems, but if such a solution were found, it could be mapped into a procedure for solving all members of the class. It is not known what features of the individual problems in NP-complete class are the cause of their difficulty. Since the NP-complete class of problems contains many situations of practical interest, heuristic methods have been developed with computational requirements proportional to small powers of N [128].

Heuristic algorithms commonly apply two different and complementary strategies for finding the global optima: divide and conquer ant iterative improvement. The former relies on dividing the problem into subproblems of manageable size, to subsequently solve each

subproblem. The solutions of the subproblems must then be patched back together. For this method to produce very good solutions, the subproblems must be naturally disjoint, and the division made must be an appropiate one, so that errors made in patching do not offset the gains obtained in applying more powerful methods to the subproblems. In iterative improvement, the algorithm evaluates the cost function of a given starting configuration. During an iterative process, the algorithm will rearrange the parameters of the system until a configuration that improves the cost function is discovered. Then, the algorithm will perform a downhill/uphill movement and the process will be repeated until no further improvement is found, or a fixed number of iterations are performed. However, these two mechanism do not neccesarily ensure that the algorithm will yield to a global optima result. Indeed none of these two proceedings implement an efficient way to scape from local optima. A naive method to do so could be to carry out the optimization process several times, starting from different randomly generated configurations, and save the best result. However, most of the heuristic methods implement tools to scape from the local optima wihout having to run the algorithm a number of times. These tools are i.e. probabilistic operators where a controlled degree of randomnes takes part. Because of this probabilistic operators, the results achieved by a certain run of the algorithm will mostly not match the ones achieved in a different attempt and in some cases the algorithm could not converge to a solution or, conversely, converge to a solution too fast, disregarding best solutions.

As long as there is no guarantee that a specific heuristic proecedure will be more succesful than another in the task of designing efficient photonic crystal structures, we addressed to three different heuristic methods, namely the Fast Simulated Annealing (FSA) [129], the Improved Harmoy Search method (IHS) [130] and the Non Sorting Genetic Algorithm II (NSGA-II)[132]. The FSA algorithm is a classic heuristic algorithm, though probably outdated, which use has noticeable decayed nowdays with the flourishing of new algorithms. However, it has proven to be very effective in a wide range of applications [133–139] and since there is no benchmark in photonic applications to compare with, we decided to use this algorithm and test its validity against the IHS algorithm, which is very popular right now. On the other hand, the NSGA-II is a more sophisticated genetic algorithm algorithm that allows to simultaneously optimize more than one objectives at the same time.

4.2.1 The Fast Simulated Annealing method

Simulated annealing (SA) technique is a well known meta-heuristic ground state search method that has been commonly applied to combinatory optimization (CO) problems [140–145]. The term simulated annealing comes from the process of annealing in metallurgy, a technique involving heating and controlled slow cooling of a material to increase the size of

its crystals and reduce their defects. The heat causes the atoms to become unstuck from their initial positions (a local minimum of the internal energy) and wander randomly through states of higher energy. The slow cooling gives them more chances of finding configurations with lower internal energy than the initial one, that is, a global minima. This method implements the ability to avoid the local optima points from the search space, which is the main drawback of simpler optimization techniques such as Hill Climbing (HC) method. For this regards it provides a mechanism to implement a non-zero probability for accepting uphill solutions which do not lower the energy of the system. The theoretical foundation of SA was led by Kirkpatrick et al. in 1983 [128], where they applied the Metropolis Monte Carlo algorithm [146], to include an artificial temperature schedule for controlling the acceptance probability of uphill moves. [1]

The method of simulated annealing consists of three functional relationships [149].

1. $g_T(x)$: Probability density of state-space of D parameteres $x = x^i; i = 1, \ldots, D$ where the subscript T means a parametrization popularly referred to as the temperature.

2. $h(\Delta E)$: Probability for acceptance of new cost-function given the just previous value.

3. $T(k)$: schedule of annealing the temperature T in annealing-time steps k, i.e., of changing the volatility or fluctuations of one or both of the two previous probability densities.

The acceptance probability is based on the chances of obtaining a new state with energy E_{k+1} relative to a previous state with energy E_k. The probability of acceptance of a new cost function follows a Boltzman distribution, which can be writen as follows [150]:

$$h(\Delta E) = \frac{e^{\frac{-E_{k+1}}{T}}}{e^{\frac{-E_{k+1}}{T}} + e^{\frac{-E_k}{T}}} = \frac{1}{1 + e^{\frac{-\Delta E}{T}}} = e^{\frac{-\Delta E}{T}}, \tag{4.1}$$

where ΔE represents the energy difference between the actual fitness of the cost function and a previous value of the cost function i.e., ΔE = fitness$_{k+1}$ - fitness$_k$. Initially the temperature parameter, T, is set to a high value. The high temperature value ensures that at the very early stage of the optimization process, a set of parameters that yields to a worse fitness value has a high chance of being accepted as an uphill movement. This process is the so called diversification stage, in which the algorithm performs a extense exploration within the search space, sacrifying some local optima values. Then, during the cooling process, the amount of

[1] However, independent credit usually goes to several other authors for independetly developing the simulated annealing algorithm [147, 148].

uphill movements is subsequently reduced and the algorithm aims to improve the fitness of the cost function by doing a thorough exploration around the local optimum.

Several alternative SA schemes have been proposed so far [151, 152], but most of these algorithms impose mayor changes in the SA implementation. In contrast, the Fast Simulated Annealing (FSA) algorithm [129] reduces significantly the required running time of the standard SA algorithm by performing a semi-local search and enhances the efficiency of the optimization process by performing a more exhaustive search around local optima points by further controlling the number of long uphill junps done in the search process of the global optima. Indeed, when the cost function has a single minimum, the conventional SA method can rapidly provide the unique ground state, and moreover, any method of gradient descent can approach the minimum. However, when the cost function has multiple extrema, a nonconvex optimization technique that allows tunneling, variable sampling and accepting hill-climbing for escaping from local minima is required. With this regards, Szu et al.[129] reformulate the acceptance probability $g(\Delta x)$, in D–dimensional space, into a Cauchy-Lorentz probability distribution as follows:

$$g(\Delta x) = \frac{T}{((\Delta x)^2 + T^2)^{\frac{D+1}{2}}}. \tag{4.2}$$

In practice, the Cauchy distribution is preferred over the normal or Gaussian (Boltzman) distribution because of its flatter tail that permits to explore more exhaustively for local minima [129]. As a result, the FSA method has an annealing schedule exponentially faster that the method of standard annealing. Once a local optimum solution is found, the FSA algorithm leads to the standard SA process, in which uphill moves are accepted with regards to a high temperature parameter. This temperature parameter is gradually decreased, according to a smooth cooling process. The algorithm systematically reduces the value of this temperature parameter regards to the annealing parameter k, which is the same as the iteration number unless a re–annealing is carried out. We proceed to update the temperature parameter as follows:

$$T = \frac{T_0}{k}, \tag{4.3}$$

where T_0 is the initial temperature of the i-th component, and k is the annealing parameter for component i. Smaller temperature leads to smaller acceptance probability. Also, larger Δ leads to a smaller acceptance probability. This unintuitive step sometimes helps to identify a new search region, i.e., by accepting points that raise the objective, the algorithm avoids being trapped in local minima in early iterations and is able to explore for better global solutions.

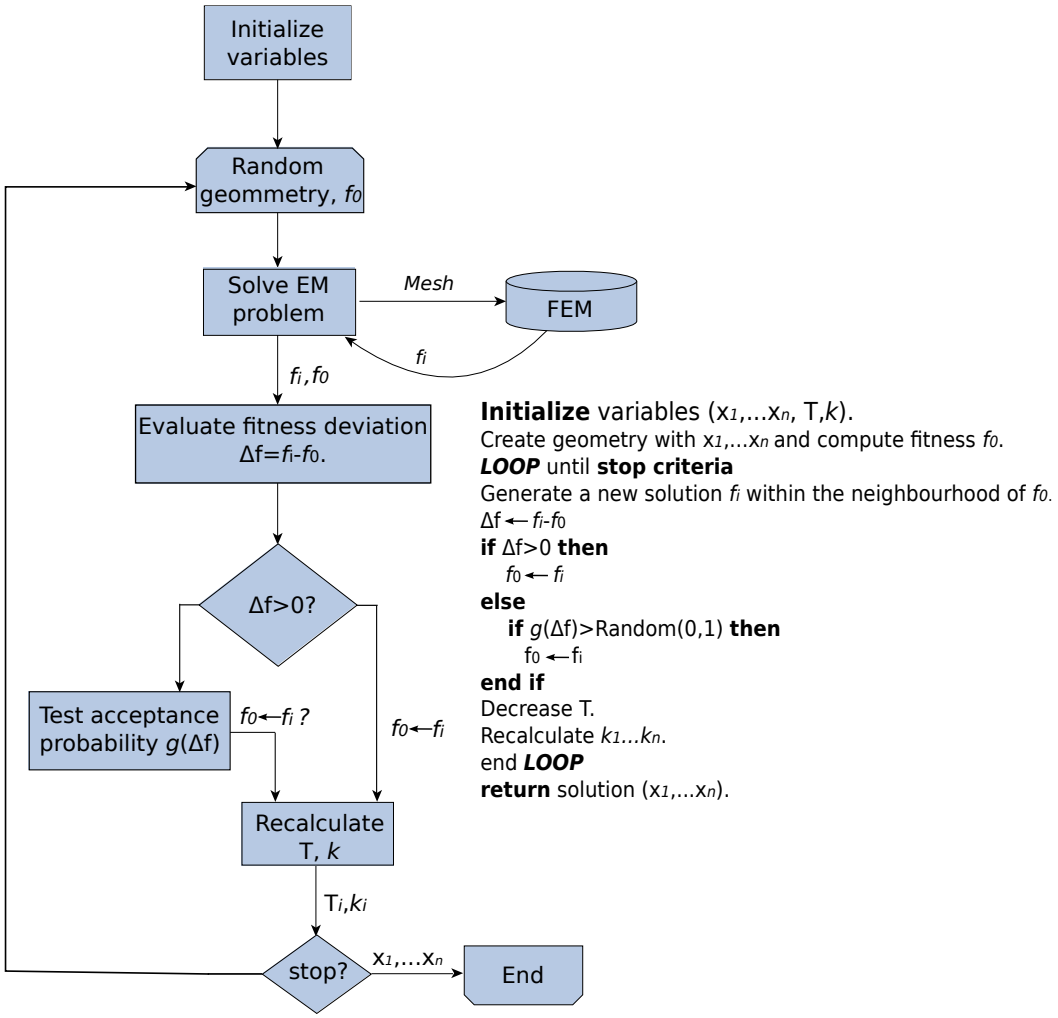

Figure 4.1 Flow chart and pseudo-code for the FSA algorithm implemented in this manuscript.

In addition, we have included a re–annealing scheme to the FSA algorithm. The reannealing attempts to unveil the range over which the relatively insensitive parameters are being searched, relative to the ranges of the more sensitive parameters. Re–annealing sets the annealing parameters to lower values than the iteration number, and raises the temperature in each dimension according to the estimated gradients of the objective function in each dimension. The annealing parameter for component i, k_i is given by the following basic formula:

$$k_i = \log\left(\frac{T_0}{T_i}\frac{max(s_j)}{s_i}\right), \tag{4.4}$$

where T_i is the current temperature for component i, and s_i is the gradient of objective in direction i times the difference of bounds in direction i. Finally, the algorithm stops when a predefined number of iterations are fulfilled and the deviation of the fitness function,

Δx converges. In Fig. 4.1 a flow chart and a pseudo-code of the FSA algorithm utilized throughout this work is detailed.

4.2.2 The Improved Harmony Search algorithm (IHS)

The Harmony Search (HS) algorithm is a meta-heuristic optimization algorithm inspired by the observation of musical improvisation process, in which the aim is to search for a perfect state of harmony. HS was proposed by Geem et al. in 2001 [153] and thenceforth it has been widely applied to a variety of combinatory optimization problems [154–156]. HS was developed to delve with continuous design variables in real world optimization problems, by avoiding the use of derivative information of the objective function and relying instead in stochastic random search. Conceptually, HS lays out an analogy between the actions performed by a jazz ensemble in the process of searching for the most harmonious melody and an engineering optimization method that improvises potentially optimal functions to the target problem. To do so, the musicians are represented by the set of decision variables, the harmony improvised at a certain time refers instead to the solution vector given at a certain iteration and the musicality of the harmony itself is quantized by the fitness of these cost functions. Therefore, in the same way that musicians play together to improve the melody, trying new notes and chords, and slowly refining the melody, the Harmony Search algorithm iteratively improves the fitness of the solution vector [157]. Further, during the process of musical improvisation, suggesting a new melody is subject to three different circumstances: a musician can either play a tune exactly in the way he has memorized or he can play something similar to a stored melody (eg. slightly adjusting the pitch), or compose new notes randomly. Based on these three options, Geem et al. made a new quantitative optimization process. These three corresponding components became: memory usage of harmonies, pitch adjustment and randomization. Following the analogy of musical inspiration, HS algorithm adopts the terminology used in music, e.g., each candidate vector is renamed as an harmony and each harmony is composed by elements known as notes. On the other hand, the Improved Harmony Search (IHS) algorithm [130] is a modified version of the original HS algorithm. IHS employs a novel method for generating new solution vectors to enhance the accuracy and convergence rate of the original HS algorithm. In particular, the IHS algorithm improves the efficiency in terms of convergence rate in performing a local search. The steps in the procedure of the IHS algorithm can be summarized as follows:

- Initialize the optimization problem and algorithm parameters. The optimization problem is usually defined as a minimization problem

$$\text{Minimize}, f(x): \quad \text{s.t.}: x_i \in X_i, \quad i = 1, 2, ..., N, \tag{4.5}$$

where $f(x)$ is the objective function; x is the set of each design variable x_i, N is the number of decision variables, X_i is the set of the possible range of values for each design variable, that is, ${}_Lx_i \leq X_i \leq {}_U\ x_i$ (for a continuous domain), and ${}_Lx_i$ and ${}_Ux_i$ are the lower and upper bounds of each decision variable, respectively. The HS algorithm parameters that are required to solve the optimization problem are also specified in this step:

- The harmony memory (HM): a matrix comprising the whole set of candidate solutions. In the initialization process the HM will be filled with random values according to ${}_Lx_i$ and ${}_Ux_i$.
- The harmony memory size (HMS): is the number of solution vectors in the harmony memory.
- The harmony memory considering rate (HMCR): the stochastic operator that defines the probability of choosing a note from the HM to generate a new harmony.
- The pitch adjusting rate (PAR): defines the probability of adjusting the pitch of a note within the set of harmonies stored in the HM.
- The random selection rate (RSR)[158]: it sets the probability of choosing a random value for a given note in the HM. Despite this operator is not present in the original HS algorithm and neither it is in the IHS algorithm, we decided to include it so as to introduce an additional randomization source in our code.
- The stopping criterion: usually fixed to a number of iterations or improvisations (NI) done by the algorithm during the optimization process.

The stochastic operators HMCR, PAR, RSR, are explained in more detail below in sec. 4.2.3

- Initialize the harmony memory with random data bounded within the feasible search space. Then these solutions are evaluated and shorted according to each fitness value,

$$HM = \begin{bmatrix} x_1^1 & \cdots & x_n^1 & | & f(\mathbf{x}^1) \\ \vdots & \ddots & \vdots & | & \vdots \\ x_1^{HMS} & \cdots & x_n^{HMS} & | & f(\mathbf{x}^{HMS}) \end{bmatrix}. \tag{4.6}$$

- Improvise a new harmony. The new harmony is created using the existing harmonies found in HM, $x' = (x'_1, x'_1, \cdots, x'_N)$. The value of a certain design variable x'_i for the new harmony can be arbitrarily chosen from any value in the HM. Here, it is possible

to choose the new value using the HMCR parameter, which varies between 0 and 1 as follows:

$$x' = \begin{cases} x'_i \in x_i^1, x_i^1, \cdots, x_i^{HMS} \\ x'_i \in X_i \quad \text{with probability} \quad (1 - HMCR) \end{cases} \tag{4.7}$$

Thus, the probability of choosing a certain value from HM for a new note x'_1 is determined by the HMCR probability operator and, otherwise, x'_1 takes a value distinct from the ones sorted in HM, with probability $(1 - HMCR)$. Subsequently, every note of the new harmony is examined to determine whether it should be pitch adjusted or not. This procedure uses the PAR parameter that sets the rate of adjustment for the pitch chosen from the HM with probability PAR, and does nothing with probability 1-PAR. The pitch adjusting process is performed only after a value is chosen from the HM and assigns a new value to x'_1 from its neighbourhood taking into account an arbitrary distance bandwidth (bw). We utilized an additional randomization tool called Random Selection Rate (RSR) suggested in [158]. It acts as the 'annealing' tool in SA or the mutation operator in GAs [159] (see section sec. 4.2.4); i.e. it adds random notes to the new harmony with probability RSR.

- Update the HM. If the new harmony vector is better than the worst harmony in the HM in terms of the objective function value, the new harmony is included in the HM and the existing worst harmony is excluded from the HM. The HM is then sorted according to the objective function value (fitness value).

- Repeat previous steps until the termination criterion is satisfied.

The IHS algorithm incorporates many of the constituents of current heuristic optimization algorithms. Indeed, it has some similarities with the Tabu search method [160], e.g. it stores a history of previously computed harmonies in the harmony memory. Besides, the use of the HMCR parameter resembles to the adaptability offered by the SA algorithm. It is also capable of handling several solutions simultaneously as it is the case in genetic algorithms, this is a very convenient feature as long as a parallel computing architecture can boost the calculation time of each iteration. However, the so called improvisation operators make a clear distinction between these kind of algorithms. These operators define how and in what extend is the acquired information will be used during the iterative process in order to generate new proposals to the solution.

4.2.3 IHS: improvisation operators

- **Harmony Memory Consideration Rate, HMCR**: is the rate of mixture of notes within the HM. This parameter measures the probability with which a particular note takes the value of any remaining harmonics included within the HS memory during the process of improvisation. The usage of harmony memory has a high relevance; it is similar to the choice of the best-fit individuals in genetic algorithms (GA) (see sec. 4.2.4). It ensures that only the best harmonies will be carried over to the new harmony memory. A low rate of HMCR means that the acquired knowledge throughout the improvisation process will remain unused, and so, a very sparse search is enhanced. On the other hand, a high HMCR rate could cause a significant loss of diversity within the population, favouring a premature convergence of the algorithm. Though its value is highly dependent on the particular problem to be treated, in this thesis we set HMCR operator value to 0.9.

- **Pitch Adjusting Rate, PAR**: is the pitch adjustment determined by a pitch bandwidth bw_{range}. In music, adjusting the pitch of a note is done by slightly modifying the frequency of the sound, whereas in IHS, pitch adjusting corresponds to generating a slightly different solution from the one found in HM. PAR measures the probability that during the process of improvisation the value of a certain note is taken from neighbour values within its alphabet[2]. Nonetheless the probability of performing a slight variation in a note is determined by the PAR operator as follows:

$$x_i' = x_i + bw \times \epsilon, \tag{4.8}$$

where x_i stands for the stored note in the HM memory, bw is the bandwidth, ϵ is a random number generated by a uniform distribution within the range $[-1, 1]$, and x_i' represents the new value for the note after adjusting the tone. Many authors consider this parameter as a kind of local search that can be used to compensate the diversification and intensification features [130]. A low PAR rate can eventually slow down the convergence of the IHS algorithm, since the search space is being limited to a very narrow subspace. Nevertheless, a high PAR rate with a high bandwidth, pulls the solution to some potentially optimum points in a much similar way as a random search algorithm would do. Consequently, typical PAR values are around $0.1 \leq 0.5$, in

[2] In this case the term *alphabet* stands for the bounded discrete or continuous range of values that a certain note can take.

most of the applications. Pitch adjustment plays a similar role as the mutation operator in genetic algorithms.

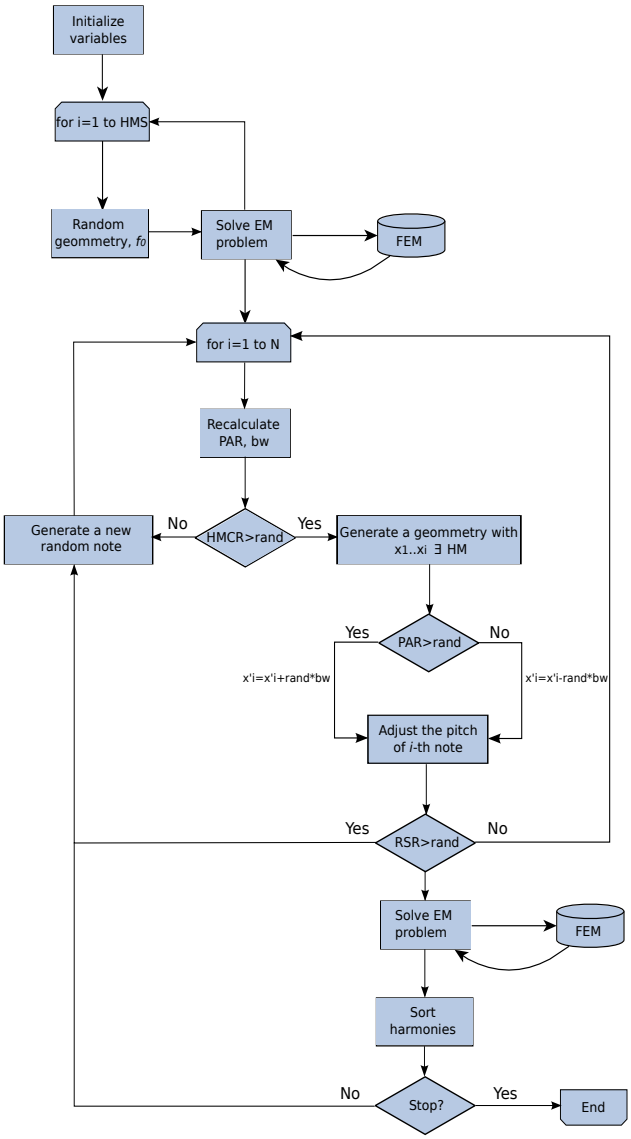

Initialize variables (x*1*,...x*n*, HM, HMCR, PAR, bw, RSR).
Fill HM with random harmonies and resolve cost functions.
LOOP until **stop criteria**
Readjust PAR and bw parameters
if HMCR>rand **then**
  x'$_i$=HM(rand(1...HM), rand(1...n))
  if PAR>rand **then**
    if 0.5>rand **then**
      x'$_i$=x'$_i$+rand*bw
    else
      x'$_i$=x'$_i$+rand*bw
    end if
  if RSR>rand **then**
    x'$_i$=random value within variable bounds
    return x'$_i$
  else
    return x'$_i$
  end if
else
  x'$_i$=random value within variable bounds.
end if

Solve harmony.
sort HM according to f_1...f_{HM}
end **LOOP**

Figure 4.2 Flow chart and pseudo-code for the IHS algorithm implemented in this manuscript.

In the original HS algorithm proposed by Geem in [153], the PAR and bandwidth parameters are fixed and do not evolve during the optimization process, thus, the election of appropriate values for these operators becomes critical and the algorithm demands a high number of iterations for locating the global optimum state. Notwithstanding, in [130], the PAR and *bw* parameters are cyclically tuned in order to enhance a smoother search, much the same as the Cauchy-Lorentz probability distribution does in the FSA algorithm. In other words, the *bw* parameter must be set to high values in initial

iterations, so as to increase the diversity of solutions, but in final generations it must be set to low values to enhance the intensification and sacrifice the diversification, i.e., to search locally instead of globally. Due to this fact, in the IHS the PAR for the iteration n is given by:

$$PAR(n) = PAR_{min} + \frac{PAR_{max} - PAR_{min}}{N} \times n, \tag{4.9}$$

where N is the maximum number of iterations set to the IHS algorithm (stop criterium). We set the PAR_{min} and PAR_{max} parameters to be 0.4 and 0.9, respectively. Then the bandwidth of each iteration *bw(n)* is given non-linearly as:

$$bw(n) = bw_{max} \times e^{c \times n}, \tag{4.10}$$

and the coefficient c is recalculated in each iteration,

$$c(n) = \frac{\ln \frac{bw_{min}}{bw_{max}}}{N}. \tag{4.11}$$

In order to cover a large number of solutions and expand the search space in which diversification has a significant relevance we set the minimum pitch adjusting rate, PAR_{min} to 0.4 ,the maximum pitch adjusting rate, $(PAR)_{max}$, to 0.9, the minimum bandwidth, BW_{min}, to 0.0001 and the maximum bandwidth, BW_{max}, to 1.

- **Random Selection Rate, RSR:** randomization increases the diversity of the solutions. Even if the PAR opertaor has a similar role, the PAR is limited to a bounded area of a certain alphabet and therefore corresponds to a local search. The use of randomization can lead the system to explore various solutions and obtain the global optimum. RSR $\in [0, 1]$, establishes the probability to pick a new value for the new note randomly from the domain of the input variables. It performs a role similar to the uphill jump probability function in SA algorithm, but in this case the perturbation in the harmony set stored in HM is performed regardless of its fitness with probability RSR. In this work we set the RSR parameter to a low value of 0.1.

HS algorithm imposes fewer mathematical requirements and does not require initial value settings of the decision variables. As the HS algorithm uses stochastic random searches, derivative information is also unnecessary. The HS algorithm generates a new vector, after considering all of the existing vectors, whereas the genetic algorithm only considers the two parent vectors.These features increase the flexibility of the HS algorithm and produce better

solutions. The optimization procedure of the HS algorithm and a pseudocode are shown in Fig. 4.2.

4.2.4 Multiobjective optimization

Multiobjective optimization means optimizing multiple conflicting objectives at the same time. In contrast with single obective optimization, multiobjective problems are much more difficult and complex. The presence of multiple objectives in a problem, in principle, gives rise to a set of optimal solutions, instead of a single optimal solution. The equation for a optimization problem with n objectives can be expressed as:

$$c(n) = \frac{\ln \frac{bw_{min}}{bw_{max}}}{N}. \tag{4.12}$$

In essence, finding a balance in a multiobjective optimization problem, where these objectives are in general interrelated, means dealing with the obscure task of choosing the set of parameters that yields to a succesful balance between mutual conflicting cost functions. In a first attempt to do so, a classical approach is to reformulate the multiobjective optimization equation eq. (4.12) into a classsical weighted sum of objectives in the form:

$$\min_{\mathbf{X}\in\mathcal{X}} f(\mathbf{X} = \sum_{i=1}^{n} \omega_i f_i(x)) \tag{4.13}$$
$$\text{subject to } g_i(\mathbf{X}) \leq c_i, \quad i = 0,\ldots,m.$$

In eq. 4.13, the multiobjective optimization problem became single objective by using the weighted method approach. The weighted method assigns a weight ω_i to each initial objective function $f_i(x)$, based on the overall relevance of $f_i(x)$ against the rest of the objectives considered in the optimization problem. However, finding the correct weigths is in most of the cases a non-trivial task that relies on a previous deep knowledge about the nature of the optimization problem. Therefore, stating the multiobjective problem in this apparently simple way can be overshadowed by the arbitrarity of the weights, ω_i, assigned to each $f_i(x)$. A much more elegant approach involves finding the Pareto optimal front. The later defines a multiobjective problem as the search for a vector of candidate solutions (also called an outcome) $X = \{X_1, X_1, \ldots, X_N\}$ with $X_n \in \mathcal{X} \forall n \in \{1,\ldots,N\}$ that optimizes the set of outcomes $f(X) = \{f_1(X), f_2(X), \ldots, f_L(X)\}$ given by the Pareto optimal solution, which is often called the Pareto front [157]. In other words, a solution is said to be Pareto optimal, or non-dominated Pareto optimal, if there is no other feassible solution fo which an improvement in one objective does not lead to a simultaneous degradation in any other remaining objectives.

Fig. 4.3 illustrates an example of a Pareto front. The boxed points represents feassible choices in the minimization task of two conflicting objectives, f_1 and f_2, respectively. Point C is not on the Pareto front beause it is dominated by both point A and point B. Points A and B are not stritly dominated by any other, and hence do lie on the frontier. Ideally, multiple Pareto points would distribute along the front uniformly, although there is no guarantee that this will happen for every optimization problem.

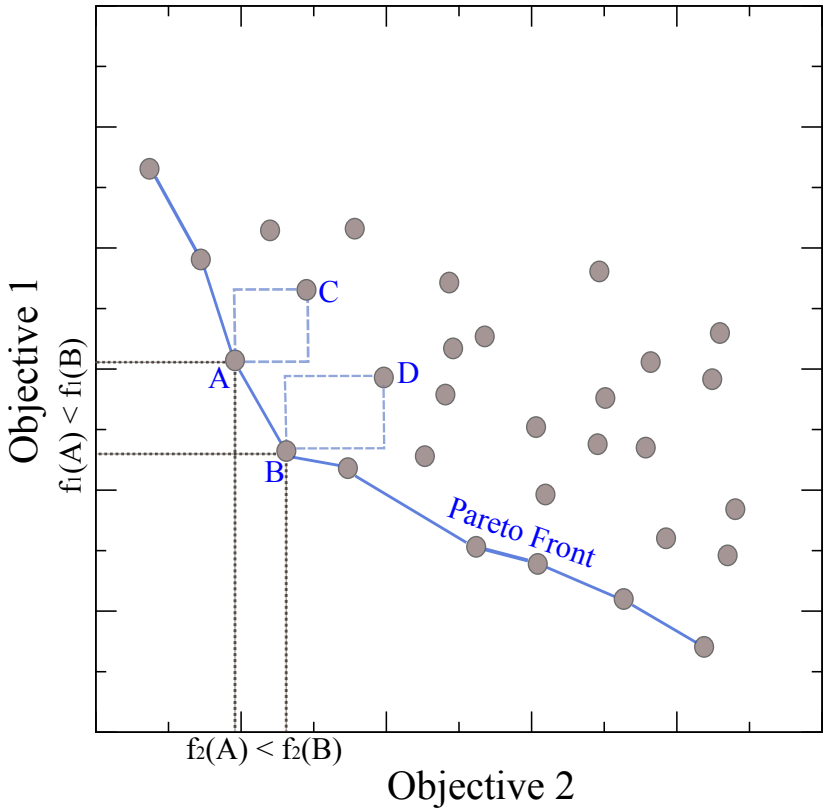

Figure 4.3 Example of a Pareto frontier, that is, the set of Pareto optimal solutions, i.e. those that are not dominated by any other solutions.

.

In the absence of any further information, one of these Pareto-optimal solutions cannot be said to be better that the other. This demands a user to find as many Pareto-optimal solutions as possible. Classical optimization methods (includding the multicriterion decision-making methods) suggest converting the multiobjective optimization problem to a single-objective optimzation problem by emphasizing one particular Pareto-optimal solution at a time. When such method is to be used for finding multiple solutions, it has to be applied many times, hopefully finding a different solution at each simulation run [161].

4.2.5 Genetic algorithms (GA)

Evolutionary algorithms are adaptative heuristic search algorithms based on the evolutionary ideas of natural selection and genetics, relying on bio-inspired operators such as mutation crossover and selection. Specifically, Genetic algorithms are a subclass of evolutionary algorithms, originally developed by John Henry Holland in the seventies [162] and are probably one of the the most successful brands of machine learning and artificial intelligence, and have been used in a wide variety of applications [163–167]. A common genetic algorithm usually starts with a randomly generated population [3] of candidate solutions, called individuals or phenotypes. Each phenotype has a set of parameters, called chromosomes or genotypes, bounded by the restrictions imposed by the optimization problem to be solved. In each generation, the algorithm evaluates the fitness of each candidate solution, according to the objetive functions. Then, it selects which individuals will remain in the pool of candidates, also called population. After, the individual's genome is modified by recombination and random mutation to form the new generation, that is the offspring population. This new population of candidate solutions is the used in the next generation of the algorithm. The algorithm terminates when either a maximum number of generations is fulfilled, a population converges, or if a satisfactory fitness value is achieved by the population. Genetic algorithms usually employ three different stochastic operators to guide the search towards the global optima. Two of these operators focus on tuning the candidate solutions to generate new ones, while the third one decides which solutions are selected as parents for the new population. One of the main differences of the canonical GA over the standard EA is the lack of a replacement strategy; in the GA, a new population starts empty, and is slowly filled with the result of the consecutive application of crossover and mutation over the parents, producing in each of them a couple of childs or new candidate solutions which will be added to the new population [157]. All these operators are sequentially applied to the population at every iteration of the algorithm, in the following fashion:

- **Selection strategy**. It defines the procedure to select which parent chromosome survives to the next generation. Despite there are multiple variants of selection strategy, the following ones are most commonly used in genetic algorithms:

  a) Fitness proportionate selection (FPS), also known as roulette selecction. This selection strategy was proposed by Holland in [162] and it stablishes a probability of being selected according to the fitness of each indivirual. Given the fitness value f_i of a crhomosome i within the chromosome population, the associated

[3] Although initialization strategies using a prior kwnoledge on the landscape of the search may be adopted

selection probability p_i is $p_i = \frac{f_i}{\sum_{j=1}^{N} f_j}$, where N is the number of individuals in the population. This process is generally conceptualized as a roulette wheel in a casino. The roulette is divided in as many sections as the size of the population, with slice widths proportional to the fitness value of each one of the individuals. Thus, to select which individuals will prevail in the next generation, the roulette is spun and the resulting individual is selected. The process will be repeated N times to select N individuals and hence preserve the same amount of individuals during the optimization process. However, while the candidate solutions with best fitness values are less likely to be discarded, there is still a chance that they may never be seleted for the mating process. However, this method permits that some weaker solutions survive the selection process, which is an advantage, as a weak solution may still include some components (genes) which could prove iseful following the recombination process. Some other selection techniques deal with this issue by slightly modifying the Roulette method, such as the stochastic universal sampling proposed by James Baker in [168].

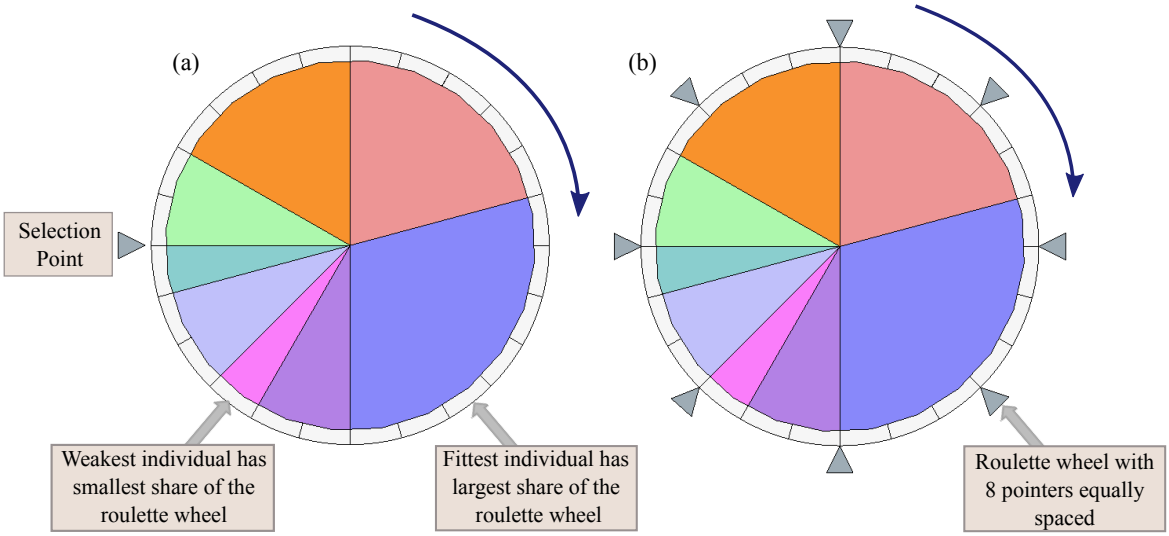

Figure 4.4 (a) Illustration of the fitness proportional selection method. Candidate solutions are drawn filling the roulette with slices proportionalto their fitness value. Then, the roulette is spinned and the selector chooses the selected chromosome. (b) Stochastic universal sampling technique. This method uses N (in this case N=8) equally spaced pointers and so, one spin of the roulette is enough to map the whole mating population. This method prevents best solutions of saturating the candidate space. Figure adapted from [169]

.

b) Stochastic universal sampling (SUS): is an improvement of the Roulette method for selecting potentially useful solutions that prevents best solutions

of saturating the candidate space. FPS can have a bad performance when a chromosome presents a very high fitness value in comparison with the rest of the population, giving weaker members of the population few chances of being selected. In the stochastic universal sampling, instead of having a single pointer that identifies the awarded candidate, it uses a set of N equally spaced pointers and so, one spin of the roulette is enough to map the whole mating population, making the selection more fair and computationally efficient.

c) Tournament: the tournament selection involves repeatedly choosing the best chromosomes among a randomly chosen subset of the population, which is commonly contextualized as running "tournaments" between these individuals. First, k individuals are selected from the population at random, where $k \leq N$ is fixed integer number. Then, the best individual is chosen from the tournament pool with probability p. Subsequenty, the second best individual is chosen with probability $p \times (1-p)$, and in case there is a third individual in the tournament pool, it will be chosen with probability $p * (1-p)^2$, and so on. Therefore, the selection pressure can be easily tailored in the tournament method by simply adjusting the tournament size k and the selection probability p. If k is set to a low value, only the highest fitness individuals will be selected, while if it is set to a high value it will also select unfit individuals, although with a smaller probabuility. For GA, the size of the tournament is usually set to 2 [157].

- **Crossover**. The crossover is the genetic operator behind the recombination process of chromosomes in GAs. It generates new chromosomes (children) with improved fitness by mixing the inherited genes of parent chromosomes. There are many crossover techniques that play with different recombination methods:

  b)Single-point crossover: It uses a single crossover point, taken at random over the total amount of genes comprisin a chromosome. Then, all data beyond that point in either chromosome is swapped generating a pair of solution, each one having two segments.

  c)Two-point crossover: in this case two points are selected randomly. Everything between the two points is swapped between the parent organism, rendering two offspring solutions.

  d)Uniform crossover: Unlike single and two point crossover techniques, the uniform crossover does not need to select any point to do the swapping of genes. Instead, each gene is evaluated for exchange with probability p.

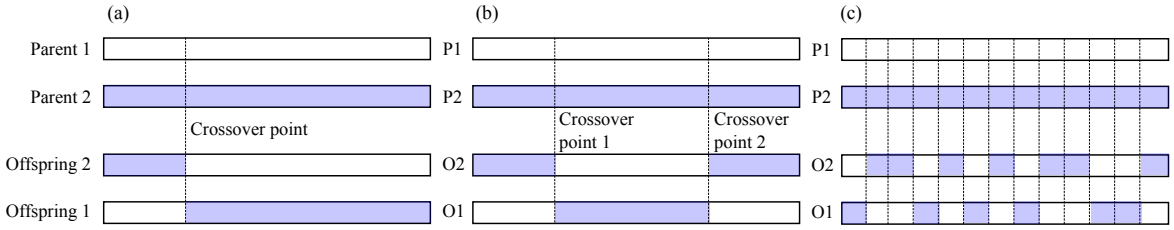

Figure 4.5 (a) The single-point crossover method. The vertical dashed line indicates a random cut point used to compose the offspring population, whereas the two-point crossover (b) uses two cut points to do it. (c) The uniform crossover does not use any cut points, instead it swapps genes according to the probability p_c. This figure was adapted from [170]

.

- **Mutation**. This genetic operator is utilized to artificially introduce genetic diversity. To this point, the reader will find that the RSR operator introduced in sec. 4.2.3 and the uphill movements in FSA, sec. 4.2.1 have identical roles to this operator. The classic example of a mutation operation involves a probability that an arbitrary bit flips to the counter binary state. Mutation should allow the GA to scape from local minima and explore new possibilities in the search landscape. At the same time, it reduces the convergence time of the algorithm by doing a permutation on several genes and thus, creating children dissimilar to the parent crhomosomes. Nevertheless, when the codification is uniform instead of binary, the standard mutation operator utilizes Normal distribution to add or substract a small amount of noise to the gene with probability p_M.

4.2.6 Overview of the Non-dominated sorting genetic algorithm-II (NSGAII)

Under the guidelines of a custom genetic algorithm provided so far, a large number of alternative and improved multiobjective evolutionary algorithms (MOEAs) have been suggested [171–174]. The primary reason for this relies in their potential to maintain a diverse set of candidate solutions while they approximate towards a true Pareto-optimal region. As a result, they can be utilized to rapidly find multiple Pareto-optimal solutions in a single simulation run. The nondominated sorting genetic algorithm (NSGA) proposed in [132] was one of the first of such evolutionary algorithms that adquired a high popularity. However, it has also been very criticized mainly due to three reasons:

I Its computational complexity follows a $O(MN^3)$ rule, where M is the number of objetives and N is the population size. This fact makes it computationally expensive

for large population sizes. This complexity arises due to the non-dominated sorting procedure in every generation.

II The original NSGA algorithms implements a non-elitism approach. The elitism is a procedure where the alforithm grants the provilege to the best gentypes to be unaltered between generations, i.e. it ensures that the geotype with the best fitness survives to the next generation.

III It requires to specify a sharing parameter σ_{share}, to ensure diversity in a population in order to get a wied variety of equivalent solutions.

The NSGA-II algorithm, alleviates all the above difficualties to some extent. Owing to the exceed of computational complexity of original NSGA method, and given a population of size N, identifying solutions of the first non-dominated front requires to compare each solution with every other solution in the ppulation to find whether this is dominated or not. The later requires $O(MN)$ comparisons for each solution. This process is repeated to find all members in the first nondominated level, raising the total complexity to $O(MN^2)$. Once this is accomplished, all the individuals comprising the first nondominated front are found. To find the individuals in the next nondominated front the procedure is repeated once again. In the worst case the task of finding the succeeding fronts also requires $O(MN^2)$ computations [132]. However, in the worst case, when there are N fronts with one solution in each front, the computational complexity required will be $O(MN^3)$. With this reagards, the NSGA-II method provides a fast non-dominated sorting approach which reduces the computational complexity to $O(MN^2)$. To do this, the NSGA-II algorithm implements two entities, the domination count n_p and S_p, a set of solutions that the solution p dominates. Insights about this sorting method are described later on in this section. The second issue is due to the lack of elitism, which has been easily provided to the NSGA-II algorithm. Last but not least, the algorithm deals with the need of providing a sustainable diversity in a population but, without having to strictly set the value of the the operator that controls this feature. The original NSGA method does this by using a sharing parameter σ_{share}, which value determines the largest value that distance metric within which any two solutions share each others fitness. It is set by the user who has probably no guidelines about the value it should take in each case. NSGAII replaces this sharing parameter with a crowed-comparison approach, that does an estimation of the density of solutions surrounding a particular solution in the population. Again, the details of the crowding-distance estimation are provided later on in this section. With all, this modification eliminates the need of any user defined parameter for maintaining the diversity among population members.

4.2.7 The proceedings of the NSGAII

The algorithm initializes the population as usual, filling the individuals with random values (subject to the constraints, if any). Then, each individual is evaluated with regards to each M objective function. Subsequently, the individuals are sorted based on nondomination into each front. To do this, each solution is assigned a fitness based on the front in which they belong. In addition to the fitness value, a new parameter called crowding distance is calculated for each individual. In the first generation, parents are selected using binary tournament selection (i.e. $k = 2$) to generate the offspring population by means of crossover and mutation operators. After, the current population and the offspring population are sorted again based on non-domination and only N individuals are preserved, while the rest are discarded. Although, the second iteration is slightly diffferent. The algorithm implements elitism, which means that these individuals with bes fitness and crowding distance will inmediatelly be selected for the next generation.

Non-domination sorting

This subsection provides a survey on the sorting of the potantial candidate solutions at each iteration of the algorithm. The sorting procedure described above follows, step-by-step, the guidelines proposed in [132, 175]. First, for each individual p in main population P do the following:

- Initialize the counter S_p, the set of all individuals that the solution p dominares, as well as the parameter that countes the number of idividuals that dominate p, n_p, to zero, i.e., $S_p = 0$ and $n_p = 0$, respectively. Then, for each individual $q \neq p$ where $q \in P$, being P the whole set of individual in the population pool:
  - If p dominates q then add q to the set S_p, i.e. $S_p = S_p \cup \{q\}$.
  - Else if q dominates p then increment domination counter n_p by one unit, i.e. $np = np + 1$.

  After finishing the whole set of comparisons, then, there might be no individuals dominating p, i.e., $n_p = 0$. In that case, p belongs to the first front set. Therefore the rank of the p individual is set to one ($p_{rank} = 1$). And the first front set is updated by adding p to it as $F_1 = F_1 \cup \{p\}$. The algorithm then looks for the subsequent Pareto fronts.

- Initialize the front counter i to one, $i = 1$, and while the i_{th} front is nonempty, i.e. $F_i \neq 0$, we proceed as follows:

- Initialize the variable Q, used to store the individuals of the $(i+1)^{th}$ front, to a zero value, i.e $Q = 0$.
- Then, for each individual p in front F_i and for each individual q, being $q \in S_p$:
  * Decrement the domination count for infividual$q$, $n_q = n_q - 1$.
  * If $n_q = 0$ then none of the individuals in the subsequent fronts would dominate q. Thus, we assign q the next rank value, $q_{rank} = i + 1$ and we update the set Q, i.e $Q = Q \cup q$.
- Whenever the former iteration is fulfilled, we increment the front counter by one, $i = i + 1$, and the Q set is assigned to the i_{th} front, i.e. $F_i = Q$.

4.2.8 Obtaining the crowding distance

The nondominated sorting classifies the individuals into different fronts by assigning ranks (fitness values) to them. However, so as to maintain a sustainable diversity in a population without using a sharing parameter, the NSGA-II method employs the so called crawding distance, which i.e. consists on finding the euclidian distance betweeen each individual in a front based on their M objectives in the M dimensional hyper-space [175, 176]. The procedure for calculating the crosing distance between N different individuals belonging to the same F_i front follows these steps:

- The euclidian distance is initialized to zero value for every individual in the front F_i, $F_i(d_j) = 0$, where j corresponds to the j^{th} individual in the front F_i.
- For each objective function m:
  - Sort the individuals in front F_i using each objective m, $I = sort(F_i, m)$.
  - Assign infinite distance to boundary values, so that boundary points are always selected, $I(d_1) = I(d_n) = \infty$, while for all other individuals the distance is calculated as:

$$I(d_k) = I(d_k) + \frac{I(k+1) \times m - I(k-1) \times m}{f_m^{max} - f_m^{min}} \tag{4.14}$$

  where $I(k) \times m$ is the value of the m^{th} objective function of the k^{th} individual in I [**?**]

4.2.9 Genetic operators in NSGAII

NSGAII uses simulated Binary crossover (SBX) [177, 178] and polynomial mutation [179], to do the crossover and mutation operations, respectively. The SBX is found to be particularly

good in problems having multiple optimal solutions and also in those problems in which the lower and upper bounds of the global optimum are not known a priori. This method creates two childs from the selected parents by applying the following transformations [175]:

$$c_{1,k} = \frac{1}{2}[(1-\beta_k)p_{1,k} + (1+\beta_k)p_{2,k}] \tag{4.15}$$

$$c_{2,k} = \frac{1}{2}[(1+\beta_k)p_{1,k} + (1-\beta_k)p_{2,k}], \tag{4.16}$$

where $c_{i,k}$ is the i^th child with k^{th} component, $p_{i,k}$ is the selected parent and β_k is a sample from a random number generated having the density

$$p(\beta) = \frac{1}{2}(\eta_c + 1)\beta^{\eta_c}, \quad \text{if} \quad \leq \beta \leq 1 \tag{4.17}$$

$$p(\beta) = \frac{1}{2}(\eta_c + 1)\frac{1}{\beta^{\eta_c+2}}, \quad if \quad \beta > 1 \tag{4.18}$$

This distribution can be obtained from a uniformly sampled random number u between (0,1). η_c is the distribution index for crossover and determines how well spread the children will be from their parents. That is:

$$\beta(u) = (2u)^{\frac{1}{\eta+1}}. \tag{4.19}$$

The polynomial mutation creates a new child c_k, from a parent p_k following

$$c_k = p_k + (p_k^u - p_k^l)\delta_k \tag{4.20}$$

with p_k^u being the upper bound on the parent component, p_k^l is the lower bound and δ_k is a small variation given by a polynomial distribution [175]

$$\delta_k = (2r_k)^{\frac{1}{\eta_m+1}} - 1, \quad \text{if} \quad r_k < 0.5 \tag{4.21}$$

$$\delta_k = 1 - [2(1-r_k)]^{\frac{1}{\eta_m+1}}, \quad \text{if} \quad r_k \geq 0.5 \tag{4.22}$$

where r_k is a uniformly sampled random number between $(0,1)$ and η_m is a mutation distribution index.

The algorithm then combines the offspring population with the actual population. Since all the previous and current best individuals are added in the population, elitism is guaranteed. The new generation is filled by each front subsequently until the population size exceeds the current population size. If by adding all the individuals in front F_j the population exceeds

the preestablished number of individuals allowed within the population memory, N, then, individuals in front F_j are selected based on their crowding distance in the descending order until the population size matches N. This procedure is iteratively repeated on each generation until the maximum number of iterations are performed or the population converges to the desired result.

Chapter 5

Inverse design and topology optimization of Photonic Crystal Circuits

In this chapter we report on the inverse design (ID) of ultra-wide bandwidth novel passive devices based on photonic crystal (PC) technology for efficiently performing the essential functionalities required by any future photonic integrated circuit (PIC). We utilize the heuristic and genetic optimization methods described in the previous chapter as an inverse design engine for achieving promising PC systems that outperform previous topologies devised on intuitive grounds. We combine the effectiveness of two alternative and well-proven optimization methods that will guide the inverse design process according to a certain pre-established criteria, with the flexibility and robustness of the FEM. With this procedure we demonstrate that both algorithms suit perfectly PC devising. PC topologies proposed throughout this chapter are constrained in order to fulfill the limitations imposed by lithographic manufacturing techniques. Therefore, these designs are not only interesting from a theoretical point of view but also of great practical importance, since they can be readily manufactured.

5.1 Inverse design method (ID)

The usual approach of experimental science can be described as follows: the observed phenomena leads to formulating hypotheses and to developing a theory, in which a model of the system is built, characterized by some relevant parameters. The theory is then used to solve the direct problem, i.e., to calculate, from the values chosen for these parameteres, the values of the measurable data, which will be compared to the experiment. In short, a theory is the formulation of a direct problem. To determine the properties of the studied system from the observed data, this is, solving an inverse problem is much more difficult, since it proceeds

opposite to the normal proccess of experimental science. The properties of a medium, such as a PC structure, completely depend on the parameters that comprise it, such as the lattice period or the dielectric index. A direct way to achieve a desired material then, consists in doing successive adjustements on a certain parameter until a consistent configuration is found. Thus, the classic approach entails inspecting successive approximations. However, this approach is only feassible in linear problems, where the data depends linearly on the parameters. Beyond linear problems, the solution may or may not exist, may be unique or not and may be stable or not when the data suffers slight variations. In contrast, the inverse approach consists of using an actual result to infer the values of the parameters that yield to that physical properties, and predicting the outcome of a measurement is called the modellization of the problem. While the forward problem has a unique solution, the inverse problem may not [180].

Currently, the process of designing a PC structure that complies with a certain required objective is still largely based on intuition rather than using a rigorous mathematical technique, in other words, the most usual design process remains being a direct approach to the problem. Owing to this fact, numerous previous studies report on several PC devices wherein the variation of a few of their constituents yields to interesting optical devices. However, achieving a significant enhancement of a certain property at certain circumstances could be a very challenging task for such trial-and error guided design techniques. Beyond these assumptions, creating PC structures to fulfil multiple conflicting objectives highly hinders the design procedure. Moreover, when studying novel PC systems based upon non-periodic scatter systems, the number of possible configurations becomes extremely large. For the sake of simplicity, let us consider a simple PC model, e.g. an arrangement of holes drilled in a dielectric material, wherein, one must decide whether to plug a hole with bulk material or to leave it at is in order to, e.g., guide the light through a certain path. Regarding to this case, the amount of possible configurations grows rapidly with the number of holes that comprise the PC cluster *(N)*; i.e. the number of distinct configurations grows as 2^N. Nonetheless, even this simple case entails dealing with a large amount of possible configurations, and it is evidently impractical to analyze each of them. The traditional approach is to allow only a small number of degrees of freedom to vary and to explore the whole landscape of values of these parameters. From this landscape, the most adequate structures are extracted. This approach is computationally very costly and, oftentimes, impractical. On the other hand, one can set the goal functionally and, by means of inverse design methods [181–183], elucidate the structure that fulfills the required functionality. This is the approach that we have developed. By using a novel combination of heuristic methods and evolutionary algorithms together with the well-known finite element method [184], we are able to identify the photonic

structures that best comply with the required target functionality. Using this technique we have designed highly efficient photonic integrated circuits of practical relevance in terms of packaging density, improved functionality and cost effectiveness. Heuristic algorithms comprise two fundamental features: the divide-and-conquer process, in which the problem is divided into a more manageable subsets and the iterative improvement that performs a sequential downhill optimization. Meta–heuristic global optimization algorithms are a long term subject in engineering casuistry. However, applying such techniques still involves an intensive computational load. In general, heuristics are applied only in those cases in which solving a candidate solution takes trivial time for machine logic. However, solving Maxwell equations for each candidate solution in a complex heterogeneous media using standard time domain electromagnetic solvers is still a tedious task. The long computing times required by the time evolution of the EM fields together with the high resources needed for each calculation, prevent the use of heuristic search techniques in these materials. Instead, the finite-element analysis (FEM) applied within a steady steady regime satisfies both, a rapid convergence of the solutions and a balanced use of computational resources [184]. This features are highly convenient as they permit to take over an iterative search in a handy way, even in large and complex systems. Besides, the ID technique used for modelling the PC structures reported below supports a constrained search of the parameter space and hence they can render PC topologies that are fully compatible with CMOS fabrication technology. We found that these methods are easily applicable to most of PC engineering design problems since they do not require any detailed knowledge of the structure of the problem and they can rely on the solver of the problem as a black-box. Therefore, we exploit the advantages of implementing a stochastically-driven optimization process and the rapidity and accuracy of the finite element method (FEM) in order to design fully functional passive optical components [184] on a triangular lattice of holes with a radius of $0.35a$, where a is the lattice period, in a 2D dielectric material with a dielectric index of 3.46. The following topologies enhance additional functionalities and enable a higher level of control in complex light paths.

5.2 Power beam splitters

Among the set of functional optical devices that perform essential functionalities that are common in electronic systems, a power beam splitter plays a fundamental role either in light transport segregation or as a primary stage for more complex devices such as Match-Zhender interferometers (MZI) and integrated optical interconnectors. Owing to this, a power-splitter mechanism is a key building block in any photonic system and i.e. in future

PICs. The fundamental feature of a power splitter is to distribute the incoming light from one of its ports equally into the output ports. Several previous studies pointed out that PC technology can be a promising field for developing nanoscale electro-optically controlled couplers/splitters and switches [185–188]. Whereas straight waveguides and bends have been studied by many groups, the very important problem of junction has not received much attention. With this regards, some reasonably good configurations have been proposed so far [185, 186], but they are mainly focused on microwave applications and extrapolating them to PC technology would be a challenging task. Besides, designing *T* and *Y* junctions in rod type PCs yields to impressive results, but when a more realistic PC-slab framework is adopted, the efficiency of these configurations tends to decrease drastically. On the other hand, the holes-in-dielectric approach encounters a different drawback: the simplest PCWGs made this way are usually multi-mode. Multi-mode operation prevents an efficient light steering through complex light paths as higher order modes are easily excited [186]. In particular, when the light path is somehow twisted or follows a different crystalline direction, new modes or a mixing of modes takes place. In any case, these mismatches produce large losses that render these power splitter very inefficient —specially when the most straightforward *T* and *Y* junction designs are used. The standard *Y*–junction design comprises three single defect waveguides joined together at 120°. This geometry leads to strong reflections and is limited to a narrowband operation range. Something similar occurs with multi-mode interference (MMI) type power splitter configurations. MMI splitters take advantage of the periodic nature of light scattering, namely, they focus the first twofold image of an even mode through a pair of output waveguides. However, the symmetry of these images occurs at different positions according to each target frequency and so, a wide bandwidth operation is still impossible to achieve.

In contrast with this background, we present some novel power-beam splitter structures using both the conventional *Y*–junction approach and a more sophisticated and compact one that resembles the one used in MMI approaches. The following photonic crystal structures were obtained using an inverse design approach steamed by the heuristic algorithms detailed in Chapter 4. However, before focusing on practical designs, we considered some trivial structures that still comprise some degree of complexity from a computational effort point of view.

5.2.1 A Toy Model Y-junction

When the amount of degrees of freedom involving a ID process is large, it is impractical to determine whether a global optimum has been reached, neither it is practical to check whether a given local optimal solution is reasonably good among the whole set of feasible

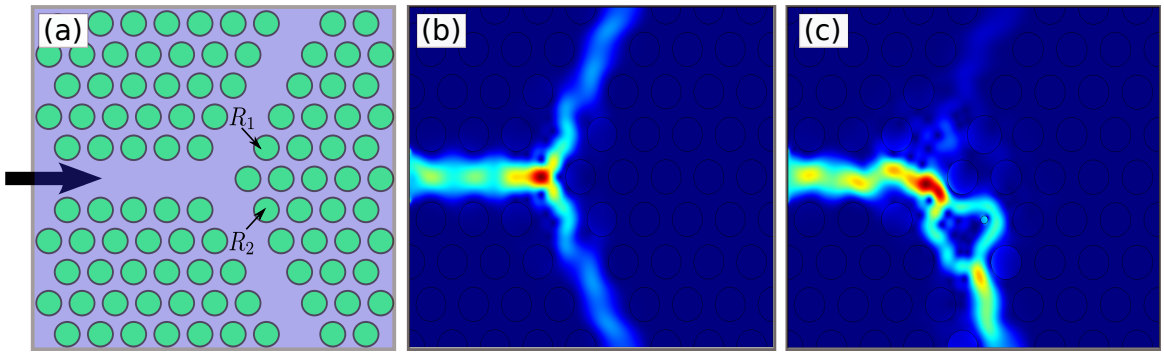

Figure 5.1 (a) Schematic view of the toy model splitter, in which the radii of two holes, namely the ones indicated by R_1 and R_2 are tuned so as to minimize the back reflected percentage of light. The black arrow indicates the direction of the light injection through the input W1 channel. (b) Time averaged power flow in an initial non-optimized Y–junction cluster. (c) Time averaged power flow for one of the solutions proposed by the ID algorithm, in which almost all the incoming light flow is redirected through one of the branches of the Y–junction.

optima. However, in a simplified stage, wherein a brute-force hard search is still feasible, it seems of practical relevance to check whether the ID process gets to good results or, conversely, if it gets stuck at some non-optimum region. With this in mind, we tested our ID method in a variety of toy–models before aplying it to more practical devices. Some of these PC configurations were previously reported by some other authors using semi-analytic techniques. In this section we demonstrate that the task of molding the flow of light through a Y-junction is trivial for the ID method and in some cases using ID one gets to a solution still better that the one posed by any other solving method.

Even if the following toy model entails an inherent simplicity, the exploration of the whole set of solutions it comprises is still a hard endeavour for non-clustered computational resources. In Fig. 5.1.a we present one of such toy model examples consisting of an input waveguide that encounters a Y-junction type splitting structure comprised of two regular W1 PCWGs bended by 60°. At this stage, one may wonder what kind of configuration yields to minimum backscattering in the input W1 waveguide, regardless of which one of the output branches is chosen as the output channel for the incoming light. This structure is not strictly a Y-junction, since it does not perform any separation of the current light power, however, this mere theoretical cluster serves to explain how the ID method tunes the geometry to get to a succesful configuration. In Fig. 5.1.a light impinges from the straight W1 waveguide and the transmittance at one of the output waveguides is computed, solving the EM field propagation using FEM in the stationary linear regime and then, the transmittance spectra is calculated with eq.3.1. The z-component of the magnetic field was set to 1 and 0 at the initial time of the

simulation on the input and output boundaries, respectively. This transmittance is calculated on the output waveguides boundary for several target frequencies. This result is further used to evaluate and quantize the goodness of each candidate model using the so called fitness value. The fitness of the proposed geometry is evaluated using the root-mean-square deviation (RMSD),

$$\mathrm{RMSD}(\theta_1,\theta_2) = \sqrt{\mathrm{MSE}(\theta_1,\theta_2)} = \sqrt{T((\theta_1-\theta_2)^2)} = \sqrt{\frac{\sum_{i=1}^{n}(x_{1,i}-x_{2,i})^2}{n}}. \qquad (5.1)$$

In this case, we defined the fitness of both algorithms in behalf of the transmission of a straight W1 PCWG composed by $0.35a$ radii holes etched into a Si material. These individual differences are also called residuals, and the RMSD serves to aggregate them into a single measure of predictive power.

As it is impractical to visualize the exploration of subspaces of more than three degrees of freedom, we limited the study of this toy model to the exploration of the radii R_1 and R_2 that best meet the desired objective (see Fig. 5.1), by thoroughly exploring 10.000 radii tuples. Thus, we ran the ID process for 60 Monte Carlo experiments using the two heuristic approaches described in section 4.2.2 and 4.2.1, namely the IHS and the FSA methods. Both algorithms yielded to global optima points in almost 100% of the cases, as it is shown in Fig. 5.2. Remarkably, the hard search exploration took more than 24 hours while a single run of the ID process typically takes only a few minutes in a regular $I3$ computer. Fig. 5.1.b shows the time averaged power flow for the initial, non-optimized, structure and Fig. 5.1.c shows the same quantity for a globally optimum solution in which light is redirected almost completely through one of the branches of the Y-junction. Due to the twofold symmetry of the PC cluster comprised in this toy model there are two global optima regions. In this context, the result yielded by a gradient-based algorithm strongly depends on the starting point. However, the heuristic algorithms resorted in this manuscript provide some critical tools for enhancing a sparse search throughout the search space. As a result, using either IHS or FSA algorithms the inverse design process manages to find both global maxima points each with an averaged 50% probability. Specifically, when the IHS algorithm is used, the harmony memory (HM) is filled with solutions corresponding to both global optima points, i.e., it finds the global optimality in a variety of configurations. Fig. 5.3.c shows the evolution of the optimization process in a single run after 5, 10, 20 and 30 iterations. The goodness of each trial solution is quantified by the fitness value. This fitness is computed according to an ideal zero-backscattering model and thus, the amount of light power redirected through the bended ports is maximized as the fitness decreases. In addition, the operators that enable a sparse exploration of optimum solutions in an IHS algorithm direct the search through both

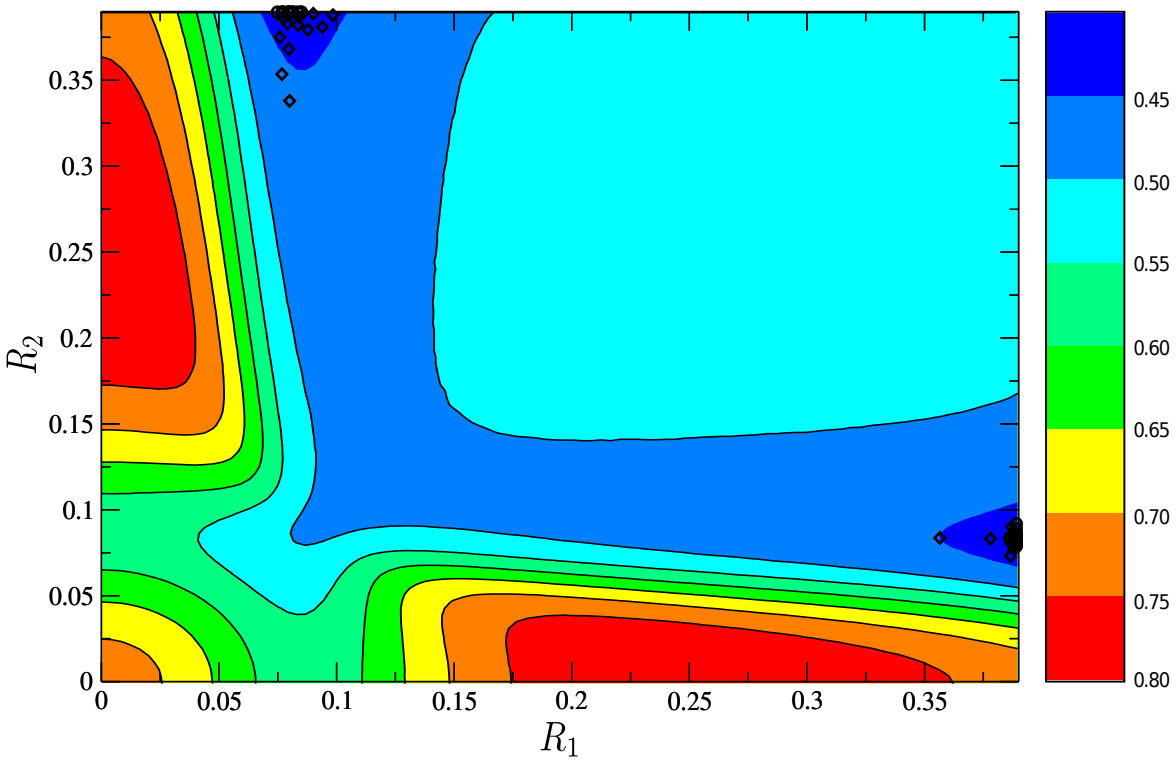

Figure 5.2 The density map depicts the value of the optimization cost function over the entire set of feasible solutions. For this purpose, the search space was discretized in 10.000 points. The circled set of points and the diamond shaped points depict the solutions yielded by the ID method using the IHS and the FSA algorithms, respectively.

global maxima points. Finally, the IHS memory is filled with solutions corresponding to both optimum solutions.

In Fig. 5.3, the averaged performance of both methods at each iteration is presented, together with the lowest and largest values of the distribution. The rapid convergence of both methods signifies that the complexity of the toy-model problem is easily solved during a reduced number of iterations using either method. This is further stressed when there are almost no instabilities in the fitness function achieved at each run, in spite of using stochastic nature processes for doing the optimization. In this case, the IHS algorithm yielded to a slightly lower fitness value. A different amount of iterations was used in IHS and FSA optimization procedures because IHS manages many solutions at every iteration and FSA works with individual solutions.

In the following subsections, new half-power splitting schemes are proposed, founded in symmetry preserving topologies that preserve light division without introducing significant reflection or radiation losses. Besides, as they can be build following the PC standards, they comply with size compactness requirements of future PICs.

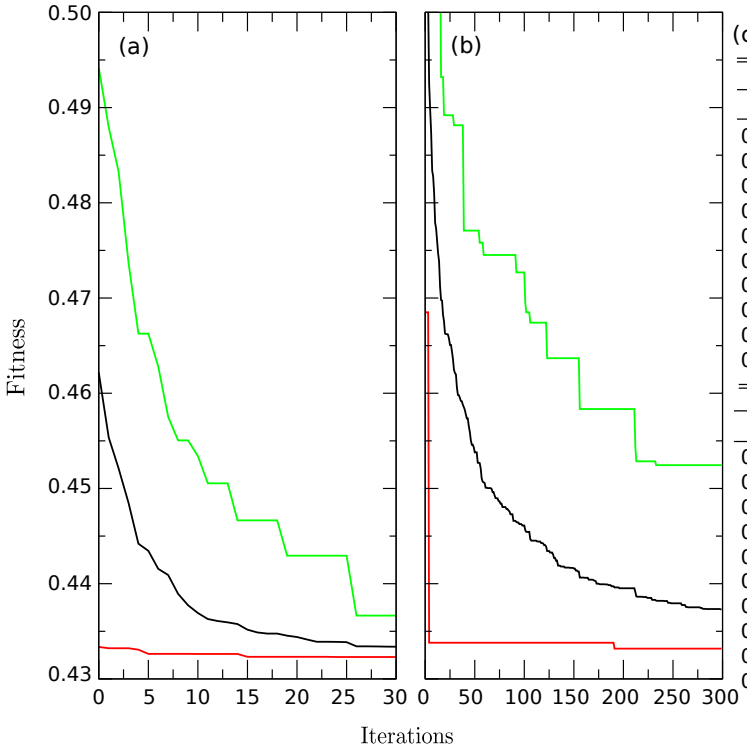

(c)

Iteration1			Iteration10		
R_1	R_2	fitness	R_1	R_2	fitness
0.083	0.334	0.457	0.39	0.088	0.434
0.315	0.084	0.463	0.07	0.387	0.441
0.078	0.305	0.472	0.072	0.387	0.441
0.101	0.268	0.473	0.101	0.384	0.448
0.154	0.108	0.488	0.101	0.384	0.448
0.154	0.134	0.495	0.364	0.079	0.448
0.065	0.334	0.498	0.364	0.076	0.451
0.197	0.356	0.516	0.072	0.373	0.451
0.203	0.226	0.517	0.101	0.373	0.453
0.197	0.305	0.518	0.101	0.370	0.454

Iteration20			Iteration30		
R_1	R_2	fitness	R_1	R_2	fitness
0.39	0.088	0.434	0.39	0.079	0.433
0.072	0.387	0.445	0.39	0.079	0.433
0.072	0.387	0.441	0.39	0.088	0.434
0.101	0.384	0.448	0.072	0.387	0.441
0.101	0.384	0.448	0.072	0.387	0.441
0.364	0.079	0.448	0.072	0.387	0.441
0.364	0.076	0.451	0.072	0.387	0.441
0.072	0.373	0.451	0.39	0.071	0.442
0.101	0.373	0.453	0.101	0.387	0.447
0.101	0.370	0.454	0.101	0.387	0.447

Figure 5.3 (a) Averaged convergence values during 60 Monte Carlos using the IHS algorithm (black line), worst solution during the iterations (green line) and best solution (red line). (b) Analogous representation when using the FSA algorithm for 300 Monte Carlos.(c) Solutions stored in the IHS memory after 1, 10, 20 and 30 ierations. The results remarked with a blue stroke belong to the group of solutions that are gathered around one of the global maximum of the problem while the ones marked with a red box belong to the other global maximum.

5.2.2 PC Y-Junction/splitters

In this section we report on some novel power-beam splitter structures using the conventional *Y*–junction approach. *Y*–junction configurations have been widely criticized due to their low transmittance response [188]. The primary splitter configuration, sketched in Fig. 5.4.a, is comprised of three W1 waveguides and a junction area. The quality of transmission depends on the strength of coupling between the waveguides and the junction section. As it will be seen in later sections(see sec. 5.3 for more details), the band gap guiding mechanism of PCWGs together with an artful design can overcome sharp bended paths along a wide range of wavelengths. However, coupling modes through a number of 120° twisted paths necessarily introduces unwanted strong reflection, at least, if no further invention is used.

In order to overcome the limitations imposed by this cumbersome topology, we have successfully applied the ID methodology.

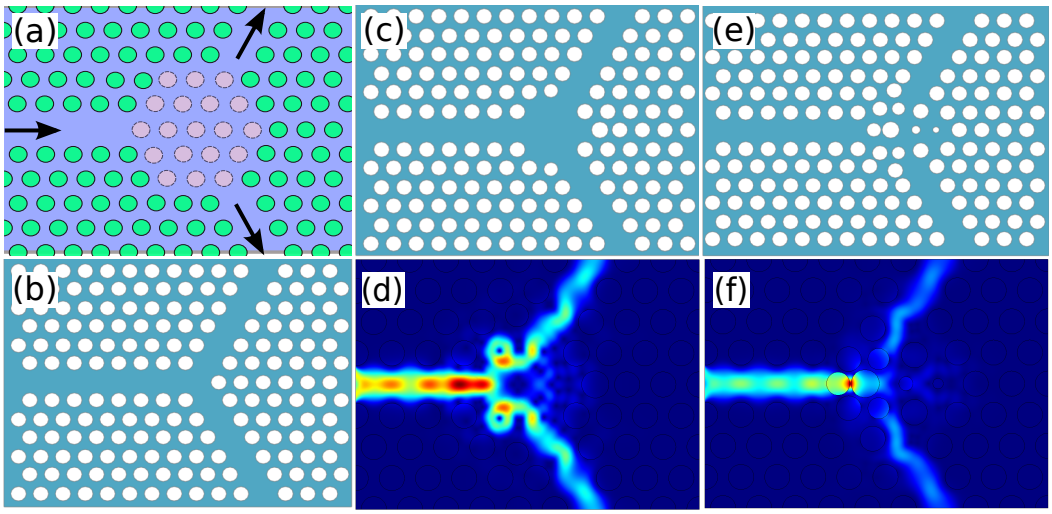

Figure 5.4 (a) Schematic view of the PC cluster wherein the ID methodology was applied for achieving an improved splitting configuration. (b) A non-optimized Y-junction. (c) Optimized Y-junction given by the IHS algorithm. (d) Power flow achieved using (c). Optimized topology yielded by the FSA algorithm. (f) Power flow using (e).

The inverse design method generates, evaluates and chooses the fittest geometries according to each situation. Besides, the reported ID methodology support a constrained search of the parameter space and hence they can render PC topologies that are fully compatible with CMOS fabrication technology. Generally, the following constraints have been imposed:

- Radii of the holes. In order to avoid arbitrary solutions that can not be easily manufactured using the standard fabrication techniques, the search space concerning to these variables has been restricted to,

$$0.1 < r_{ij} \geq 0.39. \tag{5.2}$$

  Inasmuch as the lower limit in 5.2 leads to many negligible radii that may exceed the manufacturing method threshold, the following condition is imposed,

$$\epsilon_{ij}\{n_{air} if r_{ij} \geq 0.1 n_{Si} otherwise. \tag{5.3}$$

  Therefore, for radii smaller than 0.1 the hole is filled with dielectric material. This way dispensable holes that introduce unnecessary reflections are removed, since holes with negligible radii lead to very delicate interference type solutions that are hardly manufacturable.

- Lateral relative displacement of each hole with respect its position in the regular triangular network. The lateral displacement of each hole arises independently and is bounded to

$$-0.2 < x_{ij} \geq 0.2. \tag{5.4}$$

  A negative offset will move the item to the left while a positive one will do rightwards.

- Displacement in the ordinate axis. Determines the relative shift of the hole position along the ordinate axis, analogously to the relative displacement in the abscissa,

$$-0.2 < y_{ij} \geq 0.2. \tag{5.5}$$

This way of posing the problem involves the generation of multiple solutions in which neighbouring holes may overlap each other or intersect at some point, i.e. many potentially good but hardly implementable geometries can be proposed, moreover, in some cases, the robustness of the physical device could be too challenging. However, if instead of discarding these solutions, they are merely penalized (i.e. a higher fitness value is assigned to them), there is a chance that later on these unsuitable geometries are further used to create promising solutions that comply with the aforementioned restrictions. Alternatively, we could have taken into account the radius of each element as well as the radius and the relative position of the neighbouring elements so as to define a closed domain wherein no intersections occur. However, formulating the search space of a variable implicitly according to so many other variables restricts too much the diversity of the optimization method. Besides, this way of posing the problem implies setting a hierarchy among the holes which lies again in intuition rather than in a heuristic optimization basis. All the same, we could have fixed any structure presenting structural defects such as overlapping holes, however, the number of corrections implied in some of the proposed geometries would undermine the entire optimization process led by the IHS or FSA algorithms.

Transmittance results for the simplest non–optimized, IHS and FSA optimized configurations are shown in Fig. 5.5. The non-optimized structure is clearly very inefficient due to the sharp bends and discontinuities along the light path. This geometry can only provide a maximum transmittance of 30% near 0.278 and a minimum transmittance ratio of 10% across most of the target frequency range. Therefore, instead of steering the light flow though the output ports, strong back-reflection is produced. This means that this basic geometry is not suitable for efficient integrated optics applications. On the contrary, the structures devised by means of FSA and IHS algorithms yield much better performance. They exhibit an almost flat transmittance spectra through the whole target frequency range. Almost 45% of the light

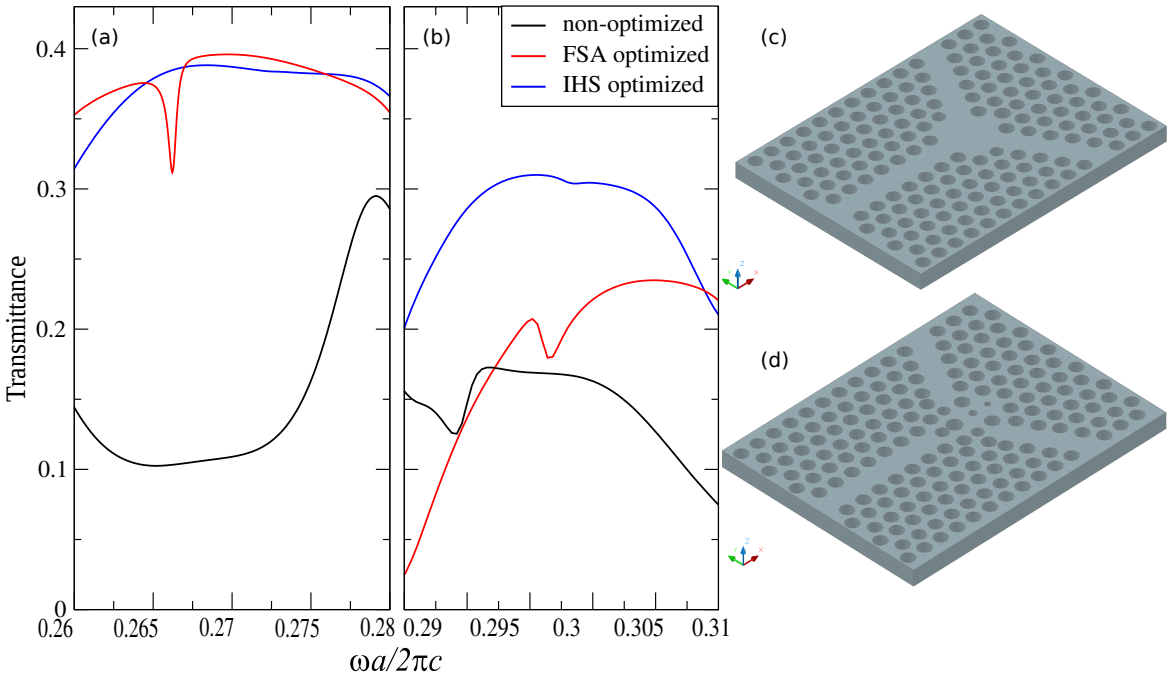

Figure 5.5 (a) Comparison of the transmittance spectra for the non-optimized, IHS optimized and FSA optimized Y–junction topologies in (a) 2D PC structure and (b) 3D PC structure. The 3D structures corresponding to the IHS and FSA topologies are shown in (c) and (d), respectively.

power is redirected to each output branch in both cases. The structure attained by using the FSA algorithm has a drop near the 0.267 point caused by the resonance that is formed within the scatterers that obstacle the flow of the light along the input waveguide. This phenomena is shown in Fig. 5.4.e. However, the reflection caused by this resonance is negligible compared with the overall transmittance of the non-optimized model.

As mentioned before, one of the main advantages of using a hole type basis against the rod type PC structures is the preservation of the light guiding capabilities attained in a 2D PC framework when a 3D environment is required for optical applications. As it is customary we used the PC slab approach for the non-optimized and the IHS and FSA optimized topologies. The simulations obtained using 3D FEM calculations are depicted in Fig. 5.5. It is worthy to mention that while the non-optimized structure remains being poorly efficient, the IHS structure redirects almost all the light percentage through both splitting branches. In contrast, the FSA geometry turns to have serious drawbacks at some lower frequencies maybe due to the change of the symmetry of the guided modes. Indeed, when the mode lossses its even symmetry, splitting the flow of light becomes very difficult. This situation is difficult to foresee in a 2D environment and thus, we believe that a different splitting architecture that fulfills the compactness requirements constitutes a better starting point for an ID design. An

example of an ultra low loss 3 dB PC splitting configuration based power splitter is shown in the next section for this purpose.

5.2.3 Optimization of a PC wavelength selective high bandwidth power-splitter, directional coupling splitters and multiple line defect waveguide like approach

In this subsection some compact power splitter configuration that do not rely on 120° bended PCWGs are presented. The starting topology used for this purpose was previously used as a multimode interference (MMI) medium for improving narrow band power splitters in [186]. An MMI approach seems to be a very convenient way of combining the usual multimode behaviour of hole-type PCWGs and the self-imaging principle for developing successful novel PC devices. The self imaging phenomena, i.e. the splitting of the input field profile into multiple copies at regular intervals, can be easily aroused by closely placing two parallel PCWGs. The proximity of these PCWGs leads to new super-modes, and thus, one can tailor the coupling region in order to force a match between the beaten of the electric/magnetic field with the modes allowed in the output guides. The simplest MMI device is composed by three parallel PCWGs, namely an input waveguide and an output region consisting of two parallel waveguides placed in proximity and a coupling/splitting area. We set a coupling area that corresponds to a W5 waveguide section. This way, a compromise between compactness and the isolation of each output ports, i.e. cross-talk losses, is guaranteed. In Fig. 5.6 a close up view of the dispersion diagram of a W5 waveguide is sketched.

As the PCWG becomes wider, the multimode feature is enhanced. In these large PCWGs new modes surge from fundamental modes. The new modes have either even or odd symmetry. As we are seeking for a two-port half splitting configuration we restrict the search to even like modes. If one chooses a working frequency, say a/λ_0=0.27, there are many modes matching this frequency, some of them describe an even parity field distribution while the rest have and odd symmetry. In the simplest case of an 1x2 splitter model one can look for the first symmetric pair of modes matching a target frequency, this is, the fundamental mode and the second-order mode. Then the separation at which the first image occurs is easy to foresee by simply applying

$$MMI_{spacing} = \frac{1}{(k_0 - k_2)}, \tag{5.6}$$

where k_0 and k_2 are the wave vectors of the fundamental mode and the second-order mode, respectively. If 5.6 is subsequently applied, one can obtain the periods (a) needed for finding

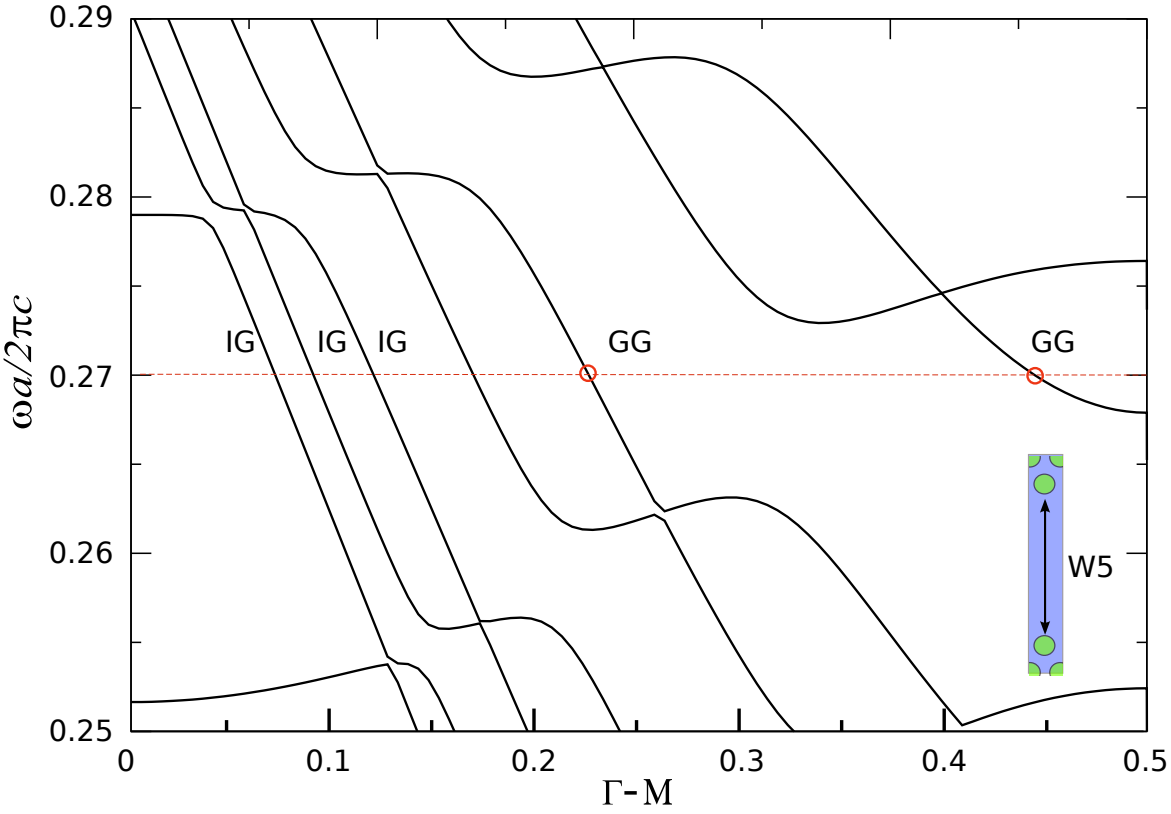

Figure 5.6 Dispersion diagram of a W5 PCWG in which many modes are allowed within the band gap. Some modes are gap guided modes (GG) and some are caused by index guiding mechanism(IG). At an arbitrary frequency a/λ=0.27, the fundamental mode and the first image are signalled by red circles.

the first twofold image that leads to a proper light splitting through the pair of output W1 waveguides. The result of these calculations is shown in Fig. 5.7.

Then, we placed a set of holes following a regular triangular distribution for steering light to the output waveguides, as it is shown in Fig. 5.7.c. However, as shown in Fig. 5.7, the beating of the first twofold is strongly frequency dependent and thus, using the MMI approach it is impossible to achieve a balanced splitting in a wide set of wavelengths, as long as a fixed PC cluster configuration is used. We tried different configurations for the MMI that satisfy the beaten requirements of some frequencies within the range of frequencies [0.26 – 0.28]. The results are shown in Fig. 5.9.

However, a MMI like structure is inherently a narrowband solution. If one takes the range of normalized frequencies comprising [0.262 – 0.267] a MMI splitter shows a twofold image after almost 5 periods while for frequencies at interval [0.268 – 0.273] it requires only around two periods to encounter a twofold symmetry. Thus, satisfying the twofold condition for the whole set of frequencies seems unreasonable. Moreover, if a target frequency falls near an

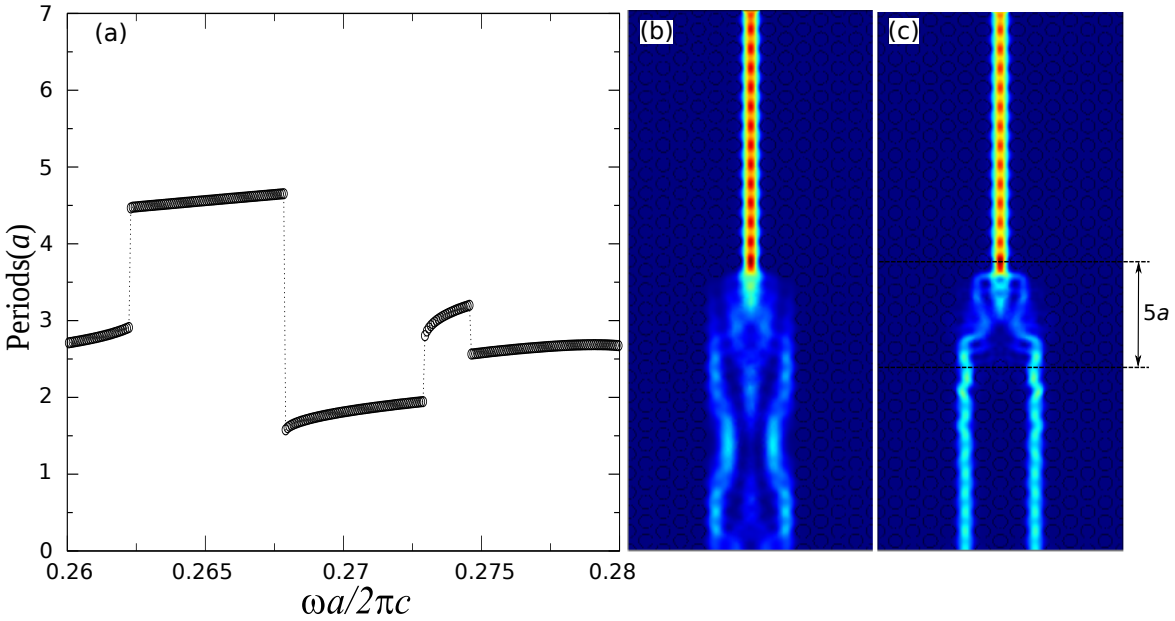

Figure 5.7 (a) When the W1 PCWG leads to a wide coupling region such as a W5 waveguide, a new set of modes appears. This coupling region rises new images of the fundamental mode and calculating the first twofold is image is straightforward using 5.6. This graph shows the number of integer periods needed for a proper splitting at each target frequency within the rage [0.26 – 0.28]. (b) Power flow profile at a/λ=0.27 and (c) placing a PC structure for separating the power through the output channels.

anticrossing point, the approximation given in eq. (5.6) yields to unexpected results. This is mainly due to some exchanges in the symmetry of the studied modes from even to odd symmetry. Anyhow, an MMI approach supplies a very compact configuration. The width and the length of such coupling region can be optimized in order to obtain even a more reduced device. Though, the beat length constitutes a fixed value that limits the size of this kind of systems.

So as to improve the performance of these systems, we applied the inverse design methodology. The ID process yielded to the structures depicted in Fig. 5.8. In particular, for the case of the structure proposed by means of IHS algorithm, it closely resembles to the splitting mechanism proposed in [187], in which a *Y*–junction provided with three scatters that steer light through each channel. In additionto this, the IHS model introduces a defect between the output waveguides that enhances light coupling in the 60° bend. On the other hand, the FSA algorithm proposes a very interesting alternative design. This structure resembles to a Multiple Line Defect Waveguide (LDW) power splitter, like the ones described in [188]. This configuration is very convenient as it prevents the use of lossy or complicated bends and relies on the light leakage from the coupled input channeling through the output

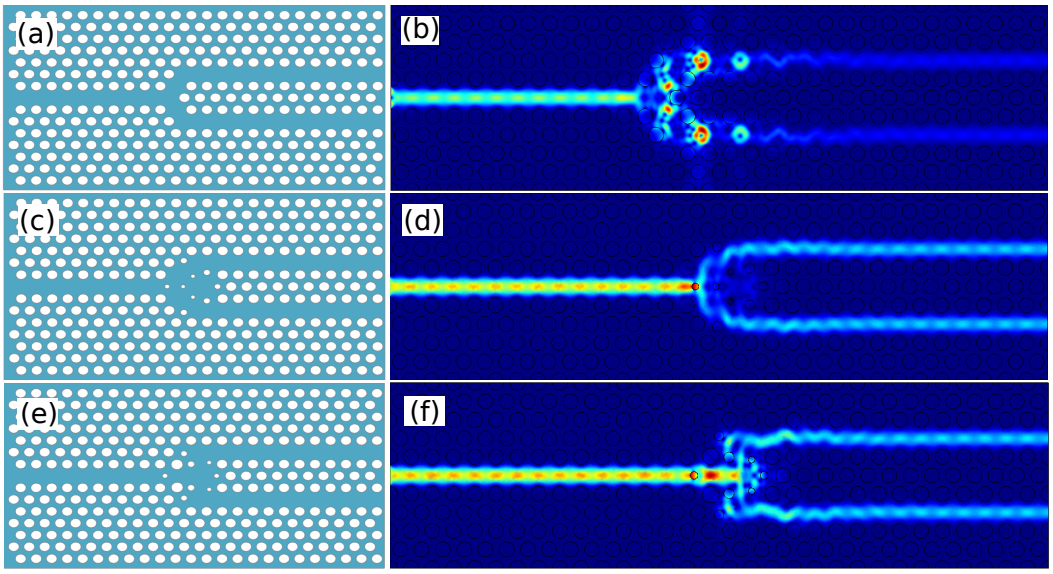

Figure 5.8 (a) Non-optimized MMI-like splitter that suffers from serious losses and does not act properly as a splitting mechanism. (b) Depicts the poor performance of the non-optimized splitter at a/λ=0.27. (c) IHS optimized power spllitter that divides the power properly as shown in (d). (e) FSA optimized design. (f) Power distribution using (e).

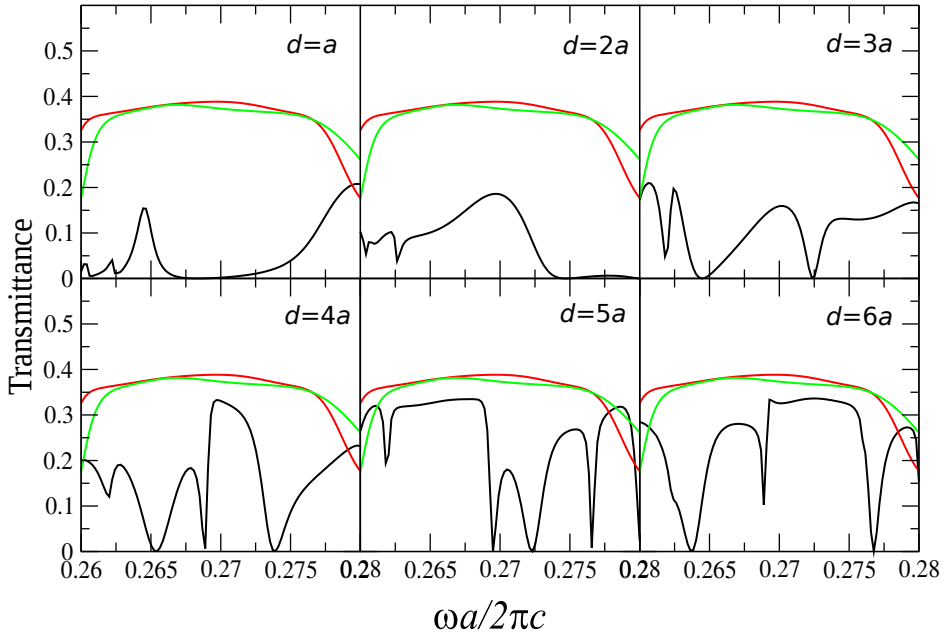

Figure 5.9 Transmittance comparison for the IHS optimized splitter shown in Fig. 5.8.c, (red), FSA optimized splitter shown in Fig. 5.8.e (green) and a regular MMI splitter (black) computed using a spacing length d ranging from 1 to a, where a is the lattice period.

waveguides using only straight W1 waveguides oriented along the $\Gamma - K$ direction of the triangular lattice and so, it requires only the tuning a few number of parameters. This result,

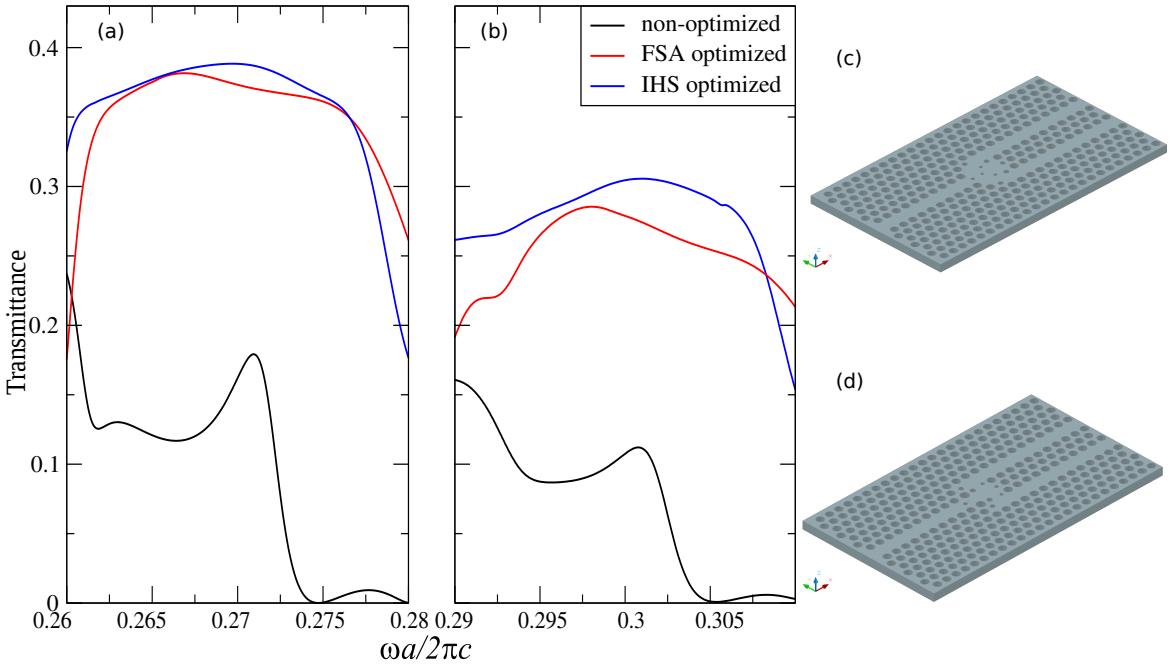

Figure 5.10 (a) Transmittance comparison for non-optimized, IHS optimized and FSA optimized splitters in 2D-PC.(b) Analogous computations solved for PC-slab splitters shown in (c) and (d). (c) IHS and (d) FSA topology built in a PC slab framework.

as well as the one attained through the IHS algorithm, are completely unintentional, i.e. the ID determined the shape of the structures given in Fig. 5.8 with no other reference except the initial configuration shown in Fig. 5.8.a. With all, the transmittance spectra calculated using these structures is shown in Fig. 5.10.

Noticeably, using inverse designed structures, almost all the incoming light is equally shared between the output channels, while the percentage of light that is back-reflected is negligible. What is more, these behaviour occurs for the whole range of target frequencies, namely for $[0.26-0.28]$ and as a result, the transmittance spectra describes an almost flat response. Apart from this highly desirable features, it is interesting to remark the impressive level of integration offered by these systems. In fact, both structures limit the coupling region to a few periods while previous studies make use of much higher coupling stages. This behaviour is sustained even in 3D-PC slab framework as it is shown in Fig. 5.10.b. Unlike in the case of Y-junction splitter optimization, this time both IHS and FSA approaches show a reassonable good performance in suspended membrane type media.

5.3 Engineering sharp PCWG bends

Section sec.3.6 presented the use of a line defect in a photonic crystal exhibiting a photonic bandgap as a waveguide. Such waveguide provides an outstanding guiding through a straight section of a engineered PhC and that would be enough to devise light paths in a PIC in which all of its components are placed one after another in a row. However, from a practical point of view, a waveguide must allow the routing of optical signal through arbitrary directions, whereas any realistic photonic device contains waveguides with multiple bends. Traditional waveguide systems, such as the photonic wires discussed in the next chapter, rely upon index guiding phenomena for steering light through curved paths. Regarding to this, the bending efficiency is highly affected by a critical bend angle that prevents total internal reflection (TIR) mechanism for guiding light modes in those sharp bends that exceed this critical angle. PCWG bends, unless conventional curved dielectric waveguides, are not limited by a critical curvature angle of the order of millimetres. Instead, they can offer a much more compact way to guide light along curved light paths [189]. This fact opens the possibility of drastically increasing the integration density of novel on-chip opto-electronic devices. Reducing the reflection from the bend region has been widely investigated in the literature [110, 111, 190–193]. The first results on PC waveguide bends were reported by Mekis et al. [190], where the transmission through a 90° bend in a 2D photonic crystal with a square lattice structure was investigated. Several techniques have been used so far in order to improve the transmission of the PC bends [110, 194, 195]. Most of the theoretical studies reported so far are founded on PCs comprised by dielectric rods in air. Waveguides created in this fashion are normally single mode. Then, it is relatively easy to carry out a significant enhancement of PCWG bends therein. In [190], Mekis et al. proposed a simplified one-dimensional scattering theory model to describe the transmission properties of a 90° bend in a 2D photonic crystal made of high index dielectric rods on a square grid, as it is shown in Fig. 5.11. In such configurations, when a light source impinges from any of the waveguides, no power can be radiated out of the waveguides, since the photonic band gap inhibits the existance of any extended mode into which the propagating mode can be coupled. Thus, light within the waveguide can only be either transmitted or reflected back. Under these considerations, Mekis et al. posed the transmission through bended waveguides as a scattering problem. Therefore, the reflection coefficient is stimated by

$$R(\omega) = \left[1 + \left(\frac{2k_1(\omega)k_2(\omega)}{[k_1^2(\omega) - k_2^2(\omega)]\sin k_2(\omega L} \right)^2 \right]^{-1}, \tag{5.7}$$

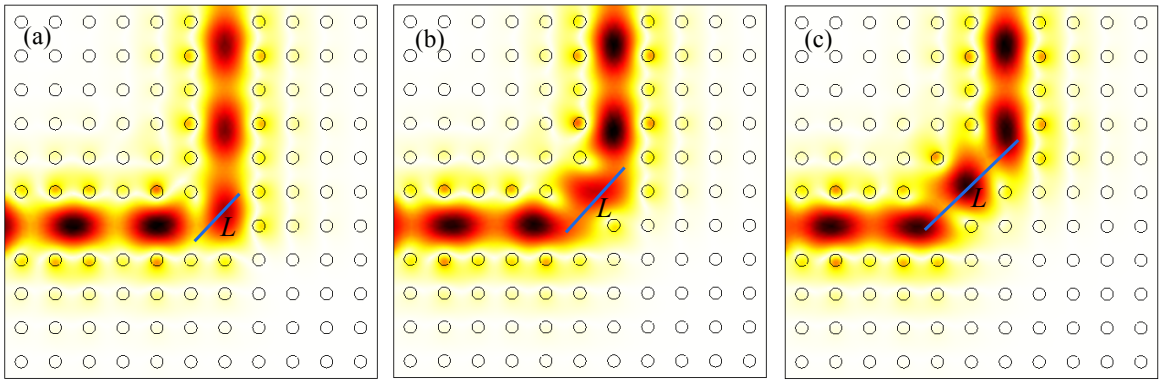

Figure 5.11 (a)A 90° photonic crystal waveguide bend created by overlapping the ends of two straight waveguides in a square lattice of GaAs rods (n=3.4) surrounded by air (n=1) as demonstrated by Mekis et al. in [190]. Light impingues from the horizontal waveguide ([10] direction). Further, in (b) and (c) the diagonal section of the waveguide, represented by the length L, is tuned to enhance the guiding of the electric field into the vertical waveguide ([01] direction).

where $k_1(\omega)$ is the wave vector for a mode propagating in both straight waveguides, i.e. [10] and [01] directions, $k_2(\omega)$ is the wavevector of the mode propagating through the bend ([11] direction) and L is a parameter which represents the effective length of the discontinuity between the pair of straigh waveguides. Therefore, the task of finding an efficient bend configuration in such structure, reduces to find the zeros of equation 5.7 for the target frequency.

However, minimizing the scattering losses caused by a discontinuity, over a large bandwidth, using a multi-mode holes-etched-in-dielectric-type PC is not as straightforward. One way to alleviate the scattering losses is to make the waveguide single mode and that is generally obtained by just reducing the waveguide width. Such single mode waveguide would increase the transmission efficiency of sharp bends without any need of modifying the lattice of air holes. However, narrow waveguides suffer more propagation losses [192], hence, it seems more practical not to limit the case of study of sharp bends to those narrow structures for which the losses are already intrinsicaly high. With all, in this section we demonstrate that an almost optimum bending efficiency is also possible for multimode W1 waveguides endowed with wide operation bandwidth, in holes-etched-in-dielectric-type PCs. To alleviate the problem of low transmission under these considerations, various solutions have been proposed so far. Among the most prominent solutions there are studies that enhance the bend efficiency by introducing some point defects near the curvature [194, 196, 197], by replacing the radii of some holes [198], by adiabatically tapering the defect size [192] or even by replacing the holes at the outer edge of the bend by exotic geometries engineered

using the popular topology optimization method [195, 199]. Instead of following one of the approaches mentioned so far, we adopted the inverse design approach to improve the transmission of optical frequencies in a waveguide including a 60° curvature and a 120° sharp bend.

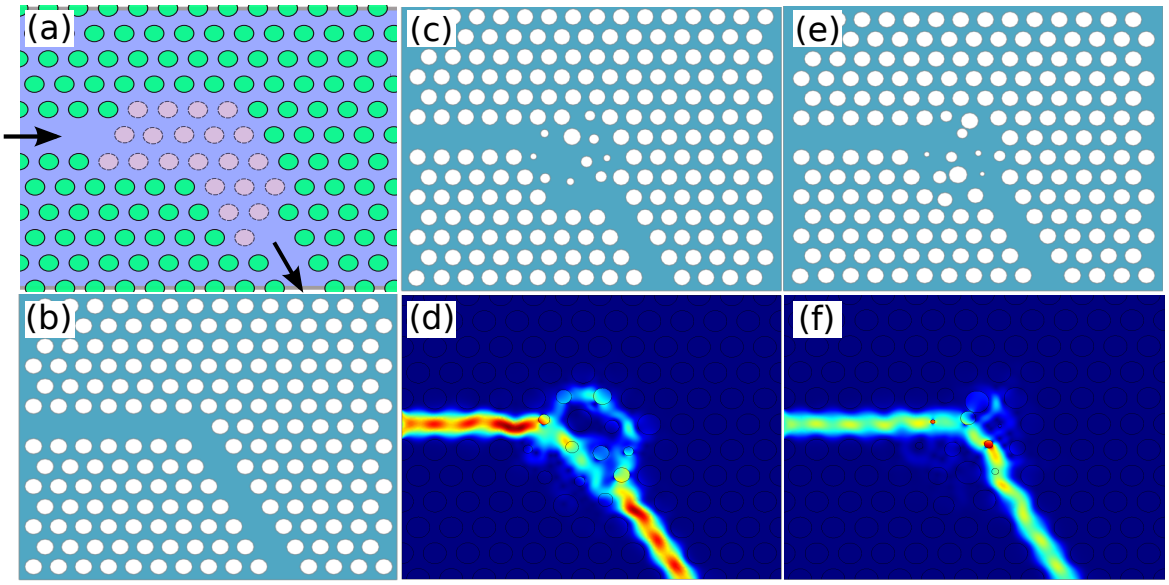

Figure 5.12 (a) Schematic view of the PC cluster used for designing a 60° bend PCWG. The air holes subject to the optimization algorithms are highlighted. (b) A non-optimized PCWG bend. (c) Optimized topology for a 60° using IHS algorithm. (d) Power flow achieved using (e). Optimized topology for a 60° using FSA algorithm. (f) Power flow using (e).

To start with, we took the original 2D photonic crystal lattice detailed in sec. 3.6, in which we eliminated several holes to draw a pair of waveguides matched by a 60° bend, as shownarc it is shown in Fig. 5.12. Such discontinuity acts as a near pefect mirror and hence, most of the power incoming from any of the wavetguides is backreflected. The low transmission ratio can also be explained by inspecting the band diagram of the original 2D W1 waveguide shown in Fig. 3.13. In essence, the guided modes allowed within the band gap in the Γ–K direction, are either not guided in Γ–M or they are evanescent, and thus they decay exponentially as they leakage to the dielectric material. All of this produces a significant drop in the transmission spectrum, as it is shown in Fig. 5.13.

The situation radically changes, however, when we apply our optimization algorithms to this structure. The resulting 2D topologies obtained by using the IHS and FSA algorithms, respectively, are depicted in Fig .5.13. Fig. 5.13 shows that the resulting structures significantly enhance the transmittance spectrum for the target frequency range, which ranges from 0.26 to 0.28. In essence, these partially disordered holes comprising the bend region highlighted in Fig 5.12, set up an efficient coupler between the waveguide modes permited in Γ–M and

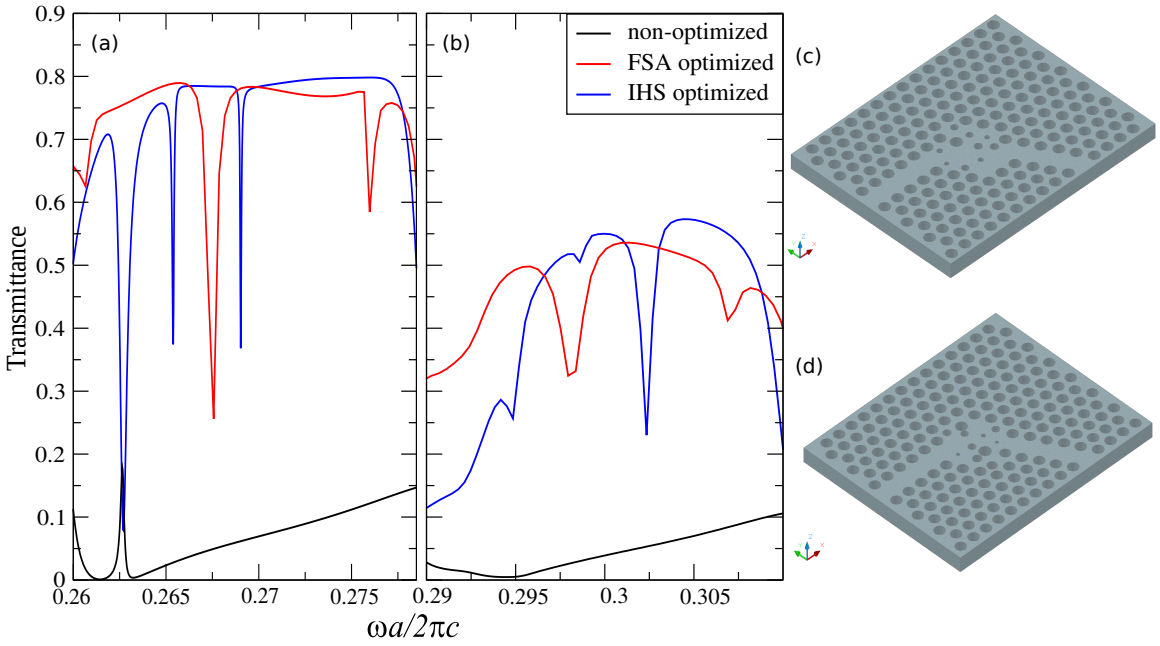

Figure 5.13 Transmittance comparison for a 60° bend IHS, FSA optimized and non-optimized PCWG structures.(b) Analogous computations for PC slab architectures. (c) Bended waveguide system proposed by the IHS algorithm and (d) FSA algorithm.

Γ–*K* directions. In principle, the election of a multimode W1 waveguide could make it easier to find a coupling for at least one of the guided modes in either direction. However, the reader should consider that the coupling obtained using the 2D configurations shown in Fig .5.13 provides a flatted transmision spectra, meaning that the coupling is extended to every guided mode. All in all, the transmission coefficients provided in Fig. 5.13 do add up to near the reference values of a straight W1 PCWG for every frequency within the optimization scope, which confirms that the heuristic technique is a very versatile and reliable tool for PC topology optimization.

When the bend curvature is increased, the decoupling of the modes between both waveguides becomes more critical. Indeed, steering light through a sharp 120° becomes a really hard task that requires the modification of a substantial number of elements that form the junction of the waveguides. Moreover, there are few papers that cover such problem, such as [200] and [201]. Indeed, in these few studies severe modifications in the PC structures are imposed for enhancing narrowband operation. For this reason, exploring new configurations that permit to transmit light within a broad bandwidth without having to break the entire spatial symmetry is essential. Recently, a waveguide that describes such curvature has been demonstrated using topological photonics [202]. We also study the topological protection guiding in the last chapter of this thesis.

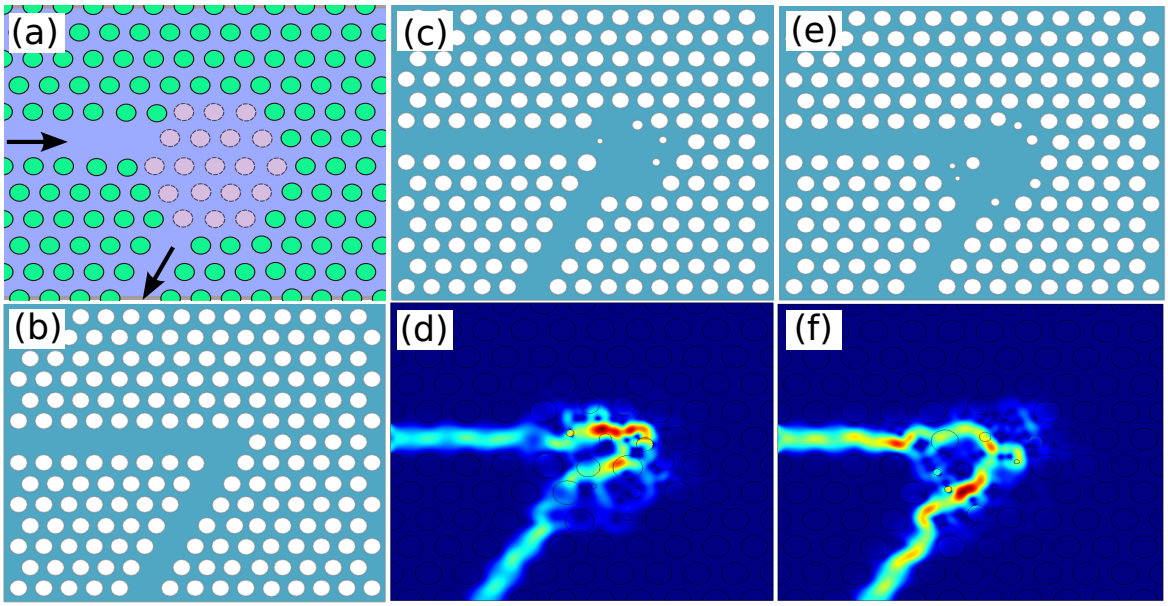

Figure 5.14 (a) Schematic view of the PC cluster used for designing a 120° bend PCWG. The air holes subject to the optimization algorithms are highlighted. (b) A non-optimized PCWG bend. (c) Optimized topology for a 120° with IHS algorithm. (d) Power flow achieved using (e). Optimized topology for a 120° with FSA algorithm. (f) Power flow using (e).

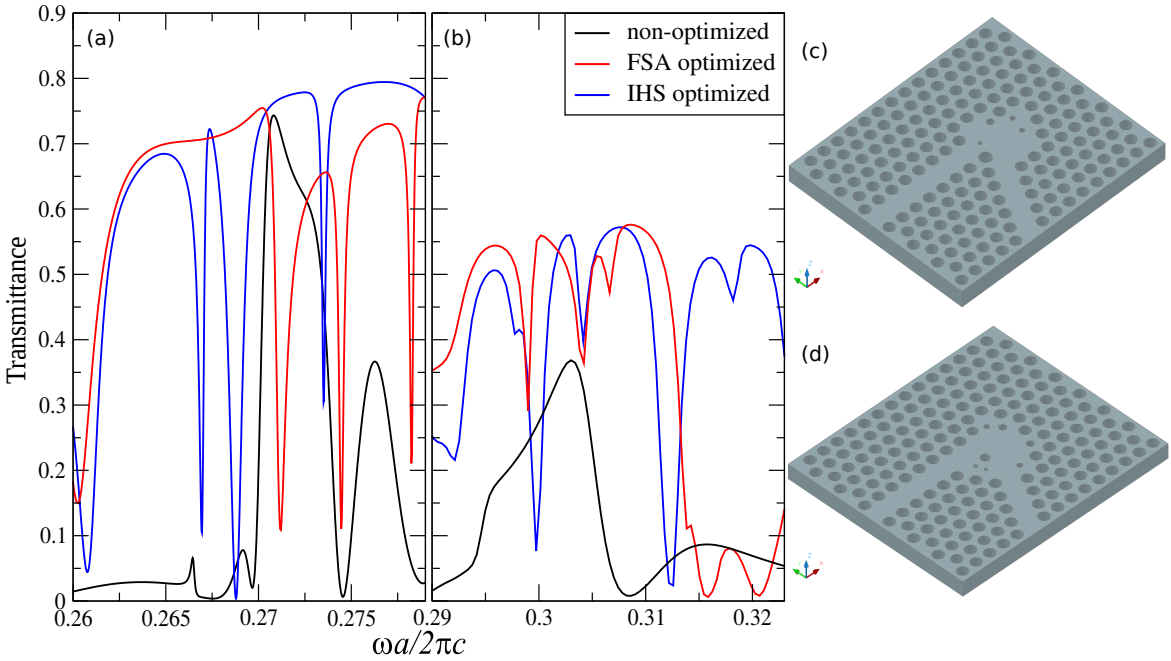

Figure 5.15 (a) Transmittance comparison for a 120° bend IHS, FSA optimized and non-optimized PCWG structures. (b) Analogous computations for PC slab architectures. (c) Bended waveguide system proposed by the IHS algorithm and (d) FSA algorithm.

To couple light through sharp curved paths we repeated the inverse design proceedings, this time for a 2D 120° bend topology depicted in Fig. 5.14.a. The corresponding optimized 2D topologies are represented in Fig. 5.14.c and Fig. 5.14.e, for IHS and FSA optimized structures, respectively. The excellent agreement between the transmission through the 120° bend and the transmittance spectra calculated for a bend-less, straight W1 waveguide demonstrates the consistency of our approach. Furthermore, the transmittance comparison sketched in Fig. 5.15 confirms that the reflection losses are minimal for optimized structures, in spite of the sharp bend. It seems that there is resonant mode occurring around $\omega = 0.273$, where even the non-optimized structure presents a high transmission, though it happens only for a narrow bandwidth. Further, we show that the results obtained so far yield to a significant improvement in the transmittance spectra even in a photonic crystal slab structure. The results depicted in Fig. 5.13 and Fig. 5.15 were verified by means of rigorous three dimensional FEM. In addition, Fig. 5.13.b and Fig. 5.15.b remark the excellent agreement between 2D and 3D simulations. Nevertheless, the effective index changes for the case of a slab structure and so they do the band gap and the guided modes.

5.4 Channel Drop Tunneling

Enhancing broadband light guiding through PC paths is essential for communication network applications. In the same way, creating highly selective filters is particularly important for adding and extracting light from waveguides. Furthermore, such channel-drop filter devices are a key element for exploiting the spectral bandwidth capabilities in dense wavelength demultiplexing systems (DWDM) [203, 204]. PCs are specially well suited for proposing such devices, on the one hand, the PBG phenomena performs an efficient discrimination of light power at a high-range of wavelengths and on the other hand, minimal structural modification of the periodic arrangement leads to light localization with high Q-factors. These PC cavities constitute a very handy mechanism for leaking light from a PCWG into another waveguide. With this regards, we devised some PC system that permit to determine the path of the light flow according to the wavelength, much in the same way as nowadays electronic interconnectors do. So far, some early studies have demonstrated PC WDM designs based on superprism effects [205, 206] and there are quite some studies that make use of resonances to perform similar performance, like in [207, 208]. The former tend to require large areas and thus they could be too bulky for a PIC module; the later scales appropiately for integration purposes but they do not support a high bandwidth operation.

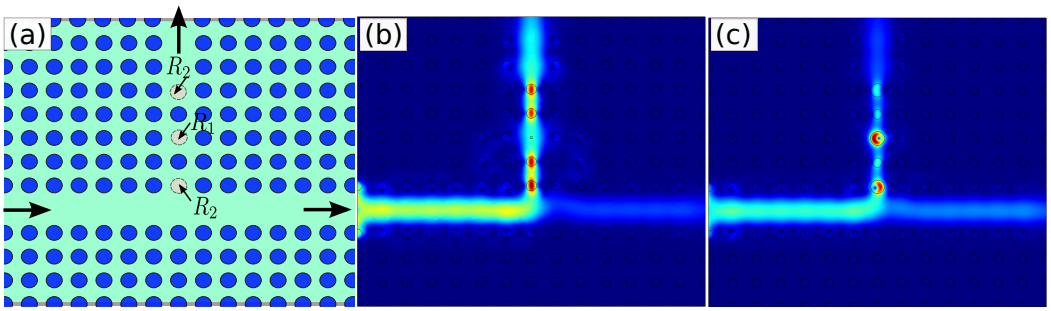

Figure 5.16 (a) Schematic view of the selective add-drop PC topology comprised by two transversal waveguides and a defect formed by the reduction of the radii R_1 and R_2. The time averaged power flow is represented at the resonance frequency of $a/\lambda = 0.37$ for (b) the configuration proposed by Ren et al., where $R_1 = 0.042a$ and $R_2 = 0.211a$, and (c) one of the configurations given by the IHS algorithm, where $R_1 = 0.388a$ and $R_2 = 0.276a$.

5.4.1 Designing a Toy Model Channel Drop Filter

In [203], Ren and co-workers reported on a three port PC channel add-drop made by tailoring only a few parameters. The original geometry proposed by Ren et al. is depicted in Fig. 5.16.a. It is comprised by a straight W1 PCWG formed by removing a row of rods with $0.2a$ radius and a refractive index of 3.4 together with a transversal W1 waveguide that is intended to be the drop channel for extracting evanescent light from the horizontal waveguide. Therein, a PC cavity traps a resonant frequency from the input waveguide and couples it to the drop port. With this elements, they applied a time coupled mode theory for determining the size of the rod comprising the PC cavity and the radii of rods close to each waveguide that enables the light coupling. Fig. 5.16.b shows the time averaged power flow at the resonant frequency, for the configuration proposed by Ren et al., where $R_1 = 0.042a$ and $R_2 = 0.211a$ radii are utilized. This figure illustrates the light coupling to the output waveuide. The theoretical analysis carried out by Ren et al. is further confirmed by computing the transmittance spectra for the vertical drop waveguide depicted in Fig. 5.18.a. Their prediction states that balancing the quality factor of the air defect cavity and the cavity formed near both waveguides yields to the best coupling system. In regards to this simple configuration where only two parameters define the coupling/drop of some guided frequencies, we explored the fitness of 10.000 feasible solutions which are shaped in the surface map shown in Fig. 5.17. Dealing with moderate and high Q factor PC cavities requires a high degree of accuracy, and thus, the running time grows up, even when fast methods are implied for such task [184]. Consequently, acquiring the information given in Fig. 5.17 took almost 250 hours. However, when using the ID method the process speeds up, i.e. a single IHS ID run takes in average

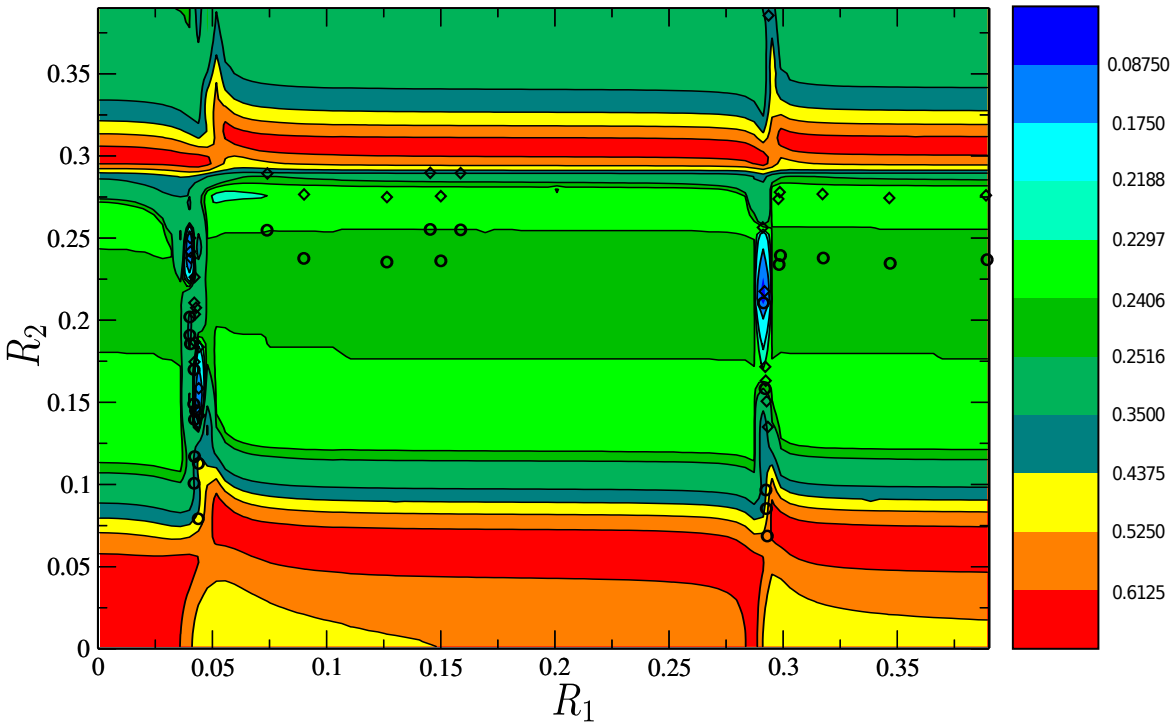

Figure 5.17 The coloured chart depicts the value of the optimization cost function over the entire set of feasible solutions. For this purpose, the search space was discretized in 10.000 points. The circled set of points and the diamond shaped points depict the solutions yielded by the ID method using the IHS and the FSA algorithms, respectively.

no longer than 17 minutes to converge and much the same happens when using the FSA algorithm.

Fig. 5.18 shows some of the solutions proposed by the ID methods using both the IHS and the FSA algorithms. They are very close to the optimum solution proposed by Ren et al. and, in some cases these designs slightly outperform the one given by the authors, i.e., the channel drop is slightly enhanced.

Fan et al. followed the proceeding posed by Wang et al. to extend the three channel filter structure to a symmetric four channel add/drop configuration [207]. The schematic diagram of the coupled system used by Fan et al. is illustrated in Fig. 5.19. Therein, they theoretically predicted that, a photonic crystal lattice, comrprised by alumina rods, can be tailored to make a propagating state excited in the waveguide A (see Fig. 5.19.a) interfere constructively into the waveguide D, whilst the optical signal can be almost completely cancelled on the remaining waveguides. Noticeably, the system proposed by Fan et al. is very similar to the one shown by Ren et al., but in this case, they proposed to modify not only the radius of some rods (i.e. the ones denoted in Fig. 5.19.a as R_1), but also the refractive index of some other elements, which are highlighted in Fig. 5.19.a.

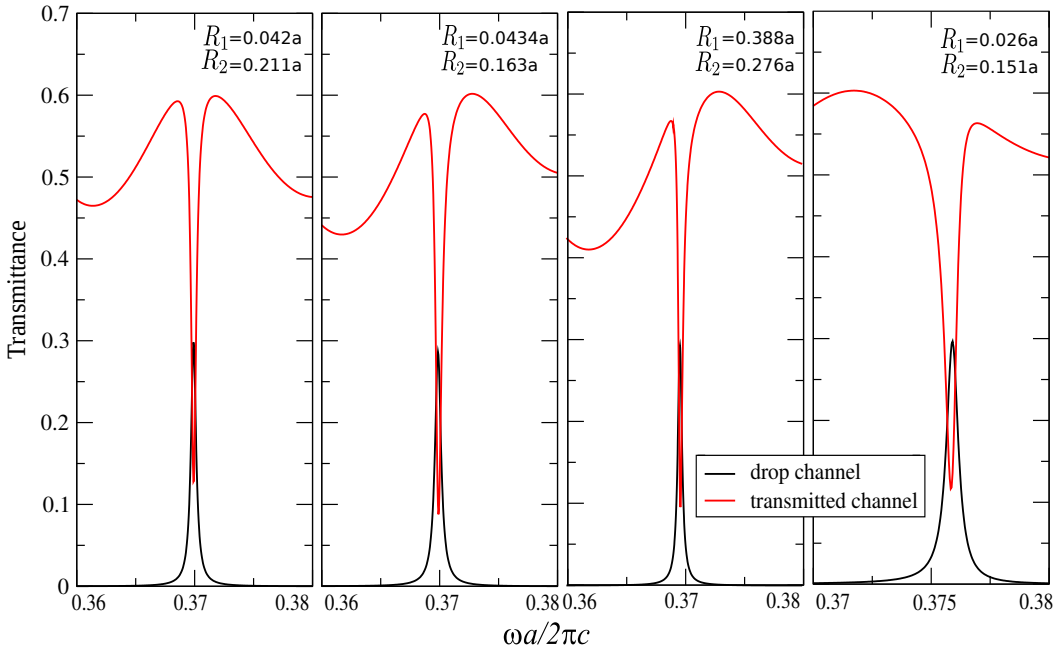

Figure 5.18 From left to right: Transmittance spectra calculated at the drop channel and at the straight channel using the configuration proposed by Ren et al., using the IHS algorithm, the FSA algorithm and an alternative solution obtained using the IHS algorithm.

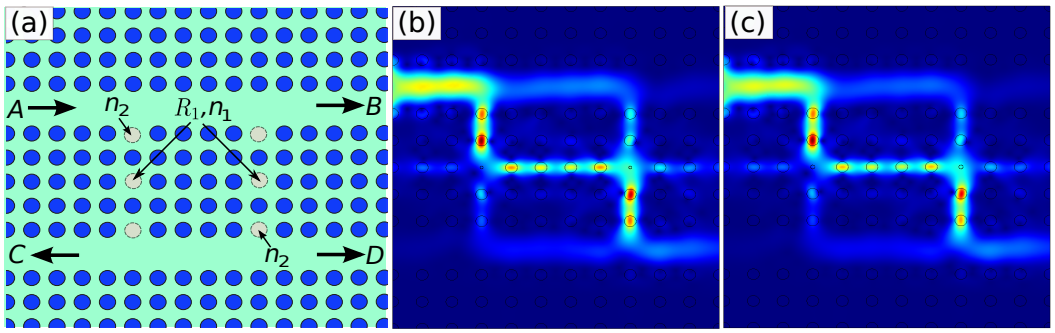

Figure 5.19 (a) PC structure proposed by Fan et al. [207], for light tunnelling through the parallel waveguides. (b) Time averaged power flow for the topology reported by Fan et al. and the one provided by the ID algorithm(c) at a/λ=0.373.

Alltogether, this model comprises three degrees of freedom and, solving such system becomes much more complicated. Therefore, the thorough exploration of the search space implies an impractical high number of calculations. However, for the sake of demonstrating the high efficiency of the ID methodology testing our approach in this stage it is of practical relevance. In Fig. 5.20 we show both, the transmittance results for the topology proposed by Fan et al. and the still better result obtained by the ID method. When setting the topology with the parameters found by the ID method the interference pattern at the sharp drop frequency

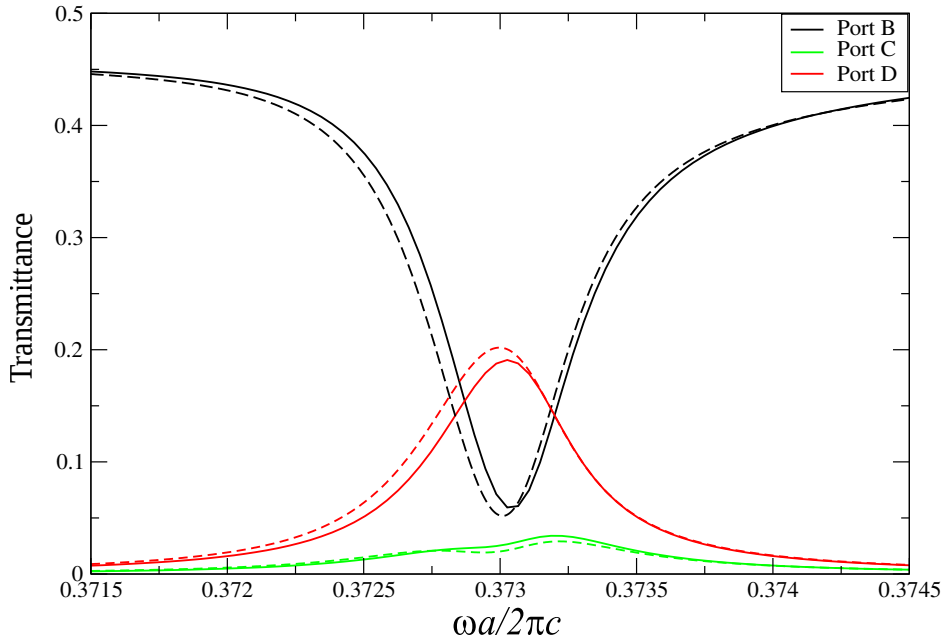

Figure 5.20 Transmittance calculation through the ports *B*,*C*, *D*, for the light tunnelling scheme suggested by Fan et al. (solid lines) and the one provided by the IHS algorithm (dashed lines).

range describes some interesting patterns, namely, it interacts destructively and minimizes the amount of light redirected to channel *C* and *B* while it acts constructively in port *D* producing a complete transfer of light. Specifically, the solution proposed by Fan et al. is formed by a square arrangement of rods, provided by a dielectric constant of 11.56 and R_1=0.05a, n_1=6.6 and n_2=9.5, while the solution obtained by means of ID uses R_1=0.0727, n_1=2.32 and n_2=10.69. In summary, we achieved a very accurate and efficient transfer of light using the cavity light leakage approach proposed by Fan. It seems that these models, which are subject of analytical studies, are an easy matter to be solved using the ID approach proposed in this paper. Besides, in this case, our solution yields slightly better results than the one proposed in [207]. According to these results, it seems reasonable to conclude that the ID method using both IHS and FSA algorithms can be useful in simple PC cluster design. Moreover, in the following section we will show that its usefulness is even more valuable when addressing much more complex configurations where many competing degrees of freedom must be handled.

5.5 Inverse designed butt-coupled PCWG tapers

Achieving an efficient coupling of light between two optical waveguides is a key feature that must be achieved for enabling complex integrated photonic devices. Besides, there is a special interest in enabling a proper coupling of the slow-light modes [209] that propagate in PCWGs, inasmuch as light–matter interactions benefit from the slow-light regimen [210–212] and can lead to non-bulky and controllable optical delay lines [192, 213]. However, coupling light into PCWG provided with a slow light regime translates into a large backscattering, at least if no further invention is used [209, 214]. The later is mainly due to the large group index mismatch between different PCWG configuration, which is further increased when ultra-low velocity modes are excited [215]. Recently, a large variety of coupling techniques and structures have been proposed for efficient interfacing PCs and different guide sections. In some cases, as in [216], a mode matching technique is employed to improve the coupling between conventional silica waveguides (see next chapter for more information regarding to silicon integrated waveguides) and a rod-type 2D-PCWG by tuning just a few parameters. Enhancing the efficient injection of light to PCWGs is a matter of mayor interest, and it has been covered by various authors theoretically as in [215] and experimentally as in [214]. Specifically, in [214], Vlasov et al. demonstrate that coupling light form a regular strip line into a PCWG can be significantly enhanced if the coupling region between these two devices is carefully tailored. Besides, they prove that this proceeding works even for extremely low velocity light modes. Much more popular approaches are founded on adiabatic or smooth transitions that gradually facilitate the transition between different guiding devices. The principle of operation of such devices relies on progressively tuning the diameter of holes/rods. This variations simulate a smooth gradient of the effective index and so, the amount of reflections due to the index mismatch are reduced. In principle, this gradual mode conversion enables tapering between a classic ridge waveguide and a PCWG [192, 217] as well as a proper coupling between different sized PCWGs, as long as the light is strongly confined in the PC waveguide [218]. Besides, this method gets impressive results when dealing with light operating at moderate velocities, but when dealing with slow light modes the impedance mismatch increases and thus longer tapers are usually required to achieve an acceptable coupling loss [219, 220]. On the other hand, adiabatic scaling of PC scatters requires very accurate manufacturing capabilities since these type of taper stages are rather sensitive to fabrication errors. Genetic algorithms have also been employed to fabricate tapers displacing some scattering cylinders [221, 222]. With all, previous studies presented either approximated solutions (often based on intuition) or discuss a semi-analytical solutions of much more simple cases that can not be extrapolated to many-scatterer PC slab waveguides.

Nonetheless, in [209], Oskooi et al. pointed that when dealing with many degrees of freedom the resulting topologies tend to be very sensitive to manufacturing errors, being this the reason that boost the election of only a few parameters for designing successful tapers, instead of proving with more ambitious topologies. Taking into account these limitations, in [209] a worst-case optimization method is proposed. Though this methodology seems to be robust and yields to good results, it is difficult to extrapolate it to more complex systems like the ones presented throughout this chapter.

5.5.1 A toy Model coupler device

To do it simple, in the following toy model, shown in the inset of Fig. 5.21, we study the coupling issue between two sections of PCWGs comprising slightly different waveguide widths. This photonic crystal structure has a line defect promoted in the Γ - M direction, this procedure yields an effective in-plane waveguide width of $\sqrt{3}a$, this section is commonly known as a W1 waveguide. According to this notation, when the next row of holes/rods is also erased, a wider waveguide is created. This wider waveguide is likely to support more guided modes but does not ensure that its modes will couple rightly with the modes allowed in W1 waveguide. Thus, in order to suppress the backscattering as well as to achieve a good transmission through a link composed by different width waveguides, a nexus structure is required.

In [223], Talneau et al. proposed some interesting tapering structures in order to adiabatically couple the guiding modes from a W3 section to a narrower W1 PCWG. The principle of operation of the coupling model proposed by Talneau et al. relies on the manufacture of holes with progresively varying diameter, which syntesizes an artificial material with a gradient effective index. One of the most basic structures proposed by Talneau et al. is sketched in Fig. 5.21.c, consisting of a set of patterned air holes obtained by etching a semiconductor material GaInAsP with a refractive index of 3.5. The transition from guide part W1 to guide part W3 is made by interrupting with a pair of diameter decreased holes, labelled as R_1 and R_2 in Fig xx. Talneau et al. optimized the guided propagation structure to ensure a low percentage of back reflection of light. We choosed this model as a toy model beacause it renders a very simple design problem that can be further simplified by considering the twofold symetry. Before running any ID calculation, we analyzed the guided modes for each waveguide section. In Fig. 5.21 the projected band diagram for both W1 and W3 waveguides is depicted in solid and dashed lines, respectively. In order to have an efficient coupling between the two PCWGs there should be an overlap between their guided modes. Noticeably, near a/λ =0.215 point there is a match between the allowed guided

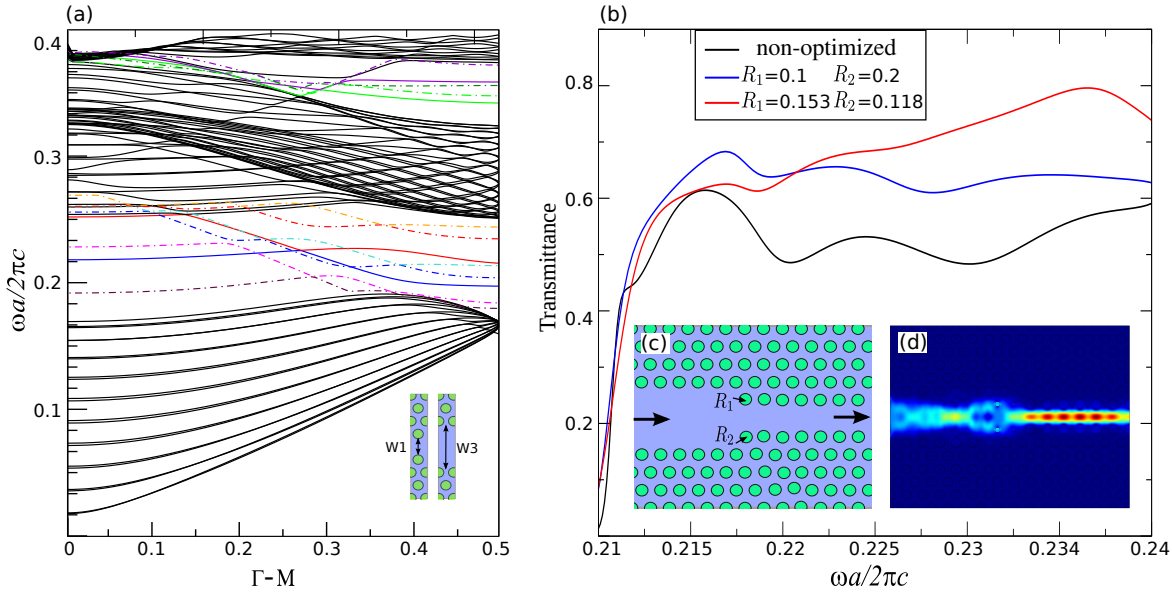

Figure 5.21 (a) Band diagram for triangular lattice of 0.295a holes drilled in a n=3.5 material in which a row of holes was eliminated (W1 waveguide) or three of these rows are filled with material (W5). For a W1 waveguide some band gap guided modes appear (thick coloured lines) but for a W3 waveguide there are many more modes allowed within the bandgap (dashed coloured lines). (b) Compariosn of the transmittance spectra obtained using a non optimized W3-W1 structure, the configuration given by the ID process and the solution proposed by Talneau et al. (c) Basic configuration of a simple taper structure that depends on the size of the radii R_1 and R_2. (d) Light power distribution using the configuration proposed by the ID method.

modes in a W1 waveguide and a W3 waveguide. However, this situation occurs only for a few frequencies and the transmittance decays sharply as it is shown in Fig. 5.21.b.

In this case, a brute-force look-up of the entire search space for the optimum R_1 and R_2 lengths is still feasible and so, we searched among 10.000 solutions points to locate the global maxima at $R_1 = 0.1531$, $R_2 = 0.118$ values. Once again, IHS and FSA algorithms agree in locating the optimum set of values but this result does not match with the one proposed by Talneau et al. Indeed, as it is shown in Fig. 5.21.b the transmittance enhancement obtained using the adiabatic configuration $R_1 = 0.1$ and $R_2 = 0.2$ proposed by Talneau et al. is extremely close to the one obtained by choosing a taper geometry given by the ID. Notwithstanding, for the optimization methods addresses here, the adiabatic solution is still a local maxima point and so if needed, the optimization escapes from this point and meets the global optimum in just few iterations. Fig. 5.22 depicts the search space according to the fitness and the solutions yielded by 60 Monte Carlos using the IHS method and another

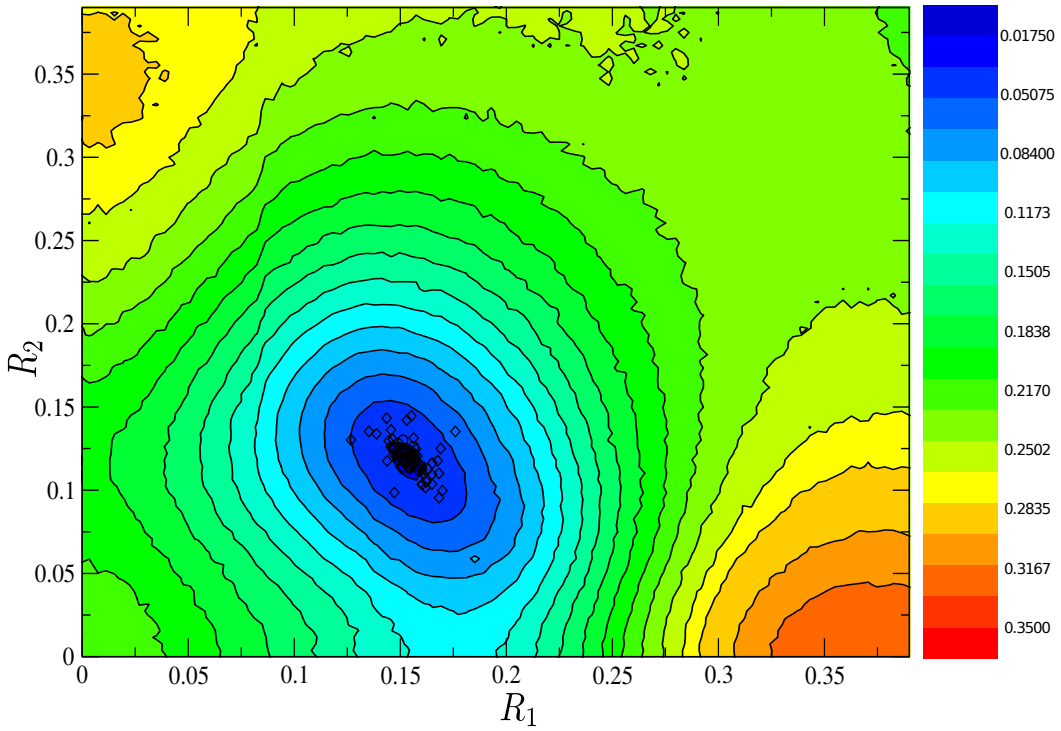

Figure 5.22 The coloured chart depicts the value of the optimization cost function over the entire set of feasible solutions. For this purpose, the search space was discretized in 10.000 points. The circled set of points and the diamond shaped points depict the solutions yielded by the ID method using the IHS and the FSA algorithms, respectively.

60 runs using the FSA method. Remarkably both methods succeed in finding the global optimum topology that maximizes the amount of light coupled to the W1 waveguide.

5.5.2 A Photonic Crystal coupler for efficient coupling light between a W5 and a W1 PCWGS

Usually, in silicon photonics, SOI waveguides are utilized as the most common means of light guiding trhough integrated components, and their feasibility for dense photonic integration has been widely demonstrated. Therefore, if a photonic crystal waveguide must be used in a PIC, this is very likely to be connected to any of these SOI waveguides, which interface section exceeds that of the W3 PCWG. This feature size difference and the corresponding low coupling efficiency between these media is one of the most relevant aspects that prevent PC from being used more frequently in PICs. Alternatively one could interface a SOI waveguide with a commensurate W5 waveguide, for which the coupling issue should not be so critical, and from this PCWG a coupling device could steer the light into a narrower W1 waveguide. All the same, coupling the light through these highly different photonic crystal

waveguides is a much more complicated task than the one done in the former toy model and, tuning just some few parameters does not ensure a proper light coupling. The geometry utilized as a initial configuration for engineering a coupler device is the one in Fig 5.23.b. Once again, we used the custom photonic crystal lattice, comprised of a triangular lattice of holes with $0.35a$ radii, where a stands for the lattice period, drilled on a 3.46 index Si material, in which we encountered a W5 waveguide against a W1 waveguide. We chose to modify a number of parameters to enhance the coupling between both media, i.e. we let the algorithms modify the radii and shift the position of those holes highlighted in Fig. 5.23.a. Both waveguides support guided modes between the range of frequencies of $[0.26 - 0.28]$ and thereupon we run the ID method with the prospect of finding those structures that flatten the transmission for this entire frequency band. To the best of our knowledge there has not been any demonstration of such a wide bandwidth operating system under similar conditions. The cluster considered in Fig. 5.23.a has a folding symmetry and thus, only a half of the geometry needs to be computed. So as to simulate this symmetry, perfect electric boundary conditions (PEC) were set to the symmetry plane boundary and perfectly matched layers were used for the outer interfaces to avoid unphysical reflections caused by the finite size of the cluster. The simulation model was illuminated placing a monochromatic plane wave source in the westernmost boundary. Then, the inverse design was carried out using both, the IHS and the FSA codes, respectively. The resulting optimized designs are shown in Figs. 5.23.c-. 5.23.e, noticeably they are very counterintuitive.

Fig.5.24.a shows the transmittance spectra obtained using the taper structures depicted in Figs. 5.23.c-. 5.23.e as well as the transmittance of a non-optimized W5-W1 taper shown in Fig. 5.23.b. On the one hand very strong reflection is observed when different width waveguides are not properly tapered, yielding to important losses in the transmission intensity. On the other hand, the light coupling is highly enhanced when the optimized taper structures are utilized. Furthermore, the transmittance spectra unveils a transmission efficiency that closely resembles to the one simulated for the reference W1 waveguide. Regarding to the transmittance of the W1 PCWG it should be pointed out that the amplitude of the transmittance lies below the 0.9 value. This fact is due to the presence of absorption boundaries, the so called PML boundaries commented in Chapter 2.

The coupling results presented by the non-tapered structure could still be sufficient for these devices operating in transmission. In contrast, in reflection operating devices, small reflections could lead to Gires-Tournois like interferences caussing damage in the operating systems. In these cases, the tapers proposed so far ensure a near-zero reflection behaviour. In addition, in both cases, the taper section goes integrated in the core PC circuit and thus it can be fabricated without adding more complexity to the fabrication process. Furthermore,

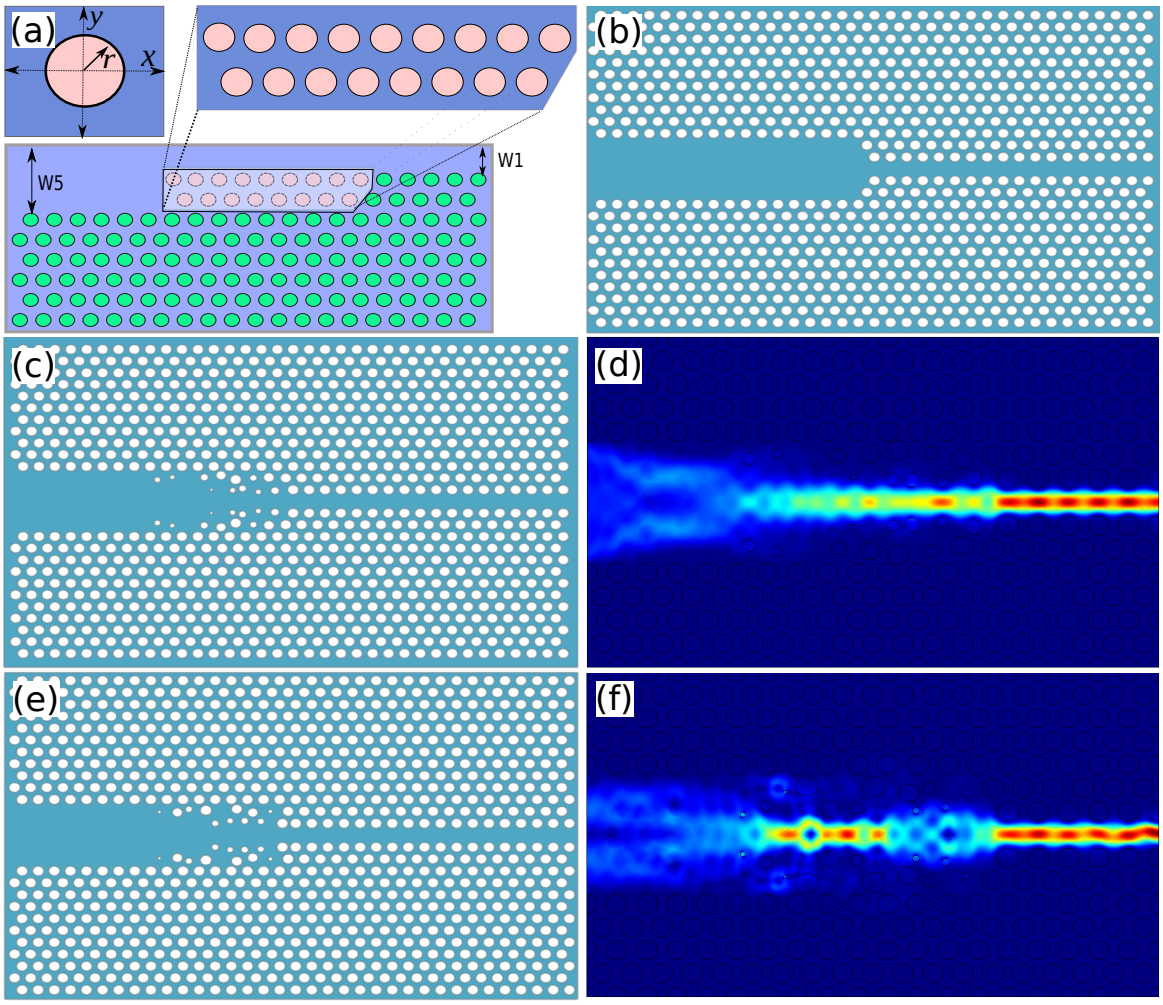

Figure 5.23 (a) Schematic view of the coupling region splitted by its symmetry plane. This system couples light from a W5 waveguide to a narrower W1 waveguide. The air holes subject to the ID process are highlighted therein. A close-up view of a unit cell wherein the radius and the position of a hole is shown. (b) A non-optimized horn-type taper design that reflects back a high-percentage of incoming light to the W5 channel (c) IHS optimized design that yields to an almost 100% coupling of light as it is shown in (d) for a/λ =0.265. (e) FSA optimized design. (f) Time averaged power flow obtained using the configuration sketched in (e).

the proposed design follows on the same geometry objects used in PCWGs, i.e. it does not use any kind of exotic geometry. Last but not least, the lengths of the taper section does not enlarge much the device, as it is comprised just by 8 periods, while most of the tapers presented so far implement long adiabatic stages for covering a less abrupt step (mainly W3-W1 tapers) like in [192]. Additionaly, we performed 3D simulations of the optimized taper structures, using a photonic crystal slab with a thickness of $0.6a$. The resulting transmittance

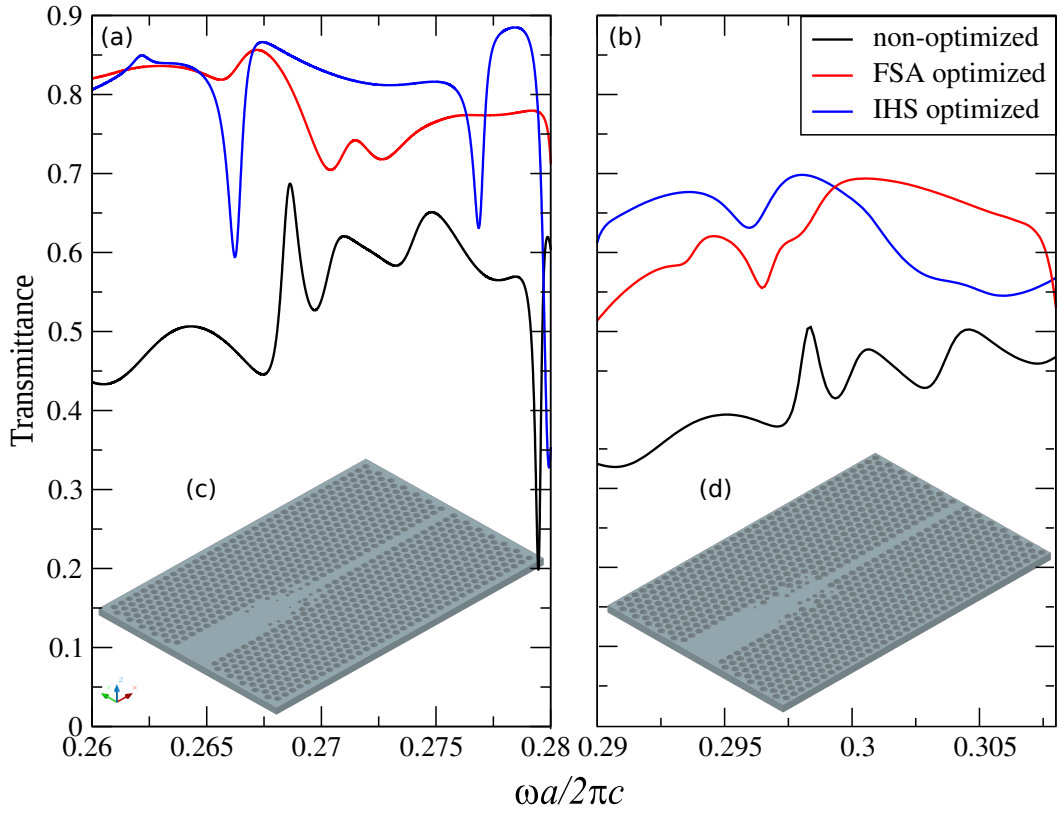

Figure 5.24 (a) Comparison of the amplitude of the transmittance spectra for the non-optimized model (black), IHS optimized (blue) and FSA optimized (red) coupler configurations in a 2D photonic crystal comprised by air holes of $0.35a$ radii in a Si (n=3.46) material. The inset shows the 3D PC slab model of the solution proposed using the IHS mehtod. (b)Analogous transmittance comparison in PC slab structures. The inset shows the 3D PC slab configuration obtained trhough the FSA method.

diagram is shown in Fig. 5.24.b. From this results we conclude that, although the tapers were designed for in a 2D PCWGs framework, they still preserve their coupling characteristics when they are implemented into a slab material. In addition, as the thickness of the slab is enlarged, the guided bands will lower in frequency and the efficiency of the taper is enhanced, approaching the transmittance obtained in Fig. 5.24.a.

5.6 Conclusions

In this chapter, we reported on the inverse design of ultra-wide bandwidth novel passive devices based on photonic crystal technology for efficiently performing the essential functionalities required by any future photonic integrated circuits. We utilize various heuristic optimization methods as the inverse design engine for achieving promising PC systems that outperform

previous topologies devised on intuitive grounds. Moreover, we present the application of these techniques for attaining a global optimum solutions. Besides, this chapter addresses PCWGs made using a holes-in-dielectric type PCs. In this situation, the PCWG becomes typically multimode and hence, higher order modes prevent an efficient mode-matching between different crystalline directions or through dissimilar PCWGs. The ID methodology is a well known tool in other engineering disciplines, but there have been very few attempts to use it in the design of complex photonic devices based on PCs. With this proceeding we demonstrate that both, FSA and IHS algorithms, suit perfectly to PC devising. Likewise, comparing the performance of FSA and IHS algorithms is somehow out of the scope of this manuscript as the models treated here are far from constituting a standard benchmark framework. Even though, for the sake of illustrating the reliability of each of the aforementioned techniques, we show some very basic PC structures, in which managing only a few degrees of freedom still comprises a challenge to an intensive exploratory search. Moreover, we demonstrate that in some of these simple cases, the ID method yields to solutions that outperform the results reported in the literature so far. The designs reported above are not only interesting from a theoretical point of view, but also of great practical importance as they are essential building blocks required for a number of more complex devices. A clear example of this is found in the optimized light coupling structures reported here. These structures maximize the mode matching between two distinct PCWG that are joined by an abrupt transition step and avoid the acute back reflection at the input waveguide, a feature that is neccessary for coupling near-zero dispersive light modes of PCWGs and to devise tunnable optical delay lines that benefit from the slow-light regime. With this regards, we show that the light coupling efficiency of these structures is near 100% for a wide range of frequencies. Last but not least, these tapers are fully compact, namely, they consists only on a few periods of PC, while most of the tapers presented so far make use of long adiabatic stages for covering a less abrupt step. In addition, we report on the extremely high efficiency of these structures in a PCWG slab using a 3D-FEM approach. The ID method has been also applied to discover light PCWGs provided by sharp bends that maximize the transmission over an ultra-wide range of frequencies. Indeed, the ability of confining light through high angle curvatures is one of the most promising features of PCWGs, but designing them for enhancing the light guiding operation in a wide bandwidth requires novel geometries. In this chapter we present PC bends that do not require any exotic lattice and thus, they are easily manufacturable using common lithography methods. Besides, as far as we are concerned, this is the first report of a wide bandwidth operating sharp 120° PCWG bend with almost optimum bending efficiency. This fact opens the possibility of building essential stages for novel integrated opto-electronics, small-scale all-optical circuits and semiconductor device

miniaturization. Along with all these models, we also demonstrated two distinct approaches of functional light splitting topologies with excellent performance. The key feature of these devices is the ability to control the mode expansion and excitation of higher order modes at the output waveguides. These simple structures support low losses within a large optical bandwidth and can be combined for distributing optical power within a PIC as well as a splitting/combining light mechanism in interferometers and optical switches. With this in mind, the structures studied in this work are difficult to obtain by using intuition as a guide, whereas they are obtained in a straightforward manner from our ID framework.

Chapter 6

Non uniform grating couplers

Photonic crystal waveguides promised to bring a flawless lossles guiding to SOI integrated circuits but, despite of being a theoretical breakthrough for light localization, it turned out that SOI waveguides were a simpler and more effective approach to guide light providing minimum losses. These light conduits are therefore extensively used to guide light at micrometer scale in planar silicon integrated circuits and are also the last frontier between the PIC and an optical fibre. This chapter starts with a brief introduction to SOI waveguides. Two typical optical waveguides are presented- strip and rib waveguides. Then, the challenge of coupling light in and out of silicon photonic slab waveguides, different coupling approaches, and the physics behind the grating couplers are described. Moreover, we use an FDTD method together with the ID methodology to design non-trivial coupling devices optimized to minimize insertion losses between optical fibres and integrated waveguides.

6.1 Waveguides in silicon photonics

Waveguides of integrated optics constitute one of the most important elements in the building of all-optical and electro-optical technology. A waveguide plays the double role of being the optical pipe that interconnects light between the components of the PIC and simultaneously acts as the interface between the PIC and single mode fibers (SMF). Considering the strong localization of light modes in PCWGs, it could seem reasonable to readily use them as indefectible light conduits. However, only these photonic crystals constructed on a three dimensional scale bestow a theoretical total confinement of light, albeit they are extremelly difficult to fabricate and prevent a wafer scale modelling of PICs. More generally, slab photonic crystal waveguides provide a solid basis for tailoring light wave propagation. Additionally, PCWGs can be used to enhance anomalous dispersion features that can be further exploited, leading to very interesting physical phenomena, such as soliton-effect pulse

compression [224] or third harmonic generation produced by the inherent slow down of group velocity [225]. However, considering the insertion losses of slab PCWGs, it turns out that less sophisticated SOI waveguides are a simpler and a more effective approach to just guide light in the linear regime. SOI waveguides, which are the optical analogue of silicon microelectronics, operate using total internal reflection and their feassibility for dense photonic integration has been widely demonstrated [226, 227]. Commonly, these waveguides are comprised of a silicon layer, set on top of a silicon oxide layer, above a host silicon lattice, as far as silicon provides a high refractive core material to confine light within a very reduced footprint and yields to minimum propagation losses to the cladding material. Nevertheless, waveguides in silicon photonics can be comprised of silicon nitride, silicon oxynitride, doped silica, doped silicon or polysilicon as waveguide materials [228].

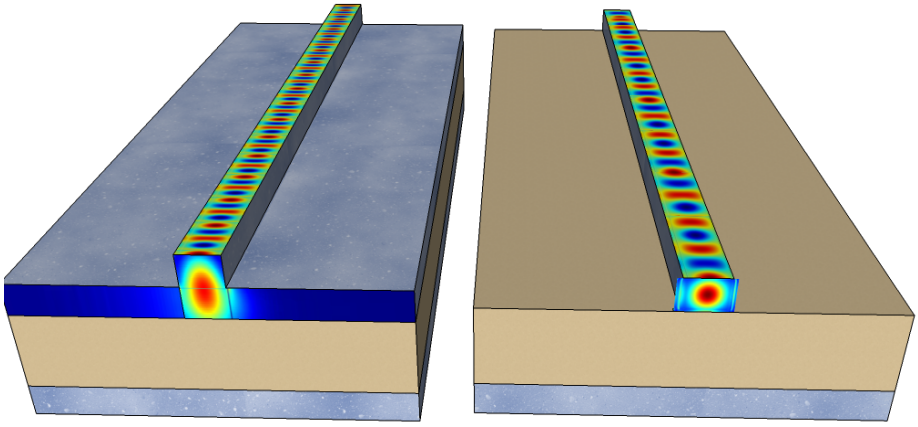

Figure 6.1 Common waveguide geometries in silicon-on-insulator. left: A 3D representation of a strip waveguide comprised by a silicon guiding layer set on top of a buried oxied layer and a silicon substrate. In this case the cladding matrial is absent(air). The strip waveguide shows the fundamental TE mode propagation pattern calculated using FDTD computations. The cross section (front) shows the shape of the fundamental TE mode simulated using a full vectorial eigenmode method. To the right: shows the corresponding information for the rib waveguide.

There are two basic sort of waveguides. On the one hand, the strip waveguide, shown in Fig.6.1.a, also known as photonic wire or channel waveguide, is the simplest optical link as it requires a single etch in its fabrication process. It allows for very tight bends with low optical losses [226]; however, it presents relatively low fabrication tolerances and high scattering losses due to sidewalls roughness [229]. The later can be understood by inspecting Fig.6.1.a. Therein, the fundamental TE mode overimposed in the front cross-section shows that a

relevant amount of the electric field spreads over the walls of the silicon strip. Therefore, fabrication imperfections in these silicon waveguide walls are the most significant sources of propagation losses, which are currently around $2-3$dB/cm using commercial processes [230, 231]. The other common type of waveguide in silicon photonics is the rib waveguide, also known as ridge or strip loaded ridge waveguide. The rib waveguide requires two edges and thus, it is more expensive to fabricate [232]. A standard rib waveguide is shown in Fig 6.1.b , where the fundamental TE mode depicted in the front cross section of the rib structure shows a remarkable spread of the field into the silicon layer beneath the guide. This larger modal area makes it particularly good for devising electro-optic componentes such as modulators [233, 234]. On the other hand, this feature increases field radiation effects and demands larger bend radius to confine light within the channel [235]. Novel strategies have recently been demonstrated for achieving ultra-low loss silicon waveguides fabricated without any silicon etching, achieving propagation loss down to 0.3dB/cm [227, 236].

Throughout this chapter we focus our study into the strip waveguides comprised of 725 μm of silicon substrate, 2 μm of oxide, known as buried oxide, or BOX, and 220 nm or 250 nm is some other cases, of cristalline silicon strip. This thickness has become a standard used in particular by multiproject wafer foundries and foundry service providers (e.g. Imec [237], LETI [238], IME [239]). Fig.6.2.b shows the electric field profile for the TE and TM fundamental modes of the asymmetric SOI strip waveguide for a number of geometries, respectively. Onward, as the slab thickness is increased, the electric field gets more localized, i.e. the evanescent field outside the silicon material decreases. However, as it is shown in Fig.6.2.a, when the thickness is increased beyond 240 μm, the waveguide becomes multi-mode. In general, multimode waveguides are undesirable in SOI circuits, as their performance can be compromised by undesirable effects such as intermodal dispersion or optical signal distorsion, among others [230]. In addition, waveguides optimized to bound TM modes are eventually lossy when they are utilized for guiding TE polarized light, the same applies to TE waveguides when they are used to guide TM modes. However, the width of the waveguide, W, is still a free parameter that the designer can tune according to each application. Again, W is usually limited in order to keep the waveguide being single mode.

6.2 Coupling to silicon waveguides

The large refractive index contrast in SOI materials, makes them an outstanding platform for designing densely integrated circuits. However, the small feature size of such compact devices complicates the light-coupling interfacing between standard single mode optical fibres and SOI circuits, causing high insertion losses and high packaging costs. This decoupling is

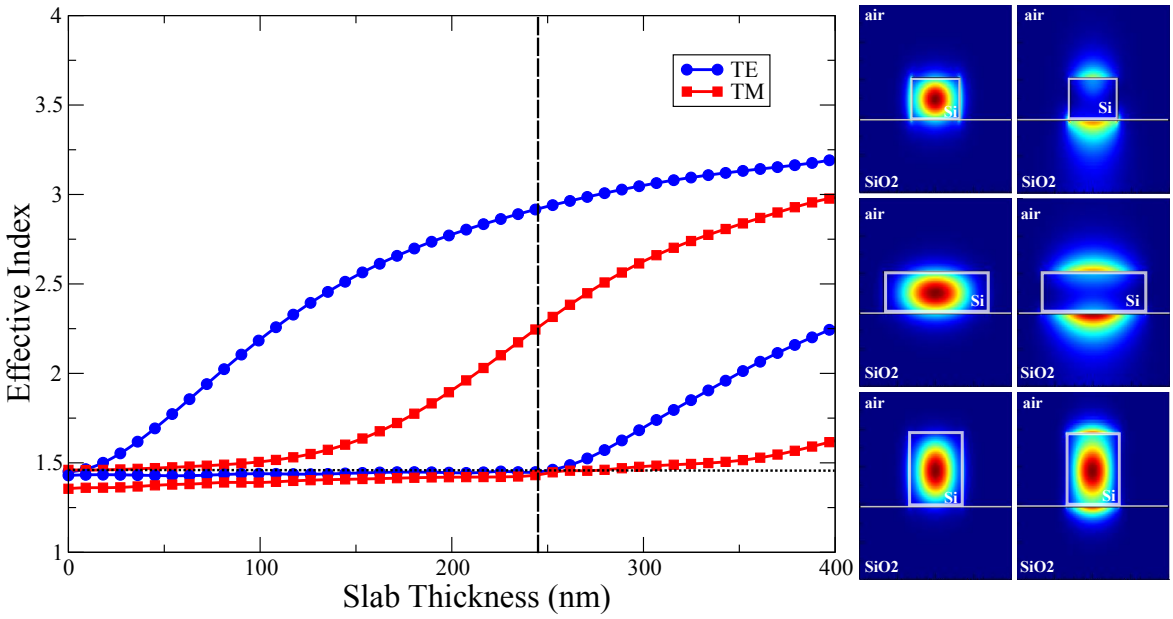

Figure 6.2 (a) The effective index simulations for different waveguide widths at a wavelength of 1550 nm. The horizontal dotted line represents the refraction index of the oxide layer. Therefore, only modes with effective index beyond this dotted line will be guided through the strip waveguide. Consequently, the vertical dotted line denotes the exact thickness value beyond which the strip waveguide becomes multi-mode. The latter is also observed in b) for the simulated TE and TM fundamental modes with a thickness of 220 nm, 500 nm and 1100 nm, respectively.

mainly due to the huge mode mismatch between the cross-sections of fibres and SOI guides. It is straightforward to observe this decoupling by calculating the overlap of the incident source field and the excited guided mode in the waveguide. The latter can be written as follows:

$$\Gamma = |\int \int S\, E_{input} \times H^{*}_{mode} dS|^2, \tag{6.1}$$

where E_{input} corresponds to the electric field profile of the incident optical mode from the fiber and H_{mode} is the excited mode in the slab waveguide. This field can be approximated by a Gaussian profile [235]:

$$E_f(x,y,z=0) = E_{max} \exp^{-\left(\frac{x^2+y^2}{\omega_0^2}\right)}, \tag{6.2}$$

where ω_0 corresponds to the beam diameter for which the amplitude of the electric field decays to $1/e$ of its maximum amplitude, E_{max}. The mode field diameter of the beam is twice the beam diameter, i.e. $MFD = 2\omega_0$. Light may be coupled into a waveguide by using an end-

fire coupling, i.e. directly focusing at one end, as it is shown in Fig.6.3.a. To excite a given mode, the transverse distribution of the incident light should match that of the mode and does not allow to selective guided mode excitation [240]. The polarization of the incident light must also match that of the desired mode. Because of the small dimensions of the waveguide slab, it is neccessary to perform a very high optical polishing of the guide cross-section to avoid optical diffusion losses. Also, focusing and alignment are usually difficult and therefore coupling using this method highly depends on the experimental conditions [235]. Given and end-fire coupling configuration between a strip waveguide with a W of 1550 nm and a SMF fiber, the former has a mode field diameter (MFD) of a few hundreds of nanometers while the latter has a MFD of around 10 µm. This MFD mismatch causes coupling losses as high as $26.7dB$ [230] for a single fiber-chip connection, meaning that extracting back the light to an output optical fiber would be twice this quantity. Light coupling inefficiency can be partially alleviated by positioning the optical fiber at some angle θ. Yet, in orther to excite the slab waveguide mode, the axial component of the wavevector of the incident wave must match the propagation constant beam of the guided mode. Such condition can be achieved by using a prism of refractive index $n_p > n_1$, where n_p and n_1, are the refractive index of the prism and the air, respectively. By adjusting the distance between the prism and the waveguide, the power coupled to the in plane guide can be significantly increased. Figure 6.3.b shows the focusing procedure using a prism. The operation may also be reversed to make an output coupler, extracting light from the slab waveguide into free space. Coupling using this technique has roots in the late 60s and modern coupler systems rarely utilize a prism mechanism. Instead, to alleviate the fibre-chip coupling issue, two main strategies are usually utilized: edge coupling methods provided with inverted tapers and out of axis coupling using periodic gratings, respectively.

Edge-coupling methods provide wide bandwidth and low insertion loss operation [230]. In general, this practice requires a tapered structure on the waveguide surface over a distance of 10 to 100 times the wavelength used to progressively couple or out-couple the incident light throughout the structure. In essence, the modal amplitude of the coupled mode is adiabatically fitted to minimize backscattering reflections. This technique is of great interest because it allows to couple both, TE and TM polarization, simultaneously. Nonetheless, this procedure still requires a lensed, high numerical aperture fibre or an inverted taper with a very sensitive fiber-guide alignment [241, 242] to match the optical mode size between the two light guiding materials. Fig. 6.3.c shows a coupling system using a lensed fiber and a tapered waveguide surrounded by a Su-8 polymer as the one utilized in [241] to highly increase the light coupling. In contrast, out-of-plane coupling, presents some major advantages over former methods. The use of this approach eludes the need of cleaved facet fibres and there

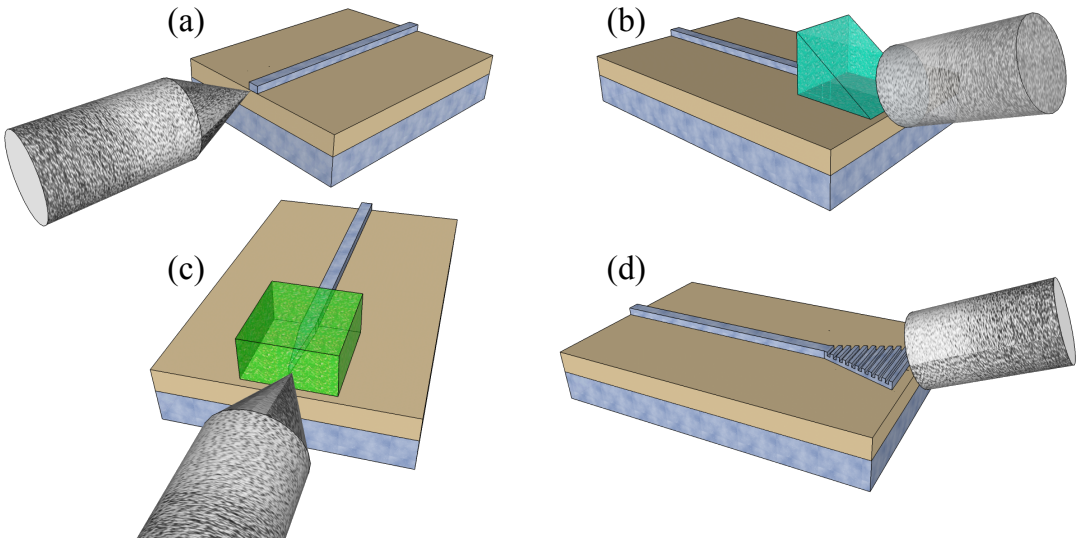

Figure 6.3 a)Illustration of the end-fire coupling principle: the fibre faces the nano waveguide directly. b) Prism coupling mechanism: the coupling is performed by adjusting the air gap distance between the prism and the slab guide. Thus, the system becomes a four layer medium(prism, air, silicon and BOX). c) Coupling mechanism utilizing an inverted taper. Usually this approach uses a low index medium as the SU-8 polymer to increase the coupling efficiency (coloured in green). d) Light incident by an angle θ_i is coupled to the waveguide using a periodic set of trenches, i.e. a grating coupler.

is no limitation for extracting/coupling light everywhere on the chip, which is a critical advantage for large scale wafers [256]. Regular solutions provide guided-mode resonances using periodic gratings directly written onto the surface of the nano-waveguide, as the one shown in Fig. 6.3.d. This approach is the most broadly used [244, 245] for PIC connection and most of the silicon photonics foundries provide them in their chips. The grating addresses the phase matching problem by modifying the wavevector of the incoming wave to satisfy the phase matching condition in the direction of the slab waveguide, as it is discussed below. Nevertheless, periodic grating designs present a small coupling strength, they are rather long, and they have a narrow bandwidth operation.

6.3 Diffraction gratings

When light incident from the fibre impinges the grooved waveguide, diffraction phenomena occurs. This process can be understood in terms of the Huygens-Fresnel principle, i.e.

the trenches of a grating create small sources of interference where the superposition of constructive and destructive wavefronts occurs. Fig. 6.4 shows the phase relation diagram for diffracted rays from adjacent etches [246]. For the sake of simplicity, the grating coupler can be represented as a one dimensional periodic structure, and thus, it can be described using Bragg's Law. In Fig. 6.4.a we assumed that the diffraction grating extends infinitely, that the incident wave is monochromatic and perfectly collimated and that the plane of incidence is perpendicular to the grating grooves. Under these conditions, incident plane waves are diffracted at an specular fashion when they encounter the dielectric medium with refractive index n_2, with an angle θ. Given the periodicity of the grating, Λ, the waves are scattered from lattice grooves separated by a distance Λ and with a path difference of $|\Lambda \sin\theta_i - \Lambda \sin\theta_m|$, where θ_m is the scattering angle for waves propagating with a wave vector k_m [246].

According to the Bragg condition there is a unique set of angles for which light scattered from these grooves is in phase and thus, interferes constructively. This condition is fulfilled whenever this path difference equals an integer multiple of the wavelength of the impinging wave. Therefore, the grating equation can be written as follows:

$$\sin\theta_m = \sin\theta_i + \frac{m\lambda}{\Lambda}, \qquad m = 0, \pm 1, \pm 2, ..., \tag{6.3}$$

where θ_i and θ_m are the angles between the incident and diffracted wave directions, λ is the wavelength and Λ is the grating period. When m is equal to zero, the grating acts as a mirror and all wavelengths are superimposed. For non specular orders ($m \neq 0$) the angle of diffraction depends on the wavelength value so that wavelengths are separated angularly [246]. For a given set of incident angles, groove spacing and wavelength values, the grating equation can be satisfied for more than one value of m. Furthermore, it is obvious that there is a solution only when $|\sin\theta_m| < 1$. Diffraction orders with number m such that condition eq. (6.3) is fulfilled are called propagation orders.

For the particular case of steering in-plane diffraction to excite the wave propagating in a slab waveguide, i.e. a propagation direction in the same plane as the grating coupler, the propagation constant is given by

$$\beta = \frac{2\pi n_{eff}}{\lambda}, \tag{6.4}$$

where n_{eff} is the effective index of the slab waveguide. Waveguide gratings are thereupon polarization dependent, as n_{eff} varies according to each polarization. On the other hand, the quantity

$$K = \frac{2\pi}{\Lambda}, \tag{6.5}$$

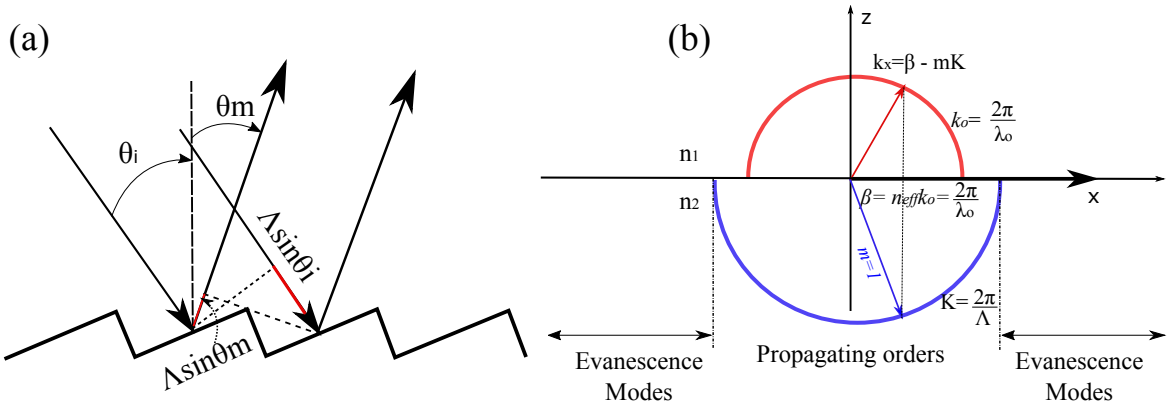

Figure 6.4 a) Illustration of the end-fire coupling principle: the fibre faces the nano waveguide directly. b) Prism coupling mechanism: the coupling is performed by adjusting the air gap distance between the prism and the slab guide. Thus, the system becomes a four layer medium (prism, air, silicon and BOX). c) Coupling mechanism utilizing an inverted taper. Usually this approach uses a low index medium as the SU-8 polymer to increase the coupling efficiency (coloured in green). d) Light incident by an angle θ is coupled to the waveguide using a periodic set of trenches, i.e. a grating coupler.

known as the grating wavenumber, describes the periodicity of the grating. Higher order diffraction gratings can be written as integer values of this quantity, i.e. $m\dot{K}$. Thus, the general form of the Bragg condition can be expressed as

$$\beta - k_x = mK, \tag{6.6}$$

where k_x is the component of the wave vector of the diffracted wave in the direction of the incident wave. This wave is traveling in the cladding with an index of refraction n_2. The diffracted light has a wave vector of

$$k = \frac{2\pi n_2}{\lambda}, \tag{6.7}$$

and describes and angle θ_m between the wavevector of the diffracted light, k, and the horizontal component k_x, of:

$$\theta_m = \sin^{-1}\frac{k_x}{k} = \sin^{-1}\frac{n_{eff}\lambda}{\Lambda}. \tag{6.8}$$

This is illustrated in Fig.6.4.b. All in all, the Bragg condition can be simplified to be

$$n_{eff} - n_2 \sin\theta_m = \frac{\lambda}{\Lambda}. \tag{6.9}$$

Regarding to the other orders of diffraction, having $|\sin\theta_m > 1|$ inplies then that the vertical component of the wavector is imaginary, these orders decrease exponentially with the distance from the grating surface, i.e. their amplitudes are proportional to [246]

$$exp(ik_{mx}x - k_{my}y), \tag{6.10}$$

with

$$k_y = \sqrt{k_x - \left(\frac{2\pi n}{\lambda}\right)^2}. \tag{6.11}$$

These orders are called evanescent orders. They can not be detected at a distance greater than a few wavelengths from the grating surface, but can play an important role in some surface-enhanced grating properties [246].

6.4 Searching for a more efficient grating coupler system

Figure 6.5 shows the schematic set-up of a regular grating coupler etched on a strip SOI wafer with a220 nm thick crystalline silicon layer which refractive index n is, $n = 3.467$, over a 2 µm thick buried oxide $n = 1.46$ layer. A single mode fibre is positioned with a tilt angle to the normal direction above the grating to avoid backreflection. In order to eliminate the fiber's facet reflection, an index-matching gel with index $n = 1.46$ is utilized filling the space between the fibre and the grating.

Aside from the consideration of these parameter, it is of practical relevance to choose the etching depth and the period of the grating. In a periodic grating coupler the period of the grating is fixed by the Bragg condition, as explained above, while the edge depth is also present in the grating equation (6.9) as it contributes to the effective index of the guiding material. Grating groove's will make the amplitude of a wave propagating through the corrugated waveguide decay exponentially [247],

$$P_{wg}(z) = P_{wg}(z = 0)e^{-2\alpha z}, \tag{6.12}$$

according to the leakage factor 2α (also called coupling strength), and those wave-vectors matching the first order diffraction will contribute to the optical power leaked to the optical fiber (upwards). Correspondingly, and if no other reflection mechanism is used beneath the waveguide layer, there will be a certain amount of optical power radiated downwards following the same reflection angle, θ. The inverse of the leakage factor is defined as the coupling length:

$$L_c = 2\alpha. \tag{6.13}$$

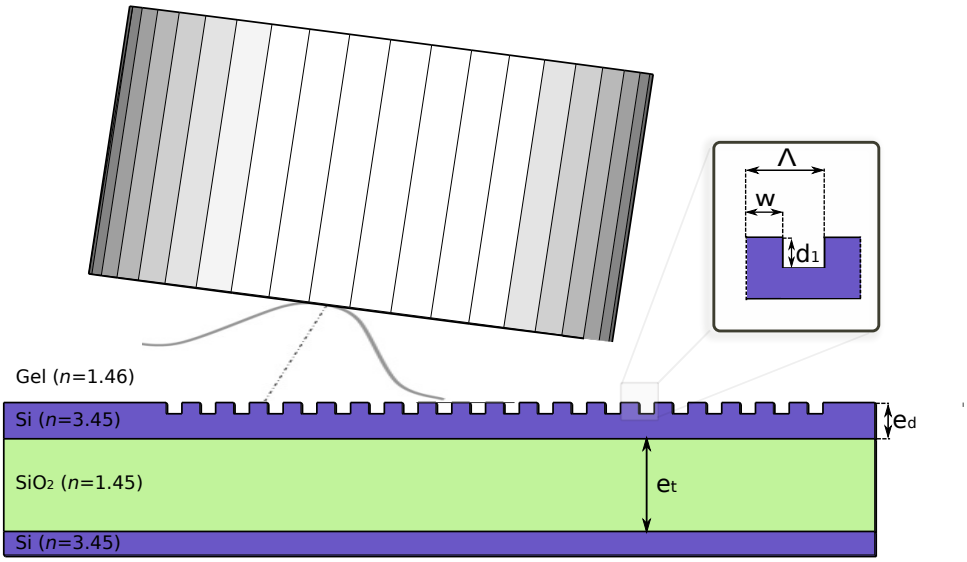

Figure 6.5 Basic configuration for a custom fiber-to-chip periodic grating coupler. A standard SMF interfaces near vertically with a diffractive grating structure defined on the surface of the silicon waveguide. The grating coupler structure is determined by the duty cicle (W), the filling factor (ff), the period (Λ) and the depth of the grooves (d_1). The rib waveguide consists of a silicon layer of thickness e_d on top of a buried oxide layer (BOX) of thickness e_t. To clearly illustrate the design, the diagram is not to scale.

For shallow etched grating couplers, α is small, making the coupling length L_c as large as the diameter of the mode of the optical fibre [229] and thus, they produce a large mode overlap between the exponential mode from the grating and the Gaussian mode of a fibre. Instead, fully etched gratings render to a high coupling strength and thus, the shorter coupling length makes it more difficult to achieve an efficient mode overlap. In the case of periodic gratings, the optimal horizontal distance, d, between the center of the fiber and the grating coupler, corresponds to the coupling length L_c. In the following simulations, we assumed a fiber Gaussian beam waist of $2\omega = 10.4\,\mu\text{m}$ and hence, we placed the fibre at a distance of $d = 5.2\,\mu\text{m}$ in the horizontal axis from the grating edge and to $1.8\,\mu\text{m}$ from the silicon top layer. This vertical gap permits to relax the tilting angle, which, in this first case was chosen to be 8° from the perpendicular plane. For the initial approach we set the SOI wafer crystalline silicon layer thickness to be 250 nm and the etching depth of the grooves was set to the custom length of 70 nm. In a preliminary approach, we delimited the search to the exploration of two coupled trivial parameters, i.e. to the duty cycle of the grating coupler W that defines the width of the grating tooth and the fill factor ff defined as the ratio of the grating period and the duty cycle ($ff = \Lambda/W$). Then, we mapped the maximum coupling efficiency between a transverse electricaly (TE) polarized Gaussian beam centred at $\lambda = 1.55\,\mu\text{m}$, where λ is the light's wavelength, spanning 0.1 μm. Each fiber-grating configuration was modelled

by means of two-dimensional Finite-Differential Time-Domain (FDTD) simulations using a uniform grid featuring elements with sizes below $\lambda/10$ and we used Perfectly Matched Layer (PML) boundary conditions surrounding the whole grating and fibre domains. The coupling efficiency (η) was then calculated using eq. (6.9).

Figure 6.6.a depicts the coupling efficiency of 10.000 combinations of *ff* and *W*. As expected in this trivial case, an almost linear relationship between the filling factor and the duty cycle can be appreciated, along with some global maxima (marked in black). In addition, we assumed that the oxide thickness, fibres tilt angle, etching deep and some other aforementioned parameters were almost optimal for a minimal downward leakage, but that is not necessarily true since all these parameters are coupled to each other, as it will be seen later on. The above analysis has proven useful for unveiling some optimal parameters in a periodic grating structure, given the initial conditions described before. However, limiting the amount of design parameters as we did, leaves far fewer degrees of freedom than are phisically possible and the resulting coupling efficiencies are still rather low. On the other hand, bringing more parameters into the coupling problem extremely complicates the brute-force approach and also would make the problem mathematically very hard to be tractable.

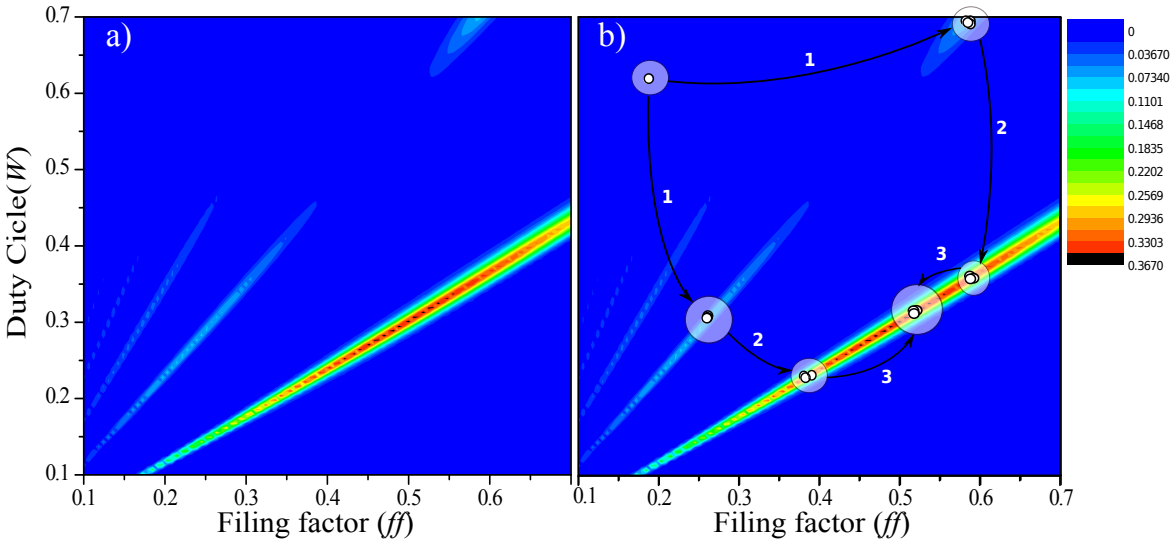

Figure 6.6 (a) The density map depicts the coupling efficiency at $\lambda = 1550\,\text{nm}$ for the entire set of *W* and *ff* combinations. b) The solution dataset calculated in (a) is over-imposed by circled set of points surrounded by a white cloud, showing the solutions given by the ID method in each step. The ID process clearly converges to the maximum coupling parameter pairs.

To counterbalance this issue, we addressed once more to the inverse design methodology so as to facilitate the prospect of optimum topologies. In the present context, it was of practical relevance to check whether an ID methodology like the one described in sec. 4.2.2

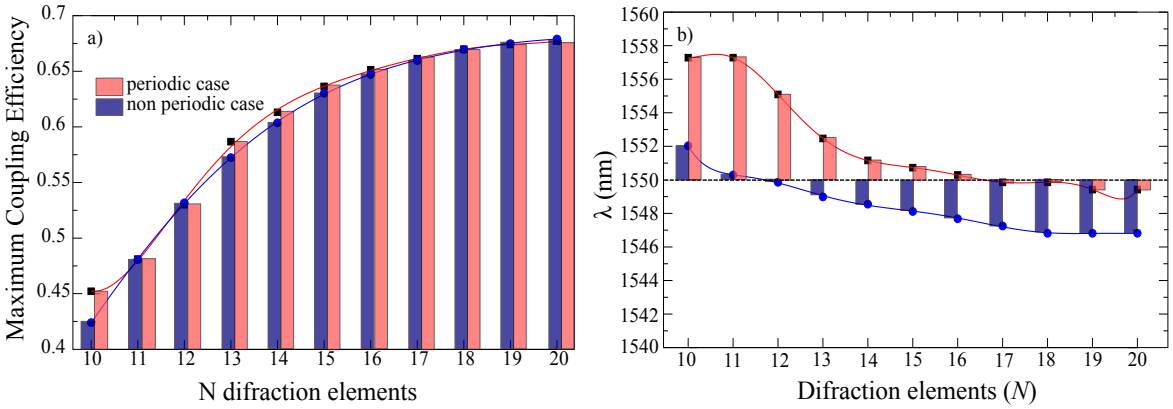

Figure 6.7 (a) Maximum coupling efficiency with regards to the number of grooves in the periodic and non-periodic gratings, sketched in red and blue respectively and the(b) deviation of the peak coupling efficiency in each case.

yields improved grating couplers or, conversely, whether conventional periodic grating couplers fare better. In Fig. 6.6.b results obtained by means of the ID mehtod using the IHS core algorithm are overlaid to the exhaustive lookup–map. Noticeably, when using the ID methodology to this problem, the solution is quickly achieved taking into account only those combinations of parameters that yield promising results. The ID method, driven by its heuristic engine jumps quickly from average fitness solutions to local optima points and subsequently splits the search through local optima points to a global optimum in just 3 steps. The whole process takes only few minutes to converge to the solution marked by white markers. Hence, even in this simplified model, introducing the ID method drastically reduces the computational time and prevents the calculation of non-profitable solutions by predicting the combination of parameters that enhances light overlapping between guide and fibre.

The key features of an effective light coupling system are compactness, low insertion loss, large alignment tolerance, and broadband operation [242]. Taking all this into account we proceed with the secont attempt to design a more efficient, still periodic, grating. With this regards, we took a 20 periods length grating profile with the parameters specified before, except that this time we let the ID algorithm decide the horizontal position of the SMF fibre, its tilt angle as well as the grating period, Λ, in order to optimize the coupling of light from the integrated waveguide to the SMF fibre. The optimum set-up for this purpose found by our code is given by $\Lambda = 640\,\text{nm}$, with a fibre displaced $5.23\,\mu\text{m}$ from the grating edge and tilted 15°. For these values, a maximum theoretical coupling efficiency of 66% is achieved with an estimated 1 dB bandwidth of 40 nm.

Considering the first diffraction order ($m = 1$), a tilt angle of 15°, and a n_{eff} around 2.8 (calculated using an eigenmode solver), equation (6.6) predicts a grating period of 610 nm

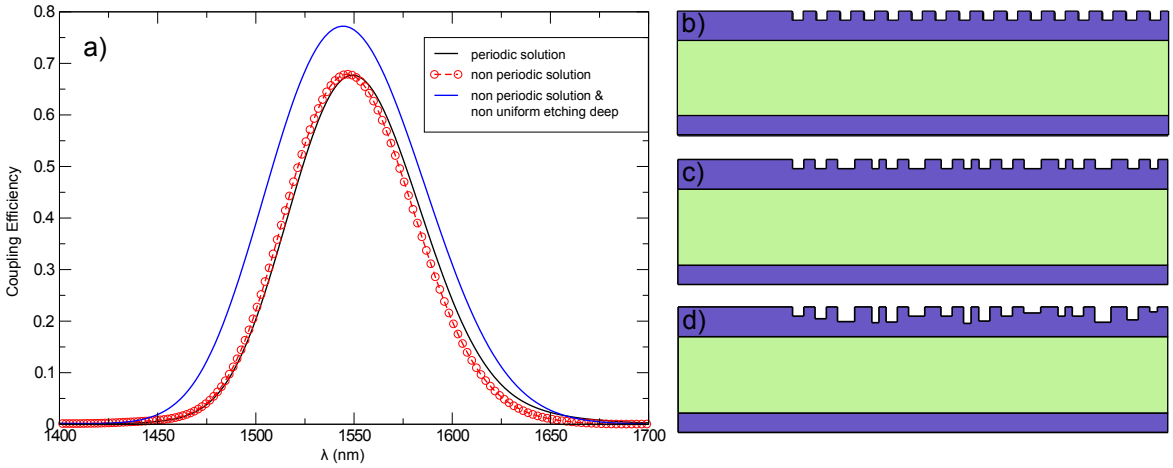

Figure 6.8 (a) Simulations results for coupling efficiency spectrum for each case of study.(b)-(d) The schematic representation of the optimized periodic grating, the aperiodic grating and the non-uniform grating made by also tuning the etch depth, respectively. The dimensions of the grooves have been exaggerated for clarity purposes.

for $\lambda = 1.55\,\mu m$, very close to the solution given by our ID method. It should be pointed out, however, that the Bragg condition is only exact for infinite structures. For finite structures, diffraction occurs for a range of wave-vectors. The decay of the coupling performance for this structure is shown in Fig. 6.7.a. The performance of the periodic grating converges when 20 grooves are etched in the silicon layer and the removal of grooves presents a polynomial decay of the coupling efficiency (see Fig. 6.7.a). However, as one disposes of just 4 periods, the peak coupling efficiency starts to deviate from the target λ, as it is shown in Fig. 6.7.b. This deviation amounts to 8 nm when only 10 periods are considered in the periodic grating. Although the etching nonuniformity is usually detrimental for most applications, brings more freedom into the design process. However, designing such non-periodic clusters entails dealing with several correlated parameters at the same time and, moreover, these kind of diffraction gratings cannot be outlined using current analytic approach, or by tuning a small number of parameters by hand [248]. Nonetheless the ID method provides a prospect way for dealing with N-parameter optimization required for non-periodic corrugated waveguides. In Fig. 6.8.c a non-uniform grating coupler scheme is represented. In this particular case, every groove is detuned at the same time, constrained to fabrication limitations, i.e. the width of these grooves does not go below 10 nm. The efficiency of the final corrugated waveguide yields slightly better coupling results when compared to the former periodic case, depicted in Fig. 6.8.b, although this non-periodic structure does not entail a significant advantage over the well-known periodic design, as it is shown in the efficiency comparison given in Fig. 6.8.a.

Specifically, it provides a peak coupling efficiency of 69 % with a 1 dB bandwidth close to 38 nm. Noticeably, the grating structure depicted in Fig. 6.8.c shows an smooth profile that ensures a good stability when the grating is shorten (see Fig. 6.7.a.). In this case, the efficiency of the coupling almost corresponds to the periodic case. On the other hand, this grating profile enhances the coupling of light close to the 1.55 μm with a maximum deviation of 3 nm, which can be compensated by adjusting the fibre tilting angle.

Fig. 6.9.b shows the almost perfect agreement between experimental measures taken on a fabricated silicon grating coupler and the efficiency calculations achieved with numerical simulations. The sample was fabricated in the Nanophotonics Technology Center (NTC) of the Universidad Politecnica de Valencia, using a commercial SOI wafer with 220 nm top silicon thickness and 3 μm buried SiO_2 thickness. An e-beam lithography method over polymethic methacrylate resist was used to create a mask that was further used to achieve the desired grating structure through dry etching by using an Inductive Coupled Plasma (ICP) system [230]. A Scanning Electron Microscope (SEM) image of fabricated grating is depicted in Fig. 6.9.a

All the same, non-periodicity did not result in any benefit in the out-off-plane coupling system so far. Due to this, we decided to include the etching depth of the periodic grooves into the design process. In this case, we constrained the etching depth and the duty cycle of each groove preventing full etching of the silicon layer or narrow grooves. The resulting grating profile is schematically shown in Fig. 6.8.d and the simulated coupling spectrum for the TE polarization is shown in Fig. 6.8.a for comparison. One can see that a maximum coupling efficiency of 78% is achieved at 1.55 μm and the 1 dB bandwidth is about 40 nm. The coupling efficiency is much larger than that for a standard uniform grating coupler and the wide bandwidth makes it very promising for C-band applications. Besides, the efficiency could be further improved using a bottom reflector [255] or a silicon overlay [250] that reduces the downward substrate leakage, but at the expense of an increased fabrication complexity. In spite of the efficiency boost provided by this last structure, it requires different etching depths for each grove, which severely complicates the fabrication of this grating, making it a mere theoretical solution. On the other hand, these results show that the non-periodicity could be utilized to further explore non-uniform grating couplers when a periodic approach has proven to be limiting, such as in the cases that we discuss in the following sections.

6.4.1 Perfectly vertical grating couplers

So far, we have reported on corrugated waveguides which rely on a slight tilt of the optical fibre facet with respect to the vertical axis that inhibits the second-order Bragg

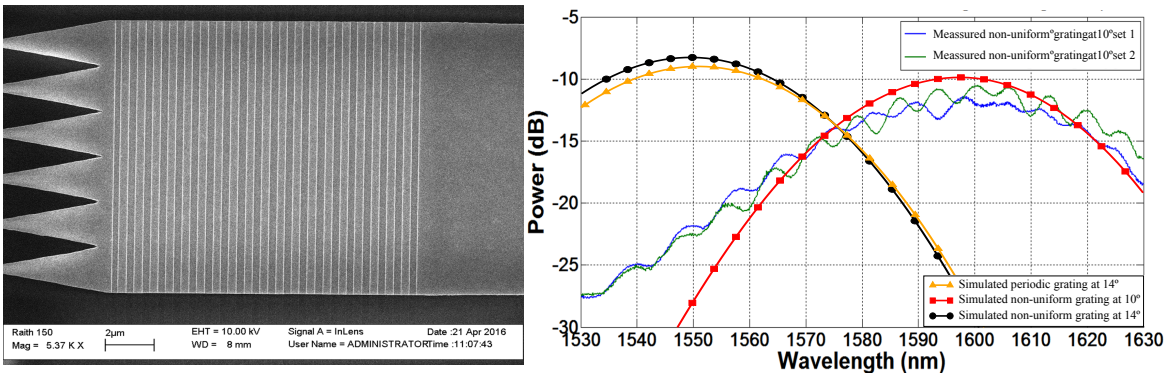

Figure 6.9 Left: SEM image of the non-uniform grating coupler fabricated at NTC. Right: Comparison of the experimental meassurements of the fabricated grating coupler at a tilt angle of 10°, and the simulated transmission spectrum provided a tilt angle of 10° and 14°.

reflection. Nearly all grating couplers demonstrated to date require an angular detuning of the input/output fibres by a significant angle from normal incidence in order to eliminate undesired back reflection and transmission problems [251]. In such configurations, a vertical interfacing of the fiber-chip set-up would drastically reduce the coupling efficiency. In addition, non vertical couplers precise a polishing of the fibre ferrule and an accurate positioning of the fibre, resulting in a more complex packaging and mounting configurations, which in turn makes them less attractive for future commercial applications. So far, little effort has been devoted to develop perfectly vertical grating couplers, though they could be a key element to prevent the need of cleaving, dicing or polishing of fibres, allowing for timely in-line wafer testing [252].

In future PICs the high density integration capabilities may urge to handle a large number of fibre ports to communicate with off-chip components, systems and networks. Considering a perfectly vertical coupling, the regular extremely closely packed SMF bundle mounted on V-grooves, with fibre-to-fibre spacing limited to the cladding diameter of a single SMF fibre of 125 µm, would ideally serve as the I/O media for future PICs. In contrast, an azimuthally tilted configuration imposes larger distances in a grating coupler design over a PIC assembling, as the grating couplers etching would have to be spaced so as to match the distance requirements of every SMF in the bundle. Previously, in section 6.4, we detailed the exact distances at which the modelled grating couplers present an optimum coupling efficiency; however, this criterion would be impossible to fulfil for every fibre in the bundle if a close packet bundle is used for this task. Moreover, even thinner fibre bundles may not work well with tilted grating couplers, because even if the tilted angle is as small as 10°, the vertical position difference among all the cores with respect to the surface of the chip can be

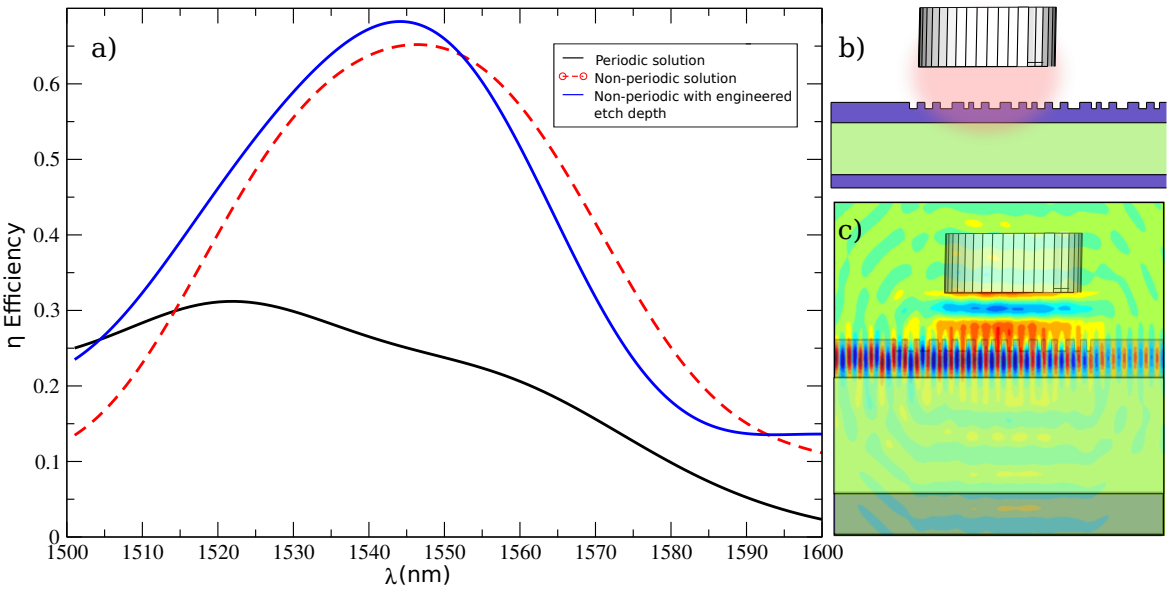

Figure 6.10 (a) Coupling efficiency between a SMF fibre positioned normal to a periodic grating coupler, as well as for non-periodic optimized structures like the one shown in the inset b). (c) Illustration of the real part of the E_z field for the fibre- grating domain.

as large as 12 μm, which suggest that an optimized grating coupler structure working best for one core, may not work well for the rest, as it is pointed out in [253]. Considering this all, a perfectly vertical grating coupler with high coupling efficiency is highly desired, as long as it significantly relaxes waveguide routing constraints near vertically emitting grating couplers. Many of the perfectly vertical grating couplers reported so far in the literature present a high coupling efficiency but most of them either rely on extremely complex structures such as slanted gratings [253], or need additional fabrication steps [254], which makes them difficult to extend to a mass-production [255]. Some others reported on the enhancement of the coupling efficiency by adding additional bottom reflectors [256]. Nevertheless, in all these cases the designing principle has only taken into account a few numbers of degrees of freedom for modelling the grating coupler, typically the period or the filling factor of the grooves/pillars. Owing to the relevance of that an effcient vertical coupler has into PIC design, once more, the ID method was used to optimize the periodic configuration in a perfectly vertical coupling situation as illustrated in the inset of Fig. 6.11.a. In this case, the light was impinged from the vertical fibre and the grating coupler was detuned in order to enhance the coupling to the leftwards direction of the waveguide. The Fibre was set to 7 μm far from the grating device in the horizontal axis and 1.5 μm in the vertical axis. As in previous calculations we used a fibre with a mode field diameter of 10.4 μm. The coupling efficiency at 1.55 μm is poor if it is compared with previous simulations presented for the

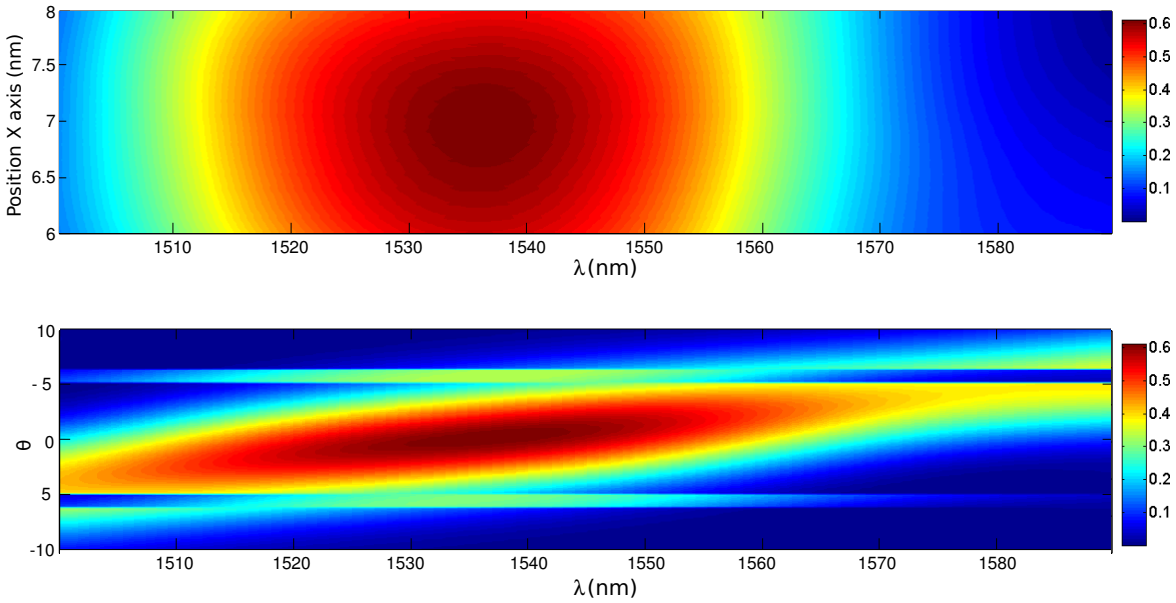

Figure 6.11 Coupling efficiency density map for the optimized non-uniform vertical coupler in which (a) the SMF is displaced along the x axis and (b) the tilt angle is deviated from the normal incidence.

non-vertical coupling systems shown in sec. 6.4. This is due to the enormous back reflection which is clearly shown in Fig. 6.10.b., where the real part of the E_z field is overimposed on the fiber-grating system. In contrast, non-uniform configuration illustrated in the inset of Fig 6.10.b, drastically minimizes the back reflection of the TE polarized field and successes in coupling the impinging light to the Si waveguide. This time the efficiency is close to the 60 % and almost all the polarized field is coupled to the waveguide. In this case, it was not possible to further improve the light coupling efficiency as light was still being coupled to the right-hand side of the wage guide. We believe that extra an engineered extra slit like the one proposed in [256] could prevent this issue and further enhance the operability of this structure.

6.5 A compact Silicon-on-Insulator Polarization Splitter

Polarization beam splitters (PBS) perform the splitting of unpolarized light into TE and TM-like polarizations. These components are essential for many applications, such as data storage [257], optical switching and routing in PICs [186] and they are a key element for enabling advanced optical modulators like dual polarization quadrature phase shift keying (DP-QPSK) [230], which improves the spectral and power efficiency [258]. In SOI technology, most of the integrated components are polarization dependent. Consequently,

their performance drasticaly varies when they handle light with an unexpected polarization state. On the other hand, single mode fibers support two orthogonal linearly polarized modes and during the propagation light will suffer changes in its elliptical polarization, mainly due to polarization mode dispersion (PMD). Even photonic waveguides exhibiting low losses, present a strong polarization dependence due to the difference in effective index between the fundamental TE and TM guided modes (see sec. 6.1). Therefore, since both mode profiles are opposed, the geometries required for successfully guiding TM and TE polarizations are inherently different. In order to deal with this issue, it is of major relevance to separate TE and TM polarizations and route each polarization to the corresponding optical connection or, otherwise, rotate one of the polarization states to ensure a complete control over the performance of the PIC. Conventional PBS are based on birrefrigence of crystals for which the separation of orthogonal polarization states is straighforward, but they are bulky, such as the ones based on a Nicol or Wollaston prisms, and are therefore unsuitable for dense integrated applications [259]. So far, a number of structures comprising directional couplers, Y-junctions and MMI couplers have been proposed [260]. These devices were fabricated using birefrigent materials such as silica, LiNbO3, GaAs-GaAlAs, InGaAsP-InP, polymers, and even in silicon, which even though it does not have any material birefrigence, the high index contrast obtained in the SOI platform and reduced waveguide dimensions makes it posible to induce significant birefrigence. Material birefrigence, stress-induced birefrigence in ion exchanged waveguides, stress-induced birefrigence in ion exchanged waveguides, and selective attenuation of orthogonal polarization states using metal over a waveguide have been employed in these polarization splitters [261–264]. Some other solutions propose the use of multilayer coatings [265, 266], but their narroband operation makes them less attractive for practical applications. All in all, these methods require additional steps for coupling light from the fibre to the polarization splitter devise and then guide light to the proper output. Instead, a PBS made by using a grating coupler approach seems to be a more convenient solution for SOI technology, inasmuch as a grating coupler could perform light coupling and separation of the polarization states in a very reduced footprint, ensuring both functionalities in a single compact device. In [267], a photonic crystal configuration is utilised as a PBS, enabling a separation of polarizations in 45° with an approximatted efficiency of 20 %. While this approach has prooved to be very promissing, it is still difficult to explore optimum 3D PC configurations by doing intensive calculations.

Implementing a grating coupler that relaxes the effective index difference for both polarizations simultaneously is a challenging task, since both polarization profiles are somehow competing ones. Therefore, in this section, we resort to the NSGA-II evolutionary algorithm described in section 4.2.6, in order to find topologies that optimize the coupling of

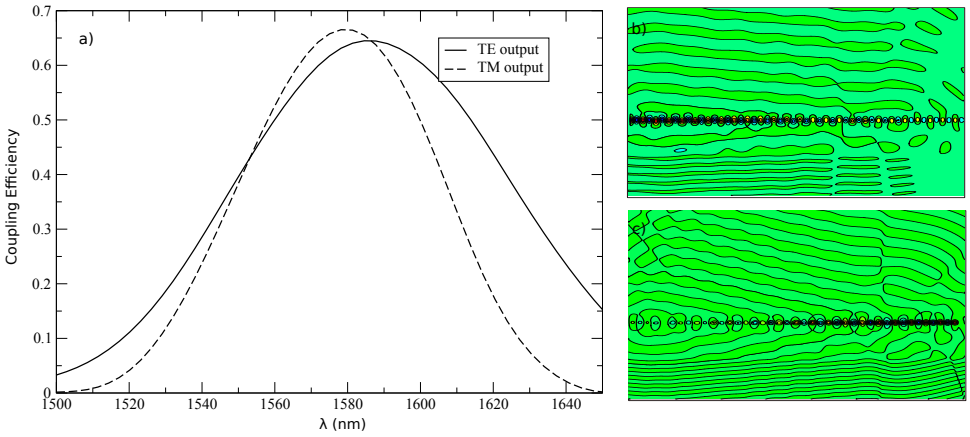

Figure 6.12 a) Coupling efficiencies achieved by means of an engineered non-uniform grating coupler like the one depicted in the inset for the TE and TM polarizations considering an SMF fibre with a modal with of 10.4 μm. b) TE field coupling to the SMF fibre tilted 15 ° from the normal plane of the grating device and c) TM field impinging from the opposite direction of the silicon waveguide also couples to the SMF fibre.

each polarization to different waveguides in a balanced way. In this case, we focused our research on 2D non-uniform grating coupler designs, in which iterative calculations are still feassible to do in a manageable computational time. The optimization process is carried out during 120 iterations. This process shifts the Pareto-optimal front to higher values of TE and TM polarization coupling efficiencies, respectively. Ideally, the Pareto front should cover also average solutions for both polarizations, but in this case the lack of these intermediate solutions corresponds to the physical impossibility of matching the effective index for both polarizations. In spite of this, we looked for those solutions that minimize the coupling losses (as much as possible) for both polarization. The performance of one of these best solutions is shown in Fig. 6.12. This BPS comprises a non-uniform grating profile performed by 70 nm deep grooves in a 220 nm width Si layer. With this configuration TE polarized light is coupled to the easternmost waveguide while the TM polarization couples to the waveguide located at the west. This structure simulaneously supports a TE/TM coupling/splitting in the C-band with an efficiency of 77 % and 55 %, for TE and TM polarization, respectively. The bandwith (at 3 dB) for the TE case is close to 80 nm while for the TM case is close to 50 nm. This structure offers an extinction ratio beyond 25 dB in a wide wavelength range.

6.6 Conclusions

In this chapter we demonstrate the usefulness of using an inverse design approach to the process of exploring new grating coupler designs. By means of this method the designer can

handle more parameters even when there is no theoretical background leading to any hints in the process of designing better couplers. We found that these methods are easily applicable to grating coupler design problems since they do not require any detailed knowledge of the structure and they can rely on the solver of the system as a blackbox. In fact, using this method, we find that the coupling efficiency of non-uniform grating couplers can outmatch custom periodic designs. Moreover, the structures proposed in this work are fully compatible with conventional manufacturing processes as they prevent the formation of exotic geometries or shallow edges. The length of the non-uniform gratings is slightly shorter than that of canonical gratings. Besides, if these gratings are shortened, then they still hold for a reliable coupling ratio with a minimal deviation in the C-band.

Chapter 7

Topological photonics

Photonic crystals are an outstanding platform for realizing a scatter-free propagation of light waves. However, in conventional PCs, unwanted structural disorder, surface roughness and all kind of fabrication imperfections rise significant losses. The breakthrough in overcoming these problems is likely to come from the synergy of the topological PCs and silicon-based photonics technology that enables high integration density, lossless propagation, and immunity to fabrication imperfections [268], leading to a robust energy transport in integrated photonic devices, all-optical circuity, and optical communication systems. Following with the conceptual analogy between electromagnetic waves in patterned dielectric media and quantum mechanical electron waves in solids, we worked on the rapidly emerging field of topological photonics for which materials still have a band gap, but they also present exotic edge states with unusual properties. In the photonic context, these edge states can be used to realize a fundamentally new class of electromagnetic wave-guides, which are able to transport light around sharp corners without backscattering [269].

One-dimensional models with topological band structures represent a simple and versatile platform to demonstrate novel topological concepts. Here we experimentally study topologically protected states in silicon at the interface between two dimer chains with different Zak phases. Furthermore, we propose and demonstrate that, in a system where topological and trivial defect modes coexist, we can probe them independently. Tuning the configuration of the interface, we observe the transition between a single topological defect and a compound trivial defect state. These results provide a new paradigm for topologically protected waveguiding in a complementary metal-oxide-semiconductor compatible platform and highlight the novel concept of isolating topological and trivial defect modes in the same system that can have important implications in topological physics.

7.1 Introduction to Topological photonics

At the beginning of this thesis, we stated the analogies between the electronic band gap materials and those periodic structures that lead to similar characteristics featuring photons instead of electrons. In both cases we used the band theory and the corresponding Bloch-Floquet modes to determine the dynamics of electrons and photons. This band theory is indeed an old, though still adequate, cornerstone of solid state physics that serves to give a simple explanation to the particular charcateristics of crystalline materials and to stablish a graphical distinction between electric insulators and conductors. In the bulk of a band insulator, the eigenstates form a set of continuum states broken by energy gaps that no electron can occupy and promoting an electron between these energy bands requires an energy cost of the order of such energy gap. In contrast, conductors render to partially filled bands in which there are plane wave states available to transmit electrons across the bulk at arbitrarily low energy [270]. However, this simple understanding of the band theory turns out to be more complicated since the breakthrough of the Quantum Hall effect in 1980 [271–274]. Considering a two-dimensional electron system, at low temperatures, the presence of a strong magnetic field forces electrons to be deviated in the bulk and forces them into delocalized edge states on the surface of the metal. Beacuse of this striking behaviour, the metal subjected to this temperature and magnetic field conditions is still insulating in its bulk, but it conducts electrons without dissipation on the edges. The Quantum Hall Effect has been a constant source of new ideas, moreover, when the role of the external magnetic field was proved to be unneccessary under certain *topological* conditions. The later was first proposed in a theoretical manner by Haldane in [275], and soon after he reported on a ground-breaking demonstration of the analogous Quantum Hall Effect in the field of photonics [276]. The first observable verifification of the topological protection came swiftly with the experimental demonstration of a photonic topological insulator using gyromagnetic media [277] in the microwave regime. Since those first theoretical proposals and this first experimental demonstration of topologically protected electromagnetic propagation, many proposals have been made to take topological concepts into the optical regime [278–281]. Experiments followed soon thereafter, demonstrating adiabatic pumping [282], and eventually photonic topological insulators [283, 284]. Conceptually, the localized modes appearing at the interface of two structures with distinct topological invariants hold the promise to play a key role in the development of robust optical circuits. The simplest model to realize these so-called photonic topological defect states in one dimension is the dimer chain (the so-called SSH model) [285]. This idea was demonstrated in optical experiments in 2009, on the edge of a binary waveguide array [286], and more recently in a non-hermitian system

involving loss [287] and in a dimer chain of microwave resonators [288]. Analogous systems to the dimer chain have been recently proposed to demonstrate onedimensional plasmonic and polaritonic topological edge states based on zigzag arrays of metallic nanoparticles [289] and micropillars [290]. Interestingly, ideas related to the SSH dimer chain were also recently explored, in the context of topological effects in one-dimensional quasicrystals, demonstrating Thouless pumping [291–293]. Therefore, topological order has opened a new frontier in photonic and the bridging between theory and experiments suggests that carefully-designed wave-vector space topologies may be a prospective mean to create interfaces that support new states of light with useful and interesting properties. In particular, it suggests the realization of unidirectional waveguides that allow light to flow around large imperfections without back-reflection as well as a wealth of potential applications regarding to slow light photonic devices, such as photonic crystal waveguides seen so far throughout this thesis, for which fabrication imperfections severelly affect to their overall performance [294]. But, what is meant by topology and how does it fall into photonic systems?. L. Lu et al. [295] briefly describe topology as follows: *Topology is the branch of mathematics that concerns quantities that are preserved under continuous deformations*. This statement, as it is, does not enlight much the role of topology in the present context of photonics, however, we wil try to provide a self contained bottom-up physical approach to topological photonics, limited to the Su-Schrieffer-Heeger model [285].

7.2 The Su-Schrieffer-Heeger (SSH) model

In this section we will consider the simplest setting for topological band theory, which is the one dimension. This will allow us to introduce several key concepts in their simplest form, which thereafter we will translate to the optical analogue in which we observed topological phase transitions. But first, a quick note: much of the information given below can be found in the unvaluable course notes of [270], and a few figures are essentially adapted from those lessons. Indeed, for a more detailed coverage of the solid state physics behind the SSH chain model, we refer the reader to the first chapter of [296] and to [297–299], and for an even more in depth view of the mathematical approach to the topological aspects, we refer the reader to these other books [300, 301].

The Su-Schrieffer-Heeger was introduced as a two band model for the conducting polyacetilene, which at half filling undergoes a Peierls instability [1] to a dimerized state [296]. This system offers the possibility to provide two different dimerized states, in which under

[1] i.e. a one-dimensional equally spaced chain with one electron per ion is inherently unstable, thus dimerization occurs only at low temperature.

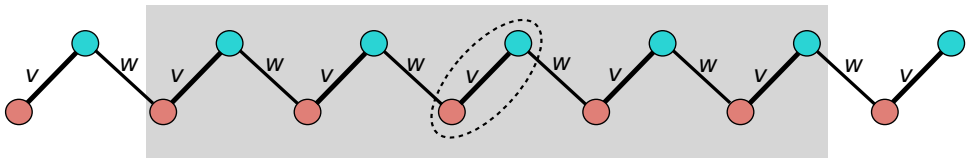

Figure 7.1 Schematic representation of the SSH mode. There are two lattices, one coloured in blue and the other in red, which we denoted A and B, respectively. They are grouped into unit cells, the $n = 4$th cell is circled by a dotted line. In this section we only refer to the Bulk states and so, the edge regions have been intentionally kept out of the shadowed box.

some circunstances (discussed below), these two states are topologically distinct. Moreover, interfaces between these states provoke zero energy boundary states. For simplicity we consider spinless electrons and that the filling is one electron per unit cell. Thus, our Su-Schrieffer-Heeger (SSH) model describes electrons hopping on a chain (one-dimensional lattice), with staggered hopping amplitudes, as shown in Fig. 7.1. The chain consist of N unit cells, each unit cell hosting two sites, one on sublattice A, and one on sublattice B. Interactions between the electrons are neglected, and so the dynamics of each electron is described by a single-particle Hamiltonian[2], given by [270]

$$\mathcal{H} = v\sum_{m=1}^{N}(|m,B\rangle\langle m,A| + h.c.) + w\sum_{m=1}^{N-1}(|m+1,A\rangle\langle m,B| + h.c.), \tag{7.1}$$

where $|m,A\rangle$ and $|m,B\rangle$ stand for the state of the chain where the electron is located on the unit cel m, being m an integer number, $m \in 1,2,\cdots,N$, and $h.c$ denotes the hermitian conjugate. To proceed with the SSH system, we will limit the study to those eigenstates yielded by an hermitian Hamiltonian, i.e. the eigenstates will be real and non negative (thus, let us assume that our *particles* are at zero temperature and zero chemical potential). In addition, hereafter we will further simplify the Hamiltonian stated in eq. (7.1) by only considering a single copy of the chain where each particle occupies a single unit cell. To further simplify the problem we will consider that the chain distances, also referred to as hopping distances or hopping amplitudes, are also real and nonnegative. These assumptions permit to drop the complex phase terms of the hopping distances and thus, the matrix form of the Hamiltonian for the SSH model is given by

[2]Here we will only refer to the bulk Hamiltonian, for a detailed analysis of the Hamiltonian of edge states, as well as a topological analysis of these edge states the reader is referred to [296], and for a brief explanationof these topics to [270]

$$\mathcal{H} = \begin{bmatrix} 0 & v & 0 & 0 & 0 & 0 & 0 & 0 \\ v & 0 & w & 0 & 0 & 0 & 0 & 0 \\ 0 & w & 0 & v & 0 & 0 & 0 & 0 \\ 0 & 0 & v & 0 & w & 0 & 0 & 0 \\ 0 & 0 & 0 & w & 0 & v & 0 & 0 \\ 0 & 0 & 0 & 0 & v & 0 & w & 0 \\ 0 & 0 & 0 & 0 & 0 & w & 0 & v \\ 0 & 0 & 0 & 0 & 0 & 0 & v & 0 \end{bmatrix}, \tag{7.2}$$

(7.3)

for a SSH chain comprised by 4 unit cells. Let us assume now that the number of unit cells in the SSH chain shown in Fig. 7.1, is large enough to disregard the effect of the boundaries (the edges of the chain). With this regards, we can now set the Hamiltonian of the SSH model in terms of the Born-von Karman periodic boundary conditions, i.e. $u_{n,\vec{k}}(\vec{r}+\vec{R}) = u_{n,\vec{k}}(\vec{r})$. The expression for such Hamiltonian is given by

$$\mathcal{H} = \sum_{m=1}^{N} (v\,|m,B\rangle\langle m,A| + w\,|(m \bmod(N)+1,A\rangle\langle m,B|) + h.c. \tag{7.4}$$

Therefore, the eigenvalue problem, considering this Hamiltonian leads to

$$|\mathcal{H}, \Psi_n(k)\rangle = |E_n(k), \Psi_n(k)\rangle, \quad n \in \{1,2,\ldots,2N\}, \tag{7.5}$$

and the translation operation applied to the 1st Brillouin zone to the 1D SSH model, allows to express the wavenumber in a plane wave basis

$$|k\rangle = \frac{1}{\sqrt{N}} \sum_{m=1}^{N} |e^{im2\pi/N}, m\rangle\,. \tag{7.6}$$

We can now redefine the Hamiltonian

$$|\mathcal{H}(k), u_n(k)\rangle = |E_n, u_n(k)\rangle\,, \tag{7.7}$$

where u_n is the set of vectors comprising the Bloch eigenstates of the $\mathcal{H}(k)$ Hamiltonian. [3] With all, the SSH model comprising 4 unit cells can be expressed using eq. (7.6) as an eigenvalue equation in a matrix form

$$\begin{bmatrix} 0 & v & 0 & 0 & 0 & 0 & 0 & 0 \\ v & 0 & w & 0 & 0 & 0 & 0 & 0 \\ 0 & w & 0 & v & 0 & 0 & 0 & 0 \\ 0 & 0 & v & 0 & w & 0 & 0 & 0 \\ 0 & 0 & 0 & w & 0 & v & 0 & 0 \\ 0 & 0 & 0 & 0 & v & 0 & w & 0 \\ 0 & 0 & 0 & 0 & 0 & w & 0 & v \\ 0 & 0 & 0 & 0 & 0 & 0 & v & 0 \end{bmatrix} \begin{bmatrix} a(k)e^{ik} \\ b(k)e^{ik} \\ a(k)e^{2ik} \\ b(k)e^{2ik} \\ a(k)e^{3ik} \\ b(k)e^{3ik} \\ a(k)e^{4ik} \\ b(k)e^{4ik} \end{bmatrix} = E(k) \begin{bmatrix} a(k)e^{ik} \\ b(k)e^{ik} \\ a(k)e^{2ik} \\ b(k)e^{2ik} \\ a(k)e^{3ik} \\ b(k)e^{3ik} \\ a(k)e^{4ik} \\ b(k)e^{4ik} \end{bmatrix}, \tag{7.8}$$

(7.9)

where $a_n(k)$ and $b_n(k)$ are the amplitudes of the plane wave solutions to the eigenstate $u_n(k)$, i.e. $|u_n(k),\rangle = |a_n(k), A\rangle + |b_n(k), B\rangle$. Fig. 7.2 shows the dispersion relation for different choices of hopping distance parameters. In those cases for which the hopping parameters are equal, that is $v \neq w$, the SSH system behaves as a conductor for electrons whitin the chain lattice, otherwise, the dispersion diagram leads to an energy gap of $2|v - w|$. The Schrödinger equation equation defining the matrix $\mathcal{H}(k)$ can be expressed as

$$\mathcal{H}(k) = \begin{bmatrix} 0 & v + we^{-ik} \\ v + we^{ik} & 0 \end{bmatrix}; \quad \mathcal{H}(k) \begin{bmatrix} a(k) \\ b(k) \end{bmatrix} = E(k) \begin{bmatrix} a(k) \\ b(k) \end{bmatrix}. \tag{7.10}$$

(7.11)

The momentum space Hamiltonian $\mathcal{H}$ of the SSH model can also be expressed as

$$\mathcal{H}(k) = d_x(k)\hat{\sigma}_x + d_y(k)\hat{\sigma}_y + d_z(k)\hat{\sigma}_z, \tag{7.12}$$

where $\hat{\sigma}$ are the Pauli matrices

$$\sigma_x = \begin{bmatrix} 0 & 1 \\ 1 & 0 \end{bmatrix}, \quad \sigma_y = \begin{bmatrix} 0 & -i \\ i & 0 \end{bmatrix}, \quad \sigma_z = \begin{bmatrix} 1 & 0 \\ 0 & -1 \end{bmatrix}, \tag{7.13}$$

(7.14)

[3] Note that both, u_n and $\mathcal{H}(k)$ are periodic, i.e. $|u_n(k + 2pi)\rangle = |u_n(k)\rangle$ and $\mathcal{H}(k + 2pi) = \mathcal{H}(k)$.

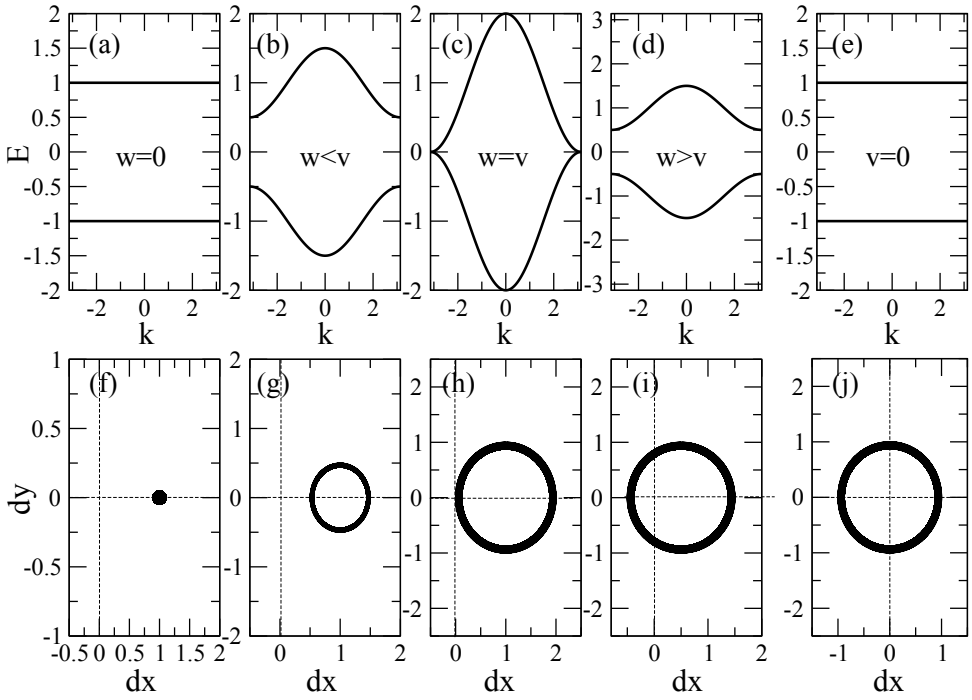

Figure 7.2 Dispersion relations of the SSH model given by Eq. (7.10), for different settings of the hopping amplitudes: (a) v = 1, w = 0; (b) v = 1, w = 0.6 (c) v = w = 1 (d) v = 0.6, w = 1 (e) v = 0, w = 1. Below: TIn each case, the path of the endpoints of the vector $d(k)$ representing the bulk momentum-space Hamiltonian, given by Eq. (7.12) and Eq. (7.15), respectively. The wavenumber is sweeped across the Brillouin zone, $k = 0 \rightarrow 2\pi$. This figure has been adapted from [270].

and **d**(k) is a vector whose cartesian components for the SSH model are given by [4]

$$d_x = v + wcos(k), \qquad d_y = W + sin(k), \qquad d_z = 0. \tag{7.15}$$

Fig. 7.2 depicts the direction described by the vector **d**(k) according to the hopping distances v and w, for several cases. In particular, the trace of this vector traces a closed circle of radius w centered at (v,0). Once again, a quick inspection of the traces of these vectors within the Brillouin zone, that is $k \in (0, 2\pi)$), unveils that those systems that behave as conductors describe a close circle centered at the origin, while those that provide an energy gap either draw a closed circle whose center is displaced from the origin of d_x, d_y plane or project this circle into a line. All in all, these circles can be used to analyze the geometrical insights of the SSH system by analyzing them using topology. Indeed, topology permits to label these circles by the calculus of an integer number called the winding number, ν.

[4] The out-of-plane vector $d_z = 0$ in our SSH model due to the Chiral symmetry of the system.

7.3 Topological overview of the SSH model

The *winding number* can be simply obtained by counting the number of times that the vector $\mathbf{d}(k)$ intersects the *line of sight of infinity*, ζ, i.e. a curve that goes from the origin of the d_x, d_y plane to infinity. Since $\mathbf{d}(k)$ is a vector quantity, a quick way to characterize the winding number ν associated to a particular SSH system comes from counting the number of times that the wavevector crosses the line of sight in each direction, adding a unit each time it crosses the line in one of these direction and substracting a unit if it does it in the opposite direction.

The winding number ν satisfies is preserved under continuous deformations of ζ or $\mathbf{d}(k)$, and therefore, it is considered a topological invariant. In essence, continuous deformations could change the traces of the $\mathbf{d}(k)$ vectors, though the symmetry of the model makes these changes pairwise, keeping ν unnaltered. In a more formal manner, we can express the winding number by the following analitical expression

$$\nu = \frac{1}{2\pi}\int \left(\tilde{\mathbf{d}}(k) \times \frac{\partial}{\partial k}\mathbf{d}(k)\right) dk \tag{7.16}$$

where we normalized the vector $\mathbf{d}(k)$ to bound it to the unit circle

$$\tilde{\mathbf{d}} = \frac{\mathbf{d}}{|\mathbf{d}|}. \tag{7.17}$$

To calculate the winding number from the Hamiltonian of the SSH model, we introduce the $\mathbf{d}(k)$ vector notation into the Hamiltonian matrix of eq.(7.10)

$$H(k) = \begin{bmatrix} 0 & h(k) \\ h^*(k) & 0 \end{bmatrix}, \tag{7.18}$$

$$\tag{7.19}$$

where the elements $h(k)$ are comprised of the vector components $h(k) = d_x(k) + d_y(k)$. With this reagards, the winding number can be calculated as an integral in the following form [270]

$$\nu = \frac{1}{2\pi i}\int_{-\pi}^{\pi} dk \frac{\partial}{\partial k} \log h(k). \tag{7.20}$$

The integral of eq. (7.20) is always real and yields to either $\nu = 0$ or $\nu = 1$ depending of the intracell and intercell hopping parameter values. Specifically, when the intracell hopping dominates the intercell hopping, i.e. $v > w$, the winding number is $\nu = 0$. Otherwise, when the intercell hopping dominates the intracell hopping, i.e. $W > v$, the winding number is $\nu = 1$

[5]. There are two ways to change the winding number. On the one hand, we could modify the intracell distance to shift the trace of the $\mathbf{d}(k)$ vectors as in Fig.7.2.a. The gradual change of the intracell parameter requires to close and reopen the bulk gap. In a similar manner, we could gradually change the value of the intercell hopping. The later results in a gradual change of the radial distance of the circular path of $\mathbf{d}(k)$. Once again this requires to close and reopen the bulk gap. On the other hand, if the chiral symmetry is somehow broken, then it is possible to lift the circle described by $\mathbf{d}(k)$ out of the plane and put it back on the plane at a different position, as illustrated in Fig. 7.2.c.

Until now we have indistinctly used the terms *gradual deformation* and *continuous deformation* to define wether the winding number could be a topological invariant on not, but what does it imply to perform a *continuous deformation*?. By definition, a continuous deformation means that the Hamiltonian is adiabatically deformed by changing the parameters continuously while the symmetry of the system is maintained and the gap at zero energy point remains open (E=0). Apart from the winding number, there is also an additional feature that is usually considered as a topological invariant in the SSH model. This second topological invariant is the number of edge states at one end of the SSH model. So far, we have focused on the bulk Hamiltonian, featuring an infinite chain for the SSH system. However, if these edge states are taken into account, then one realyzes that the number of edge states does not change either under adiabatic deformations. Remarkably these edge states do not only occur at the boundaries of the chain, but also at interfaces between different domains of the same chain.

7.4 The observation of the optical analogue of topologically protected modes and the beating with trivial defects

In this section we turn back to the domain of photonics. In an analogy to the SSH model described above, we now experimentally study the simplest model to realize the so-called photonic topological defect states in one dimension. The theoretical understanding of topologically protected modes in a chain of dimers was presented in [302], in the context of elucidating the existence of edge states in graphene ribbons. From the results in [302] it follows that interfacing two dimer chains with different topological invariants gives rise to a topological transition and to the existence of a topologically protected defect state at the interface. In the dimer chain system, the property that remains invariant under continuos deformations, that is, the topological invariant is called the Zak phase [303]. The Zak phase is

[5] We obviate the trivial case in which $v = w$, for which there is no energy gap and the winding number is undefined.

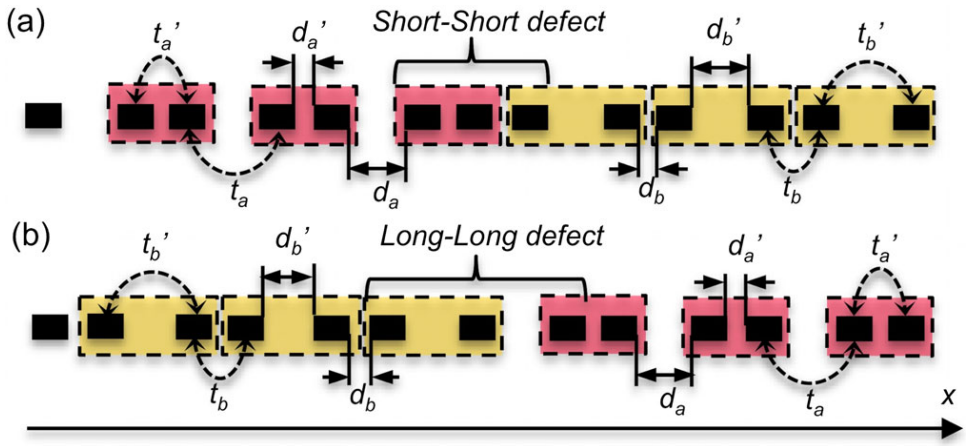

Figure 7.3 Interfaces between dimer chains. (a) Two chains of dimers connect through a short-short defect. (b) Two chains of dimers connect through a long-long defect. The dimers shaded in red (yellow) have an intra-dimer hopping parameter of t_a' (t_b'), an interhopping parameter t_a (t_b), and distances between waveguides of d_a and d_a' (d_b and d_b').

half the solid angle of the winding path of the unit vector $\hat{n} = (h_x, h_y, h_z)/\sqrt{h_x^2 + h_y^2 + h_z^2}$, with h_i are the components of the Hamiltonian of the two band system, i.e. $\mathcal{H} = h_x\sigma_x + h_y\sigma_y + h_z\sigma_z$ [6]. The exact configuration of the waveguides around that interface determines the shape of the topological defect mode and it may give rise to the appearance of trivial defect states coexisting with the topological defect. Since these trivial defect modes are also localized at the interface and can have populations comparable to that of the topological defect, beating between the trivial and topological defect modes can arise. In [304, 305] we reported the experimental demonstrations of the existence of this compound topological-trivial defect state that propagates localized at the interface and undergoes recurrent periodic propagation. The transition from the compound trivial state to a single topological defect is possible by varying the configuration of the waveguides at the interface between the two silicon waveguide dimer chains with different topological invariants. The realization that the topological defect mode can be probed separately from the trivial defect modes provides deeper understanding of the nature of topologically protected transport in photonic systems [275–277, 306], and suggests that such phenomena are universal; that is, they should exist also in other physical systems, such as condensed matter physics [307] or atomic physics [308]–wherever topological and trivial states coexist. In addition to its fundamental interest, our physical setting represents a new platform for topologically protected waveguiding in silicon and opens the door to realizing optical circuits with immunity to fabrication imperfections or environmental changes in a complementary metal-oxidesemiconductor (CMOS) compatible platform.

[6] More generally, the Zak phase is the Berry phase in one dimension.

Let us consider the two potential configurations of a system comprising two dimer chains with different topological invariants, as shown in Fig. 7.3.a and Fig. 7.3.b. It was shown in [302] that the ratio between the hopping parameters between two elements in the same dimer t' and the hopping parameter between two dimers t determines the value of the Zak phase, for which the analitical expression is given by

$$\mathcal{Z} = i \oint dq \, \langle u_q | \partial_q u_q \rangle , \tag{7.21}$$

where $|u_q\rangle$ are the Bloch wave functions [303]. In particular, $\mathcal{Z} = 0$ when $t'/t > 1$ and $\mathcal{Z} = \pi$ when $t'/t < 1$. The topological transition $\mathcal{Z} = 0 \longleftrightarrow \mathcal{Z} = \pi$ corresponds to the emergence of edge states, and $\mathcal{Z} = \pi$ gives the number of topological states localized at the edge of each chain [302]. In Fig. 7.3.a and Fig. 7.3.b we interface a dimer chain with $t'_a/t_a > 1$, whose dimers are shaded in red, with a dimer chain with $t'_b/t_b < 1$, whose dimers are shaded in yellow. At the interface the inter- and intradimer hopping parameters are equal, i.e., $t'/t = 1$, and a topological transition $\mathcal{Z} = \pi \longleftrightarrow \mathcal{Z} = 0$ occurs right at the interface. The connection between dimers can be arranged so that there is a short-short defect at the interface, as in Fig. 7.3.a, or a long-long defect, as in Fig. 7.3.b.

In coming to design our system –the photonic waveguide array– the separation between waveguides plays an important role. We chose the separation between waveguides such that the contrast between the intra- and interdimer hopping parameters is maximized, which guarantees a large band gap and in turn strong topological protection. However, certain practical issues restrict us. The minimum separation between waveguides is determined by the minimum feature size defined by the fabrication process, so as to avoid proximity effects. The maximum separation between waveguides is limited by the minimum spatial overlap between the individual waveguide modes, which defines the coupling coefficient between adjacent waveguides. In our experiment, it is very important that the propagation length in the waveguide array is large enough, at least 10 coupling lengths. With these considerations, we chose the proper parameters that ensure robust experimental observation of all the phenomena involved.

Consider first the particular case where each element of the dimer chains is a silicon waveguide of refractive index $n_{Si} = 3.48$ at 1550nm, width $w = 450$nm, height $h = 220$nm, and length $L = 500\mu$m. We fix the total number of waveguides to $n = 203$ and consider that the waveguides are separated by air ($n_{air} = 1$). For the short-short defect case we chose $d'_a = d_b = 182$nm and $d_a = d'_b = 324$nm as the separation distances between waveguides. Using the silicon waveguide parameters above, we obtain the coupling constants for each separation distance, and subsequently the hopping parameters. This yields $(t'_a/t_a) = 3.26$ and

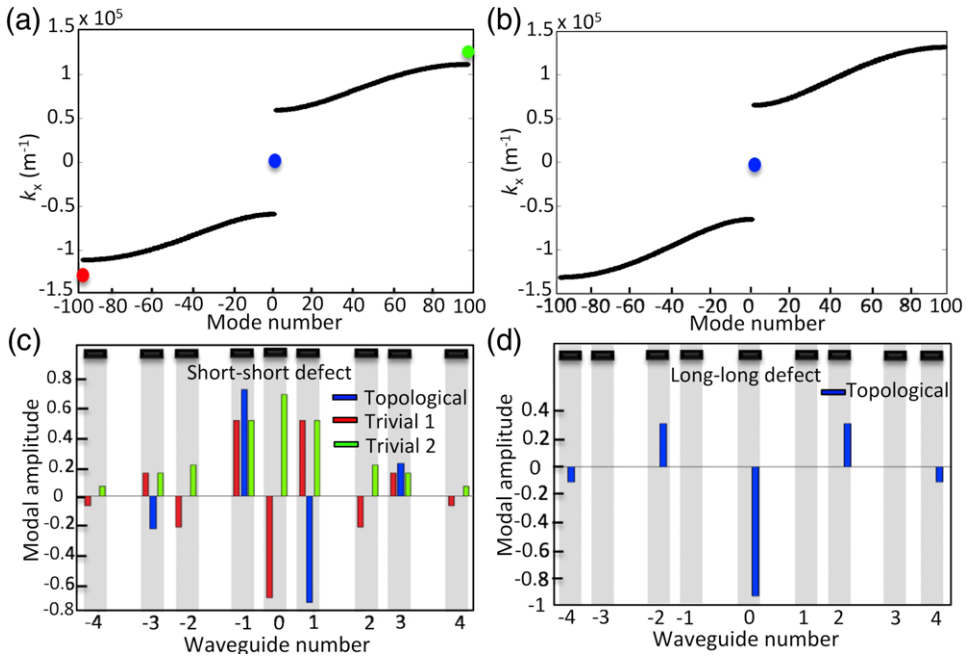

Figure 7.4 Band diagrams and modal amplitudes around the defects. (a) Transverse propagation constant (k_x) of the modes at the short-short defect structure. The blue dot represents the topological defect mode, the red and green dots represent two trivial defect modes, the black curve represents the extended states. (b) k_x of the modes at the long-long defect structure. Only the topological defect and the extended states are supported by this system. (c) Modal amplitude of the topological (blue) and the two trivial defect modes (red and green) for the short-short defect case. (d) Modal amplitude of the topological defect mode for the long-long defect case.

$(t'_b/t_b) = 0.31$. For the long-long defect case we chose $d'_a = d_b = 166$nm and $d_a = d'_b = 294$nm, giving the relations $t'_a/t_a = 2.96$ and $t'_b/t_b = 0.34$.

The transverse propagation constants at each waveguide for the short-short defect and the long-long cases are shown in Figs. 7.4.a and 7.4.b, respectively. The band diagram in both cases is characterized by two bands separated by a band gap, as expected from one-dimensional dimer chains [302]. As a consequence of the defect, the topological transition occurs at the interface between the left and right dimer chains, and a topological defect state emerges in the middle of the band gap, as represented by the blue dots in Figs. 2(a) and 2(b). The transverse propagation constant of this topological defect is zero, which implies that the mode will remain exponentially localized at the interface, i.e., around waveguide number 0. The modal amplitudes of the topological defect mode across the nine central waveguides, for the short-short and long-long cases, are depicted by blue bars in Figs. 7.4.c and 7.4.d respectively. As anticipated, the configuration of the waveguides at the vicinity of the interface determines the shape of the defect mode. The short-short defect gives rise to an

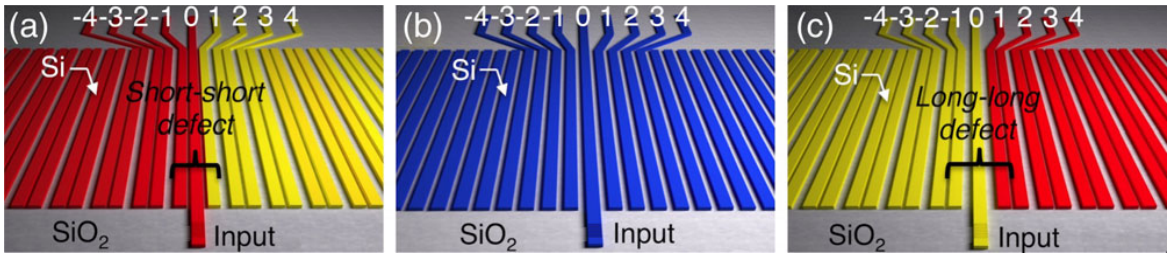

Figure 7.5 Fabricated silicon-on-insulator structures. (a) Two silicon dimer chains connected by a short-short defect. (b) Array of equidistant coupled waveguides. (c) Two silicon dimer chains connected by a long-long defect.

antisymmetric modal amplitude with maxima in the odd waveguides and minima in the even waveguides, as shown in Fig. 7.4.c, and the long-long defect generates the complementary defect state modal amplitude with maxima in the even waveguides and minima in the odd waveguides, as shown in Fig. 7.4.d.

In addition to the topological defect state, the short-short defect case allows for two trivial defect states, represented by the red and green dots in Fig. 7.4.a. These trivial defects appear because the short-short defect, formed by three waveguides closely spaced, constitutes a region of higher refractive index than the rest of the structure. Hence, as shown by the red and green bars in Fig. 7.4.c, the power of the light populating these trivial defects is localized in the defect in the same spatial region as the topological defect. In this situation, the excitation (the input beam) determines the population of each mode and it can be used to isolate the topological mode from the compound trivial mode. The two topological structures studied in Fig. 7.4.a and Fig. 7.4.b are fabricated in a silicon-on-insulator chip using deep-UV lithography at Interuniversity MicroElectronics Center (IMEC). To highlight the behavior of topological structures with respect to trivial structures, a third structure is fabricated: a coupled 1D waveguide array with equidistantly spaced silicon waveguides [309, 310]. These three fabricated structures are depicted in Figs. 7.5.a- 7.5.c. The red and yellow waveguides in Fig. 7.5.a and Fig. 7.5.c represent, respectively, the dimer chains with $(t'_a/t_a) > 1$ and $(t'_b/t_b) > 1$, similar to Fig. 7.3. The waveguides in Fig. 7.5.b are all blue to indicate that they are equidistantly spaced ($d_a = d'_a = d'_b = d_b = 230$nm). Both the input and output waveguides have 10-deg grating couplers at their ends. We couple light (1550 nm wavelength) into the structures by using an input waveguide that merges into waveguide number 0 of the arrays. To measure the light at the output, the nine central waveguides flare out at the output of the structures.

We first examine the underlying phenomena using simulations, which assume nearest-neighbor coupling. With our parameters, any residual next-neighbor coupling is exceedingly small due to the tightly confined silicon modes. The simulations in Figs. 7.6.a- 7.6.c show

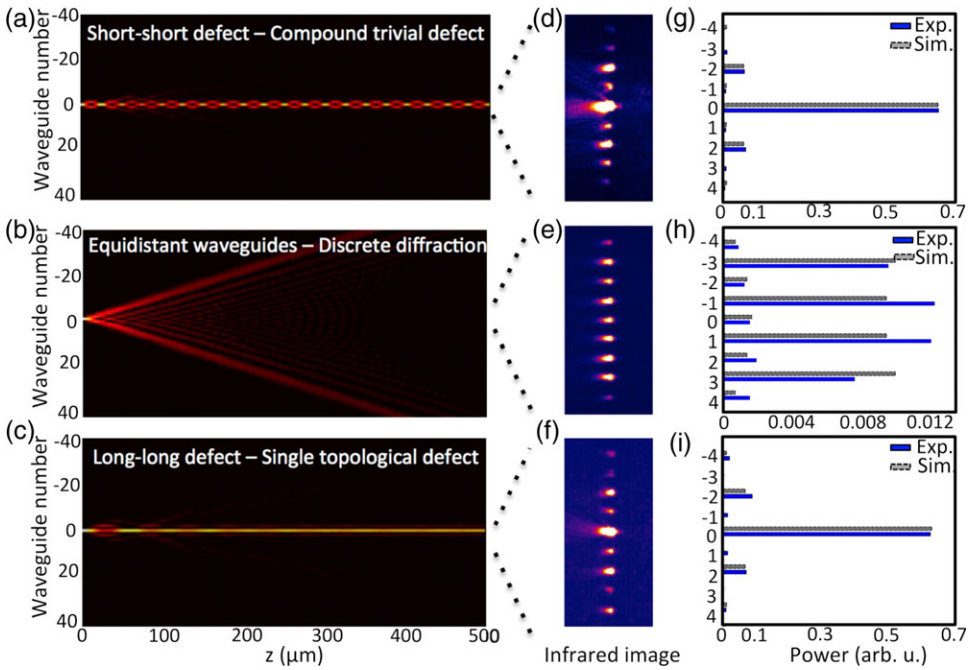

Figure 7.6 Experimental and numerical results showing the transition from the guided trivial compound state to the guided topological defect state. (a)–(c) Propagation simulations of the input signal propagating through the structures of Figs. 7.5.a- 7.5.c, respectively. (d)–(f) NIR images at the output of the structures of Figs. 7.5.a– 7.5.c, respectively. (g)–(i) Power measurements (blue) and simulation results (gray) at the output of the structures of Figs. 7.5.a– 7.5.c, respectively.

the propagation of that input signal across the $500-\mu$m-long silicon waveguide structures represented in Figs. 7.5.a- 7.5.c, respectively. Note that only the central 80 waveguides are shown. Fig. 7.6.a shows a characteristic beating pattern corresponding to the mix of the trivial defects. Throughout propagation, the power of this compound trivial defect remains localized around the short-short defect, in a recurrent fashion. The propagation behavior observed in the simulation of Fig. 7.6.b is explained by the well-known phenomenon of discrete diffraction [311, 312]. The light coupled into waveguide number 0 spreads as it propagates through the waveguide array, until at the output most of the power resides in two sidelobes far away from the center waveguide. These two sidelobes constitute the most distinct feature of diffraction in an equidistance waveguide array, a phenomenon known as *discrete diffraction*[311, 312], which is fundamentally different than diffraction in bulk systems (where most of the power remains in the center). The propagation simulation in Fig. 7.6.c shows a singular topological defect that propagates in the structure while always being exponentially localized around the defect.

We provide two different types of measurements to examine the propagation dynamics. First, to get a visual characterization of the power distribution at the output, we image the nine outputs of each structure using a 10x objective and a near-infrared (NIR) camera (Xenics Xeva 2785) set on a superior plane at an angle similar to the output angle of the grating couplers. The photographs in Figs. 7.6.d- 7.6.f correspond to the output of the structures of Figs. 7.5.a– 7.5.c), respectively. Second, to provide accurate measurements of the power distribution, we collect the light from each of the nine output grating couplers, using a fiber at a 10-deg angle, and measure it with a power meter. The normalized power extracted from these measurements is represented by blue bars in Figs. 7.6.g- 7.6.i, corresponding to the output of the structures in Figs. 7.5.a– 7.5.c, respectively. The gray bars in Figs. 7.6.g- 7.6.i correspond to the propagation simulation results at the output. The elongated tails at the left of each bright spot in Figs. 7.6.d- 7.6.f are an aberration caused by the ultrahigh sensitivity of the NIR camera combined with the fact that it cannot be placed at exactly the same angle as the output of the grating couplers.

The measurements and simulations displayed in Figs. 7.6.d- 7.6.g show a power maximum at the central waveguide, a zigzag intensity structure on either side with minima in the odd waveguides, and an exponential decay farther away on both sides. This is the result of the beating between the two trivial defect modes, which yields a particular linear combination of the intensities of the two modes at each propagation distance. The output intensities are, therefore, extremely dependent on the length of the silicon waveguides. As illustrated by the simulation in Fig. 7.6.a, 490-μm-long silicon waveguides (just 10 μm shorter than in the experiments) would give rise to a very different output power distribution—with a local minimum in the central waveguide and maxima at the odd waveguides. Naturally, instead of varying the propagation distance, one can vary the wavelength, which would scale accordingly. Hence, Fig. 7.7 shows measurements at different wavelengths to emulate various propagation lengths and so illustrate several linear combinations of interference (beating) between the trivial defect modes.

The measurements represented by the blue bars in Fig. 7.6.h show that, for the array with equidistant waveguides, very low power remains at the output facet of the nine central waveguides. This is because most of the power resides in two sidelobes. Furthermore, there is a zigzag behavior observed in the measurements and simulations, and no monotonic decrease (away from the central waveguide) is observed, again consistent with discrete diffraction in an equidistant array. The experimental measurements and the simulations follow the same trends, although the quantitative agreement between them is not as good as in the structures with a topological defect. This is due to the fact that the fabrication imperfections significantly affect the optical transport in the extended structure experiencing

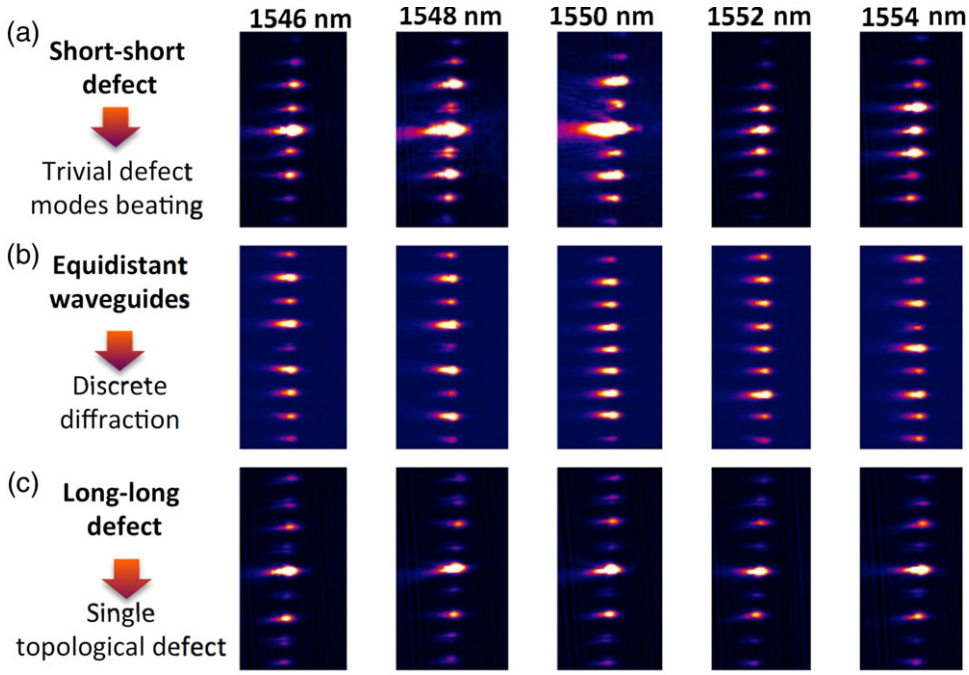

Figure 7.7 Wavelength-dependent behavior. NIR images at five wavelengths at the output of (a) the short-short defect structure, illustrating beating between trivial modes, (b) the array of equidistant waveguides, and (c) the long-long defect structure, illustrating the robustness of the topological defect to operational changes.

discrete diffraction, whereas the topologically protected defect state propagates immune to them.

Finally, the measurements at the output of the long-long defect structure, represented by the image in Fig. 7.6.f and the blue bars in Fig. 7.6.i, provide experimental proof of topologically protected waveguiding. The measurements show a single topological defect exponentially localized in the central waveguide, as predicted by the simulation (grey bars). Altogether, the simulations and experimental measurements shown in Fig. 7.6 illustrate the transition from a compound trivial defect mode, composed by the mix of two colocalized trivial modes, to a single topological defect mode by simply tuning the configuration of the waveguides at the interface.To demonstrate the beating behavior between trivial defects, we vary the wavelength across an 8-nm range around the central wavelength 1550 nm and study the output. Figures 7.7.a- 7.7.c show the NIR camera images at the output of each of the three considered cases for five different input wavelengths. The images in Fig. 7.7.a show that varying the wavelength leads to different output power distributions, from having a maximum in the center and a zigzag behavior with minima in the odd waveguides for wavelengths of 1546 to 1550 nm, to a local minimum in the central waveguide at 1554 nm, passing through a maximum in the center with a monotonic decay for 1552 nm. Varying the

wavelength causes a change on the coupling coefficient between adjacent waveguides and, hence, changes the beating period. It is, therefore, analogous to moving along the propagation length and seeing the different power distributions shown in the simulation of Fig. 7.6.a Figure 7.7.b illustrates how discrete diffraction [311, 312] is greatly influenced by the input wavelength, which determines the coupling length, and, therefore, different wavelengths lead to very different power distributions at the output. Finally, Fig. 7.7.c demonstrates that the topological defect mode maintains its power distribution at the output of the structure across the entire wavelength range.

7.5 Conclusions

In conclusion, the results presented here provided experimental evidence of topologically protected waveguiding in silicon. Further, we proved that transitioning from the compound trivial defect to a single topological defect is possible by tuning the defect configuration. By performing a wavelength-dependent study we demonstrated the robustness of waveguiding by a single topological defect in a silicon platform, as opposed to the discrete diffraction and beating by trivial modes. The experimental realization that one can independently probe colocalized topological and trivial modes could bring important fundamental implications to topological photonics and suggest similar phenomena in condensed matter systems and other physical systems—wherever topological and trivial states coexist. Further, this demonstration of topologically protected guiding of light at telecommunication wavelengths in silicon provides new ideas for developing CMOS-compatible devices immune to backscattering and environmental alterations. Likewise, among our future lines of work is studying the combined effects of topology and nonlinearity in these systems, exploring concepts similar to [313].

Conclusion and future work

In this thesis we developed a rigorous computational technique that alleviates the inherent difficulties of designing novel nanophotonic devices comprised of aperiodic dielectric structures. Optical components devised in this fashion could play a significant role in lightwave technology because they allow to confine and manipulate photons on the nanometer scales, thus enabling new functionalities or improving the functionality of existing optical and electronic devices. Such devices are important for the realization of compact optical integrated circuits, high-speed communications, information processing, and on-chip and chip-to-chip optical light guiding. Last, but not least, this thesis also focus on one of the most exciting fields of contemporary nanophotonic research: the study of topologically protected states in silicon photonics. In particular, the present thesis led to the following results:

- We proved that the finite element method is an effective and stable tool for point defect cluster quality factor calculation, wherein for each quality factor calculation, the full width at half maximum value was accurately determined by means of Brent's algorithm. This technique allows to determine the essential information needed for quality factor calculations in a speedy and computationally effective way. Consequently, we demonstrate that significant improvement in computational efficiency can be attained using the finite element method without sacrificing calculation accuracy.

- An inverse design computational framework based on various heuristic optimization methods has been developed to achieve promising photonic crystal systems that outperform topologies devised on intuitive grounds. To test initially the performance of the inverse design method, we applied this procedure to some simple and limited toy model photonic structures. Furthermore, we showed that our method allows to design arbitrarily complex photonic structures and it requires very short computation times (of the order of minutes), whereas a thorough exploration technique requires many hours to achieve the optimum configuration. Thereafter, this inverse design method was applied to tailoring more complex photonic structures of practical relevance.

- Using our inverse design framework, we demonstrated two distinct approaches of functional light splitting topologies with excellent performance. Specifically, while a non optimized splitting structure exhibits a maximum transmittance value of 30% near the target optical wavelength and a minimum transmittance ratio of 10% across most of the target frequency range, the optimized structures yield much better performance: they exhibit an almost flat transmittance spectra through the whole target frequency range, where almost 45% of the light power is redirected to each output branch. The key feature of these devices is the ability to control the mode expansion and excitation of higher order modes at the output waveguides. These simple structures support low losses within a large optical bandwidth and can be combined for distributing optical power within a photonic integrated circuit as well as a splitting/combining light mechanism in interferometers and optical switches. With this in mind, the structures studied in this thesis are difficult to obtain by using intuition as a guide, whereas they are obtained in a straightforward manner from our inverse design framework.

- The inverse design method was also applied to taylor photonic crystal waveguides with sharp bends that maximize the transmission over an ultra-wide range of frequencies. Indeed, the ability of confining light through high angle curvatures is one of the most promising features of photonic crystal waveguides, but designing them for enhancing the light guiding operation in a wide bandwidth requires novel geometries. In this thesis we present photonic crystal bends that do not require any exotic lattice and thus, they are easily manufacturable using common lithography methods. Besides, as far as we are concerned, this is the first report of a wide bandwidth operating sharp 120° photonic crystal waveguide bend with almost optimum bending efficiency up to 78% in two dimensional geometries that due to radiative losses offer a transmittance efficiency of 55% in a photonic crystal slab framework. This fact opens the possibility of building essential stages for novel integrated opto-electronics, small-scale all-optical circuits and semiconductor device miniaturization.

- We designed optimized light coupling structures. These structures maximize the mode matching between two distinct photonic crystal waveguides that are joined by an abrupt transition step and avoid the acute back reflection at the input waveguide, a feature that is necessary for coupling near-zero dispersive light modes of photonic crystal waveguides and to devise tunable optical delay lines that benefit from the slow-light regime. With this regards, we show that the light coupling efficiency of these structures is near 100% along a bandwidth of 100 nm. Last but not least, these tapers are fully compact, namely, they consists only on a few periods of photonic crystals, while most

of the tapers presented so far make use of long adiabatic stages for covering a less abrupt step. In addition, we report on the extremely high efficiency of these structures in a photonic crystal waveguide slab using a 3D-finite element method approach.

- We proposed new grating coupler designs. By means of the inverse design method proposed in this thesis, we found that the coupling efficiency of non-uniform grating couplers can outmatch custom periodic designs. Specifically, we showed a grating coupler structure with a peak coupling efficiency of 69% and a 1 dB bandwidth close to 38 nm at 1.55 μm. Therefore, the coupling efficiency is larger than that for a standard short-length and uniform grating coupler and the wide bandwidth makes these gratings very promising for C-band applications. Moreover, the structures proposed in this work are fully compatible with conventional manufacturing processes as they prevent the formation of exotic geometries or shallow edges. Besides, if these gratings are shortened, then they still hold for a reliable coupling ratio with a minimal deviation in the C-band. In addition, our computational results showed that considering also the groove etching depth in the coupler design process, the coupling efficiency can be further boosted. This way, a maximum coupling efficiency of 78% can be achieved at 1.55 μm, for which the 1 dB bandwidth is about 40 nm.

- We designed a perfectly vertical grating coupler that drastically minimizes the back reflection of the TE polarized field and successes in coupling the impinging light to the silicon waveguide with an efficiency of 60% at 1.55 μm, i.e., twice the efficiency calculated for a periodic grating coupler. Nearly all grating couplers demonstrated to date require an angular detuning of the input/output fibres by a significant angle from normal incidence in order to eliminate undesired back-reflection and transmission problems. In such configurations, a vertical interfacing of the fiber-chip set-up would drastically reduce the coupling efficiency. However, this kind of grating couplers could be a key element to prevent the need of cleaving, dicing or polishing of fibres, allowing for timely in-line wafer testing.

- We demonstrated that a polarization beam splitter combined with a grating coupler device can be realized in a single compact optical structure. The polarization beam splitter proposed in this thesis comprises a non-uniform grating profile performed by 70 nm deep grooves in a standard 220 nm width silicon layer and supports simultaneous electric and magnetic field splitting in the C-band up an efficiency of 77% and 55%, for transversal electric and transversal magnetic polarization, respectively. The bandwidth (at 3 dB) raises to 80 nm and 50 nm, for the transversal electric and transversal magnetic polarizations, respectively, and offers an extinction ratio beyond 25 dB in a wide

wavelength range. Polarization beam splitters are essential for many applications, such as data storage, optical switching and routing in photonic integrated circuits and they are a key element for enabling advanced optical modulators.

- In the context of exotic photonic phenomena, the results presented in this thesis provided experimental evidence of topologically protected waveguiding in silicon. We worked on the rapidly emerging field of topological photonics for which materials still have a band gap, but they also present exotic edge states with unusual properties. In the photonic context, these edge states can be used to realize a fundamentally new class of electromagnetic wave-guides, which are able to transport light around sharp corners without backscattering. By performing a wavelength-dependent study, we demonstrated the robustness of waveguiding by a single topological defect in a silicon platform, as opposed to the discrete diffraction and beating by trivial modes. This demonstration of topologically protected guiding of light at telecommunication wavelengths in silicon provides new ideas for developing complementary metal-oxide-semiconductor compatible devices immune to backscattering and environmental alterations.

- We proposed and demonstrated for the first time that, in a system where topological and trivial defect modes coexist, it is possible to tune the configuration of the defect configuration to force a transition between a single topological defect and a compound trivial defect state. These results provide a new paradigm for topologically protected waveguiding in a complementary metal-oxide-semiconductor compatible platform and highlight the novel concept of isolating topological and trivial defect modes in the same system that can have important implications in topological physics and suggest similar phenomena in condensed matter systems and other physical systems—wherever topological and trivial states coexist.

Future research should pave the way to manufacture these devices and characterize their performance in a fully compact photonic integrated circuit. On the one hand, we believe that the inverse design technique used to design former topologies could also be applied to non-linear optical regimes, leading to more flexible and interesting electro-optical devices such as polarization switching devices and optical modulators, just to cite some.

The study of different grooved structures in grating coupler devices could also lead to new optical devices which allow to do an efficient wavelength selective splitting and routing withing a complementary metal-oxide-semiconductor platform.

Further, the demonstration of topologically protected guiding of light at telecommunication wavelengths in silicon provides new ideas for developing CMOS-compatible devices immune

to backscattering and environmental alterations. Likewise, among our future lines of work is studying the combined effects of topology and nonlinearity in these systems, exploring concepts similar to [313]. As a first approach to this topic, we started to study these effects in a sample made of in a Gallium Lanthanum Sulphide chalcogenide glass.

Publications in this thesis

Papers in peer-reviewed journals

- I. Andonegui, A. J. Garcia-Adeva, *The finite element method applied to the study of two dimensional photonic crystals and resonant cavities*, Optics Express, **21**, 4072–4092, (2013).
- I. Andonegui, I. Calvo, A. J. Garcia-Adeva, *Inverse design and topology optimization of novel photonic crystal broadband passive devices for photonic integrated circuits*, Applied Physics A, **115**, 433–438, (2014).
- A. Blanco-Redondo, I. Andonegui, M. J. Collins, G. Harari, Y. Lumer, M. C. Rechtsman, B. J. Eggleton, and M. Segev, *Topological Optical Waveguiding in Silicon and the Transition between Topological and Trivial Defect States*, Physical. Review. Letters, **116**, 163901, (2016).

Publications in International Conferences

Invited papers and oral presentations

- I. Andonegui, I. Calvo, A. Blanco, A. J. Garcia-Adeva, *Inverse design of novel nanophotonic structures*, 15th International Conference on Transparent Optical Networks (ICTON), Cartagena, Spain (2013).
- I. Andonegui, I. Calvo, A. J. Garcia-Adeva, *Towards silicon all-optical nanophotonic circuitry*, 16th International Conference on Transparent Optical Networks (ICTON), Graz, Austria (2014).
- I. Andonegui and A.J. Garcia Adeva, *Coupling light into photonic integrated circuits using non-periodic surfaces*, 17th International Conference on Transparent Optical Networks (ICTON), Budapest, Hungary (2015).
- I. Andonegui, A. Blanco-Redondo, M. J. Collins, G. Harari, Y. Lumer, M. C. Rechtsman, B. J. Eggleton, and M. Segev, *Topological optical waveguiding in SOI structures*, 18th

International Conference on Transparent Optical Networks (ICTON), Trento, Italy (2016).

Contributed paper and oral presentation

- I. Andonegui, Itziar Landa-Torres, Diana Manjarres and A. J. Garcia-Adeva, *Novel light coupling systems devised using a Harmony Search algorithm approach*, The 3rd International Conference on the Harmony Search Algorithm (ICHSA'17), Bilbao, (2017).

- A. Blanco-Redondo, I. Andonegui, M. J. Collins, G. Harari, Y. Lumer, M. C. Rechtsman, B. J. Eggleton, and M. Segev, *Observation of waveguiding by topological defects in silicon photonic platform*, Australian and New Zealand Conference on Optics and Photonics (ANZCOP), (2016).

- I. Andonegui, I. Calvo, A. J. Garcia-Adeva, *Advanced Photonic Crystal Structures for Nano-scale Photonic Integrated Circuitry*, Progress In Electromagnetics Research Symposium (PIERS), Stockholm, Sweden (2013).

- I. Andonegui, A. J. Garcia-Adeva, *Inverse design and topology optimization of novel photonic crystal broadband passive devices for photonic integrated circuits*. The 4th International Conference on Metamaterials, Photonic Crystals and Plasmonics (META), Sharja, United Arab Emirates (2013).

- A. Blanco, I. Andonegui, Joseba Zubia, *Optical buffer memories based on photonic crystals*. Micro and Nano- photonic materials and devices (MINAP), Trento, Italy (2011).

Posters

- I. Andonegui, A. J. Garcia-Adeva, *Inverse design of photonic cristal based photonic integrated circuits*, Silicon Photonics Summer School, Ghent, Belgium (2014).

- I Andonegui, A. Blanco, A. J. Garcia-Adeva, *Characterization of slow light regime in 2D photonic cristal waveguides*. Imagenano-Conference on Plasmonics Photonics and Magnetooptics, Bilbao, Spain (2011).

References

[1] N. W. Ashcroft and N. D. Mermin, *Solid state Physics*, Philadelphia: Saunders College, (1976).

[2] C. Kittel, *Introduction to solid state physics* Dunod, (1983).

[3] D. W. Prather, S. Shi, A. Sharkawy, J. Murakowsky and G. J. Schneider, *Photonic Crystals: Theory, Applications, and Fabrication* Wiley, New Jersey, (2009).

[4] J. J. Joannopoulos, R. D. Meade, J. N. Winn, *Photonic crystals: molding the flow of light* Princeton University Press, New Jersey, (1995).

[5] K. Sakoda, *Optical Properties of Photonic Crystals* Springer, Berlin, (2001).

[6] C. Lopez, *Material Aspects of Photonic Crystals*, Advanced Materials **15**, 1679-1704, (2003).

[7] E. Istrate and E. H. Sargent, *Photonic crystal heterostructures*, Reviews of Modern Physics, **78**, 455-481, (2006).

[8] Yu. A. Vlasov, M. A. Kaliteevski, and V. V. Nikolaev, *Different regimes of light localization in a disordered photonic crystal*, Phys. Rev. B, **60**, (1999).

[9] C. M. Soukoulis, *Photonic Crystals and Light Localization in the 21st Century*, Springer, (2012).

[10] T. Baba, *Slow light in photonic crystals*, Nature Photonics, **2**, 465–473, (2008).

[11] A. Blanco-Redondo, C. Martijn de Sterke,J.E. Sipe, Thomas F. Krauss,Benjamin J. Eggleton, Chad Husko, *Pure-quartic solitons*, Nature Communications, **7**, (2015).

[12] S. Boutami, B. Benbakir, J.-L. Leclercq, P. Viktorovitch, *Compact and polarization controlled* 1.55 μ*m vertical-cavity surface-emitting laser using single-layer photonic crystal mirror*, Applied Physics Letters, **91**, (2007).

[13] Onur Kilic, Michel Digonnet, Gordon Kino and Olav Solgaard, *External fibre Fabry–Perot acoustic sensor based on a photonic-crystal mirror*, Measurement Science and Technology, **18**, (2007).

[14] Dirk Englund, David Fattal, Edo Waks, Glenn Solomon, Bingyang Zhang, Toshihiro Nakaoka, Yasuhiko Arakawa, Yoshihisa Yamamoto, and Jelena Vučković, *Controlling the Spontaneous Emission Rate of Single Quantum Dots in a Two-Dimensional Photonic Crystal*,Phys. Rev. Lett., **95**, (2005).

[15] Peter Lodahl, A. Floris van Driel, Ivan S. Nikolaev, Arie Irman, Karin Overgaag, Daniël Vanmaekelbergh, Willem L. Vos, *Controlling the dynamics of spontaneous emission from quantum dots by photonic crystals*, Nature, **430**, 654–657 (2004).

[16] Shanhui Fan, Pierre R. Villeneuve, J. D. Joannopoulos, E. F. Schubert, *Controlling the dynamics of spontaneous emission from quantum dots by photonic crystals*, Phys. Rev. Lett., **78**, (1997).

[17] A. Blanco-Redondo, C. Husko, D. Eades, Y. Zhang, J. Li, T.F. Krauss, B.J. Eggleton, *Observation of soliton compression in silicon photonic crystals*, Nature Communications, **5**, (2014).

[18] M. Ebnali-Heidari, C. Monat, C. Grillet, and M. K. Moravvej-Farshi, *A proposal for enhancing four-wave mixing in slow light engineered photonic crystal waveguides and its application to optical refeneration*, Optics Express, **17**, 18340–18353, (2009).

[19] T. H. Nguyen et al., *Phase-Preserving Power Limiting Function Using InP on SoI Photonic Crystal Nanocavity*, IEEE Photonics Technology Letters, **26**, (2014).

[20] S. M. Lo, S. Hu, G. Gaur, Y. Kostoulas, S. M. Weiss and P, M. Fauchet, *Photonic Crystal microring resonator for label-free biosensing*, Optics Express, **25**,7046–7054, (2017).

[21] K. Saurav, S. Kumari and N. L. Thomas, *CMOS Fabricated Large Array of Free Standing Substrate-Less Photonic Crystal Cavities for Biosensing Applications*, IEEE Photonics Journal, **9**, (2017).

[22] J. Zhou et al, *Parabolic Tapered Coupled Two Photonic Crystal Nanobeam slot Cavities for High-FOM Biosensing*, IEEE Photonics Technology Letters, **29**, (2017).

[23] Q. Nirmal et al., *Light Trapping in Inverted Organic Photovoltaics With Nanoimprinted ZnO Photonic Crystals*, IEEE Journal of Photovoltaics, **7**, (2017).

[24] A. C. Arsenault et al., *From colour fingerprint to the control of photoluminiscence in elastic photonic crystals*, Nature Materials, **5**, 179–84, (2016).

[25] F. Priolo, T. Gregorkiewicz, M. Galli and T. F. Krauss, *Silicon nanostructures for photonics and photovoltaics*, Nature Nanotechnology, **9**, 19–32, (2013).

[26] S. G. Johnson, S. Fan, P. R. Villeneuve, J. D. Joannopoulos, L. A. Kolodziejski, *Guided modes in photonic crystal slabs*, Phys. Rev. B, **60**, (1999).

[27] Shanhui Fan, J. D. Joannopoulos, *Analysis of guided resonances in photonic crystal slabs*, Phys. Rev. B, **65**, (2002).

[28] P. Vukusic and J. R. Sambles, *Photonic structures in biology*, Nature, **424**, 852–855, (2003).

[29] P. Simonis and S. Berthier, *How Nature Produces Blue Color*, Photonic Crystals: Introduction, Applications and Theory, InTech, (2012).

[30] S. Berthier, *Iridiscences: the physical color of insects*, Springer New York, (2006).

[31] P. Exner, *Analysis of guided resonances in photonic crystal slabs*, Phys. Rev. Lett., **74**, (1995).

[32] H.-S. Cho and Paul R. Prucnal, *New formalism of the Kronig-Penney model with application to superlattices*, Phys. Rev. B, **36**, (1987).

[33] J. W. S. Rayleigh, *On the remarkable phenomenon of crystalline reflexion described by Prof. Stokes*, Phil. Mag, **26**, 256–265, (1888).

[34] D.N. Chigrin, A.V. Lavrinenko, D.A. Yarotsky, S.V. Gaponenko, *Observation of total omnidirectional reflection from a one-dimensional dielectric lattice*, Applied Physics A, **68**, 25–28, (1999).

[35] D.N. Chigrin, A.V. Lavrinenko, D.A. Yarotsky, S.V. Gaponenko, *All-dielectric one-dimensional periodic structures for total omnidirectional reflection and partial spontaneous emission control*, Journal of Lightwave Technology, **17**, (1999).

[36] R. Slavík, S. Doucet and S. LaRochelle, *High-Performance All-Fiber Fabry-Pérot Filters With Superimposed Chirped Bragg Gratings*, Journal of Lightwave Technology, **21**, (2003).

[37] A.A.M. Saleh, J. Stone, *Two-stage Fabry-Perot filters as demultiplexers in optical FDMA LANs*, Journal of Lightwave Technology, **7**, (1989).

[38] J. Sun et al., *A broadband antireflective coating based on a double-layer system containing mesoporous silica and nanoporous silica* , J. Mater. Chem. C, **3**, 7187–7194, (2015).

[39] W. W. Bewley, C. L. Felix, I. Vurgaftman, R. E. Bartolo, J. R. Lindle, and J. R. Meyer, *Mid-infrared photonic-crystal distributed-feedback laser with enhanced spectral purity and beam quality*, Applied Physics Letters, **79**, (2001).

[40] L.-D. Haret, T. Tanabe, E. Kuramochi, M. Notomi, *Extremely low power optical bistability in silicon demonstrated using 1D photonic crystal nanocavity*, Optics Express, **17**, 21108–21117, (2009).

[41] E. Yablonovitch, *Inhibited Spontaneous Emission in Solid-State Physics and Electronics*, Physical Review Letters, **17**, 2059–2062, (1987).

[42] S. John, *Strong localization of photons in certain disordered dielectric superlattices*, Physical Review Letters, **58**, 2486–2489, (1987).

[43] G. Franzo, A. Irrera, E. C. Moreira, M. Miritello, F. Iacona, D. Sanfilipo, G. Di Stefano, R. G. Fallica, F. Priolo, *Electroluminiscence of silicon nanocrystals in MOS structures*, Applied Physics A, **74**, 1–5, (2002).

[44] O. Painter, R. K. Lee A.Scherer A.Yariv J.D. O'Brien P.D. Dapkus I. Kim, *Two dimensional Photonic Band gap Defect Mode Laser*, Science, **284**, 1819–1821, (1999).

[45] L. Li, H. Lin, S. Qiao, Y. Zou, S. Danto, K. Richardson, J. D. Musgraves, N.Lu and J. Hu, *Integrated flexible chalcogenide glass photonic devices Nature Photonics*, Nature Photonics, **8**, 643–649, (2014).

[46] A. Faraon, I. Fushman, D. Englund, N. Stoltz, P. Petroff and J. Vuckovic, *Dipole induced transparency in waveguide coupled photonic crystal cavities*, Optics Express, **16**, 12154, (2008).

[47] A. Moroz, *Three-Dimensional Complete Photonic-Band-gap Structures in the Visible*, Physical Review Letters, **83**, (1999).

[48] A. Blanco, E. Chomski, S. Grabtchak, M. Ibisate, S. John, S. W. Leonard, C. Lopez, F. Meseguer, H. Miguez, J. P. Mondia, G. A. Ozin, O. Toader, H. M. van Driel, *Large-scale synthesis of a silicon photonic crystal with a complete three-dimensional bandgap near* 1.5 *micrometres*, Nature, **405**, 437–440, (2000).

[49] Angel J. Garcia-Adeva, *Band gap atlas for photonic crystals having the symmetry of the kagome and pyrochlore lattices*, New Journal of Physics, **8**, (2006).

[50] Angel J. Garcia-Adeva, *Band structure of photonic crystals with the symmetry of a pyrochlore lattice*, Physical Review B., **73**, (2006).

[51] A.-P. Hynninen, J. H. J. Thijssen, E. C. M. Vermolen, M. Dijkstra, A. van Blaaderen, *Self-assembly route for photonic crystals with a bandgap in the visible region*, Nature Materials, **73**, 202–205, (2007).

[52] M. Deubel, G. von Freymann, M. Wegener, S. Pereira, K. Busch, C. M. Soukoulis, *Direct laser writing of three-dimensional photonic-crystal templates for telecommunications*, Nature Materials, **3**, 444–447, (2004).

[53] J. R. Piper, S. Fan, *Total Absorption in a Graphene Monolayer in the Optical Regime by Critical Coupling with a Photonic Crystal Guided Resonance*, ACS Photonics, **1**, 347–353, (2014).

[54] A.-P. Hynninen, J. H. J. Thijssen, E. C. M. Vermolen, M. Dijkstra, A. van Blaaderen, *A super narrow band filter based on silicon 2D photonic crystal resonator and reflectors*, Optics Communications, **363**, 13–20, (2016).

[55] M. Y. Mahmoud, G. Bassou, A. Taalbi and Z. M. Checkround, *Optical channel drop filters based on photonic crystal ring resonators*, Optics Communications, **285**, 368–372, (2012).

[56] K. Hirose, Y. Liang, Y. Kurosawa, T. Sugiyama and S. Noda, *Watt-class high power, high beam-quality photonic crystal lasers*, Nature photonics, **8**, 406–411, (2014).

[57] Y. Cai, X. Chen, N. Li and Y. Wang, *Electrically punped photonic crystal laser constructed with organic semiconductor*, Lasers Physics, **27**, (2017).

[58] K. Ishizaki, M. Koumura, K. Suzuki, K. Gondaira and S. Noda, *Realization of three-dimensional guiding of photons in photonic crystals*, Nature Photonics **7**, 133–137, (2013).

[59] A. Chiappini, A. Piotrowska, M. Marciniak, M. Ferrari and D. Zonta, *Design and fabrication of mechanochromic photonic crystal as strain sensor*, Proceedings of SPIE-The International Society of Optical Engineering ISBN: 9781628415384, (2015).

[60] I. El-Kady, M.M. Reda Taha and M. F. Su, *Application of photonic crystals in submicron damage detection and quantification*, Appl. Phys. Lett., **88**, (2006).

[61] F. Tani, F. Köttig, D. Novoa, R. Keding, and P. St.J. Russell, *Effect of anti-crossings with cladding resonances on ultrafast nonlinear dynamics in gas-filled photonic crystal fibers*, Photonics Research, **6**, 84–88, (2018).

[62] P. St.J. Russell, *Photonic-Crystal Fibers*, Journal of Lightwave Technology, **24**, (2006).

[63] E. Yablonovitch, T. J. Gmitter, and K. M. Leung, *Photonic band structure: The face-centered-cubic case employing nonspherical atoms*, Physical Review Letters **67**, 2295-2299, (1991).

[64] S. G. Johnson and J. D. Joannopoulos, *Block-iterative frequency-domain methods for Maxwell's equations in a planewave basis*, Optics Express **8**, no. 3, 173-190 (2001), http://www.opticsexpress.org/abstract.cfm?URI=OPEX-8-3-173. See also http://ab-initio.mit.edu/wiki/index.php/MIT_Photonic_Bands.

[65] MPB on-line manual, http://ab-initio.mit.edu/wiki/index.php/MPB_manual.

[66] F. J. Garcia de Abajo, *Multiple scattering of radiation in clusters of dielectrics*, Physical Review B **60**, 6086-6102, (1999).

[67] CAvity Modelling FRamework software (CAMFR), http://camfr.sourceforge.net/.

[68] A. Taflove, *Computational Electrodynamics* (Artech House, Norwood, 1995).

[69] J. Jin, *The finite element method in electromagnetism*, (Wiley–IEEE press, New York, 2002).

[70] M. -C. Lin and R. -F. Jao, *Finite element analysis of photon density of states for two-dimensional photonic crystals with in-plane light propagation*, Optics Express **15**, 207 (2007).

[71] W. R. Frei and H. T. Johnson, *Finite-element analysis of disorder effects in photonic crystals*, Physical Review B **70**, 1651161–11 (2004).

[72] A. Sopaheluwakan, *Defect states and defect modes in 1D photonic crystals* (MSc Thesis, University of Twente, 2003).

[73] J. D. Jackson, *Classical Electrodynamics*, Wiley, New York, (1999).

[74] J. L. Garcia-Pomar and M. Nieto-Vesperinas, *Transmission study of prisms and slabs of lossy negative index media*, Optics Express **12**, 2081–2095, (2004).

[75] D. W. Prather, S. Shi, A. Sharkawy, J. Murakowski and G. J. Schneider, *Photonic Crystals: Theory, Applications, and Fabrication* Wiley, Pure and Applied Optics, (2009).

[76] K. Innoue, K. Ohtaka, *Photonic Crystals: Physics, Fabrication and Applications* Springer Optical Sciences, New York, (2004).

[77] A. Taflove and S. C. Hagness, *Computational Electrodynamics: The Finite-Difference Time-Domain Method*, 3rd ed. Boston: Artech House, (2005).

[78] J. Jin, *The Finite Element Method in Electromagnetics*, Wiley, New York (1993).

[79] K. S. Yee, *Numerical solution of initial boundary value problems involving MAxwell's equations*, IEEE Trans. Antennas and Propagation, **14**, 6934–6936, (1966).

[80] Elmer – Finite Element Software for Multiphysical Problems, http://www.csc.fi/elmer/index.phtml.

[81] The *unofficial* numerical electromagnetic code archives, http://www.si-list.org/swindex2.html.

[82] The EMAP Finite Element Modeling Codes, http://www.emclab.umr.edu/emap.html.

[83] Comsol multiphysics and Electromagnetics module, http://www.comsol.com.

[84] T. A. Davis, UMFPACK 4.6: Unsymmetric MultiFrontal sparse LU factorization package, http://www.cise.ufl.edu/research/sparse/umfpack/.

[85] S. G. Johnson and J. D. Joannopoulos, *Block-iterative frequency-domain methods for Maxwell's equations in a planewave basis*, Optics Express **8**, no. 3, 173-190 (2001), http://www.opticsexpress.org/abstract.cfm?URI=OPEX-8-3-173. See also http://ab-initio.mit.edu/wiki/index.php/MIT_Photonic_Bands.

[86] A. Taflove, *Computational Electrodynamics* (Artech House, Norwood, 1995).

[87] Edo Waks and Jelena Vuckovic, *Coupled mode theory for photonic crystal cavity-waveguide interaction*, Optics Express **13**, 5064-5073 (2005).

[88] C.Sibilia, T.M.Benson, M.Marciniak and T.Szoplik, *Photonic crystals: Physics and technology*, Springer, (2008).

[89] B. Temelkuran, Mehmet Bayindir, E. Ozbay, R. Biswas, M. M. Sigalas, G. Tuttle and K. M. Ho, *Photonic crystal-based resonant antenna with a very high directivity*, Journal of Applied Physics **87**, 603-605, (2000).

[90] T. Tanabe, M. Notomi, E. Kuramochi, A. Shinya and H. Taniyama, *Trapping and delaying photons for one nanosecond in an ultrasmall high-Q photonic-crystal nanocavity*, Nature Photonics **1**, 49-52, (2007).

[91] T. Baba, T. Kawasaki, H. Sasaki, J. Adachi and D. Mori, *Large delay-bandwidth product and tuning of slow light pulse in photonic crystal coupled waveguide*, Optics Express **16**, 9245-9253, (2008).

[92] D.-Sung Song, S.-Heon Kim, H.-Gyu Park, C.-Kyu Kim and Y.-Hee Lee, *Single-fundamental-mode photonic-crystal vertical-cavity surface-emitting lasers*, Applied Physics Letters **80**, 3901-3903, (2002).

[93] R. V.Nair and R. Vijaya, *Photonic crystal sensors:An overview*, Progress in Quantum Electronics **34**, 89-134, (2010).

[94] S.L. McCall, P.M. Platzman, R.Dalichaouch, David Smith and S.Schultz, *Microwave propagation in Two Dimensional Dielectric Lattices*, Physical Review Letters (67), 2017–2020, (1991).

[95] D. R. Smith, R. Dalichaouch, N. Kroll, S. Schultz, S. L. McCall and P. M. Platzman, *Photonic band structure and defects in one and two dimensions*, Journal of the Optical Society of America B **10**, 314-321, (1993).

[96] S.-Heon Kim and Y.-Hee Lee, *Symmetry Relations of Two-Dimensional Photonic Crystal Cavity Modes*, IEEE Journal of Quantum Electronics **39**, 1081-1085, (2003).

[97] S. J. Cox and David C. Dobson, *Maximizing Band Gaps In Two-Dimensional Photonic Crystals*, SIAM Journal of Appllied Mathematics **59**, 2108–2120, (1999).

[98] L.F. Shen, Z. Ye, and S. He, *Design of two-dimensional photonic crystals with large absolute band gaps using a genetic algorithm*, Physical Review B **68**, 035109-5, (2003).

[99] J.M. Geremia, J. Williams, and H. Mabuchi, *Inverse-problem approach to designing photonic crystals for cavity QED experiments*, Physical Review E **66**, 066606-12, (2002).

[100] R.P. Brent, *Algorithms for Minimization without Derivatives*, Prentice-Hall, (1973).

[101] P. Lalanne, C. Sauvan and J. Paul Hugonin, *Photon confinement in photonic crystal nanocavities*, Laser and Photonics Reviews **2**, 514-526, (2008).

[102] K. J. Vahala, *Optical Microcavities*, Nature **424**, 839-846, (2003).

[103] A. Taflove and S. C. Hagness, *Computational Electrodynamics: The Finite-Difference Time-Domain Method*, Artech, (2000).

[104] J. Berenger, *A perfectly matched layer for the absorption of electromagnetic waves*, Journal of Computational Physics **114**, 185-200, (1994).

[105] Z. Sacks, D. M. Kingsland, R. Lee, and J. F. Lee *A perfectly matched anisotropic absorber for use as an absorbing boundary condition*,IEEE Transactions on Antennas and Propagation **43**, 1460-1463, (1995).

[106] A. F. Oskooi, L. Zhang, Y. Avniel and S. G. Johnson, *The failure of perfectly matched layers and towards their redemption by adiabatic absorbers*, Optics Express **16**, 11376-17, (2008).

[107] A. F. Oskooi, D. Roundy, Mihai Ibanescu, Peter Bermel, J. D. Joannopoulos and S. G. Johnson, *MEEP: A flexible free-software package for electromagnetic simulations by the FDTD method*, Computer Physics Communications **181**, 687–702, (2010).

[108] V. A. Mandelshtam and H. S. Taylor, *Harmonic inversion of time signals*, Journal of Chemical Physics **107**, 6756-6769, (1997). Erratum, ibid. **109**, 4128 (1998).

[109] A. Petrov, *Slow light photonic crystal line-defect waveguides*, Cuvillier Verlag, (2007).

[110] S. Noda, K. Tomoda, N. Yamamoto, A. Chutinan, *Full Three-Dimensional Photonic Bandgap Crystals at Near-Infrared Wavelengths*, Science, **289**, 604–606, (2000).

[111] S.-Y. Lin, E. Chow, V. Hietala, P. R. Villeneuve, J. D. Joannopoulos, *Experimental Demonstration of Guiding and Bending of Electromagnetic Waves in a Photonic Crystal*, Science, **282**, 274–276, (1998).

[112] S.Shoji and S. Kawata, *Photofabrication of three-dimensional photonic crystals by multibeam laser interference into a photopolymerizable resin*, Appl. Physics Lett., **76**, 2668–2670, (2000).

[113] M. Loncar, D. Nedeljkovic, T. Doll, J. Vuckovic and A. Scherer, *Waveguiding in planar photonic crystals*, Appl. Phys. Lett., 77, 1937–1939, (2000).

[114] L. J. Stockmeyer, *The polynomial time hierarchy*, Theoretical Computer Science, **3**, 1–22, (1977).

[115] D. Nguyen and I. Pak, *Complexity of short Presburger arithmetic*, arXiv:1704.00249, (2017).

[116] E. Lalla-Ruiz, C. Expósito-Izquierdo, S. Taheripour and S. Voß, *An improved formulation for the multi-depot open vehicle routing problem*, OR Spectrum, **38**, 175–187, (2016).

[117] G. Hiermann, J. Puchinger, S. Ropke and R. F. Hartl, *The Electric Fleet Size and Mix Vehicle Routing Problem with Time Windows and Recharging Stations*, European Journal of Operational Research,**252**, 995–1018, (2016).

[118] F. Hernandez, M. Gendreau, J.-Yves Potvin, *Heuristics for tactical time slot management: a periodic vehicle routing problem view*, International Transactions in Operational Research, **252**, 1233–1252, (2017).

[119] K. Z. Gao, P. N. Suganthan, Q. K. PanT. J. Chua, T. X. Cai and C. S. Chong, *Discrete harmony search algorithm for flexible job shop scheduling problem with multiple objectives*, Journal of Intelligent Manufacturing, **27**, 363–374, (2016).

[120] J.Kuhpfahl and C.Bierwirth, *A study on local search neighborhoods for the job shop scheduling problem with total weighted tardiness objective*, Computers & Operations Research, **66**, 44–57, (2016).

[121] H. Kellerer, V. Kotov, M. Gabay, *An efficient algorithm for semi-online multiprocessor scheduling with given total processing time*, Computers & Operations Research, **18**, 623–630, (2015).

[122] B. Tripathy, S. Dash, S. K. Padhy, *Multiprocessor scheduling and neural network training methods using shuffled frog-leaping algorithm*, Computers & Industrial Engineering, **80**, 154–158, (2015).

[123] D. Chistikov and C. Haase, *On the complexity of quantified integer programming*, Proceedings of the 44th International Colloquium on Automata, Languages, and Programming (ICALP), (2017).

[124] R. E. Bryant, *On the complexity of VLSI implementations and graph representations of Boolean functions with application to integer multiplication*, IEEE Transactions on Computers, **40**, 205–213, (1991).

[125] K. Binder and D. Heermann, *Monte Carlo Simulation in Statistical Physics: An Introduction*, Springer Science & Business Media, (2013).

[126] H. Karimi, G. Rosenberg, H. G. Katzgraber, *Effective optimization using sample persistence: A case study on quantum annealers and various Monte Carlo optimization methods*, arXiv:1706.07826, (2017).

[127] R. Y. Rubinstein and D. P Kroese, *Simulation and the monte carlo method, 3rd ed.*,John Wiley & Sons, (2016).

[128] S. Kirkpatrick, C. D. Gelatt, M. P. Vecchi, *Optimization by simulated annealing*, Science, 220, 671–680, (1983).

[129] H. Szu, R. Hartley, *Fast simulated annealing*, Phys. Lett. A, 122, 157–162, (1987).

[130] M. Mahdavi, M. Fesanghary, E. Damangir, *An improved harmony search algorithm for solving optimization problems*, Applied Mathematics and Computation, 188, 1567–1579, (2007).

[131] I. Landa-Torres, S. Gil-Lopez, S. Salcedo-Sanz, J. Del Ser, J.A. Portilla-Figueras, *A novel grouping harmony search algorithm for the multiple-type access node location problem*, Expert Systems with Applications, **39**, 2012.

[132] K. Deb, A. Pratap, S. Agarwal and T. Meyarivan, *A fast and elitist multiobjective genetic algorithm: NSGA-II*, IEEE Transactions on Evolutionary Computation, **6**, 181–197, (2002).

[133] L. Ingber, *Simulated Annealing: Practice versus Theory*, Mathl. Comput. Modelling, **18**, 29–57, (1993)

[134] E. Lessard and J. Pouliot, *Inverse planning anatomy-based dose optimization for HDR-brachytherapy of the prostate using fast simulated annealing algorithm and dedicated objective function*, Medical Physics, **28**,773-779, (2001.)

[135] T. -Chieh Chen and Y. -Wen Chang, *Modern floorplanning based on Bsup -tree and fast simulated annealing*, IEEE Transactions on Computer-Aided Design of Integrated Circuits and Systems, **25**, (2006).

[136] D. I. Svergun, *Restoring Low Resolution Structure of Biological Macromolecules from Solution Scattering Using Simulated Annealing*, Biophysical Journal, **76**, 2879–2886, (1999).

[137] I. Pavlyukevich, *Levy Flights, Non-local Search and Simulated Annealing*, Journal of Computational Physics, **226**, 1830–1844, (2007).

[138] S. Webb, *Optimisation of conformal radiotherapy dose distribution by simulated annealing*, **34**, (1989).

[139] M. Duque-Anton, D. Kunz and B. Ruber, *Channel assignment for cellular radio using simulated annealing*, IEEE Transactions on Vehicular Technology, **42**, (1993).

[140] H. H. Szu, R. L. Hartley, *Nonconvex optimization by fast simulated annealing*, Proceedings of the IEEE, **75**, 1538–1540, (1987).

[141] G. S. Mageras, R. Mohan, *Application of fast simulated annealing to optimization of conformal radiation treatments*, Medical Physics, **20**, 639–648, (1993).

[142] T.-Chieh Chen and Y.-Wen Chang, *Modern fllorplanning based on B/sup */-tree and fast simulated annealing*, IEEE Transactions on computer-Aided Design of Integrated Circuits and Systems, **25**, 637–650, (2006).

[143] N. Ryden and C. Byong Park, *Fast simulated annealing inversion of surface waves on pavement using phase-velocity spectra*, Geophysics, **71**, 49–58, (2006).

[144] J. Puliot, D. Tremblay, J. Roy and S. Filice, *Optimization of permanent*^{125}*I prostate implants using fast silumated annealing*, International Journal of Radiation Oncology*Biology*Physics, **36**, 711–720, (1996).

[145] M. Betke and N. C. Makris, *Fast object recognition in noisy images using simulated annealing*, Proceedings of IEEE International Conference on Computer Vision, (1995).

[146] N. Metropolis, A. W. Rosenbluth, M. N. Rosenbluth and A. H. Teller, *Equation of State Calculations by Fast Computing Machines*, J. Chem. Phys., 21, 1087–1092, (1953).

[147] V. Cerny, *A thermodynamical approach to the travelling salesman problem: an efficient simulation algorithm*, Report, Bratislava, Czechoslovakia, Comenius University, (1982).

[148] M. Pincus, A Monte Carlo method for the approximate solutions of certain types of constrained optimization problems, Oper. res., **18**, 1225–1228, (1970).

[149] L. Ingber, *Adaptative Simulation Annealing (ASA), Lesons learned*, Invited paper to a special issue of the Polish Journal Control and Cybernetics on "Simulated Annealing Applied to Combinatorial Optimization", (1995).

[150] K. Binder and D. Stauffer, A simple introduction to Monte Carlo simulations and some specialized topics, Springer: Applications of the Monte Carlo Method in Statistical Physics, Berlin, (1985).

[151] B. Apolloni, C. Caravalho, D. De Falco, *Quantum stochastic optimization*, Stochastic Processes and their Applications, 33, 233-244, (1989).

[152] L. Ingber, *Adaptative simulated annealing (ASA): lessons learned*, *J. Control and Cybernetics*, 25, 33–54, (1996).

[153] Z. W. Geem, J. H. Kim, G. V. Loganathan, *A New Heuristic Optimization Algorithm: Harmony Search*, Simulation, 76, 60–68, (2001).

[154] R. Forsati, A. T. Haghighat, M. Mahdavi, *Harmony search based algorithms for bandwidth-delay-constrained least-cost multicast routing*, Computer Communications, 31, 2505–2519, (2008).

[155] Z. W. Geem, *Harmony Search in Water Pump Switching Problem*, Advances in Natural Computation, 3612, 751–760, (2005).

[156] R. Zhang, L. Hanzo, *Iterative Multi-user Detection and Channel Decoding for DS–CDMA Using Harmony Search*, IEEE Signal Processing Letters, 16, 917–920, (2009).

[157] C. A. Garcia Santiago, *Metaheuristic Approaches for Energy Efficient Production Optimization in Manufacturing Facilities*, PhD Thesis, Universidad de Alcala, (2015).

[158] I. Landa-Torres, S. Gil-Lopez, S. Salcedo-Sanz, J. Del Ser, J.A. Portilla-Figueras, *A novel grouping harmony search algorithm for the multiple-type access node location problem*, Expert Systems with Applications, 39, 5262–5270, (2012).

[159] A. M. Mohsen, A. T. Khader, D. Ramachandram, *An Optimization Algorithm Based on Harmony Search for RNA Secondary Structure Prediction*, Studies in Computational Intelligence, 270, 163–174, (2010).

[160] F. Glover and M. Laguna, *Tabu Search*, Handbook of Combinatorial Optimization, 2nd Ed. Springer, 3261–3362, (2013).

[161] Y. Hadas and O. E. Nahum, *Urban bus network of priority Lanes: a Combined Multi-objecive and Multi Criteria Approach*, Transport Policy, **52**, 186–196, (2016).

[162] J. H. Holland, *Adaptation in Natural and Artificial Systems*, University of Michigan Press, (1975).

[163] J. J. Grefenstete, *Genetic Algorithms and their applications*, Proceedings of the Second International Conference on Genetic Algorithms, Psychology Press, **21**, (2013)

[164] D. Dasgupta and Z.Michalewicz, *Evolutionary Algorithms in Engineering Applications*, Springer Science & Business Media, (2013).

[165] D. C. Mattfeld, *Evolutionary Search and the Job Shp: Investigations on Genetic Algorithms for Production Scheduling*, Springer Science & Business Media, (2013).

[166] Y. Yoon and Y.-Hyuk Kim, *An Efficient Genetic Algorithm for Maximum Coverage Deployment in Wireless Sensor Networks*, IEEE Transactions on Cybernetics, **43**, 1473–1483,(2013).

[167] H. Hejazi, I. Toloue, M. S. Jaafar and J. Noorzaei, *Optimization of Earthquake Energy Disipation System by Genetic Algorithm*, Computer-Aided Civil and Infrastructure Engineering, **28**, 796–810, (2013).

[168] J. E. Baker, *Reducing Bias and Inefficiency in the Selection Algorihtm*, Proceedings of the Second International Conference on Gentic Algorithms and their Application, Hillsdale, New Jersey, 14–21, (1987).

[169] Newcastle University Engineering Design Centre, online resource, www.edc.ncl.ac.uk/highlight/rhjanuary2007g02.php.

[170] J. del Ser, *Study and Development of Advanced Meta-Heuristic Approaches for Resource Allocation in Intelligent Communication Systems*, PhD thesis, Universidad de Alcala, (2013).

[171] A. Zhou, B.-Y. Qu, H. Li, S.-Z. Zhao, P. N. Suganthan and Q. Zhang, *Multiobjective evolutionary algorithms: A survey of the state of the art*, Swarms and Evolutinoary Computation, **1**, 32–49, (2011).

[172] D. A. Van Veldhuizen and G. B. Lamont, *Multiobjective evolutionary algorithms: Analyzing the State-of-the-Art*, Evolutionary Computation, **8**, 125–147, (2006).

[173] E. Zitzler, K. Deb and L. Thiele, *Comparison of Multiobjective Evolutionary Algorithms: Empirical Results*, Evolutionary Computation, **8**, 173–195, (2000).

[174] A. Abraham, L. Jain, R. Goldberg, *Evolutionary Multiobjective Optimization: Theoretical Advances and Applications*, Springer: Advanced Information and Knowledge Processing, (2005).

[175] A. Seshadri, *NSGA-II: A multi-objective optimization algorithm*, MAT-Lab Central, Implementierung, (2009).

[176] N. Srinivas and K. Deb, *Multiobjective Optimization Using Nondominated Sorting in Genetic Algorithms*, Evolutionary Computation, **2**, 221–248, (1994).

[177] H. G. Beyer and K. Deb, *On Self-Adaptative Features in Real-Parameter Evolutionary Algorithm* , IEEE Transactions on Evolutionary Computation, **5**, 250–270, (2001).

[178] K. Deb and R. B. Agarwal, *Simulated Binary Crossover for Continuous Search Space Complex Systems*, Complex Systems, **9**, 115–148, (1995).

[179] M. M. Raghuwanshi and O. G. Kakde, *SSurvey on multiobjective evolutionary and real coded genetic algorithms*, In Proceedigns of the 8th Asia Pacific Symposium on Intelligent and Evolutionary Systems, 150–161, (1994).

[180] A. Tarantola, *Inverse Problem Theory and MEthods for Model Parameter estimation*, The Society for Industrial and Applied Mathematics (SIAM), (2005).

[181] I. Andonegui and A. J. Garcia-Adeva, *Inverse Design and Topology Optimization of novel Photonic Crystal broadband Devices for Photonic Integrated Circuits*, Proceedings of META'13: The 4th International Conference on Metamaterials, Photonic Crystals and Plasmonics, Sharjah (UAE), (2013).

[182] I. Andonegui and A. J. Garcia-Adeva, *Designing integrated circuity in nanoscale photonic crystals*, SPI Newsroom Nanotechnology, DOI:10.1117/2 1201311.005035, (2013).

[183] I. Andonegui and A. J. Garcia-Adeva, *Inverse Design and Topology Optimization of novel Photonic Crystal broadband Devices for Photonic Integrated Circuits*, Applied Physics A, **115**, 433–438, (2014).

[184] I. Andonegui and A. J. Garcia-Adeva, *The Finite Element Method Applied to the Study of Two-Dimensional Photonic Crystals and Resonant Cavities*, Optics Express, **21**, 4072–4092, (2013).

[185] L. Wu, M. Mazilu, J.-F. Gallet, T. F. Krauss, A. Jugessur and R. M. De La Rue,*Planar photonic crystal polarization splitter*, Opt. Lett., **29**, 1620–1622, 2004.

[186] T. Liu, A. R. Zakharian, M. Fallahi, J. V. Moloney and M. Mansuripur, *Multimode Interference-Based Photonic Crystal Waveguide Power Splitter*, J. Lightw.Tech., **22**, 2842–2846, (2004).

[187] R. Wilson, T. J. Karle, I. Moerman and T. F. Krauss, *Efficient photonic crystal Y-junctions*, J. Opt. A: Pure Appl. Opt., **5**, 76–80, (2003).

[188] I. Park, H.-S. Lee, H.-J. Kim, K.-M. Moon, S.-G. Lee, B.-H. O, S.-G. Park and E.-H. Lee *Photonic crystal power-splitter based on directional coupling*, Opt. Express, **12**, 3599–3604, (2004).

[189] E. Chow, S. Y. Lin, J. R. Wendt, S. G. Johnson and J. D. Joannopoulos, *Quantitative analysis of bending efficiency in photonic-crystal waveguide bends at* $\lambda = 1.55\,\mu m$ *wavelengths*, Opt. Lett., **26**, 286–288, (2001).

[190] A. Mekis, J. C. Chen, I. Kurland, S. H. Fan, P. R. Villeneuve and J. D. Joannopoulos, *High transmission through sharp bends in photonic crystal waveguides*, Phys. Rev. Lett., **77**, 3787–3790, (1996).

[191] J. D. Joannopoulos, P. R. Villeneuve and S. Fan, *Photonic crystals:putting a new twist on light*, Nature, **386**, 143–149, (1997).

[192] A. Talneau, *Slow light modes for optical delay lines: 2D photonic crystal-based design structures, performances and challenges*, J. Opt., **12**, 1–7, (2010).

[193] A. Chutinan, M. Okano and S. Noda, *Wider bandwidth with high transmission through waveguide bends in two-dimensional photonic crystal slabs*, Appl. Phys. Lett., **80**, 1698–1700, (2002).

[194] K. Rauscher, D. Erni, J. Smajic and Ch. Hafner, *Improved Transmission for 60° Photonic Crystal Waveguide Bends*, Progress in Electromagnetic Research Symposium, Pisa, Italy, March 28 –31, (2004).

[195] A. Têtu, M. Kristensen, L. H. Frandsen, A. Harpøth, P. I. Borel, J. S. Jensen and O. Sigmund, *Broadband topology-optimized photonic crystal components for both TE and TM polarizations*, Opt. Express, **13**, 8606–8611, (2005).

[196] K. Miura and Y. Ohtera, *Reduction of Propagation and Bending Losses of heterostructured Photonic Crystal Waveguides by use of a high delta structure*, Opt. Lett., **28**, 734–736, (2003).

[197] S. Olivier, H. Benisty, C. Weisbuch, C. J. M. Smith, T. F. Krauss, R. Houdre, and U. Oesterle, *Resonant and non resonant transmission through waveguide bends in a planar photonic crystal*, Appl. Phys. Lett., **79**, 2514–2516, (2001).

[198] M. K. Moghaddam, M. M. Mirsalehi and Ar. R. Attari, *A* 60° *photonic crystal waveguide bend with improved transmission characteristics*, Optica Applicata, **39**, 307–317, (2009).

[199] J. S. Jensen, O. Sigmund, L. H. Frandsen, P. I. Borel, A. Harpøth and M. Kristensen, *Topology Design and Fabrication of an Efficient Double 90 Photonic Crystal Waveguide Bend*, IEEE Photonics Technology Letters, **17**, 1202–1204,(2005).

[200] M. Tokushima, *Lightwave propagation through a 120° sharply bent single-line-defect photonic crystal waveguide*, Appl. Phys. Lett., **76**, 952–954, (2000).

[201] Y. Zhang and B. Li, *Photonic crystal-based bending waveguides for optical interconnections*, Opt. Express, **14**, 5723–5732,(2006).

[202] T. Ma, A. B. Khanikaev, S. H. Mousavi and G. Shvets, *Topologically protected photonic transport in bianisotropic meta-waveguide*, eprint arXiv:1401.1276(2014).

[203] H. Ren, C. Jiang, W. Hu, M. Gao, J. Wang, *Photonic crystal channel drop filter with a wavelength-selective reflection micro-cavity*, Opt. Express, **14**, 2446–2458, (2006).

[204] A. Sharkawy, S. Shi and D. W. Prather, *Multichannel wavelength division multiplexing using photonic crystals*, Appl. Opt., **40**, 2247, (2001).

[205] K. B. Chung and S. W. Hong, *Wavelength demultiplexers based on the superprism phenomena in photonic crystals*, Appl. Phys. Lett., **81**, 1549–1551, (2002).

[206] A. Jugessur, L. Wu, A. Bakhtazad, A. Kirk, T. Krauss and R. De La Rue, *Compact and integrated 2-D photonic crystal super-prism filter-device for wavelength demultiplexing applications*, Opt. Express, **14**, 1632–1642, (2006).

[207] S. Fan, P. R. Villeneuve and J. D. Joannopoulos, *Channel Drop Tunneling through Localized States*, Phys. Rev. Lett., **80**, 960–963, (1998).

[208] B-. K. Min, J-. E. Kim and H. Y. Park, *Channel drop filters using resonant tunneling processes in two dimensional triangular lattice photonic crystals slabs*, Optics Communications, **237**, 59–63, (2004).

[209] A. Oskooi,A. Mutapcic,S. Noda,J. D. Joannopoulos, S. P. Boyd and S. G. Johnson, *Robust optimization of adiabatic tapers for coupling to slow-light photonic-crystal waveguides*, Opt. Express, **20**, 21558–21575, (2012).

[210] T. Baba, *Slow light in photonic crystals*, Nature Photonics, **2**, 465–473, (2008).

[211] C. Monat, B. Corcoran, C. Grillet, M. Ebnali-Heidari, D. J. Moss1, B. J. Eggleton, T. P. White, L. O'Faolain and T. F. Krauss*Slow Light Enhanced Nonlinear Effects in Silicon Photonic Crystal Waveguides*,Opt. Express, **4**, 2944–2953,(2009).

[212] M. Soljacic´, S. G. Johnson, S. Fan, M. Ibanescu, E. Ippen and J. D. Joannopoulos, *Photonic-crystal slow-light enhancement of nonlinear phase sensitivity*, J. Opt. Soc. Am. B, **19**, 2052–2059, (2002).

[213] S. Nishikawa, S. Lan, N. Ikeda, Y. Sugimoto, H. Ishikawa and K. Asakawa, *Optical characterization of photonic crystal delay lines based on one-dimensional coupled defects*, Optics Lett., **27**, 2079–2081, (2002).

[214] Y. Vlasov and S. McNab, *Coupling into the slow light mode in slab-type photonic crystal waveguides*, Opt. Letters **31**, 50–52, (2006).

[215] J. Hugonin, P. Lalanne, T. White and T. F. Krauss, *Coupling into slow-mode photonic crystal waveguides* Opt. Letters, **32**, 2638–2640, (2007).

[216] P. Sanchis, J. Marti, W. Bogaerts, P. Dumon, D. V. Thourhout and R. Baets, *Experimental results on adiabatic coupling into SOI photonic crystal coupled-cavity waveguides*, IEEE Photon. Tech. Letters **17**, 1199–1201, (2005).

[217] M. Palamaru and P. Lalanne, *Photonic crystal waveguides: out of plane losses and adiabatic modal conversion*, Appl. Phys. Letters, **78**, 1466–1468, (2001).

[218] T. Happ, M. Kamp and A. Forchel, *Photonic crystal tapers for ultracompact mode conversion*, Opt. Letters, **26**, 1102–1104, (2001).

[219] M. L. Povinelli, S. G. Johnson and J. D. Joannopoulos, *Slow-light, band-edge waveguides for tunable time delays*, Opt. Express, **13**, 7145–7159, (2005).

[220] A. Mutapcic, S. Boyd, A. Farjadpour, S. G. Johnson and Y. Avniel, *Robust design of slow-light tapers in periodic waveguides*, Engineering Optimization, **41**, 365–384, (2009).

[221] A. Håkansson, P. Sanchis, J. Sánchez-Dehesa, and J. Martí, *High-efficiency defect-based photonic-crystal tapers designed by a genetic algorithm*, J. Lightw. Tech., **23**, 3881–3888, (2005).

[222] P. Sanchis, P. Bienstman, B. Luyssaert, R. Baets and J. Marti, *Analysis of butt coupling in photonic crystals*, IEEE Journal of Quantum Electronics, **40**, 541–550, (2004).

[223] A. J. Talneau, P. Lalanne, U.S. Patent No. 7242837 B2, (2007).

[224] A. Blanco-Redondo, C. Husko, D. Eades, Y. Ahang, J. Li, T. F. Krauss and B. Eggleton, *Observation of soliton compression in silicon photonic crystals*, Nat. Comm., **5**, (2014).

[225] B. Corcoran, C. Monat, D. J. Moss, B. J. Eggleton, T. P. White, L. O'Faolain and T. F. Krauss, *Green light emission in silicon through slow light enhanced third-harmonic generation in photonic-crystal waveguides*, Nat. Photonics, **3**, 206–210 (2009).

[226] K. K. Lee, D. R. Lim, L. C. Kuimerling, J. Shin and F. Cerrina, *Fabrication of ultralow-loss Si/SiO2 waveguides by roughness reduction*, Optics Letters, **26**, 1888-1890, (2001).

[227] Y. A. Vlasov and S. J. McNab, *Losses in single-mode silicon-on-insulator strip waveguides and bends*, Optics Express, **12**, 1622-1631, (2004).

[228] L. Pavesi, David J. Lockwood, *Silicon Photonics*, Springer–Verlag, (2004).

[229] Y. Wang,*Grating Coupler Design Based on Silicon-On-Insulator*, PhD Thesis, The University of British Columbia, (2013).

[230] J. V. Galan,*Addressing Fiber-to-Chip Coupling Issues in Silicon Photonics*, PhD Thesis, Universidad Politecnica de Valencia, (2010).

[231] http://epixnet.org

[232] L. Chrostowsky, *Silicon Photonics Design: From Devices to Systems*, Cambridge University Press, (2015).

[233] C. Angulo Barrios, V. R. Almeida, *Electrooptic Modulation of Silicon-on-Insulator Submicrometer-Size Waveguide Devices*, Journal of Lightwave Technology, **21**, 2332-2339, (2003).

[234] T. Shi, C. Chen, Y. Shao, T. I. Su and D. Pan, *Silicon-based rib-waveguide modulator and fabrication method thereof*, U.S. Patent 9429776 (2016).

[235] B. E. A. Saleh and M. C. Teich, *Fundamentals of Photonics 2nd edition*, Wiley-Interscience, (2007).

[236] J. Cardenas, C. B. Poitras, J. T. Robinson, K. Preston, L. Chen, and M. Lipson, *Low loss etchless silicon photonic waveguides*, Optics Express, **17**, 4752–4757, (2009).

[237] http://www.imec-int.com

[238] http://www.leti-cea.com

[239] http://www.a-star.edu.sg

[240] A. Boudrioua, *Photonic Waveguides, Theory and Applications*, Wiley, (2006).

[241] T. Shoji, T. Tsuchizawa, T. Wanatabe, K. Tamada, H. Morita, *Low loss mode size converter from 0.3 um square Si wire waveguides to simglemode fibers*, Electron. Lett., **38**, 1669–1670, (2002).

[242] D. Tallaert, F. V. Laere, M. Ayre, W. Bogaerts, D. Van Thourhout, P. Bienstman, R. Baets, *Grating Couplers for Coupling between Optical Fibers and Nanophotoni Waveguides*, Japanese J. of Appl. Phys., **45**, 6071–6077, (2006).

[243] F. V Laere, W. Bogaerts, D. Taillaert, P. Dumon, D. V. Thourhout, R. Baets, *Grating couplers for coupling between optical fibers and nanophotonic waveguides* , J. Lightwave Tech., **25**, 151–156, (2007).

[244] Y. Wang, X. Wang, J. Flueckinger, H. Yun, W. Shi, R. Bojko, N. A. F. Jaeger, L. Chrostowski, *Focusing sub-wavelength grating couplers with low back reflections for rapid prototyping of silicon photonic circuits*, Opt. Express, **22**, 20652–20662, (2014).

[245] R. Topley, L. O'Faolain, D. J. Thomson, F. Y. Gardes, G. Z. Mashanovich, G. T. Reed, *Planar surface implanted diffractive grating couplers in SOI*, Opt. Express, **22**, 1077–1084, (2014).

[246] Erwin G. Loewen and Eugeny Popov, *Diffraction Gratings and Applications*, Marcel Dekker, (1997).

[247] D. Taillaert, *Grating couplers as Interface between Optical Fibres and Nanophotonic Waveguides*, PhD thesis, Universiteit Gent, (2005).

[248] A. Y. Piggott, J. Lu, T. M. Babinec, K. G. Lagoudakis, J. Petykiewicz, J. Vuckovic,*Inverse design and implementation of a wavelength demultiplexing grating coupler*, Sci. Rep., **4**, (2014).

[249] G. Roelkens, D. V. Thourhout, R. Baets, *High efficiency grating coupler between silicon-on-insulator waveguides and perfectly vertical optical fibers*, Opt. Lett., **32**, 1495–1497, (2007).

[250] G. Roelkens, D. Vermeulen, D. V. Thourhout, R. Baets, *High-efficiency fiber-to-chip grating couplers realized using an advanced CMOS-compatible Silicon-On-Insulator platform* , Opt. Express, **17**, 18278–18283, (2010).

[251] J. Covey, R. T. Chen, *Efficient perfectly vertical fiber-to-chip grating coupler for silicon horizontal multiple slot waveguides*, Opt. Express, **21**, 10886–10896, (2013).

[252] S. Wang, Y. Hong, Y. Zhu, J. Chen, S. Gao, X. Cai, Y. Shi and L. Liu, *Compact high-efficiency perfectly-vertical grating coupler on silicon at O-band*, Opt. Express, **25**, 22032–22037, (2017).

[253] B. Wang, J. Jiang and G. P. Nordin, *Embedded slanted grating for vertical coupling between fibers and silicon-on-insulator planar waveguides*, IEEE Photonics Technology Letters, **17**, (2005).

[254] L. Dai, M. Da, Y. Xu, M. Lu, X. Liu and Y. Chen, *Highly efficient and perfectly vertical chip-to-fiber dual layer grating coupler*, Optics Express, **23**, 1691–1698, (2015).

[255] G. Roelkens, D. V. Thourhout, R. Baets, *High efficiency grating coupler between silicon-on-insulator waveguides and perfectly vertical optical fibers*, Opt. Lett., **32**, 1495–1497, (2007).

[256] F. B. Laere, G. Roelkens, M. Ayre, J. Schrauwen, D. Tallaiert, D. V. Thourout, T. F. Krauss and R. Baets, *Compact and highly efficient grating couplers between optical fiber and nanophotonic waveguides*, J. Lightwave Technology, **25**, 151–156, (2007).

[257] R. K. Kostuk, T. Kim, G. Campbell, C. W. Han, *Diffraction optic polarization sensing element for magneto-optic storage heads*, Optics Lett., **19**, 1257, (1994).

[258] A. Hakansson et al., *Silicon CMOS Photonic Platform for Enabling High-Speed DQPSK Transceivers*, Proceedings of ICTON, (2013).

[259] J. Feng, Z. Zhou, *Polarization beam splitter using binary blazed grating coupler*, Optics Lett., **32**, 1162–1164, (2007).

[260] I. Kiyat, A. Aydinli, N. Dagli, *A Compact Silicon-on-Insulator Polarization Splitter*, IEEE Photonics Technology Letters, **17**, 100–102, (2005).

[261] A. Miliou, R. Srivastava, and R. V. Ramaswamy, *A 1.3-μm directional coupler polarization splitter by ion exchange*, J. Lightw. Technol., **11**, 120–225, (1993).

[262] K. Okamoto, M. Doi, T. Irita, Y. Nakano, and K. Tada, *Fabrication of TE/TM mode splitter using completely buried GaAs/GaAlAs waveguide*, Jpn. J. Appl. Phys., **34**, 114–115, (1990).

[263] P.-K. Wei and W.-S. Wang, *A TE-TM mode splitter on lithium niobate using Ti, Ni, and MgO diffusions*, IEEE Photon. Technol. Lett., **6**, 245–248, (1994).

[264] C. Pu, Z. Zhu, and Y.-H. Lo, *Surface micromachined integrated optic polarization beam splitter*, IEEE Photon. Technol. Lett., **10**, 988–990, (1998).

[265] R. C. Tyan, A. A. Sakevar, H. P. Chou, C. C. Cheng, A. Scherer, P. C. Sun, F. Xu and Y. Fainman,, *Design, fabrication and characterization of form-birefrigent multilayer polarization beam splitter*, J. Opt. Soc. Am. A, **14**, 1627–1636, (1997).

[266] K. Tan, Y. Huang, G.-Q. Lo, C. Lee, C. Yu, *Three-dimensional polarization splitter and rotator based on multi-layer Si_3N_4-onSOI platform*, International Conference on Optical MEMs and Nanophotonics, Singapore, (2016).

[267] D. Taillaert et al.,*A compact two dimensional grating coupler used as a polarization splitter*, Photonics Technology Letters, **15**, 1249–1251, (2003).

[268] M. I. Shalaev, S. Desnavi, W. Walasik and N. M Litchinitser, *Reconfigurable topological photonic crystal*, New Journal of Physics, **20**,(2018).

[269] X. Ni, D. Smirnova, A. Poddubny, D. Leykam, Y. Chong, and A. B. Khanikaev, *PT phase transitions of edge states at PT symmetric interfaces in non-Hermitian topological insulators*, Physical Review B, textbf98, 165129, (2018).

[270] J. A. Asboth L. Oroszlany and A. Palyi, *A Short Course on Topological Insulators: Band Structure and Edge States in One and Two Dimensions*, Springer, Lecture Notes in Physics 919, (2015).

[271] D. R. Yennie, *Integral Quantum Hall Effect for Nonspecialists*, Rev. Mod. Phys.,**59**, 781–824, (1987).

[272] K. Klizing, *25 Years of Quantum Hall Effect (QHE) A Personal View on the Discovery, Physics and Applications of this Quantum Effect*, Progress in Mathematical Physics, **45**, 1–21, (2005).

[273] M. Z. Hasan and C. L. Kane, *Colloquium: Topolological insulators*, Reviews of Modern Physics, **82**, 781–824, (1987).

[274] D. Tong, *Lectures on Quantum Hall Effect*, arXiv: 1606.06687, (2016).

[275] F. Haldane and S. Raghu, *Possible Realization of Directional Optical Waveguies in Photonic Crystals with Broken Time-Reversal Symmetry*, Physical Review Letters, **100**, (2008).

[276] S. Raghu and F. Haldane, *Analogous of Quantum Hall Effect Edge States in Photonic Crystals*, Physical Review A, **78**, (2008).

[277] Z. Wang, Y. Chong, J. D. Joannopoulos and M. Soljacic, *Observation of unidirictional Backscattering-Immune Topological Electromagnetic States*, Nature, **7**, 1001–1006, (2009).

[278] R. O. Umucalilar and I. Carusotto, *Artificial Gauge Field for Photons in Coupled Cavity Arrays*, Phys. Rev. A, **84**, 043804, (2011).

[279] M. Hafezi, E. A. Demler, M. D. Lukin, and J. M. Taylor, *Robust Optical Delay Lines via Topological Protection*, Nature Phys., **7**, 907, (2011).

[280] K. Fang, Z. Yu, and S. Fan, *Realizing effective magnetic field for photons by controlling the phase of dynamic modulation*, Nature Phot, **6**, 782, (2012).

[281] X. Cheng, C. Jouvaud, X. Ni, H. Mousavi, A. Z. Genack and A. B. Khanikaev, *Robust reconfigurable electromagnetic pathways within a photonic topological insulator*, Nature Mater., DOI:10.1038NMat4573, (2016).

[282] Y. E. Kraus, Y. Lahini, Z. Ringel, M. Verbin, and O. Zilberberg, *Topological States and Adiabatic Pumping in Quasicrystals*, Phys. Rev. Lett., **109**, 106402, (2012).

[283] M. C. Rechtsman, J. M. Zeuner, Y. Plotnik, Y. Lumer, D. Podolsky, F. Dreisow, S. Nolte, M. Segev, and A. Szameit, *Strain-induced pseudomagnetic field and Landau levels in photonic structure*, Nature (London), **296**, 196, (2013).

[284] M. Hafezi, S. Mittal, J. Fan, A. Migdall, and J. M. Taylor, *Imaging Topological Edge States in Silicon*, Nature Phot, **7**, 1001, (2013).

[285] W. P. Su, J. R. Schrieffer, and A. J. Heeger, *Solitons in Polyacetylene*, Phys. Rev. Lett., **42**, 1698, (1979).

[286] N. Malkova, I. Hromada, X. Wang, G. Bryant, and Z. Chen, *Observation of optical Shockley-like surface states in photonic superlattices*, Opt. Lett., **34**, 1633–1635, (2009).

[287] J.M. Zeuner, M.C. Rechtsman, Y. Plotnik, Y. Lumer, S. Nolte, M.S. Rudner, M. Segev and A. Szameit, *Observation of a Topological Transition in the Bulk of a Non-Hermitian System*, Phys. Rev. Lett, **115**, 040402, (2015).

[288] C. Poli, M. Bellec, U. Kuhl, F. Montessagne, and H. Schomerus, *Selective enhancement of topologically induced interface states in a dielectric resonator chain*, Nature Comm., **6**, 7710, (2015).

[289] A. P. Slobozhanyuk, A.N. Poddubny, A. E. Miroshnichenko, P. A. Belov, and Y. S. Kivshar, *Subwavelength Topological Edge States in Optically Resonant Dielectric Structures*, Phys. Rev. Lett., **114**, 123901, (2015).

[290] D. D. Solnyshkov, A. V. Nalitov, and G. Malpuech, *Kibble-Zurek Mechanism in Topologically Nontrivial Zigzag Chains of Polariton Micropillars*, Phys. Rev. Lett., **116**, 046402, (2016).

[291] M. Verbin, O. Zilberberg, Y. E. Kraus, Y. Lahini, and Y. Silberberg, *Observation of Topological Phase Transitions in Photonic Quasicrystals*, Phys. Rev. Lett., **110**, 076403, (2013).

[292] M. Verbin, O. Zilberberg, Y. Lahini, Y. E. Kraus, and Y. Silberberg, *Topological pumping over a photonic Fibonacci quasicrystal*, Phys. Rev. B, **91**, 064201, (2015).

[293] The topological effects in quasicrystals are fundamentally different than those of the SSH dimer chain. Namely, the defect states embedded in the one-dimensional quasicrystal are not topological zero modes associated with the lattice. Rather, they are states that can be mapped to twodimensional quantum Hall systems, which are protected in the two-dimensional space. Those states are not protected in any way in one dimension, unlike the topological defect observed in this chapter (Figs. 2,4, and 5), which is topologically protected as an outgrowth of the SSH model.

[294] M. Minkov, *Numerical study and optimizaiton of photonic crystals*, PhD Thesis, Ecole Polytechnique Federale De Lausanne, (2016).

[295] L. Lu, J. D. Joannopulos and M. Soljacic, *Topological Photonics*, Nature Photonics, **8**, 821–829, (2014).

[296] C. L. Kane, *Topological Insulators*, Elsevier, (2013).

[297] C. L. Kane, *Topological Insulators: Dirac Equation in Condensed Matters*, Springer Series in Solid State Sciences, (2012).

[298] A. M. Turner and A. Vishwanath, *Topological Insulators*, Elsevier, (2013).

[299] B. A. Bernevig and T. L. Hughes, *Topological Insulators and Topological Superconductors*, Princetown University Press, (2013).

[300] J. Munkres, *Topology*, Pearson, 2nd ed., (2000).

[301] M. Nakahara, *Geommetry, Topology and Physics*, Graduate Student Series in Physics, Institute of Physics Publishing, Bristol 2nd ed., (2013).

[302] P. Delplace, D. Ullmo and G. Montanbaux, *The Zak phase and the existence of edge states in graphene*, Phys. Rev. B, **84**, 195452, (2011).

[303] J. Zak, *Berry's phase for energy bands in solids*, Phys. Rev. Lett., **62**, 2747, (1989).

[304] A. Blanco-Redondo, I. Andonegui, M. J. Collins, G. Harari, Y. Lumer, M. C. Rechtsman, B. J. Eggleton and M. Segev, *Topological optical waveguiding in silicon and the Transition between Topological and Trivial Defect States*, Phys. Rev. Lett., **116**, 163901, (2016).

[305] A. Blanco-Redondo, I. Andonegui, M. J. Collins, G. Harari, Y. Lumer, M. C. Rechtsman, B. J. Eggleton and M. Segev, *Erratum:Topological optical waveguiding in silicon and the Transition between Topological and Trivial Defect States*, Phys. Rev. Lett., **117**, 129901, (2016).

[306] Z. Wang Y. D. Chong, J. D. Joannopoulos, and M. Soljacic, *Reflection-Free Onw Way Edge Modes in a Gyromagnetic Photonic Crystal*, Phys. Rev. Lett., **100**, 013905, (2008).

[307] Y. L. Chen, J. G. Analytis, J.-H. Chu, Z. K. Liu, S.-K. Mo, X. L. Qi, H. J. Zhang, D. H. Lu, X. Dai, Z. Fang, S. C. Zhang, I. R. Fisher, Z. Hussain and Z.-X. Shen, *Experimental realization of a three-dimensional topological insulator,* Bi_2Te_3, Science, **325**, 178, (2009).

[308] A. S. Sørensen, E. Demler, and M. D. Lukin, *Fractional Quantum Hall states of Atoms in Optical Ĺattices*, Phys. Rev. Lett., **94**, 086803, (2005).

[309] A. L. Jones, *Coupling of Optical Fibers and Scattering in Fibers*, J. Opt. Soc. Am., **55**, 261, (1965).

[310] S. Somekh, E. Garmire, A. Yariv, H. L. Garvin, and R. G. Hunsperger, *Precise meassurement of coupling between optical waveguides*, Appl. Phys. Lett., **22**, 46, (1973).

[311] D. N. Christodoulides, F. Lederer, and Y. Silberberg, *Review article Discretizing light behaviour in linear and nonlinear waveguide lattices*, Nature, **424**, 817–823, (2003).

[312] F. Lederer, G. I. Stegeman,D. N. Christodoulides,G.Assanto, M. Segev, and Y. Silberberg, *Discrete Solitons in Optics*, Phys. Rep, **463**, 1–3, (2008).

[313] Y. Lumer, Y. Plotnik, M. C. Rechtsman, and M. Segev, *Self-Localized States in Photonic Topological Insulators*, Phys. Rev. Lett., **111**, 243905, (2013).